Charged particle beam acceleration and strong discharge currents' fields generation by laser : a study on laser-driven ion sources and beam transport suited for application in high-energy-density physics experiments

Michael Ehret

THÈSE EN COTUTELLE PRÉSENTÉE

POUR OBTENIR LE GRADE DE

DOCTEUR DE

L'UNIVERSITÉ DE BORDEAUX

ET DE L'UNIVERSITÉ TECHNIQUE DE DARMSTADT

ÉCOLE DOCTORALE Nº 209 À BORDEAUX

DÉPARTEMENT DE PHYSIQUE À DARMSTADT

SPÉCIALITÉ ASTROPHYSIQUE, PLASMAS, NUCLÉAIRE

Par Michael EHRET

Accélération laser de particules chargées et génération de forts champs associés à des courants de décharge induite par laser

Une étude sur les faisceaux d'ions issues de l'interaction laser-plasma et de leur transport vers l'application dans des expériences de physique à haute densité d'énergie

Sous la direction de Prof. Markus ROTH et de Prof. João SANTOS

Soutenue le 09/07/2021

Membres du jury :

M. CONSOLI, Fabrizio	Contract Researcher, ENEA (Italy)	Rapporteur
M. FLACCO, Alessandro	Assistant Professor, LOA /ENSTA (France)	Rapporteur
M. SCHRAMM, Ulrich	Professor, HZDR (Germany)	Rapporteur
M. ALBER, Gernot	Professor, TU-Darmstadt (Germany)	Examinateur, Président
M. ROTH, Markus	Professor, TU-Darmstadt (Germany)	Direction
M. SANTOS, João	Professor, U-Bordeaux (France)	Direction
Mme. HANNACHI, Fazia	Professor, U-Bordeaux (France)	Invitée
M. ROMAGNANI, Lorenzo	CNRS Researcher, LULI (France)	Invité

Charged particle beam acceleration and strong discharge currents' fields generation by laser – a study on laser-driven ion sources and beam transport suited for application in high-energy-density physics experiments

International collaborative doctoral thesis affiliated to Université de Bordeaux and Technische Universität Darmstadt, conducted at Laboratoire CELIA UMR5107

THÈSE EN COTUTELLE DE M.SC. MICHAEL EHRET PRÉSENTÉE POUR OBTENIR LE GRADE DE DOCTEUR DE L'UNIVERSITÉ DE BORDEAUX ET DE L'UNIVERSITÉ TECHNIQUE DE DARMSTADT, SOUTENUE PAR L'ÉCOLE DOCTORALE N° 209 EN SPÉCIALITÉ ASTROPHYSIQUE, PLASMAS, NUCLÉAIRE SUR BORDEAUX ET LE DÉPARTEMENT DE PHYSIQUE À DARMSTADT
Sous la direction de Prof. Markus ROTH et de Prof. João SANTOS, soutenue le 09/07/2021

Membres du jury / Disputationskomitee:
M. CONSOLI, Fabrizio – Contract Researcher, ENEA (Italy) – Rapporteur
M. FLACCO, Alessandro – Professor, LOA/ENSTA (France) – Rapporteur
M. SCHRAMM, Ulrich – Professor, HZDR (Germany) – Rapporteur
M. ALBER, Gernot – Professor, TU-Darmstadt (Germany) – Examinateur, président du jury
M. ROTH, Markus – Professor, TU-Darmstadt (Germany) – Direction
M. SANTOS, João – Professor, U-Bordeaux (France) – Direction
Mme. HANNACHI, Fazia – Professor, U-Bordeaux (France) – Invité
M. ROMAGNANI, Lorenzo – CNRS Researcher, LULI (France) – Invité

Zur Erlangung des Grades eines Doktors der Naturwissenschaften (Dr. rer. nat.)
Vorgelegte Dissertation von M.Sc. Michael Ehret aus Mannheim (Matrikelnummer: 1796818)
Tag der Einreichung: 27/05/2021, Tag der Prüfung: 09/07/2021

1. Gutachten: Dr. Fabrizio Consoli
2. Gutachten: Prof. Alessandro Flacco
3. Gutachten: Prof. Ulrich Schramm
4. Gutachten: Prof. Gernot Alber
5. Gutachten: Prof. Markus Roth
6. Gutachten: Prof. João Santos
Darmstadt – D 17

TECHNISCHE UNIVERSITÄT DARMSTADT
CELIA Université de BORDEAUX

Physics Department
AG M. Roth and
Groupe PETRUX

Charged particle beam acceleration and strong discharge currents' fields generation by laser – a study on laser-driven ion sources and beam transport suited for application in high-energy-density physics experiments
International collaborative doctoral thesis affiliated to Université de Bordeaux and Technische Universität Darmstadt, conducted at Laboratoire CELIA UMR5107

Submitted doctoral thesis by M.Sc. Michael Ehret
(Student ID: 1796818)

1. Review: Dr. Fabrizio Consoli
2. Review: Prof. Alessandro Flacco
3. Review: Prof. Ulrich Schramm
4. Review: Prof. Gernot Alber
5. Review: Prof. Markus Roth
6. Review: Prof. João Santos

Date of submission: 27/05/2021
Date of thesis defense: 09/07/2021

Darmstadt – D 17

La chance ne sourit qu’aux esprits bien préparés. — Louis Pasteur

Charged particle beam acceleration and strong discharge currents' fields generation by laser – a study on laser-driven ion sources and beam transport suited for application in high-energy-density physics experiments

International collaborative doctoral thesis affiliated to Université de Bordeaux and Technische Universität Darmstadt, conducted at Laboratoire CELIA UMR5107

Approved dissertation by Michael Ehret from Mannheim

1. Review: Dr. Fabrizio Consoli
2. Review: Prof. Alessandro Flacco
3. Review: Prof. Ulrich Schramm
4. Review: Prof. Gernot Alber
5. Review: Prof. Markus Roth
6. Review: Prof. João Santos

Date of submission: 27/05/2021
Date of disputation: 09/07/2021

Darmstadt – D17

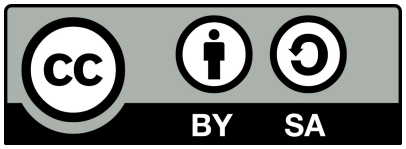

Hiermit versichere ich, Michael Ehret, die vorliegende Dissertation ohne Hilfe Dritter und nur mit den angegebenen Quellen und Hilfsmitteln angefertigt zu haben. Alle Stellen, die Quellen entnommen wurden, sind als solche kenntlich gemacht worden. Diese Arbeit hat in gleicher oder ähnlicher Form noch keiner Prüfungsbehörde vorgelegen.

Mir ist bekannt, dass im Fall eines Plagiats (§ 38 Abs. 2 APB) ein Täuschungsversuch vorliegt, der dazu führt, dass die Arbeit mit 5,0 bewertet und damit ein Prüfungsversuch verbraucht wird. Abschlussarbeiten dürfen nur einmal wiederholt werden.

Bei der abgegebenen Thesis stimmen die schriftliche und die zur Archivierung eingereichte elektronische Fassung überein.

Datum: Unterschrift:

Title – Titel – Titre

Charged particle beam acceleration and strong discharge currents' fields generation by laser – a study on laser-driven ion sources and beam transport suited for application in high-energy-density physics experiments

Lasergestützte Beschleunigung von geladenen Teilchenstrahlen und Felderzeugung durch starke Entladungsströme – eine Studie zu Ionenquellen und Strahltransportelementen geeignet für die Anwendung in Hochenergiedichtephysikexperimenten

Accélération laser de particules chargées et génération de forts champs associés à des courants de décharge induite par laser – une étude sur les faisceaux d'ions issues de l'interaction laser-plasma et de leur transport vers l'application dans des expériences de physique à haute densité d'énergie

Home Institutions

Groupe PETRUX
Laboratoire CELIA (Centre Lasers Intenses et Applications)
Université de Bordeaux, CNRS, CEA, UMR 5107
43 Rue Pierre Noailles
33400 Talence
France

AG M. Roth
Institut für Kernphysik
Technische Universität Darmstadt
Schlossgartenstraße 9
64289 Darmstadt
Germany

Keywords – Stichworte – Mots clés

laser-plasma interaction; ion acceleration from near critical density; magnetic lenses; electromagnetic lenses; MV/m dicharge pulse; kA return current

Laser-Plasma-Wechselwirkung; Ionenbeschleunigung aus nahezu kritischer Dichte; magnetische Linsen; elektromagnetische Linsen; MV/m Entladungspuls; kA Rückstrom

intéraction laser-plasma; accélération d'ions dans des plasmas de densité quasi-critique; lentilles magnétiques; lentilles électromagnétiques; impulsions de décharge MV/m; courants de retour kA

Erklärungen laut Promotionsordnung

§8 Abs. 1 lit. c PromO

Ich versichere hiermit, dass die elektronische Version meiner Dissertation mit der schriftlichen Version übereinstimmt.

§8 Abs. 1 lit. d PromO

Ich versichere hiermit, dass zu einem vorherigen Zeitpunkt noch keine Promotion versucht wurde. In diesem Fall sind nähere Angaben über Zeitpunkt, Hochschule, Dissertationsthema und Ergebnis dieses Versuchs mitzuteilen.

§9 Abs. 1 PromO

Ich versichere hiermit, dass die vorliegende Dissertation selbstständig und nur unter Verwendung der angegebenen Quellen verfasst wurde.

§9 Abs. 2 PromO

Die Arbeit hat bisher noch nicht zu Prüfungszwecken gedient.

Darmstadt, 27/05/2021

M. Ehret

Preface – Vorwort – Préface

The present work was created during my work as a doctoral student in a binational project of two working groups, respectively in the departments of physics at the universities TU Darmstadt and Université de Bordeaux under the direction of Prof. Dr. Markus Roth and Prof. Dr. João Jorge Santos. The starting point for interest in the topic is my previous scientific work in the plasma physics working group at the Society for Heavy Ion Research in Darmstadt-Wixhausen, in the French national master's course Sciences de la Fusion and in the Laboratoire CELIA at the Université de Bordeaux. The work was directly funded by the German Academic Exchange Service for international work in the context of internships and doctorates, the French Embassy in Berlin for Franco-German cooperation and the French Ministry of the Interior with a full doctoral position. Parts of the work benefited indirectly from ongoing projects of the respective working groups from 2015 until 2021. I would like to thank Prof. Dr. Markus Roth and Prof. Dr. João Jorge Santos very much for the dedicated support of my work.

Die vorliegende Arbeit entstand während meiner Tätigkeit als Doktorand in einem binationalen Projekt zweier Arbeitsgruppen, jeweils in den Fachbereichen Physik der Universitäten TU-Darmstadt und Université de Bordeaux unter der Leitung von Herrn Prof. Dr. Markus Roth und Herrn Prof. Dr. João Jorge Santos. Den Außgangspunkt zu der behandelten Thematik bilden meine vorausgegangenen wissenschaftlichen Arbeiten in der Arbeitsgruppe Plasmaphysik an der Gesellschaft für Schwerionenforschung in Darmstadt-Wixhausen, im französischen nationalen Masterstudiengang Sciences de la Fusion und im Laboratoire CELIA der Université de Bordeaux. Die Arbeit wurde direkt gefördert durch Mittel des Deutschen Akademischen Austauschdienstes für internationale Arbeit im Rahmen von Praktika und Promotionen, der französischen Botschaft in Berlin für deutsch-französische Zusammenarbeit und dem französischen Innenministerium mit einer vollen Promotionsstelle. Teile der Arbeit profitierten indirekt von laufenden Projekten der jeweiligen Arbeitsgruppen von 2015 bis 2021. Herrn Prof. Dr. Markus Roth und Herrn Prof. Dr. João Jorge Santos danke ich sehr herzlich für die engagierte Betreuung meiner Arbeit.

Le présent travail a été créé lors de mon travail en doctorat dans un projet binational de deux groupes de travail, dans les départements de physique des universités TU Darmstadt et Université de Bordeaux sous la direction du Prof. Dr. Markus Roth et Prof. Dr. João Jorge Santos. Mes précédents travaux scientifiques au sein du groupe de travail Physique des plasmas de la Society for Heavy Ion Research à Darmstadt-Wixhausen, au Master national français en Sciences de la Fusion et au Laboratoire CELIA de l'Université de Bordeaux constituent le point de départ du sujet en discussion. Les travaux ont été directement financés par le service allemand d'échanges universitaires pour les travaux internationaux dans le cadre de stages et de doctorats, l'Ambassade de France à Berlin pour la coopération franco-allemande et le ministère français de l'Intérieur avec un doctorat à part entière. Certaines parties du travail ont bénéficié indirectement des projets en cours des groupes de travail respectifs entre 2015 et 2021. Je tiens à remercier chaleureusement Prof. Dr. Markus Roth et Prof. Dr. João Jorge Santos pour le soutien dévoué de mon travail.

Abstract

This work aims at both, the experimental benchmark of laser-driven ion acceleration from targets in the near-critical density regime and the exploration of laser-driven open-geometry platforms for spatial and spectral ion beam tailoring. Theoretically described mechanisms and dynamics predicted by numerical simulations are compared to novel experimental findings that are supported by new particle in cell simulations and heuristic models. Results comprise (i) demonstration of Helium ion acceleration from ultra-relativistic laser-driven near-critical density gas jet targets employing shock nozzles, (ii) further investigation of the driving mechanisms of charged particle beam lensing platforms in the quasi-static regime driven by ns-laser and in the transient regime driven by sub-ps laser, and (iii) studies of transport and tailoring of laser accelerated particle beams by EM fields and B-fields.

The Helium ion source shows broad spectra cut-off energies above 55 MeV, a regime suitable for isotope production in alpha-therapy. Hence, the destruction of nozzles in the violent experimental environment and the perspective to HRR operation underlines the need of mass producible nozzles with automatized nozzle exchange and vacuum systems able to maintain good vacuum levels.

Ns-laser driven magnetic lenses show current amplitudes in the same order of magnitude for the spontaneous B-fields of the plasma and the consumer loop, which favours the theoretical modelling of the platform as a plasma-diode power source. During the laser drive, space charge effects arise with the arrival of the laser-plasma in vicinity of the magnetic lens, representing a possible threat to efficient lensing of ion beams. A target geometry is presented that decreases space charge effects.

Short laser-pulse driven solid target discharge gives rise to the propagation of a pulsed potential guided by the target geometry along its surface. This work shows that EM discharge pulses emanating the interaction region are followed by a pulse discharge current from the ground, both transporting kA-range currents through the target rod. The observed pulsed current dynamics on timescales of tens of ps indicates the presence of a hot surface plasma. The temperature and electron density of the surface plasma are promising control parameters of the discharge pulse dispersion. The high branch of the dispersion relation is responsible for a group velocity different from the speed of light. Solutions on the low branch of the dispersion relation agree with modulations of the target potential in their spatial dimensions and temporal growth rate.

Experimental and numerical studies of short laser pulse driven platforms show their applicability to spectral shaping of ion beams, with a perspective to temporal compression of beams for cases where low energy parts of the spectrum get efficiently post-accelerated. Presented are the experimental study of a simple double-coil geometry and a numerical study of a helical coil target.

This work motivates junction of presented approaches for future experiments aiming at HRR laser accelerated high energy density ion beams for applications, notably medical isotope production, or fundamental research, ranging from studies on collective stopping effects, warm dense matter generation to an optimized particle injector for fast ignition.

Zusammenfassung

Diese Arbeit umfasst sowohl eine experimentelle Machbarkeitsstudie zur Laserionenbeschleunigung aus Materie im Bereich der nah-kritischen Dichte, als auch die Untersuchung von Mechanismen, Limitationen und Einsatzmöglichkeiten von lasergetriebenen elektrischen Strömen für eine räumliche und spektrale Formung von Ionenstrahlen. Vorhandene konzeptuelle und numerische theoretische Vorhersagen werden mit neuen experimentellen Befunden verglichen, und im Weiteren unterstützt durch neue PIC Simulationen und heuristische Modelle. Die Ergebnisse umfassen (I) eine Demonstration von Laserheliumionenbeschleunigung aus Gasen nah der kritischen Dichte durch ultrarelativistische Laserpulse unter Verwendung von Schockdüsen, (II) die weitere Ergründung der felderzeugenden Mechanismen in elektromagnetischen Linsen für geladenen Teilchenstrahlen, im sowohl quasi statischen Regime angetrieben durch ns Laser als auch im transienten Regime angetrieben durch sub-ps Laser, und (III) Studien zum Transport von laserbeschleunigten Ionenstrahlen durch elektromagnetische und magnetische Felder.

Die Heliumionenquelle zeight breite Spektren mit Maximalenergien über 55 MeV. Dieser Energiereich ist für die Isotopenproduktion im Rahmen der Alpha-Therapie geeignet. Die Zerstörung von Schockdüsen in der strapaziösen Versuchsumgebung und der Ausblick auf den Betrieb mit hoher Wiederholungsrate unterstreichen die Notwendigkeit von massenproduzierbaren Düsen mit automatisiertem Düsenaustausch und leistungsstarken Vakuumsystemen.

Linsenplattformen getrieben durch ns Laser zeigen eine vergleichbare Stromstärke im Plasma und der Verbraucherschleife, was die theoretische Modellierung der Plattform als Plasma-Dioden-Stromquelle am besten zu deuten vermag. Während der Bestrahlung mit dem Laser treten durch das expandierende Laserplasma in der Nähe der magnetischen Linse starke Raumladungseffekte auf, die einer effizienten Strahlführung von Ionen im Wege stehen. Es wird eine Geometrie der Plattform vorgestellt, die Raumladungseffekte verringert.

Die Entladung von Festörpern durch kurze Laserpulse führt zu einer gepulsten Ausbreitung des elektrischen Potentials entlang der Oberfläche. Diese Arbeit zeigt, dass ein Impulsendladungsstrom ausgehend von der Erdung auf diesen elektromagnetischen Endladungsimpuls folgt. Beide tragen Ströme im kA-Bereich. Experimentelle Beobachtungen der gepulste Stromdynamik auf Zeitskalen von mehreren zehn ps deuten das Vorhandensein eines heißen Oberflächenplasmas an. Temperatur und Elektronendichte des Oberflächenplasmas sind vielversprechende Kontrollparameter für die Endladungsimpulsdispersion. Der obere Zweig der Dispersionsrelation ist für eine von der Lichtgeschwindigkeit verschiedenen Gruppengeschwindigkeit verantwortlich. Lösungen auf dem unteren Zweig stimmen mit Modulationen des Potentials in räumlicher Dimension und zeitlicher Wachstumsrate überein.

Experimentelle und numerische Studien der durch kurze Laserpulse angetrieben Plattformen zeigen deren Anwendbarkeit auf spektrale Ionenstahlformung, insbesondere die Realisierbarkeit von zeitlicher Kompression durch die effiziente Nachbeschleunigung von niederenergetischen Teilen des Spektrums. Die experimentelle Untersuchung einer einfachen Doppelspulengeometrie und die numerische Untersuchung einer Helixspule werden präsentiert.

Diese Arbeit motiviert die Verbindung der vorgestellten Ansätze für zukünftige Experimente, die laserbeschleunigte Ionenstrahlen mit hoher Wiederholungsrate benötigen. Eine mögliche Anwendung ist die Herstellung von Isotopen und mögliche Grundlagenforschung reicht von Studien zu kollektiven Effekten beim Energieverlust von Teilchen in Materie über die Erzeugung warmer dichter Materie bis hin zu einer optimierten Zündpartikelquelle für Fusionsexperimente.

Résumé

Ce travail comprend à la fois une étude de faisabilité expérimentale sur l'accélération des ions par laser à partir de la matière dans le domaine de la densité proche critique, ainsi que l'étude de la source, des limites et de l'utilité des courants électriques générés par laser pour la mise en forme spatiale et spectrale des faiseaux d'ions. Les prédictions théoriques conceptuelles et numériques existantes sont comparées à de nouvelles découvertes expérimentales, et soutenues par de nouvelles simulations PIC et des modèles heuristiques. Les résultats comprennent (I) une démonstration de l'accélération des ions hélium par un laser ultrarelativiste à partir des cibles gazeuses proches de la densité critique à l'aide de buses de choc, (II) une exploration plus approfondie des mécanismes générateurs de champ dans les lentilles électromagnétiques applicable aux faisceaux de particules chargées, à la fois dans un régime quasi-statique piloté par des lasers ns et également en régime transitoire piloté par des lasers sub-ps, et (III) études sur le transport de faisceaux d'ions accélérés par laser dans des champs électromagnétiques et magnétiques.

La source d'ions hélium génère des spectres larges avec des énergies maximales de 55 MeV. Cette gamme d'énergie est adaptée à la production d'isotopes dans le cadre de la thérapie alpha. La destruction des buses de choc dans l'environnement experimentale violente et la perspective d'un fonctionnement avec un taux de répétition élevé soulignent le besoin de buses fabriqué par une production de masse avec échange de buses automatisé et de puissants systèmes de vide.

Les plates-formes de lentilles electromagnetiques pilotées par des lasers ns montrent une intensité de courant comparable dans le plasma et la boucle consommateur, ce que la modélisation théorique de la plate-forme en tant que diode plasma peut le mieux interpréter. Pendant l'irradiation avec le laser, le plasma en expansion crée de forts effets de charge d'espace au voisinage de la lentille magnétique, qui font obstacle à un guidage efficace des faisceaux d'ions par une telle lentille. Une géométrie de la plate-forme est présentée qui réduit les effets de charge d'espace.

La décharge de solides par de courtes impulsions laser conduit à une propagation pulsée du potentiel électrique le long de la surface. Ce travail montre qu'un courant de décharge pulsé originaire de la terre suit cette impulsion de décharge électromagnétique. Les deux transportent des courants dans la gamme de kA. Des observations expérimentales de la dynamique d'impulsion de décharge pendant plusieurs dizaines de ps indiquent la présence d'un plasma de surface chaude. La température et la densité électronique du plasma de surface sont des paramètres de contrôle prometteurs pour la dispersion des impulsions de décharge. La branche supérieure de la relation de dispersion est responsable d'une vitesse de groupe différente de la vitesse de la lumière. Les solutions sur la branche inférieure correspondent à des modulations observées du potentiel en dimension spatiale et en taux de croissance temporelle.

Des études expérimentales et numériques des plates-formes pilotées par de courtes impulsions laser montrent leur applicabilité à la mise en forme spectrale des faisceaux ioniques, en particulier la faisabilité de la compression temporelle grâce à la post-accélération efficace des parties à faible énergie du spectre. L'étude expérimentale d'une géométrie à double bobine et l'étude numérique d'une bobine hélicoïdale sont présentées.

Ce travail motive la connexion des approches présentées pour les expériences futures qui nécessitent des faisceaux d'ions accélérés par laser avec un taux de répétition élevé. Une application possible est la production d'isotopes et les recherches fondamentales possibles vont des études sur les effets collectifs de la perte d'énergie des particules dans la matière et la génération de matière chaude et dense à une source de particules optimisée pour d'allumage dans des expériences de fusion.

Contents

Acronyms

2D two dimensional

3D three dimensional

Al Aluminium

ASE Amplified Spontaneous Emission (of light)

Au Gold

B-dot-probe inductive magnetic field probe

B-field magnetic field

CH Hydrocarbon

CLPU Centro de Láseres Pulsados (Salamanca, Spain)

CMAM Centro de Micro-Análisis de Materiales (Madrid, Spain)

CPA Chirped Pulse Amplification

CR-39 Columbia Resin #39

CSA Collisionless Shock Acceleration

Cu Copper

CW Continuous Wave

DCE Direct Coulomb Explosion

E-field electric field

e.g. for example (*exempli gratia*)

EM electromagnetic

EMDP electromagnetic discharge pulse

EMP electromagnetic pulse

FFT Fast Fourier Transform

FWHM Full Width at Half Maximum

GEMP Giant Electro-Magnetic Pulses

GSI Helmholtz Centre for Heavy Ion Research (Wixhausen, Germany)

H Hydrogen

He Helium

HEDP High Energy Density Physics

HRR high repetition rate

ICF inertial confinement fusion

Kapton poly(pyromellitimide-1,4-diphenyl ether)

laser light amplification by stimulated emission of radiation (*commonly used as synonym for:* light amplified by stimulated emission of radiation)

LET Linear Energy Transfer

LIGHT Laser Ion Generation, Handling and Transport (collaboration)

LULI Laboratoire pour l'Utilisation des Lasers Intenses (Ecole Polytechnique, Palaiseau, France)

MAU Medical Accelerator Unit

MCF magnetic confinement fusion

Mylar biaxially-oriented polyethylene terephthalate

N Nitrogen

NIR near infrared (light)

OD optical density

OECD Organization for Economic Co-operation and Development

PAFIN Particle Field Interaction (Simulation Code)

PHELIX Petawatt High Energy Laser for Heavy Ion Experiments

PIC Particle in Cell (Simulations)

PiN Acceptor-Neutral-Donor (Semiconductor Layers)

PySTarT Pythonic Stopping and Track Analysis for Particle Detectors by Transport of Ions in Matter

RAW digitized record of measurement values

RCF Radio-Chromic Film

REB relativistic electron beam

REL Restricted Energy Loss

RF radio frequency

ROI region of interest

RPA Radiation Pressure Acceleration

Si Silicon

SRIM Stopping and Range of Ions in Matter (Simulation)

SSTD Solid State Track Detector

TCC Target Chamber Centre

TGG Terbium Gallium Garnet

Ti:Sa Titanium doped Sapphire Crystal

TNSA Target Normal Sheath Acceleration

ToF Time of Flight

TRIM Transport of Ions in Matter

UV ultra violet (light)

1 Motivation

The social and economic development of the last 200 years has led to an improvement in the biological living conditions for large parts of the world's population, and is therefore associated with population growth due to increased life expectancy, reduced child mortality, lower disease mortality and optimized productivity. The world population is prospected to reach $10 \cdot 10^9$ from today $8 \cdot 10^9$ for the period between 2055 and 2060 [DES09]. Expected is a decline towards zero net-growth only after 2100, then already having reached $11 \cdot 10^9$ persons alive. The growing population challenges availability of resources and foundation of social peace, demanding a sustainable form of economy and energy production.

On the contrary, the economic activities yield persistent anthropogenic destruction of Earth, marked by climate change [IPC14] and massive reduction in biological diversity [Bro+19]. This alteration of our biosphere is mainly caused by worldwide deforestation, animal husbandry and energy generation based on fossil fuels. The total energy consumption globally is steadily increasing. According to forecasts before the COVID19 pandemic, energy consumption in non-OECD countries was about to increase by almost 70% between 2018 and 2050 and in OECD countries by 15% [Adm], then stemming from proportionally more or less the same energy sources which means mostly from fossil resources. Most of the cumulative emissions from existing infrastructure are expected to come from the energy (55%) and heavy industry (26%) sectors [IEA20b]. Today's energy infrastructure alone, if it were to continue to operate as in the past, would cause a temperature increase of 1.65 °C [IEA20c].

The globalization of human activity was first framed at the end of the epoch of imperialist colonialism as planetization of problems in technology and science, as a leveling of culture and economy, but also as manifestation of globally equal human aspirations and longings, accompanied by the awareness of the finiteness of space on the planet [Jas32]. From this, roots of a world society have developed for several decades [Luh75; Luh98] through novel means of telecommunication, albeit without real democratic political institutionalization. The international awareness of problems and the collaborative development of solutions represent an excellent opportunity to shape the earth for future generations in such a way that they can achieve an improved quality of life and equal prosperity.

A recent international achievement is the Paris Agreement [COP15]. Its goal is to reach the global peaking of greenhouse gas emissions in the close future in order to to limit global warming to 1.5 °C. Even though past years do show a net increase of energy consumption, the ratio of energy consumption to human productivity decreases [IEA20c]. This improvement to lower energy intensity is partially due to warmer weather and changes in the economic interplay, but mostly due to technological enhancements and a shift towards sustainable energy sources.

The COVID19 pandemic is a threat to such policies aiming at climate-neutrality and sustainability of all human activity. The global economy is set to shrink by 6% in 2020 [Coz20] and economic growth falls by an estimated 4.6% [IEA20a], with approximately $300 \cdot 10^6$ jobs lost during the second quarter of the year. The energy market suffers a fall in electricity demand and the resulting reduced revenues in the private energy sector make it more difficult to finance optimization and innovation. Lower energy prices have extended

payback periods for key energy efficiency measures by 10% to 40% [IEA20a], making them less attractive than other investments. In total, global energy related investments are expected to shrink by 20% in 2020 [Coz20], as never before. That is reflected directly in a smaller improvement of energy intensity in 2020, declined to half the rate of previous years [IEA20a] and now below the level needed to achieve global climate and sustainability goals.

Overall reduced investments endanger major gird construction projects worldwide [Coz20]. The enhancement of grids is the backbone of energy supply based on renewable sources such as hydro power, bio-gases, solar-energy and wind-energy. Renewables depend on environmental factors and their efficient use requires a smart-grid that enables the fluid interplay between a supply by dynamically allocated sources and a stock-holding in enormous energy storage capacities. The only energy sources with growing demand and investment attractiveness since the pandemic have been renewable [IEA20c], but an absence of adapted grids will render it impossible to deliver produced energy.

The struggle of the private sector currently motivates multiple pandemic-related economic stimulus programs by governments and intergovernmental organizations, but the support for energy efficiency that is announced in policies as of October 2020 is several trillion Euros below potential investment opportunities identified in the IEA Sustainable Recovery Plan (SRP) [Coz20]. The SRP is an international proposal of measures that are necessary to meet the long-term energy and climate goals, with 2019 as the year of all-time peak emission.

The loss of nuclear capacity in the sector of load-based thermal power plants especially in the US and EU will further hinder climate mitigation activities. Nuclear fission power plants became politically discredited for catastrophic accidents, for example (*exempli gratia*, *e.g.*) related to mismanaged operation as in Chernobyl or natural catastrophes in Fukushima, and for the potentially destructive uncertain long-term implications of the nuclear fuel cycle, from mining to enrichment, fabrication and waste disposal [Coz20].

The profit maximization principle of the private sector, the absence of sufficient funds in government development programs and a withdrawal from the nuclear energy sector make a failure likely to achieve climate goals, even though the problems are precisely outlined and solutions are designed based on the actual technological readiness and market reality. Motivation for this work was to contribute to research on the pathway to a novel type of nuclear power plant. Fusion power plants may close the gap of early retired nuclear fission plants. Such power plants could operate load-based in existing conventional grid infrastructure and in proximity of energy intensive industry such as steel and Aluminium (Al) manufacturing. Their appearance will remove stress from the overall need of investment towards climate neutrality. The nuclear fusion approach further causes potentially less damage to the ecosystem than traditional nuclear fission.

In all nuclear power plants, a net output of energy is archived by an induced exothermic nuclear reaction. Energy is conserved in nuclear reactions and a release in form of meta-stable activation of products, high energy photons and kinetic energy of products is only possible if the net binding energy in reactants is lower than in products. The average binding energy per nucleon as function of the number of nucleons in a nucleus is shown in fig. 1.1. The binding energy denotes the minimum energy necessary to ionize an atom. ^{56}Fe has the highest binding energy, exothermic reactions for atoms of higher mass are due to nuclear fission, for atoms of lower mass due to nuclear fusion.

In the traditionally employed fission process, the nucleus of a heavy atom is split into two or more fragments. Current nuclear power reactors employ either ^{235}U or ^{239}Pu, projected so-called thorium reactors would make use of ^{233}U. The fission process has a wide probabilistic range of output channels other than typical spontaneous radioactivity. Elements that undergo neutron emitting fission, when triggered by collisions with thermal neutrons, are referred to as nuclear fuels. This characteristics allows nuclear fuels to deliver energy from self-sustaining chain reactions. The energy production can be controlled by controlling the neutron

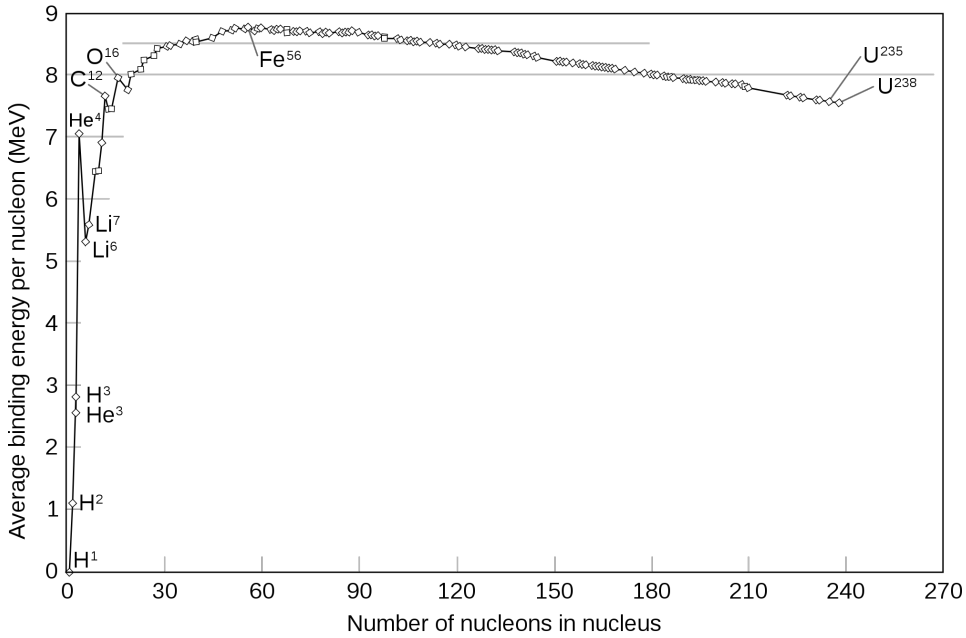

Figure 1.1: Graph of the nuclear binding energy of an atom as a function of its nucleons – energy is released from nuclear fission reactions above the maximum and from fusion reactions underneath. Figure taken from Wikimedia Commons [Fas08].

bombardement. The downside of the fission approach comprises the limited amount of nuclear fuel that is available on earth and the long half-life times of radioactive products.

Nuclear fusion is based on quantum tunneling through the Coulomb barrier between two close nuclei. Thermonuclear fuel can constitute widely available isotopes of light elements such as Hydrogen, Helium and Boron. The cross section σ_f for key thermonuclear fusion reactions is depicted with fig. 1.2, it increases above the kinetic energy needed to overcome the Coulomb barrier until it peaks typically for several ten to hundred keV of fuel temperature. This energies well above typical electron binding energies of several eV correspond to temperatures above $100 \cdot 10^6$ °C, pointing to the plasma state for the thermonuclear fuel. Fusion of Deuterium ^{2}H and Tritium ^{3}H has the highest cross sections for lowest centre-of-mass energies. The reactants must overcome a Coulomb barrier of 100 keV, then combining to unstable ^{5}He under liberation of 17.6 MeV energy. The produced nucleus directly ejects neutrons, thus transforming to stable alpha particles ^{4}He. The kinetic energy divides to 14.07 MeV for the neutron and 3.52 MeV for the alpha particle, following conservation of energy and momentum. Tritium does not appear naturally on earth due to its short half life time of about 10 years, but can be bread by bombardment of ^{6}Li with slow neutrons ^{1}n or ^{7}Li with fast neutrons. Thus, lithium moderation and reactor shielding seems handy to for a possible reactor design. Similarly neutron emitting is the fusion of pure Deuterium fuel. The Deuterium fusion reactions read

$$^2\mathrm{H} + {}^3\mathrm{H} \longrightarrow {}^5\mathrm{He} + 17.59\,\mathrm{MeV} \longrightarrow {}^4\mathrm{He}_{\,3.52\,\mathrm{MeV}} + {}^1\mathrm{n}_{\,14.07\,\mathrm{MeV}} \tag{1.1}$$

$$^2\mathrm{H} + {}^2\mathrm{H} \xrightarrow{50\,\%} {}^3\mathrm{He}_{\,820\,\mathrm{keV}} + {}^1\mathrm{n}_{\,2.45\,\mathrm{MeV}} \tag{1.2}$$

$$\xrightarrow{50\,\%} {}^3\mathrm{H}_{\,1.01\,\mathrm{MeV}} + {}^1\mathrm{H}_{\,3.02\,\mathrm{MeV}} \tag{1.3}$$

$$^2\mathrm{H} + {}^3\mathrm{He} \longrightarrow {}^4\mathrm{He}_{\,3.67\,\mathrm{MeV}} + {}^1\mathrm{H}_{\,14.68\,\mathrm{MeV}} \quad . \tag{1.4}$$

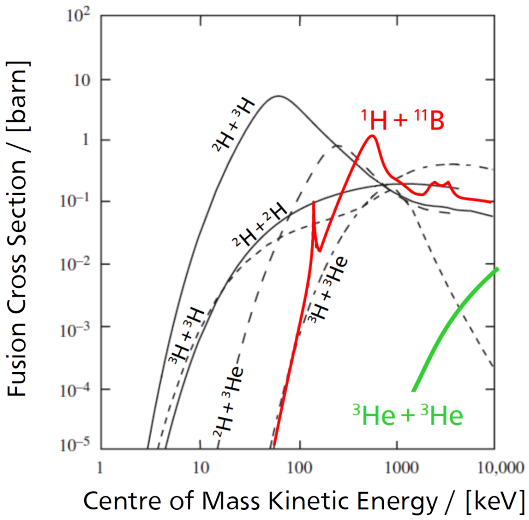

Figure 1.2: Fusion cross section in function of the centre of mass energy of the reactants in the nuclear fuel, data from [NS00] (black), [AV04] (red), [Eri19] (green).

The amount of energy released depends stronger on the exact fused isotopes than for fission processes. Reactants and products are not radioactive or of short half-life time. The burn of pure Deuterium fuel produces Tritium and proton ^{1}H projectiles, that can enter further fusion reactions with Deuterium. The ^{2}H - ^{2}H-fusion represents the beginning of the Deuterium cycle that sums up to

$$6 \times {}^{2}\mathrm{H} \longrightarrow 2 \times {}^{4}\mathrm{He} + 2 \times {}^{1}\mathrm{H} + 2 \times {}^{1}\mathrm{n} + 43.2\,\mathrm{MeV} \quad . \tag{1.5}$$

However, emission of high energy neutrons leads to nuclear reactions in the reactor casing which potentially produce radioactive isotopes, dangerous to the environment. Aneutronic fusion reactions besides ^{2}H - ^{3}He-fusion are

$$^{1}\mathrm{H} + {}^{11}\mathrm{B} \longrightarrow 3 \times {}^{4}\mathrm{He} + 8.68\,\mathrm{MeV} \tag{1.6}$$

$$^{3}\mathrm{He} + {}^{3}\mathrm{He} \longrightarrow {}^{4}\mathrm{He} + 2 \times {}^{1}\mathrm{H} + 12.86\,\mathrm{MeV} \quad . \tag{1.7}$$

Helions ^{3}He are not available in large quantity on earth, but may be available in future with mining on the moon [Kim+19] and planets in the solar system. For the fusion of protons and Boron ^{11}B the cross section peaks at ≈1 b a centre of mass energy of 500 keV, in reach for proton beams from available secondary sources or in a temperature range that is typical for hot dense plasma.

Fusion processes are naturally observed in stars. Nuclear fusion is also well known for its most destructive application in uncontrolled form as H-bomb, whereas power plants for controlled fusion are not shovel-ready. The state-of-art understanding in plasma physics already conducted to first large scale fusion projects in the domain of magnetic confinement fusion (MCF), such as JET, ITER and Wendelstein, yet not to working reactors. Even though the working principles and problems are known since the 1950s, the proximity of solutions to military applications renders an open collaborative international fusion project difficult. This work in experimental laser-plasma physics will explore two aspects in the field of inertial confinement fusion (ICF).

First, the generation of high energy density ion beams leads towards the so-called fast ignition approach, where irradiation with an ion beam kicks-off a rapid burn wave in an inertially confined fuel. Second, further explored ultra-strong magnetic fields are apt to be deployed in magneto-inertial fusion, where a sample implodes in a magnetic field meant to suppress inability growth and to confine hot charged particles.

Fusion science is not only relevant for the energy sector in terms of reactor design. Direct applications comprise propulsion engines for spacecraft needed for interplanetary activities, and experimental platforms for high energy density physics research towards a better understanding of astrophysical processes and processes in so called warm dense matter. This work can further contribute to innovation in many sectors, *e.g.* to improve the means of medicine for combating old and modern diseases. The state-of-art of ion beam acceleration and tailoring is compared to novel platforms archived by means of plasma physics, and widened towards new technologies and coupled applications.

With all possible improvements, it is nevertheless very important to note that no technological revolution allows disregarding far-reaching changes in individual and economic activities. The focus must be on minimizing consumption, recycling in closed-loop value creation networks, emphasizing education and creating profound individual solutions for all problems of the Anthropocene that have already arisen.

2 Introduction

After this short introduction of essential concepts follows an in-depth presentation of theoretical foundations to EM fields, particle beam acceleration by laser, the build-up of electrical potential on laser-driven targets, and interaction of ionizing radiation and matter. Thereafter mentioned are practical considerations and physics concepts for deployed experimental diagnostics. This first three sections provide the essential to support the following chapters with experimental results and data interpretation concerning three pillars of this work: (a) laser-ion acceleration from near-critical density gas-jet targets, (b) controlled B-fields for ion beam lensing and (c) EM lensing applied to ion beam sources. The thesis concludes with suggestions for future work and conclusions of achievements.

In a first step, the state-of-art in laser-ion acceleration and tailoring is briefly outlined. Secondly, applications for fusion and medicine are mentioned with their requirements.

2.1 Laser-Plasma Acceleration based Ion Beam Sources

Plasma is a state of matter that can be framed as an ionized gas. In plasma, collisions between particles are important for thermalization as in gases, but far more important are collective effects due to long distance action of EM fields and resonating waves. The charge separation in species of ionized atoms and free electrons gives rise to electric field (E-field) effects, and current dynamics induces B-fields. The term plasma was firstly defined by Langmuir [Lan28] in 1928. Since a plasma can be generated under supply of energy from the gaseous state, it is frequently referred to as the fourth state of matter. For ionization and the further supply with energy, photons issued by the light amplification by stimulated emission of radiation (laser) technique are used in this work.

Laser sources emit EM radiation of large coherence length that can be focused to high intensity into small volumes. Since the advent of the high-power short-pulse laser technology [SM85a], a focus in high-energy-density- (HED) and plasma-physics has been the development of high-energy, high-quality ion sources based on strong EM fields issuing from laser-plasma interaction [DNP12b; MBP13]. Motivation are many potential applications of such sources [Alb+20], including radiography of HED plasmas [Bor+04], time-resolved probing of transient EM phenomena [Rom+05], the fast ignition approach to laser-driven fusion [Rot+01a], isochoric heating of matter [Pat+03], exploratory experiments in nuclear physics [LMS03] and new tools of dose delivery for medical physics [Led+14; Spe+01]. The particular suitability of laser-driven ion beams for this applications is based in the high number of accelerated ions of typically $10 \cdot 10^6$ to $1 \cdot 10^{12}$ issued from a compact source.

Focus in research for laser-plasma based ion accelerators [DNP12a; Alb+20] lies on small-scale ultra-strong EM field structures with high energy coupling efficiency. The so-far best understood [RS16] laser-acceleration mechanism for ions is Target Normal Sheath Acceleration (TNSA) [Sna+00; Wil+01] from sharp cliffs in the

target material density. Here, ions are accelerated by space charge fields originating the dynamics of laser heated electrons. The efficiency of TNSA increases for increased absorption efficiency from laser energy to electron motion, as will be specified later in this chapter. An important aspect of TNSA is emission of ion beams with exponential spectrum in target normal direction. For transparent plasma, efficient laser absorption concentrated in a small volume can yield a depletion of the plasma electron population by relativistic electrons escaping the coulomb potential in vicinity of the plasma. Remaining ions experience a repulsive force resulting in a Direct Coulomb Explosion (DCE), accelerating a broad spectrum to all solid angles. If on the contrary absorption is minimized and the mass of an opaque target is small, targets can be pushed as piston in the scheme of Radiation Pressure Acceleration (RPA). Other acceleration mechanisms deal with advanced targetry, of which this work discusses in detail the approach of ion acceleration from near-transparent gas targets aiming at the drive of a collisionless shock wave that reflects some counter-propagating ions in the plasma bulk to twice its velocity. A collisionless shock is not transported via Coulomb collisions but by the collective effects in a plasma, where the shock front length scale is smaller than the collisional mean free path of any plasma species. This mechanism is referred to as Collisionless Shock Acceleration (CSA), and has the advantage to produce quasi-mono-energetic spectra.

One acceleration event results in one short ion bunch, which can be called micro-bunch. Most applications rely on steady beam currents in macro-bunches, which are pulse trains of micro-bunches. The limiting factors for the generation of pulse trains are the repetition rate of the driving laser system and target exchange or regeneration [Pre+17]. The new generation of Titanium doped Sapphire Crystal (Ti:Sa) laser systems allows principally production of thousands of laser pulses per second, and systems allowing amplification to the petawatt (PW) level for tens of pulses per second now become operational all over the world. This puts emphasis on the importance of development of advanced targetry. Where TNSA is based on targets that require complex technological tweaks to be high-repetition rate ready, CSA from gas targets is only limited by plasma cooling times of typically hundreds of nanoseconds (ns) and the gas flow characteristics upon eventual return current dynamics. Finally limiting factors will be the automatized geometrical alignment of laser focus and target.

In conditions of exploratory experiments, one must keep in mind that many of the before-mentioned mechanisms can co-exist, either due to the overlap of regimes or for reasons of spatial and temporal uncertainties in the interaction conditions of the target and the driving laser pulse.

This work makes use of ion acceleration by TNSA and aims at exploration of the CSA domain. Targeted are ion sources with low divergence and possibly mono-energetic multi-MeV beams, regardless the acceleration mechanisms at play. Direct applicability will be highlighted throughout the work.

2.2 Laser Induced Electromagnetic Tailoring of Ion Beams

Ion beams must be tailored spatially and regarding their spectrum in order to achieve both a controlled dose rate and total energy deposition at specific spatial positions in irradiated samples. Absolute timing of the irradiation process is possible in all-optical laser-driven systems, for the femtosecond (fs) accuracy with which laser beams can be synchronized, and taking into account the Time of Flight (ToF) of projectiles along their known geometrical trajectories. Important ion beam characteristics are the energy-depended emittance and temporal dispersion. The beam emittance determines the minimum size to which the beam can be down-focused. The temporal dispersion of the beam yields lateral stretching and compression of parts of the spectrum with ToF. EM fields can be externally applied to charged particle beams in order to modify

the phase space during and after laser-acceleration, aiming at smallest possible lateral and transverse focal spots with highest possible particle density.

This work explores ion beam tailoring by conventional large scale accelerator technology and novel approaches that rely on laser-driven EM lenses and cavities.

2.3 Laser Driven Fusion

The success of a fusion device is linked to whether the reactor is able to produce more energy than is consumed in starting the fusion. Further the fusion reaction can be self-sustaining if the rate of energy production exceeds the rate of losses to the environment. The reaction efficiency Ξ_{eff} of a fusion reactor is

$$\Xi_{\text{eff}} = \frac{P_{\text{out}}}{P_{\text{fus}} - P_{\text{rad}} - P_{\text{con}}} \quad , \tag{2.1}$$

with P_{out} the output power, P_{rad} radiative losses and P_{con} conductive losses carried away with particles leaving the plasma. The energy production rate by fusion reactions P_{fus} results from the product of volume fusion rate f_{fus} and the liberated energy into charged particles E_{fus} in one fusion process with $P_{\text{fus}} = f_{\text{fus}} \cdot E_{\text{fus}}$. The volume fusion rate, which is the number of reactions per volume per time, calculates as product of the number densities of both reactants multiplied by the mean value of the product of relative velocity and fusion cross section over the velocity distribution of reactants

$$f_{\text{fus}} = \left(\prod_{i \in \{\text{X,Y}\}} n_i \right) \cdot \langle \sigma_{\text{f}} v \rangle \tag{2.2}$$

where ${}^{A}\text{X}$ and ${}^{B}\text{Y}$ represent the constituents of the fuel with number densities n_i. Starting from cold Decaboran ${}^{11}\text{B}_{10}{}^{1}\text{H}_{14}$ fuel at nominal density of $940 \cdot 10^{-3}\,\text{g}\,\text{cm}^{-3}$, loss terms can be neglected. An impinging particle beam of mono-energetic protons at 1 MeV with $1 \cdot 10^{12}$ protons in 50 µs long micro-bunches would yield $\int_V f_{\text{fus}}\, \text{d}V \approx 25\,\text{ns}^{-1}$ fusion reactions. The liberated energy of 1.7 µJ is much lower than the energy required to accelerate such particle beam, and the reactor design with cold fuel is energetically inefficient. The minimum requirement for a self-sustaining reactor is given by the Lawson criterion [Law57] for ignition

$$f_{\text{fus}} \overset{!}{\geq} \frac{P_{\text{loss}}}{E_{\text{fus}}} \quad . \tag{2.3}$$

The total rate of energy loss $P_{\text{loss}} = P_{\text{rad}} + P_{\text{con}}$ can be estimated as the total energy density per unit volume W_{p} divided by a confinement time of the plasma τ_{p}. For an equilibrium plasma of fuel constituents and electrons with Maxwellian velocity distribution characterized by the temperature T_{p},

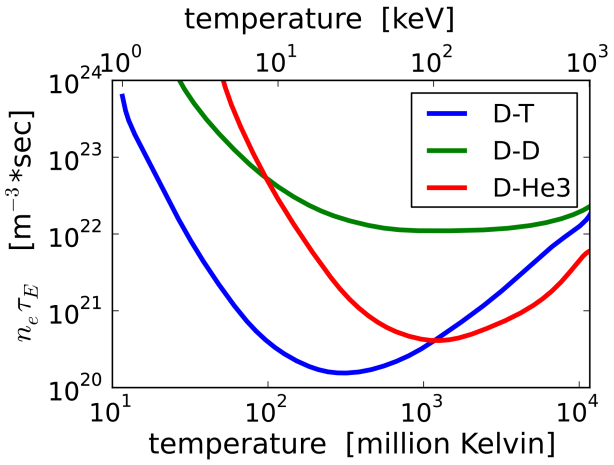

Figure 2.1: Lawson self-heating condition for Deuterium-cycle fusion reactions. Plasma characteristics must exceed the plotted curves for fusion self-heating to overcome energy loss. Graph extracted from [Str10].

$$W_\mathrm{p} = \frac{3}{2}\left(\sum_{i\in\{\mathrm{e,a,b}\}} n_i\right) k_\mathrm{B} T_\mathrm{p} \quad , \tag{2.4}$$

$$\overset{\text{eq. (2.3)}}{\Rightarrow} \tau_\mathrm{p} \cdot \frac{\prod_{i\in\{\mathrm{X,Y}\}} n_i}{\sum_{i\in\{\mathrm{e,X,Y}\}} n_i} \overset{!}{\geq} \frac{k_\mathrm{B} T_\mathrm{p}}{E_\mathrm{fus} \cdot \langle \sigma_\mathrm{f} v \rangle} \quad , \tag{2.5}$$

k_B denotes the Boltzmann constant. The minimum requirement for ignition simplifies to a bottom limit for the product of confinement time and a number density depended function, that can be readily calculated. The left hand side of eq. (2.5) calculates to $\tau_\mathrm{p} \cdot n_\mathrm{p}/12$ for Deuterium fusion reactions with fuel of electron number density n_p. The right hand side is a function of fuel temperature with an absolute minimum, that determines the absolute lower limit of the product of confinement time and plasma density necessary for ignition, see fig. 2.1.

Controlled fusion in plasma is mostly divided into two approaches: either one maintains the fuel density moderately high for a long confinement time, or one is obliged to archive extremely high densities for short confinement times. This delimits the domains of MCF deploying magnetic traps and ICF where imploding fuel is confined by its own inertial forces.

For hot Decaboran fuel in a equilibrium plasma state, the relevant temperatures for high fusion cross sections of hundreds of keV mean important losses due to Bremsstrahlung with $P_\mathrm{loss} \gg P_\mathrm{fus}$ [MV+96]. A possible solution follows a strategy referred to as fast ignition (FI) [Tab+94]. There, fuel is pre-compressed to a high-density core as in ICF but at lower equilibrium plasma temperature than needed to ignite. The dense core is subsequently irradiated to crate a hot spot which is ought to trigger a burn wave, faster than the ion-electron relaxation time in order to maintain a high ion-electron temperature gap. The efficient energy deposition in the dense core is a hot topic in High Energy Density Physics (HEDP), starting with the energy deposition cross sections for different types of radiation ranging from EM radiation, such as laser beams

and high energy photons, to massive charged particles, such as electrons or heavy ions. A further important constraint is that laser driven implosion yields production of low density plasma around the imploding fuel.

The fast ignition approach to ICF relevant to this work relies on the energy deposition by ion beams [Rot+01a], with the advantages that ions have a high energy deposition only at the end of their propagation range and a low scattering cross section in the coronal plasma. Most important parameters demanded for the ion beam are a spectrum suitable for maximum energy deposition inside the dense core and a possibly small emittance to achieve highest energy densities after down-focusing with an auxiliary EM lens. Fast ignition at the National Ignition Facility (NIF) requires a total energy deposition of 7 kJ to 11 kJ into a typical hot core of about 20 µm size [Rot+01a], during a pulse duration of 13 ps to 16 ps.

The other strategy relevant to this work is magneto-inertial fusion, a hybrid of ICF and MCF that relies on magnetization of the imploding sample prior to its drive [Wur+16]. The ramping up field amplitudes during compression reduce thermal transport and enhance the heating by charged fusion products as ultra-strong magnetic fields confine both electrons and ions in the plasma on their respective Larmor radii. At the moment of maximum compression, the energy density of the magnetic field must be more important than the energy density of the plasma. State-of the art experiments deploy a seed magnetisation with tens of T that is compressed to the order of several kT, aiming at higher seed field amplitudes for more burn efficiency.

2.4 Laser Driven Medical Applications for Radiation Therapy

Radiation therapy aims at the targeted destruction of a cancerous tumor and metastases by radiation in vivo. One approach is based on radiation from external sources. The therapy of tumors in several cm depth of the human body and possibly inside bone can benefit from the high energy deposition only at the end of ion ranges. Electron beams or high energy photons depose dose in larger volumes all across their trajectory, then destructive to healthy tissue. The irradiation of living tissue in living organisms requires precisely applied depth dose profiles, which must be regulated at precise dose rates of micro- and macro-bunches. The therapeutic use thus demands a majority of the laser-ion acceleration technology, but might be embraced in the frame of the novel FLASH [Fav+14] irradiation concept. It was only discovered recently that micro-bunch dose rate [Bru+20] and macro-bunch repetition rate [Bay19] majorly influence cytotoxicity. In depth application requires projectile energies of several hundred MeV u^{-1} [Eic+98], and doses of several Gy per therapeutic application [Jäk+99].

Alpha therapy is a further promising approach for clinical oncology [Cha+18]. This form of radiotherapy is not carried out by external radiation, but by administering radioactive substances to the patient. The cells are reached through the bloodstream. Unlike chemotherapy, the treatment is aimed at diseased cells due to the targeted binding properties of compound molecules and thus reduces possible side effects [IAE18]. Alpha-emitting radionuclides can be produced by interaction of ionizing radiation with a suited target material, which is a major challenge for reasons of the needed quantities [Cha+18]. Astatine-211 is a suited candidate for its intermediate half live time of 7.2 h and low risk for side effects [Mak+18], which can be produced in a $(\alpha, 2n)$ reaction by irradiating Bismuth-209 with alpha particles of 28 MeV. Beam currents of several hundred µA are necessary for efficient isotope production.

The delivery of high doses in short amounts of time for both applications is only available at large scale Synchrotron facilities – and might become accessible by laser-ion acceleration.

3 Theoretical Foundations and Physics Concepts

This chapter introduces basic concepts of EM fields, the laser technique and laser-plasma interaction. Here the focus is set on laser acceleration of charged particles, especially electron heating, with an accentuation of ion acceleration by TNSA and CSA. Further, the interaction of charged particle beams and high energy photons with solid density matter are summarized, and important principles of optics are laid out. The introduction is inspired by textbooks [AV04; Mac13; Ren17; Mul20], if not otherwise indicated.

The spatial dimensions important for this work are of the order of hundreds of µm to several mm, the size of acceleration and beam tailoring platforms in experimental configuration. The temporal evolution of electric currents and fields ranges from several ps up to the ns, laser pulses have Full Width at Half Maximum (FWHM) durations ranging from tens of fs up to the ns. Amplitudes of induced EM fields range up to hundreds of T and several GV m^{-1}. Ions and electrons move with a kinetic energy of up to a few 10 MeV, demanding a relativistic consideration.

3.1 Electromagnetic Fields

Electric, magnetic and EM fields with the underlying mechanisms responsible for their build-up are of fundamental importance for this work. A direct access to the three-dimensional electric and magnetic vector field is given by the Maxwell equations

$$\vec{\nabla} \cdot \vec{E} = \frac{\rho}{\epsilon_0} \tag{3.1}$$

$$\vec{\nabla} \cdot \vec{B} = 0 \tag{3.2}$$

$$\vec{\nabla} \times \vec{E} = -\partial_t \vec{B} \tag{3.3}$$

$$\vec{\nabla} \times \vec{B} = \mu_0 \left(\vec{J} + \epsilon_0 \cdot \partial_t \vec{E} \right) \tag{3.4}$$

– $\vec{B}$ stands for the magnetic and $\vec{E}$ for the electric field, ρ is the charge density, ϵ_0 is the permittivity of vacuum, μ_0 is the permeability of vacuum and $\vec{J}$ is the current density vector. These equations govern the EM dynamics important for this work: (a) the propagation of light in vacuum, where no charges ($\rho = 0$) and no currents ($\vec{J} = 0$) are present, and (b) the spatial characteristics of static fields induced by charges and currents. For static fields the Maxwell equations simplify to

$$\vec{\nabla} \cdot \vec{E} = \frac{\rho}{\epsilon_0} \tag{3.5}$$

$$\vec{\nabla} \cdot \vec{B} = 0 \tag{3.6}$$

$$\vec{\nabla} \times \vec{E} = 0 \tag{3.7}$$

$$\vec{\nabla} \times \vec{B} = \mu_0 \vec{J} \tag{3.8}$$

The E-field can be calculated with regard to a continuous space charge density. The respective equations for divergence and curl lead to the E-field for any spatial point $\vec{r}$, by integration over the applied charge density

$$\vec{E}\left(\vec{r}\right) = \frac{1}{4\pi\epsilon_0}\int \mathrm{d}\vec{r}'\left(\rho\left(\vec{r}'\right)\frac{\vec{r}-\vec{r}'}{|\vec{r}-\vec{r}'|^3}\right) \quad . \tag{3.9}$$

For a magnetic field, the general Maxwell equations can be solved introducing the vector potential $\vec{A}$ of the field $\vec{B}$. With Φ as the electric scalar potential, the vector potential is given by

$$\vec{\nabla}\times\vec{A} = \vec{B} \tag{3.10}$$

$$\partial_t\vec{A} + \vec{\nabla}\Phi = -\vec{E} \quad . \tag{3.11}$$

The later satisfy the condition of having no source of the magnetic field. Using the general Coulomb gauge condition, setting $\partial_t\Phi = 0$ in static fields, this set of equations and equation (3.8) lead directly to

$$\vec{\nabla}\times\left(\vec{\nabla}\times\vec{A}\right) = \mu_0\vec{J} \tag{3.12}$$

$$\Leftrightarrow \vec{\nabla}\left(\vec{\nabla}\cdot\vec{A}\right) - \Delta\vec{A} = \mu_0\vec{J} \mid \text{with } \vec{\nabla}\cdot\vec{A} = 0 \tag{3.13}$$

$$\Rightarrow \Delta\vec{A} = -\mu_0\vec{J} \quad . \tag{3.14}$$

A solution can be constructed with the Green's function for the three dimensional (3D) Laplace operator,

$$\vec{A}\left(\vec{r}\right) = \frac{\mu_0}{4\pi}\int \mathrm{d}\vec{r}'\left(\frac{\vec{J}\left(\vec{r}'\right)}{|\vec{r}-\vec{r}'|}\right) \quad , \tag{3.15}$$

From this the B-field is accessible for a given current density distribution

$$\vec{B}\left(\vec{r}\right) = \frac{\mu_0}{4\pi}\int \mathrm{d}\vec{r}'\ \vec{\nabla}_r\times\left(\frac{\vec{J}\left(\vec{r}'\right)}{|\vec{r}-\vec{r}'|}\right) = \frac{\mu_0}{4\pi}\int \mathrm{d}\vec{r}'\ \vec{J}\left(\vec{r}'\right)\times\left(\frac{\vec{r}-\vec{r}'}{|\vec{r}-\vec{r}'|^3}\right) \quad . \tag{3.16}$$

This is the integral form of Biot-Savart's law, basis for numerical calculations and estimates in this work. For numerical simulations, it is useful to determine the vector potential with equation (3.15) to increase the speed of calculations. The resulting field is found with equation (3.10) by curling the vector potential. E-fields will be implemented analytically or by solving equation (3.9). Self-induced E-fields due to $\partial_t\vec{A}$ become only important for quickly rising currents, seperately discussed in the course of this work.

3.2 Light Amplification by Stimulated Emission of Radiation

The induced phosphorescence of coherent directional monochromatic EM waves from an energetically stimulated medium is referred to as light amplification by stimulated emission of radiation (laser). First laser operation was achieved in 1960 [Mai60], producing an EM wave of wavelength $\lambda_\mathrm{L} = 694.3\,\mathrm{nm}$ from optically excited ruby as crystalline gain medium. Under irradiation with EM waves of 550 nm wavelength, the triply ionized Cromium impurity in the Sapphire crystal is excited from its ground state ${}^4F_{3/2}$ to the unstable state ${}^4F_2$, from which it decays quickly to the meta-stable ${}^2E$ state. The decay is a non-radiative transition with

energy released in phonons. This excitation method is called optical pumping. The meta-stable state has a long lifetime of ≈5 ms, allowing to populate it in higher number than the ground state throughout the medium. This is called the population inversion. A single photon emitted by spontaneous emission in such a medium can be seed of a chain reaction of stimulated emission events, otherwise impossible. In stimulated emission, the phase, frequency, polarization, and direction of travel of incident photon and emitted photon are equal, thus amplification of the EM wave is achieved.

Energy gain efficiency of the laser beam can be increased by placing the active medium between two mirrors: photons bouncing between the mirrors will efficiently increase their number until the number of atoms in the excited state drops underneath the number of atoms in the ground state. In order to keep photons in phase, the distance between the mirrors must be a multiple of $\lambda_\mathrm{L}/2$. Such construct is called optical resonator and the cascade of photon multiplication along the resonator axis is called lasing. A resonator of length L allows cavity modes with spacing $\frac{c}{2L}$ in the frequency domain – and thus amplification of a broad spectrum and not just one single wavelength. Optical pumping of the gain medium results in a broad laser gain bandwidth, which in intersection with the cavity modes leads to the amplified spectrum. The technological evolution of laser machines, shortly called laser themselves, went over different active media implying different spectra on the amplified light, and introduced different tweaks to the cavity allowing for different modes of operation. The introduction of powerful optical pumping and the placement of a leaking mirror on one side of the resonator allows steady out-coupling of EM radiation. This mode of laser operation is called Continuous Wave (CW) laser.

Further introduction of a variable attenuation inside the resonator allows to inhibit lasing from a random spontaneous emission event and thus to attain a higher number of atoms in the meta-stable state. The controlled removal of attenuation then allows for lasing with a higher energy gain for the possibility of larger amounts of photons. Such attenuator results in a modification of the quality factor of the optical resonator defined as ratio between energy stored and energy dissipated per power-loss cycle, and is therefore named Q-switch. Switching to zero attenuation allows for release of a higher photon number for a shorter amount of time when compared to a CW laser. The result is a short pulse train of EM radiation, called laser pulse.

The time needed for flipping the switch limits the pulse duration. A further increase of the energy flux is possible by imposing a fixed phase relation to all modes of the resonator, in order to benefit from constructive interference. Essential tweak for short-most pulses is to deploy a gain medium with large bandwidth, that incorporates multiple of all possible cavity modes. The larger the bandwidth, the smaller the spatial region of constructive interference, or in other words the shorter the laser pulse. The else independent modes can be mode locked, *e.g.* by elements in the cavity that allow only most intense pulses to bounce. Pulse compression to even shorter duration is possible by employing optical fibres to enlargen the spectrum through self-phase modulation.

A single photon of wavelength λ_X has the energy $E_\mathrm{X} = hc/\lambda_\mathrm{X}$, where h is the Planck constant and c the speed of light. The energy of a photon with the lasing wavelength of a ruby laser is $287 \cdot 10^{-21}$ J. Laser pulses are often guided through multiple amplification stages after leaving the optical resonator, then reaching energies of up to hundreds of J. Non-linear effects arise in gain media for high laser pulse intensities and alter the pulse properties, *e.g.* by distortions of the laser phase front.

Short pulses of large spectrum can be further amplified by Chirped Pulse Amplification (CPA) [SM85b]. First the pulse is stretched by varying the optical path length for every frequency in the laser spectrum, *e.g.* based on group velocity dispersion in optical fibres or the double-passage through a double-grating arrangement. Then the chirped pulse with spatio-temporally separated frequencies is at lower intensity compared to the short pulse and can be amplified to higher energies. Finally the laser pulse is coupled into a reflective-double-passage double-grating compressor. The frequencies arriving first in the chirped pulse are forced to a longer optical

path than later arriving frequencies. After double passage, the frequencies overlap spatially and form a short laser pulse.

3.3 Electromagnetic Forces

The interaction of charged particles with electric and magnetic fields is governed by the Lorentz force $\vec{F}_\mathrm{L}$

$$\vec{F}_\mathrm{L} = q \cdot \left(\vec{E} + \vec{v} \times \vec{B} \right) \quad , \tag{3.17}$$

with q the charge of the particle, $\vec{p}$ the momentum, m the mass at rest, $\vec{v}$ the velocity of its inertial system. The relativistic description of the problem makes it necessary to transform the momentum and the forces. The transformation rules of a Newton force are depending on the field components parallel or perpendicular to the actual direction of movement of the particle,

$$\vec{p}^\mathrm{R} = \gamma m \vec{v} \quad , \tag{3.18}$$

$$\vec{F}_\parallel^\mathrm{R} = \gamma^3 m \, \mathrm{d}_t \vec{v}_\parallel \quad , \tag{3.19}$$

$$\vec{F}_\perp^\mathrm{R} = \gamma m \, \mathrm{d}_t \vec{v}_\perp \quad , \tag{3.20}$$

$$\gamma = \left(1 - \frac{v^2}{c^2} \right)^{-1/2} \quad , \tag{3.21}$$

with c the speed of light. $\vec{F}_\parallel^\mathrm{R}$ denotes the relativistic parallel component and $\vec{F}_\perp^\mathrm{R}$ is the relativistic perpendicular component. γ is the so-called relativistic gamma-factor. Following eq. (3.17), the relativistic equation of motion is

$$\gamma^3 m \, \mathrm{d}_t \vec{v}_\parallel = q \cdot \vec{E}_\parallel \tag{3.22}$$

$$\gamma m \, \mathrm{d}_t \vec{v}_\perp = q \cdot \left(\vec{E}_\perp + \vec{v}_\parallel \times \vec{B} \right) \quad . \tag{3.23}$$

Which allows simplification to

$$\mathrm{d}_t \vec{v}_\parallel = \frac{q}{\gamma^3 m} \cdot \vec{E}_\parallel = \frac{\vec{F}_\mathrm{L} \cdot \vec{v}_\parallel}{\gamma^3 m} \cdot \frac{\vec{v}_\parallel}{v_\parallel^2} \quad , \tag{3.24}$$

$$\mathrm{d}_t \vec{v}_\perp = \frac{q}{\gamma m} \cdot \left(\vec{E}_\perp + \vec{v}_\parallel \times \vec{B}_\perp \right) = \frac{1}{\gamma m} \cdot \left(\vec{F}_\mathrm{L} - \left(\vec{F}_\mathrm{L} \cdot \vec{v}_\parallel \right) \cdot \frac{\vec{v}_\parallel}{v_\parallel^2} \right) \quad . \tag{3.25}$$

3.4 Particle Beam Acceleration by Laser

The energy transfer from laser energy to projectile energy is fundamental to laser driven charged particle beam acceleration and target discharge. This work discusses all-optical platforms, where laser pulses are used for the ionization of charged particle species from neutral media and the successive acceleration of electrons and ions. A material in gaseous or solid state can be transformed into a plasma by interaction with a laser.

Either the E-field is strong enough to accelerate stochastically present free electrons to energies needed for collisional ionization of the atoms; or the laser liberates bound electrons at higher field amplitudes, where the atomic potential may distort and tunnelling ionization becomes more likely; or the laser field is of the order of the Coulomb force and the electron is able to escape. After first electrons are set free, the target is ionized in an avalanche to the plasma state. Electrons the most efficiently heated species for their low mass.

To understand the acceleration of charged particle beams from laser-plasma, first discussed are effects of EM waves on single particles, then collective plasma effects are introduced. The later lead to a description of state-of-the-art ion acceleration from solid state targets as well as from near-critical density targets

3.4.1 Relativistic Laser-Plasma Interaction

The EM wave of a laser is described by a plane wave vector potential with wave vector $\vec{k}_\mathrm{L}$ and angular frequency ω_L. The EM wave shall propagate along the z-axis with a linear polarization in the plane perpendicular to z, thus $A_z = 0$, and

$$\vec{A} = A_0 \cdot \cos\left[k_\mathrm{L} z - \omega_\mathrm{L} t\right] \cdot \vec{e}_\perp \quad . \tag{3.26}$$

The relativistic electron motion in an EM wave is described by the relativistic equation of motion

$$\mathrm{d}_t \vec{p}^\mathrm{R} = q \cdot \left(-\partial_t \vec{A} + \vec{v} \times \left(\vec{\nabla} \times \vec{A}\right)\right) \quad . \tag{3.27}$$

For a plane wave follows $\partial_x A_y = 0 = \partial_y A_x$. Substituting $\vec{\xi}_\perp = \xi_x \vec{e}_\mathrm{x} + \xi_y \vec{e}_\mathrm{y}$ for any vector gives

$$\mathrm{d}_t \vec{p}^\mathrm{R}_\perp = -q \cdot \left(\partial_t \vec{A}_\perp + v_z \cdot \partial_z \vec{A}_\perp\right) = -q\ \mathrm{d}_t \vec{A}_\perp \mid \text{with } z_e(t) = \int_0^t v_z\ \mathrm{d}\tau \quad , \tag{3.28}$$

$$\mathrm{d}_t p^\mathrm{R}_z = q \cdot \left(\vec{v}_\perp \cdot \partial_z \vec{A}_\perp\right) \quad . \tag{3.29}$$

Integration of perpendicular momentum (3.28), under the assumption of initially resting particles, leads to another form of the parallel component's equation of motion,

$$\mathrm{d}_t p^\mathrm{R}_z = -\frac{q^2}{2\gamma m} \partial_z \vec{A}^2_\perp \quad . \tag{3.30}$$

Equation (3.30) shows that the acceleration in direction of wave propagation depends on the intensity-gradient of the EM wavefront as $A^2 \propto E^2 \propto I_L$. I_L describes the intensity of the EM wave under regard. The temporal evolution of the kinetic energy $E_c = (\gamma - 1)mc^2$ with $\partial_{\vec{p}^R} E_c = \vec{v}$ is useful to construct a conservation law,

$$\mathrm{d}_t E_c = \partial_t E_c = \partial_{\vec{p}^R} E_c \cdot \partial_t \vec{p}^R = \vec{v} \cdot \partial_t \vec{p}^R \quad , \tag{3.31}$$

$$\overset{(3.27)}{=} -q\vec{v} \cdot \partial_t \vec{A} = -\frac{q}{\gamma m} \vec{p}_\perp \cdot \partial_t \vec{A}_\perp \quad , \tag{3.32}$$

$$\overset{(3.28)}{=} \frac{q^2}{2\gamma m} \partial_t \vec{A}^2_\perp \quad . \tag{3.33}$$

Further, the conservation law arises precisely on the definition of a wave equation as we see in the dependency $\vec{A} = \vec{A}(\omega \cdot (t - {}^{z}/_{c}))$. Addition of equation (3.33), and (3.30) multiplied by the speed of light leads to

$$\mathrm{d}_t \left((\gamma - 1)mc^2 - c \cdot p_z^{\mathrm{R}}\right) = \frac{q^2}{2\gamma m}\left(\partial_t \vec{A}_\perp^2 + c \cdot \partial_z \vec{A}_\perp^2\right) = \frac{q^2}{2\gamma m} \cdot 0 \quad , \tag{3.34}$$

$$\Leftrightarrow \left((\gamma - 1)mc^2 - c \cdot p_z^{\mathrm{R}}\right) \overset{\vec{v}(0)=0}{=} 0 \quad . \tag{3.35}$$

In summary results,

$$\vec{p}_\perp^{\,\mathrm{R}} = -q\vec{A}_\perp \quad , \tag{3.36}$$

$$p_z^{\mathrm{R}} = (\gamma - 1)mc \mid \text{via } \gamma = \left(1 + \frac{\vec{p}^{\,2}}{m^2c^2}\right)^{1/2} \quad , \tag{3.37}$$

$$\Rightarrow p_z^{\mathrm{R}} = \frac{\left(\vec{p}_\perp^{\,\mathrm{R}}\right)^2}{2mc} \quad . \tag{3.38}$$

As the charge of projectiles has no influence, the parallel component of the momentum vector is positive and particles accelerate in direction of the wave propagation. The exact angle in between wave propagation direction and particle trajectory is given by

$$\tan\left[\Phi\right] = \frac{p_\perp^{\mathrm{R}}}{p_z^{\mathrm{R}}} = \left(\frac{2}{\gamma - 1}\right)^{1/2} \quad . \tag{3.39}$$

Relativistic electrons with $\gamma \gg 1$ move in direction of the laser propagation and non-relativistic electrons with $\gamma \approx 1$ oscillate in the polarization plane. By convention, movements are designated as relativistic if $\gamma > 2$ and movements with $\gamma > 100$ are named ultra-relativistic. Relativistic and non-relativistic regime are distinguishable with the normalized vector potential a_0 by combining (3.26), (3.37) and (3.38). Therefore, we assume the perpendicular oscillation motion with its peak velocity during the first half period leading to a maximum γ_M. It follows

$$a_0 := \frac{qA_0}{mc} = \left(2\left(\gamma_M - 1\right)\right)^{1/2} \approx \left(\gamma_M - 1\right)^{1/2} \quad . \tag{3.40}$$

For $a_0 \ll 1$, particles can be described classical, for $a_0 \approx 1$ particles approach the speed of light and become relativistic. Ultra-relativistic motion is achieved by $a_0 \gg 1$. The interaction in between an EM wave and a plasma is called relativistic if electrons in the plasma oscillate with relativistic velocities, and so forth. From the Maxwell equations and Poynting's theorem of energy conservation for the interaction between EM fields and charged particles, follows that the energy transfer from time-varying EM fields is perpendicular to this fields. The intensity is thus defined as

$$I_L = \frac{1}{\mu_0}\left\langle \vec{E} \times \vec{B} \right\rangle_{{}^{2\pi}/_{\omega_L}} = \frac{1}{\mu_0 c} \cdot \frac{\left(A_0\omega_L\right)^2}{2} \quad . \tag{3.41}$$

The intensity regime necessary for relativistic interaction is $10^{18}\,\mathrm{W\,cm^{-2}} < I_L < 10^{22}\,\mathrm{W\,cm^{-2}}$ with electrons and a wavelength $\lambda_L \approx 1\,\mu\mathrm{m}$. Pulsed laser systems commonly provide such intensities, *e.g.* laser pulses amplified via CPA containing several 100 J at a typical pulse duration of about $\tau \approx 1\,\mathrm{ps}$. For a laser with $I_L = 10^{19}\,\mathrm{W\,cm^{-2}}$ and $\lambda_L = 1.053\,\mu\mathrm{m}$, like it is used in some of the the underlying experiments, we estimate a

normalized vector potential $a_{0,e} \approx 2.8$ for electrons. Protons can be described classically with $a_{0,p} \approx 1.6 \cdot 10^{-3}$, their small quiver motion is located in the polarization plane.

Trajectories for electrons can be calculated by using the wave's local time frame $\chi := t - {}^{z}/_{c}$ which allows $\mathrm{d}_t \chi = {}^{1}/_{\gamma}$ to avoid problems with the relativistic description:

$$\mathrm{d}_t \vec{r} = \frac{\vec{p}^{\mathrm{R}}}{m\gamma} \tag{3.42}$$

$$\Leftrightarrow \ \mathrm{d}_\chi \vec{r} = \frac{\vec{p}^{\mathrm{R}}}{m} = \frac{\vec{p}_\perp^{\mathrm{R}} + p_z^{\mathrm{R}} \vec{e}_\mathrm{z}}{m} \underset{(3.38)}{\overset{(3.36)}{=}} \frac{e}{m}\vec{A}_\perp + \frac{e^2}{2m^2 c} A_\perp^2 \vec{e}_\mathrm{z} \tag{3.43}$$

$$\overset{(3.26)}{=} c \cdot \left(a_{0,e} \cdot \cos\left[\omega_\mathrm{L}\chi\right] \cdot \vec{e}_\perp + \frac{a_{0,e}^2}{2} \cos^2\left[\omega_\mathrm{L}\chi\right] \cdot \vec{e}_\mathrm{z} \right) \tag{3.44}$$

$$\Rightarrow k_\mathrm{L} \cdot z(\chi) = a_{0,e} \cdot \sin\left[\omega_\mathrm{L}\chi\right] \tag{3.45}$$

$$k_\mathrm{L} \cdot x_\perp(\chi) = \frac{a_{0,e}^2}{8} \cdot \left(2\omega_\mathrm{L}\chi + \sin\left[2\omega_\mathrm{L}\chi\right]\right) \tag{3.46}$$

It is a transversal sinusoidal motion in the wave's field. However, the forward propagation oscillates in speed and reaches minima due to a vanishing electrical field component, thus twice per oscillation period of the EM wave. The numerically calculated trajectory of an electron with $a_{0,e} = 2.8$ is shown in figure 3.1.

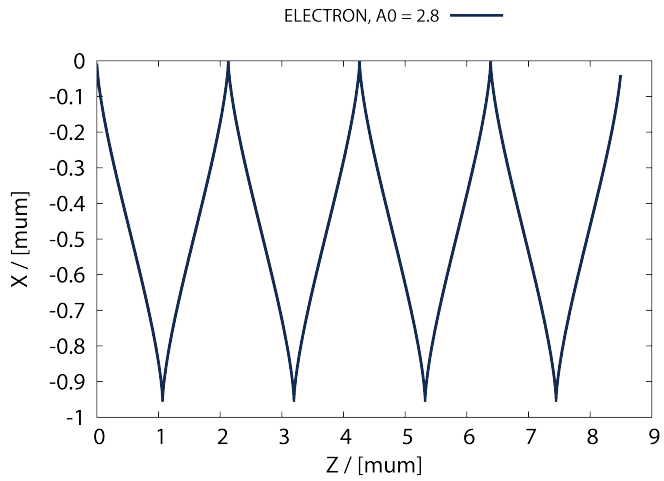

Figure 3.1: Relativistic electron quiver motion in a laser field with $a_{0,e} = 2.8$ and $\lambda_L = 1.053\,\mu\mathrm{m}$. The laser propagates in z direction, the E-field oscillates in transverse x direction.

A real laser-pulse is finite in space and time. If we consider an infinite plane wave with a temporal Gaussian intensity profile, electrons initially at rest are transported in direction of laser propagation but only during the time intensity is in the relativistic regime. After the pulse passed, electrons will be at rest again, displaced by a certain distance. If we consider a spatially finite flat top intensity wave with an infinite duration, electrons will escape if their quiver motion leads them to regions which are not affected by the EM wave. Thus, electrons can leave the laser-plasma interaction zone with a net gain of energy E_P for a real spatially and temporally finite laser pulse. They are called ponderomotive scattered electrons. For further investigation with real pulse profiles see Galkin et al. [Gal+07].

The picture of a ponderomotive potential is often used for a better understanding of the interaction between a single particle and a laser field. It is simpler to introduce a potential based description than to solve the equation of motion for a realistically shaped laser pulse. Considering such a laser pulse, finite in space and time, equation (3.30) gives a force $\vec{F}_\mathrm{P}$ that pushes any particles in opposite direction of the EM intensity gradient. Variation of laser intensity leads to variation of this force, thus the ponderomotive force is a low frequency effect of high frequency EM forces within spatially not uniform EM fields.

Plane waves with perpendicularly equal a_0 cause a drift in z-direction only. If we consider a spatially finite Gaussian wave, electrons will escape if their quiver motion leads them to regions which are barely affected by the EM wave. In addition, any perpendicular spatial gradient of intensity leads to a perpendicular drift of the quiver motion's centre. The drift is not only along the z-axis because surfaces with equal a_0 are curved. Considering this, we change ∂_z with a full $\vec{\nabla}$ operator. The average force $\left\langle \vec{F}_\mathrm{P} \right\rangle$ over a laser period τ is the ponderomotive force

$$\left\langle \vec{F}_\mathrm{P} \right\rangle_\tau = \left\langle \, \mathrm{d}_t p_z^\mathrm{R} \right\rangle_\tau = -\frac{q^2}{2m \left\langle \gamma \right\rangle_\tau} \cdot \vec{\nabla} \left\langle \vec{A}_\perp^2 \right\rangle_\tau \quad . \tag{3.47}$$

The right hand side of the equation can be simplified with $\langle \gamma \rangle = \left(1 + {}^{\langle \vec{p}^2 \rangle}/_{m^2 c^2}\right)^{1/2}$ and a momentum representation equivalent to equation (3.43), we obtain

$$\vec{\nabla} \left\langle \gamma \right\rangle_\tau^2 = \frac{q^2}{m^2 c^2} \cdot \vec{\nabla} \left\langle \vec{A}_\perp^2 \right\rangle_\tau \quad . \tag{3.48}$$

The average force depends only on the gradient of the relativistic factor. This form of a conservative force allows re-writing with introduction of a ponderomotive potential U_P. With U_P ranging between zero in infinity, the maximum energy gain of accelerated particles results with

$$\Rightarrow \left\langle \vec{F}_\mathrm{P} \right\rangle_\tau = -\frac{mc^2}{2 \left\langle \gamma \right\rangle_\tau} \cdot \vec{\nabla} \left\langle \gamma \right\rangle_\tau^2 = -mc^2 \cdot \vec{\nabla} \left\langle \gamma \right\rangle_\tau \tag{3.49}$$

$$\Leftrightarrow \left\langle \vec{F}_\mathrm{P} \right\rangle_\tau = -m \cdot \vec{\nabla} U_\mathrm{P} \mid \text{with } U_\mathrm{P} = c^2 \cdot \left(\left\langle \gamma \right\rangle_\tau - 1 \right) \tag{3.50}$$

$$\Rightarrow E_\mathrm{P} = mc^2 \cdot \left(\left\langle \gamma \right\rangle_\tau - 1 \right) = mc^2 \cdot \left(\left(1 + a_0^2 \right)^{1/2} - 1 \right) \quad . \tag{3.51}$$

and thereby a mass related potential with a possible peak energy transfer of E_P. Especially in the case of a perpendicularly drifting electron, a net energy gain is possible. The deceleration after the passage of the peak intensity is caused by lower potential niveaus.

To summarize, in a temporally finite pulse of a spatially uniform intensity distribution, a particle can't gain energy. This is known as Lawson-Woodward criteria. When spatial uniformity holds in free space, the interaction of a laser pulse with a target material might yield spatial non-uniformity. In such cases, particles can gain energy, *e.g.* if they penetrate through the critical density that is discussed in the next section. Cases in which the above derivation based on the ponderomotive potential is not valid are short laser pulses, which are too short to allow a quiver motion, and the presence of external B-fields. In a temporally finite and spatially non-uniform pulse, a net acceleration due to a ponderomotive potential is likely.

3.4.1.1 Collective Effects in Plasmas

Plasma electrons react more easily to external EM forces than the positive ion background for their lower mass. If electrons are displaced with regard to the ions due to an external force like the ponderomotive force, an electrostatic potential builds up. The charge separation leads to a restoring force which can be explained by introducing a density perturbation in Poisson equation. The electrons start to oscillate with the characteristic electron plasma frequency ω_{pe} and the perturbation wave starts propagation within the plasma. The oscillation period depends on the electron number density n_e and is given by

$$\omega_{\text{pe}} = \left(\frac{n_e q_e^2}{\epsilon_0 m_e} \right)^{1/2} \quad . \tag{3.52}$$

Plasma waves caused by laser-plasma interaction can accelerate electrons. In their own co-propagating frame, a plasma wave is equal to a potential wave. The gradient between regions of high electron density and low energy density produces a force which can accelerate wave-co-propagating electrons.

With the Maxwell-Ampère and Maxwell-Poisson equation of a transverse EM wave within a plasma, the plasma dispersion relation is obtained as

$$\omega^2 = \omega_{\text{pe}} + k^2 c^2 \quad , \tag{3.53}$$

where ω is the angular frequency of the EM wave, and with k follows the specific absolute wave vector. The dispersion relation neglects thermal effects. In presence of a B-field $\vec{B}$, the dispersion relation shows anisotropy

$$\frac{c^2 k^2}{\omega^2} = 1 - \frac{\omega_{\text{pe}}^2}{\omega^2} \cdot \begin{cases} 1, & \vec{A} \nparallel \vec{B} \\ \frac{\omega^2 - \omega_{\text{pe}}^2}{\omega^2 - \omega_{\text{pe}}^2 - \omega_{\text{B}}^2}, & \vec{k} \perp \vec{B} \quad \vec{A} \perp \vec{B} \\ \frac{1}{1 - \omega_{\text{B}}/\omega}, & \vec{k} \nparallel \vec{B} \quad - \text{ circular polarization} \\ \frac{1}{1 + \omega_{\text{B}}/\omega}, & \vec{k} \nparallel \vec{B} \quad + \text{ circular polarization} \end{cases} \quad . \tag{3.54}$$

with the electron gyration frequency $\omega_{\text{B}} = q_e B / m_e$, and $\vec{k}$ the wave vector pointing in direction of wave propagation with $k = 2\pi/\lambda_{\text{X}}$.

EM waves with $\omega \leq \omega_{\text{pe}}$ are not able to propagate in the plasma, their E-field is shielded by the plasma electrons. The critical plasma density n_{cr} is defined as the electron density for which $\omega = \omega_{\text{pe}}$. A laser with ω_L cannot penetrate beyond the spatial plane of critical density with $\omega_L = \omega_{\text{pe}}$. Relativistic particle motion on the laser axis, as seen in the last section, leads to a modification of the particle momentum. With the Maxwell-Ampère and Maxwell-Poisson equation of a laser wave within a plasma, a relativistic dispersion relation is obtained $\omega^2 = \omega_{\text{pe}}^2/\gamma + k^2 c^2$. We obtain the relativistic relations

$$\omega_{\text{pe\_rel}} = \left(\frac{n_e e^2}{\epsilon_0 \langle \gamma \rangle_\tau m_e} \right)^{1/2} \tag{3.55}$$

$$n_{\text{cr}} = \frac{\epsilon_0 \langle \gamma \rangle_\tau m_e \omega_L^2}{e^2} = \frac{1.11 \cdot 10^{21}\,\text{cm}^{-3}}{(\lambda_L \cdot 10^6)^2} \langle \gamma \rangle_\tau \,, \tag{3.56}$$

with $\langle \gamma \rangle_\tau = \sqrt{1 + a_0^2}$, see eq. (3.51). The critical density for $a_0 \approx 1$ corresponds to an electron density of $n_{\text{cr}} = 1.7 \cdot 10^{21}\,\text{cm}^{-3}$ for the central lasing wavelength of a Ti:Sa, which is 800 nm; and $1.11 \cdot 10^{21}\,\text{cm}^{-3}$ for Nd-YAG laser systems of ≈1 µm wavelength.

As the laser itself modifies transparency, the relativistic effect is called self-induced transparency. Using the electric permitvity $\epsilon(\omega) = {}^{k^2c^2}/_{\omega^2}$ we obtain the refractive index in a non-magnetic material $\eta(\omega) = (\epsilon(\omega))^{1/2}$

$$\eta(\omega_L) = (\epsilon(\omega_L))^{1/2} = \left(\frac{k^2c^2}{\omega^2}\right)^{1/2} = \left(1 - \left(\frac{\omega_{\text{pe\_rel}}}{\omega_L}\right)^2\right)^{1/2}. \tag{3.57}$$

Compared to peripheral areas of the laser focus, higher intensities are present in the centre for typical beam shapes such as Gaussian beams or flat-top beams. Thus, the plasma in the centre is more relativistic. Due to the then reduced refractive index in the centre compared to the outer regions, the plasma acts as a focusing lens. The laser focusing in the plasma is called relativistic self-focusing [Max+74]. A higher electron density in the centre due to a higher ionization tend to attenuate the self focusing effect. Competitively, the ponderomotive scattering due to a high intensity gradient diminishes electron density and thereby increases self focusing, Result is a self guiding of the laser beam with undulating beam envelope [Esa+97].

3.4.1.2 Electron Heating in Plasmas

Laser plasma interaction leads to various non-linear collective effects which can not only accelerate a directed beam of electrons but also heat the plasma by inducing isotropic motion. Depending on the experimental conditions, different regimes have to be distinguished. In discussed experiments, we use initially solid targets where electrons are efficiently heated from the critical density boundary, and largely transparent near-critical density targets where a critical density may arise. In literature, underdense plasmas are used for acceleration with the laser wakefield mechanism. This was firstly shown by Mangles et al. [Man+04], by Geddes et al. [Ged+04] and by Faure et al. [Fau+04].

During laser interaction with solid targets, the rising edge of the pulse creates a dense pre-plasma on the target front surface, in such a way the main intensity peak interacts with a boundary of critical density. Considering a plasma with a critical density, the maximum energy gain of electrons due to ponderomotive effects is given with equation (3.51). Thereby, the relative effective temperature of the electron beam can be assumed with

$$k_\text{B}T = mc^2 \cdot \left(\left(1 + a_0^2\right)^{1/2} - 1\right) \tag{3.58}$$

where k_B is the Boltzmann constant. This relation was proposed by Wilks et al. [Wil+92] and experimentally proven by Malka et al. [MM96]. With $a_{0,e} = 2.8$ in our experiment, a beam temperature of $k_\text{B}T \approx 1\,\text{MeV}$ is likely.

Resonant absorption [Fre72; EVK75] is the dominant absorption mechanism of oblique laser pulses at steep plasma density gradients, notably to be distinguished from instability heating for normal incidence. The mechanism is most effective for plasma densities ranging from critical density to densities largely exceeding the critical density [For+77]. Hot electrons are accelerated from the high energy tail of the cold plasma electron distribution, maintaining the energy balance. Cold electrons mostly define the plasma pressure that is in equilibrium with the laser pressure at the maximum penetration depth, maintaining momentum balance.

Brunel heating and $\vec{J} \times \vec{B}$ heating are further important non-linear effects related to dense plasmas. Brunel heating describes the interaction of an intense p-polarized obliquely incident laser beam with a dense plasma. The laser coming from $-\infty$ propagates to the critical density at $z = 0$ and is reflected. Thereby it crosses a thin layer of underdense pre-plasma or a steep density gradient. The incidence angle ϕ allows the separation into a normal and perpendicular E-field component. The field component perpendicular to the plane of critical

density as well as the laser intensity gradient are able to accelerate electrons as already discussed in section 3.4.1. The E-field normal to the plasma density gradient has to vanish at the critical density. During the first laser half period with $E_z > 0$, electrons initially at rest are pulled out of the plasma surface to maintain a zero field on the critical density seen as a perfect conductor's surface. A potential builds up and decelerates electrons. During the second laser half cycle, both, potential and laser field, accelerate outer electrons towards the critical density. These electrons cross the critical density with a net gain of energy in the order of the ponderomotive potential with an effective $a_p = a_0 \sin[\phi]$. The efficiency of this process was first discussed by Brunel [Bru87] in 1987.

So called $\vec{J} \times \vec{B}$ heating [KE85] is an effect of relativistic electron motion in B-fields normal to the critical density due to the oscillating component of the ponderomotive force. Assuming a p-polarized incident laser beam, the normal B-field component is given by $F_z = -qv_\perp B$. P-polarization and a first order approximation of velocities exclusively due to a perpendicular E-field allow this two-dimensional description with $\vec{B}$ in the plane $z = 0$. $v_\perp$ and B are oscillating with a phase shift of $\pi/2$. Using all relations obtained in section 3.4.1 leads to:

$$F_z = -qv_\perp B = -q\frac{p_\perp}{\gamma m}B \tag{3.59}$$

$$= +q\frac{-qA_0 \cos\left[k_\mathrm{L} z - \omega_\mathrm{L} t\right]}{\gamma m} k_L A_0 \sin\left[k_\mathrm{L} z - \omega_\mathrm{L} t\right] \tag{3.60}$$

$$= -mc^2 \cdot \frac{a_0^2 k_L}{2\left(1 + a_0^2\right)^{1/2}} \cdot \sin\left[2\left(k_\mathrm{L} z - \omega_\mathrm{L} t\right)\right] \tag{3.61}$$

Twice per laser oscillation, electrons are moved away from critical density in direction of free space. In analogy to Brunel heating, a potential builds up until accelerating force and decelerating electrostatic field are in equilibrium. Acceleration towards the critical density is then triggered by both, the sign change of F_z and the electric potential.

Once passed the critical density, the accelerated electrons propagate further in the plasma. They interact with plasma waves, plasma electrons and their own self-induced fields. An important return current builds up to compensate the lack of electrons on the target front side. This causes ohmic heating of the plasma, explained in more detail in [Pas+04] and [Tik02]. Plasma resistivity variation strongly depends on the temperature. That gives rise to a spatial variation of the return current driving E-field which causes an azimuthal B-field to rise, seen in [BK03]. On the basis of self-focusing, the angular spread of accelerated electrons remains small. In a finite target, electrons finally arrive the rear side. The successive dynamics is discussed in the following section.

3.4.2 Laser Driven Acceleration of Ion Beams

Two main regimes of laser-plasma interaction depend on the transparency properties of the ionized medium. For electron densities lower than the critical density, the laser pulse can propagate over large distances in the plasma, generating a strong plasma wake. Experimentally, low densities are achieved by using gaseous targets – gas jets or cells. Ion acceleration up to the MeV-level has been reported in this regime [Lif+14; Wil+06], with origin in the charge separation in the ponderomotive channel that is formed at the laser wake. Note that electron beams can be accelerated even up to the GeV [Ami+98; Lee+14].

In the regime of so-called over-critical densities ranging between $10 \cdot 10^{21}$ cm^{-3} to $100 \cdot 10^{21}$ cm^{-3}, plasmas are generated from high-pressure gas, solid and liquid targets. The acceleration mechanism at play usually is

TNSA [Sna+00; Wil+01] at density discontinuities, the Break-Out-Afterburner (BOA) [Don+03; Yin+06; Wen+18] acceleration in relativistically induced transparent targets and Hole Boring (HB) [Wil+92] at the laser position. Directional broadband proton beams have been reported, achieving maximum energies of 100 MeV [DNP12b; MBP13].

Fewer studies have addressed the case of intense short laser pulses interacting with so-called near-critical plasmas, where $n_e \approx n_{\mathrm{cr}}$. This interaction regime offers the optimized energy coupling between laser and plasma, compared to the typical scaling for over and under dense cases [Wil+09; Fiú+12; Syl+13; Deb+17]. Multiple possible ion acceleration scenarios have been proposed referring to this kind of interaction. An intense short laser pulse impinging onto a near-critical plasma can drive a strong charge separation and electron energization, which could trigger a collisionless shock into the plasma. When moving down a density gradient, this plasma structure is predicted to accelerate a fraction of the background ions via CSA to energies higher those attained through standard TNSA [Fiú+12; Sil+04; Liu+16; d'H+10; d'H+13]. CSA is predicted to generate narrow and spectrally peaked ion beams, with up to 100s MeV of energy. Other acceleration mechanisms are also proposed in near-critical interaction and may appear simultaneously, such as the Magnetic Vortex Acceleration (MVA) [Bul+10; Nak+10; Syl+12a; Hel+16; Par+19] and TNSA.

3.4.2.1 Target Normal Sheath Acceleration

The interaction of an ultra-intense laser with a initially solid target produces a divergent multi-energetic quasi neutral particle beam and some relativistic electrons from target front- and rear-surface. The mechanism of acceleration is known as TNSA and was described firstly by Snavely et al. [Sna+00] and Wilks et al. [Wil+01].

An ultra-intense laser of $I_L > 10^{18}\,\mathrm{W\,cm^{-2}}$ has a steep intensity gradient but finite spatial contrast. On a TNSA target front surface, a pre-plasma is formed before the peak intensity arrives. Electrons are accelerated by the laser on the target's front surface by various mechanisms, discussed in the previous section. In addition, a shock is formed due to ablation pressure. Forward accelerated electrons cross the plasma, overtake the shock and propagate through the undisturbed solid part. Targets typically have a thickness of 1 µm to 100 µm. In our experiment, we use a gold foil of 10 µm.

Within the target, electrons become scattered, which broadens the beam. If the electrons are energetic enough, they can leave the target on the rear side and overcome the rising potential barrier. They escape in the free space and a negative potential builds up across the target. The more relativistic electrons escape, the bigger the potential barrier grows and the steeper it becomes. It holds back slower electrons which form a electron sheath above the target's rear surface. Front-sided escape and recirculation of the halted rear side sheath electrons yields a sheath above the target front surface, too. Due to electrostatic equilibrium, this sheaths arise parallel to the target surface. If targets become thicker, the rear side sheath becomes more and more an ideal plane due to the scattered broad beam of electrons escaping the target rear side. The disadvantage of scattering is the energy loss of electrons heating the target. Less energetic electrons are not as likely to escape the potential barrier, which diminishes the sheath potential.

Atoms on the target surface are ionized by the E-field in the order of $\mathrm{TV\,m^{-1}}$ [Heg+03] and subsequently accelerated. TNSA thus is interesting as source of charged particle beams of several MeV due to its short acceleration track compared to standard accelerators with lower E-fields. Accelerated ion species are composed of the usually undesired contamination on the target's surface due to contamination with water or oil. The composition of such a layer was investigated in [Hof14]. As protons have the highest charge to mass ratio, their acceleration is most likely. They trespass the electron sheath, taking with them some co-propagating electrons. The main propagation direction is parallel to the normal vector of the target's rear surface because

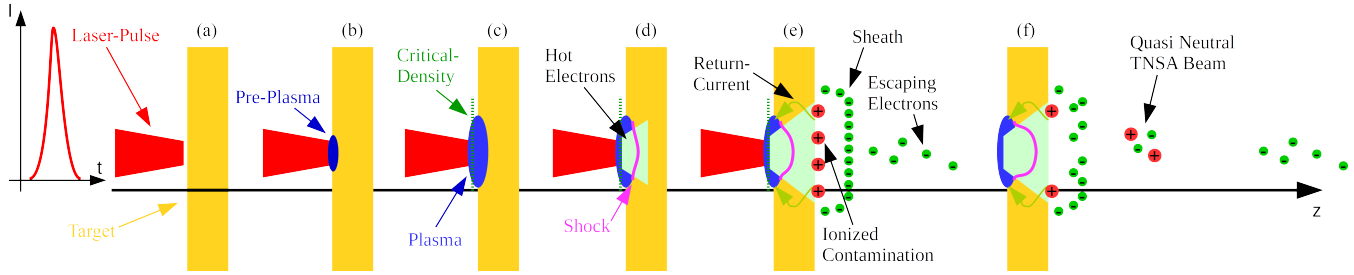

Figure 3.2: TNSA process leading to laser driven proton acceleration by (a) a laser with finite contrast interacting with a initially solid target. The rising edge of laser intensity creates a pre-plasma (b) and heats it. Plasma density rises up to a critical density (c) where the intensity peak becomes reflected. A shock wave is created (d) and meanwhile electrons become forward-accelerated. Escaping fast electrons build up a potential that stops slower electrons which re-circulate and form a sheath (e). Contamination on the target rear side is ionized and subsequently accelerated (f). Accelerated ions take electrons with them forming a quasi-neutral TNSA beam. The process ends due to a disturbance by the shock or by the end of laser-electron acceleration. With ongoing time less electrons are within the sheath and acceleration efficiency drops.

the electron sheath ideally builds up spatially uniform and parallel to the rear side. The whole process is illustrated in figure 3.2.

To summarize, a TNSA beam consisting out of three species: relativistic MeV electrons on the one hand and the co-moving quasi-neutral MeV protons and relatively low energetic electrons on the other hand. Co-propagating protons and electrons form a low density plasma cloud in which recombination can be neglected. This cloud is expanding perpendicular to the main propagation axis, seen as little angular beam divergence in the laboratory frame. In real experiments the electron sheath depends on target thickness and laser intensity. Due to a non-ideal sheath additional beam divergence may occur. Low proton energies have a big divergence of a few tens of degrees, high proton energies show a small divergence of a few degrees. However, beam-divergence is big compared to standard-accelerators, which is reason for our beam tailoring experiment.

Protons moving within the quasi-neutral cloud have a broad range of energies up to a maximum energy which is lastly defined by the laser intensity and contrast assuming a thin target of several µm. In experiments, we obtain exponentially sloping energy distributions with a sharply dropping edge for a maximum energy [Bor+06]. The dependence on target thickness is illustrated in figure 3.3 taken from [Nee+06]. The inset in this figure shows an energy-resolved proton spectrum with exponential part and cut-off energy. Variation in target thickness leads to a maximum energy cut-off related to 10 µm thickness for Al targets. For further investigation of the dependence on target thickness and laser intensity as well as laser pre-pulses due to Amplified Spontaneous Emission (ASE), see [Kal+04]. At the Petawatt High Energy Laser for Heavy Ion Experiments (PHELIX) system, research was carried out by Wagner et al. [Wag+16]. According to a quasi-static model of Passoni and Lontano [PL08], which is supported by experimental data, the maximum energy for sub-picosecond pulses is given with

$$E^{\max} = k_{\mathrm{B}}T \cdot (4.8 + 0.8 \cdot \ln[E_{\mathrm{J}}]) \tag{3.62}$$

where E_{J} is the laser energy in J and $k_{\mathrm{B}}T$ is the hot electrons' temperature in terms of energy. This model holds for pulses of 100 mJ $< E_{\mathrm{L}} <$ 500 J, a pulse duration of 40 fs $< \tau_{\mathrm{L}} <$ 900 fs and high laser intensities of

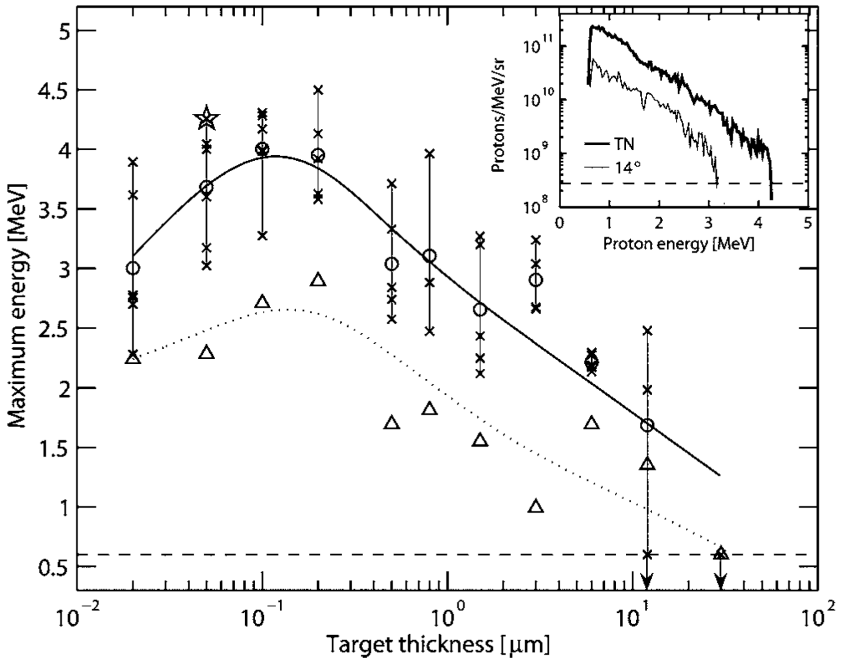

Figure 3.3: Maximum TNSA proton energies obtained as a function of Al-target thickness. Cut-off energies measured along the target normal (crosses). The solid line gives a fit to the on-axis average value for each thickness (circles). Triangles represent average data measured for a $14°$ off-normal, their fit is given with the dotted line. The dashed line represents the detection limit. The inset shows both energy resolved proton-spectra obtained during the shot labled with a star. Laser pulses with 33 fs pulse duration, $10^{19}\,\mathrm{W\,cm^{-2}}$ intensity and an energy of $300\,\mathrm{mJ}$ for on target contrast of 10^{10} archieved using a plasma mirror. Figure taken from [Nee+06].

$3 \cdot 10^{18}\,\mathrm{W\,cm^{-2}} < I_\mathrm{L} < 300 \cdot 10^{18}\,\mathrm{W\,cm^{-2}}$. T is estimated on the basis of the ponderomotive force with

$$k_\mathrm{B}T \approx mc^2 \cdot \left(1 + \frac{2E_\mathrm{P}}{mc^2}\right)^{1/2}, \tag{3.63}$$

following [Wil+01], where E_P is the ponderomotive potential energy of the laser with

$$E_{\mathrm{P,\,eV}} \approx 9.33 \cdot 10^{-14} \cdot I_{\mathrm{W\,cm^{-2}}} \cdot \lambda^2_{\mu\mathrm{m}}. \tag{3.64}$$

For a laser with $I_L = 10^{19}\,\mathrm{W\,cm^{-2}}$, $\lambda = 1.053\,\mu\mathrm{m}$ and $E = 50\,\mathrm{J}$ one can estimate a maximum proton energy of $E^\mathrm{max} \approx 9\,\mathrm{MeV}$ if the laser is absorbed perfectly.

3.4.2.2 Acceleration from Near-critical Density Targets

Direct Coulomb Explosion (DCE) from uniformly charged spheres result in straight longitudinal phase-space profiles [Pea+07]. The ion energy distribution $\mathrm{d}_E N$ is proportional to

$$f(E) = \frac{3R_0(4\pi\epsilon_0)}{2q_\mathrm{i}^2(1-1/\chi_\mathrm{i})^{3/2}} \cdot \sqrt{E_\mathrm{i}/E_\mathrm{C}} \quad , \tag{3.65}$$

with R_0 the initial radius of the sphere, E_i the ion energy for ions with charge q_i, $E_\mathrm{C} = q_\mathrm{i}^2 N_\mathrm{i0}/4\pi\epsilon_0 R_0$ the cut-off energy of the spectrum with initial number of N_i0 ions in the sphere, and χ_i the expansion factor constant for all ions. The later is time depended and can be calculated with the ion plasma frequency ω_pi via

$$\sqrt{\chi_\mathrm{i} \cdot (\chi_\mathrm{i} - 1)} + \log\left[\sqrt{\chi_\mathrm{i}} + \sqrt{\chi_\mathrm{i} - 1}\right] = \sqrt{\frac{2}{3}} \cdot \omega_\mathrm{pi} t \quad . \tag{3.66}$$

For charged spheres with radially decreasing charge density profiles, acceleration of innermost ions yields higher energies than for outermost ions. Inner ions overtake outer ions and eventually form a shock-like shell in the ion phase space. The accelerated ion energy spectrum depends fully on the initial plasma density and size as well as the electron temperature distribution. Simplifying the origin of the dynamics to a quasi-neutral region of radius R_0 filled with cold ions and hot electrons with Maxwellian energy distribution, the full acceleration dynamics can be characterized by a dimensionless parameter,

$$\mathfrak{T} = \frac{Z_\mathrm{i} k_\mathrm{B} T_0}{E_\mathrm{C}} = \frac{4\pi\epsilon_0 Z_\mathrm{i} k_\mathrm{B} T_0 R_0}{q_\mathrm{i}^2 N_\mathrm{i0}} = 3 \cdot \frac{\epsilon_0 k_\mathrm{B} T_0}{n_\mathrm{e0} q_\mathrm{e}^2 R_0^2} = 3 \cdot \frac{\lambda_\mathrm{D,e}^2}{R_0^2} \quad . \tag{3.67}$$

Ion number density distributions asymptotically approach the solution for uniformly charged spheres in the limit of $\mathfrak{T} \to 1$, for all $\mathfrak{T} > 0.5$ the ion spectra rise monotonic. For $\mathfrak{T} < 0.5$, the spectra show a maximum for low energies. The actual spectral cut-off energy can be fitted with

$$E_\mathrm{SCO} = \frac{2.28 \cdot \mathfrak{T}^{3/4}}{\left(1 + (2.28 \cdot \mathfrak{T}^{3/4})^{1.43}\right)^{1/1.43}} \cdot E_\mathrm{C} \quad , \tag{3.68}$$

and the energy corresponding to the maximum of the number density distribution was found to follow a power law

$$E_\mathrm{MND} = 0.3 \cdot \mathfrak{T}^{0.9} \cdot E_\mathrm{C} \quad . \tag{3.69}$$

Thus, E_MND depends weakly on the density distribution and is mostly defined by the electron kinetics.

Collisionless Shock Acceleration (CSA) starts in such a shock-like mechanism as during strong asymmetrical DCE in near-critical density plasma with steep density profile. The shock shell is formed in the decreasing plasma density gradient after the rapid build up of a charge imbalance by means of ultra-relativistic electron acceleration [d'H+10]. Ions located downstream can be reflected if the ion wave launched during this process overcomes the ion sound speed [Nov+15], resulting in acceleration to twice the shock velocity. The energy of the shock is ultimately dissipated by wave breaking in the plasma density down-ramp, driven by the strong E-field in this region that is mostly created by the laser-heated electron dynamics.

Considered targets typically have longitudinal profiles with tens of µm FWHM and peak electron densities of several tenth of one critical density. Note, that TNSA is also a possible from near-critical density targets at extremely sharp density gradients.

The possibility of several simultaneous ion acceleration mechanisms and the presence of many different non-linear plasma effects, such as relativistic self-focusing [Syl+13], magnetic vortex generation [Syl+12a; Nak+10] and magnetic self-channelling [PV96], make the controlled ion acceleration from near-critical targets in experiments especially complex.

3.5 Beams of Ionizing Radiation

In the frame of the target material, the transferred energy per unit length of propagation is referred to as Linear Energy Transfer (LET). The typical dependency of energy loss and scattering cross-sections on mass, charge and energy are reflected in quite different evolution of LET with penetration depth, see fig. 3.4. Massive charged particles such as electrons and protons have a maximum LET for low kinetic energy. Concerning proton beams, the LET and therewith the deposited energy per unit mass, the dose, is maximized just at the end of the particles' projected range. The dose deposition of individual electrons resembles this peaked evolution along the trajectory, but scattering events yield a quite different statistical sum projected to the initial forward direction. EM radiation such as high energy photons (X-rays) attenuate, with a peaked dose deposition for shallow penetration depth due to the build up of dose deposition by ionized electrons in the material. The following section details on the exact energy deposition mechanisms.

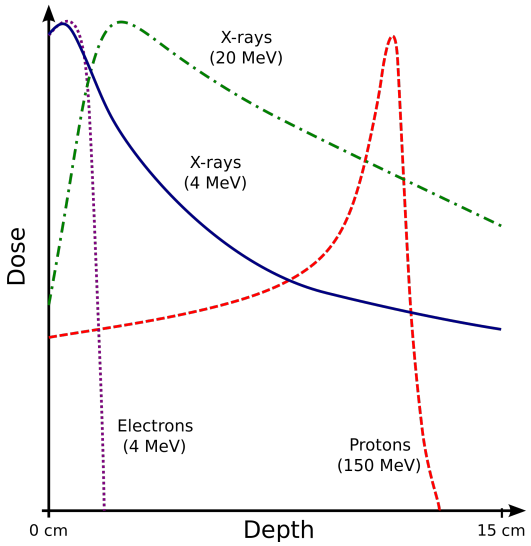

Figure 3.4: Averaged LET dose deposition in function of the penetration depth for typical ionizing radiation, assumed to impact in statistically relevant number from free space into a solid-state target material resembling tissue [Whi+89] at a given impact energy. Image extracted from [Cep10].

3.5.1 X-ray Absorption and Attenuation in Matter

High energy photons interact with matter due to incoherent scattering (Compton scattering), coherent scattering (Rayleigh scattering), photoelectric absorption as well as pair production processes in both the field of nuclei and electrons. The summed total cross section σ_{X} with one atom species is depending on the photon energy. The absorption in a material sample is proportional to the concentration of an attenuating species with its characteristic σ_{X}, and to the optical path length across the sample. The linear attenuation coefficient μ_{lac} in homogeneous media calculates with

$$\mu_{\mathrm{lac}} = \sum_i \sigma_{\mathrm{X},i} n_i \quad , \tag{3.70}$$

as summed contribution over all present species i with individual number densities n_i. The mass attenuation coefficient calculates as ratio

$$\mu_{\text{mac}} = \frac{\mu_{\text{lac}}}{\rho} \quad , \tag{3.71}$$

with mass density ρ. Process-individual and total mass attenuation coefficients for iron are plotted in fig. 3.5. Losses due to incoherent scattering decreases towards low energy radiation, as the scattering evolves from inelastic (Compton effect), to elastic Thomson scattering, then with no alteration of the photon frequency. Losses due to coherent scattering increase towards low energy radiation, due to large sized wavelengths compared to resonant scattering bodies. The polarizability increases and therefore the capacity of re-radiation at the same frequency.

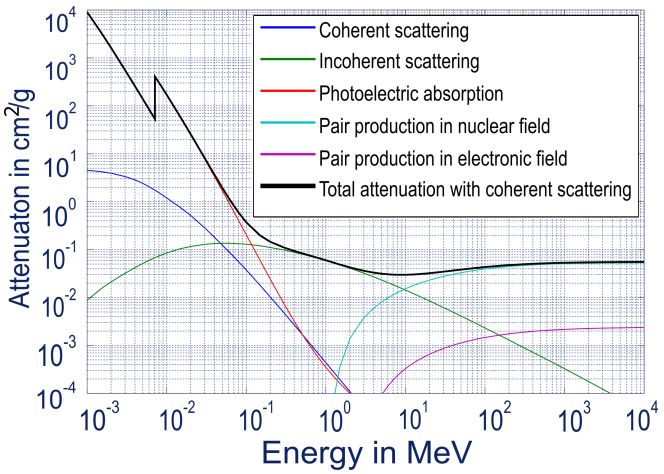

Figure 3.5: Photon mass attenuation coefficients for iron for the most likely absorption mechanisms. Extracted from [Mat+10].

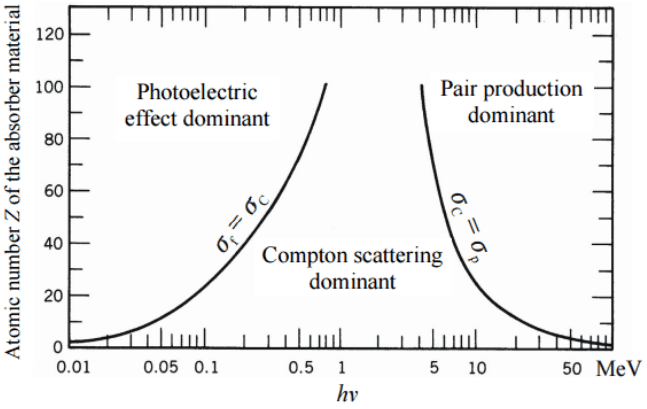

Figure 3.6: Dependency of photoelectric effect, Compton scattering and pair production on photon energy and atomic number in interactions with solid matter. Image extracted from [pow20].

The photoelectric effect describes the ionization of an orbital electron with binding energy lower than the photon energy. Photoionization is especially efficient if the photon energy is equal to a particular binding energy.

Absorption by pair production concerns photons sufficiently energetic to overcome the total rest mass energy of the particle-antiparticle pair, *e.g.* electron-positron pair and muon-antimuon pair. Pair production from one photon must occur in vicinity of a recoiling interaction partner, such as nucleus or electron, for the momentum conservation.

The energy range for the respective dominance of photoelectric effect, Compton scattering and pair production varies with the atomic number Z, see fig. 3.6. Attenuation follows as an exponential decay of the intensity of a photon bunch with penetration depth x, the so called Lambert-Beer law

$$I_{\text{X}}(x) = I_0 \exp\left[-x \cdot \mu_{\text{lac}}\right] \quad , \tag{3.72}$$

with initial intensity I_0.

3.5.2 Stopping Power on Massive Projectiles

The stopping power (SP) is the ability of a medium to impose energy loss on penetrating massive projectiles through collisional and radiative damping mechanisms. The deposited energy of a projectile in a target medium along a trajectory with coordinate x can be calculated if the stopping power $S = \mathrm{d}_x E$ of the medium on a given type of projectile is known. When fast charged particles move through solid matter, they perform inelastic collisions with the material's shell electrons and interact with the atomic nuclei themselves. This leads to excitation and ionization, nuclear scattering or even nuclear reactions of the atoms. Secondary photons in the vicinity of the strong E-field of a nucleus are furthermore reported to give raise to pair production [BH34] and therewith shielding effects. As a net result, the traversing particle looses energy.

Assumptions common to most theoretical treatment of the problem are that the particles interact only via the EM force and nuclear reactions are discarded. It is required that the charge state of the projectile does not alter for the whole interaction. Furthermore, it can be derived that massive high energy projectiles transfer more energy to the electrons of the target than to the nuclei. The ratio of nuclear SP to electron SP is

$$\frac{S_\mathrm{n}}{S_\mathrm{e}} >= \frac{m_\mathrm{e} \cdot Z_\mathrm{t}}{M_\mathrm{t}} \quad , \tag{3.73}$$

with Z_t and M_t the target atomic number and weight in u respectively [Bet30], and m_e the electron rest mass. For hydrogen targets this ratio evaluates to 0.05 % and for carbon targets to 0.03 % - even considering experimental data, this ratio remains below $100 \cdot 10^{-3}$ % [Zie99]. For low projectile energies, nuclear interaction dominates.

3.5.2.1 Stopping Power on Heavy Ions

The following relativistic relationship approximates this momentum transfer from projectile to target electrons for charged particles heavier than electrons [Mol32; Bet32], in its first version proposed by Hans Bethe in 1930 and derived through quantum mechanical perturbation theory [Bet30]. Bethe extends the Rutherford differential cross section [Ros52; Bic06] for scattering from free electrons with a term taking into account the bound state of electrons.

$$S = \mathrm{d}_x E = -\frac{4\pi n_\mathrm{e} Z_\mathrm{i}^2}{m_\mathrm{e} c^2 \beta_\mathrm{i}^2} \cdot \left(\frac{q_\mathrm{e}^2}{4\pi\epsilon_0}\right)^2 \cdot \left[\ln\left(\frac{2 m_\mathrm{e} c^2 \beta_\mathrm{i}^2}{I_\mathrm{e} \cdot (1-\beta_\mathrm{i}^2)}\right) - \beta_\mathrm{i}^2\right] \quad , \tag{3.74}$$

for projectiles with maximim charge state Z_i and velocity $v_\mathrm{i} = \beta_\mathrm{i} \cdot c$, where c is the speed of light and β_i the relative particle velocity. q_e denotes the elementary charge, ϵ_0 the E-field constant, n_e the electron density of the target material, and I_e the mean excitation potential of the target material. This formulation incorporates relativistic effects and the atomic energy structure of the target medium. Note that in general, for practical purposes in high energy density physics calculations, the mass of ion projectiles is neglected as it has only a small influence on the maximum energy that a charged particle can transfer to a bound electron [Tan+18, in sec. 33].

The mean excitation potential or energy of the material is the logarithmic average over each excitation energy weightened by the corresponding oscillator strength [Fan63]. It is determined experimentally and reported from the of the International Commission on Radiation Units (ICRU) [Icra; Icrb], see fig. 3.7.

Experimental observations in discrepancy with the analytic expression eq. (3.74) motivated formulation of many corrections that correspond to higher powers of Z_i.

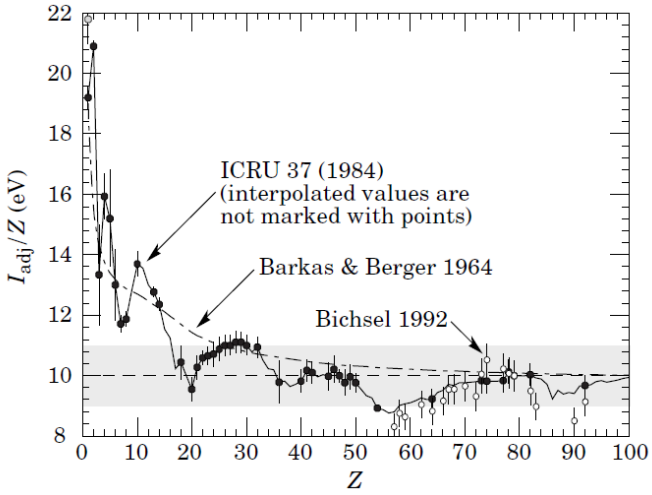

Figure 3.7: Mean excitation potential I_e renormalized to the atomic charge Z_t of the target material, as function of the atomic charge Z_t in accordance with ICRU [Icrb]. Experimental measurements with error bars are plotted together with interpolated values in this extract from [Tan+18]. Two distinct points are measured for $Z_t = 1$ with the grey data point employing liquid H_2 and the black data point for H_2 gas. Open circles show data obtained by Bichsel [Bic92] for higher Z_t. The dash-dotted curve is from the approximate formula of Barkas [Bar64].

The Bloch-correction [Blo33; MM12] builds the bridge between the quantized Bethe formalism and the classical Bohr calculation [Boh13]: Bloch shows that Bethes initial assumptions on the nature of the electron waves are valid in the limit of low momentum transfer and Bohrs classical derivation would be the limit solution for large momentum transfer [Zie99]. The Bloch-correction is proportional to Z_i^4.

Two more major extensions of the stopping power formulation are Shell Correction and Density Correction [Fan63]. The Shell Correction term corrects for the electron velocity distribution in the target and is important when the projectile velocity is not large compared to the velocities of atomic electrons. This term vanishes for flat distributions of many electrons and is therefore invers proportional to the atomic charge of the target Z_t^{-1}. The Density Correction term corrects for a possible dielectric polarization of the target and gains importance, counteracting the increasing distant-collision contribution, for increasing particle energies.

As further theoretical refinement, Barkas-splitting and Barkas-Andersen-correction [SS] refer to corrections in Z_i^3. Barkas-splitting describes that the stopping power on a positively charged particle can be larger than for its antiparticle [Smi+53; Bar56; Bar63] and the Barkas-Andersen-correction concerns a velocity dependent deviation $\Delta S(Z_i^2(v_i))$ for light projectile ions [And+69; And+77a; And+77b].

The complete formalism is referred to as Bethe-Bloch Theory nevertheless Bethe, Bloch, Barkas, Fermi and Fano are all equally important contributors. The formalism describes the energy loss of pions, muons and ions with $\beta_i \cdot \gamma_i$ ranging up to several 10s [Bic+05], here γ_i denotes the relativistic factor of projectiles. Radiative effects are essential contributor to an exponential increase of energy loss for higher energies. For the low energy limit, the formalism is only valid for ion energies high enough to prevent a pick-up of charges from the medium. Such lowering of the ion charge state lowers the stopping power. The lower limit of validity are projectile energies of $E_i <= M_i(Z_i - 1.5)$ for $Z_i > 2$ with a limit of 500 keV for protons [Bic92] where M_i denotes the atomic mass in u and E_i results in MeV. Fits to experimental data are widely used to predict stopping power for low ion energies [ST; Zie], or the so called effective charge for partially neutralized

projectiles is introduced as fitting parameter to predict stopping according to Bethe-Bloch beyond the theory's limits. An extract from the [ST] data base for protons traversing iron is plotted in fig. 3.8.

The accuracy of stopping power calculations compared to the use of experimental data is difficult to evaluate, as experimental errors and structural differences in targets already cause a significant discrepancy between experimental data sets. For hydrogen and helium projectiles on a nickel target, 30 experimental data sets show an agreement to $\pm 3\,\%$ [Zie99], which is related to ion channelling in crystalline structures among other causes.

However, ions loose most of their energy shortly before the end of the penetration range in the stopping power maximum. The characteristic shape of ionic energy loss with respect to the travel range is a slowly increasing deposition rate, called tail, followed by a rapidly growing deposition rate due to the stopping power peak for small particle energies. It is called Bragg-peak, after William Henry Bragg who discovered it in 1903 [Sig06]. The dose-depth profile of a particle beam can be calculated by probabilistic numerical simulations, so called Monte-Carlo simulations, also taking into account scattering events and cascade effects according to their likelihood. With the code Pythonic Stopping and Track Analysis for Particle Detectors by Transport of Ions in Matter (PySTarT), this work presents a pythonic pilot of Stopping and Range of Ions in Matter (SRIM) [Zie] to calculate ion ranges and dose-depth profiles, see section 7.4.

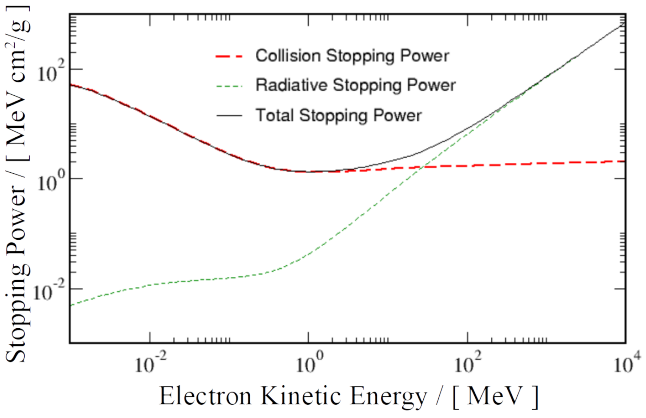

Figure 3.8: Stopping power for electrons in solid iron. Data extracted from [ST].

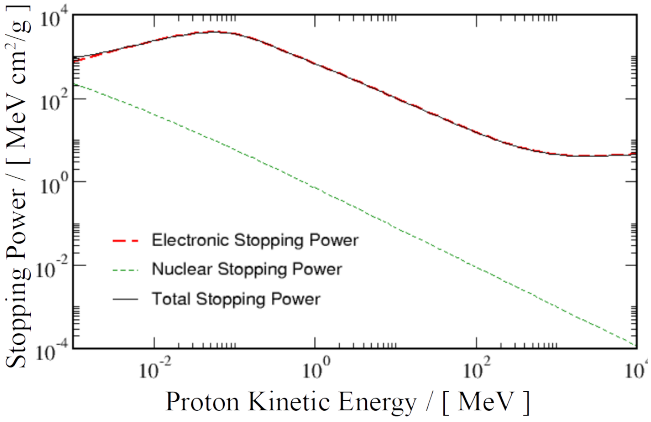

Figure 3.9: Stopping power for protons in solid iron. Data extracted from [ST].

3.5.2.2 Stopping Power on Electrons

Low energy electron collisions with nuclei are quasi-elastic, for the high mass of nuclei. Electrons' inelastic collisions can excite orbital electrons, followed by radiative an non-radiative de-excitation channels that trigger secondary radiation and material heating respectively. From ionization result secondary electrons and reaction cascades such as the Auger effect, where the inner-shell vacancy is filled by an outer-shell electron under emission of a photon or an outer shell electron. High energy electrons dissipate their energy due to radiative effects such as Bremsstrahlung and Cherenkov radiation into photons of broad continuous spectra. Bremsstrahlung is radiation produced during the deceleration of a charged particle in an EM field. The term mostly refers to a broad spectrum of photons that results from deceleration of a charged particle in vicinity of another charged particle, but comprises radiation from radial acceleration (so called Synchrotron Radiation), electron-positron-emission during beta decay and radiation emitted from atoms due to their polarizability by

incident charged particles. Cherenkov radiation is emitted from charged particles that traverses a dielectric medium with a speed greater than the speed of light in the medium.

Collisional and radiative losses yield a total energy depended SP, an extract from the [ST] data base for electrons traversing iron is plotted in fig. 3.9.

Especially for low electron energies, models that predict two dimensional (2D) dose-depth profiles are not satisfactory due to difficulties to model the cross section of collisions. The deposited dose can be calculated for a linear range following the electron trajectory, simply by means of tabulated stopping power values. With pyPEST, this work embodies a pythonic script to calculate electron path-lengths for several published tabulated materials, see section 7.3.

3.5.3 Material Damage by Ionizing Radiation

Ionizing radiation describes particles and EM waves that carry sufficient energy to liberate electrons from their orbitals, whether or not the energy and species depended cross-section for reactions involving ionization are higher than for other reaction channels. This work will regard material damage as the change of the target material away from its initial state. Damage mechanisms comprise displacement damage, excitation and ionization. For displacement damage, the type of radiation is less important and dose and dose rate are important. For excitation and ionization reactions, the type of radiation is important due to different interaction mechanisms and chain-reactions, *e.g.* neutrons (a) enter binary collisions, with efficient energy transfer to nuclei of similar mass, (b) knocked atoms recoil and cause secondary effects such as ionization and excitation of electrons and displacement of other atoms, and (c) high energy photons from radiative transitions interact as discussed here-before. Likely damage by ions, electrons and photons follows respectively from the processes discussed above. The atomic or molecular damage can cause chemical reactions, such as radical formation.

The primary energy transfer can also cause phonon excitation in solid material. From phonon de-excitation results ultimately an increase of target material temperature, as from all non-radiative de-excitation transitions. Thus, energizing can cause phase transitions, such as melting.

LET beyond the ionization threshold triggers secondary radiation by liberated electrons, that transport energies away from the primary track. The maximum energy that can be transferred from a massive projectile to a free electron is

$$T_{\mathrm{max}} = \frac{2 \cdot m_{\mathrm{e}} c^2 \cdot \left(\gamma_{\mathrm{i}} \beta_{\mathrm{i}}\right)^2}{1 + 2\gamma_{\mathrm{i}} m_{\mathrm{e}}/M_{\mathrm{i}} + \left(m_{\mathrm{e}}/M_{\mathrm{i}}\right)^2} \quad , \tag{3.75}$$

with projectile mass M_{i}. This maximum energy represents the higher energy cut-off of the spectrum of energetic secondary electrons. Such energetic electrons are referred to as δ-rays. The form of the spectrum depends on projectile species, for further reading see [Bic+05]. Third order effects occur due to photons due to the interaction of secondary electrons, and so forth.

3.6 Concepts of Optics

Two major approaches to describe the propagation of radiation in the wavelength range of light between the ultra violet (UV) and near infrared (NIR) regimes between 10 nm and 1.4 µm are geometrical optics and

Fourier optics. Geometrical optics argues with Fermat's principle of the least time and the Huygens-Fresnel principle, Fourier optics considers propagating EM waves as being naturally made up of a set of eigenmodes. The following derivations deploy the approach of geometrical optics, based on derivations in [Dre99; HL18], recommended for further reading also on a more physical derivation.

The ratio between the speed of light c in vacuum and the frequency specific phase velocity of an EM wave $v_{\text{ph,X}}$ in a material defines the refractive index

$$\eta_{\text{m}} := \frac{c}{v_{\text{ph}}} = \sqrt{\epsilon(\omega)\mu(\omega)} \quad , \tag{3.76}$$

with electric permittivity $\epsilon(\omega)$ and magnetic susceptibility $\mu(\omega)$. It is depended of material and wavelength and often approximated in second order to

$$\eta_{\text{m}} \approx A_{\text{m}} + B_{\text{m}}/\lambda_{\text{X}}^2 + i \cdot \mu_{\text{ext,m}} \quad , \tag{3.77}$$

with material constants A and B and an imaginary part containing an extinction coefficient $\mu_{\text{ext,m}} = \lambda_{\text{X}}\mu_{\text{lac}}/4\pi$. The dependence on the wavelength causes dispersion, the spatial division of an initially co-propagating broad spectrum. At the interface between two media of different refractive index, EM waves with oblique incidence are deflected. This so-called refraction is due to the different phase speed in both media, that forces the wave front to bend. It follows Snell–Descartes' law

$$\eta_{\text{m1}} \sin(\theta_{\text{m1}}) = \eta_{\text{m2}} \sin(\theta_{\text{m2}}) \quad , \tag{3.78}$$

for waves traversing the inter-phase between two media m1 and m2, with angles θ respectively measured from the normal of the boundary. If one of the angles results to be larger than $\pi/2$, the wave is totally reflected at the boundary. The incidence angle for total reflection is called critical angle.

The transmission into the medium is imperfect, resulting in partial specular reflection with equal incidence and reflection angles. Whenever $\theta_{\text{m1}} + \theta_{\text{m2}} = \pi/2$, the reflected wave does not bear a *p*-polarized component with polarization in the plane of incidence direction and interface normal, known as Brewster's law. The reflection is *s*-polarized, with polarization perpendicular to the plane of incidence direction and interface normal.

The focus of a focusing element, such as a curved mirror or a lens, is the point on which incoming collimated light that propagates parallel to the optical axis has the smallest beam waist after the focusing element. The focal length f_{foc} is the distance between the centre-plane of a focusing device and this point. For light propagating on the symmetry axis of a focusing lens, referred to as the optical axis, the focal length in an ambient medium with $\eta \approx 1$ can be calculated with the lensmaker's equation [HL18]

$$\frac{1}{f_{\text{foc}}} = (\eta_{\text{foc}} - 1) \cdot \left[\frac{1}{R_1} - \frac{1}{R_2} + \frac{(\eta_{\text{foc}} - 1) - d_{\text{foc}}}{\eta_{\text{foc}} R_1 R_2}\right] \quad , \tag{3.79}$$

with refractive index of the lens material η_{foc}, both radii of curvature R_1 for the surface facing the incoming beam and R_2 the focus point, and the thickness of the lens along the optical axis d_{foc}. The radii are of positive value for convex curvature and of negative value for concave curvature resulting in positive valued focal length for converging lenses and negative valued focal length for diverging lenses. Real focus points are only obtained for positive focal length.

Lenses have different kind of aberrations that inhibit a perfect focus point. For all incident EM wave packages (a) chromatic aberration due to dispersion yields a wavelength dependent focal position, and (b) spherical aberration due interface geometries that yield a focal position dependent on the distance from the optical axis. For waves in oblique incidence with respect to the optical axis arise (c) an astigmatic aberration due to different focal spots for rays in perpendicular planes yielding a focal line, and (d) coma as additional spherical aberration. Coma can be understood regarding parabolic mirrors that are free of spherical aberration when light enters on the optical axis, but show spherical aberration for obliquely incident light, then called coma. A further aberrations is (e) distortion that is a deviation from rectilinear projection.

Chromatic aberrations can be corrected for a pair of wavelength using systems of one convex and one concave lens, so-called Achromatic Doublets. In so called Aplanats, spherical aberration and coma are corrected for a single wavelength.

Light passing through a finite aperture is diffracting. The diffraction of collimated light of waist d_{beam} by a circular lens results in a radially undulating pattern of adding and annihilating interference in the focus plane, with central maximum called Airy disk. The Airy disk diameter a_{airy} of a spatially flat-top beam is

$$a_{\text{airy}} = 2.44 \frac{f_{\text{foc}} \cdot \lambda_{\text{X}}}{d_{\text{beam}}} \quad . \tag{3.80}$$

Imaging with focusing lenses can be realized in two geometries. In parallel-transport configuration, one positions the object in the focal plane of a lens, thus collimating fluorescence and scattered light. The image plane is created in the focus plane of a successive second lens. Imaging is perfect if entering collimated light exits the system collimated, thus when both inner focal planes superpose. The magnification of such system results from the ratio of the focal length of the imaging lens to the focal length of the collimating lens $m_{\text{mag}} = f_{\text{img\_foc}}/f_{\text{col\_foc}}$.

In convergent-convergent configuration, imaging of an object at distance g to a focusing element yields production of an image at distance b with

$$f_{\text{foc}}^{-1} = g^{-1} + b^{-1} \quad , \tag{3.81}$$

the magnification of the imaging system results to $m_{\text{mag}} = b/g$.

The optical resolution of an imaging system is limited by the diffraction limit, reached when two neighboring Airy-discs can not be distinguished from one another. The so-called Rayleigh criterion defines two points in to be resolved in the image just until the maximum of one's Airy disk overlaps with the minimum boundary of the other's. Following Abbe's law of limiting resolution one can calculate the Airy disk of light coming from point sources, located in an object plane with $g > f_{\text{foc}}$. The smallest measurable distance between objects results with

$$a_{\text{obj\_res}} = 2.44 \frac{\lambda_{\text{X}}}{4 \sin \theta_{\text{NA}}} \quad , \tag{3.82}$$

with half opening angle of the collecting lens $\theta_{\text{NA}} = \arctan\left(d_{\text{foc}}/2g\right)$, depending on the lens diameter d_{foc}. Thus, two distinguishable points in the image plane are $a_{\text{img\_res}} = a_{\text{obj\_res}} \cdot m_{\text{mag}}$ apart.

4 Experimental Diagnostics

Diagnostics are tools that allow to measure designated input and output channels as well as the dynamics of a process in a region of interest (ROI). Temporal diagnostics record time resolved measurements, *e.g.* the auditory perception of organisms is the temporal diagnostics of sound waves. Spatial diagnostics capture projections and images, *e.g.* a photo camera system is a spatial diagnostics by imaging the 3D world on a 2D canvas. Diagnostics often comprise multiple elements to realize the measurement, such as imaging lens and film in a camera.

A limitation common to all measurement devices is the existence of a highest resolved frequency. This so-called Nyquist frequency ν_{nyq} can be resolved by a detector with sampling rate $2\nu_{\text{nyq}}$. E.g. for spatial detectors, this means that a line pair of bright and dark areas is not resolved when it under-spans two pixels of the sensor.

A concept common to all measurements, especially meaningful for imaging systems, is the contrast C_{con}, a metrics on the difference between two measurements I_1 and I_2 that calculates via

$$C_{\text{con}} = \frac{\|I_1 - I_2\|}{\|I_1\| + \|I_2\|} \quad . \tag{4.1}$$

All experiments discussed in this work rely on a similar set of diagnostics. The main diagnostics aim at characterization of laser- and plasma-parameters and measurement of accelerated massive projectiles and induced EM fields.

4.1 Laser Pulse Characterization

In this work, laser pulses serve as essential tool to drive plasma and to probe dynamic processes. Temporal pulse-profile and spatial intensity profile majorly define the temporal evolution of laser intensity and therewith the laser-plasma interaction mechanisms. Laser pulses are characterized for their temporal pulse-profile, their FWHM pulse length and their pulse energy. High driver intensities can only be archived if initially wide laser beams are focused down to small focal spots - characterized by 2D imaging of the time integrated spatial focus intensity distribution. Comparability of results is only possible, if laser-pulses are steadily monitored and re-adjusted.

The temporal pulse profile is measured with multi order intensity autocorrelator systems. A fraction of the collimated laser pulse is split into two equal portions that are focused into a non-linear dielectric material, with small angle between each other. One of both pulses is guided over a optical delay line prior to focusing, which allows to modify the optical path and introduce a time delay τ_{del} between the arrival of both pulses in the dielectric material. Material such as SHG crystals will emit second-harmonic beams of light in function of

the overlapping intensity, directed co-propagating with both pulses and into the half-angle between them. The later beam allows measuring an amplitude $A(\tau_{\text{del}})$ with a slow photo-diode,

$$A(\tau_{\text{del}}) = \int I(t) \cdot I(t - \tau_{\text{del}}) \, \mathrm{d}t \quad . \tag{4.2}$$

The contrast of pulse-peak intensity to the level of ASE on the timescale of hundreds of ps can also be determined from such measurements, *e.g.* with the third harmonic [Sch+17]. Several pre- and post-pulses may arise due to elements in oscillator and laser transport. Too much energy in pre-pulses may cause so-called pre-plasma and renders monitoring important.

Typically, pulse energy is measured by calorimetry. A calorimeter comprises a absorbing material with high heat capacity $C_{\text{cap,m}}$ and a temperature measurement probe. The calorimeter, positioned in such a way it can absorb the full laser pulse, determines the pulse energy via

$$E_{\text{L}} = C_{\text{cap,m}} \cdot \Delta T_{\text{m}} \tag{4.3}$$

with the temperature change of the material ΔT_{m} before and after impact.

Focusing of a laser beam by focusing optics such as lenses or parabolas allows to attain ultra-high intensities. The focal spot size of typically some µm can be measured by the so-called Hartman technique or by imaging with a high magnification imaging system. The Hartman technique utilizes a thin absorbing plate with multiple holes, which is used as aperture to cut-out beamlets from the collimated laser beam in close vicinity to the focusing element. The focus can be measured with high energy shots onto a metallic foil in the focus plane. The beamlets interfere in the focusing plane and imprint the interference pattern on the metal by means of plasma ablation.

Imaging systems typically pick up the diverging laser beam after the focus plane. Low energy pulses are used to avoid damage to optical elements and distortions by non-linear effects. This makes the diagnostic susceptible to miss non-linear effects in the laser beam transport that alter wave-front and thus the focal spot size. Presuming reproducible laser shot conditions, best focus alignment renders individual shots at least comparable.

The imaging lens after the focal spot is referred to as collector, it is important that the spatial envelope of the diverging beam at the lens position is smaller than the lens diameter and that the resolution of the collector is smaller than the laser focal spot. Best results are obtained for microscope objectives closely positioned to the focal spot. Imaging is done typically on CCD chips, connected to a recording device. The image space resolution on the CCD chip is limited by the Nyquist frequency and the resolution of the imaging system.

4.2 Plasma Characterization

This section details on the underlying principles for methods to derive plasma parameters such as density and EM effects such as B-fields in plasma.

Pump-probe experiments deploy short laser pulses as probe to back-light fast processes triggered in a main interaction by a pump laser. Diagnostics of this scheme comprise shadowgraphy, schlieren imaging and interferometry to determine the driven plasma density or density gradients, as well as polarimetry [Seg95] for measurement of B-fields in dielectric matter. The temporal resolution of these diagnostics benefits from the

short laser pulse duration reached in CPA systems, yielding a time integrated measurement mostly impacted by trespass times.

Time resolved measurements of fluorescence effects are possible by streaked imaging of one spatial dimension (1D) with a sweep over time as second image axis. Streaking is practically realized by imaging EM radiation on a thin cathode. The cathode emits electrons that are imaged on a phosphorous screen, passing by a sweeping voltage that deflects them according depending on their ToF. Streaking of plasma self-emission is useful to identify hot plasma regions, streaking of long-pulse back-lighted plasma can be used to determine expansion and cooling times.

4.2.1 Spatial Filtering Techniques as for Shadowgraphy and Schlieren Imaging

Focusing optics are fourier analysers, they allow discrimination of the impinging superposing natural modes in their focus plane. The Fourier transform of the space in the focus plane in front of a lens is formed in the focus plane after the lens. Introduction of masks in the focus plane allows to eliminate certain modes by blocking their propagation. This type of Fourier filtering is referred to as spatial filtering. A low-pass filter allows further propagation of modes close to the optical axis, such as the Airy disk, and a high-pass filter suppresses this modes.

Imaging of an object that is back-lighted by a collimated laser beam through a system with a high-pass filter is one form of schlieren imaging, generally used to visualize zones of changing refractive index which are source to diffraction composed of higher modes. Shadowgraphy, in parallel, deploys a low-pass filter to visualize transmitted light, *e.g.* to conclude on the optical density (OD) of the object.

At typical set-up deployed for schlieren imaging of dynamic processes in this work is illustrated in fig. 4.1. The diagnostic is also known as strioscopic imaging or strioskopy. The term strioscopic is directly referring to the measurement of stripes resulting from diffraction at edges. Here, the diagnostic has a spatially resolving arm with CCD detector and a temporally resolving arm with fast photodiode connected to an oscilloscope.

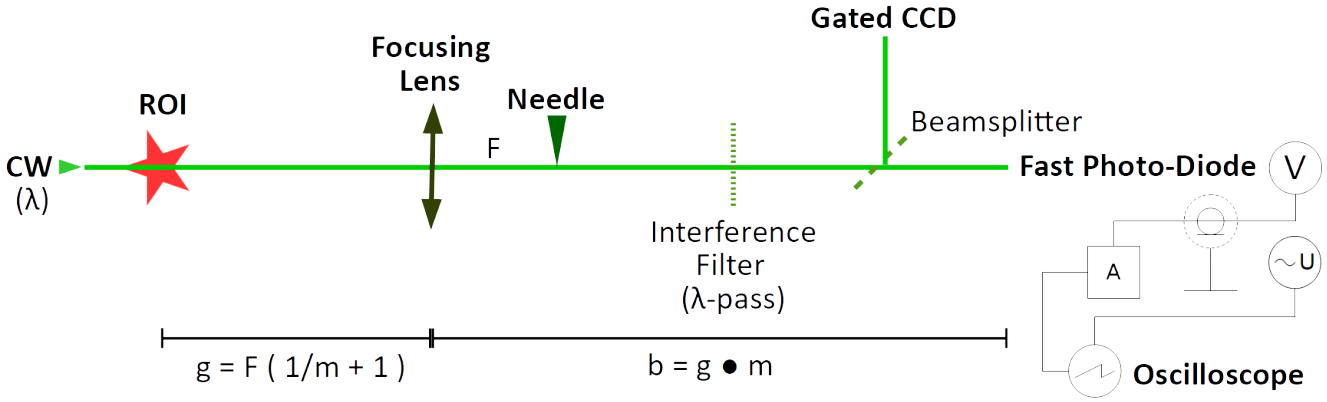

Figure 4.1: Schlieren imaging diagnostics of a dynamic process in the ROI in the object plane of the lens.

The primary constraint is imposed by the magnification m suitable to image the ROI on the CCD and fast photodiode. The ratio of ROI size and respective minimum chip size defines the optimum magnification of the system. Focusing lenses are chosen to achieve a sensor limited rather than optically limited resolution, thus by limiting the optical resolution by the spatial Nyquist frequency of the CCD $a_{\text{img\_res}} < a_{\text{pix}}$, with pixel size a_{pix} for quadratic pixels. In the small angle approximation follows $f_{\text{foc}}\lambda_{\text{X}}/d_{\text{foc}} < a_{\text{pix}}/(1.22(m_{\text{mag}}+1))$. The

wavelength range is constraint by available CW sources, so the focal length and lens diameter are the principle free parameters. Practical boundary conditions imposed by the experimental set-up geometry are further narrowing the parameter range. Finally, the spatial filter can be designed based on the Airy disk size of the lens, in order to block efficiently incoming collimated CW light, *e.g.* with an opaque ball glued to a needle's tip. An interference filter in the beamline, matching the CW wavelength, betters the quality of imaging by suppressing stray light from processes in the ROI.

The success of the temporally resolved measurement depends only on the correct choice of equipment such as fast photo diodes and oscilloscopes of suitable bandwidth.

4.2.2 Interferometric Measurements with a Nomarski Interferometer

Interferometry describes measurement techniques that record interference effects of re-combined space-time separated monochromatic wavefronts on a detector screen. Nomarski interferometry aims at determination of the difference in optical path between two distinct trajectories in space. The difference in optical path can be quantified by measuring the phase shift imprinted into a wavefront after passage of a medium. Particularly, the wavefront is guided through the ROI in such a way that the beam waist also encloses a region that is not affected by any dynamic process. E.g. the phase shift between the wavefront passing through a plasma and the adjacent free space can be measured with a Nomarski interferometer, if the wavefront passes also through vacuum regions not reached by the plasma dynamics.

The interferometer used for parts of this work is based on imaging Nomarski interferometry with a Wollaston prism for wavefront separation. The Wollaston prism is a cubic prism split in two wedges from uni-axial birefringent material. Birefringence follows from the dependency of the refractive index on the polarization direction of light. In case of uni-axial birefringence, waves propagating along the optical axis of the material have the same refractive index η_o for all polarization directions. Waves propagating perpendicular to this axis experience a different refractive index $\eta(\alpha_\mathrm{pol}))$ depending on the angle between wave polarization and optical axis. An initially linearly polarized beam entering the prism perpendicularly to the optical axis and with an angle $\alpha_\mathrm{pol} = \pi/4$ can be decomposed in two projections: in a component with polarization perpendicular to the optical axis, the ordinary beam, and a component with polarization parallel to the optical axis, the extraordinary beam. For $\alpha_\mathrm{pol} = \pi/2$ follows $\eta(\pi/2) = \eta_\mathrm{o}$ and for $\alpha_\mathrm{pol} = 0$ it is defined $\eta(0) =: \eta_\mathrm{e}$. Dispersion yields the wavefront separation in two components of perpendicular polarization. The optical axis of the second wedge is set perpendicular to the optical axis of the first wedge, in such a way the extraordinary beam of the first wedge transforms to the ordinary beam of the second. This enhances the wavefront separation, which is also proportional to the wedge angle α_w. For a divergent ray with initial angle θ to the optical axis, the exiting rays have both angles $\beta_{+/-} = \theta \pm (\eta_\mathrm{e} - \eta_\mathrm{o})\alpha$ [SSP72]. Thus, the wavefront is separated by an angle $\epsilon_\mathrm{w} := 2(\eta_\mathrm{e} - \eta_\mathrm{o})\alpha_\mathrm{pol}$.

The diagnostic is based on a plane wavefront probing both the ROI of diameter D_ROI and a reference region at a centre distance R. The optical axis of the successive imaging system is centred with the observation space of diameter $G_\mathrm{OBS} = (2D + R)$. The plane wavelets are transformed into spherical waves by the focusing optics, converging to the focal point and diverging from there. The Wollaston prism is positioned in the diverging section at distance v from the focus plane, see fig. 4.2.

In front of the prism, a polarizer filters for the unperturbed linear polarization of the wave. In the prism, the spherical wave is split in two wavefronts, with two imaginary sources in a plane parallel to the focal plane. An analysing polarizer is introduced after the prism to obtain visible interference effects, setting its polarization

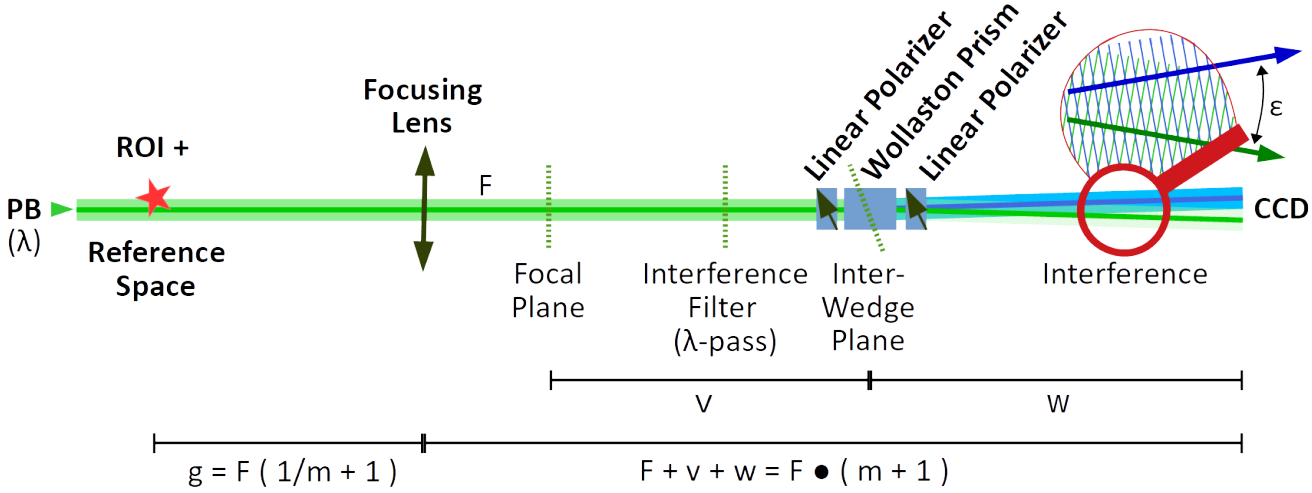

Figure 4.2: Imaging Nomarski interferometry with a Wollaston prism.

parallel to the impinging polarization direction. The undisturbed fringe spacing at distance w from the prism centre plane in forward direction calculates to

$$l = \frac{\lambda_x}{\epsilon_w} \cdot \left(1 + \frac{w}{v}\right) \quad . \tag{4.4}$$

In order to narrow down the parameter range, the following refers to geometrical boundary conditions and constraints on the resolution. The application defines a minimum for G_{OBS}. All optical elements must not clip the beam of diameter $d_b > G_{OBS}$, imposing

$$d_{foc} \geq d_b \quad , \tag{4.5}$$

$$d_w \cdot f_{foc} \geq v \cdot d_b \quad , \tag{4.6}$$

with diameters d_{foc} and d_w in the lens and the inter-wedge plane respectively. Imaging is typically performed with a CCD camera of chip size C_{CCD} and pixel size a_{pix}. The CCD chip should capture the full ROI,

$$D_{ROI} \cdot m_{mag} \leq C_{CCD} \quad , \tag{4.7}$$

$$\Leftrightarrow m_{mag} \leq \frac{C_{CCD}}{D_{ROI}} \quad . \tag{4.8}$$

and goal is a not optically limited resolution

$$\frac{0.61\lambda_x}{\sin\left(\arctan\left(\frac{d_{foc}}{2f_{foc}\left(m_{mag}^{-1}+1\right)}\right)\right)} \leq a_{pix} \quad . \tag{4.9}$$

The fringe spacing l should be by a factor ξ_{airy} larger than a_{img_res}, thus

$$\left(1 + \frac{w}{v}\right) \cdot \sin\left(\arctan\left(\frac{d_{foc}}{2f_{foc}\left(m_{mag}^{-1}+1\right)}\right)\right) \geq 0.61\xi_{airy} \cdot \epsilon_w \quad , \tag{4.10}$$

with typically $\xi_{\text{airy}} > 5$. The overlap of both wave fronts in the image plane should allow interference over the full ROI, thus

$$D_{\text{ROI}} \cdot m_{\text{mag}} \leq 2 \cdot \left(\frac{d_{\text{b}} \cdot (v+w)}{f_{\text{foc}}} - w \tan(\epsilon_{\text{w}}) \right) \quad , \tag{4.11}$$

and the imaging equation eq. (3.81) can be simplified to

$$f_{\text{foc}} \cdot m_{\text{mag}} = v + w \quad . \tag{4.12}$$

Combination of above equations in the limit of small angles $1 \gg d_{\text{foc}}/2f_{\text{foc}}$ yields

$$f_{\text{foc}} \leq \frac{d_{\text{foc}}}{1.22\,(1 + D_{\text{ROI}}/C_{\text{CCD}})} \cdot \min\left[\frac{a_{\text{pix}}}{\lambda_{\text{X}}}; \frac{1 + w/v}{\xi_{\text{airy}} \cdot \epsilon_{\text{w}}} \right] \quad , \tag{4.13}$$

$$\frac{1.22\lambda_{\text{X}} \cdot f_{\text{foc}}}{a_{\text{pix}} \cdot d_{\text{foc}} - 1.22\lambda_{\text{X}} \cdot f_{\text{foc}}} \leq m_{\text{mag}} \leq \min\left[\frac{C_{\text{CCD}}}{D_{\text{ROI}}}; \frac{v \cdot \tan(\epsilon_{\text{w}})}{f_{\text{foc}} \cdot \tan(\epsilon_{\text{w}}) - d_{\text{b}} + D_{\text{ROI}}/2} \right] \quad . \tag{4.14}$$

The parameter space can be further narrowed by limiting the inter-fringe-space s_{OBS} projected back to the observation plane. This spatial resolution calculates as ratio of fringe spacing and magnification and delimits thus

$$s_{\text{OBS\_min}} \leq \frac{\lambda_{\text{X}} \cdot \left(1 + \frac{w}{v}\right)}{\epsilon_{\text{w}} \cdot m_{\text{mag}}} \leq s_{\text{OBS\_max}} \tag{4.15}$$

$$\Leftrightarrow s_{\text{OBS\_min}} \leq \frac{f_{\text{foc}} \cdot \lambda_{\text{X}}}{\epsilon_{\text{w}} \cdot v} \leq s_{\text{OBS\_max}} \quad . \tag{4.16}$$

For a laser wavelength with $\lambda_{\text{X}} \geq \xi_{\text{airy}}\epsilon_{\text{w}}/a_{\text{pix}}$, the range of f_{foc} is limited by eq. (4.13) $\Rightarrow f_{\text{foc}} \leq d_{\text{foc}}a_{\text{pix}}/1.22\lambda_{\text{X}}(1+ D_{\text{ROI}}/C_{\text{CCD}})$. Further choice of the limits on s_{OBS} allows to calculate the appropriate range for v with eq. (4.16). Then, a range for m_{mag} follows from eq. (4.14). The ranges for magnification and focal length allow to retrieve a range for the total optical path length of the full diagnostic. The choice of the pair f_{foc} and m_{mag} can be adapted to the experimental set-up geometry.

The density map of the plasma can be deconvoluted from the interference pattern under assumption of a cylindrical symmetry for the electron density distribution [Hut02]. The relation between index of refraction of a plasma and its density leads us to the phase shift, which in turn can be directly obtained from measurements by means of a Fourier-Transform.

From the definition of the refractive index eq. (3.76) follows for plasma in absence of B-fields

$$\eta_{\text{m}} = \sqrt{1 - \frac{\omega_{\text{pe}}^2}{\omega^2}} \quad , \tag{4.17}$$

depending on the plasma electron density. With also $v_{\text{ph}} = \omega/k$ one derives the non-relativistic dispersion relation in cold plasma $\omega^2 = \omega_{\text{pe}}^2 + k^2c^2$, and thus for the absolute wavevector

$$k_{\text{plasma}} = \frac{\omega}{c} \cdot \sqrt{1 - \frac{\omega_{\text{pe}}^2}{\omega^2}} \quad . \tag{4.18}$$

Compared to a wave propagating through free space with $k_{\text{free}} = \omega/c$, the difference in wave-number

$$\Delta k = k_{\text{plasma}} - k_{\text{free}} \quad | \cdot c \tag{4.19}$$

$$\Leftrightarrow c \cdot \Delta k = \omega - \omega \cdot \sqrt{1 - \frac{\omega_{\text{pe}}^2}{\omega^2}} \quad | \text{ a Tylor expansion at } \quad \frac{\omega_{\text{pe}}}{\omega} = 0 \quad \text{for} \quad \frac{\omega_{\text{pe}}}{\omega} \ll 1 \tag{4.20}$$

$$\Leftrightarrow c \cdot \Delta k \approx \omega \cdot \left(\frac{\omega_{\text{pe}}^2}{2\omega^2} \right) = \frac{n_{\text{e}} q_{\text{e}}^2}{2\epsilon_0 m_{\text{e}} \omega} \quad , \tag{4.21}$$

causes a phase difference $\Delta\Theta$ building up for wave propagation along the optical axis z

$$\Delta\Theta = \int_{-\infty}^{\infty} \Delta k \, \mathrm{d}z = \frac{q_{\text{e}}^2}{2\epsilon_0 m_{\text{e}} c \omega} \cdot \int_{-\infty}^{\infty} n_{\text{e}} \, \mathrm{d}z \quad . \tag{4.22}$$

For a cylindrical symmetry of the plasma in each probed half-space (x, y), underneath and above the plane defined by probe beam propagation and plasma symmetry axis y, eq. (4.22) can be brought to the form of an Abel integral equation. Such allows inversion to deduce the electron density distribution from a measurement of $\Delta\Theta(x, y)$. One assumes that a ray of light passes the plasma in a distance x perpendicular to y and defines $r^2 = z^2 + x^2$ as radial coordinate, then the integral eq. (4.22) can be changed with $\mathrm{d}_r z = r/z = r/\sqrt{r^2 - x^2}$ to

$$\Delta\Theta(x, y) = \frac{q_{\text{e}}^2}{\epsilon_0 m_{\text{e}} c \omega} \cdot \int_x^R \frac{r \cdot n_{\text{e}}(x, y)}{\sqrt{r^2 - x^2}} \, \mathrm{d}r \quad , \tag{4.23}$$

where the cut-off radius R precise a distance with vanishing electron distribution. The Abel inversion yields

$$n_e(r, y) = \frac{q_{\text{e}}^2}{2\epsilon_0 m_{\text{e}} c \omega} \cdot \frac{-1}{\pi} \cdot \int_r^R \frac{\partial_x \Delta\Theta(x, y)}{\sqrt{x^2 - r^2}} \, \mathrm{d}x \quad . \tag{4.24}$$

Noise in experimental data is amplified by numerical integration schemes, therefore a derivative-free elaborate inversion technique was proposed [DB82]. An unknown function $g(r, y)$ can be derived from a known quantity $G(x, y)$ with

$$g(r, y) = \frac{-1}{\pi} \left(\frac{G(R, y) - G(r, y)}{\sqrt{R^2 - r^2}} + \int_r^R \frac{G(x, y) - G(r, y)}{\sqrt{x^2 - r^2}^3} \cdot x \, \mathrm{d}x \right) \quad . \tag{4.25}$$

The inversion can be further enhanced by spline-fitting the data, which allows analytical integration in function of the chosen coefficients [DNP90].

The 2D phase map $\Delta\Theta(x, y)$ follows from the Fourier-Transform of a measured interferogram. The central lobe of the Fourier spectrum of interferometric data corresponds to the Fourier-Transform of the background function $b(x, y)$, whereas the side lobe around the spatial frequency of the interfringes is the shifted Fourier-Transform of the visibility $v(x, y)$. The background function encodes the amplitude distribution and therewith changes in signal brightness, and the visibility encodes the phase shift. To obtain the visibility [CS05] (a) one Fourier transforms the measured interferogram, (b) shifts the centre of the Fourier spectrum to one of the the first order peak centres, and (c) inverse Fourier transforms the changed spectrum clipped around the shifted peak. The phase shift results with [ZS+17]

$$\Delta\Theta(x, y) = \arctan \left(\frac{\mathrm{Im}[v(x, y)]}{\mathrm{Re}[v(x, y)]} \right) \quad . \tag{4.26}$$

The electron density distribution can be readily obtained by an Abel inversion, if cylindrical symmetry is presumed.

Temporal resolution can be managed by gated CCDs or ultra-short laser pulses as probe beam.

4.2.3 Polarimetry

Polarimetry aims at the characterization of a B-field by magneto-optical effects. The propagation of an EM wave through a medium, or its reflection at an interface, can be affected by the presence of a magnetic field, if magnetization induces an anisotropic permittivity $\epsilon(\omega)$, that then causes variations in the phase speed $v_{\mathrm{ph}} = \sqrt{\epsilon_r}^{-1}$, with relative permittivity ϵ_r. Media that show such effects are referred to as magneto-optical materials. When a EM wave propagates through magneto-optical materials, circularly polarized (CP) light of mathematically positive and negative rotating polarization (from the point of view of the source) shows a differing phase speed. For the following, this can be efficiently described with a difference in refractive index $\Delta\eta_{\mathrm{CP}}$.

The Faraday effect describes cases where the B-field is parallel to the wave propagation direction, the Cotton-Mouton effect cases for which the B-field is parallel to the wave polarization and perpendicular to the propagation.

The set-up for polarimetry in this work aims at measurement of the Faraday effect in a magneto optical Terbium Gallium Garnet (TGG) crystal that is aligned in vicinity of the investigated magnetic field. The EM wave of a linearly polarized ultra-short laser pulse is guided through the crystal, therein the magneto-optic effect yields the rotation of the polarization direction around the optical axis. This can be understood if the wave of linear polarization is decomposed in two waves, of negative and positive circular polarization respectively. Their superposition is always a linearly polarized wave and their different phase speed $v_{\mathrm{ph,+}}$ and $v_{\mathrm{ph,-}}$ yields a rotating polarization. The polarization rotation angle Φ results as half the phase difference $\Delta\Theta$ at the back of the crystal with length L_{CRY} along the optical axis. One calculates from the different passage times of the phase in homogeneous media

$$\Phi = \frac{\Delta\Theta}{2} = \frac{\omega_{\mathrm{P}} \cdot \Delta t}{2} = \frac{\omega_{\mathrm{P}} \cdot L_{\mathrm{CRY}}}{2} \cdot \left(v_{\mathrm{ph,-}}^{-1} - v_{\mathrm{ph,+}}^{-1} \right) = \frac{\omega_{\mathrm{P}} \cdot L_{\mathrm{CRY}} \cdot \Delta\eta_{\mathrm{CP}}}{2c} \quad . \tag{4.27}$$

$\Delta\eta_{\mathrm{CP}}$ depends on the longitudinal component of the magnetic field, the angular frequency of the probe beam ω_{P}, and material properties. In a more general form [Gin70]

$$\Phi = \frac{\omega_{\mathrm{P}}}{2c} \cdot \int_{-\infty}^{\infty} \Delta\eta_{\mathrm{CP}} \, \mathrm{d}z \quad . \tag{4.28}$$

Introducing a frequency dependent material constant referred to as Verdet constant, allows to re-write

$$\Phi = -V_{\mathrm{B}} \cdot \int_{-\infty}^{\infty} \vec{B} \cdot \vec{k} \, \mathrm{d}z \quad , \tag{4.29}$$

with optical axis z, and for this work $V_{\mathrm{B}} = V_{\mathrm{TGG}}(808\,\mathrm{nm}) = -60\,\mathrm{rad\,T^{-1}\,m^{-1}}$.

The rotation of polarization is measured with a polarizer-analyser configuration, see fig. 4.3. The intensity of the incoming probe beam I_0 is reduced by a polarizer to I_{P} according to the initial polarization and the respective polarizer angle. This intensity is supposed constant if no changes to the alignment for incoming

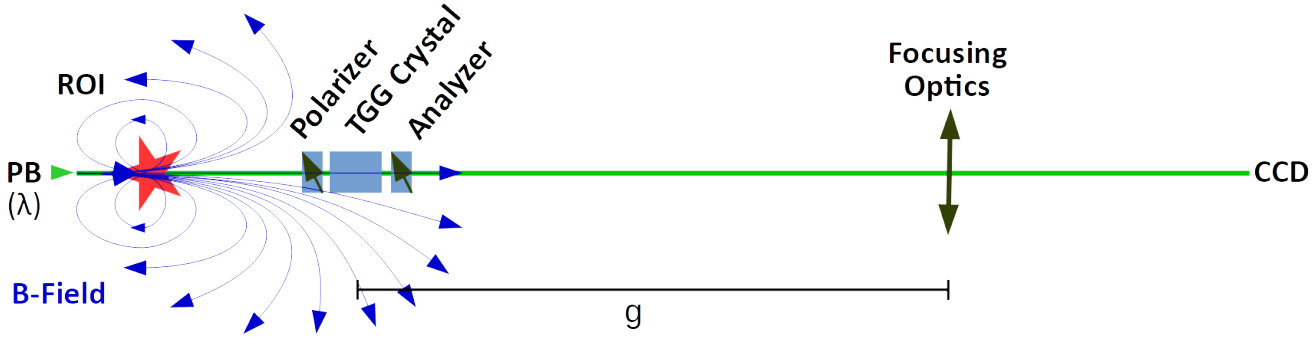

Figure 4.3: Faraday rotation polarimetry with a TGG crystal.

light and the polarizers are done. The polarized probe beam passes the ROI and thereafter a second polarizer, the analyser. Analyser and polarizer pass-orientations are aligned with large angle Θ, and the small angle $\beta = (\pi/2) - \Theta$ follows. The complex amplitude of the E-field after passage projects to $E_\mathrm{A} = E_\mathrm{P} \cdot \sin(\beta)$. The intensity reduces to $I_\mathrm{A} = \eta/2 \cdot c\epsilon_0 \cdot \|E_\mathrm{A}\|^2 = I_\mathrm{P} \cdot \sin(\beta)^2$. This formulation for intensity is valid for non-magnetic ambient media with refractive index η. With magnetized crystal in the ROI, the polarization rotates and the signal output intensity yields $I_\mathrm{S} = I_\mathrm{P} \cdot \sin(\phi + \beta)^2$. For small rotation angles we derive

$$\phi = -\beta + \arcsin\left(\sqrt{\frac{I_\mathrm{S}}{I_\mathrm{A}}} \cdot \sin(\beta)\right) \cdot \begin{cases} \operatorname{sgn} V_\mathrm{B}, & I_\mathrm{S} < I_\mathrm{A} \quad \vec{k} \downarrow\uparrow \left\langle \vec{B} \right\rangle \\ \operatorname{sgn} V_\mathrm{B}, & I_\mathrm{S} > I_\mathrm{A} \quad \vec{k} \uparrow\uparrow \left\langle \vec{B} \right\rangle \end{cases} \tag{4.30}$$

where $\operatorname{sgn} V_\mathrm{B}$ is the sign of the Verdet constant.

Some practical considerations follow. The crystal with possibly high and uniform Verdet constant is best positioned in plateaus of B-fields or in regions with small variation of $B/\mathrm{d}_z B$. The spatial extend of the crystal should be smaller than this respective regions. With this constraint on the localization of the crystal, the best sensitivity of the diagnostic is achieved when measuring rotation angles in in the quasi linear regime of $\sin(\alpha)^2$, thus with $\alpha = \phi + \beta$ in a range from approximately 30° to 60°. This dynamic range of $\Delta\alpha \approx 30°$ imposes a constraint on the range of B-field amplitudes that can be measured. Setting $\beta = 30°$, the effective value for a B-field that suits the quasi linear range is

$$L_\mathrm{CRY} \cdot \langle B \rangle_\mathrm{ext,z} = \frac{\Delta\alpha}{V_\mathrm{B}} \quad . \tag{4.31}$$

Therewith we may adapt the rotation angle β and if necessary the crystal width to suit field amplitudes in the selected optimum position.

If neither the geometrical configuration of crystals nor β can be tuned, the position of the crystal must be de-optimized. E.g. for the case of a perfect circular coil with one turn, the B-field on the coil axis z calculates to

$$B_\mathrm{z}(z) = \frac{\mu_0 r_\mathrm{C}^2 I_\mathrm{C}}{2\left(r_\mathrm{C}^2 + z^2\right)^{3/2}} \tag{4.32}$$

with the coil radius r_{C} and the coiling current I_{C}. Then, the B-field integral through the crystal slap positioned co-planar at z_{CRY} from the coil centre is

$$L_{\mathrm{CRY}} \cdot \langle B \rangle_{\mathrm{CRY}} = \frac{\mu_0 I_{\mathrm{C}}}{2} \cdot \left[\operatorname{arcsinh}\left(z/r_{\mathrm{C}}\right) - \frac{z}{\sqrt{r_{\mathrm{C}}^2 + z^2}} \right]_{z=z_{\mathrm{CRY}}}^{z=z_{\mathrm{CRY}}+L_{\mathrm{CRY}}} \tag{4.33}$$

Equating eq. (4.31) and eq. (4.33) allows to define a crystal position with respect to chosen polarizer-analyser angles.

Using a pulsed laser allows for a high temporal resolution τ_{res}. It is limited by the pulse length and the ToF through the crystal, extending over a width of L_{CRY} along the optical path.

$$\tau_{\mathrm{res}} = \tau_{\mathrm{L}} + \frac{L_{\mathrm{CRY}}}{\partial_k \omega(\omega_{\mathrm{P}})} \quad , \tag{4.34}$$

with the group velocity $\partial_k \omega \leq c$. The best possible temporal resolution is $\tau_{\mathrm{opt\_res}} = \tau_{\mathrm{L}} + L_{\mathrm{CRY}}/c$.

4.2.4 Complex Interferometry

Complex Interferometry [Kal03; Kal15] aims at detection of so called Spontaneous Magnetic Fields (SMF) in laser driven plasma [KS66], predominantly arising due to thermoelectric currents, resonance absorption and growing parametric instabilities [Pis+15]. This fields of the order of hundreds of T [SR75] are studied for their relevance to transport properties of laser fusion plasma [Cha+73; WT73] and will be of importance in this work for their impact on the target-discharge in ns-laser driven EM lenses.

Thermal EM fields arise in laser driven plasma due to the angle between the respective gradients for local plasma temperature T_{e} and density n_{e} [Sta+71; Bas+87]. Their magnetic component reads

$$\triangle \vec{B} = -\frac{4\pi\sigma}{c \cdot q_{\mathrm{e}}} \cdot \left(\vec{\nabla} T_{\mathrm{e}} \times \vec{\nabla} \ln\left[n_{\mathrm{e}}\right] \right) \quad , \tag{4.35}$$

where σ is the conductivity and q_{e} the electron charge.

Resonant absorption from laser into plasma waves at the critical density yields electron motion giving raise to B-fields [Tho+75]. In the limits of a stationary solution of an obliquely incident intense laser pulse ($>10^{16}\,\mathrm{W\,cm^{-2}}$) the maximum value for the B-field perpendicular to the plane defined by laser polarization and target normal calculates with

$$\langle B_{\perp} \rangle \approx -\frac{c}{16\pi \cdot \langle j_{\mathrm{n}} \rangle \cdot L} \cdot \left(E_{\mathrm{n}} E^*_{\perp \mathrm{n}} + \mathrm{c.c.} \right) \tag{4.36}$$

balancing the field's growth rate from laser heating with a convective term representing the charges accelerated into free space by the resonantly excited waves. L denotes the plasma density scale length which here is supposed of the order $L \approx c^2 \lambda_{\mathrm{L}} / 2\pi v_{\mathrm{th,e}}^2$ with $v_{\mathrm{th,e}}$ the thermal electron velocity.

Aperiodic parametric instabilities excited from small perturbations by powerful periodic E-fields with frequencies close to the plasma frequency [AKS70] can grow if their growth rate exceeds the damping rate of Langmuir oscillations. Then yielding steadily growing non-equilibrium E-fields [AB79] that induce B-fields oriented perpendicularly to the perturbation wave vector and the seed E-field. In a laser plasma with non-negligible

density gradients, the spatial extend of such B-field was determined to one third of the density in-homogeneity and therewith the corona.

Complex interferometry unites in one frame interferometry and polarimetry of a sample. The distribution of phase shift is obtained by means of a Fourier-Transform of the data, described in section 4.2.2. Furthermore, for plasma the Faraday effect eq. (4.28) simplifies to

$$\Phi_{\mathrm{F}} = \frac{q_{\mathrm{e}}^3}{2\epsilon_0 m_{\mathrm{e}}^2 c \omega_{\mathrm{P}}^2} \cdot \int_{-\infty}^{\infty} n_{\mathrm{e}} \cdot \frac{\vec{k} \cdot \vec{B}}{k} \, \mathrm{d}z \tag{4.37}$$

and the Cotton-Mouton effect yields [Pis+90]

$$\Phi_{\mathrm{C}} = \frac{q_{\mathrm{e}}^3}{2\epsilon_0 m_{\mathrm{e}}^2 c \omega_{\mathrm{P}}^2} \cdot \frac{q_{\mathrm{e}} c}{m_{\mathrm{e}} c \omega_{\mathrm{P}}} \cdot \int_{-\infty}^{\infty} n_{\mathrm{e}} \cdot \left(\frac{\vec{k} \times \vec{B}}{k} \right)^2 \mathrm{d}z \quad . \tag{4.38}$$

The order of magnitude of both effects varies. E.g. probing a expanding laser plasma perpendicular to its axis of symmetry lets us estimate both extreme cases $\vec{k} \upharpoonright\upharpoonright \vec{B}$ and $\vec{k} \perp \vec{B}$ for an infinitesimal propagation δz, assuming cylindrical symmetry of the B-field structure. Then $\Phi_{\mathrm{F}}/\Phi_{\mathrm{C}} \approx m_{\mathrm{e}}\omega_{\mathrm{P}}/q_{\mathrm{e}}B \approx 10710 \cdot B_{\text{in T}}\lambda_{\text{in µm}}$. For laser-plasma with B-fields of several T and probing laser pules of µm wavelength, the Faraday effect dominates polarimetry over the Cotton-Mouton effect. This is discussed in more detail in [CDB18]. The vanishing Cotton-Mouton effect leads us to the quasi-longitudinal regime, where polarimetry results largely reflect the Faraday effect.

Complex interferograms of laser driven plasma shown hereinafter take into account only the Faraday effect and neglect the Cotton-Mouton effect in the quasi-longitudinal approximation. The generally in-homogeneous electron density, velocity, and temperature of plasma are also likely to change the polarization of the probing wave. It is argued in [Pis+90], that SMF measurements with complex interferometry are possible in the limit of

$$B > \frac{\Delta z}{8 L_{\mathrm{p,z}}^2} \cdot \frac{n_{\mathrm{e}}}{n_{\mathrm{cr}}} \cdot \frac{c m_{\mathrm{e}}}{q_{\mathrm{e}}} \quad , \tag{4.39}$$

with Δz the longitudinal size of the plasma, and $L_{\mathrm{p,z}}$ the characteristic gradient length in the plasma. For typical laser plasma parameters with gradient length of tens of µm, sizes of hundreds of µm and densities of several $100 \cdot 10^{18}\,\mathrm{cm}^{-3}$, this holds true with B-fields stronger than several tens of T.

The experimental realization of the diagnostic is based on an ultra-short probe laser pulse of initially linear polarization. The probe beam passes through a waveplate-polarizer pair that allows adjustment of the polarization plane of the probe passing through the ROI filled with laser-plasma, see fig. 4.4. Phase and polarization-plane of the probe are affected by the plasma, and detected by the analyser-wedge pair on the imaging side. Note that it was postulated [Pis+90]: if one employs three such channels in parallel, then a general analysis is possible coping for depolarization and unknown axis-symmetric distributions of electron density and B-fields.

The measurement of the phase shift is based on Nomarski interferometry with a half-wedge, merging rays from respective regions in the ROI with and without plasma.

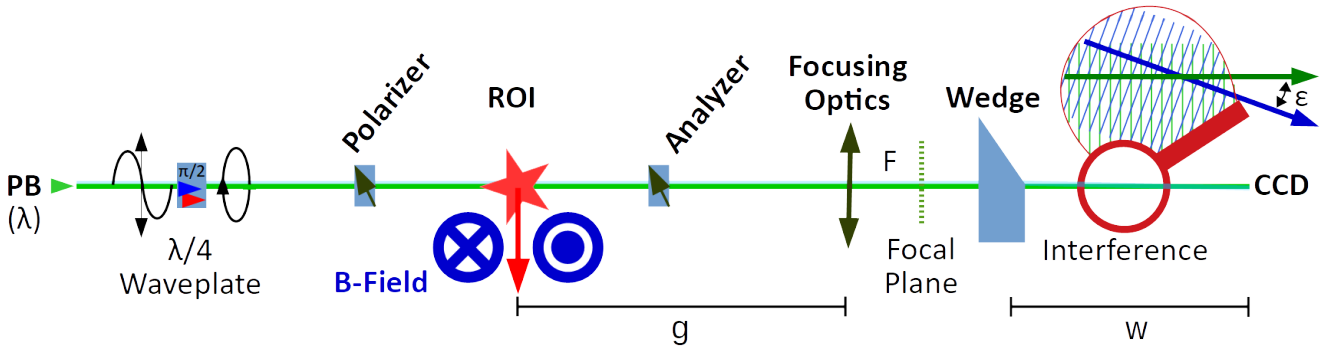

Figure 4.4: Complex interferometry comprises polarimetry and interferometry of a laser-plasma with SMF.

The optimum polarizer-analyser angle to measure the Faraday effect in plasma is deduced by [Pis+90; Pis+15]

$$\beta = \arcsin\left(\sqrt{\frac{1-\frac{I_\mathrm{P}}{I_\mathrm{p}(\omega_\mathrm{P})}\cdot(K_1-K_2)}{2+\frac{I_\mathrm{P}}{I_\mathrm{p}(\omega_\mathrm{P})}\cdot[2\,(K_1+K_2)+1]}}\right) \quad , \tag{4.40}$$

with I_P the probe beam intensity and $I_\mathrm{p}(\omega_\mathrm{P})$ the intensity of plasma self emission at the probe beam frequency, the coefficient of polarization $K_1 \approx 0$ for vanishing Cotton-Mouton effect, and $K_2 = I_S/I_\mathrm{FB}$ the degree of polarization at the analyser defined as ratio of intensities of passing signal wave and forward-blocked EM wave in presence of a plasma.

If interferograms show axial symmetry of the expanding plasma, good approximations for Faraday rotation angle $\phi = \Phi_\mathrm{F}$ and the phase shift Θ are [Pis+20]

$$\phi(x,y) = 5.24\cdot10^{-17}\cdot\lambda^2\cdot\int_x^R \frac{B_\phi(r,y)n_e(r,y)}{\sqrt{r^2-x^2}}\,\mathrm{d}r \quad , \tag{4.41}$$

$$\Theta(x,y) = 8.92\cdot10^{-14}\cdot\lambda\cdot\int_x^R \frac{n_e(r,y)r}{\sqrt{r^2-x^2}}\,\mathrm{d}r \quad , \tag{4.42}$$

where $r^2 = z^2 + x^2$ is the radial coordinate for cylindrical symmetry around plasma-axis y and $B_\phi(r,y)$ is the azimuthal SMF in a plasma slice at y with cut-off radius R. The equations were brought to the form of Abel integral equations, thus an Abel inversion yields respectively

$$n_e(r,y) = -\frac{8.92\cdot10^{-14}\cdot\lambda}{\pi}\cdot\int_r^R \frac{\partial_x\Theta(x,y)}{\sqrt{x^2-r^2}}\,\mathrm{d}x \tag{4.43}$$

$$\frac{B_\phi(r,y)\cdot n_e(r,y)}{r} = -\frac{5.24\cdot10^{-17}\cdot\lambda^2}{\pi}\cdot\int_r^R \frac{\partial_x\phi(x,y)}{\sqrt{x^2-r^2}}\,\mathrm{d}x \quad . \tag{4.44}$$

The distribution of the SMF is determined by the expression [Pis+20]

$$B_\phi(r,y) = \frac{1.7\cdot10^5}{\lambda}\cdot\left[\frac{rf_B(r,y)}{f_n(r,y)}\right] \quad , \tag{4.45}$$

$$f_n(r,y) := 4.46\cdot10^{-14}\cdot\lambda\cdot R\cdot[n_e(r,z)] \quad , \tag{4.46}$$

$$f_B(r,y) := 2.62\cdot10^{-15}\cdot\lambda^2\cdot R\cdot\left[\frac{B_\phi(r,y)n_e(r,y)}{r}\right] \tag{4.47}$$

where $f_n(r)$ and $f_B(r)$ are determined by the abelizations in square brackets and the B-field is in units of T.

4.3 Ion Beam Diagnostics

Laser accelerated particle beams are a important output channel of laser driven plasma, for their possible application as secondary source but also as diagnosis of dynamic processes inside the plasma. This section discusses active and passive particle beam detectors, such as films to record 2D projections, 3D track detectors as well as HRR ready ToF detectors. Note that many more diagnostics are used to detect ion beams, *e.g.* Imaging Plates (IP) that do have advantages to determine absolute ion numbers - and also nuclear activation that can be sensed with a Germanium detector.

4.3.1 Stacks of Radio-Chromic Films

To capture the spatial and spectral properties of ion beams, stacks of Radio-Chromic Film (RCF) are commonly used [N+09]. The films self-develop in the interaction with ionizing radiation and show a change of colour. A key feature is that the changes in the absorption spectrum of a film are bijective with respect to the received dose D. The films contain sub-µm sized cromophore components that allow a very good spatial localization of the impact of projectiles after radiosynthesis. This means that a space-resolved measurement of the wavelength dependent OD $\iota(\lambda, \vec{x})$ can be transformed into a localised dose measurement $D(\vec{x})$. As the received total dose is proportional to the energy transfer from single ion–stack interactions, it is possible to retrieve both spectrum and phase space of an ion beam of known species.

The modification of structural properties of the active film component by ionizing radiation is the key feature of RCF films [MC65; Hum89; McL96]. This self-developing films generally consist of 100 µm thick plastic layers that are transparent in the visible wavelength range and that support a 10 µm thin active layer. Irradiation triggers a topochemical polymerization process of ordered diacetylene monomers in the active crystalline medium [WM11; Mil+18; Bau72; Enk84]. The monomers cross-link by developing chemical bonds between them. For such polymerization, monomers optimally are only several Å apart which makes the active layer a dense detection array. The polymerized chromophore polydiacetylene is reported to have a size of 750 nm [Soa06] defining the maximum resolution of RCF. The result of the radiosynthesis can be appreciated due to a visible change in colour of the active film layer and the colour change can be related to the deposited dose via calibration data. In addition to the material properties of the active layer of the RCF, both dose rate and total dose have an influence on the response function of the RCF as a dose detector.

Historically, RCFs have evolved from the dose range of a few to hundreds of kGy to lower doses of cGy, a wide range of dose detection commercially available today [Soa06]. The films serve as detectors with micrometric resolution for deposited doses in industry [Aea; ISO13] and medicine [But+03]. Key features are their low projectile-energy response variation [Mue+91], a low dose-rate dependency of the response [Say+88] and a high uniformity of the film [Chu+90].

Given that the stack of RCF contains N_{RCF} layers in depth, each layer n represents a two dimensional dose measurement $D(\vec{x}) = D(x, y, \int_{z\in n} \mathrm{d}z)$. With known film density $\rho_{\text{RCF}}(n)$ and layer thickness $d_{\text{RCF}}(n)$, the deposited energy E per surface area A in layer n calculates from the received dose D with

$$\mathrm{d}_A E(x, y)_n = D(x, y, \int\limits_{z\in n} \mathrm{d}z) \cdot \rho_{\text{RCF}}(n) \cdot d_{\text{RCF}}(n) \quad . \tag{4.48}$$

The total deposited energy in one layer comprises the summed energy deposition ΔE of each individual ion i in the beam I along its trajectory $\vec{t}$,

$$\mathrm{d}_A E(x,y)_n = \sum_{i \in I} \left(\int_{z \in n} \Delta E(\vec{t}_i) \mathrm{d}z \right) \quad . \tag{4.49}$$

For high particle numbers, a likelihood map of deposited energy per projectile $\Delta\mathfrak{E}(\vec{x})_i$ in a solid-density target can be calculated or simulated via a stopping power calculation (see section 3.5.2.1). This map is unique to all ion species within the ion beam and varies for different impact parameters as the stopping power and scattering cross sections depend also on the ion charge state and kinetic energy and not only on target material properties. For m grouped ion populations with a subset of i_m projectiles respectively,

$$\mathrm{d}_A E(x,y)_n = \sum_{m \in I} i_m \cdot \Delta\mathfrak{E}_m(x, y, \int\limits_{z \in n} \mathrm{d}z) \quad . \tag{4.50}$$

If the ion beam is mono-energetic and consists of one species with known mass and charge state, only one population exists and the number of traversing particles $N(x,y)_n$ can be calculated, provided it is sufficiently large. Equating eq. (4.48) and eq. (4.50) yields

$$N(x,y)_n = \frac{D(x, y, \int_{z \in n} \mathrm{d}z) \cdot \rho_{\mathrm{RCF}}(n) \cdot d_{\mathrm{RCF}}(n)}{\Delta\mathfrak{E}(x, y, \int_{z \in n} \mathrm{d}z)} \quad . \tag{4.51}$$

where integration over the full (x,y)-plane gives an equal total particle number N for each layer in the stack that is reached by the ions.

For an ion beam of one single species that is not mono-energetic we search the particle number spectrum per unit energy $\mathrm{d}_E N$ instead. Set a normalized distribution $f(E) = \frac{\mathrm{d}_E N}{N}$ with $\lim_{E \to \infty} f(E) = 0$, thus from eq. (4.50) follows

$$\mathrm{d}_A E(x,y)_n = \int_{E \in n} N \cdot f(E) \cdot \Delta\mathfrak{E}_E(x, y, \int\limits_{z \in n} \mathrm{d}z) \, \mathrm{d}E \tag{4.52}$$

$$= \int_{E \in n} \mathrm{d}_E N \cdot \Delta\mathfrak{E}_E(x, y, \int\limits_{z \in n} \mathrm{d}z) \, \mathrm{d}E \quad . \tag{4.53}$$

The total energy deposited in a layer results from a convolution of spectrum and detector response function - in order to retrieve the particle number, assumptions on the shape of the spectrum are necessary.

The depth of penetration into a stack of multiple RCF is proportional to the ion impact energy. On the simulation side, a projectile penetration range calculation in a well characterized target material allows to estimate the delimiting energies E^{in}, the minimum energy necessary for an ion to reach a film layer, and E^{out}, the minimum energy necessary to pass a film layer. Performing an iterative calculation over a wide range of energies allows to map this energy-to-range relation for the full stack with any precision required.

On the experimental data side, the range of the highest energy projectiles is visible as the depth of the last coloured film because the change from coloured films to uncoloured films is sudden. The particularity of ion stopping with respect to electron- and photon-stopping is a maximum of the stopping power for low ion energies: The stopping power maximum is always located at the end of the penetration range, in the Bragg peak. The film response to ions can be easily distinguished from background electrons, that may even traverse the stack, as their imprints faint only slowly with increasing depth. Thus the cut-off energy of the spectrum E^{max} can be estimated with the value E^{out} of the last coloured film. Only if the highest projectile energy is stopped within the stack, deconvolution of imprints is possible.

If RCF films are thin with respect to features in the ion beam spectrum, we can simplify the problem further by presuming a flat spectrum within the energy bounds of the last coloured layer n_{last}. Furthermore, we transform the likelihood map with dependence on both the stack-depth z and particle energy E in a map with energy dependence only. Therewith we equate eq. (4.48) and eq. (4.50)

$$D(x, y, \int_{z \in n_{\text{last}}}) \cdot \rho_{\text{RCF}}(n_{\text{last}}) \cdot d_{\text{RCF}}(n_{\text{last}}) = N \cdot f(n_{\text{last}}) \cdot \int_{E^{\text{in}}_{n_{\text{last}}}}^{E^{\text{out}}_{n_{\text{last}}}} \Delta\mathfrak{E}(x, y, E)\, \mathrm{d}E \tag{4.54}$$

$$\Leftrightarrow N \cdot f(x, y, n_{\text{last}}) = \frac{D(x, y, n_{\text{last}}) \cdot \rho_{\text{RCF}}(n_{\text{last}}) \cdot d_{\text{RCF}}(n_{\text{last}})}{\int_{E^{\text{in}}_{n_{\text{last}}}}^{E^{\text{out}}_{n_{\text{last}}}} \Delta\mathfrak{E}(x, y, E)\, \mathrm{d}E} \quad . \tag{4.55}$$

From this point $(N \cdot f(x, y, n_{\text{last}}), E \in n_{\text{last}})$ on, a step-wise iteration through the stack is possible, always subtracting all higher energy particles from the deposited energy in a film layer j before retrieving the particle number per unit energy $N \cdot f(x, y, n_{\text{j}})$,

$$N \cdot f(x, y, n_j) = \frac{D(x, y, n_j) \cdot \rho_{\text{RCF}}(n_j) \cdot d_{\text{RCF}}(n_j) - \sum_{l=j+1}^{n_{\text{last}}} N \cdot f(x, y, n_l)}{\int_{E^{\text{in}}_{n_j}}^{E^{\text{out}}_{n_j}} \Delta\mathfrak{E}(x, y, E)\, \mathrm{d}E} \quad . \tag{4.56}$$

Such a procedure allows us to obtain the particle number spectrum per unit energy in the limit of the assumption of a flat spectral evolution over the energy bin defined by the depth of one film. Otherwise, $f(E)$ must be known to derive $\mathrm{d}_E N$. Due to measurement uncertainties and features in the ion beam spectrum we may take into account deviations $\delta(E)$ to $f(E)$ via $\mathrm{d}_E N = N \cdot (f(E) + \delta(E))$. Then we can solve eq. (4.53) for the total particle number in the ion beam N and the deviation distribution $\delta(E)$, *e.g.* by minimization of $\sum_n |f(n) - \delta(n)|$.

4.3.1.1 Ashland GAFCHROMIC

In the course of this work, RCFs based on Gafchrom film were used: different types of GAFCHROMIC developed as near tissue equivalent for medical applications and distributed by Ashland (Ashland Speciality Ingredients, Bridge Water, NJ, USA). This films are designed for dosimetry of photons in the range from 100 kV to several MV [Por16b; Lew16; Por16a] but are also successfully applied to dosimetry of ion beams [Sei+15].

The specifications of GAFCHROMIC films evolved over the past decades with respect to the dimensioning and stacking of polyethylene terepthalate plastic layers and active layers as well as with respect to chemical composition of layers, see table 8.2. The latest generation films are named HD-V2, MD-V3 and EBT-3. All films employ the same active component: lithium pentacosa-10,12-diynoate (LiPCDA) [Lew10] embedded in a gelatin matrix with marker dye [Kir11; Gca], but the films are designed to suit detection in different dose ranges. The active layer composition was developed first for EBT-2 film. The absorption spectrum for EBT-2 is well reported, see fig. 4.5. We see separated spectra of active component and marker dye. The well defined absorption peaks of the active component are situated at 582 nm and 633 nm after irradiation with 50 cGy. An irradiation independent broad absorption maxima in the marker dye is located at 425 nm.

The crystalline form of the radiopolimerized active medium varies for all film types. For HD-V2, the difference in pronounced in a shifted absorption spectrum [Por16b], compare fig. 4.6 – for EBT this difference is pronounced in a light polarizing property [Lew10]. Besides, different spatial resolutions of the film types are delimited by the respective crystal sizes. The crystalline form depends with its structural properties on the manufacturing procedure and shows batch-to-batch variations. The coating technique during manufacture

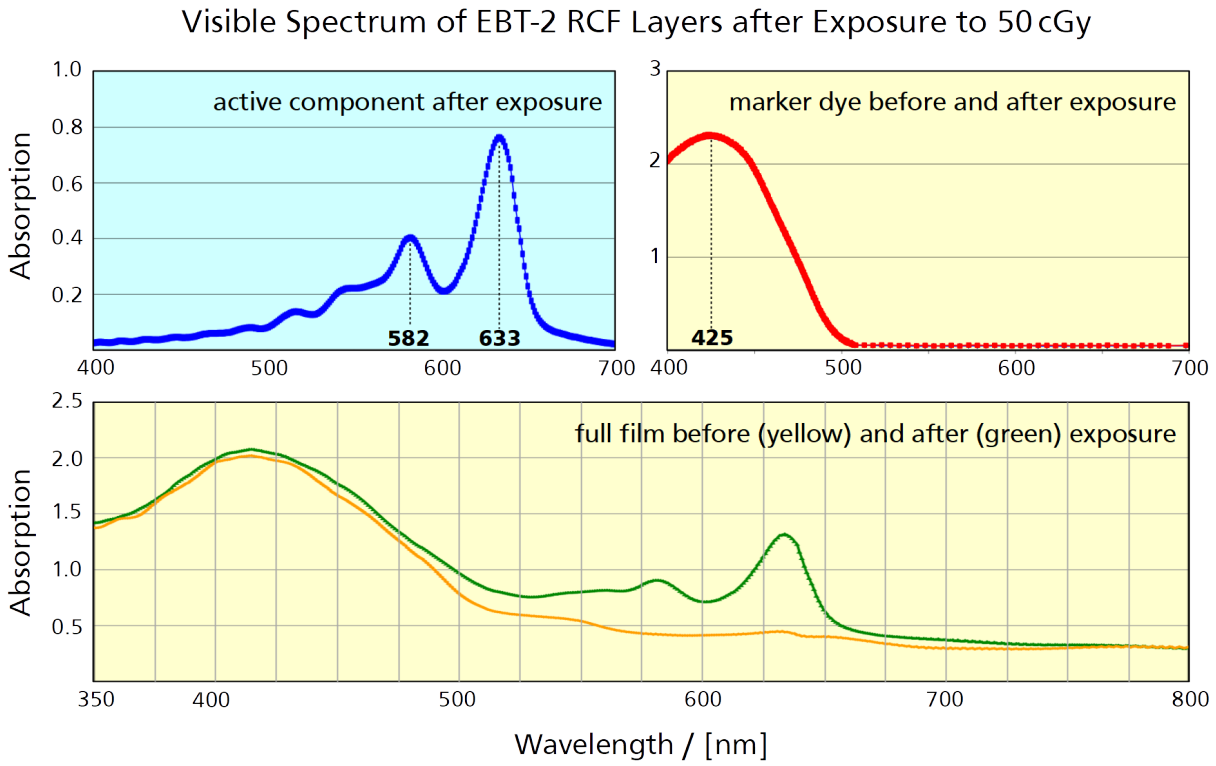

Figure 4.5: Absorption spectrum of GAFCHROMIC EBT-2 RCF in the visible wavelength range. Films comprise biaxially-oriented polyethylene terephthalate (Mylar) layers and a layer containing active component and marker dye. The mean position of the two well-pronounced high-end absorption maxima are 583 nm and 633 nm. The absorption maxima blue-shift for increasing dose values. Images extracted from [Lew10].

defines if the crystals are either rod shaped or squared. Their orientation-distribution influences whether RCF select on the polarization of transmitted light or not. In addition, some batches employ a matte-polyester substrate to eliminate Newton's Rings artefacts during post-exposure data digitizing with scanner systems.

HD-V2 [Por16b] are the most performant with respect to their spatial resolution and dose range. Nominally, this films consist of an active layer of 12 µm thickness with spatial resolution of 5 µm coated upon a 97 µm thick polyester substrate. The polymer formed after irradiation is blue coloured with absorption maxima at 670 nm. An exemplary absorption spectrum of HD-V2 for different doses can be seen in fig. 4.6. We see that low doses can be best characterized in the red wavelength range whereas the respective lower opacity in green and blue bands allows a characterization of higher doses respectively. HD-V2 is designed for the dose range of 10 Gy to $1.000 \cdot 10^3$ Gy. Detection of heavy ions or low energy ions is possible due to the active layer on the surface.

Nominally, MD-V3 [Lew16] consist of an active layer of 10 µm thickness with a spatial resolution below 25 µm sandwiched between two layers of 125 µm thick polyester substrate [Lew16]. The polymer formed after irradiation is blue coloured with absorption maximum around 635 nm. MD-V3 can be applied best in an intermediate dose range of 1 Gy to 100 Gy.

EBT-3 [Por16a] has a 25 µm resolution and is meant to suit a low dose range of $100 \cdot 10^{-3}$ Gy to 20 Gy. The polymer formed after irradiation is blue coloured with absorption maximum around 635 nm.

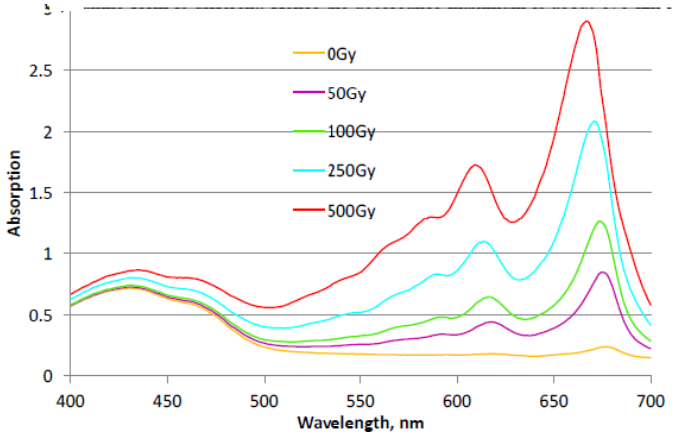

Figure 4.6: Absorption spectrum of GAFCHROMIC HD-V2 RCF in the visible wavelength range. Compared are the answer function of the film to different doses of ionizing radiation. The mean position of the two well-pronounced high-end absorption maximum are 615 nm and 670 nm. The absorption maxima blue-shift for increasing dose values. Image extracted from [Por16b].

The presence of marker dye in all active layers of all recently produced films allows for multi-channel dosimetry [Gca].

The manufacturer reports a projectile energy dependent response difference of less than 5 % when exposed to 1 MeV electrons with respect to 18 MeV electrons. EBT-3 films show the same low response difference for electrons within an enhanced range of $100 \cdot 10^{-3}$ MeV to 18 MeV.

The dose fractionation response varies with less than 5 % comparing a single exposure of

- HD-V2 to 100 Gy with respect to five cummulative 20 Gy doses at 30 min intervals,
- MD-V3 to 100 Gy with respect to five cummulative 20 Gy doses at 30 min intervals,
- EBT-3 to 25 Gy with respect to five cummulative 5 Gy doses at 30 min intervals.

GAFCHROMIC RCF show a dose rate response difference of below 5 % for an exposure of 10 Gy with rates of 3.4 Gy min^{-1} compared with $34 \cdot 10^{-3}$ Gy min^{-1}.

The manufacturer's specifications concern electrons and photons. We are interested in multi-MeV ions, which do have a more promounced LTE than electrons in the same energy range, see fig. 4.7. The ion LTE increases with decreasing projectile energy due to the Bragg-Peak and may lead to saturation of the RCF response. For older RCF models, under-responses of 25 % to 35 % for carbon ions between 100 MeV u^{-1} to 400 MeV u^{-1} are reported [MJ10]. Whereas this result indicates complications for heavy ions, no saturation was constated down to a proton energy of 50 MeV u^{-1}.

GAFCHROMIC films are not only sensitive to ionizing radiation but also to high temperature and sunlight. Not to alter the films proper functionality, one must beware of careless handling of the films. The manufacturer specifies that films should not be exposed to temperatures above 50 °C and stored even below 25 °C. Especially the later is often not respected and leads to visible darkening of the films over time.

After exposure, the final colour of RCF is reached after 48 h [Say+88] for old film types and after 2 h for the new film types used for this work [Lew10] – even though this only means that the darkening curve reaches a flattening. The manufacturer specifies for the OD $\iota(\lambda)$ a stability in dark room conditions below $\Delta\iota = 500 \cdot 10^{-6}\,\mathrm{d}^{-1}$ at 23 °C.

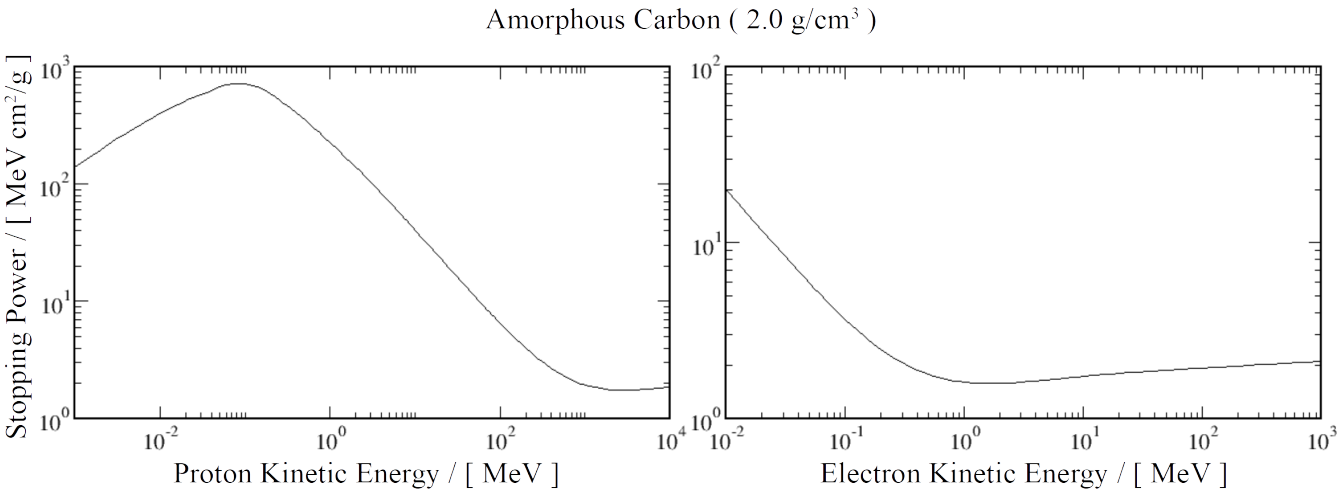

Figure 4.7: Plot of tabulated values for the electron and proton Stopping Power in Carbon. Images extracted from [ST].

4.3.1.2 Data Digitization

The analogue RCF are digitalized either by dedicated laser scanner systems [SG91; Fen+18] or commercial professional flat-bed scanners [Ste+96; LG+18]. For this work, we perform scans with the EPSON EXPRESSION11000XL flat-bed scanner that comprises a cold fluorescent Xenon light source for illumination and a CCD array for image acquisition. The spectrum of the light source and the RGB-colour channel data acquisition sensitivity bands of the CCD array are known, compare fig. 4.8. One sees narrow emission peaks for 486 nm, 542 nm, 592 nm, 610 nm and 626 nm whereas the sensitivity bands are large with $\mathrm{ch_R} = [611\,\mathrm{nm}, 661\,\mathrm{nm}]$, $\mathrm{ch_G} = [550\,\mathrm{nm}, 600\,\mathrm{nm}]$ and $\mathrm{ch_B} = [400\,\mathrm{nm}, 500\,\mathrm{nm}]$ [LG+18].

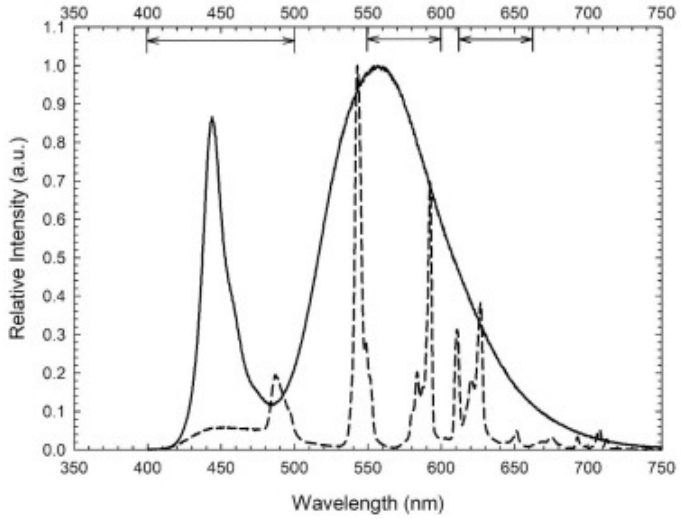

Figure 4.8: Emission spectrum of the cold fluorescent Xenon light source of the EPSON EXPRESSION11000XL flatbed scanner as dashed line compared to the detection band of the RGB colour channels indicated with arrow bars. A Light-Emitting Diode light source is compared as solid line. Image extracted from [LG+18].

Note, that the EPSON EXPRESSION 11000XL primarily used in this work fails to detect the most defined absorption maximum for HD-V2, present around 670 nm after radiosynthesis. Nevertheless, the second absorption maximum around 615 nm is well lit and acquired within $\mathrm{ch_R}$. For both other film types, MD-V3 and EBT-3, the first absorption maximum around 635 nm is not well lit but acquired in $\mathrm{ch_R}$. The second absorption maximum, presumably in the interval from 580 nm to 585 nm (compare fig. 4.5), is well lit and acquired within $\mathrm{ch_G}$. The combination of a quick data acquisition procedure that offers good spatial resolution makes the digitization via flat-bed scanners advantageous with respect to a spectrometric scan, even though we must accept a less precise dosimetry due to the missmatch of emission spectrum, acquisition bands and absorption spectrum.

Scanning Procedure

The light source needs a heat up prior to usage that is done automatically after switching on the EPSON EXPRESSION 11000XL. It is crucial to respect the heating time and perform an initial full-bed blank scan to start operation with a lamp that is warm and scan-to-scan inter-comparable.

No software-dependent image correction tools must be applied during a 48 bit RGB multi-exposure scan. This is important to allow comparability to any absolute calibration of the scanner, discussed in a later section. The software `SilverFast 8.8` is used for scans with settings specified in section 8.2. Scans in transmission or reflection obtain different results – all scans for this work are done in transmission.

A priori, the scanner answer function must be suspected to be dependent on the coordinates (x, y) of the flat-bed. The software allows to select frames within the full flat-bed array to reduce the size of scans and improve on the time needed to do one scan – it is important to keep track of the coordinates of this frames, see section 4.3.1.2. For absolute comparability, the RCF in a stack must be scanned at the exact same position.

The orientation of the RCF during a scan plays a major role due to the polarization effects that may arise with differences in the crystalline type of the active compound in several film-types. Changing the orientation by $\frac{\pi}{2}$ can lead to a maximum variation of results, which is of the order of several % as will be shown in a later section. On one hand side it is possible to perform several scans of one single film in order to have a full angular response curve - on the other hand side, the RCF absorption spectrum alters due to the heating by the scanner light source. This renders a general comparability of scans desirable. The tracking of the RCF orientation must start with the unwrapping, well before exposure and probably month before scanning operation. Hereinafter, a comparable corner and the landscape orientation of films is documented following a standard convention, depicted in fig. 4.9a. This assures that whatever the manufacturing procedure was, intercomparability of the films in a batch is garanted. For RCF type HD-V2 it is easy to mark the originally slited corner – one should find a applicable solution for both types MD-V3 and EBT-3. Especially EBT-3 must be marked, for which a rotation changes results dramatically. For this work, the upper-right corner of the films after removal from the envelope are marked, to stay consistent with HD-V2. Finally, the scanning angle is logged - this angle is measured between the short side of an un-cutted RCF and the long side of the scanner. A scheme is illustrated in fig. 4.9b.

Note, that the heating of the scanner lamp represents a low-level threat to RCF data [Ste+96] due to their temperature sensitivity. If multiple scans are performed, a scanner cool-down should be respected. We find, for initially unexposed HD-V2 films, the mean grayscale value alters for a series of 10 scans without cooldown up to 1 %. The standard deviation of the mean values does not grow but remains stable. This allows some confidence on the uncertainty of grayvalues in scans.

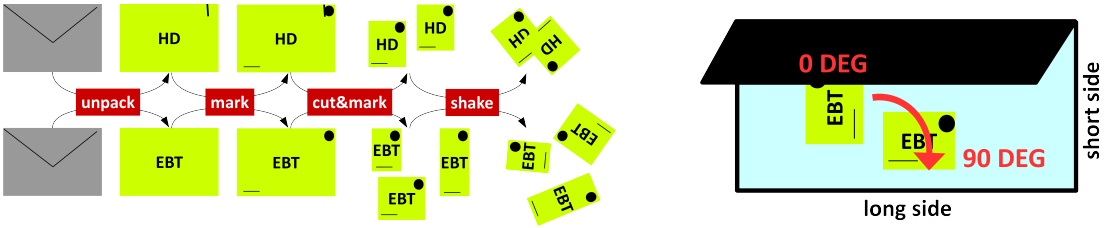

(a) cutting and marking

(b) angular positioning

Figure 4.9: A convention for cutting, marking and scanning of the RCF is of paramount importance to facilitate any later-on data analysis that requires absolute comparability of each film in a stack, an possibly with calibration data.

Transformation of Scan Grayscale to Optical Density

The final grayscale value of a film scan depends on the absorption in the RCF on one hand side. On the other hand it depends on the flat-bed scanner emission spectrum and acquisition bands with their respective efficiency – the machine answer function of the scanner. The scanner light source emission is important as the acquisition bands of the scanner fig. 4.8 are large compared to the absorption peaks of the RCF fig. 4.6. A transformation of grayscale data into OD allows to de-couple the machine function from the analysis.

The OD ι_{ch} of each colour channel ch $\in \{R; G; B\}$ in a pixel (m, n) of the acquired scan image (ch, m, n) is defined as

$$\iota_{\text{ch}}(m,n) = \log_{10}\left(\frac{I_0(m,n)}{I(m,n)}\right) \tag{4.57}$$

where $I(m, n)$ represents the transmitted grayscale intensity of pixel (m, n). $I_0(m, n)$ is the scanner response for a scan without sample.

Kodak WRATTEN 2 n°96 OD foils with well defined spectral properties are used as reference data for scanner calibration in transmission scans. We model the grayscale answer of a flat-bed scanner with respect to changes in OD is sucessfully with,

$$\langle I_{\text{ch}}(m,n)\rangle = A_{\text{ch}} \cdot \exp\left[-B^{\text{fit}}_{\text{ch}} \cdot \iota_{\text{ch}}\right] \tag{4.58}$$

$$\text{with} \quad A_{\text{ch}} = \exp\left[B^{\text{fit}}_{\text{ch}} \cdot C^{\text{fit}}_{\text{ch}}\right] \quad , \tag{4.59}$$

where the inverse $B^{\text{fit}}_{\text{ch}}$ and $C^{\text{fit}}_{\text{ch}}$ are scanner specific fit parameters. $B^{\text{fit}}_{\text{ch}}$ is the inverse scale parameter for the exponential decay. $C^{\text{fit}}_{\text{ch}}$ is the OD for which the scanner answer is 1 on the greyscale, thus the minimum detectable transmittance. Note, that a more detailed fitting could also take into account an offset to this minimum detectable transmittance, *e.g.* due to the size of samples with respect to the flatbed. A_{ch} is the dynamic range on the greyscale, *e.g.* for a zero minimum detectable transmittance it corresponds to the grayscale value of a completely transmissible sample. This parameter is intentionally not fix in order to deduce an uncertainty. In turn, the uncertainty range of the parameter can be compared to the bit-range of scans to judge the quality of the fit. The inverse function reads

$$\iota_{\text{ch}} = \frac{\ln\left[A_{\text{ch}}\right] - \ln\left[\langle I_{\text{ch}}(m,n)\rangle\right]}{B^{\text{fit}}_{\text{ch}}} \quad . \tag{4.60}$$

To avoid fitting difficulties, we transform the relation to a linear form

$$y = B_{\text{ch}}^{\text{fit}} \left(C_{\text{ch}}^{\text{fit}} - \iota_{\text{ch}} \right) \tag{4.61}$$

$$\mid \text{with} \quad y = \ln \left[\langle I_{\text{ch}}(m,n) \rangle \right] \quad . \tag{4.62}$$

Results obtained for the EPSON EXPRESSION 11000XL flat bed scanner are summarized in table 4.1. This calibration only holds for the scanner used for this work, as a precice measurement of the scanner light source emission was not performed and de-coupled.

Table 4.1: Grayscale to OD transformation parameters for the EPSONEXPRESSION 11000XL according to fit function eq. (4.60).

Parameter	Best Value	Standart Deviation	Parameter	Best Value	Standart Deviation
$B_{\text{R}}^{\text{fit}}$	2.254	0.012	$C_{\text{R}}^{\text{fit}}$	4.922	0.022
$B_{\text{G}}^{\text{fit}}$	2.320	0.020	$C_{\text{G}}^{\text{fit}}$	4.766	0.034
$B_{\text{B}}^{\text{fit}}$	2.339	0.012	$C_{\text{B}}^{\text{fit}}$	4.740	0.022

The parameters for a EPSON V750-PRO, notably deploying the same type of light source [Hua+21], are given with table 4.2. Two major differences are that (a) the exponential is less steep and (b) the minimum detectable transmittance varies more in function of different colour channels. (a) could be due to a brighter light source or less thick flatbed glass, (b) due to a different composition of the flatbed glass.

Table 4.2: Grayscale to OD transformation parameters for the EPSON V-750-PRO according to fit function eq. (4.60), derived from [Hua+21].

Parameter	Best Value	Standart Deviation	Parameter	Best Value	Standart Deviation
$B_{\text{R}}^{\text{fit}}$	1.333	0.011	$C_{\text{R}}^{\text{fit}}$	8.311	0.067
$B_{\text{G}}^{\text{fit}}$	1.351	0.011	$C_{\text{G}}^{\text{fit}}$	8.199	0.067
$B_{\text{B}}^{\text{fit}}$	1.471	0.011	$C_{\text{B}}^{\text{fit}}$	7.532	0.056

Homogenity of the Scanner Answer

RCF are homogeneous and do not require reference data of the very same spot on the film in unexposed state with respect to the exposed state. Nevertheless, the scanner answer function is not homogeneous over the full flat bed. Scanning is performed by a slider moving in direction of the long side of the scanner – the scan axis – which has a light source parallel to the short side of the scanner – the lateral axis.

Scanning a homogeneous sample in transmission results in laterally fainting data for off-centre positions superposed with large-area fluctuations and with background noise. The lateral fainting is widely observed and due to the illumination - for polarizing types of RCF, this fainting then becomes more pronounced with increasing dose. The large-area variations relative to the signal corrected for fainting are due to oil films

or chippings in the flat-bed glass. The background noise can be due to dust particles, droplets, scratches or inhomogeneities in the detection CCD array.

In order to grant relative comparability of scans performed at different positions on the flat bed, a calibration of lateral-fainting and large-area fluctuations is required. The background noise is accepted to contribute to the standard deviation of the signal mean value.

For lateral fainting, the difference of flat-bed centre- and edge-value is comparable for all colour channels, for data depicted in fig. 4.10c. The relative error is minimum for the red and maximum for the blue channel. The relative changes $\Delta^{\text{sweet}}_{\text{edge}}(\text{channel})$ – which are the scanner's mean answer at the edge with respect to the answer on the centre axis, the so called sweet-axis – are

$$\Delta^{\text{sweet}}_{\text{edge}}(\text{red}) = 0.95 \tag{4.63}$$
$$\Delta^{\text{sweet}}_{\text{edge}}(\text{green}) = 0.95 \tag{4.64}$$
$$\Delta^{\text{sweet}}_{\text{edge}}(\text{blue}) = 0.91 \quad . \tag{4.65}$$

A second-order polynomial calibration function seems appropriate for fitting. Figure 4.10 contrasts data and fit and gives the fit parameters. Thus, we obtain the off-axis correction functions $c_{\text{channel}}(x)$, where $x = 0\,\text{mm}$ is the long side of the scanner which is not connected to the scanner's top but faces the user,

$$c_{\text{red}}(x) = (1 \pm 0.002) - (2.1 \pm 0.1) \cdot 10^{-6} \cdot (x - (149 \pm 3))^2 \tag{4.66}$$
$$c_{\text{green}}(x) = (1 \pm 0.002) - (2.0 \pm 0.2) \cdot 10^{-6} \cdot (x - (146 \pm 4))^2 \tag{4.67}$$
$$c_{\text{blue}}(x) = (1 \pm 0.002) - (4.1 \pm 0.2) \cdot 10^{-6} \cdot (x - (148 \pm 2))^2 \quad , \tag{4.68}$$

where the adjusted value $a_{\text{channel}}\,(\text{scan}(x))$ for films scanned at off-axis positions x measured in mm can be calculated by

$$a_{\text{channel}}\,(\text{scan}(x)) = \frac{\text{scan}(x)}{c_{\text{channel}}(x)} \quad . \tag{4.69}$$

As result of this calibration, the scanner can only be used for directly comparable scans in proximity of the sweet axis in its lateral centre. There, all scans to different doses have the same flat top answer. All scans which will be done in off-centre positions are valuable for absolute analysis only with correction.

4.3.1.3 Ion Beam Deflectometry - Ultra-fast Imaging with Stacks of Radio-Chromic Film

Ion beam deflectometry is commonly used to spatially and temporally characterize EM fields. Mono-energetic laminar ion beams are ideal probe beams for fast material transformation processes and electrodynamic fields. Their speed reaches several $10\,\mu\text{m}\,\text{ps}^{-1}$ for kinetic energies of several $\text{MeV}\,\text{u}^{-1}$. This means that µm-sized structures can be resolved with a temporal resolution of several tens of ps. The temporal uncertainty of such a measurement on a time integrating 2D ion detector is dominated by the width of the spectral peak. The beam bunch length grows laterally with time-of-flight prior to probing a sample.

Laser-accelerated ion beams posses a large spectrum in the $\text{MeV}\,\text{u}^{-1}$-range. The spectral width smears out the temporal resolution for measurements with 2D ion detectors such as Imaging Plates or RCF. Stacking of 2D detectors is the key for ultra-fast imaging techniques with time-integrating passive detectors. A stack detector is able to resolve different projectile energies due to the characteristic Bragg-peak position for every

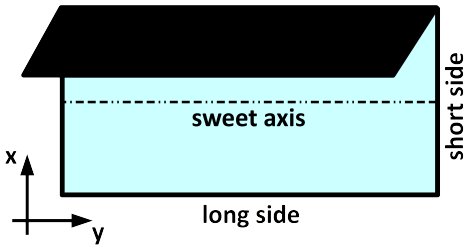

(a) geometry of the sweet-axis

EBT Dose: 0 Deg | Channel: 1
Function: sat − const (−shift + variable)^2

	Estimate	Standard Error	t-Statistic	P-Value
sat	169.054	0.291813	579.323	2.1317×10^{-49}
const	0.000354322	0.0000242595	14.6055	3.99344×10^{-13}
shift	149.082	3.00989	49.5307	7.06935×10^{-25}

EBT Dose: 0 Deg | Channel: 2
Function: sat − const (−shift + variable)^2

	Estimate	Standard Error	t-Statistic	P-Value
sat	163.271	0.364143	448.371	7.72714×10^{-47}
const	0.000328683	0.0000302774	10.8557	1.58867×10^{-10}
shift	146.102	4.0819	35.7925	1.13157×10^{-21}

EBT Dose: 0 Deg | Channel: 3
Function: sat − const (−shift + variable)^2

	Estimate	Standard Error	t-Statistic	P-Value
sat	84.9607	0.191672	443.261	1.00577×10^{-46}
const	0.000347485	0.0000159342	21.8075	7.27498×10^{-17}
shift	148.239	2.01949	73.4044	8.79416×10^{-29}

(b) fits for all channels

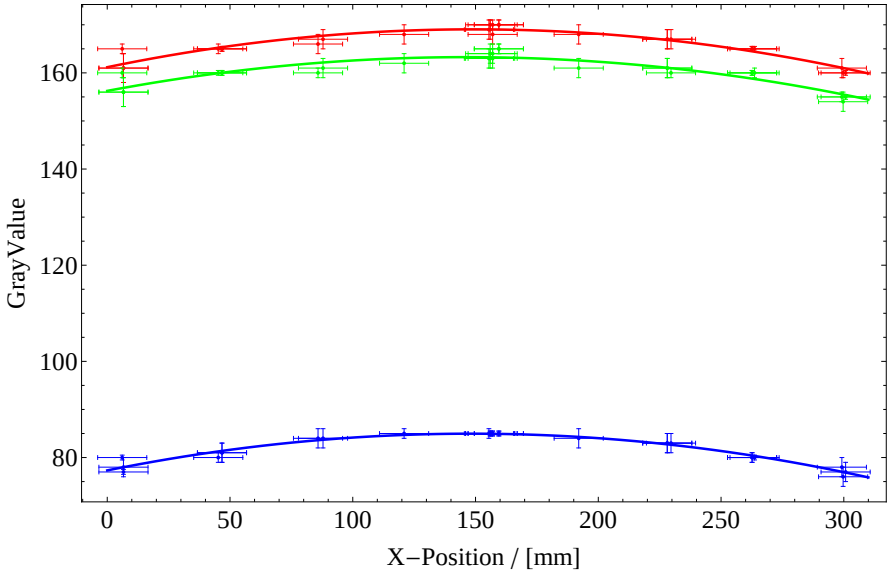

(c) mean respons and standard deviation of non-irradiated EBT-3 at different positions on the flat bed scanner glas

Figure 4.10: Calibration for off-axis scans of RCF is necessary due to the inhomogeneity of the scanner illumination: (a) the symetry axis of the response function, here named sweet axis, is centred on the short side and (c) scans results of blank films on different positions with their fit (b).

impact energy $d_{\mathrm{BP}}(E_{\mathrm{kin}})$, see section 3.5.2.1. For stacks of RCF, the time-of-flight uncertainty of imprints in each active layer varies with the spectral range that the active layer covers. A typical value are several ps for ions with $\mathrm{MeV\,u^{-1}}$.

Stacks of RCF and their characteristic stopping of proton beams are simulated using SRIM [ZBZ13], within the runtime environment PySTarT, see section 7.4. Sequences of active layers and polyester substrate layers are modelled with perfectly plane successive solid material slaps. Within one layer atoms are uniformly distributed, and their composition is implemented in ratios according to their stoichiometric coefficients. The ion beam spectrum is rasterized by single mono-energetic simulations. Result of the calculation is a matrix with Bragg-peak position dependent on impact ion energy over an energy range of interest.

The first layer of the stack contains information of all ions that do not stop prior to it. This comprises ions that stop in the active layer but also all of which traverse the layer. The Bragg-peak itself is the predominant range of dose deposition but ions decelerate already prior to the peak with a flat stopping power curve. The slimmer the Bragg-peak is at a given depth in the stack, the better is the spectral resolution and therewith temporal uncertainty of adjacent active layers. The wider the spectral range of the particle beam, the more trespassing particles integrate over the first layers and the less pronounced is the actual Bragg-peak signal in such layers.

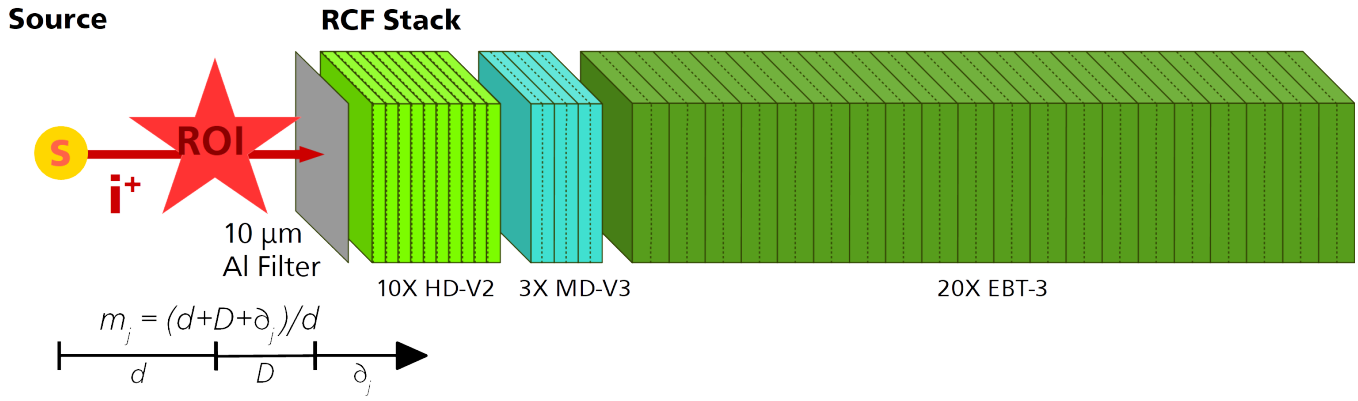

Figure 4.11: Exemplatory RCF stack of 10 × HD-V2 followed by 3 × MD-V3 and 20 × EBT-3 with ion beam arriving from the left hand side, traversing first a filter foil, then HD-V2 sensitive to high doses, followed of MD-V3 for intermediate doses and finally EBT-3 for low doses. Such stack design with increasing sensitivity in depth suits a TNSA particle beam spectrum with exponential decay of the number-density distribution for higher energies. The magnification of a region of interest depends on source to ROI distance, ROI to detector distance and the position of the detecting active layer within the stack.

A given active layer of thickness d_{active} covers a larger spectral bandwidth if positioned as first layer of a stack than if it is among the last imprinted layers. Separation of the layers by filters renders stacks cheaper especially for detection of high-energy ions – with respect to available film types. Notably, thin metal foils or additional foils of biaxially-oriented polyethylene terephthalate (Mylar) may be added to a stack in order to modify and widen the covered energy range minimizing the number of used RCF to the necessary. Aiming at a specific proton energy range, RCF stacks may be fitted regarding energy range, energy resolution and binning. The code PySTarT is used for stack design prior to experiments.

Laser driven charged particle beam deflectometry is often based on the robust TNSA mechanism and proton projectiles. The broad exponential energy distribution enables for time resolved deflectometry measurements of EM field evolution on a scale of hundreds of ps, depending on the ToF. The following discusses an exemplary RCF stack of 10 × HD-V2 followed by 3 × MD-V3 and 20 × EBT-3, see fig. 4.11. Such stack is suited for TNSA beams with 30 MeV cut-off. In fig. 4.12, we see the stopping of different proton energies within this stack. Al shields are introduced to protect the films from low energy electrons, X-Rays, macroscopic projectiles and irradiation by laser light. They render it impossible to obtain signals from the lowest energies in the spectrum underneath the cut-off for the ions themselves.

The uncertainty for the simulated mapping of active layer to proton energy is set by two sources. First, the active layer thickness d_{active} embodies the Bragg peak of an interval of proton energies ranging from E_{a} to E_{b}. Here the display of a peak-to-peak width is chosen, where one may prefer to use the FWHM of the descending and ascending Bragg-peak for E_{a} and E_{b} respectively. Second, the projected stopping range may be large compared to the thickness of layers in the stack which is reflected by an uncertainty ΔE corresponding to half the FWHM of Bragg peaks in the vicinity of the layer. Detailed information about energies resolved in the stack is given with table 7.1, for results depicted in fig. 4.12. Note that one encounters growing stopping range uncertainties for ions that traverse the full simulation range, comprising here a stack followed by a buffer zone filled with Mylar. This is an artefact of the simulation: SRIM is not able to determine the ion range directly and PySTarT uses the ionization curve of the projectiles in the target to estimate value and uncertainty of

the projectile range. The broader and broader low-stopping foot in advance of the Bragg-peak is visible with larger and larger uncertainties on a maximum value. Thus, plotted maximum values and uncertainties are not related to the range once an ion leafs the stack.

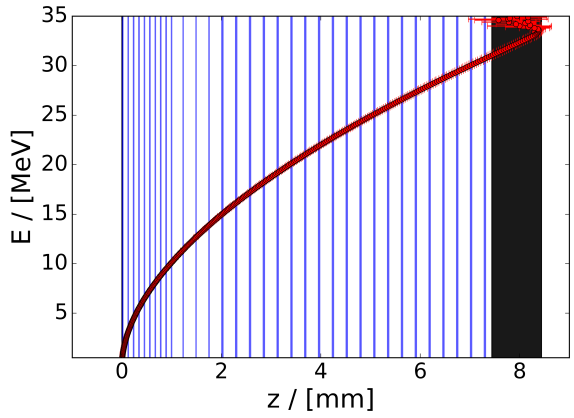

Figure 4.12: Stopping ranges for protons in RCF stacks with energies ranging from 500 keV to 30 MeV. Stacks comprise 10 layers of HD-V2, 3 layers of MD-V3 and 20 layers of EBT-3 protected by a preceding 10 µm thick Al-filter. Active layers are highlighted with blue colour, filters and auxiliary buffer layer are highlighted in black.

4.3.1.4 Absolute Dose calibration of Films

The dose deposition for calibration data is performed at a Medical Accelerator Unit (MAU) at Institut Bergonié, Bordeaux, for clinical oncology based on electron- and photon irradiation. MAUs usually deliver small doses to patients. There, we could not deliver a high dose in a single short bunch, which is required to investigate the dose rate response difference. In laser-ion-acceleration experiments, RCF the formation of radicals in the active medium occurs on the timescale of acceleration phenomenon from several fs up to a few ps, stretched in time by the ion-beam time-of-flight. For typical MeV energies of ions, and detector distances of some cm, experimental results are acquired with ns bunches of particles. Note that the darkening of films, which is linked to the polymerization reactions, happens on longer timescales of hours – longer than any irradiation event discussed in this work. We compare the calibration done at the MAU with an independent calibration done with a proton particle beam at a large scale Cockcroft–Walton type electrostatic accelerator [Hua+21]. Measurements were performed at the Centro de Micro-Análisis de Materiales (CMAM) [CF04; Pas04] at Universidad Autónoma de Madrid (UAM) in Madrid, Spain.

Calibration Dose Deposition

The MAU is source to electrons or photons with variable energies that can be used to deposit energy in the RCF, with a dose precision better than 1 %. For dose irradiation hereinafter, electrons with an initial energy of 9 MeV are used. Only one dose - 10 Gy - was chosen to compare the imprint on all RCF types regarding 6 MV photons. All film types show no evident difference in their answer to photons or electrons.

Films are irradiated uniformly for all doses. The irradiation by a flat-top square beam is shaped by a 15 cm $\times$ 15 cm aperture for electrons and a 10 cm $\times$ 10 cm aperture for photons before passing through the water

equivalent plastic and arriving on the film. The flat top profile has steep variations at the edges, see fig. 4.13 for photons. Calibration RCF of cm-size are positioned in the centre of the aperture or in groups with a maximum distance of 2 cm from the centre axis – this leads to an uniformity-deviation of $100 \cdot 10^{-3}$ % to $500 \cdot 10^{-3}$ % on the edges of the films relative to the centre dose value. The centring of the films relative to the beam is ensured by a cross-hair. Instead of dose maps $D(x, y)$, we assume hereinafter deposition of the nominal dose D with a standard deviation of 1 %.

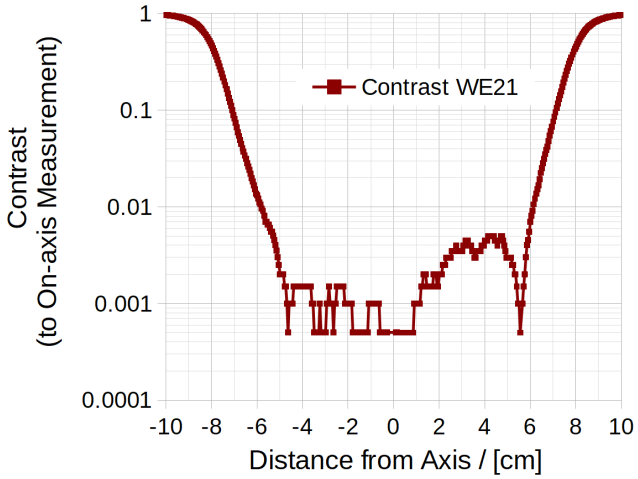

Figure 4.13: Contrast of dose measurements of the transverse dose profile with respect to the dose deposited on-axis. The MAU is adjusted to 100 cm source distance and doses are deposited in a water equivalent depth of 2.1 cm, shaped by a 15 cm $\times$ 15 cm aperture.

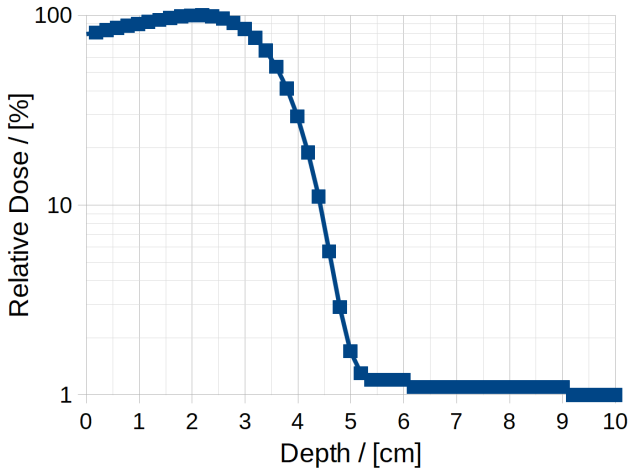

Figure 4.14: Percentage depth dose profile of 9 MeV electrons in water equivalent material on the centre axis. Plotted is the peak-normalized dose per depth in water. The MAU is adjusted to 100 cm source distance and a plateau is obtained for water equivalent depth of 2.1 cm.

The dose deposition at a MAU is calibrated with respect to depth in water to suit the medical application case. Principally, MD-V3 and EBT-3 can be investigated under water as their active layer is well protected against water immersion. To avoid contact between the on-surface active layer of HD-V2 with water, all measurements are done in a dry environment using water equivalent RW3[1] slab phantoms. Their characteristic dose-depth curve is plotted in fig. 4.14. The plateau of the dose deposition in a water equivalent depth of 2.1 cm accumulates due to electron scattering and secondary photons.

Shots with electrons are performed under a source-to-RCF distance of 100 cm on top of a pile of 10 RW3 plates of 1 cm thickness, to ensure nominal back-scattering of the electron beam. Pre-stopping of electrons is performed using $2\times$ 1 cm and $1\times$ 1 mm of RW3, to irradiate within the dose-depth plateau. The slaps are squares of 30 cm sides, centred with the irradiation axis. A single layer of RCF is thin and fits in the gap of two large plates without tilt effects on the plate. Comparative shots with photons are performed under a source-to-RCF distance of 95 cm using $1\times$ 1 cm $+1\times$ $500 \cdot 10^{-3}$ cm of RW3 for pre-stopping.

The dose is delivered in bunches of 1 cGy with a dose rate of 10 Gy min^{-1} with a macro-bunch length maximum of 50 Gy. Macro-bunches are intersected by a mandatory operator request that takes approximately 10 s for performance in average.

[1] RW3 slab phantoms were delivered by PTW Freiburg GmbH

At CMAM, a Titanium Hydride (TiH_2) sputtering source delivers protons that are accelerated up to $10.0(4)$ MeV and collimated by two successive 2 m distant squared Tantalum (Ta) masks to a transverse section of $S = 4.4\,\mathrm{mm}^2$. The experiment is performed in a secondary vacuum with pressure of $10 \cdot 10^{-6}$ mbar. The proton beam is guided into a stack of RCF enveloped in a thin metallic filter foil. Diagnosis of the beam current $\partial_t Q$ is done by a Faraday cup mounted as beam shutter in front of the stack. The shutter was controlled to open for a time Δt, giving passage of $N = \Delta t \cdot \partial_t Q / q_\mathrm{e}$ projectiles. Additionally, a charge integrator connected to the RCF stack holder was used to measure the total absorbed beam charge Q and derive the particle number $N = Q/q_\mathrm{e}$. The deposited dose per active layer is calculated by a LET simulation per projectile and extrapolated to the particle number N. Various RCF stacks were exposed once to a proton beam, each with different N.

Note that it was assured for both characterization campaigns that all reference films for zero-exposure had the same life cycle as the exposed film, except of course the irradiation.

Calibration Doses Range

The following calibration doses are suited for calibration curve fitting regarding the dynamic range of the respective film types and small increments in sections of large second derivative. First result of this calibration effort is, that the dose range that can be used in RCF dosimetry is larger than the manufacturer specified.

HD) 0 Gy, 5 Gy, 10 Gy, 50 Gy, 80 Gy, 100 Gy, 150 Gy, 250 Gy, 500 Gy, 1 kGy, 2 kGy, 3 kGy

MD) 0 Gy, 5 Gy, 10 Gy, 15 Gy, 25 Gy, 50 Gy, 100 Gy

EBT) 0 Gy, $10 \cdot 10^{-3}$ Gy, $100 \cdot 10^{-3}$ Gy, 1 Gy, 2 Gy, 4 Gy, 6 Gy, 10 Gy, 20 Gy, 40 Gy, 80 Gy

One precisely archives this dose values using the MAU, but the experiment at CMAM faced problems to deliver doses lower than several 100 Gy for the limited shutter speed. At CMAM exposures were 2 s to 12 s long and doses from 250 Gy to 3.5 kGy were reached within the stack of 10 $\times$ HD-V2 beyond a 10 µm thick filter foil.

Coping for Flaws of a Flat-Bed Scanner

For data digitization, all flatbed scanners have the disadvantage that their light sources change the illumination properties with increasing age. This potentially eliminates the comparability of any absolute calibration of a scanner system to data scans. At the beginning of each scan, the EPSON EXPRESSION 11000XL checks the colour response by means of a white balance. This is automatically done in the zone above the scan zone, indicated by arrows on the scanner itself. The white balance compensates for the ageing of the light source, but it may cause trouble: the full acquisition band is being re-normalized and eventually changing peak to peak-intensity ratios are ignored. For this work, calibration scans and data scans for experiment analysis are performed within time spans of several month and often the only scan events for the used system.

Further it is important to ensure that the scanner glass does not get dirty, *e.g.* with oily deposits - or worse, that it does not experience damage caused by scratches.

If multiple scans on one film were performed, the calibration films were scanned in regular intervals of 30 min with films removed from the scanner in pauses. This interval was set in order to be large enough to cool down the scanner flat bed and lamp, for comparable initial conditions of each scan.

Dose Response Fit for Calibration RCF

The scan-system specific transformation from RCF scan image-arrays $g(\text{ch}, x, y)$ (in grayscale) to dose maps $D(x, y)$ (in Gy) can be performed via channel-wise direct comparison to calibration data $D(\text{ch}, x, y)$ with $\text{ch} \in \{R; G; B\}$. Note that $D(\text{ch}, x, y) = D$ is uniform within the irradiation uncertainty. In order to avoid comparability issues between calibration and data, the scanning protocol section 4.3.1.2 is respected, scans are with orientation of 90° in the centre of the scanner flat-bed.

In order to obtain maps of $g(\text{ch}, x, y)$, the full film is scanned, comprising it's edges and any surface artefact. The scan delivers a matrix with a gray-value for each colour in each pixel, among which we need to select the data. The colour channels are processed separately. To obtain a mean grayscale $\langle g_{\text{ch}} \rangle$ with an standard deviation, a Gaussian peak is fitted to the histogram of the respective colour channel. With such procedure, influences of dark dust, light scratches, white background and black edge effects as well as marks on the film are discarded. Scanning with a higher resolution pronounces edge colour-artefacts and demands a fit by a so called 'Johnson SU-Distribution'. Result is a colour-channel dependent mean grayscale to dose correspondence, a data point for fitting.

The RCF manufacturer proposes [Gca] a fit function for calibration of flat-bed scanners that reads

$$D = c_{\text{ch}}^{\text{fit}} + \frac{b_{\text{ch}}^{\text{fit}}}{\langle g(\text{ch}) \rangle - a_{\text{ch}}^{\text{fit}}} \quad . \tag{4.70}$$

This function became a well established standart fit model for RCF calibrations as it is easy to invert. The inverse function

$$\langle g(\text{ch}) \rangle = a_{\text{ch}}^{\text{fit}} + \frac{b_{\text{ch}}^{\text{fit}}}{D - c_{\text{ch}}^{\text{fit}}} \quad , \tag{4.71}$$

can be fitted to calibration data. The rather abstract fit parameter values for $c_{\text{ch}}^{\text{fit}}$, $b_{\text{ch}}^{\text{fit}}$ and $a_{\text{ch}}^{\text{fit}}$ are only constant for a given batch of a specific film-type scanned with a specific flat-bed scanner. In order to render this model more physical, we define $A_{\text{ch}}^{\text{fit}} = b_{\text{ch}}^{\text{fit}} / c_{\text{ch}}^{\text{fit}}$ and $g_{0,\text{ch}}^{\text{fit}} = a_{\text{ch}}^{\text{fit}} - A_{\text{ch}}^{\text{fit}}$. The intercept $g_{0,\text{ch}}^{\text{fit}}$ denotes the grayscale response of a non-irradiated film and the scale parameter $A_{\text{ch}}^{\text{fit}}$ represents the dynamic range of the RCF in grayscale due to radiosynthesis and $c_{\text{ch}}^{\text{fit}}$ unravels as scaling parameter for which lower absolute values indicate the onset of sensitivity for lower doses,

$$\langle g_{\text{ch}} \rangle = g_{0,\text{ch}}^{\text{fit}} + A_{\text{ch}}^{\text{fit}} \cdot \frac{D}{D - c_{\text{ch}}^{\text{fit}}} \quad . \tag{4.72}$$

We see with a fit on the HD-V2 batch number 11171601 that in the limit of infinite doses $g_{0,\text{ch}}^{\text{fit}} + A_{\text{ch}}^{\text{fit}} < 0$ bit for $\text{ch} \in \{R; G\}$, compare fig. 4.15. This is unphysical, as the infinite dose can only saturate the film up to no transmission. The maximum range of validity is $D_{\text{ch}} \in [0; c_{\text{ch}}^{\text{fit}} - c_{\text{ch}}^{\text{fit}} \cdot A_{\text{ch}}^{\text{fit}} / (g_{0,\text{ch}}^{\text{fit}} + A_{\text{ch}}^{\text{fit}})]$ Gy for channels ch with negative limit value. We evaluate $D_{\text{R}} \in [0; 73264.]$ Gy and $D_{\text{G}} \in [0; 25198.]$ Gy. The blue colour channel saturates at $\lim_{D \to +\infty} \langle g_{\text{B}} \rangle = 1972$ bit and its calibration fit is valid for all doses.

The dose calibration function proposed by the manufacturer is adapted to the limit of low doses only. Modification of eq. (4.70) to obtain a more physical fit function ultimately leads to a reduction by one parameter. In order to respect the limit for high doses we impose $a = 0$ – a modification that makes the model fail to reproduce low doses accurately.

Scanned data in grayscale can be transformed into OD arrays $\langle \iota \rangle (g(\text{ch}, x, y))$, compare section 4.3.1.2. Then, a physical representation of the sensitometric curve for the OD of each colour channel ι_{ch} can be obtained

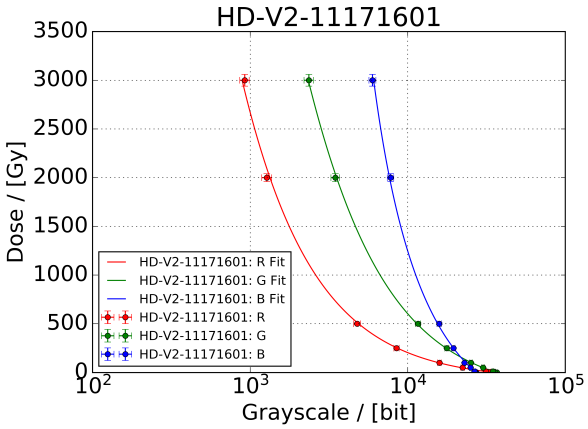

(a) data and fit for all channels

```
HD-V2-11171601 Ch:R
 A = -35362.0 +/- 343.0
 c = -80.89 +/- 2.98
 g_0 = 35323.0 +/- 351.0

HD-V2-11171601 Ch:G
 A = -36782.0 +/- 326.0
 c = -235.8 +/- 11.4
 g_0 = 36441.0 +/- 312.0

HD-V2-11171601 Ch:B
 A = -25003.0 +/- 531.0
 c = -589.3 +/- 55.0
 g_0 = 26975.0 +/- 241.0
```

(b) fit reports for all colour channels

Figure 4.15: Fit of the dose response model proposed by the manufacturer, performed to calibration data for HD-V2 batch number 11171601 obtained at the MAU.

with the universal dose response model [Cue+15],

$$\iota_{\mathrm{ch}} = A_{\mathrm{ch}}^{\mathrm{fit}} \cdot \left(1 - (1 + \frac{D}{k_{\mathrm{ch}}^{\mathrm{fit}}})^{\theta}\right) + \iota_{0,\mathrm{ch}}^{\mathrm{fit}} \quad . \tag{4.73}$$

where $A_{\mathrm{ch}}^{\mathrm{fit}}$ and $k_{\mathrm{ch}}^{\mathrm{fit}}$ are parameters depending channel and scanner system, the off-set $\iota_{0,\mathrm{ch}}^{\mathrm{fit}}$ depends on the life-cycle of the non-irradiated film and $\theta = 0.436 \pm 0.005$ [Cue+15] represents a universal constant that depends on the sensitive material.

Such calibration can be compared to published calibration data, or used as calibration data for comparable flat-bed systems, if the emission spectrum of the scanner light sources are characterized respectively and found identical after renormalization. All calibrations done within this work are valid only for the EPSON EXPRESSION 11000XL situated at Laboratoire CELIA (Univ. Bordeaux, France), which is Xenon gas cold cathode fluorescent lamp based. This is due to the fact that we did not perform a dedicated measurement of the emission spectrum.

Most authors prefer to subtract the OD of the non-irradiated film $\iota_{0,\mathrm{ch}}^{\mathrm{fit}}$ for presentation of calibration data. In order to better judge comparability of ones RCF to a certain calibration, this value has the major advantage of beeing accessible even without dose-calibration campaign and should always be part of the model. For calibration data obtained for HD-V2 batch #11171601, see the exemplatory characterization fit with parameters in fig. 4.16.

We appreciate the different sensitivity of the colour channels. Note that for low doses, the uncertainty on the determination of the OD of a measurement dominates the uncertainty of deduced dose values. For high doses the calibration curve flattens and the uncertainty of the calibration fit yields large uncertainties of deduced doses. The red channel has the largest variation in it's response, the blue channel the lowest. We do not observe saturation on the calibrated range from 0.0 kGy to 3.0 kGy.

The calibration at CMAM was performed one year before the calibration at the MAU, with films out of the same envelope for HD-V2 batch #11171601. There, the zero-reference film scanned with a EPSON V750-PRO yields optical densities $\iota_{0,\{\mathrm{R;\,G;\,B}\}}^{\mathrm{scan}} = \{0.277 \pm 0.009; 0.278 \pm 0.010; 0.425 \pm 0.009\}$. The aging of HD-V2 films yields a

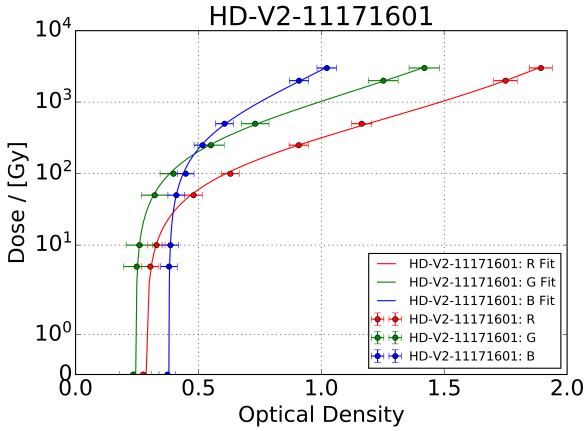

(a) data and fit for all channels

```
HD-V2-11171601 Ch:R
 A = 2.3678 +/- 0.093
 k = 248.8 +/- 32.8
 OD_0 = 0.2874 +/- 0.0202

HD-V2-11171601 Ch:G
 A = 2.164 +/- 0.247
 k = 611.0 +/- 190.0
 OD_0 = 0.2448 +/- 0.0285

HD-V2-11171601 Ch:B
 A = 1.38 +/- 0.255
 k = 957.0 +/- 410.0
 OD_0 = 0.3798 +/- 0.0174
```

(b) fit reports for all colour channels

Figure 4.16: Fit of the universal dose response model to calibration data for HD-V2 batch number 11171601 obtained at the MAU.

darkening in a OD range from $73 \cdot 10^{-3}$ to $180 \cdot 10^{-3}$ for one year, thus the zero-reference for both calibration campaigns agree in the margin of their uncertainty for the red colour channel – green and blue channel show lighter shades which can not be explained. Note that the calibration films are scanned with different scanner, but which is from the same manufacturer with the same type of light source. Scans performed with both systems possibly average differently over the transmission spectrum of RCF, hence they can not be presumed to be directly comparable.

The calibration curves of both campaigns are plotted in fig. 4.17a, thoroughly showing higher optical densities for high doses at CMAM. Focusing on the red colour channel and comparing MAU to CMAM, one notes positive shifts of $50(2) \cdot 10^{-3}$, $260(2) \cdot 10^{-3}$ and $260(2) \cdot 10^{-3}$ optical densities for 10 Gy, 100 Gy and 1 kGy respectively. The collective effects of a high beam current on material damage possibly result in more material damage, *e.g.* due to a higher reaction rate from radicals to joint chains, or ohmic heating. The relative difference between the OD values is respectively $3.6(22)\,\%$, $8.8(16)\,\%$ and $4.0(11)\,\%$.

The influence of the scanner light source and image acquisition system to the outcome of calibration is highlighted in fig. 4.17, by comparison to the modelled channel-averaged response curve to doses delivered by high energy high flux particle beams [Bin+19]. The model predicts that higher beam currents yield less damage than observed at CMAM. Note that the deployed scanner has different characteristics and the calibrations can not be compared, the model is not universal. Systematically decoupling data from the spectral characteristics of scanner systems would allow for direct comparability.

This work also makes use of batch #06251801 of type U-EBT-3 and the batch #CLPU201810 of EBT-3 provided at Centro de Láseres Pulsados (CLPU) in October 2018 (equal to #10251701), the respective calibrations are presented in fig. 4.18 and fig. 4.19.

We see that the EBT type has a different response than the HD type. EBT are applicable to lower doses as HD. For EBT, there are two distinct slopes for both green and red channel, whereas the blue channel does show a smooth curve. The blue channel is dominated by the marker dye and a flat response in both cases, such that it remains comparable despite for variations in the film thickness. The response in red and green channels is influenced by changes of the film absorption spectrum.

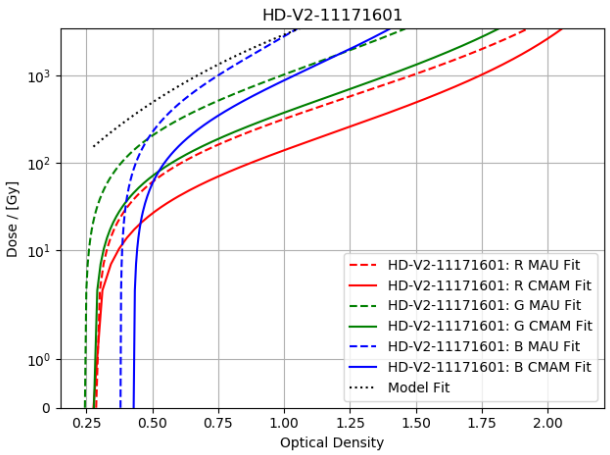

(a) comparison of fit for all channels

```
HD-V2-11171601 Ch:R
 A = 2.243 +/- 0.144
 k = 96.3 +/- 25.5
 OD_0 = 0.2771 +/- 0.0277

HD-V2-11171601 Ch:G
 A = 2.238 +/- 0.17
 k = 260.0 +/- 57.6
 OD_0 = 0.2789 +/- 0.0277

HD-V2-11171601 Ch:B
 A = 1.687 +/- 0.233
 k = 557.0 +/- 212.0
 OD_0 = 0.4297 +/- 0.0411
```

(b) fit reports for all colour channels

Figure 4.17: Fit of the universal dose response model to calibration data for HD-V2 batch number 11171601 obtained at CMAM, for which data is extracted from [Hua+21]. The model curve refers to channel averaged calibrations done recently with high energy high flux particle beams [Bin+19].

Batch to Batch Variations

Note that calibration results depends not only the type of film but also the batch the films were produce in - the manufacturer states a batch-to-batch difference in response of up to 10 %. One compares to different batches with fig. 4.18d and fig. 4.18b, bought two years from each other. Calibration curves have slightly different slopes and shapes, but all parameters agree in their respective margins of uncertainty.

Differences of the Scanner Answer due to Polarization Effects

The polarization effect is due to polymerization reactions that are preferentially aligned in the so-called down-web direction, which is parallel to coating direction. Therefore RCF are weak polarizers after exposure [Lew10], and the rotational orientation α_{ori} of films on the flatbed matters to the answer function. Note that the angle convention for scan orientation used in this work is $\alpha_{\text{ori}} = \pi/2$, that is corresponding to the case with the line-like scanner light source parallel down-web direction.

Most pronounced are polarization effects in recent batches of EBT-3, shown in fig. 4.20. The sinusoidal can be best fitted with

$$\langle g(\text{ch,D}) \rangle \left(\alpha_{\text{ori}}\right) = g_{45}(\text{ch,D}) + g_{\text{AMP}}(\text{ch,D}) \cdot \cos\left(\alpha_{\text{ori}}\right) \quad , \tag{4.74}$$

where parameters are depending on the dose. Recent batches of HD-V2 do show polarization effects too, shown in fig. 4.21. The variance of data is larger, but the same sinusoidal can be best fitted. Note that the amplitude is of the order of the %, which would represent a small error.

The third type of RCF, MD-V3, did not show polarization effects for calibration campaigns undertaken to carry out this work.

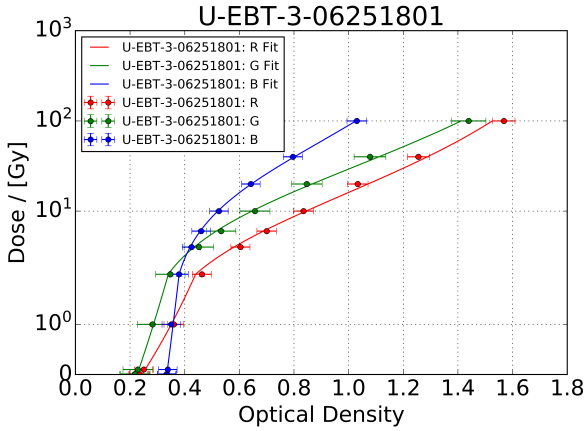

(a) data and fit for all channels

```
U-EBT-3-06251801 Ch:R
 A = 1.8316 +/- 0.0774
 k = 6.735 +/- 0.919
 OD_0 = 0.2435 +/- 0.0186

U-EBT-3-06251801 Ch:G
 A = 1.965 +/- 0.182
 k = 13.59 +/- 3.4
 OD_0 = 0.2258 +/- 0.0267

U-EBT-3-06251801 Ch:B
 A = 1.378 +/- 0.176
 k = 25.23 +/- 7.47
 OD_0 = 0.3344 +/- 0.0157
```

(b) fit reports for all colour channels

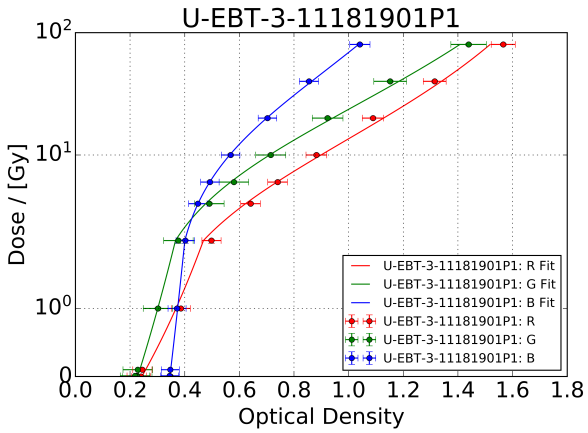

(c) data and fit for all channels

```
U-EBT-3-11181901P1 Ch:R
 A = 1.8402 +/- 0.0802
 k = 5.727 +/- 0.799
 OD_0 = 0.2432 +/- 0.0189

U-EBT-3-11181901P1 Ch:G
 A = 1.955 +/- 0.179
 k = 10.91 +/- 2.73
 OD_0 = 0.2279 +/- 0.0275

U-EBT-3-11181901P1 Ch:B
 A = 1.384 +/- 0.18
 k = 20.66 +/- 6.17
 OD_0 = 0.3458 +/- 0.0159
```

(d) fit reports for all colour channels

Figure 4.18: Fit of the universal dose response model to calibration data for U-EBT-3 batch numbers 06251801 and 11181901P1.

4.3.1.5 Stacks of Radio-Chromic Film as Spectrometer

The above calibrations allows one to transform scanned imprints on RCF to 2D dose maps, that in turn are energy resolved according to the LET characteristics in the stack. Results depend on the channel, as each channel concerns a different part of the absorption spectrum, and can be regarded as separate measurement with independent uncertainty. Channel-wise dose data is transformed to number density maps with decon_RCF, see section 7.5.

Following the protocol established in [N+09], the code deconvolves imprints issued by high energy ions on layers they traverse. Starting with the last imprinted layer and the highest ion energy, it calculates a particle number spectrum pixel-wise following eq. (4.56). Basic assumption for the current version of the code is a flat spectrum between two layers. This has a major influence on the results as one pre-defines the form of the spectrum, which is a huge bias due to the limited amount of samples RCF stacks deliver.

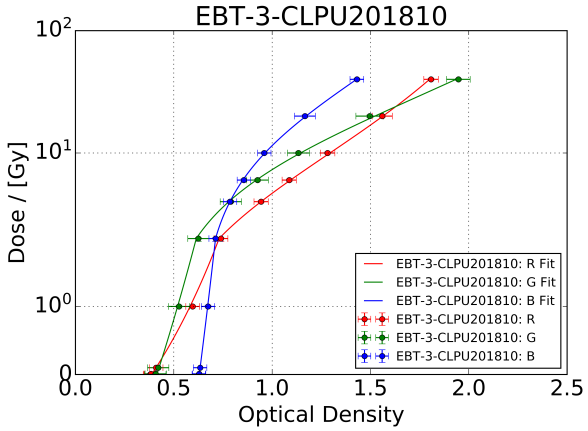

(a) data and fit for all channels

```
EBT-3-CLPU201810 Ch:R
 A = 2.2052 +/- 0.0944
 k = 4.219 +/- 0.535
 OD_0 = 0.3872 +/- 0.0196

EBT-3-CLPU201810 Ch:G
 A = 3.327 +/- 0.359
 k = 13.06 +/- 3.0
 OD_0 = 0.414 +/- 0.0279

EBT-3-CLPU201810 Ch:B
 A = 2.178 +/- 0.377
 k = 21.52 +/- 6.96
 OD_0 = 0.6296 +/- 0.017
```

(b) fit reports for all colour channels

Figure 4.19: Fit of the universal dose response model to calibration data for EBT-3 batch number CLPU201810.

4.3.2 Solid State Track Detectors - Columbia Resin #39

Solid State Track Detectors (SSTDs) are used to measure ionizing radiation by quantifying material damage [You58; DB87], some require a secondary development process. Chemical reactions in and around the projectile track cause permanent structural changes that can be measured and related to projectile species and impact energy. Other than RCF, SSTDs allow to determine the exact number density of projectiles by giving access to singular projectile tracks. The three-dimensional projectile traces are accessible across the entire detector slap. We will focus hereinafter on Columbia Resin #39 (CR-39) plane plate detectors [CSP78; Rud+80], a high sensitivity high resolution variety of SSTD. CR-39 widely used to confirm appearance of projectile species in charged particle beam acceleration experiments, we will develop further on the idea to use them as spectrometer.

4.3.2.1 Composition and Irradiation Reaction of Columbia Resin #39

CR-39 are made of polyallyl diglycol carbonate polymers with diethylene glycol bis(allyl carbonate) monomer $C_12H_{18}O_7$. The thermosetting plastic polymer is widely available as it is industrially used for plastic eyeglass lenses. The plastic is transparent in the visible wavelength range with absorption spectrum depicted in fig. 4.22. As the first manufacturer for such lenses was situated in California, some confuse CR-39 with California Resin #39. Historically, the plastic was firstly used as glass-replacement for the fuel tanks of long-range bombers allowing a weight reduction and therefore either more load or wider operation radii.

During exposure to ionizing radiation, projectiles collide with the polymer chains and some of them break. Structurally, the polyallyl chains in CR-39 are joined by diethyleneglycol dicarbonate links. The polyallyl chain was found to be unaltered by irradiation [SP86] which points to the diethyleneglycol dicarbonate links as radiation sensitive. Decarboxylation, the splitting of a given molecule in molecular carbon dioxide (CO_2) and a residual, is a common radiation reaction of polymers like polyester and polycarbonate [Mau87]. This endorses the carbonate group as radiation sensitive in CR-39 [TD95], which was confirmed by measurement of concentrations of CO_2 in post-exposure CR-39 [Cho+97].

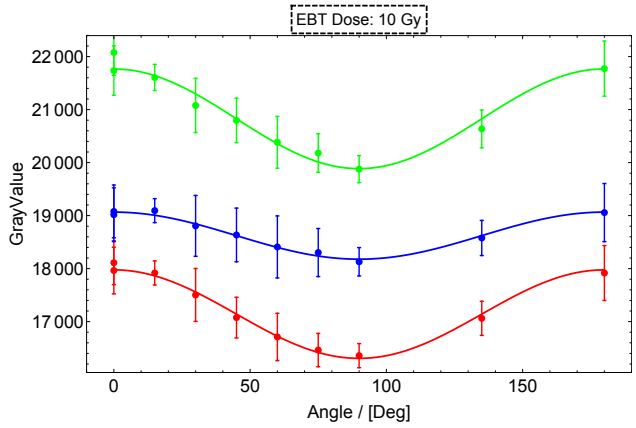

(a) data and fit for all channels

```
EBT-3-CELIA2016/spring
Ch   g_45           g_AMP
R    17141 +/- 24   835 +/- 31
G    20826 +/- 53   940 +/- 69
B    18622 +/- 17   444 +/- 21
```

(b) fit report for all colour channels

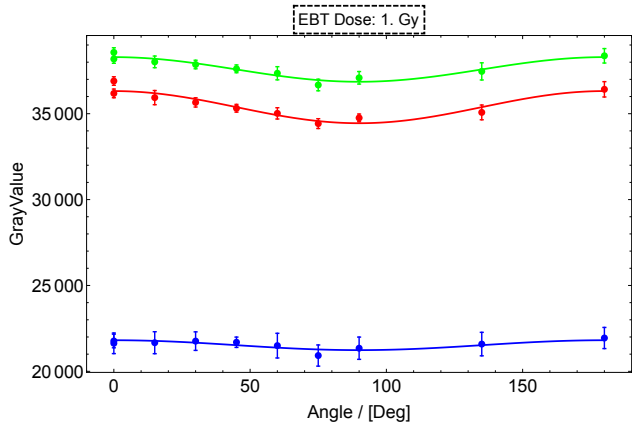

(c) data and fit for all channels

```
EBT-3-CELIA2016/spring
Ch   g_45           g_AMP
R    35382 +/- 97   935 +/- 125
G    37577 +/- 63   717 +/-  82
B    21523 +/- 58   288 +/-  75
```

(d) fit report for all colour channels

Figure 4.20: Dependence of the scanner answer with respect to the rotational orientation of EBT-3, unknown batch bought by CELIA in spring 2016.

4.3.2.2 Damage Mechanism and Dose Response

The damaged region in the polymer is known but the driving damage mechanism at play is subject to discussions. The stopping of ion projectiles in CR-39 ionizes the material by ion-molecule interaction on the ion track and yields energetic electrons. Furthermore, energy is transferred to recoiling target atoms, that may get knocked-off their position. As secondary radiation, electrons and knocked-off target atoms contribute to distant polymer chain fractionation by transporting energy into the region in the vicinity of the ion track.

Fractured bonds can be categorized in irreparable, also referred to as latent, and partially damaged. The zone where irreparable damage occurs is denominated as latent track [DB87]. With the unaltered chain, this yields three possible states of the polymer after irradiation. The first-order transitions are total damage yielding latent cracks as well as partial damage yielding long living radicals. In second order, a post-exposure dynamics related to the partially damaged bonds leads to a partial reconstitution of intact polymers and a partial transfer into latent cracks. Overall, it is reported that concentrations of free oxygen play an important role to the formation of latent tracks [YOM92], as they are available reaction partner of radicals during their lifetime. The three states with four transitions could be described by a system of differential equations that yields a solution with a saturation therm minus two negative exponential therms, representing the dose response.

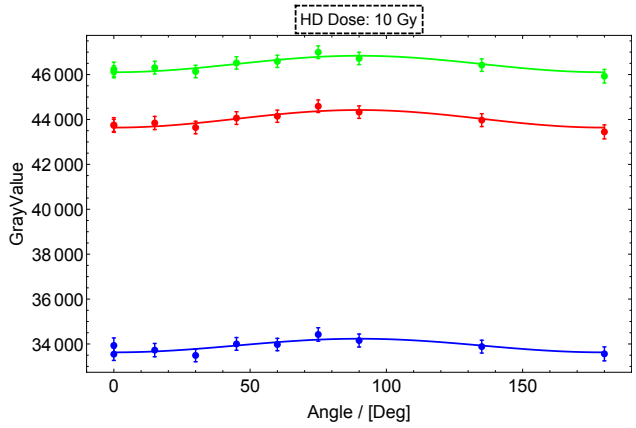

(a) data and fit for all channels

```
HD-V2-CELIA2016/spring
Ch   g_45           g_AMP
R    44030 +/- 50   -391 +/- 65
G    46471 +/- 46   -367 +/- 60
B    33929 +/- 60   -303 +/- 78
```

(b) fit report for all colour channels

Figure 4.21: Dependence of the scanner answer with respect to the rotational orientation of HD-V2, unknown batch bought by CELIA in spring 2016.

4.3.2.3 Data Exploration Methodologies

There are two methodologies to investigate the cracks along projectile tracks, both of which can be used complimentary. The first approach, barely pursuit, is based on detection of the radiation reaction product CO_2 by optical spectroscopic methods. The molecular CO_2 is slowly diffusive and measurements are reported based on Fourier-transform infrared spectroscopy [Mal+01].

We will focus hereinafter on the second approach which makes the projectile track visible via a chemical post-exposure etching of the SSTD material. Therefore SSTDs are sometimes referred to as etched track detectors. Etching the CR-39 with an alkali solution yields ablation of surface material due to reactions of the polymer with the hydroxide ions. The ablation rate is constant for a pure homogeneous plastic, given that the reaction environment with hydroxide concentration and ambient temperature and pressure is constant. Hydroxide cuts the carbonate links [SP86] as ionizing radiation does. For exposed regions along tracks with already broken links, the ablation rate is higher and a crater develops, often referred to as etch pit.

The bulk etching rate v_B, in units of an ablation speed, is depending on material parameters and the life cycle of the CR-39. The etching rate along ion tracks v_T depends in addition on the irradiation response of the plastic. Recent studies found the bulk etching rate also to be sensitive to high doses of X-rays [RH+15].

Main observables of the etch pits at the detector surface are depth and diameter. Additionally, the direction of projectiles can be retrieved from the inclination of the crater axis to the detector surface and the ellipticity of the crater. Most authors in HEDP use the diameter evolution with etching time as observable that then is compared to calibration data, also the crater inclination is used for background subtraction [Ing+18]. We will see hereinafter, that the track length is more directly coupled to the track etching rate. This work relates to a more complete analysis of the depth-diameter evolution and employs analysis of singularly etched SSTD material based on both observables.

4.3.2.4 Description of the Etch Pit Growth

The following derivation follows the discussion in [DB87]. First, we assume the ion track to be punctual on the detector surface, not taking into account the secondary material destruction triggered by ionized electrons.

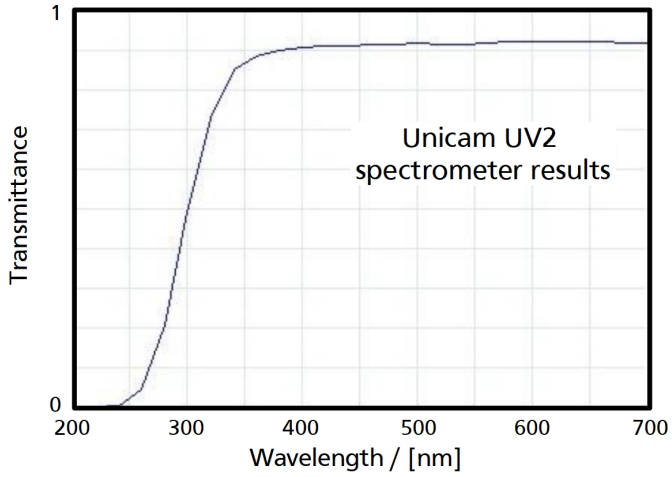

Figure 4.22: Transmission of a TASTRAK CR-39 Plastic Sheet of $1.5\,\mathrm{mm}$ thickness for EM radiation in the visible range, extracted from [Wor14].

We presume a proportionality of track etching rate v_T and energy deposition $S_j(\Delta z)$ with no final decision for the leading mechanism $j \in \{\text{total}; \rightarrow \text{electrons}; \rightarrow \text{recoils}\}$. Furthermore the ion track shalt be normal to the detector surface. Then, $v_\mathrm{T}(-S_j(\Delta z))$ depends on the stopping power at a given depth Δz. v_B is presumed a material constant. Following the Huygens-Fresnel principle for elementary wave propagation, we derive the pit growth initiated by a point moving along the z-axis with velocity $v_\mathrm{T}(-S_j(z))$ that launches spherical etching waves at constant speed v_B. We also take into consideration that the bulk material ablates over the full surface with constant rate v_B, and therewith the plane into which the pit ends. The track length growth rate $\mathrm{d}_t L$ for a given exposure time t to the etchant solution can be calculated by

$$\mathrm{d}_t L(t) = -v_\mathrm{B} + v_\mathrm{T}(-S_j(z(t))) \quad . \tag{4.75}$$

A coordinate transform is necessary to find $S(t)$,

$$t(z) = \int_0^z \frac{1}{v_\mathrm{T}(-S_j(\check{z}))} \mathrm{d}\check{z} \quad , \tag{4.76}$$

where $z(t=0) = 0$. Then the track length is

$$L(t) = -v_\mathrm{B} \cdot t + \int_0^t v_\mathrm{T}(-S_j(\check{t}))\mathrm{d}\check{t} \quad , \tag{4.77}$$

For constant etching rates this yields

$$L(t) = t \cdot (v_\mathrm{T} - v_\mathrm{B}) \quad , \tag{4.78}$$

a form that can be applied to projectiles of relatively uniform energy deposition, *e.g.* to ionic projectiles of high energy to mass ratio. Note that this yields growth of a cone with semi-cone angle $\delta = \arcsin {}^{v_\mathrm{B}}/_{v_\mathrm{T}}$. The pit diameter D calculates to

$$D = 2 \cdot L \cdot \tan\delta \tag{4.79}$$

$$= 2 \cdot t \cdot (v_\mathrm{T} - v_\mathrm{B}) \cdot \left(\frac{v_\mathrm{B}}{\sqrt{v_\mathrm{T}^2 - v_\mathrm{B}^2}} \right) \tag{4.80}$$

$$= 2 \cdot t \cdot v_\mathrm{B} \cdot \sqrt{\frac{v_\mathrm{T} - v_\mathrm{B}}{v_\mathrm{T} + v_\mathrm{B}}} \quad . \tag{4.81}$$

With both, diameter and track length, we are able to understand dynamically formed major characteristics of the etch pit. Dividing eq. (4.78) by eq. (4.81) yields,

$$\frac{L}{D} = \frac{1}{2} \cdot \sqrt{\left(v_{\mathrm{T}}/v_{\mathrm{B}}\right)^2 - 1} \quad . \tag{4.82}$$

The limit of $v_{\mathrm{B}} \ll v_{\mathrm{T}}$ yields a narrow pit cone with $\lim_{v_{\mathrm{T}} \to \infty} D = 2 \cdot t \cdot v_{\mathrm{B}}$. For $v_{\mathrm{B}} \approx v_{\mathrm{T}}$, no pit is developped. With eq. (4.82), it is already possible to measure track etching rates. They can be compared to calibration data to derive projectile energies.

Second, we want to widen the scenario for cases with non-constant v_{T}. For detailed analysis it is important to take into account the variation of the energy deposition along the track, especially for ions with Bragg-peak close to the surface. The coordinate r is set perpendicular to z, just in the manner of general cylindrical coordinates assuming cylindrical symmetry. See fig. 4.23 for illustrations on the geometry.

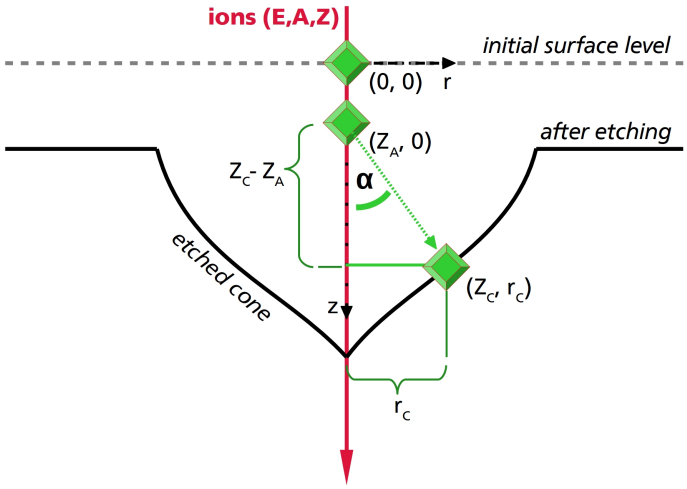

Figure 4.23: Side view on an etch pit of CR-39, with superposed idealised ion track. The surface position before etching is set to be $z(t = 0) = 0$. Assuming radial symmetry, the radial coordinate points away from the ion track with zero position on the track which then is also symmetry axis of the pit. Every point on the etched cone is reached by the etchant according to Fermat's principle of the least time, which allows to deduce either the track etching rate measuring the full cone or to simulate tack length and pit diameter with known track etching rate.

With two distinct regions of differing etching rate, notably bulk material and ion track, every point $(z_{\mathrm{C}}, r_{\mathrm{C}})$ on the conical pit surface is reached after a linear combination of etching along the track until a point $(z_{\mathrm{A}}, 0)$ followed by etching through the bulk material. The time $\check{t}$ needed to reach $(z_{\mathrm{C}}, r_{\mathrm{C}})$ coming from $(0, 0)$ via $(z_{\mathrm{A}}, 0)$ is

$$\check{t} = \left(\int_0^{z_{\mathrm{A}}} \frac{1}{v_{\mathrm{T}}(-S_j(\check{z}))} \mathrm{d}\check{z} \right) + \frac{\sqrt{\left(z_{\mathrm{C}} - z_{\mathrm{A}}\right)^2 + r_{\mathrm{C}}^2}}{v_{\mathrm{B}}} \quad . \tag{4.83}$$

Employing the principle of the least time, we minimize $\check{t}$ to obtain the most likely division of the path,

$$\mathrm{d}_{z_\mathrm{A}}\check{t} = \frac{1}{v_\mathrm{T}(-S_j(z_\mathrm{A}))} - \frac{z_\mathrm{C} - z_\mathrm{A}}{v_\mathrm{B} \cdot \sqrt{(z_\mathrm{C} - z_\mathrm{A})^2 + r_\mathrm{C}^2}} \stackrel{!}{=} 0 \tag{4.84}$$

$$\Leftrightarrow z_\mathrm{C} - z_\mathrm{A} = \frac{r_\mathrm{C}}{\sqrt{\left(v_\mathrm{T}(-S_j(z_\mathrm{A}))/v_\mathrm{B}\right)^2 - 1}} \quad . \tag{4.85}$$

Geometrically interpreted, eq. (4.85) is an expression for the cathetus $z_\mathrm{C} - z_\mathrm{A}$ of the triangle $(z_\mathrm{A}, 0)$–$(z_\mathrm{C}, r_\mathrm{C})$–$(z_\mathrm{C}, 0)$. We find

$$\alpha(v_\mathrm{T}(-S_j(z_\mathrm{A})), v_\mathrm{B}) = \arctan\left[\sqrt{\left(v_\mathrm{T}(-S_j(z_\mathrm{A}))/v_\mathrm{B}\right)^2 - 1}\right] \quad , \tag{4.86}$$

the angle between etching wavefront and ion track for point $(z_\mathrm{A}, 0)$. With a constant bulk etching rate, the etching wave front in all points on the cone wall $(z_\mathrm{C}, r_\mathrm{C})$ is perpendicular to the corresponding vector $(z_\mathrm{A}, 0)$–$(z_\mathrm{C}, r_\mathrm{C})$. Therefore $\alpha(v_\mathrm{T}(-S_j(z_\mathrm{A})), v_\mathrm{B})$ is imprinted into the local semi-cone opening angle $\delta(z_\mathrm{C}, r_\mathrm{C}) = {}^{\pi}/_{2} - \alpha(v_\mathrm{T}(-S_j(z_\mathrm{A})), v_\mathrm{B})$.

For better reading, we name the time partition needed for the etchant to reach the point $(z, 0)$, let

$$\Lambda\left[v_\mathrm{T}(-S_j(z)), z\right] \stackrel{!}{=} \int_0^z \frac{1}{v_\mathrm{T}(-S_j(\check{z}))}\mathrm{d}\check{z} \quad . \tag{4.87}$$

We substitute either cathetus in eq. (4.83) in terms of eq. (4.85) for a known total etching time t. First the cathetus $z_\mathrm{C} - z_\mathrm{A}$ to obtain the coordinate r_C

$$t = \left(\int_0^{z_\mathrm{A}} \frac{1}{v_\mathrm{T}(-S_j(\check{z}))}\mathrm{d}\check{z}\right) + \frac{r_\mathrm{C}}{v_\mathrm{B} \cdot \sqrt{1 - \left({}^{v_\mathrm{B}}/_{v_\mathrm{T}(-S_j(z_\mathrm{A}))}\right)^2}} \tag{4.88}$$

$$\stackrel{4.87}{\Leftrightarrow} r_\mathrm{C} = \left(t - \Lambda\left[v_\mathrm{T}(-S_j(z_\mathrm{A})), z_\mathrm{A}\right]\right) \cdot v_\mathrm{B} \cdot \sqrt{1 - \left({}^{v_\mathrm{B}}/_{v_\mathrm{T}(-S_j(z_\mathrm{A}))}\right)^2} \tag{4.89}$$

$$\stackrel{4.86}{\Leftrightarrow} r_\mathrm{C} = \left(t - \Lambda\left[v_\mathrm{T}(-S_j(z_\mathrm{A})), z_\mathrm{A}\right]\right) \cdot v_\mathrm{B} \cdot \sin\left[\alpha(v_\mathrm{T}(-S_j(z_\mathrm{A})), v_\mathrm{B})\right] \quad , \tag{4.90}$$

and second the cathetus r_C to obtain z_C in analogy

$$z_\mathrm{C} = z_\mathrm{A} + \left(t - \Lambda\left[v_\mathrm{T}(-S_j(z_\mathrm{A})), z_\mathrm{A}\right]\right) \cdot v_\mathrm{B} \cdot \cos\left[\alpha(v_\mathrm{T}(-S_j(z_\mathrm{A})), v_\mathrm{B})\right] \quad . \tag{4.91}$$

Equation (4.90) and eq. (4.91) describe the etch pit's cone wall only depending on the etching rates and a single parameter z_A. Plugging eq. (4.91) into eq. (4.90) yields

$$r_\mathrm{C} = \frac{z_\mathrm{C} - z_\mathrm{A}}{v_\mathrm{B} \cdot \cos\left[\alpha(v_\mathrm{T}(-S_j(z_\mathrm{A})), v_\mathrm{B})\right]} \cdot v_\mathrm{B} \cdot \sin\left[\alpha(v_\mathrm{T}(-S_j(z_\mathrm{A})), v_\mathrm{B})\right] \tag{4.92}$$

$$= (z_\mathrm{C} - z_\mathrm{A}) \cdot \tan\left[\alpha(v_\mathrm{T}(-S_j(z_\mathrm{A})), v_\mathrm{B})\right] \tag{4.93}$$

$$\stackrel{4.86}{=} (z_\mathrm{C} - z_\mathrm{A}) \cdot \sqrt{\left(v_\mathrm{T}(-S_j(z_\mathrm{A}))/v_\mathrm{B}\right)^2 - 1} \quad . \tag{4.94}$$

This expression eq. (4.94) is handy for direct analysis of experimental results as well as for numerical track simulations. On one hand side, it is possible to derive the track etching rate along z if we can appreciate

the exact shape of a given pit by measurement. The etching rate of the bulk material can be experimentally deduced by etching non-irradiated samples. From eq. (4.94) follows

$$v_{\mathrm{T}}(-S_j(z_{\mathrm{A}})) = v_{\mathrm{B}} \cdot \sqrt{1 + \left(\frac{r_{\mathrm{C}}}{z_{\mathrm{C}} - z_{\mathrm{A}}}\right)^2} \quad . \tag{4.95}$$

$z_{\mathrm{A}}(z_{\mathrm{C}})$ can be deduced by the intersection of the surface normal in $(z_{\mathrm{C}}, r_{\mathrm{C}})$ and the ion axis.

On the other hand side, knowing both etching rates enables us simulation of the characteristic pit diameter D. We choose the point point $(z_{\mathrm{C}}, r_{\mathrm{C}})$ to be on the intersection of etch pit and ablated surface. For a given etching time t, let

$$z_{\mathrm{C}} \overset{!}{=} v_{\mathrm{B}} \cdot t \tag{4.96}$$

$$\Rightarrow D(t) = 2 \cdot r_{\mathrm{C}} \overset{4.94}{=} 2 \cdot (v_{\mathrm{B}} \cdot t - z_{\mathrm{A}}) \cdot \sqrt{\left({}^{v_{\mathrm{T}}(-S_j(z_{\mathrm{A}}))}/_{v_{\mathrm{B}}}\right)^2 - 1} \quad . \tag{4.97}$$

Calculation of $D(t)$ requires knowledge about z_{A}. We develop eq. (4.91) for now known coordinates of $(z_{\mathrm{C}}, r_{\mathrm{C}})$ to

$$v_{\mathrm{B}} \cdot t = z_{\mathrm{A}} + (t - \Lambda\left[v_{\mathrm{T}}(-S_j(z_{\mathrm{A}})), v_{\mathrm{B}}\right]) \cdot v_{\mathrm{B}} \cdot \cos\left[\alpha(v_{\mathrm{T}}(-S_j(z_{\mathrm{A}})), v_{\mathrm{B}})\right] \tag{4.98}$$

$$\Leftrightarrow t = \frac{{}^{z_{\mathrm{A}}}/_{v_{\mathrm{B}}} - {}^{v_{\mathrm{B}}}/_{v_{\mathrm{T}}(-S_j(z_{\mathrm{A}}))} \cdot \left(\int_0^{z_{\mathrm{A}}} \frac{1}{v_{\mathrm{T}}(-S_j(\check{z}))} \mathrm{d}\check{z}\right)}{1 - {}^{v_{\mathrm{B}}}/_{v_{\mathrm{T}}(-S_j(z_{\mathrm{A}}))}} \tag{4.99}$$

Solutions may be found numerically, *e.g.* with Newton's method. The most reported general form of this relations, following the derivation in [DB87, chapter 4], are equivalent

$$D(t) = 2 \cdot (z_{\mathrm{A}} - v_{\mathrm{B}} \cdot \Lambda\left[v_{\mathrm{T}}(-S_j(z_{\mathrm{A}})), z_{\mathrm{A}}\right]) \cdot \sqrt{\frac{v_{\mathrm{T}}(-S_j(z_{\mathrm{A}})) + v_{\mathrm{B}}}{v_{\mathrm{T}}(-S_j(z_{\mathrm{A}})) - v_{\mathrm{B}}}} \tag{4.100}$$

$$\mid \text{with} \quad t = \frac{{}^{z_{\mathrm{A}}}/_{v_{\mathrm{B}}} - {}^{v_{\mathrm{B}}}/_{v_{\mathrm{T}}(-S_j(t))} \cdot \Lambda\left[v_{\mathrm{T}}(-S_j(z_{\mathrm{A}})), z_{\mathrm{A}}\right]}{1 - {}^{v_{\mathrm{B}}}/_{v_{\mathrm{T}}(-S_j(t))}} \quad . \tag{4.101}$$

Even though the detailed characteristic pit evolution is a numerical problem, we may derive key features from above formulations. For a constant etching rate v_{T}, eq. (4.99) can be approximated and introduced to eq. (4.97),

$$t \overset{v_{\mathrm{T}}=\text{const.}}{=} \frac{z_{\mathrm{A}}}{v_{\mathrm{B}}} \cdot (1 + {}^{v_{\mathrm{B}}}/_{v_{\mathrm{T}}}) \tag{4.102}$$

$$\Rightarrow D(t) = 2 \cdot t \cdot v_{\mathrm{B}} \cdot \sqrt{\frac{v_{\mathrm{T}} - v_{\mathrm{B}}}{v_{\mathrm{T}} + v_{\mathrm{B}}}} \quad , \tag{4.103}$$

here we find the same result as above in eq. (4.81). We understand that v_{T} is required only to be constant until z_{A}, which is a far weaker criterium than requiring a constant etching rate for the full pit. Knowing energy deposition curves of ions and their proportionality to the track etching rate, we estimate the relative change of track etching rate to follow

$$\frac{v_{\mathrm{T}}(-S_j(z))}{v_{\mathrm{T}}(-S_j(0))} \approx \frac{S(z))}{S(0)} \quad . \tag{4.104}$$

We can estimate maximum etching times t for which a constant v_T is a good presumption. With criterium $\|S(z)) - S(0)\| < \epsilon$ and derived z_A for $\|S(z_\mathrm{A})) - S(0)\| = \epsilon$ in the rising slope of the Bragg-peak, one obtains

$$t < \frac{z_\mathrm{A}}{v_\mathrm{B}} \cdot \frac{1 - \left({}^{v_\mathrm{B}}/_{v_\mathrm{T}(-S_j(0))}\right)^2 \cdot (1+\epsilon)}{1 - {}^{v_\mathrm{B}}/_{v_\mathrm{T}(-S_j(0))} \cdot (1+\epsilon)} \quad . \tag{4.105}$$

Increasing ion energies cause decreasing ionization in the material surface layer after impact and therefore their pits can be etched longer.

If the track etching rate $v_\mathrm{T}(-S_j(z))$ is a function of the Bragg curve $S(z)$, all information about the incident particle's impact energy and its species is available with the track etching rate $v_\mathrm{T}(z)$ with $z \in \{0, z(t)\}$ in function of etching time t. The track etch rate completely controls the observed pit growth in the CR-39 when immersed in the caustic solution. Measurement of the depth growth rate $\mathrm{d}_t L(t)$ allows a quantification of $v_\mathrm{T}(z(t))$ at the end of the pit and observation of the diameter $D(t)$ allows a quantification of $v_\mathrm{T}(z_\mathrm{A})$. z_A ist the axial origin of the etch wave reaching the crater edge at time t. Therefore two independent measurements of $v_\mathrm{T}(z)$ are available for $z \in \{0, z_\mathrm{A}\}$. Vice-versa, knowing $v_\mathrm{T}(-S_j(z))$ allows to retrieve $S(z)$ for two independent positions which beneficial for determining impact energy and ion-charge the same time. The full set of equations reads

$$\mathrm{d}_t L(t) = -v_\mathrm{B} + v_\mathrm{T}(-S_j(z(t))) \quad , \tag{4.106}$$

$$D(t) = 2 \cdot (v_\mathrm{B} \cdot t - z_\mathrm{A}) \cdot \sqrt{\left({}^{v_\mathrm{T}(-S_j(z_\mathrm{A}))}/_{v_\mathrm{B}}\right)^2 - 1} \quad , \tag{4.107}$$

$$t = \frac{{}^{z_\mathrm{A}}/_{v_\mathrm{B}} - {}^{v_\mathrm{B}}/_{v_\mathrm{T}(-S_j(z_\mathrm{A}))} \cdot \left(\int_0^{z_\mathrm{A}} \frac{1}{v_\mathrm{T}(-S_j(\check{z}))} \mathrm{d}\check{z} \right)}{1 - {}^{v_\mathrm{B}}/_{v_\mathrm{T}(-S_j(z_\mathrm{A}))}} \quad . \tag{4.108}$$

4.3.2.5 Practical Considerations for Etching of Columbia Resin #39

We employ NaOH solution of 6.25 N in distilled water for etching the CR-39 from all sides in a bath at constant temperature of 70 °C. The molarity and temperature of the etchant are of paramount importance for the etching rates, the etch rates' ratio is not constant! Depicted in fig. 4.24, optimum molarity and temperature depend on the ion species and impact energy. We see the etch rates' ratio ${}^{v_\mathrm{T}}/_{v_\mathrm{B}}$ for low energy He^{2+} with respect to the etchant molarity. The ratio reaches a distinct maximum for each impact energy. From 2 MeV to 6.1 MeV the molarity for a maximum ratio is approximately 6.25, given a constant temperature of 70°. Furthermore illustrated is the etch rates' ratio with respect to the deposited energy along the ion track for different temperatures of the etchant solution. We appreciate a huge difference between low temperature and high temperature etching, with growing etch rates' ratio for rising temperatures at a given Restricted Energy Loss (REL).

We will hereinafter experimentally use TASTRAK CR-39 Plastic Sheets. Naturally, different manufacturers produce with differing quality and methodology – inter-comparability of calibrations can not be presumed but is sometimes found [Zha+19]. The bulk etching rate and its temperature dependency of TASTRAK CR-39 are almost the same as for CR-39 of Page Mouldings (Pershore) Limited. This is of further importance as we rely hereinafter on third-part calibration data acquired with CR-39 of Page Mouldings (Pershore) Limited.

One must also beware of composition changes due to optimization processes by manufacturers. As reported with [RH+15], large batch-to-batch differences may occur.

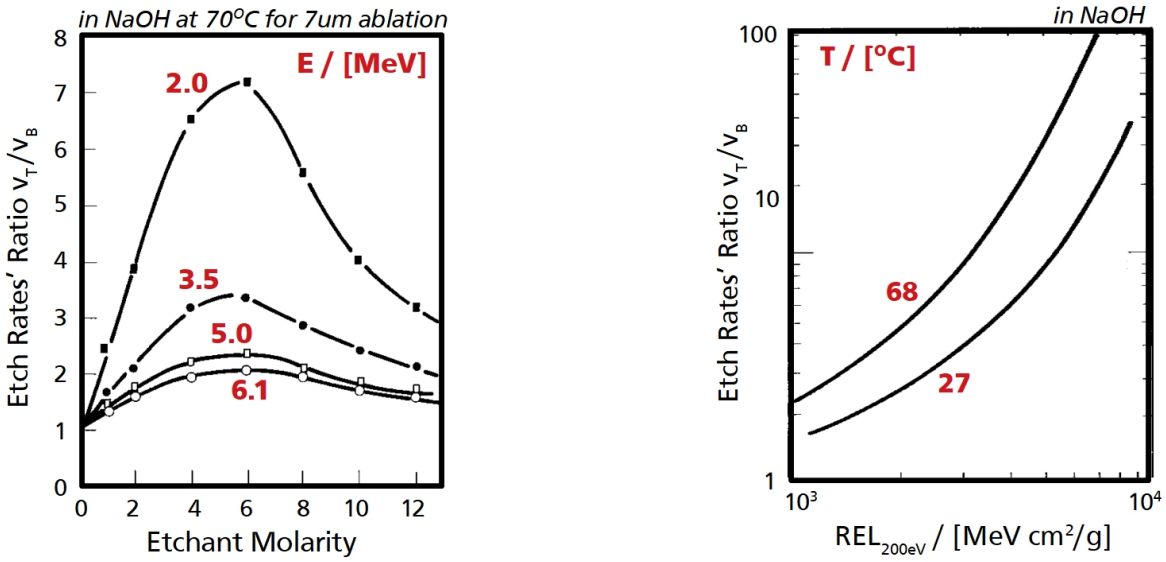

(a) variation of molarity

(b) variation of temperature

Figure 4.24: The etch rates' ratio in CR-39 for He^{2+} ions depend on (a) the molarity of the etchant solution and (b) the temperature on which the etching is carried out. Here, the chosen unit for the deposited energy is REL, with an upper cut-off energy 200 eV. Both graphs adapted from [DB87], evolution with respect to molarity originally extracted from [Gre+82] and temperature dependency originally extracted from [Fow+80].

4.3.2.6 Columbia Resin #39 as Particle Spectrometer

There are different approaches when trying to turn the CR-39 into a particle spectrometer, all aiming at measurement of incident particle mass A, impact charge state Z, and initial kinetic energy E. For ions of high energy to mass ratio, the total amount of deposited energy can be derived from Bethe's stopping power formulation. It is proportional to Z_i^2/β^2. In the limit of high ion velocities, the ratio of track and bulk etching rate was found to be proportional to $v_T/v_B \approx 1 + (Z_i/C_{const} \cdot \beta)^3$ [CSP78]. C_{const} is a fit parameter constant for a given sample. We see the dependency on ion charge state and velocity. Therefore, the etch pit characteristics can be related to projectile species and impact energies. For fully ionized ion beams, such relation offers the possibility to construct a number density spectrum. The number of ions per species per steradian can be determined by simple counting of similar pits.

Of general importance is to either predict the function $v_T(-S_j(z))$ as a benign function of enery deposition mechanism $S_j(z)$, or to tabulate values of $v_T((A, Z, E), z)$. For both approaches, the dynamic track etching rate can be directly related to a species (A, Z, E) – or employed to derive the static etch pit observables (L, D).

Following a presumed functional dependence of $v_T(-S_{total}(z))$, we obtain a relation between the pit observables and the ion species. With Bethe's formalism, $S_{total} \propto Z_i^2/\beta^2 \propto A_i^2 \cdot Z_i^2/E_i$ and in the limit of constant rates $L \propto A_i^2 \cdot Z_i^2/E_i$. This proportionality is ambiguous even for fully ionized projectiles. Absolute deconvolution of species and energy is possible by placing a magnet in front of the detector. The Lorentz force selects on ratios of momentum per charge arriving at a given position - this renders the pit diameter into a detector for atomic mass of the projectiles [Hic99].

A first discussion concerns the purely theoretical prediction of the etching rates. A second fully empirical

approach is to link measured values for $v_{\mathrm{T}}(z)$ directly to the particle properties (A, Z, E). Such a calibration catalogue allows comparison of experimental data with tabulated values. A third, semi-empirical approach relates $v_{\mathrm{T}}(-S_j(z))$ with the energy losses $\mathrm{d}_z E(-S_j(z))$ or, equivalently, with the damage to the material (*e.g.* ionization $S(z)$).

Prediction of Etching Rates for Columbia Resin #39

Theoretical prediction of both etching rates based on the initial conditions of SSTD material and ionic projectiles is the holy grail for CR-39 etched track detectors.

The simplified model for high ion velocity discussed here-before, as others, is based on the total loss of energy of projectiles in matter – a concept firstly proposed by [Fle+67b]. It fails for very high and very low projectile energies. For low ion velocities, especially in the vicinity of the stopping power maximum, Bethes formalism is not valid. For high ion energies, experimental data does not match predictions [Fle+67a]. A more detailed account of the deposited energy per penetration depth and the driving mechanisms for material damage is necessary, *e.g.* by referring to calibration data or simulations tracking material damage.

A vast zoo of models highlight different physical energy deposition mechanisms that lead to etchable tracks, see [DB87, chapter 3]. In a second approach, the number of primary ionizations was considered a possible candidate [DB87]. The model does only take into account the number of ionized electrons by projectile-target interactions. All secondary ionizations and any relation to dose are ignored, and therefore this model is not physical. The model of REL [BN69] interprets the dose in the vicinity of the ion track majorly important and therefore cancels the contribution of the high-energy electrons that carry energy far off the track. In practice, the energy deposition to target electrons is calculated via a stopping power calculation, during which energy loss to ionized electrons with kinetic energy above a limit are not taken into account. The choice of the limit W_0 is arbitrary and reported from 200 eV to $1.000 \cdot 10^3$ eV – the limit often is used as fitting parameter [DB87]. This means that interactions including possible ionizations caused by secondary electrons with energies above W_0 are discarded. On the opposite, it is possible to only consider the secondary electron energy loss (SEEL) [KK68]. The SEEL model finds self-consistent thresholds for track formation in some materials by assuming that only many collision events by a considerable amount of secondary electrons are able to cause an etchable track. Unfortunately, it fails for minerals where direct exposure to high energy density electron beams did not trigger tracks for calculated thresholds [DB87]. Furthermore, the radius-restricted energy loss (RREL) [Par78] takes all primary and secondary energy deposition events into account, but only within a critical radius around the particle trajectory. Such radius can be reasoned to be of the order of several nm [Fle+75, section 1.3]. The radius unfortunately remains a fitting parameter, even though the authors of [Par78] propose the concept of linear event density (LiED) that should count the number density of primary and secondary ionizations as criterion – not their energy. The later may be a good metric upon which track etching rates can be modelled. As of today and to our best knowledge, all publicly available modelling remains inconclusive, which favours the use of calibration data.

Empirical Calibration for Etch Pit Growth in Columbia Resin #39

Empirical calibration aims at direct comparison between experimentally obtained data and calibration data. Etch pit characterizations are available for most ion species, but commonly at distinct energies in limited ranges. E.g. the accessibility of ^{241}Am isotopes that emit 5.4 MeV alpha particles causes most accessible calibration data on alpha particles to be in the range from several 100 keV to 5.4 MeV. Rather rare are studies

that employ particle accelerator facilities to investigate various types of ions at once, for which the respective Bragg-peak is in vicinity of the detector surface. In order to cover the impact energy range of 1.87 MeV to 26.41 MeV for ions from 1 u to 16 u, we emphatize data from [AANAJ12; AHAJ13].

Extrapolation of calibration data to energies not directly covered by the calibration data set requires fitting routines that do neither diverge from physical limits nor produce unphysical values. A carefull fit model is reported with [AANAJ12], it reads

$$L(t) = A_{\mathrm{Az1}} \cdot \left(\tanh \left[\exp \left[\frac{t - A_{\mathrm{Az2}}}{A_{\mathrm{Az3}}} \right] \right] \right)^{\left(A_{\mathrm{Az1}} \cdot A_{\mathrm{Az2}} \cdot A_{\mathrm{Az3}} \cdot 1\,\mu\mathrm{m}^{-1} \right)^{-1}} \quad , \tag{4.109}$$

with length L in µm and times in h. The parameters are fit functions of (A, E), best fitting with [AHAJ13]

$$A_{\mathrm{Az1}}(A, E) = \frac{17.38122 \cdot E^{1.2}}{A^{1.3531}} \cdot \left(1 + 1.35 \cdot \exp \left[-\frac{(A-9)^2}{2} \right] - 1.4 \cdot \exp \left[-\frac{A^2}{1.2} \right] \right) \tag{4.110}$$

$$A_{\mathrm{Az2}}(A, E) = E^2 \cdot \exp \left[12.8217 \cdot \exp \left[-\frac{A}{10.6845} - 10.0631 \right] \right] \tag{4.111}$$

$$A_{\mathrm{Az3}}(A, E) = \frac{A^{0.5}}{7.8636 \cdot E^{0.5} - 3.8706} \quad , \tag{4.112}$$

with energy in MeV, and atomic mass number A in u. All calibration data was is made available following an etching procedure conducted with NaOH etchant at 70 °C and normality of 6.25 N. The bulk etching rate of the CR-39 was found to be $1.32\,\mu\mathrm{m\,h}^{-1}$. Direct application of the best fit is only possible if such environment is reproduced and if the bulk etching rate matches.

Parameter units are µm for A_{Az1} and h for A_{Az2}, A_{Az3} then is required to be in h. The parameter A_{Az1} corresponds to the saturation value of the track depth L_{max}, attained after etching passed the range of projectiles. The second parameter A_{Az2} defines the transition from negative to positive exponential behaviour and is mostly controlling the track length saturation time t_{sat}. A_{Az3} is a shape determining parameter defining the slope, and together with A_{Az1} it influences the smoothness of transition between growing track length and saturated track length.

The significance of the parameters allows comparability to the projectile range R_{i} with

$$R_{\mathrm{i}} = L_{\mathrm{max}} + t_{\mathrm{sat}} \cdot v_{\mathrm{B}} \quad . \tag{4.113}$$

The best fit eq. (4.110) is applicable to various ion species and can be improved if species-wise analysis is performed. For extrapolation of the energy range of individual species, we find it handy to depart from

$$L_{\mathrm{max}} = a_1 \cdot E_{\mathrm{i}}^{a_2} \tag{4.114}$$

$$t_{\mathrm{sat}} = a_3 \cdot E_{\mathrm{i}}^2 \tag{4.115}$$

$$\Rightarrow R_{\mathrm{i}}\left(E_{\mathrm{i}}\right) = a_1 \cdot E_{\mathrm{i}}^{a_2} + a_3 \cdot E_{\mathrm{i}}^2 \cdot v_{\mathrm{B}} \quad , \tag{4.116}$$

in analogy to eq. (4.110), but with no further refinement of dependencies on the atomic mass number and with a free parameter a_2. We obtain the parameters a_1, a_2 and a_3 by fitting range data, *e.g.* issued by a SRIM simulation.

The above eq. (4.116) is implemented in the code PySTarT, see section 7.4, with modules for CR-39 analysis. For alpha particles of 1 MeV to 40 MeV impact energy into a CR-39 of 1 mm thickness and density of 1.31 g cm^{-3}, we obtain from the minimum of the absolute difference between range data and parametrisation

$$a_1 = 2.47(1) \tag{4.117}$$
$$a_2 = 1.22(1) \tag{4.118}$$
$$a_3 = 0.353(1) \quad . \tag{4.119}$$

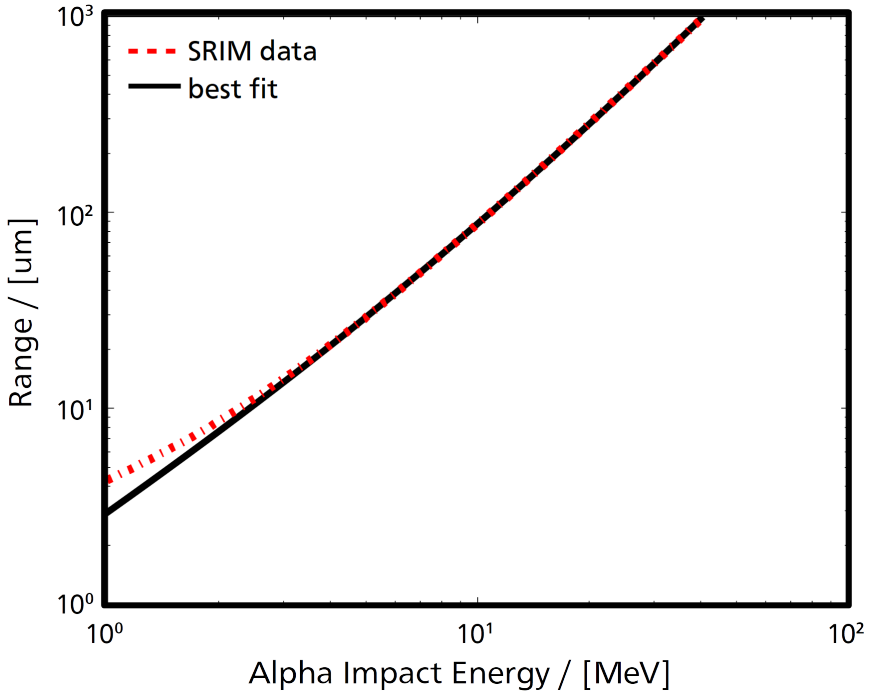

Figure 4.25: Best fit of eq. (4.116) to SRIM output for alpha particle ranges with variation of the initial kinetic energy when entering a CR-39 track detector. Modelling performed following [AHAJ13].

The best fit is shown in fig. 4.25. For alpha particles, [AANAJ12] reports explicitly $a_1 = 2.45$, $a_2 = 1.2$ and $a_3 \approx 0.27$ (in a graphic). The fit based on SRIM range data is in good agreement and motivates further steps with refined parameters $A_{\text{Az1}}(A, E) = L_{\text{max}}$ and $A_{\text{Az2}}(A, E) = t_{\text{sat}}$. $A_{\text{Az3}}(A, E)$ remains explicit. The three parameters are illustrated with fig. 4.26. $A_{\text{Az1}}(E)$ and $A_{\text{Az2}}(E)$ are monotonically increasing, $A_{\text{Az3}}(E)$ remains larger than $10 \cdot 10^{-3}$ h in the range from 1 MeV to 40 MeV.

With knowledge of $L(t)$, we readily obtain $v_{\text{T}}(t)$ plugging eq. (4.109) into eq. (4.75). One may obtain $D(t)$ by numerical solution of the system eq. (4.97) and eq. (4.99), first mapping $t(z)$ with $z(t) = L(t) + t \cdot v_{\text{B}}$ in order to find $v_{\text{T}}(z)$. Otherwise, it is possible to derive $D(t)$ geometrically, applying Huygens' principle to spherical etch-waves that depart from the tip of the pit $z(t)$. Then the pit diameter is given with the largest intersection of any sphere and the surface.

The presented implementation of eq. (4.109) into the code PySTarT diverges for high energies above 14 MeV. The exponent $t - A_{\text{Az2}}(E)/A_{\text{Az3}}(E)$ underflows, out of the valid range of 64 bit floats that python operates in. The

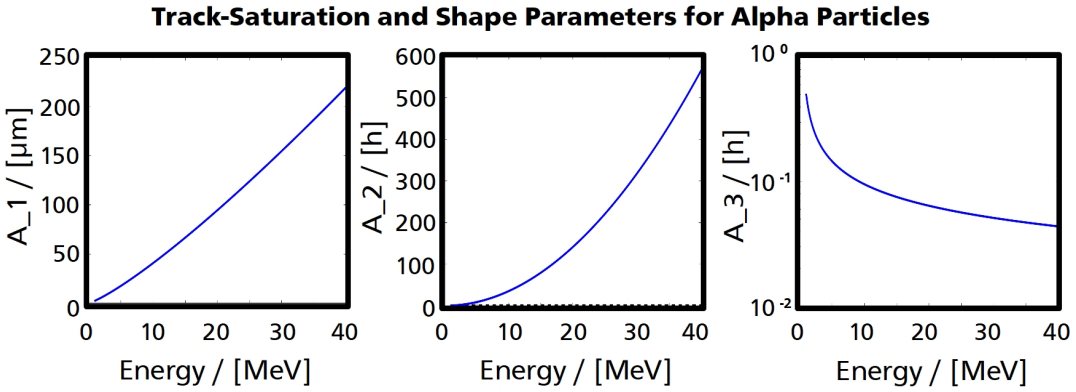

Figure 4.26: Parameters $A_{\text{Az1}}(E)$ for the maximum track length, $A_{\text{Az2}}(E)$ for the saturation time when this maximum length is etched free and $A_{\text{Az3}}(E)$ the shape of the track length evolution for alpha particles.

direct calculation of the exponent is not necessary, developing $v_{\text{T}}(t, E)$ for small exponents allows us to avoid tiny numbers

$$\chi(t, E) \overset{!}{=} \exp\left[\frac{t - A_{\text{Az2}}(E)}{A_{\text{Az3}}(E)}\right] \tag{4.120}$$

$$v_{\text{T}}(t, E) \overset{\text{eq. (4.75)}}{=} v_{\text{B}} + \frac{\left(\tanh\left[\chi(t, E)\right]\right)^{-1+\left(A_{\text{Az1}}(E)\cdot A_{\text{Az2}}(E)\cdot A_{\text{Az3}}(E)\cdot 1\,\mu\text{m}^{-1}\right)^{-1}} \cdot \chi(t, E)}{A_{\text{Az2}}(E) \cdot A_{\text{Az3}}(E)^2 \cdot \left(\cosh\left[\chi(t, E)\right]\right)^2 \cdot 1\,\mu\text{m}^{-1}} \tag{4.121}$$

$$\lim_{\chi(t,E)\to 0} v_{\text{T}}(t, E) = v_{\text{B}} + \frac{\left(\chi(t, E)\right)^{-1+\left(A_{\text{Az1}}(E)\cdot A_{\text{Az2}}(E)\cdot A_{\text{Az3}}(E)\cdot 1\,\mu\text{m}^{-1}\right)^{-1}} \cdot \chi(t, E)}{A_{\text{Az2}}(E) \cdot A_{\text{Az3}}(E)^2 \cdot (1)^2 \cdot 1\,\mu\text{m}^{-1}} \tag{4.122}$$

$$= v_{\text{B}} + \frac{\left(\chi(t, E)\right)^{\left(A_{\text{Az1}}(E)\cdot A_{\text{Az2}}(E)\cdot A_{\text{Az3}}(E)\cdot 1\,\mu\text{m}^{-1}\right)^{-1}}}{A_{\text{Az2}}(E) \cdot A_{\text{Az3}}(E)^2 \cdot 1\,\mu\text{m}^{-1}} \tag{4.123}$$

$$= v_{\text{B}} + \frac{\exp\left[\frac{t - A_{\text{Az2}}(E)}{A_{\text{Az1}}(E)\cdot A_{\text{Az2}}(E)\cdot A_{\text{Az3}}(E)^2\cdot 1\,\mu\text{m}^{-1}}\right]}{A_{\text{Az2}}(E) \cdot A_{\text{Az3}}(E)^2 \cdot 1\,\mu\text{m}^{-1}} \quad . \tag{4.124}$$

For larger energies, the fraction in the exponent goes to zero. Then eq. (4.77) is used to integrate $v_{\text{T}}(t)$. The resulting $L(t)$ is plotted with fig. 4.27 (a) and compared to the overflowing casefig. 4.27 (b) via their ratio fig. 4.27 (c). The corrected track length underestimates the exact value for small exponents up to 10 % due to rounding errors and discretization of the integration.

For calculation of $D(t)$ we choose to follow Huygen's principle as the geometrical solution is computationally not as expensive as the minimization problem. The track diameter growth rate $\mathrm{d}_t D$ is compared with the track length growth rate $\mathrm{d}_t L$ in fig. 4.28 for different total times of etching. $\mathrm{d}_t L$ and $\mathrm{d}_t D$ are depicted for a given total etching time. In each plot we also indicate the maximum of the respective rate evaluated for the full evolution until this time is reached.

For low energy alpha particles with ranges smaller than the track tip's position, $\mathrm{d}_t L$ is zero. This corresponds to so called saturated tracks. For higher energies, $\mathrm{d}_t L$ is proportional to material damage which is pronounced in a sharply rising peak followed by monotoneous falling edge. The spectral maximum of both growth rates reflects the maximum energy deposition of impact particles $\mathrm{d}_t D$ does not only depend on the track etching

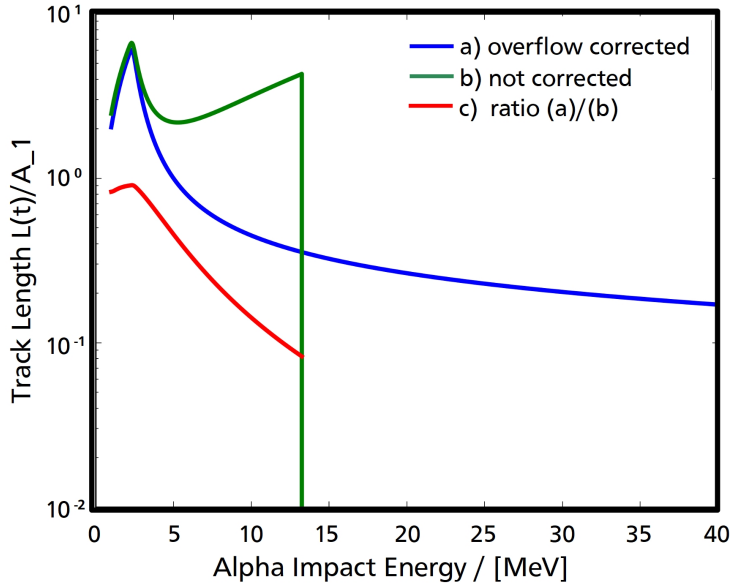

Figure 4.27: Comparison between indirect iterative calculation (a) and direct analythical calculation (b) of the track length normalized with the parameter $A_{\mathrm{Az1}}(E)$ for several MeV impact energy for alpha particles. (c) is the ratio of both and illustrates the error up to 10 % introduced by the method for small exponents.

rate but also on the bulk etching. For a maximum track etching rate, $\mathrm{d}_t L$ is at it's maximum and the etch pit walls are the most inclined at the etch pit's tip. For this maximum inclination, the bulk etching attacks the pit walls most perpendicularly to the track axis and $\mathrm{d}_t D$ is at its maximum.

Both growth rates attain a common spectrally resolved maximum, here at 2.3 MeV, when evaluated on the full evolution until the respective total etching time. The etched cone is fromed by superposing etch waves that depart from the track axis. The offset of the origin of the etch wave and the tip of the track causes the difference in time for which the maxima are obtained. Here, both maxima diagnose the track etching rate v_{T} at an initial target depth reached by the track after 2 h of etching. Then, the total etched path along the track $v_{\mathrm{B}} \cdot t + L(t)$ is $8.6(1)$ µm. The diameter evolution is dominated by etch waves coming from this point after 2 h of etching. Qualitatively comparing the spectral width of both maxima, we directly see that observation of $\mathrm{d}_t L$ allowed a more precice data analysis than measurement of $\mathrm{d}_t D$.

Most authours refer to the evolution of $L(t)$ or $D(t)$ if comparing calibration data to experimentally obtained data points of unknown projectile energy. With fig. 4.28 we see the depth and diameter growth rates of the order of several µm h^{-1}. Therefore etching times with precisions of min result in rather small uncertainties of hundreds of nm for the detector response function. The largest influence to the uncertainty of analysis with optical methods will be related to the measurement of track diameters and length.

We check on the simulation of $L(t)$ and the evaluation of $D(t)$ with model-independent experimental data for the track diameter. In order to apply the model, the etched track detector and etching procedure must be of comparable kind as in [AHAJ13] – with a CR-39 at bulk etching rate of $v_{\mathrm{T}} = 1.32\,\mu\mathrm{m\,h}^{-1}$ etched in NaOH etchant at 70 °C and normality of 6.25 N. Latest studies report similar behaviour of differently manufactured CR-39 [Zha+19], including the CR-39 used for the modelling. The authors report the track diamater for alpha particles of low impact energies, which we compare to PySTarT results in fig. 4.29. We see, PySTarT

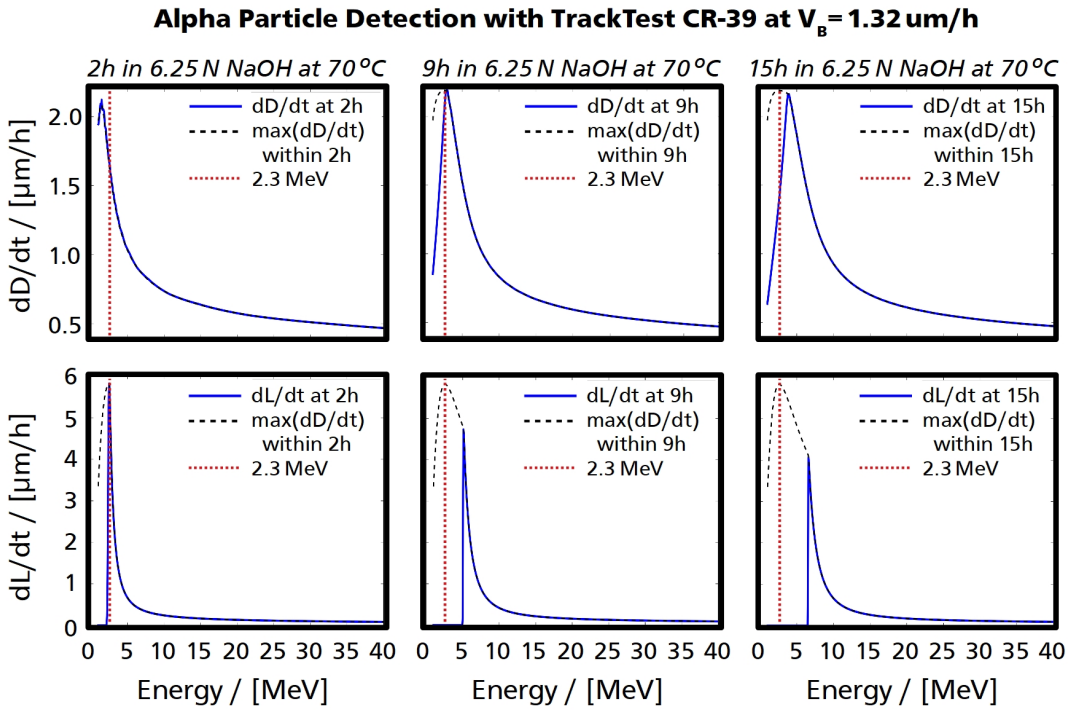

Figure 4.28: Characteristic etch-pit growth rates for varying alpha particle impact energy. Here, a CR-39 with bulk etching rate $v_T = 1.32\,\mu m\,h^{-1}$ is kept in NaOH etchant at $70\,°C$ and normality of 6.25 N for three distinct total etching times. Both spectrally resolved rates are illustrated for a given total etching time as blue line, and as dashed black line we indicate the maximum of the respective rate evaluated for the full evolution until this time is reached. Simulated with the CR-39 plug-in of the code PySTarT, section 7.4.

underestimates systematically the etch-pit diameter. This corresponds to the systematic error of the track length calculation. There is a good agreement in the peak position and slopes.

The combined etch-pit characteristics for a varying alpha particle impact energy are depicted in fig. 4.30 for two distinct total etching times. Every etching time resolves bijectively the full spectrum of impact energies. The characteristic loop shape of the depth-diameter diagram is due to the retarded character of $D(t)$ with respect to $L(t)$. The impact energy of 2.3 MeV, discussed in detail here-before, is highlighted. The falling edge mostly resolves impact energies situated between a maximum for which the range equals the pit's tip position and a minimum for which the etching wave creates the etch pit diameter. The diagnostic has it's best energy resolution for energies with ranges little larger than the pit's tip position. There, we can appreciate single simulations with 50 keV energy spacing as singular dots.

Following a model for the etch track length proposed by [AHAJ13], we derived a python based tool for computation of the full set of etch pit characteristics: diameter and length with their respective growth rates. Computer routines to calculate track characteristics are available in Fortran [NY06; NY08], and herewith in a pythonic hands-on version. Where traditional analysis focuses on individual representation of $L(t)$ and $D(t)$, we emphasize the representation of data in $L(D)$ diagrams to obtain an integral impression of the impact ion spectrum. Etch pits are evaluated with an additional uncertainty of 10 % on length and diameter due to numerical methodology that may be improved in future versions of the underlying code PySTarT.

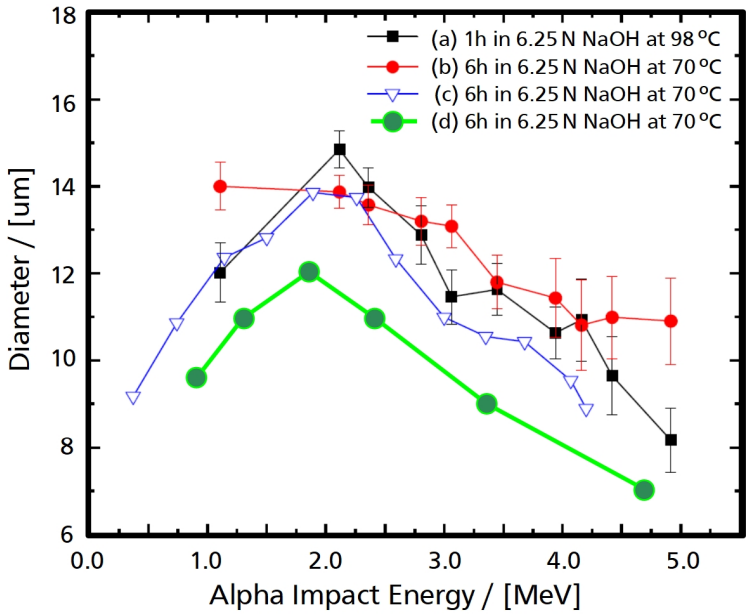

Figure 4.29: Comparison between etch-pit diameters for alpha particles of several MeV impact energy, obtained by experimental data (a-c) and a PySTarT simulation (d). The experimental data is independent from the data used to find the model employed by the simulation routine, (a) and (b) are reported by [Zha+19], (c) is reported by [Sad+97]. The ideal pit diameter is systematically smaller than the experimental data suggests, but shows good agreement in the peak position and slopes. Original graph from [Zha+19].

Semi-empirical Calibration of Etch Pit Growth in Columbia Resin #39

Semi-empirical modelling aims at a self-consistent description of the track etching rates based on known physical parameters. Recent publications in HEDP focus on the energy transfer of ions to electrons through Rutherford scattering without application of thresholds. This approach is based on a power model endorsed in [Hic99, appendix B] that reads $v_T/v_B \approx 1 + k \cdot (S_{\rightarrow \text{electrons}})^m$. Even though it can not be applied in the vicinity of the Bragg-peak, the method yields satisfactory results [NY04].

Contrary to this, publications in the SSTD community [D+99; D+97a; D+97b; DHK02; D+02] focus on a model following the concept of REL. In their work, only electrons with energies lower than 350 eV are presumed to give a contribution to material damage. The track length for several distinct etching times is measured for various incident particle species with differing impact energies and the track etching rate is derived. For a given particle (E, A), combining the measured $v_T(z)$ with the calculated REL δE at depth z enables one to find a relationship $v_T(\delta E)$. With this generalisation, the model can be used to predict tracks of all particle species.

For incident protons and alpha particles, a fairly satisfactory relationship is found [D+02] with

$$v_T(\delta E) = v_B \cdot \begin{cases} 0.93 + 3.14 \cdot 10^{-3} \cdot \delta E - 7.8 \cdot 10^{-6} \cdot \delta E^2 & \\ +1.11 \cdot 10^{-8} \cdot \delta E^3 - 5.27 \cdot 10^{-12} \cdot \delta E^4 & 33\,\text{MeV cm}^{-1} \leq \delta E \leq 560\,\text{MeV cm}^{-1} \\ 1.3 + 3.8 \cdot 10^{-4} \cdot \delta E - 4.9 \cdot 10^{-7} \cdot \delta E^2 & 560\,\text{MeV cm}^{-1} < \delta E \end{cases} \quad (4.125)$$

with fitted data for both species overlapping in $v_T(\delta E)$.

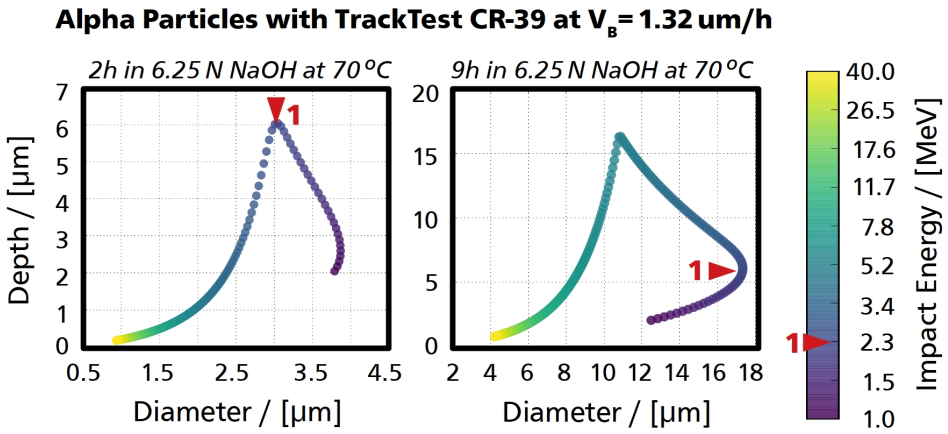

Figure 4.30: Etch-pit characteristics for varying alpha particle impact energy. Here, a CR-39 is kept in NaOH etchant at $70\,°C$ and normality of 6.25 N for two distinct total etching times. Marker (1) illustrates an energy of $2.3\,\mathrm{MeV}$ with range of $8.8(1)\,\mu\mathrm{m}$ in the continuous-slowing-down approximation. This energy attains the maximum track depth after $2\,\mathrm{h}$ of etching where the total etched path along the track $v_B \cdot t + L(t)$ is $8.6(1)\,\mu\mathrm{m}$. This simplified view yields underestimation of the energies for both maxima as it does not take into account the detailed temporal integration necessary to obtain the track length from the etching rates eq. (4.77). The maximum track diameter for this energy is reached after approximately $9\,\mathrm{h}$, when the spherical etch wave launched after $2\,\mathrm{h}$ gives the largest intersection with the etched surface. Simulated with the CR-39 plug-in of PySTarT, section 7.4.

SRIM gives access to the energy loss of projectiles to electrons and offers the possibility to ignore ionization cascades triggered by recoiling or displaced target atoms. The code also gives access to the energy lost to target atom recoils. Principally, it is possible to explore simulation data based on both portions of the total deposited energy and their relation to the REL and therewith the track etching rate.

Unfortunately, modelling was performed with a CR-39 is kept in NaOH etchant at $70\,°C$ and normality of 7.25 N. The changing normality leads to changes in the bulk etching rate. To our best knowledge, the latest systematic case study of bulk etching rates in function of etching temperature and etchant normality concerns CR-39 of old age that do not correspond to latest CR-39 [Fro+91]. We will not further pursuit data analysis based on semi-empirical modelling in this work.

4.3.2.7 Environmental Bias

The downsides of CR-39 as etched track detector comprise the dependence of identical CR-39 for calibration and data acquisition and the variability of results depending on environmental variables. Fractionation of CR-39 exposed to UV light by photochemical changes is reported [TNY06] and motivates careful handling of slaps ment to be used for data acquisition. For HEDP experiments, it is important to obtain a pure batch of CR-39, avoiding artificial pits due to material inhomogeneity. Furthermore, the concentration of free oxygen during the lifetime of radicals plays a crucial role for the formation of latent cracks [GT92; YOM92]. Therefore, the etch pit diameter depends on the degree of out-gassing under vacuum prior to exposure and the delay of exposure and venting procedure. Depicted in fig. 4.31, CR-39 show a decreasing etch pit diameter for the same type of irradiation if they are kept in vacuum for long times prior to exposure and if they are kept in vacuum

for long times after exposure. Both dependencies seems to saturate. Keeping the slaps for $1.000 \cdot 10^3$ min in vacuum prior to exposure and 150 min after exposure, stabilizes the response function on respective limits. Also, the lengthy experimental data analysis comprises a potentially falsifying chemical post processing. In addition, digitization is difficult due to µm-sized track tracing observables.

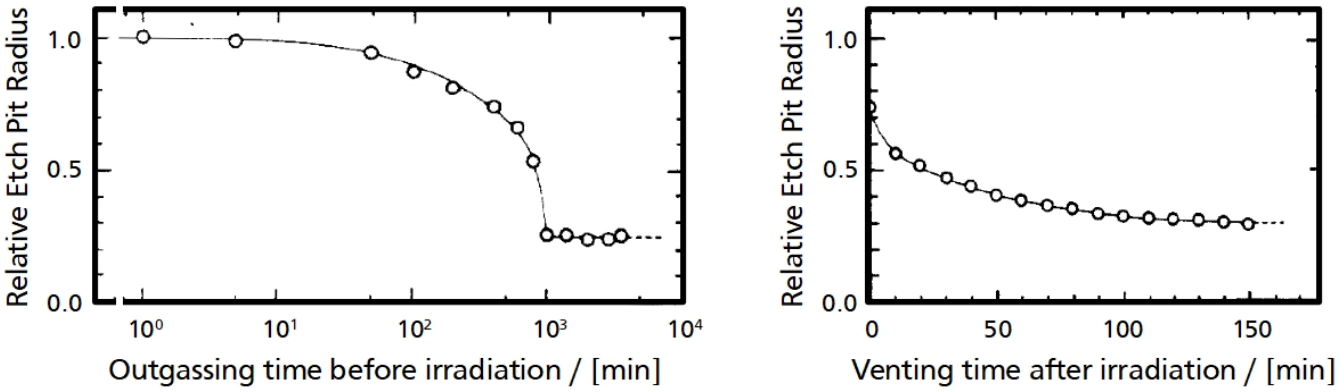

Figure 4.31: Relative changes in the etch pit radius of CR-39, type SUPER GRADE of manufacturer Pershore Mouldings, depending on the time out-gassing was possible (left) and on the time interval between irradiation and venting with ambient air (right). Extracted from [YOM92].

Projectiles with a low energy transfer below $10\,\mathrm{keV\,\mu m^{-1}}$ to $15\,\mathrm{keV\,\mu m^{-1}}$ do not lead to the formation of tracks [Haj+08]. Thus, single electrons do have no influence on CR-39 track formation but electrons in high doses of several kGy change collectively both etching rates and their ratio [CS88]. A behaviour that can be modelled [WM05]. The same applies for gamma rays [Oda+97]. Background comprises neutrons, high Z cosmic rays and contaminating radioactive elements in the vicinity of the detector, such as radon in ambient air. There may occur also a contribution of spontaneous fission from mineral traces enclosed in the plastic itself [DB87, chapter 4].

4.3.3 Active Time-of-Flight Particle Detectors

On-line energy spectra of accelerated charged particles can be acquired by ToF detectors located at a distance $a_{\mathrm{ToF}} \pm \Delta a_{\mathrm{ToF}}$ from the ROI, see fig. 4.32. Projectiles impacting on ToF detectors alter proportionally the detector voltage. This diagnostics rely on time resolved voltage signal read-out, *e.g.* by fast oscilloscopes.

The ratio of kinetic energy to rest mass energy T can be calculated by the relativistic energy balance to

$$T = \left(1 - \left(\frac{a_{\mathrm{ToF}}}{c \cdot \tau_{\mathrm{ToF}}}\right)^2\right)^{1/2} - 1 \quad , \tag{4.126}$$

with the drift time τ_{ToF} between projectile acceleration and detection. More sophisticated detector schemes do incorporate filter foils, which induce stopping and must be taken into account, and stack configuarations. For a discussion of ToF schemes see [Sal21].

Essential is that simple ToF detectors can not discriminate between different particle species. A more elaborate set-up could do this, *e.g.* by adding a magnet spectrometer in the trajectory.

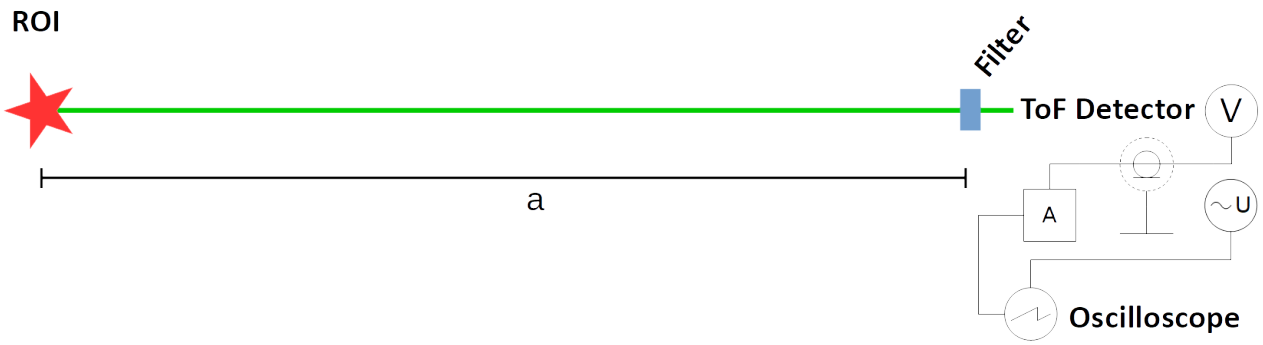

Figure 4.32: ToF diagnostics detect projectiles emitted in a dynamic process in the ROI by recording arrival events - an absolute timing reference is needed for data evaluation.

4.3.3.1 Semiconductor Diodes

This work makes use of Silicon (Si) Acceptor-Neutral-Donor (PiN) photodiode ToF detectors. The diode substrate is preceded by a Si layer and extra filtering by thin foils in order to avoid diode saturation by the strong photopeak expected for hot laser-plasma.

The PiN configuration of the diodes includes an extra neutral layer ”i” in the middle of the doped acceptor layer ”P” and donor layer ”N”, which allows for a quantum efficiency enhancement by increasing the cross-section of ionizing radiation with the diode substrate, and a faster response in absence of a minority carriers current that delays the signal current formation. The temporal resolution is of the order of several ns FWHM. The bias voltage of tens of V is comparatively low to other ToF detectors such as micro-channel plates, which are polarized with bias voltages of the order of kV at risk of short-circuit currents through the imperfect vacuum in experimental conditions.

Filters are handy to distinguish between several possible species. They impose a low energy cut-off to massive projectiles reaching the detector. The related maximum detectable ToF per species allows to conclude on weather or not a species can cause a signal for detection times. E.g., electrons are generally present among laser accelerated species and can be easily distinguished from ions by a filter design that blocks all electrons that arrive after the photopeak.

The excitation and cooling of laser-plasma yield efficient emission of X-rays. The detector shows them upon arrival as peaked response, the so-called photopeak. An example of the obtained signal is plotted in figure fig. 4.33. It is pronounced with a first sharp rising edge of the signal allowing one to retrieve a reference time τ_{php} for projectiles traveling with the speed of light c. This timing fiducial is advantageous for absolute determination of $\tau_{\mathrm{ToF}} = \tau_{\mathrm{m}} - \tau_{\mathrm{php}} + a_{\mathrm{ToF}}/c$ for detection times τ_{m}.

The signal from massive high energy projectiles is partially superposed to the photopeak. Only ion beam signals much larger than the shot-to-shot variance in the photopeak can be detected, thus the photopeak is effectively a high energy cut-off to the dynamic range of the detector.

Once the photopeak contribution has been subtracted, the original signal must be obtained by performing a deconvolution with the photodiode’s impulse response. For this work, the detector’s impulse response is an exponentially modified Gaussian known from [ESLOB+20]. The detector’s response function and the deconvolution result can be seen in fig. 4.34. The diode response was measured at CLPU by directly irradiating

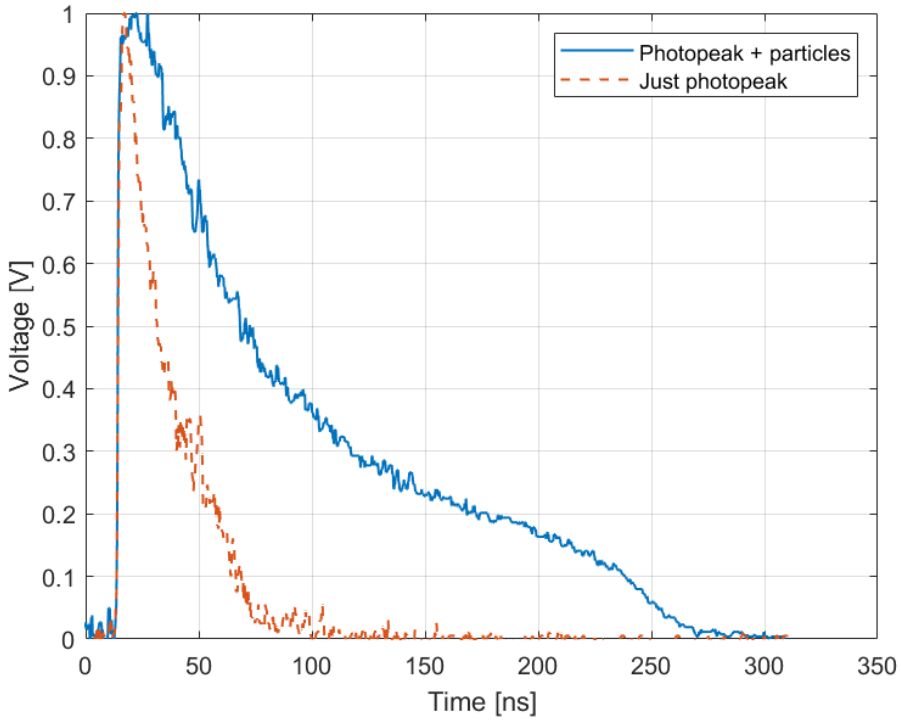

Figure 4.33: Comparison between the detector digitized record of measurement values (RAW) signal comprising photopeak and all accelerated particle species (blue full line) and a signal with photopeak only (orange dashed line). Data related to an experiment discussed hereinafter, see section 5.1.

the diode with low energy laser pulses[2]. Here, the low energy laser pulses are concidered as an impulse in-put signal, the output signal is then plotted in fig. 4.34 (left). Note that diode and scope were not directly connected but via a passive biasing network. The used Bias Tee causes a larger time-constant of the circuit, but the detector response was independent from the applied bias voltage. Finally the energy resolved spectrum can be obtained by presuming a species and transforming detection times into particle energies.

[2]Results transmitted by personal communication with Valeria Ospina.

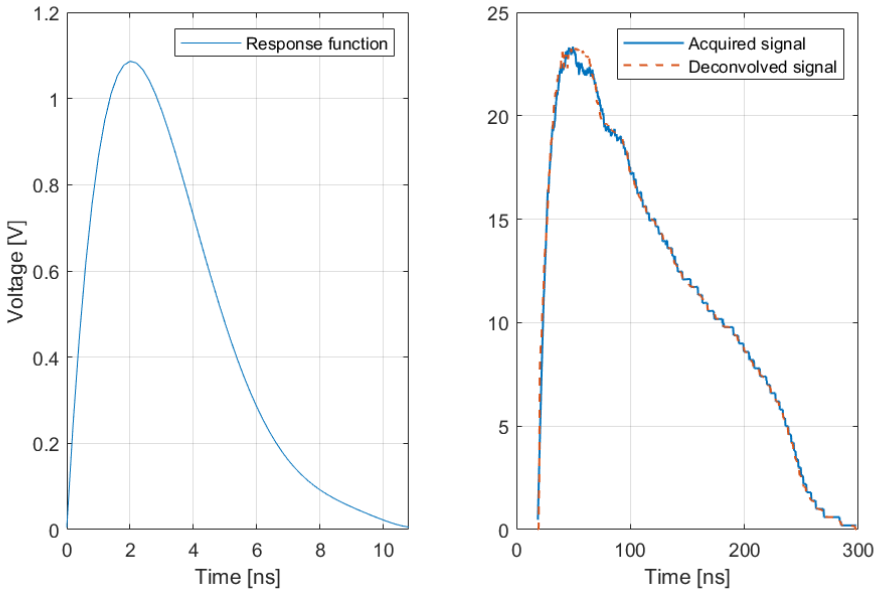

Figure 4.34: Photodiode detector impulse response (left) and signal after deconvolution (right). Extracted from [ESLOB+20]. A passive biasing network was used and causes a larger time-constant of the circuit, but the detector response was independent from the applied bias voltage.

5 Experimental Results and Analysis

Intense ion sources of low divergence are in strong need for many applications ranging from fundamental research in atomic physics, *e.g.* the exploration of collective stopping power effects and generation of warm dense matter, to medicine, *e.g.* isotope production for cancer therapy and heavy-ion treatment. Ion beam sources based on laser-plasma interaction [Alb+20] deliver orders of magnitude more particles per micro-bunch than standard accelerator facilities, not only able to deliver high doses under short irradiation but also to attain extremely high dose rates of several $1 \cdot 10^9\,\mathrm{Gy\,s^{-1}}$ for durations of the order of ns [BFD19]. Plasma-accelerators might become available at lower cost than standard accelerator facilities because of a much smaller size [Alb+20]: the electric field strengths supported in plasma make accessible accelerating gradients of above $\mathrm{GeV\,cm^{-1}}$, compared to $\mathrm{MeV\,cm^{-1}}$ in standard accelerators.

This work presents an experimental benchmark of laser-driven ion acceleration from targets in the near-critical density regime and the exploration of open-geometry platforms for spatial and spectral ion beam tailoring driven by either sub-ps or ns laser pulses. Aiming at ion sources with the lowest possible emittance, magnetized TNSA is demonstrated from solid plastic targets injected in ns-laser-driven quasi-static B-fields, and an attempt of ion beam tailoring with sub-ps driven targets of micro-helmholtz coil geometry is shown. Individual case study results underpin the overall idea of joint use-case scenarios: bright ion sources at high-repetition rate, *e.g.* key for alpha-therapy isotope production, may be sources of low divergence ion beams than can be guided more efficiently within small volumes through beamlines that also comprise pulsed beam-guiding elements for longitudinal and transverse phase-space compression as well as post-acceleration, *e.g.* essential towards heavy-ion therapy and fast ignition. Such beamline terminated with an ultra-strong magnetic lens renders high-energy-density physics experiments possible.

Particular experimental achievements are first, the generation of MeV ion beams from near-critical gas jet targets that unravel low-divergence particle beams with a broad spectrum. Interpreted as alpha particles, projectiles have cut-off energies above 55 MeV and peaked particle number densities of several $10^8\,\mathrm{MeV^{-1}}$ for $22(2)\,\mathrm{MeV}$. Second, EM charged particle beam lensing platforms and their modelling are revised and characterized with respect to applications. Detailed investigations of rapid ps-laser driven pulsed EM lenses hint the sensitivity of the dispersion relation to the target surface temperature and electron density of the surface plasma. Electro-magnetic discharge pulses emanating the interaction region are followed by a pulse discharge current from the ground, both transporting kA-range currents through the target rod. A surface plasma offers promising control over key properties such as discharge pulse speed and target-surface potential modulations. The platform based on laser-induced target discharge is suitable to attain high energy density ion beams by focusing effects and ToF compression. The further exploration of ns-laser driven magnetic lenses with ultra-strong fields up to the hundreds of T leads us to optimization that allows to decrease space-charge effects which reduce the effective field sent by traversing ions. Thirdly, EM lenses applied to magnetized TNSA resulting in brighter proton beams and in an ultra-fast Helmholtz-coil showing evidence of cavity effects.

5.1 Ion Beam Generation from Near Critical Density Gas Jets

This work pursuits an approach to HRR ion acceleration based on jet targets and HRR lasers. Studied is the interaction of an ultra-short Ti:Sa laser pulse in the regime of hundreds of TW tightly focused into a high density gas jet. The electron density reaches after ionization a level similar to the critical density for the central laser wavelength. Thus, the near critical sample may turn over-critical [Fiú+12] or remain in a regime where the laser propagates through the full target [CAB17]. Which conditions apply does not only depend on the target parameters but also the laser pre-pulse that is able to pre-ionize the target. Note that pre-pulse is stable on a shot-to-shot basis, but the target parameters are not. This work demonstrates a low variance of characteristics for laser-accelerated multi MeV beams under only slight alterations of the target, and tries to find hints for acceleration mechanisms at play.

5.1.1 Set Up and Experimental Diagnostics

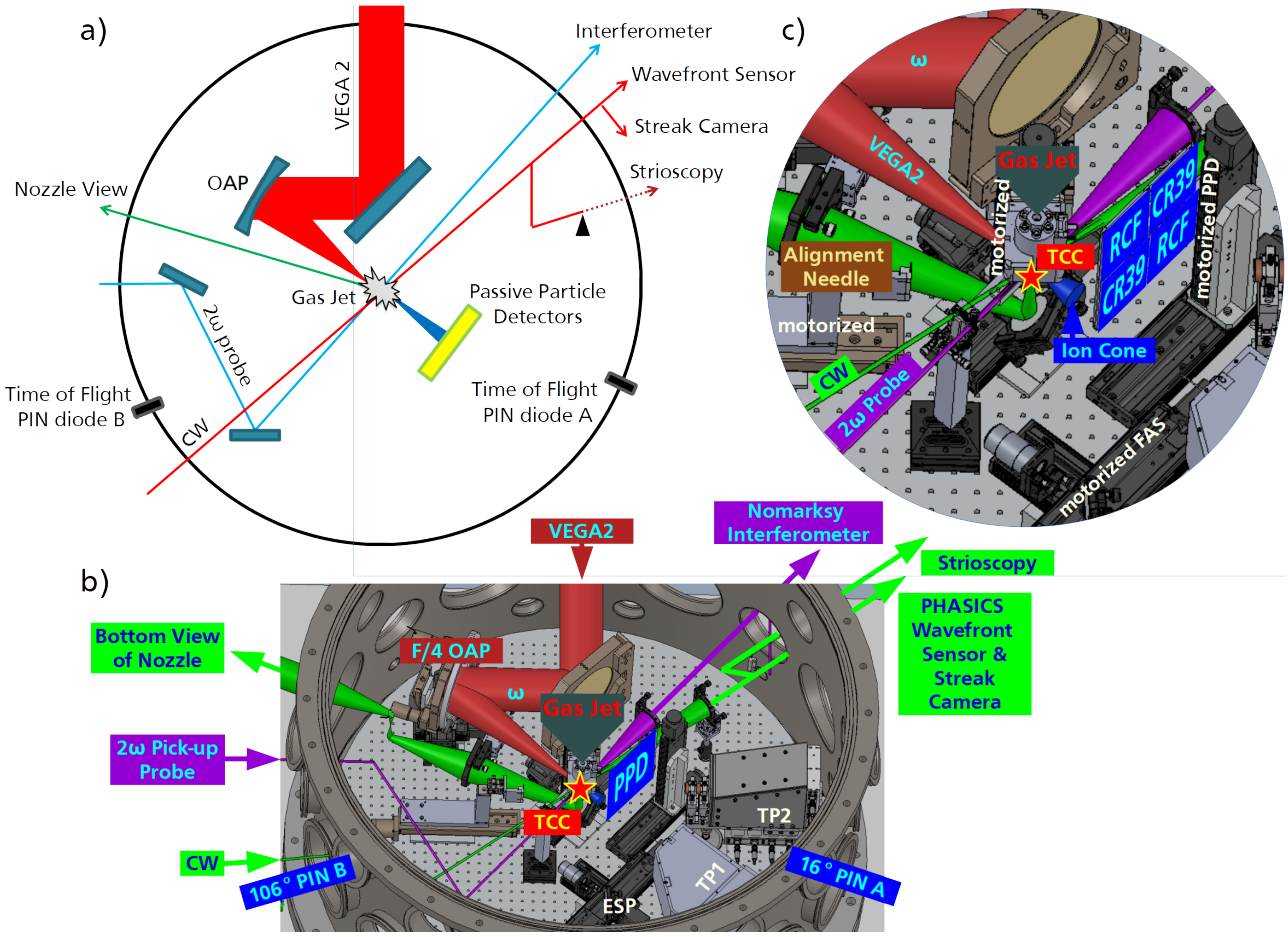

Figure 5.1: (a) Principle diagnsotics and sketch of experimental set-up for the campaign IONGASJET-2018 with the VEGA-2 laser at CLPU. Details are given with (b) the 3D Computer-Aided Design and a (c) zoom on the Target Chamber Centre (TCC) around the interaction zone.

The underlying experiment was conducted with a pulse energy of 3.00(36) J on target, with pulses of approximately 30 fs FWHM duration issued by the 200 TW VEGA 2 laser at CLPU [Vol+19]. The CPA Ti:Sa laser, with a central wavelength of 800 nm, was focused by an F/4 off-axis parabolic (OAP) gold coated mirror onto the gaseous target, as shown in fig. 5.1. The focal spot size was regularly measured at low energy by a high magnification imaging system, resulting in a reproducible FWHM of 7 µm from shot to shot. The averaged intensity in the FWHM extrapolated to the full energy is up to $120 \cdot 10^{18}\,\mathrm{W\,cm^{-2}}$. The contrast to the ASE level on the timescale of hundred ps is determined to $5 \cdot 10^{-12}$, from measurement with a third order autocorrelator system. Measurements looking at earlier times have not been performed. Several pre- and post pulses have been identified, see fig. 5.2. The ps contrast of the main pulse is $20 \cdot 10^{-6}$, after attaining $8 \cdot 10^{-9}$ at -10 ps and $50 \cdot 10^{-9}$ at -5 ps. The ramp up from contrast $50 \cdot 10^{-9}$ to $20 \cdot 10^{-6}$ appears to be exponential.

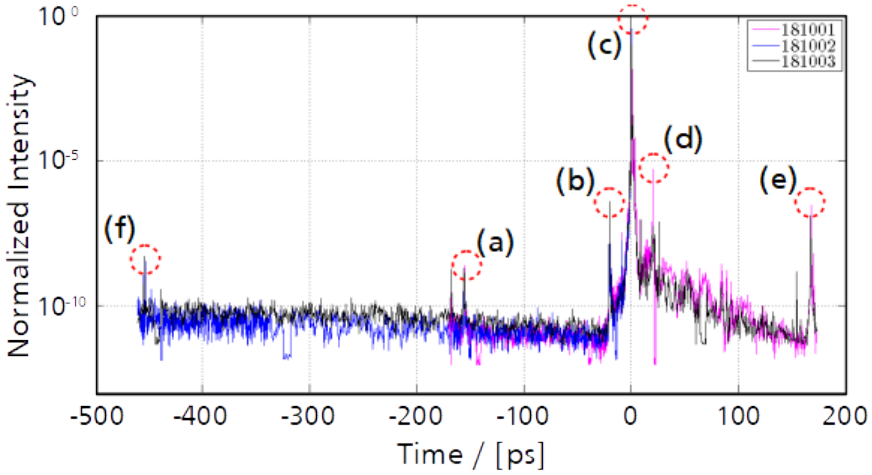

Figure 5.2: Sequoia measurement of the temporal contrast at best compression with a 10^{-10} to 10^{-11} ASE level on the order of hundred ps. Identified pre- and post-pulses are located at (a) -156 ps due to the pockels cell at the regenerative amplifier, (b,d) ± 20 ps as likely artifacts of the measurement itself and (e) 167 ps due to the pockels cell at the regenerative amplifier. (f) is unidentified, (c) indicates the main pulse.

The desired near-critical density target is produced in a controlled way with a commercially available SL-GT-10 gas jet system (SourceLab) equipped with supersonic shock nozzles [Syl+12b]. The sub-mm shock nozzle is attached to a ms-fast electro-valve with a maximum of 400 bar gas backing pressure. At several Hz issued gas jets yield a narrow density profile of approximately 100 µm FWHM such as the peak density reaches the critical density of the Ti:Sa laser wavelength after ionization. The gas jet was fully characterized by means of interferometric methods using the commercially available SID-4 wavefront sensor (PHASICS) [Pri+05] in advance, and also for monitoring during the experiment. Here, a CW laser is used as backlighter. By bottom-view imaging, the nozzle is visually inspected regarding surface damage and perfect cylindrical geometry. The shot-to-shot characterization leads us to evaluate the laser damage of the nozzle and its effect on the gas jet profile. A three axis motorization system for the valve holder and two perpendicular imaging systems allow the proper alignment of the density peak at the interaction point. The timing of laser and shocked density is monitored via a strioscopic imaging of the ROI, capturing scattered light of the driver pulse and the stroscopic image of the gas based on the CW backlighter.

Studied are gas jets of pure Helium (He) and mixtures of Nitrogen (N) and He with a ratio of 9 to 1. Due to its fluid properties, addition of N is beneficial for proper operation of the gas valve. The He doping yields ions

with high charge-to-mass ratio in the bulk of the plasma, expected more susceptible to acceleration.

Main diagnostics are on-shot interferometry to determine the driven plasma density, the streaked imaging of plasma self-emission to identify hot plasma regions, and passive particle detectors as well as ToF detectors to measure ion beam spectra. Note that the two visible Thomson Spectrometers (TP)[1] were not performing during the campaign: they were deployed with Lanex screens imaged with CCD cameras. Even after multiple re-alignment procedures, no parabolas were detected, neither X-ray spots. Also, with voltages turned off, no traces or spots were seen. One hypothesis for the failure of the diagnostics is that the CCD were not acquiring images when triggered, but with a delay.

A frequency-doubled ultra-short pick-up probe is derived from the edge of the main laser pulse before focusing, and the synchronization with the main beam in the Target Chamber Centre (TCC) is done with the help of a delay line and a streak camera. The probe back-lights the plasma dynamics perpendicularly to the main driver beam axis, with a delay of $\approx$1 ns to the arrival of the main beam. One half of the cm-scale probe beam is aligned to propagate through free space several mm aside TCC. The full beam encounters an optical path in function of the radially symmetric density profile with mm-scale wings of low gas density. The resulting phase shift was measured with a Nomarski interferometer. The electron density was then retrieved with methodology discussed here-before, see section 4.2.2.

A fast streak camera (Hamamatsu C7700), with ps resolution, measured the plasma self-emission under an angle of 82° with respect to the main laser axis in the horizontal plane, protected from scattered laser light and other NIR photons with a BG38 [Sch14] filter.

On-line energy spectra of the accelerated particles are acquired by two Si PiN photodiode ToF detectors. Both photodiodes are located vertically inclined, with 19° at 67 cm from the interaction point. They are positioned at different horizontal angles of (A) 16° and (B) 106° with respect to the driver laser propagation axis, see fig. 5.1 (a). The diode substrate is preceded by a Si layer of 750 nm and extra filtering by Mylar foils with 40 nm thick Al coating, in order to avoid diode saturation by the strong photopeak from the laser-target interaction. Mylar foils are (A) 2 µm and (B) 4 µm thick. Signal acquisition with a 1 GHz oscilloscope (Tektronix DPO4104) is performed at a maximum sampling rate of 200 ps per sample. The temporal resolution of the ToF diagnostic is 4.5 ns FWHM. 20 dB attenuation is applied to both channels to avoid saturation. The low bias voltage of -60 V is an advantage, with pressurized gas entering the vacuum chamber. For details on data deconvolution, see section 4.3.3.1.

Solid state passive particle detectors are used to capture the spatial and spectral properties of forward accelerated ion beams in single-shot operation, with stacks of RCF and slaps of CR-39. RCF undergo a colour-changing radio-synthesis that allows to retrieve the dose-depth curve from stacked films and therewith an absolute projectile number spectrum, given the projectile species is known, see section 4.3.1. To confirm appearance of projectile species, we make use of CR-39 as solid state track detector, see section 4.3.2.

Two different types of GAFCHROMIC RCF (Ashland) are deployed, commercially available EBT-3 [Por16a] (batch CLPU201810) and especially manufactured U-EBT-3 (batch 06251801). Each RCF stack comprises 4 layers of U-EBT-3 and 2 layers of EBT-3 and is enveloped in 10 µm Al filter foil. CR-39 are of type TasTrak CR-39 Plastic Sheet bought in February 2015. CR-39 are enveloped in an opaque Al coated 2 µm thick Mylar foil. Note, slaps are kept for $1.000 \cdot 10^3$ min in vacuum prior to exposure and 150 min after exposure, which stabilizes the response function on values close to known calibrations in literature.

The passive particle detector surfaces are aligned 60 mm from TCC - and detector slaps are perpendicular to the laser axis. Active layers of U-EBT-3 face TCC.

[1] For further reading on TP see a late review in [Val20].

Both detectors come in sheets and required cutting with a sharp blade. Each cut layer is large enough to fill the area in a detector casing behind one or multiple open squared frames with 40 mm sides. The casing was made of 3 mm thick Al plates. A grid of three times four recesses is used to hold either three strips of RCF upright or singular CR-39 squares. The grid is fixed to a 2D motor system in the target chamber, which allows the detectors to be freely moved behind a 5 mm thick Al plate that acts as shielding. The shielding plate has a squared opening of 40 mm times 40 mm. One shot uses the detector in one position, all other positions are well shielded. The RCF stacks and CR-39 slaps are assembled in a clean room and carefully pre-aligned with respect to horizontal and vertical orientation.

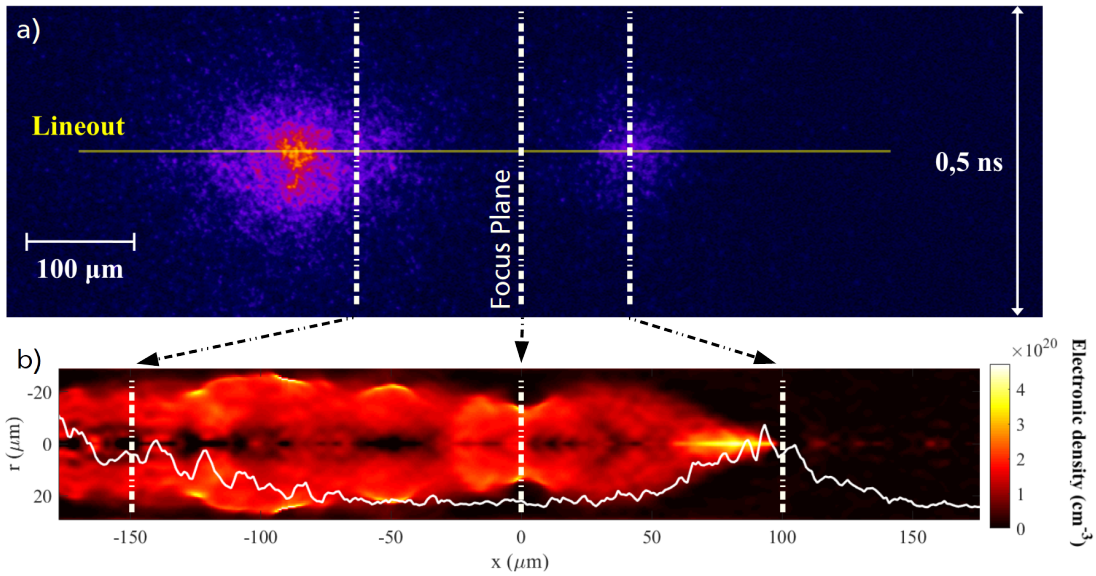

Figure 5.3: Optical plasma diagnostics show strong self emission from dense narrow regions of the plasma. We see from shot #63 (a) a raw streak camera measurement of the self-emission of the plasma with indication of the laser focal plane and (b) the retrieved electronic density of the plasma, measured with the Normarsky interferometer (see fig. 5.4), 1 ns after the interaction starts. In (b) the jet shock point and the laser focal spot are on $(x = 0, r = 0)$; the laser travels left to right; and the plasma self-emission streak-camera measurement line-out in white (arb. units) is included.

5.1.2 Experimental Results and Analysis

The two following studies focus on ion acceleration depending on the target properties without variation of driver laser parameters, despite day-to-day changes. In the fist data set, different gas jet density profiles are deployed with the driver laser aiming at the density maximum. Here the laser pulse length is $29.8(1)$ fs. For the second set of data with $27.0(2)$ fs laser pulses, the interaction region changes from the density maximum into the wings of the jet.

5.1.2.1 First Study: Variation of the Target Properties

Target parameters are determined with respect to their molecular density profiles prior to laser shots and compared on a shot-to-shot basis with respect to self-emission and electron density. For laser shot #63, deploying a pure helium jet, figure fig. 5.3 illustrates results of optical diagnostics, with fig. 5.3 (a) the

streaked self emission of the plasma and fig. 5.3 (b) the electronic density map of the plasma. As expected, taking into account that the measurement is made 1 ns after the interaction, the plasma has been able to expand and the average density is a fraction of the critical density, $\approx 0.1 n_c$. The plasma channel originates either from direct laser heating or from heating by accelerated electron beams. The scaled line-out of the self-emission, with position indicated in fig. 5.3 (a), is visible as white line in fig. 5.3 (b). The plasma self-emission in fig. 5.3 (a) is imaged with an opened slit of the streak system. Note, a thin line was observed in shots with closed slit, since the duration of the emission is shorter than the ps-time resolution of the streak with a 2 ns streak window.

In order to calculate the electron density from Nomarski interferograms, a routine[2] first calculates the phase from data and reference by the Fourier Transform technique, unwraps the phase and obtains the phase shift by subtraction of reference from data. Then, the coordinates in the spatial derivative of the phase are abelized (in the 3 inversion way) and the electron density is calculated from the spatial derivative of the difference of optical path in plasma and vacuum. For streaked self emission and interferometry diagnostics, images of micro-tips under vacuum positioned at the interaction point are aquired every day. Images are centred around the interaction point and further characterized are horizontal movements of the tip to establish the respective horizontal plane. The respective magnification is determined with vertical movements. This procedure allows to bring both acquisitions to the same scale, to rotate the acquired images to a common horizontal axis and to translate the acquired images to show the interaction point in the same pixel. For data representation, the streaked results are projected onto the interferometric coordinates, for which the angle between the axis of both diagnostics is characterized with the reflection of a CW and a goniometer.

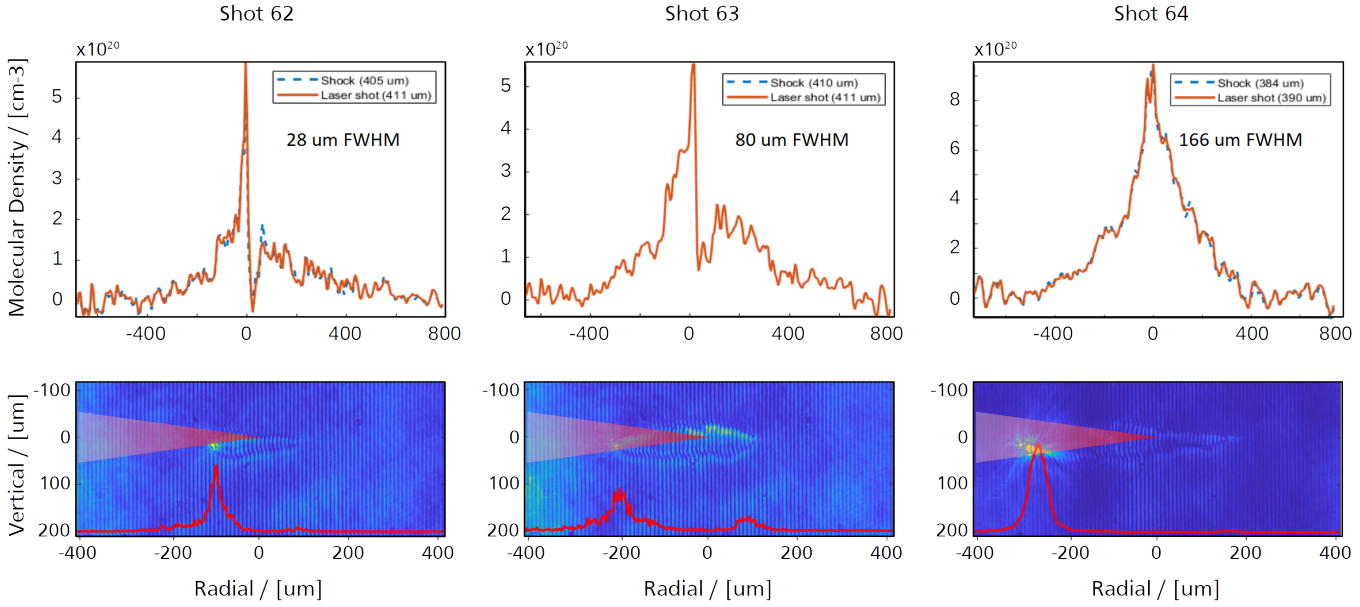

Figure 5.4: For three consecutive shots varying the pure Helium gas jet density profile, see the (top row) longitudinal gas jet density profile before laser shots obtained with the PHASICS system, and the (bottom row) interferometric image superposed to aligned laser beam and plasma self-emission in arbitrary units as red line. The laser is focused to $(0, 0)$, the coordinates of the jet shock point.

For the first study, laser shots #62, #63 and #64 deployed different gas jet density profiles, depicted in figure fig. 5.4 (top row), without varying other parameters than the gate opening time of the gas reservoir and its

[2] Script and results communicated by Carlos Salgado.

backing pressure, throughout the experiment pressurized around 400 bar. The gate opening time was set to the order of tens of ms, long enough in order to allow stabilization of the gas jet density profile but not much longer in order to limit the gas inflow into the interaction chamber. A line-out of the prompt self emission in arbitrary units is superposed to the interferometry in fig. 5.4 (bottom row). Self emission is prominent at both ends of the plasma channel, but not at the position where the laser focus was encountered without gas. One observes a plateau like feature in the density profile on the left hand side, right before the density peak fig. 5.4 (62, top row). The position of the plateau and the location of the self emission peak coincide for shot #62. The plateau density rises in shot #63 and likely becomes part of the rising edge of the peak for shot #64. Thus, for this series of shots, from shot to shot, the laser has to traverse a rising areal density of gas before reaching the peak. Regarding the full longitudinal gas profile, lowest areal densities are recorded in shot #63. There, a second self emission zone appears in vicinity of the end of the plasma channel. Comparing fig. 5.4 (top row) and fig. 5.4 (mid row), we observe that the first self emission peak corresponds to a initial molecular density of $120 \cdot 10^{18}\,\mathrm{cm}^{-3}$ to $160 \cdot 10^{18}\,\mathrm{cm}^{-3}$.

Dose converted RCF data is shown in fig. 5.5, laser photons and particles propagate out of the sketch plane. One sees active layer imprints over the full RCF stack, layers are numbered in ascending order in direction of particle propagation. A beam-like feature with similar divergence and amplitude is clearly pronounced in all shots. The average FWHM divergence of the beam is 9°. The presumed laser axis according to pre-alignment coincides with the centre of depicted frames for shots #62 and #63, not superposing the position with maximum dose. This may be due to a alignment error, the RCF stack is not thick enough to confidently determine the particle beam trajectory.

The deposited dose decreases slowly throughout the stack. The depth of the last active layer in the stack corresponds to an alpha particle range for ≈42 MeV projectiles and an electron range for ≈410 keV projectiles. Without a working diagnostics able to discriminate charge to mass ratio or the sign of the charge, this ambiguity will become further pursuit by a later comparison to ToF data.

To give an upper limit for possible ion number densities in the spectral range covered by the RCF stack, we derive ion number densities per pixel, presuming alpha particle projectiles, a beam cut-off directly after the last layer of the stack and a step-wise flat spectral shape between two active layers. Note that the number densities in figure fig. 5.5 are relative to one pixel, with scanner resolution of 600 dpi.

With no further diagnostics of the background signal issued by high energy electrons and photons, we presume the signal of an alpha particle beam with small angular divergence superposed to a broad background. Number density maps are fitted with the sum of two 2D Gaussian functions for the particle beam, superposed with a second order polynomial in both x- and y-dimension representing the background signal. This is chosen to allow for distorted Gaussian signals, fitting of which gives a smaller deviation between data and fit than a pure Gaussian. The reason for the fit is to be able to integrate the obtained ion number for the full beam and not only for the fraction clipped by the RCF frame. The typical Gaussian fit function reads,

$$a = \frac{\cos\theta^2}{2\cdot\sigma_x^2} + \frac{\sin\theta^2}{2\cdot\sigma_y^2} \tag{5.1}$$

$$b = -\frac{\sin 2\cdot\theta}{4\cdot\sigma_x^2} + \frac{\sin 2\cdot\theta}{4\cdot\sigma_y^2} \tag{5.2}$$

$$c = \frac{\sin\theta^2}{2\cdot\sigma_x^2} + \frac{\cos\theta^2}{2\cdot\sigma_y^2} \tag{5.3}$$

$$g(x,y) = C + A\cdot\exp\left(-(a\cdot((x-x_0)^2) + 2\cdot b\cdot(x-x_0)\cdot(y-y_0) + c\cdot((y-y_0)^2))\right) \quad , \tag{5.4}$$

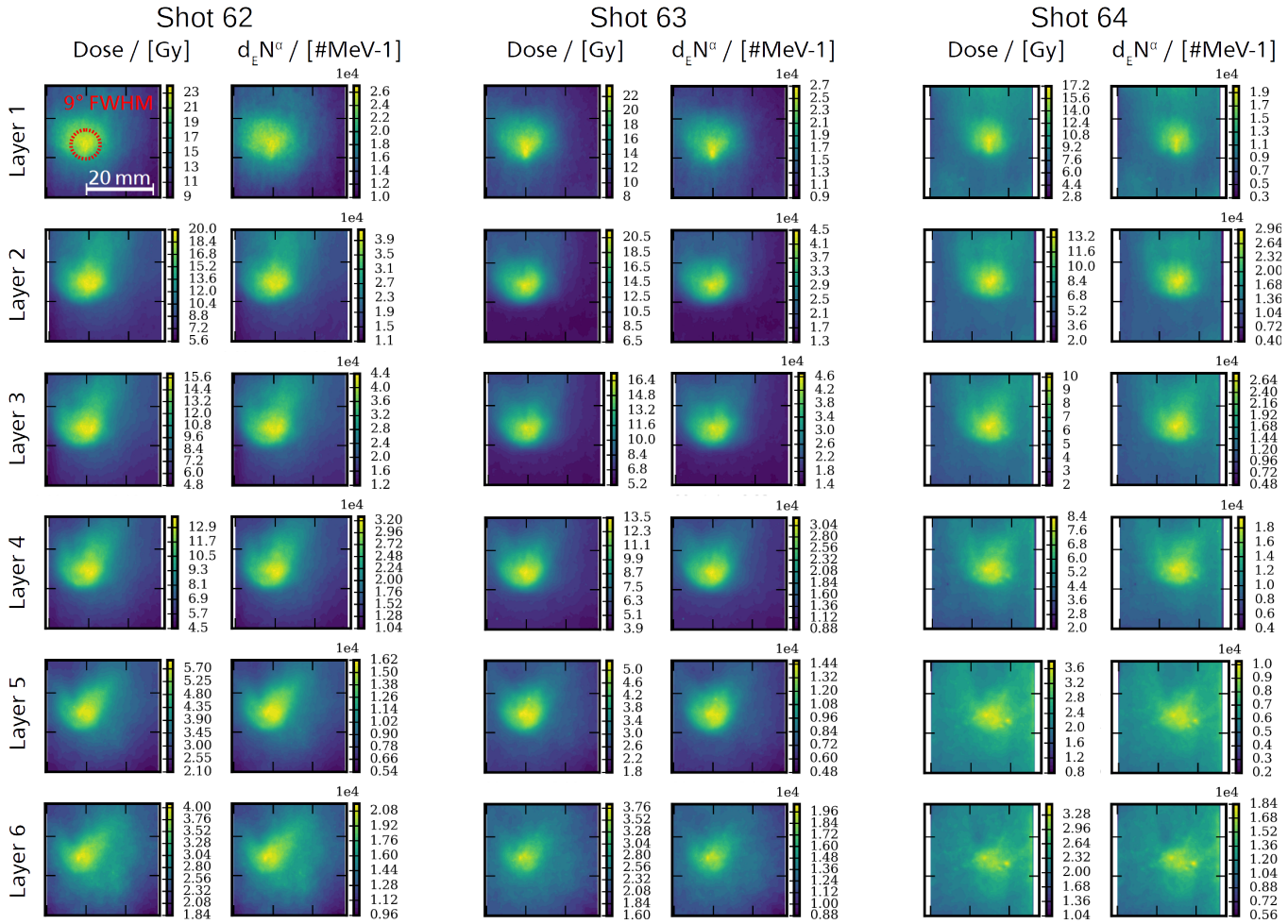

Figure 5.5: RCF imprints converted to dose and hypothetical alpha particle number density for three consecutive shots varying the gas jet density profile from lower to higher peak density. All layers of the stack are shown. The conversion to number density presumes the acceleration of alpha particles, a cut-off energy equal to the last signal layer and a step-wise flat spectral shape between active layers. The typical FWHM divergence angle of the beam imprint is 9°, all images have the same spatial scale. Note that number densities are normalized to one pixel with a $600\ \mathrm{dpi}$ resolution. For shots #62 and #63, the presumed pre-aligned laser axis corresponds to the centre of the illustrated frames. For shot #64 this does not apply.

where C is a constant offset from zero, A denotes the peak amplitude, x_0 and y_0 are the peak centre on a 2D map and σ_x^2 and σ_y^2 the variance for both dimensions tilted by an angle θ respectively. The integral of this function is $G(x, y) = A \cdot \pi \cdot \sigma_x \cdot \sigma_y / 2$. The general form of a polynomial of order m on n dimensions with signal z reads

$$z = \sum_{i=1}^{n} \left(\sum_{j=0}^{m} a_{i,j} \cdot x_i^j \right) + \prod_{i=1}^{n} \left(\sum_{j=1}^{m} b_{i,j} \cdot x_i^j \right) \quad . \tag{5.5}$$

Fits do not converge without a weighting of the data: after visual centring of the peak signal on a fit-canvas, the uncertainty of pixels is linearly and concentrically increased from 100 % at the peak to 167 % in the corners. No further adjustment is done. Examples for corresponding fits and data are depicted in fig. 5.6.

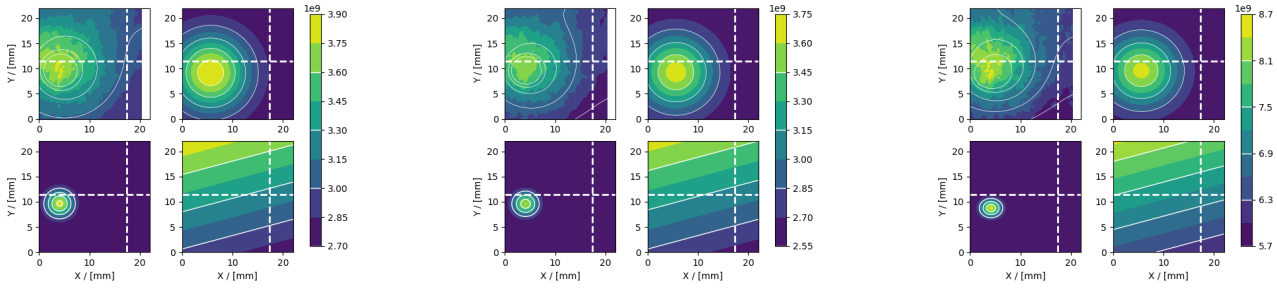

(a) red (b) green (c) blue

Figure 5.6: Zoom of the peak visible on the first layer U-EBT-3 for shot #62. Each subplot shows one colour channel. Therein, clockwise from the top-left corner, (1) the data with contours indicating a fit, for which then separately illustrated are (2) a large two dimensional Gaussian that is superposed to (4) a small Gaussian and (4) a second order polynomial background. The horizontal plane is parallel to the x-axis and the vertical plane parallel to the y-axis. The colour bar is indicative to allow comparison of the four sub-plots with each other. The intersection of white dashed lines indicate the pre-aligned laser axis position.

The number density transformed data for each of the three colour channels is depicted in the upper left panel respectively. The overlaid contours display the best fit result. The fit is illustrated with its constituents in three additional panels. Both 2D Gaussian fits can be seen in the upper right and in the lower left corner, the background in the lower right corner of the plot panel. We appreciate a low level background signal that is close to a linear evolution, fainting from left to right and bottom to top. The dashed white lines intersect on the laser axis. The background is not symmetric with respect to the laser axis. The Gaussian fits allow to retrieve the total amount of particles per energy by integration over the full beam. The integrated particle number within both Gaussians is plotted in figure fig. 5.7.

The alpha particle spectrum incorporates a peak with following exponential decay. Note that the increase at the end of the spectrum is artificial due to the assumption of a cut-off energy of 42 MeV, yielding an overestimation of the number density influenced by all higher energy projectiles that may have been present. The spectra for shots #62 and #63 are similar in the range of their error. The number density maximum of $200 \cdot 10^6\,\mathrm{MeV}^{-1}$ to $300 \cdot 10^6\,\mathrm{MeV}^{-1}$ is attained for $22(2)$ MeV alpha particles. Note that both shots have comparable neutral gas density peaks. Shot #64, with higher gas density peak, shows a thoroughly lower particle number density and the spectral peak at lower energy. $80 \cdot 10^6\,\mathrm{MeV}^{-1}$ are attained for $16(2)$ MeV alpha particles.

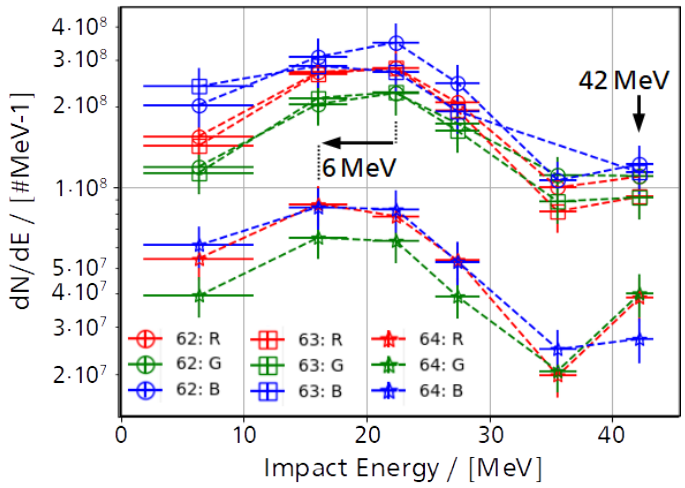

Figure 5.7: Hypothetical alpha particle spectrum for three consecutive shots varying the gas jet density profile, with similar densities for shots #62 and #63 and a higher density for shot #64. RCF colour channels R, G and B are independently analysed. Here the full dose on RCF that shows a Gaussian distribution is attributed to alpha particles to give an estimate for the upper bound of possible ion number densities.

ToF detector results give more confidence on alpha particle detection. The recorded oscilloscope data shows a clearly pronounced photopeak blinding the detector, that is followed by a signal tail extending over hundreds of ns. The photo peak of comparable shots is fitted and subtracted from the signals, such as the resulting ToF signal represents massive projectiles arriving at the detector position. The photopeak signal was found to be almost constant in intensity and decay time from shot-to-shot and to follow an exponential decay with a mean τ constant equal to $200 \cdot 10^{-3}$ ns. Earliest particles can be detected 11.3 ns after the rise of the photopeak, delimiting projectile energies with an upper bound. If electrons were the detected species, the kinetic energy range yielding recorded arrival times would be of $\approx$10 keV and below. Note, that applied filtering in front of the diodes cuts off electrons below 10 keV. Thus, comparison of RCF ranges and ToF signals indicate the presence of alpha projectiles. The deconvolved spectra for alpha projectiles obtained with the transversely oriented photodiode B is plotted in fig. 5.8 (left panel).

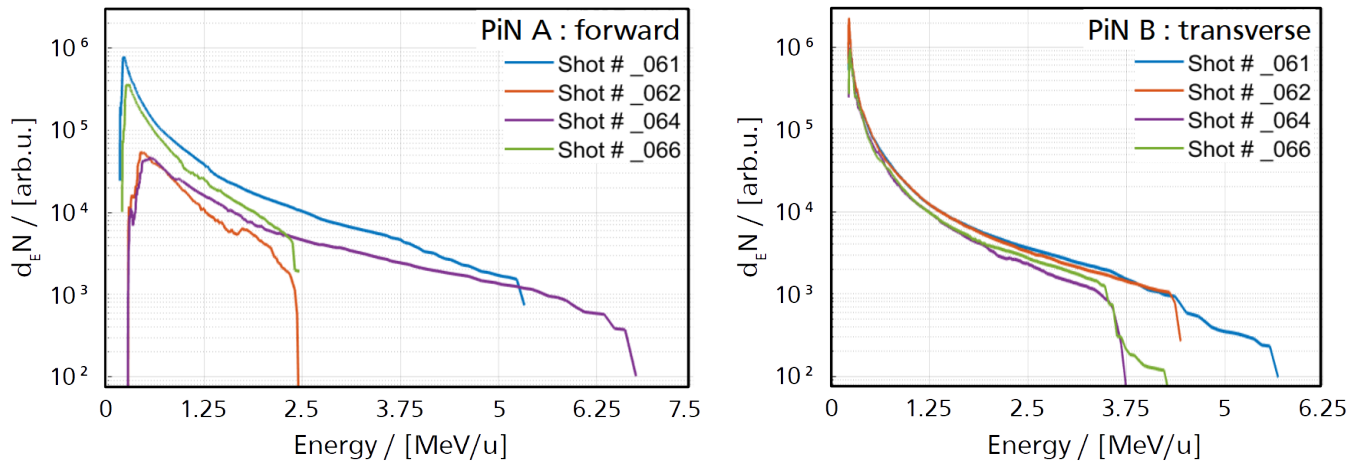

Figure 5.8: ToF results yield similar spectra in laser-forward direction (PiN A, left panel) and transverse direction (PiN B, right panel) when comparing shots with similar plasma and self emission characteristics, here for pairs #61 - #62 and #64 - #66. Results obtained under a small angle in laser-forward direction are influenced by the passive particle detector, present for shots #62 and #64, that acts as a thick filter with low energy cut-off of 44 MeV for alpha particles.

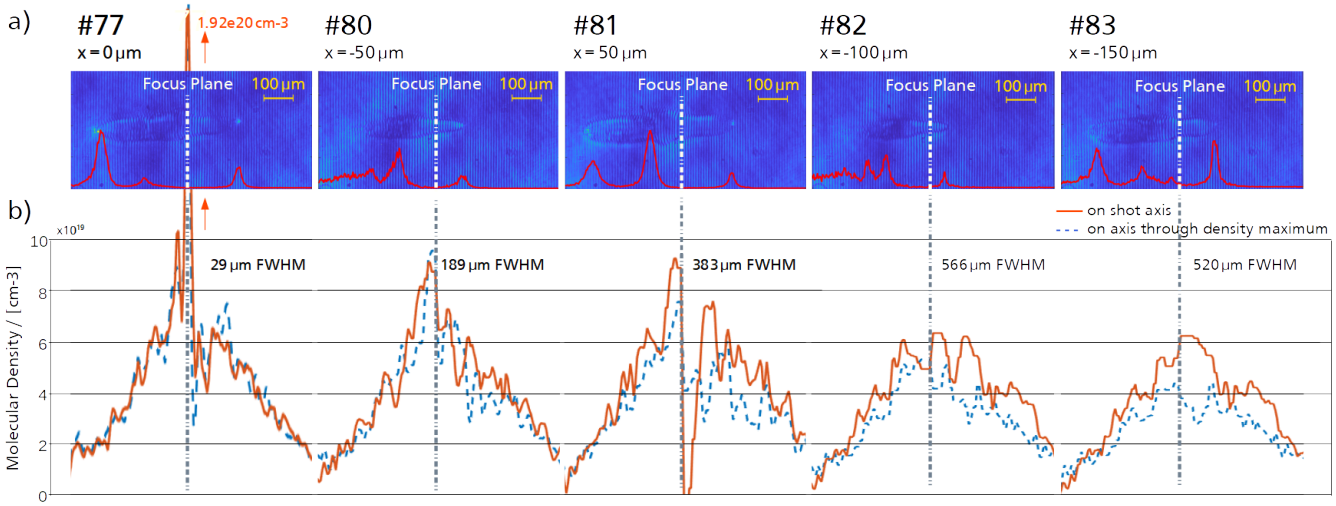

Figure 5.9: (a) Interferometric images overlaid by self-emission line-outs for shots with variation of the transverse position of the laser-gas interaction. The longest plasma channel is recorded for shot #81 with positive transverse displacement – the length of the channel decreases for the series of shots towards negative transverse displacements. The last shot of the series #83 does not agree with this assessment and shows a longer channel again. Note that (b) gas density profiles acquired prior to corresponding shots show visual changes from shot-to-shot, indicating changes to the nozzle. This agrees with a qualitative difference of the nozzle surface between shot #77 and #83, presented with fig. 5.10. Further, the drop to zero density for (b) #81 might be a measurement artefact.

The ToF spectra for particles accelerated under a small angle from the laser forward direction are shown in fig. 5.8 (left panel). The deployed RCF stack in shots #62 and #64 acts as a high-pass filter and cuts off

alpha particles with energies below 44 MeV and yields important scattering of those just passing. For this shots, the spectral cut-off energy is well separated from the photopeak cut-off. Overall, alignment precision of the recesses holding the RCF was not well enough monitored to exclude possible clipping of the direct line between laser-focus and ToF photodiode A. The cut-off energies can not be direclty compared. Results have to be understood as lower limit to the unperturbed projectile energy. Therefore, the below limit for the highest recorded projectile energy calculates to 55 MeV for alpha particles of ≈4 u from shot #62, and the below limit for the upper bound results with 70 MeV for shot #64. For jets of higher gas density and FWHM, ToF results indicate possibly a larger extend of the spectral range.

Result of the first study are the acceleration of alpha particles with energies of tens of MeV and laser-forward directed beams of ionizing radiation with minor shot-to-shot changes for small variations in the target gas density profile. Alpha particle acceleration in laser-forward direction is indicated with cut-off energies above 55 MeV, in transverse direction only lower energies could be measured. Spectra obtained from RCF show peaked particle number densities of several 10^8 MeV^{-1} for 22(2) MeV projectiles, which remain unconfirmed by other diagnostics. Note that the pairs of shots #61 – #62 and #64 – #66 have respectively similar longitudinal profiles for the gas jet, comparable interferometric images of the driven plasma at late times and a plasma self emission of same order of intensity. For smaller volumes of plasma and lower self-emission amplitude in #61 – #62, transverse ToF results show a higher particle number and a higher cut-off energy, when compared to #64 – #66 with larger volumes of plasma and higher self-emission amplitude. The decrease of particle number and the shift of spectral features to lower energy aligns with the forward accelerated spectra retrieved with RCF for shots #62 and #64.

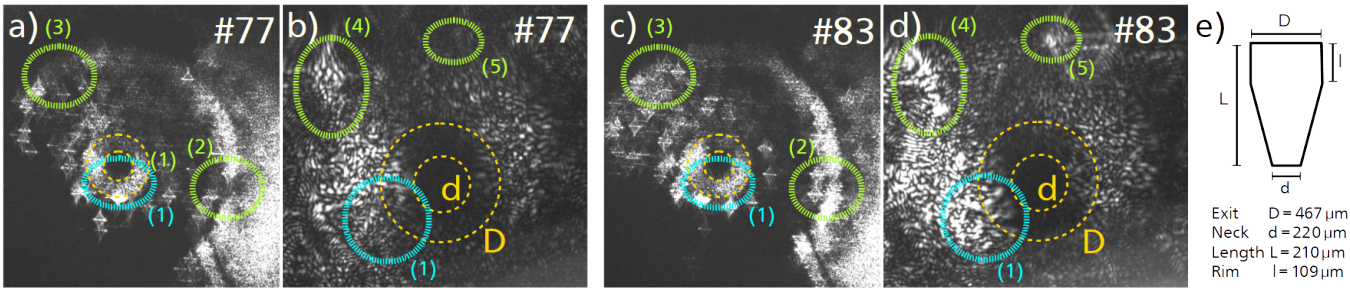

Figure 5.10: The shock nozzle deployed for the series of shots #77 to #87 shows visual changes after some laser shots. The bottom view image of the original nozzle before #77 (a) and a magnified image (b) are compared to the respective images taken before #83 in (c) and (d). The shock nozzle geometry (e) is initially cylindrical symmetric and mechanical changes to the shape and the surface quality impact the gas flow. Note areas that show visual changes in (a–d) with highlighted areas (1–5), of which (1) affects directly the nozzle cone (exit and neck diameter are indicated with orange dashed lines).

5.1.2.2 Second Study: Variation of the Interaction Region and Target Properties

The second study aims at the influence of the transverse laser focus position with respect to the gas jet density maximum. Deployed is a gas mix of Helium and Nitrogen in a ratio 1 to 9 for the gas jet. The gas jet density was not deliberately altered, but changed with the successive destruction of the nozzle on a shot-to-shot basis. Areal density and molecular peak density of the gas target are lower than in the previous study, see fig. 5.9. For a full plasma ionization, the driven electron density is smaller by a factor of about 2. In shots with clear first self emission peak, the emission zone has an molecular density of $\approx 20 \cdot 10^{18}$ cm^{-3}, and therewith an

electron density of $130 \cdot 10^{18}\,\mathrm{cm}^{-3}$ for a fully ionized plasma. The later is comparable to values found in the first study. The bulk gas shows only small shot-to-shot differences. The first self emission peak moves towards the focus plane for larger transverse displacements, likely to raise at the above mentioned fixed density value in the lobes of the density profile.

Damages were inspected visually with the nozzle viewing system, see fig. 5.10, and due to alteration of the gas jet density profile. From gas profiles in fig. 5.22 (top row) and fig. 5.9 (b), nozzle damage is likely due to laser shots #79 and #81. Further, interferometric data in fig. 5.9 (a) shows a particularly long plasma channel for shot #83 even though the laser was focused far from the largest areal density in vicinity of the supposed gas density peak. This hints severe damage to the nozzle that destroyed the cylindrical symmetry of the gas jet with shot #82.

The study is organized as follows, a first part discusses accelerated species and a second part relates variations of interaction region and target properties with changes in ion spectra.

Determination of Accelerated Species

A first qualitative view on the RCF data for shots #79, #85 and #87 (for target and plasma characteristics see fig. 5.22) with transverse displacement of 0 µm, −50 µm and 50 µm respectively is given in figure 5.11. For display purpose, data is averaged over the three colour channels. The related energies of both possible ion species correspond to impact energies of ions with a Bragg-peak in the centre of the active layer, layers are numbered in ascending order in direction of particle propagation.

The laser axis is indicated with a red-white marker, its size represents the alignment uncertainty to the laser axis in air pressure. Note that the laser pulse is p-polarized, i.e. the E-field oscillates horizontally. Photons and particles propagate out of the sketch plane, towards the dear reader. Three features are repetitive and clearly pronounced in all shots. First and most prominently, a small spot like peak appears aside the aligned laser axis. Its FWHM half-opening angle is 3°, its location approximately 5 mm right of the laser axis and 1 mm underneath the horizontal plane through TCC. The beam is elliptical and the major axis of the ellipse is perpendicular to the laser polarization direction. The sharp imprint faints quickly from first to second layer and is only roughly visible in the third layer. The fourth layer does not allow to distinguish the feature. Second, a wide Gaussian peak fills the entire RCF. The FWHM half-opening angle is 11°, the centre position is superposing the laser axis. The Gaussian is visible throughout the RCF stack, from first to last layer. A dip in its centre can be found in proximity of the laser axis for the last two layers, highlighted on the last layer of shot #87 with a white arrow. Third, four lopes appear to be clearly visible on the last layers, highlighted with a cyan circle, two maxima and two minima. Both maxima are horizontally aligned next to each other, the minima are aligned vertically above them. This horizontal separation direction is coinciding with the laser polarization. Two more features appear on the first layer, also highlighted by white arrows. For shot #87 there is a shadow visible that demarcates a clear cut from a region of high dose to a region with lower dose. For shot #79, there is a faint maximum visible at the bottom right corner of the film.

For this study, rectangles of RCF were deployed, that filled also areas between recesses for shots. On the first layers of U-EBT-3, the area between dose signals of different shots on the same RCF layer shows no exposure to dose. The Al shielding plate was efficiently protecting the RCF from irradiation, there is no cross-talk between shots. Both last layers of EBT-3 show signal on this areas and detect overall higher doses than the fourth layer. This is indicative for a mismatch between the histories of the films used for calibration and the films used during the experimental campaign. The complete life cycle of the U-EBT-3 was carefully monitored, from

manufacturing to calibration, whereas singular sheets of EBT-3 may have been exposed to high temperature fluctuations for quite a time before the experiment took place.

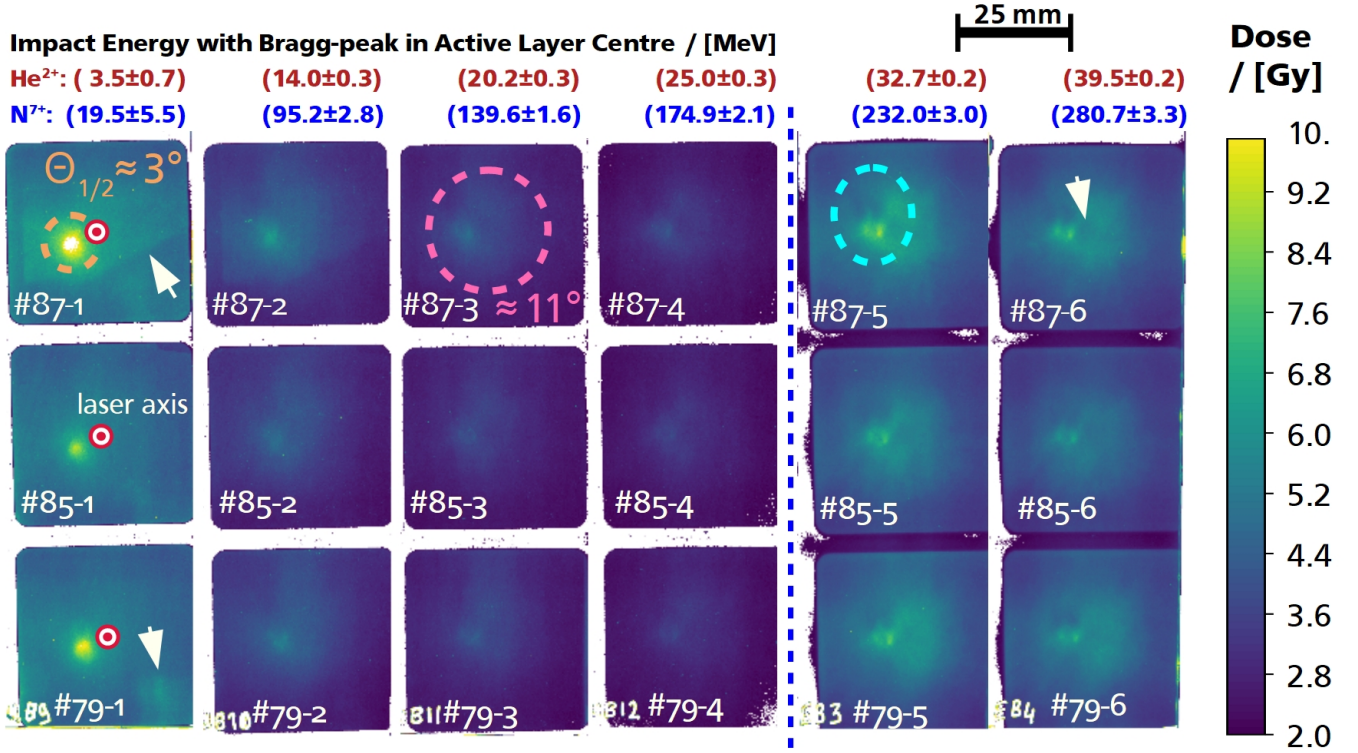

Figure 5.11: RCF results for shots #79, #85 and #87 as 2D dose maps, with indication of corresponding Bragg-peak energies in the respective active layers presuming either impact of alpha particles or fully ionized Nitrogen projectiles. The high background on both last layers is indicative for a mismatch between the histories of the films used for calibration and the films used during the experiment.

The following analysis focuses first on the spot like beam feature, with low angular divergence, and secondly on all features. The spot shows a steeply decreasing dose throughout the stack, but with a slope not fitting mono-energetic X-ray or electron beams. This opens the possibility for photon, electron, Nitrogen ion or alpha projectiles of a large spectrum. A more detailed channel-wise plot of digitized record of measurement values (RAW) data and 2D dose maps for U-EBT layers is depicted in fig. 5.12, exemplary for shot #79. The horizontal and vertical plane through the aligned laser axis are drawn as dashed white lines in the dose maps. The red colour channel is most sensitive for this type of RCF. Both, red and green channel give a clear signal with similar amplitudes. The blue channel shows thoroughly larger dose amplitudes. Note, the blue channel is not suited for doses underneath 10 Gy due to a flat response curve.

In order to resolve the ambiguity of the accelerated species we deploy CR-39. Ions with doses of several Gy are expected to show clearly cracked tracks in the SSTD. On the contrary, if the beam consists of electrons or photons, such doses are not expected to yield cracked tracks. For data exploration of CR-39 as etched track detector, the manufacturer notes use-case specific information [Wor14] and recommends etchant normality of 6.25 N NaOH-solution. This suits the model discussed here-before, implemented in the code PySTarT. The manufacturer also recommends etching at 98 celsius – a temperature not broadly covered by published calibration data. We perform etching at 70 celsius, which was found to yield satisfactory results for this

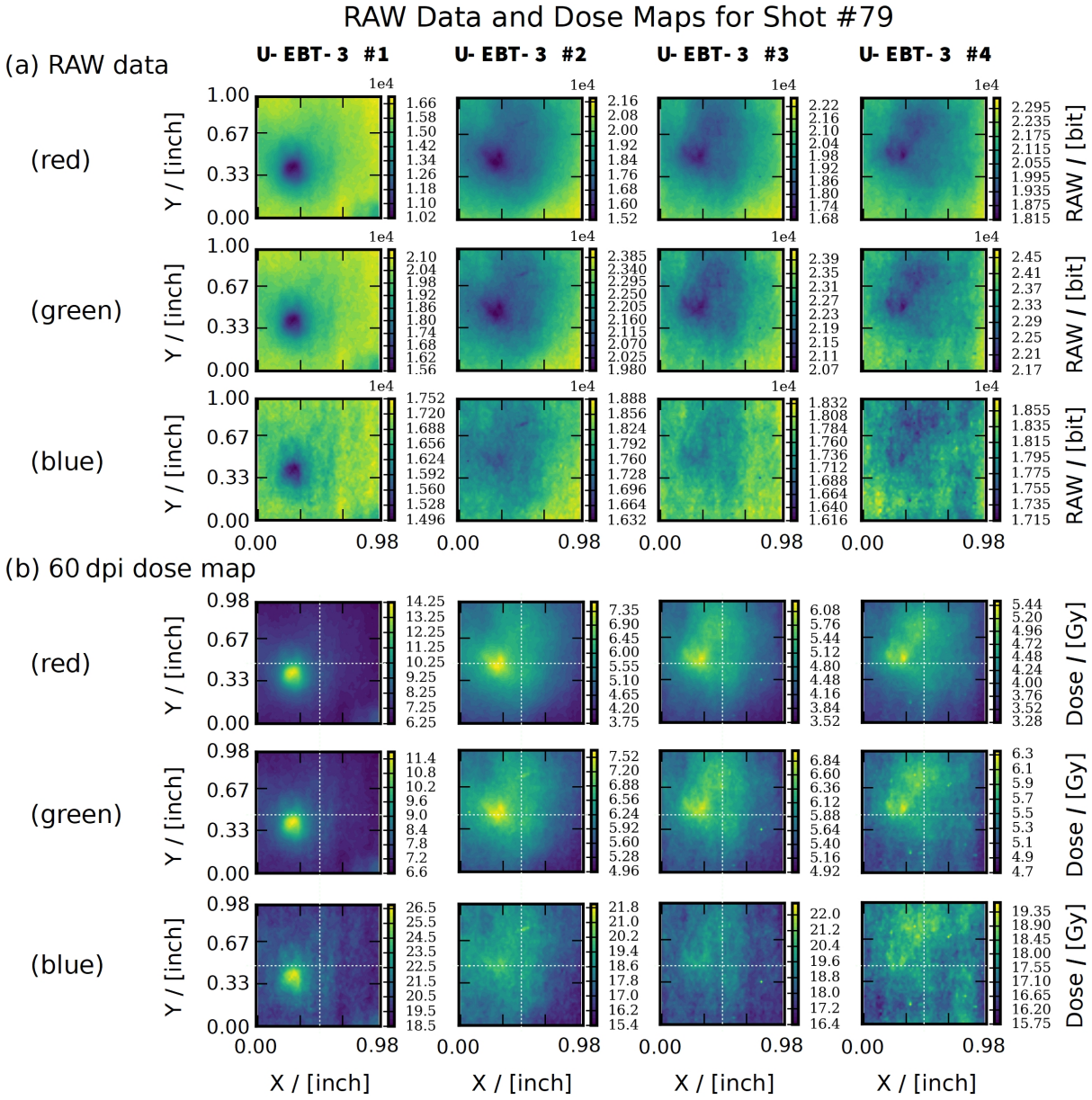

Figure 5.12: RCF stack of shot #79, with visualization limited to the first four layers. The 4 $\times$ U-EBT-3 were protected by a $10\,\mu m$ Al foil and lower film numbers face the experiment. Compared are (a) RAW data in garayscale and (b) 60 dpi dose maps in Gy. The horizontal plane of the experiment is parallel to the x-axis and the vertical plane parallel to the y-axis, the alignment axis for the laser is indicated in (b) by dotted lines.

detector type [Zha+19]. Therefore, 23.9 g of natrium hydroxid UN1823 in form of pellets manufactured by ROTH with 40 g mol^{-1} and 2.13 g cm^{-3} were dissolved in 100 ml of double distilled water.

The surface of etched CR-39 is photographed in a series of 447.63 µm × 335.4 µm microscope images acquired in 12 bit with the fully motorized CarlZeiss microscope 12-25-E-0941 (3834004357) with approximately 2 µm resolution. A large area in vicinity of the aligned aligned laser axis was analysed on the basis of a view million single microscope images, see fig. 5.13. The chemical etching post-processing unravels clear etch pits, an indication for the presence of ion species in laser forward direction for all shots. Craters are highlighted as tiny red spots on the left hand side, where squares of different gray shade are single microscope acquisitions of variable contrast. An isolated view on the location of craters corresponding to small-angle impact events is given on the right hand side.

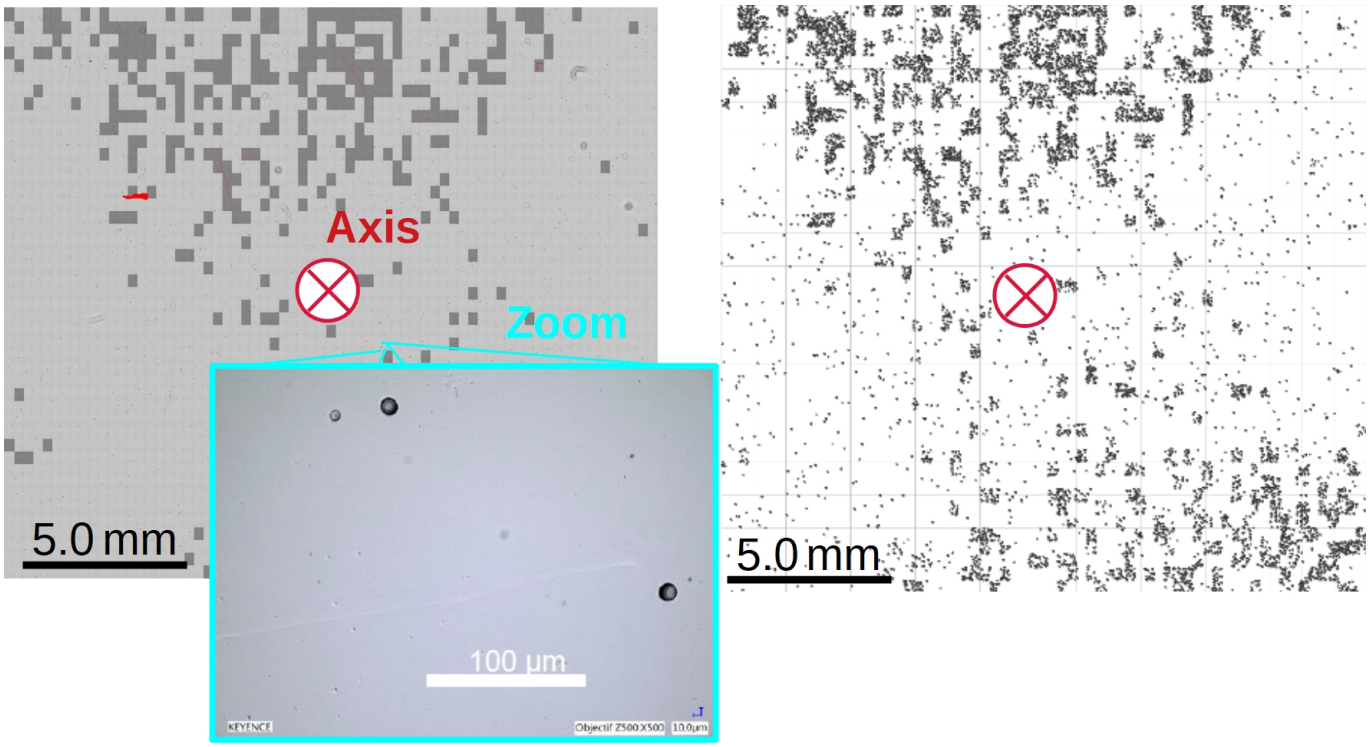

Figure 5.13: Region of interest in vicinity of the presumed laser axis as a stitched microscope images of a TasTrak CR-39 after 15 h of etching with 6.25 N etchant at 70 °C. For imaging, ta CarlZeiss microscope was employed with a maximum resolution of ≈2 µm. A zoomed canvas, acquired with a fully digital KEYENCE system, illustrates the typical etch pits with higher resolution. Small, features pronounced on RCF are not visible on CR-39.

The track density map in the vicinity of the laser axis shows an overall uniform etch pit distribution over all pit sizes. Note that areas with high contrast, visible as gray pixels on the left hand side, do allow registration of smaller crater diameters, corresponding to regions of denser points on the right hand side. The presence of a wide range of crater sizes unravels a broad spectrum for the impacting ion beam. Compared to RCF imprints, neither the lobes nor the spot-like feature are pronounced. One directly notes, that the later are most likely not ionic and that craters are related to the wide Gaussian feature.

We base a first analysis on the pit diameter evolution with etching time. One individual etch pit in vicinity of the presumed laser axis is selected that grew to approximately 20.0 µm during 15 h of etching. Figure 5.14

shows strioscopic microscope images with the growing pit after different times of etching, highlighted with white arrows. Neighboring several small craters do show smaller growth rates, and lead to perturbations to the symmetry, highlighted with orange arrows.

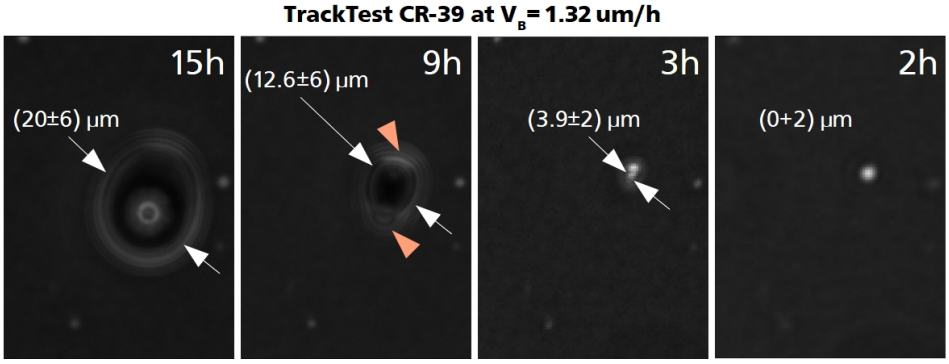

Figure 5.14: Diameter evolution of an individual etch pit on a TasTrak CR-39 with strioscopic snapshots at 2 h, 3 h, 9 h and 15 h of etching with 6.25 N etchant at 70 °C. The diameter evolves conciderably and is not detected for 2 h of etching as it may be underneath the resolution of the microscope system.

The diameter evolution of the fastest growing pit corresponds well to the expected evolution for alpha particles of 5.4(42) MeV within the margin of the measurement uncertainty. The pit has a diameter underneath the detection limit for 2 h of etching which is expected for crack tracks formed by alpha particles of such energies. In the same figure, small etch pits of 10(5) µm are visible that are present even for the earliest time, which can not be related to alpha particles of any impact energy. If they belonged to low energy alpha particles, they were expected to grow with about the same growth rate as the finally large etch pit. If they belonged to high energy alpha particles, they should not yet be visible. Their size does not match any energy of Nitrogen projectiles, neither. They could be related to high Z ions with tens of MeV or detector material impurities.

Choosing another typical area far from the laser axis aims at confirmation of the appearance of alpha particles. Etch pits with diameters at the detection threshold are investigated, see fig. 5.15. The respective dashed circles indicate all etch pits in the field of view, other circular features are microscope artifacts. For overall better comparison, the dashed circles are located at the same position for both images taken after 2 h and 9 h of etching.

We see that etch pits grow inclined with the surface, their centre shifts with an inclination that is pointing to the laser axis for most pits. Group (a) with already large pits with 5.8(9) µm diameters for 2 h and slow growth to 6.8(19) µm for 9 h follows an evolution that suits neither projectiles. We see craters (b) of 9(6) µm that are visible for short but not for long etching, which are most likely shallow suface artefacts. Inversely, the most populated group of pits (c) is underneath the detection limit for short etching and reveals pits with diameters from 6(2) µm to 13(3) µm for 9 h of etching. Such pits suit either alpha particles with energies from 4 MeV to 40 MeV or Nitrogen within an energy range of 15 MeV to 50 MeV. Grouped with (d) are pits that are at the detection limit for 2 h with diameters of 2(2) µm to 5(2) µm. The pits grow to 5.8(10) µm to 7.4(20) µm after 9 h. Where diameters are well above the microscope resolution, the craters must be very shallow to show a fainting image. Such pits suit Nitrogen within an energy range of 1.2 MeV to 2 MeV. Furthermore we see tracks with coherent but different inclination (e), not coming from the presumed laser axis.

It is noteworthy that alpha energies in the MeV range are typical for alpha particles from the decay of natural radon gas and its chain of decay. The closest neighbors in the decay series are illustrated with fig. 5.16.

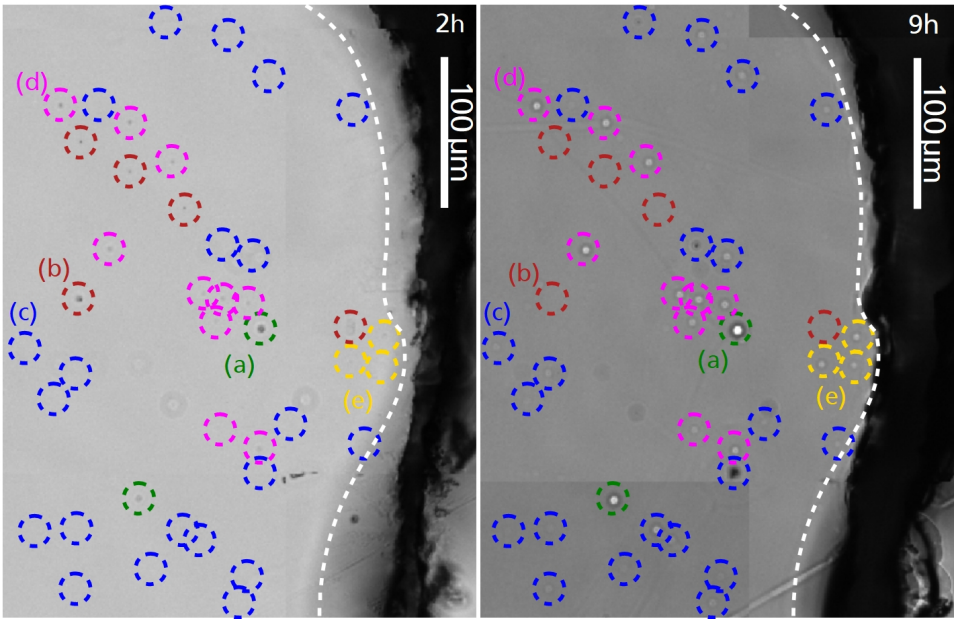

Figure 5.15: Diameter evolution for similar groups of etch pits on a TasTrak CR-39 with snapshots at 2 h, and 9 h of etching with 6.25 N etchant at 70 °C. Highlighted are groups (a,b,d,e) with circles concentric to the etch pit position for the short etching time and (c) with circles concentric to the pit position for long etching time. The dashed line delimits a scratched area, we do not see the edge of the plastic sheeth.

^{222}Rn has a half life time of 3.824 d and splits into alpha particles of 5.49 MeV and ^{218}Po. The ^{218}Po and all of the following chain has short half life times until ^{209}Bi and ^{210}Pb are reached, that decay only over years. Isotopes may be present in the vicinity of the detector for such short times. The MeV alpha projectiles that can traverse cm of air and impact on the detector. The gas occurs wherever there is granite in the subsurface. The pits grouped in (e) may be indeed issued by a chain of radon decay within cm in the vicinity of the CR-39. Inclined tracks are visible all over the CR-39 with even steeper inclination, *e.g.* see fig. 5.17.

For a broader statistical approach, a computer routine is set up to count all craters of eccentricity smaller than 0.5 with radii from 1 µm to 100 µm within the full region of interest around the laser axis. The relative counts are plotted for respective diameters in fig. 5.18. Three different blue shaded colours indicate the distributions for diameters of mean measurement value (M) with their lower uncertainty limit (L) and upper uncertainty limit (U) derived from subtraction and addition with the standard deviation respectively. Superposed are simulated diameters in function of impact energy for alpha particles and fully ionized Nitrogen.

We see distribution and expected values at three different total etching times in the upper row of graphs. The lower row of graphs highlights in addition projectile energies of either species, that correspond to etch pit diameters with peaks or features in the distribution obtained for 15 h of etching.

For one etching time, results are ambiguous: one specific diameter can be result of two impact energies. The rate $\partial_E D$ of diameter D in function of impact energy E is smaller for respective upper energies, thus their uncertainty is larger. Etch pits grow smaller towards higher energies, such as the high energy tail of the spectrum overlaps with small traces of surface damage and material impurities. The distribution for shortest etching does not show clear peaks, but changes in the slope that may be related to singular or superposing peaks. We will follow the history of peaks backwards, in order to relate the diameter distribution to particles

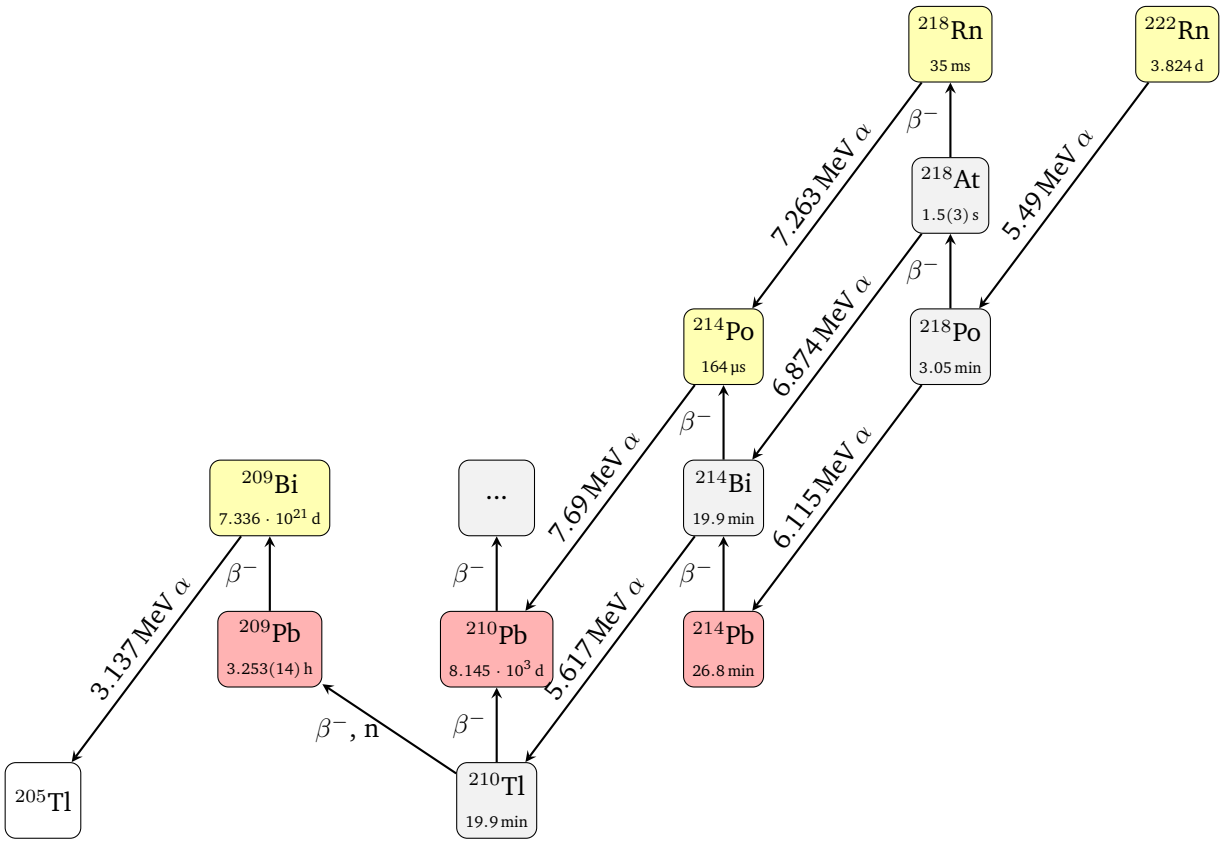

Figure 5.16: Decay of natural radon gas and decay chain.

of distinct species within a certain impact energy range.

The largest peaked diameter for 15 h is 27.0(18) µm, followed by a second peak for 20.0(12) µm. A 27.0 µm etch pit can be produced by alpha particles of 3.0 MeV and also by fully ionized Nitrogen of both 10.0 MeV and 22.4 MeV. A 20.0 µm etch pit can be produced by alpha particles of 1.3 MeV and 5.0 MeV and as well by fully ionized Nitrogen of both 5.0 MeV and 33.2 MeV. This particular pairings of energies and projectiles are now compared with the distribution for 9 h of etching. There, N^{7+} with 33.2 MeV do not correspond to any noticeable change in the slope of the distribution. All lower energy pairings with 1.3 MeV, 3.0 MeV, 5.0 MeV, 10.0 MeV and 22.4 MeV correspond to diameters that are part of bumps in the distribution. The largest diameters are consistently fit 10.0 MeV N^{7+} and 3.0 MeV He^{2+}. It is remarkable that the etch pit distribution covers the full range of likely diameters over all ion energies of both species and does not allow us to determine upper or lower limits for energy ranges.

We further observe a short plateau in the distribution for 15 h that suddenly drops for 10.0(14) µm diameters. Impact energies higher than 11.2 MeV for alpha particles and both ranges lower than 1.5 MeV and above 48.2 MeV for N^{7+} projectiles may cause such etch pit diameter. For 9 h of etching, 48.2 MeV N^{7+} correspond to a peak for 4.5 µm pit diameter for a plateau that also fits energies lower than 1.2 MeV N^{7+}. Alpha particles with energies above 11.2 MeV are also possible cause of the plateau.

After 2 h of etching, the diameter distribution does not allow to further repartition features between alpha particles and N^{7+}, partially due to the limited resolution of the microscope system, partially due to the poor quality of the detector with many scratches that render the automatized analysis difficult.

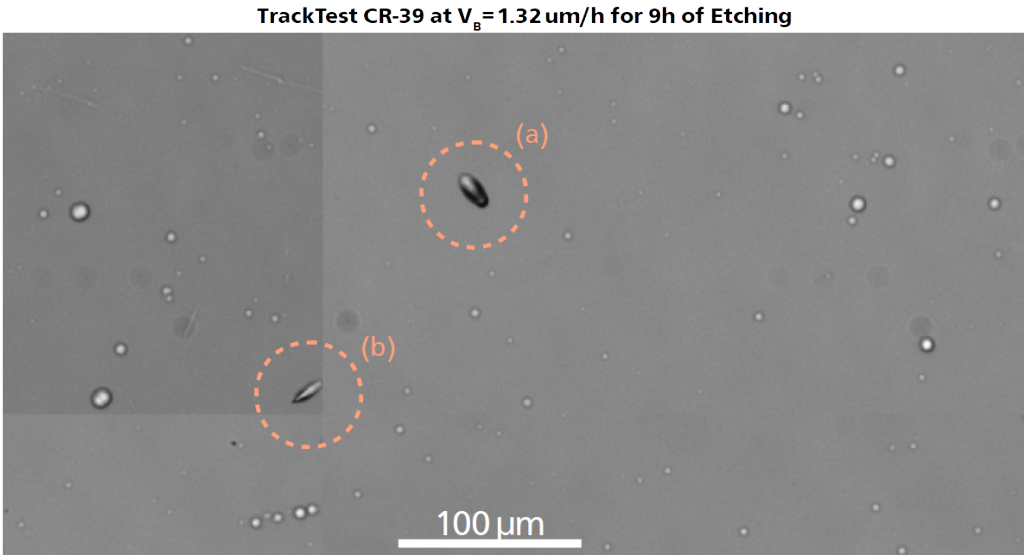

Figure 5.17: Two inclined etched pits (a) and (b) on a TasTrak CR-39 in a snapshots at $9\,\mathrm{h}$ of etching with 6.25 N etchant at 70 °C.

In summary, many possibilities result from the statistical analysis. Concerning N^{7+}, we may either observe $48.2(55)$ MeV ion bunches or projectiles with impact energy lower than 1 MeV. Ambiguously, $10.0(20)$ MeV N^{7+} or $3.0(10)$ MeV He^{2+} are indicted by the largest observed diameters. For alpha particles, a broad spectrum with energies superior to 11.2 MeV is plausible cause of smallest diameters. ≈5.0 MeV particles of both species may be part of the most pronounced features in the diameter distribution, *e.g.* a pronounced peak at 15 h.

Overall, the diameter evolution hints the presence of multi MeV alpha particles in a range of 4 MeV to 40 MeV and is not excluding alphas of different energies. Particularly alpha particles of 5.4 MeV were detected. N^{7+} from 1.2 MeV to 2 MeV are the only plausible cause for a certain group of pits. Note that Nitrogen ions up to 13.2 MeV are stopped within the filter foil in front of the RCF and therefore non contributing to the signal. The alpha impact energy range corresponds to the stopping range covered by the thickness of the RCF stack.

A second analysis strategy focuses on a Z-scan of one typical area containing all diameters of craters. We vary the focusing position of the imaging system in µm steps and follow crater walls from tip to surface to determine the length of the etched tracks. The diameter of pits is determined at the respective etched surface. Results are compared to interpolations of calibration data calculated with the code PySTarT in fig. 5.19. Data points are underlain with a relative point number density colour map in gray-scale and the simulated spectrally resolving species specific $L(D)$ lobes.

Most etch pits are shallow and of small diameter. Smallest diameters of $3.5(15)$ µm belong to craters with a large variation of depth with $4.5(30)$ µm. Deeper tracks in a range from $6.0(2)$ µm to $12.0(2)$ µm form a linear slope with their respective diameters from $4.0(2)$ µm to $10.0(2)$ µm. Two singular data points with $9.0(2)$ µm and $11.0(2)$ µm track length do not follow this trend, both of $12.0(2)$ µm diameter. Overall, the number density of craters decreases with increasing diameter. In the sample sequence, there is only one crater with a large diameter, here of $23.0(2)$ µm and $16.0(2)$ µm depth. From the few data points, it is difficult to conclude on a continuous relation between different types of craters.

Larger etch pits show characteristics similar to simulated alpha particles of $4.5(3)$ MeV. The data distribution for etch pits with diameters smaller than 10 µm makes it difficult to distinguish alpha particles of $6.7(3)$ MeV

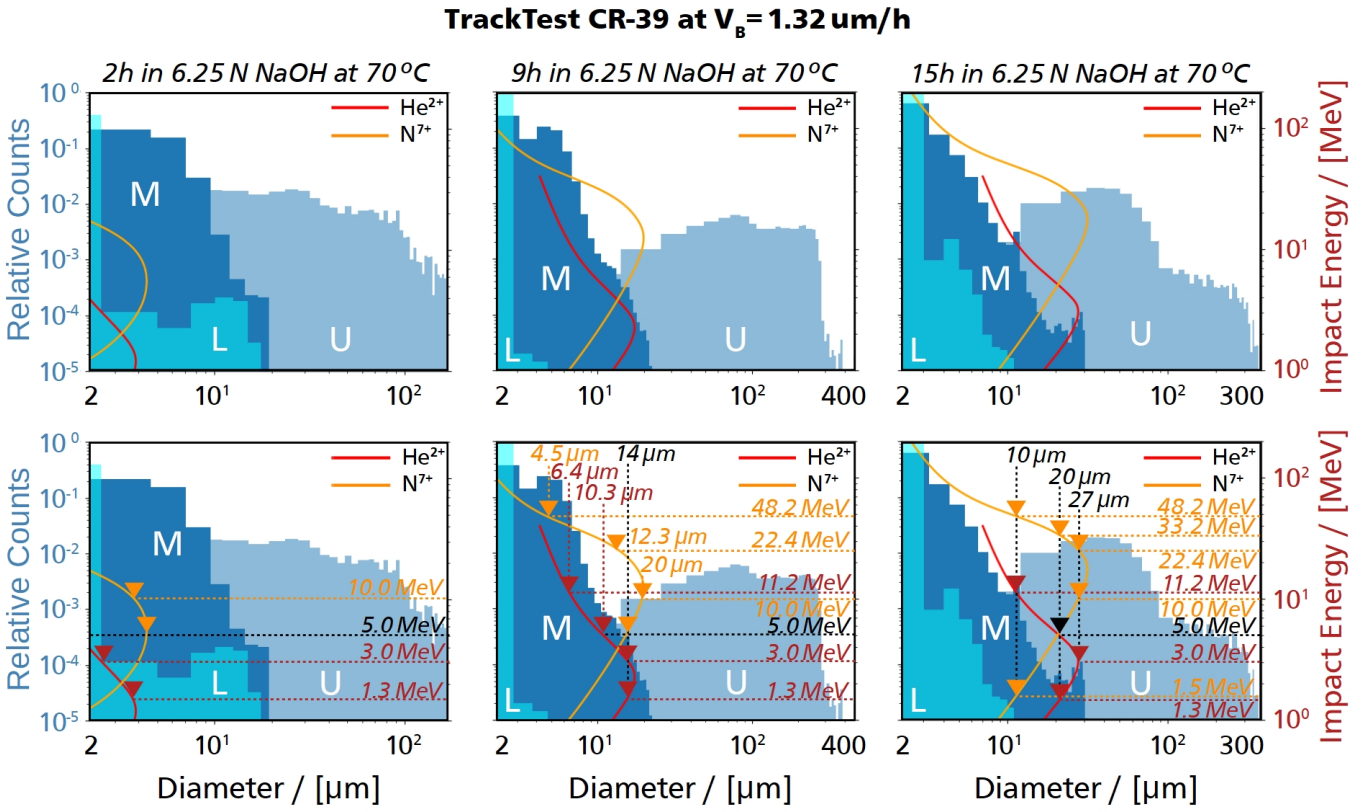

Figure 5.18: Diameter evolution of etched pits on a TasTrak CR-39 with snapshots at 2 h, 9 h and 15 h of etching with 6.25 N etchant at 70 °C. The diameter distribution of etch pits is determined within a 20 mm × 18 mm square centred with the presumed laser axis. The distribution of mean measurement value (M) is relativised by the distribution of upper uncertainty limits (U) and lower uncertainty limits (L). Solid lines indicate simulated spectrally resolving species speciffic etch pit diameters for alpha particles and for fully ionized Nitrogen ions. Upper and lower graphs correspond, but projectile energies that correspond to peaks in the distribution for 15 h are highlighted in the lower row of graphs with the respective etch pit diameter. Simulated with the CR-39 plug-in of PySTarT, see section 7.4.

to 40(14) MeV or Nitrogen ions of 56(2) MeV to 200(50) MeV. Oppositely assuming the small diameter pits to be detector noise from impurities in the material, all of the three singular etch pits with diameter above 10 µm are closer to the lobe for alpha particles than for fully ionized Nitrogen. The TasTrak CR-39 was expected to be noisy, see section 4.3.2.7, which makes it difficult to decide weather or not smallest observed etch pits are issued by impacting ions.

Note, that for alpha particles there is a numerically determined 10 % underestimation of the track length and diameter. For Nitrogen, simulations do not show such numerical discrepancy and results are within the scope of the model and fitted experimental data [AHAJ13]. Note further, that simulations for alpha particles and fully ionized Nitrogen performed here-before for the purpose of data interpretation are indicative but not conclusive, as no specific calibration was performed to check on the employed CR-39. Especially the effect of out-gassing can alter etching rates. For completeness we must mention that the analysed CR-39 was kept in a low pressure environment at <1 mbar without oxygen for 250 min before irradiation and for 15 min after.

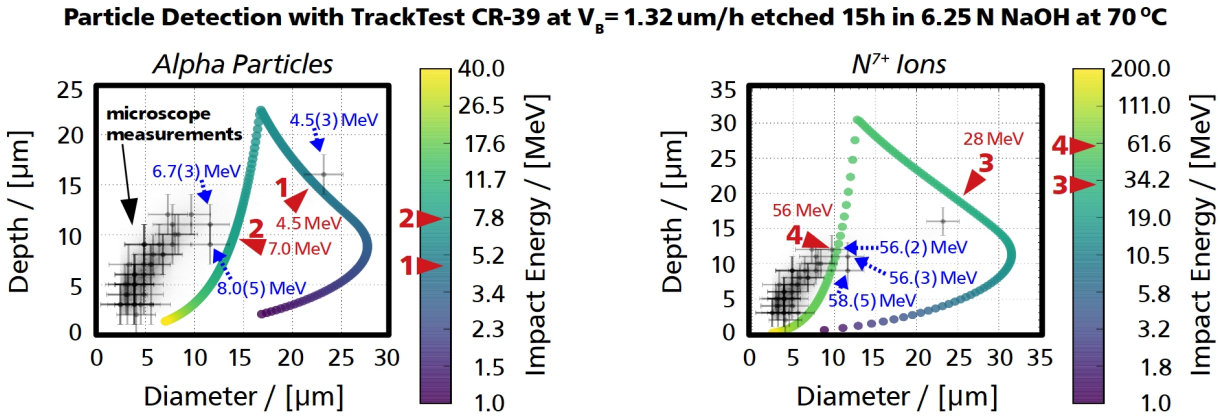

Figure 5.19: Depth-scan of etched pits on a TasTrak CR-39 after $15\,\mathrm{h}$ of etching with 6.25 N etchant at $70\,°\mathrm{C}$. Experimental data points are underlain with a relative point number density colour map in grayscale. The simulated spectrally resolving species speciffic $L(D)$ lobes are for alpha particles on the left hand side and for fully ionized Nitrogen ions on the right hand side. Specific impact energies are highlighted with red marker arrows (1–4). Experimental data points that overlap with the lobes in the range of their uncertainty are denoted with the closest corresponding energy on the lobe. Simulated with the CR-39 plug-in of PySTarT, see section 7.4.

In summary, taking into account the energy lost in the $2\,\mu\mathrm{m}$ filter prior to impact on the CR-39, we detected two individual representative low energy alpha particles with $5.6\,\mathrm{MeV}$ and $4.6(3)\,\mathrm{MeV}$, indicative for the presence of He^{2+} with energies of the order of $\mathrm{MeV\,u^{-1}}$. Further likely is acceleration of Nitrogen ions up to energies of $3\,\mathrm{MeV}$ to $4.5\,\mathrm{MeV}$. Higher energy ions of both kind can not be discarded based on the CR-39 analysis.

ToF results can now be employed to compare transverse and forward accelerated ion spectra. The spot beam and all features in its vicinity have a too little opening angle to reach the ToF detector, such as its recordings concern the background, perceived so far as uniform. Spectra from the ToF signal, can be seen in fig. 5.20.

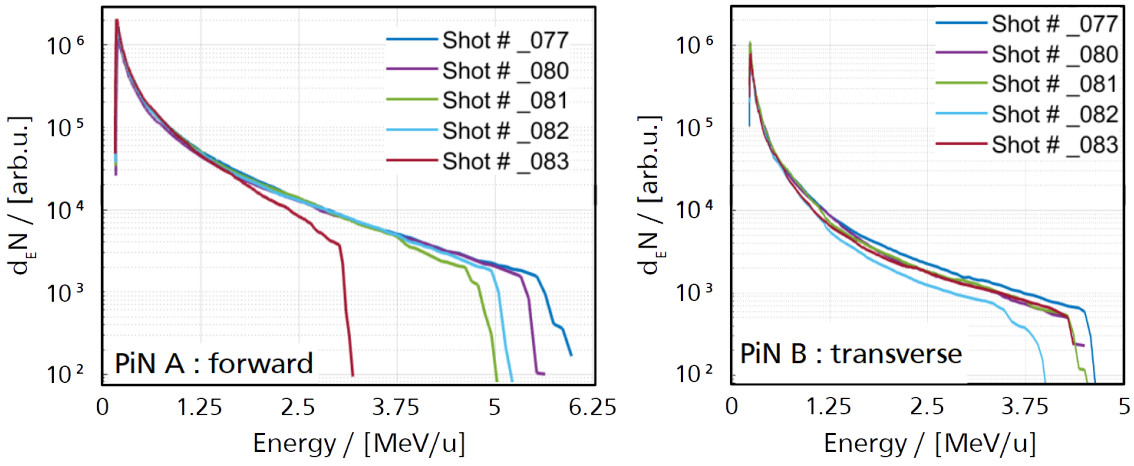

Figure 5.20: Unit-mass normalized spectra obtained after the analysis of the time-of-flight A (left) and B (right) signals assuming ion acceleration for five different shots.

Particle energies per atomic mass unit vary from 2.5 MeV u^{-1} to 6.5 MeV u^{-1} for the laser forward emission (16° from the laser axis) and from 3.75 MeV u^{-1} to 6 MeV u^{-1} for the transverse emission (106° from the laser axis). Maximum energy cut-offs are less spread in the transverse emission. The number of particles that arrive to the front detector (PiN A) is slightly higher than the number of particles arriving to the transverse detector (PiN B). Note that the upper cut-off energy is determined by the detector blinding effect of the photopeak, and does not represent the cut-off of the spectrum.

The results of PPD and ToF detectors in forward direction are graphically summarized in fig. 5.21. The overview compares the resulting spectral ranges presuming either He^{2+} and N^{7+} projectiles. For ambiguous cases, mutually exclusive pairs are indicated with the same letter or number. Ambiguous are results which could not be attributed to one species within the capabilities of one detector. Comparing all results hints the acceleration of Helium to be responsible for high velocity projectiles and the acceleration of Nitrogen only to cover projectiles of low speed.

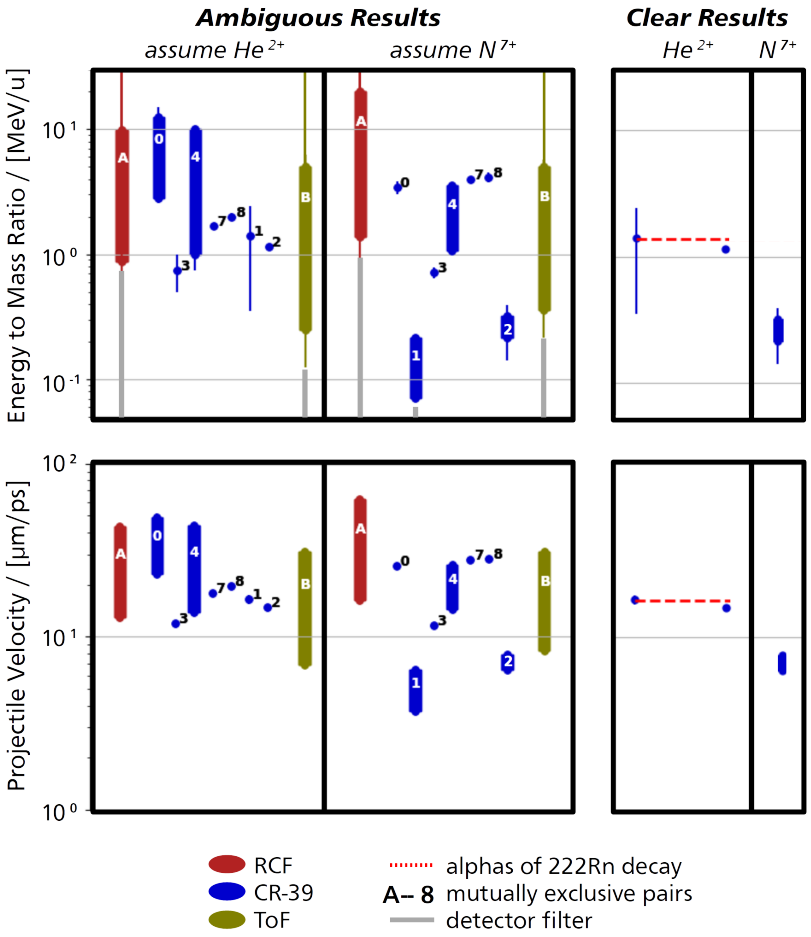

Figure 5.21: For all detectors, detected energy to mass ratio (top) and projectile velocities (bottom). Presumed is only the appearance of He^{2+} and N^{7+}. Ambiguous results in the respective left panel are compared to un-ambiguous results on the right. The ambiguous data may be associated to one or the other species, the respective pairs are indicated by an equal ID.

With the certain presence of low energy Nitrogen projectiles, the ambiguous groups one and two could be attributed to Nitrogen. Low energy alpha particles are not detected by any of the detectors, notably not by

CR-39 with the thin-most filter foil. Furthermore detected are two alpha particles with energies similar to the alpha-decay of natural radon, one of which impacts with an inclination pointing away from the interaction zone. It is thus at least one of both not related to the laser-plasma interaction. CR-39 give evidence of alpha projectiles with impact energies that can reach last layers in the RCF stack, whereas there is no indication for high energy Nitrogen. The broad and uniform background registered on RCF might be related to the uniformly distributed ion traces on CR-39. In parallel, there is no evidence that the spot-like beam or described high-dose features are ion beams. All features visible on RCF have no direct representation on CR-39.

Correlation between Variations in the Interaction Region and Signal Changes

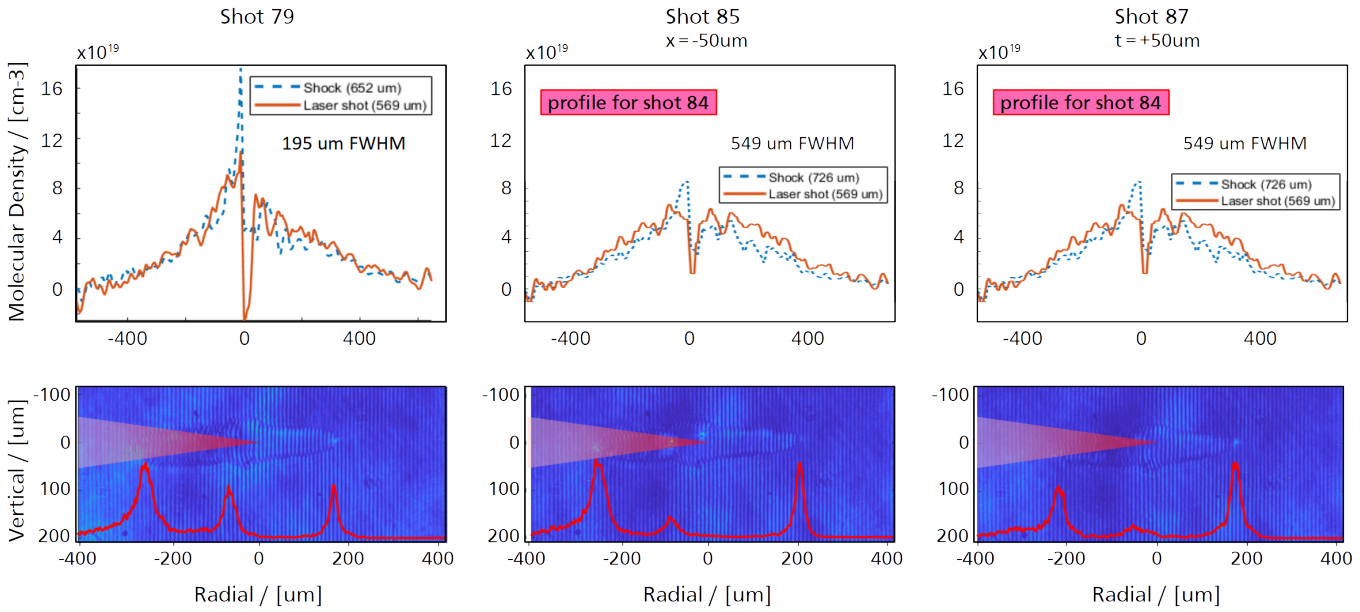

Figure 5.22: Shot-to-shot variation of the gas jet density profile using a mix of Helium and Nitrogen in a ratio 1 to 9, (top row) longitudinal un-driven gas jet density profile, and (bottom row) interferometric image superposed to a sketch of the aligned laser beam and the plasma self-emission signal in arbitrary units as red line, $1\,\mathrm{ns}$ after the interaction starts. The laser is focused to $x = 0, y = 0$, the coordinates of the jet's shock point, but transversely displaced by $0\,\mu\mathrm{m}$ and $\pm 50\,\mu\mathrm{m}$.

Characteristics of the driven plasma and gas density profiles are now compared to spectral features of the broad background signal of alpha particles. The molecular density of the gas jet in the respective laser shots and the on-shot interferograms overlaid by line-outs of the streaked self emission are depicted in fig. 5.22 and fig. 5.9, corresponding to shots with RCF (see fig. 5.11) and ToF detectors (see fig. 5.20) respectively.

Transversely, the highest ion numbers are recorded for shot #77 which is the only shot of the series with a pronounced peak in the gas density profile. Shots #80 and #81 with the same small radial displacement in opposite directions yield comparable transverse spectra. Both later shots do have plasma channels of different length, but approximately the same level of self emission intensity in the first self emission peak. Shot #83 shows a similar self emission in the first peak, and agrees with #80 and #81 for the transverse spectrum. Tiny differences between the spectra of this three shots arise for energies from $1\,\mathrm{MeV\,u^{-1}}$ to $1.5\,\mathrm{MeV\,u^{-1}}$: the shorter the plasma channel, the more particles populate this range. Shot #82 with the least pronounced self emission and the shortest plasma channel has the lowest particle number densities. Shot #77 has the most

pronounced self emission peak, but not the longest plasma channel. The self emission peak has a stronger correlation with the transverse spectrum.

The forward accelerated projectiles show only for shot #83 a much lower number density, a shot for which the third self emission peak is the most pronounced.

For this work without dedicated diagnostics, it is not possible to further determine the nature of the the features visible on RCF. A longer plasma channel and a higher first self-emission peak coincide with lower doses in the peak feature, comparing shots #79, #85 and #87. The transverse displacement of the gas jet with respect to the laser focus and the shot-to-shot damage to the nozzle do only slightly alter the features. Projectiles may come from the interaction in the bulk gas rather than from the density peak.

Interferograms show a less bright self-emission into the 2ω probe beam channel, and the apparition of two more successive self emission peaks, thus the laser may propagate deeper into the gas. Wakefield electrons may be reason for the small-angle peak prominent on first RCF layers, and small angle relativistic Thomson forward scattering [Li+02] could cause the lobes. Electrons of about hundreds of keV could reach the depth of several mm in the RCF stack. The filter in front of RCF attenuates photons of several keV by tens of %, then entering the plastic material which attenuates them down to $\exp[-1]$ over hundreds of µm. This ranges fit the observed penetration ranges.

Further regarding the dipped Gaussian, the trapping of relativistic electrons in the laser-channel can produce angular distributions of the electron beam with 2D projections resembling doughnuts [Ros+19; Pug+16]. Trapping results small Larmor orbits in ultra-strong quasi static B-fields induced by the return current dynamics.

5.1.3 Summary of Results

Accelerated alpha-particles are detected with energies between several MeV and cut-off energies above 55 MeV, with similar number density distributions for shots with similar gas target density profiles. Gross changes of the gas jet density yield clear modifications of the ion spectrum, compare fig. 5.8 and fig. 5.20. Changes of the FWHM of gas jets and small variations of the areal density of gas in front of the peak show no clear correlation with spectra of forward accelerated alpha particles.

Alpha projectiles show higher number densities per unit energy and larger cut-off energies in laser-forward direction than transversely. ToF spectra for low density targets in a range from $10^{19}\,\mathrm{cm}^{-3}$ to $10^{20}\,\mathrm{cm}^{-3}$ show this in small magnitude, see fig. 5.20. Higher target densities ranging from $10^{19}\,\mathrm{cm}^{-3}$ to $10^{20}\,\mathrm{cm}^{-3}$ allow to forward accelerate much higher energies than transversely, see fig. 5.8. Here, transverse spectra are similar for shots with similar longitudinal profiles for the un-driven gas jet, comparable interferometric images of the driven plasma at late times and a first laser-sided plasma self emission peak of same order of intensity. For smaller volumes of plasma at late times and less plasma self-emission, one observes a higher particle number and a higher cut-off energy but a lower particle number density at the cut-off energy, when compared to shots with larger volumes of plasma and larger self-emission signature.

Remarkably for all shots, the first self-emission peak is situated at the beginning of the plasma channel observed at late times, and only for some shots other peaks are observable: one in vicinity of the aligned gas density peak and another at the end of the plasma channel. Presuming full ionization of the un-driven gas density, the first self-emission peak arises thoroughly in regions of electron densities ranging from $130 \cdot 10^{18}\,\mathrm{cm}^{-3}$ to $320 \cdot 10^{18}\,\mathrm{cm}^{-3}$, which is 7.6 % to 18.8 % of the critical density. Similar to what is reported in [Che+17], shots with lower target electron density show lower beam ion number density for high energies towards the cut-off energy.

Similar spectral cut-off energies in forward and transverse direction point to DCE as possible acceleration mechanism. The occurrence of broad spectral peaks in forward direction then may be rooted in a shock wave propagating down a density gradient. With respect to DCE, the cut-off energy E_C is proportional to $Z_i^2 n_i V_0^{2/3}$ – where the plasma is presumed spherical and V_0 denotes its volume; and the number density at the cut-off energy $f(E_C)$ scales with $V_0^{1/3}$, see section 3.4.2.2. Either relating wider and larger self-emission peaks to larger volumes of hot plasma at early times, or comparing the plasma volume seen in interferograms at late times, the observed larger ion number density at the cut-off energy for larger volumes of plasma agrees with what is expected for DCE. For quantitative comparison one follows section 3.4.2.2. The laser pulse with $a_{0,e} \approx 7.5$ can ponderomotively accelerate electrons to $k_B T_0 \approx 3.3\,\mathrm{MeV}$. With an electron density of $320 \cdot 10^{18}\,\mathrm{cm}^{-3}$ and a heated area with radius equal to the laser focal spot size, the governing dimensionless parameter results to $\mathfrak{T} \approx 0.14 < 0.5$, which describes in agreement with experimental results a spectrum comprising a peak for low energies. The theory underestimates the spectral position of the peak by one order of magnitude with 2.4 MeV. Note one possible reason, the spherical nature of the plasma which is one founding presumption for the theoretical derivation was not directly measured experimentally. The Rayleigh length corresponding to the 7 µm FWHM of the plasma calculates to 100 µm, such as the plasma volume is presumably cylindrical.

It can not be excluded, that TNSA at steep density gradients in the shocked gas jet is source to parts of the spectra. Note that in one set of comparable shots, a flatter spectrum with lower energy peak and possibly larger cut-off energy is produced for a gas jet density profile without sharp rear-side gradient. This can not be reasoned solely based on one acceleration mechanism, or one only shock wave, and is clear motivation for future experiments with diagnostics regarding the plasma density at early time, electron spectra and EM in the plasma.

Note further that shots on targets with larger gas density peak and smaller gradients allow to accelerate beams of ionizing radiation with a $\exp[-1]$-opening of $65(10)$ mrad. Shots on targets with larger gradients show asymmetric beams, that can be fitted by two superposed Gaussians with a $\exp[-1]$-opening of $5.5(30)$ mrad and $30(5)$ mrad respectively.

Seen the energy range of alpha particles, a penetration depth into tissue of several hundred µm is possible, beneficial for therapy of skin related tumours and experimental therapy of tumours [Bey+17]. The opening angle of beams is large when compared to standard accelerators, it leads to a decreasing beam intensity with distance to the source. For distant applications, ion beam lensing is required after acceleration. The results motivate further studies towards improved beams with higher energies and lower opening angle. This work will now discuss approaches to beam tailoring with the next sections.

5.2 Controlled Magnetic Fields for Ion Beam Lensing

Spectral tailoring of charged particle beams by electric, magnetic and EM lenses aims at both, maximizing the number of particles in a energy bin of interest given a certain application, and minimizing the emittance of this particles respectively. Laser accelerated MeV-ion beams are typically emitted with large divergence and laterally extended virtual source size, requiring EM fields for beam shaping with several $\mathrm{GV\,m}^{-1}$ and hundreds of T.

B-fields focus charged particles in various configurations, among which we will draw our attention to mostly cylindrical symmetric solenoid type fields. This work aims at further exploration of tailoring techniques based on all-optically driven metallic Coil Targets (CT). It contributes to a better understanding of the laser generated current- and potential-dynamics in the laser-plasma and their evolution over the solid target. The focusing

power of coil fields is well understood [Rei08]. Due to effective negative radial acceleration on particles propagating along the B-field axis, the particle beam gets deflected towards the axis. The focal length f of a thin solenoid magnetic lens, where the beam rotation inside the lens does not alter the radius of projectiles, in the paraxial limit with small transverse displacement r from the axis z is

$$\frac{1}{f} = \frac{q_\mathrm{i}^2}{\left(2p_{z,\mathrm{i}}\right)^2} \int_{-\infty}^{\infty} B^2(r=0,z)\,\mathrm{d}z \quad . \tag{5.6}$$

Note the quadratic proportionality to the projectile momentum $p_{z,\mathrm{i}}$ and the inverse quadratic proportionality to the projectile charge q_i and to the axial B-field $B(r=0,z) = B_z(z)$ integrated over the projectile trajectory. Laser accelerated protons of ≈10 MeV, currently used aiming at cancer therapy in ears of mice [Zei+13], require fields of tens of T in pulsed high-field solenoids with tens of cm length to achieve focusing over distances of tens of cm. Short focal distances are important for down-focusing of the beam to small volumes, following the conservation of beam emittance. For a deeper application of the ion beam, *e.g.* for proton beam ranges corresponding to the depth of the human lungs, higher proton energies in broad spectral ranges up to 200 MeV are needed [JC11]. Maintaining the same focal distance using long solenoids demands application of B-fields of 45 T, only available with state of the art high field superconducting solenoids [Sch+08; Oud+16]. Laser driven coil targets represent a well established platform for the generation of B-fields up to the $1 \cdot 10^3$ T [SBGE+18]. In the limit of a perfect coil from eq. (5.6) follows

$$f \approx \frac{A_\mathrm{i} E_\mathrm{i}}{Z_\mathrm{i} R_\mathrm{c} B_0^2} \cdot 703.8\,\mathrm{cm} \quad , \tag{5.7}$$

with A_i the projectile mass in terms of atomic unit mass, the unit of coil radius R_c in cm, the peak B-field B_0 in T and the projectile energy E_i in MeV. Note that the focal length is proportional to the square of coil current and inverse proportional to the coil radius, as $B_0 = \mu_0 I / 2R_\mathrm{c}$. 200 MeV proton focusing over tens of cm requires coil currents of hundreds of kA in mm sized coils.

Besides the field amplitude, predictability of the field's lifetime and its evolution is a fundamental aspect for future applications. In contrast to standard pulses solenoids operating with radio frequencies, small coils for ultra-strong B-field generation operate on timescales comparable to the pulse duration of the driving laser. MeV protons propagating at tens of µm ps^{-1} traverse a mm sized field in some 100 ps. A stable amplitude required for a steady-sate operation must last for

$$\tau_f \approx \frac{s}{\sqrt{1 - \left(\frac{E_\mathrm{i}}{1000 \cdot A_\mathrm{i}} + 1\right)^{-2}}} \cdot 33\,\mathrm{ps} \quad , \tag{5.8}$$

with longitudinal particle propagation length s through the magnetic lens, where the same units for distances, energy and mass are used as here-before. Scaling to higher ion energies relaxes the constraint on temporal stability (if upscaling of the current is possible). Some applications may even benefit from tailored chromatic aberration, *e.g.* to create a density controlled focusing stripe.

We will show B-field production by laser driven currents, but also refer to preceding EM effects. We present and compare experimental studies and optimization prospects of two distinct robust open-geometry CT platforms.

Hereinafter ultra-strong B-fields are driven by laser pulses of $10 \cdot 10^{15}\,\mathrm{W\,cm^{-2}}$ to $100 \cdot 10^{15}\,\mathrm{W\,cm^{-2}}$ containing hundreds of J, and pulses of $1 \cdot 10^{18}\,\mathrm{W\,cm^{-2}}$ to $100 \cdot 10^{18}\,\mathrm{W\,cm^{-2}}$ drive ps-scale transient EM fields followed by neutralization current induced B-fields. The advantage of tailoring laser generated ion beams by laser driven CT platforms is that fields are only required in small volumes and that fields can be timed precisely aiming at particular areas in the ion beam phase space. We will asses CT capabilities hereinafter, with great care of the actual state of the art and findings unrevealed in the course of this work.

Another application of ultra-strong B-fields is the mitigation of instabilities in HED plasmas, where ionic and electronic temperatures increase if the plasma is magnetized [Pol+06; Fro+07; Mon+15]. Ultimately, the use of B-fields is intended to ease ignition. A better alpha particle and heat confinement have been numerically archived for 20 T to 60 T applied to an imploding fuel capsule in the indirect drive approach [Per+13]. In ICF experiments, a higher neutron yields has been observed applying B-fields below 10 T [Hoh+12]. Strong B-fields are also an important tool to create suitable conditions for laboratory astrophysics experiments and for atomic physics experiments [Ehr+19; Buk+20; Law+20].

5.2.1 Ultra-strong Magnetic Fields

B-fields with ns life time are generated employing ns-laser pulses of several hundred J focused at $10^{14}\,\mathrm{W\,cm^{-2}}$ to $10^{17}\,\mathrm{W\,cm^{-2}}$ onto so called Capacitor Coil Targets (CCT) [KM79]. The targets comprise two parallel plates connected by a coil-shaped wire. Therefore they are also referred to as Double Plate Ω-coil Targets. Laser energy is deposited via the dominant resonant absorption mechanism on one plate, typically in such a way that the plasma expansion is driven into the gap between both plates. A net target discharge is produced due to escaping electrons, and current dynamics in the plasma arises not only due relativistic electrons but also due to thermoelectric currents and parametric instabilities. As observable result, a current through the wire section builds up.

Experimental observations witness currents looping through the coil circuit, yielding a ns-scale strong B-field [KM79; See83; Dai+86]. Recently reported current amplitudes of hundreds of kA induce B-fields up to the order of $1 \cdot 10^3$ T [Fuj+13; San+15; Law+16; Goy+17]. The fields have a rise time on the scale of the driver laser pulse length and a short stability plateau thereafter. Quasi-static effects on a timescale of hundreds ps are achieved on mm spatial scales for non-relativistic projectiles of energy to mass ratio $E_\mathrm{i}/A_\mathrm{i} > 500\,\mathrm{keV\,u^{-1}}$, with respect to the steady-state requirement eq. (5.8). This energy to mass ratio is typical for heavy ions such as carbon in the energy regime of interest for plasma stopping power experiments [Cay+17] and for light ions such as protons in an energy range commonly accessed via TNSA [RS16] and Helium as seen here-before. Focusing of such ion beams to high beam intensities yields a high energy density regime not yet attained in experiments, suitable *e.g.* for exploration of collective effects, efficient heating of auxiliary samples to the warm dense matter state or the fast ignition approach.

Regions with high field amplitudes can trap charged particles on their radius of gyration. Ampere's law gives for a straight infinite conductor of radius R_w carrying the uniform current I the azimuth B-field $B_\phi(r) = \mu I/2\pi r$ for $r > R_\mathrm{w}$. Defining particles as trapped which encounter a gyroradius of the order of the conductor radius when located at a distance of $\kappa \cdot R_\mathrm{w}$ from the conductor centre, implies trapping for

$$\gamma_\mathrm{i} v_{\perp,\mathrm{i}} \leq \frac{Z_\mathrm{i}}{A_\mathrm{i}} \cdot \frac{R_\mathrm{c} B_0}{\kappa} \cdot 102 \cdot 10^{-3}\,\mathrm{\mu m\,ps^{-1}} \quad , \tag{5.9}$$

in the limit of a perfect coil with $R_\mathrm{w} \ll R_\mathrm{c}$ – with A_i the projectile mass in terms of atomic unit mass, the unit of coil radius R_c in cm, the peak B-field B_0 in T, Z_i the projectile charge in multiples of electron charges and $v_{\perp,\mathrm{i}}$ the projectile's velocity perpendicular to the field lines. We note that the initial projectile velocity for parts of the beam is perpendicular to the azimuthal field for lensing applications with coils smaller than the diverging beam at the coil position. Trapping of light ions at distances with $\kappa \approx 1$ requires field strength B_0 of the $1 \cdot 10^3$ T, for velocities ranging over tens of µm ps^{-1}. The same applies for moderately relativistic electrons with $\gamma < 10$. Laser accelerated ion beams have co-moving non-relativistic electron clouds that are trapped already with several T strong B-fields. All estimates are presuming the same scaling as here-before, notably mm sized coils.

This work will shed light on possible threats to ion beam lensing with the Double Plate Ω-coil Target platform that arise due to trapping of electrons on small Larmor orbits in vicinity of the target wires. Accumulation of space charge builds up E-fields de-stabilizing magnetic focusing effects. Equalizing the focal length of a perfect coil eq. (5.7) with the small angle off-axis deflection due to a charged ring yields

$$\lambda_\mathrm{c} \approx \frac{Z_\mathrm{i} R_\mathrm{c}^3 B_0^2}{\gamma_\mathrm{i} A_\mathrm{i} R_\mathrm{w}} \cdot 1.709\,\mathrm{nC\,cm^{-1}} \quad , \tag{5.10}$$

where λ_c denotes the linear charge density that is necessary to compensate for magnetic focusing. Note that this estimate holds only for space charges and projectiles with opposed charge, as equal charge transforms the charged ring in an electric lens. Thus, the coiling wire must be charged to -1 µC mm^{-1} in order to perturb par-axial proton focusing, presuming target wires of tens of µm radius and $B_0 \approx 100$ T in a mm-sized coil. The resulting 1 µC of negative charge required in vicinity of the coil is smaller than typical values for laser driven total target discharge. Tens of 10 µC are reported for ns-laser driven solid targets [Cik+14].

A strategy to suppress space charge accumulation is introduced and an experiential benchmark is presented. Further, the mechanisms maintaining the field inducing currents are not fully understood, this work investigates modelling approaches of the current generator and a presentation of experimental results comparing current dynamics in the plasma with coiling current.

5.2.1.1 Magnetic Fields Perturbed by Charge Accumulations

First indications of accumulated charge in vicinity of the small coil stem from experimental results obtained at the Laboratoire pour l'Utilisation des Lasers Intenses (LULI) pico2000 laser facility, which evidence a discrepancy of field amplitudes derived on one hand side with proton deflectometry of the coil and on the other hand side with space integrating inductive field probes [San+15; SBGE+18]. Diagnostics are applied to probe a ns-laser pulse driven Double Plate Ω-coil Target with B-fields of tens of ns lifetime and amplitudes of up to hundreds of T, induced by currents of hundreds of kA. The distance of Ω-loop and laser interaction region is on the scale of mm. Numerical studies with synthetic deflectometry show that the B-field strength estimation based on charged particle beam deflection can be biased by accumulation of charges in the vicinity of the B-field for late probing times. This section aims at finding likely spatial distributions and the amount of charge, that efficiently shield the B-field off the probing particles and yield agreement with experimental deflectometry results.

In experiments at the LULI laser facility, the Double Plate Ω-coil Target is driven by a 500 J flat-top 1 ns laser pulse of 1.06 µm wavelength, focused to 10^{17} W cm^{-2} intensity. Double Plate Ω-coil Targets have an inner Ω-loop radius of 250 µm. The Ω-loop has a full opening Angle of $\pi/4$. The targets are laser cut from 50 µm

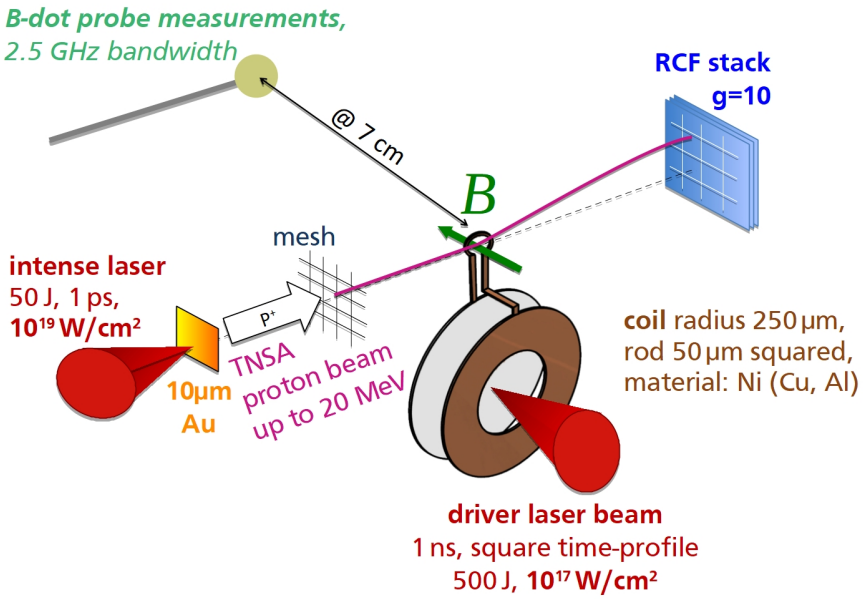

Figure 5.23: Generation of ultra-strong magnetic fields with Double Disc Ω-coil Targets driven by an intense ns pulse at $10^{17}\,\mathrm{W\,cm^{-2}}$ for experimental campaign 15-PS-FX at the LULI pico2000 laser facility. The platform is diagnosed by proton deflectometry and inductive magnetic field probes (B-dot-probes).

thick Nickel sheets and assembled in one piece by hand folding. All wire sections have a squared profile. The target has a 1 mm diameter hole in one of the capacitor plates through which the ns-driver laser aims at the other plate respectively.

The set-up comprises an auxiliary short laser driver for proton deflectometry. TNSA from a 10 µm thin Gold (Au) foil is driven by a 1 ps 50 J laser pulse focused to $10^{19}\,\mathrm{W\,cm^{-2}}$. The charged particle beam source is positioned at 5 mm from the coil centre. The proton beam passes a 600/inch mesh at 2 mm from the Au foil to obtain a spatial resolution of deflections. The stack of RCF is positioned at 45 mm from the coil – images have a magnification of $g_\mathrm{c} = 10$ for the vicinity of the coil and $g_\mathrm{m} = 25$ for the mesh. The all-optical scheme with two independent driver laser pulses allows to time protons of distinct energies to probe arbitrary and exact times of the field evolution.

Independent measurements on the B-field are performed with distant inductive field probes in auxiliary shots without proton deflectometry, particularly high-frequency B-dot-probe. The set-up is depicted with fig. 5.23. The B-dot-probe is a moebius loop [Dun74] of type RB230, it is positioned with its axis parallel to the coil axis at several cm distance inside the vacuum chamber. The probe has a radiation hardened protection to withstand the violent environment. The direct line of sight between ns-plasma and detector is partially blocked by the double-plate geometry. Both outputs are connected to a Balun located outside the vacuum chamber, in turn connected to an oscilloscope standing right aside the chamber inside a commercial Faraday Cage. It is taken care of a 2.5 GHz bandwidth of the network. Shielding outside the camber is done by wrapping the complete cabling in Al foil and blinding Baluns and the scope with it. The Al foil shielding is conductively connected to chamber and the surface of the Faraday Cage, the length of the bridge is between 1 m and 3 m.

The field probes record field strength of above 500 T with several ns duration with a very good shot-to-shot stability on differing targets of the same type, see fig. 5.24. The peak value and the rise time of the B-field

are reproducible, consistent with the reproducible driver laser pulse. The rise time of the field is equal to the driver laser pulse duration of 1 ns. For a detailed description of the analysis, see [M. 17].

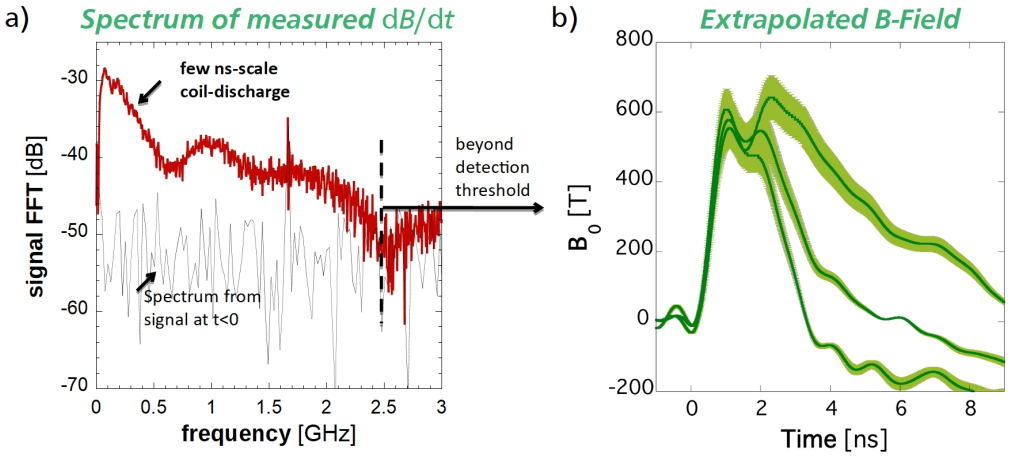

Figure 5.24: (a) Fast Fourier Transform (FFT) of B-dot-probe measurements at 7 cm distance from the coil centre of a Nickel Double Disc Ω-coil Target driven by laser shots with ≈500 J pulse energy in a 1 ns flat top profile at $10^{17}\,\mathrm{W\,cm^{-2}}$. (b) Extrapolation of the B-field amplitude at the centre of the coil presuming an ideal field configuration according to the target wire geometry, from [M. 17].

Figure 5.25 shows the RCF imprints of bulb shaped deflectometry caustics for protons passing the vicinity of the ROI around the coil. The target, viewed from the TNSA particle source, is superposed to experimental data and simulated detector output in fig. 5.25 (a). Protons probe perpendicularly to the coil axis. Bulb shaped caustics corresponding to deflections of several $10 \cdot 10^{-3}$ rad are a widely observed phenomenon [San+15; Bra+20a; Pee+20]. Their origin is the horizontal component of the coil current density, here imposing a pulling Lorentz force in the coil top and a repelling force in the coil bottom, see fig. 5.25 (b). The bulb width is proportional to the coil current, indicated with fig. 5.25 (c) is the induced B-field in the centre of the Ω-coil. The imprints fig. 5.25 (d–h) are dominated by doses deposited from 13(1) MeV protons, adjusted in timing to probe the coil with differing delays to the Double Plate Ω-coil Target ns-driver pulse. The experimental data in fig. 5.25 (e,g) is compared to synthetic deflectographs in fig. 5.25 (f,h), from charged particle transport simulations. Derived currents are compared to results of B-dot-probe measurements, showing good agreement for early times but disagreement and an inverse trend for late times.

For the probing time of $600 \cdot 10^{-3}$ ns after the driver-laser interaction started, B-dot-probe results indicate a B-field induced by a coil current of 129 kA but bulbs correspond to a coil current of only 21 kA. It is noteworthy that the overall shape of the experimental deflectometry bulb agrees with simulated patterns. For later probing times of 1.1 ns, B-dot-probe measurements indicate an increase of the coil current to 240 kA and the corresponding bulb hints a decrease of the coil current to 13 kA. Aside the difference of both measurements in order of magnitude and trend, we see a slightly different shape for the measured bulb compared to the synthetic bulb.

Possible explanations comprise either the partial compensation of the B-field strength by diamagnetic plasma in the vicinity of the coil [Col97] or the presence of a net negative charge distribution that is the source of an E-field [San+15]. As inductive field probes observe rising amplitudes, any induced counter-streaming plasma current is not likely to cause efficient shielding. A significant negative charge density may arise either due to photo electrons from the conductive wire, knocked out of the material by X-ray heating in the violent

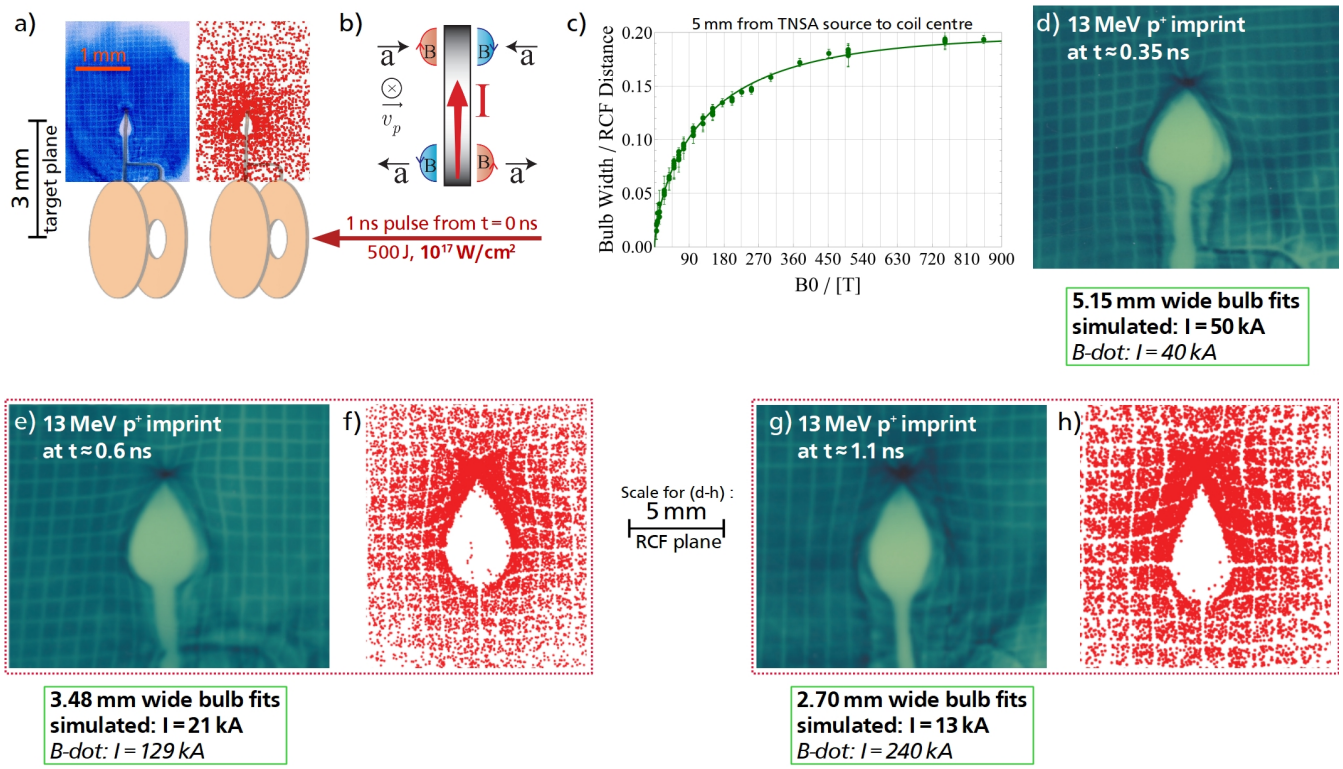

Figure 5.25: Experimentally obtained RCF scans compared to synthetic simulation data for proton deflectometry with a point like particle source 5 mm from the ROI around the Ω-coil centre. (a) The target with coil axis perpendicular to the probing axis is superposed to data and simulation. Imprints show the shadow of the target and bulb shaped deflections in the vicinity of the coil. (b) The bulb shape is directly related to the Lorenz force from B-field components originated in the horizontal sections of the coil loop. (c) The simulated bulb width with respect to the B-field in the coil centre is plotted normalized to the RCF to ROI distance. Points represent simulation results, the solid line is a fit employing a power law. (d) The simulated bulbs correspond to experimental bulbs for early probing times. (e–h) For late probing times, we obtain a significant underestimation of the coiling current with respect to measurements of the field probes. (f,h) Nevertheless, the overall shape of bulbs agrees, even for late times.

experimental environment [Pee+20], or due to the plasma expanding from the ns-driver laser interaction beneath the coil, or due to trapped co-moving TNSA electrons.

The remainder of this section is organized as follows: in a first step, purely magnetic deflections are characterized; secondly, the origin of the charge distribution is discussed; and finally, the effect of superposed E-fields is investigated.

Magnetic Field Signature in Charged Particle Beam Deflectometry

Synthetic deflectometry was carried out with the 3D transport code Particle Field Interaction (PAFIN), see section 7.2. The simulated particle source is fitted to the typical divergence of experimentally obtained particle beams, the forward directed altitude angle is assumed fully Gaussian and the source emits azimuthally

uniform. Particles in thin energy intervals corresponding to the RCF imaged energy ranges are created within 1 ps source emission. The target is modelled as current distribution with four finite element strings within the squared target rod of 50 µm sides, with finite elements of 50 µm length. Biot-Savart's law eq. (3.16) is used to determine the B-field at every point of the particle trajectory.

Note, that the bulb sizes for this Ω-coil configuration of a Double Plate Ω-coil Target depend on the Ω opening angle, studied in great detail in [M. 17]. Thus also influential is the shape of the connection of Ω-coil and legs, which here is right-angled.

Simulating a wide range of coiling currents allows us to find a power law relation between the B-field in the centre of the coil and the bulb width normalized to the ROI-to-RCF distance, see fig. 5.25 (c). The normalized value corresponds to the opening angle which is twice the deflection angle. The bulb size has a monotonously decreasing growth rate for increasing currents, which is related to the quickly decreasing amplitude of the B-field for larger distances from the coil. The power law relating coil current I_C and relative bulb width w^R reads

$$w_0^R(I_C) = S \cdot (1 - \exp\left[-k_1 \cdot (I_C - x_0)^{p_1}\right]) \tag{5.11}$$

$$+ m \cdot (I_C - x_0)^{p_2} \quad , \tag{5.12}$$

where m is a free parameter that ensures flexibility with regard to steadily rising bulbs due to steadily rising B-field amplitudes for larger coil-currents. Fits were obtained with a simulated range from 0 T to 1.5 kT in the coil centre. For that range, m and p are not yet found accurately, leading to the conclusion that they are not essential to parametrize the problem in the sub kT regime. The parameters for this experiment fit best to $S = 0.202$, $k_1 = 0.066$, $p_1 = 0.66$ and $m = 0$ with no importance to p_2.

Accumulation of Space Charge

Electrons with energies up to tens of keV can be trapped on small Larmor-orbits by very strong B-fields in proximity to the coil wire. There are three likely sources of space charge. X-rays from the laser-plasma can photoionise electrons of the wire material, but those may escape the vicinity of the wire before the B-field rises to significant amplitude. The co-moving TNSA electrons could reach the coil, but for MeV protons they are of low energies that are deviated from their initial trajectories long before reaching the coil. Trapped may be only the small fraction of electrons that is in the vicinity of the coil during the field's ramp up. This work focuses hereinafter on charges coming from the laser driven plasma. Demonstrated are heuristic transport simulations and self-consistent Particle in Cell (PIC) simulations regarding formation dynamics of the electron cloak and its spatial distribution.

For a first heuristic view, an electron source is simulated that emits hot electrons at the position of the ns-driver laser interaction 3 mm underneath the coil centre. A PAFIN simulation follows their trajectories over hundreds of ps. Experimentally, the supra-thermal electron population in the plasma on the coil target was characterized by a $T_\mathrm{h} = 40(5)$ keV temperature [San+15], as measured by X-ray spectroscopy. The temperature of the thermal electron component became characterized to $T_\mathrm{e} = 1.2(3)$ keV by Bragg diffraction spectroscopy coupled to atomic physics calculations [SBGE+18]. Following this measurements, the source is set to eject electrons of 40(5) keV kinetic energy.

Further assumed is the linear raise of a B-field at 500 T ns^{-1} at the coil centre, in accordance with the B-dot-probe measurements. The current amplitude in the wire is supposed to be equal at all positions of the wire, no current is modeled on the capacitor plates. Results are presented in fig. 5.26.

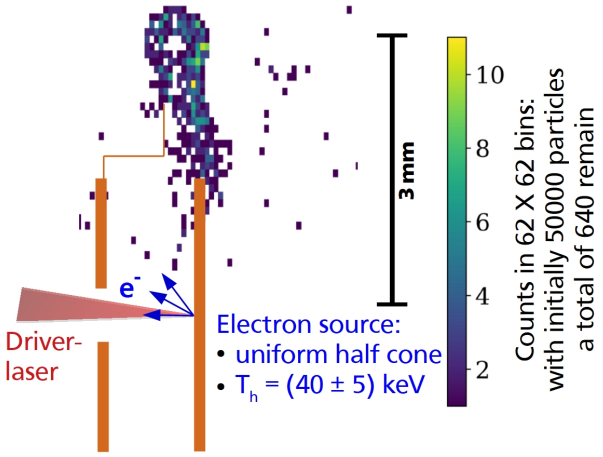

Figure 5.26: Evolution of an electron cloud emerging the laser-plasma interaction region in a heuristic approach: a source with $40(5)$ keV effectively emits electrons for 100 ps. Illustrated is the electron population 300 ps after simulation start, clinging to the strong B-field around the wire.

Only electrons emitted during the first 50 ps are able to pass the rising B-field issued by the horizontal wire section of the target on their way up to the coil. Thereafter, electrons are directed back into the capacitor gap. Most of electrons are lost when they impact on the front plate, where the simulation code can not find valid predictions of the trajectory. Electrons that arrive between the Ω-legs are kept in the surrounding of the target wire as the B-field there is the strongest. The electrons orbit on the Larmor radius but the same time keep their initial precision in direction of the B-field lines. Thus they successively follow the target geometry. Electrons cling to the rod of counter-streaming current density due to the deflection by the strong field between the legs. On the timescale of hundreds of ps, the electron cloud is confined around the target wire and has the toroidal ring-form of the coil itself. The filling of the coil section by an electron accumulation is effective after 300 ps and has a maximum outer radius of about 300 µm, consistent with experimental timescales.

This particle tracing simulations with PAFIN do not take space charge effects into account and neglect the quasi-neutrality of the plasma issued from the driver laser interaction. In order to give a more refined view, the plasma dynamics is simulated with 3D PIC simulations deploying SMILEI [Der+18]. Plasma is modelled as a cloud present in the vicinity of the Ω-legs with voids in the regions occupied by the conductor, see fig. 5.27. The initial maximum density of $2 \cdot 10^{18}\,\mathrm{cm}^{-3}$ and the full width half maximum of the order of 1 mm are typical values which will be motivated in further sections of this work. The centre of the plasma cloud is located 1.5 mm underneath the coil centre.

The plasma comprises three species: hydrogen like ions with mass $1836 \cdot m_\mathrm{e}$, elementary charge and with 1 keV ion temperature; a cold electron population with temperature 4 keV; and a hot electron population at temperature 200 keV. This parameters are larger than measured values in order to reduce simulation time and to investigate weather the dynamics of more energetic plasma would also be affected by the B-field of the coil. Initially, there are 10 ion macro particles per cell in neutrality with 10 macro particles for each type of electrons. Electrons are weighted in such a way that 90% are cold and 10% are hot. In addition to thermal expansion, the cloud is set into motion towards the coil centre, to reduce calculation time. The initial velocity of the plasma cloud is ten times the thermal velocity of cold electrons. The resulting high energy ions are an artefact of this PIC simulation on large space and timescales, which must be concidered unphysical.

The Ω-section of the Double Plate Ω-coil Target is modelled based on its real-size with a constant current

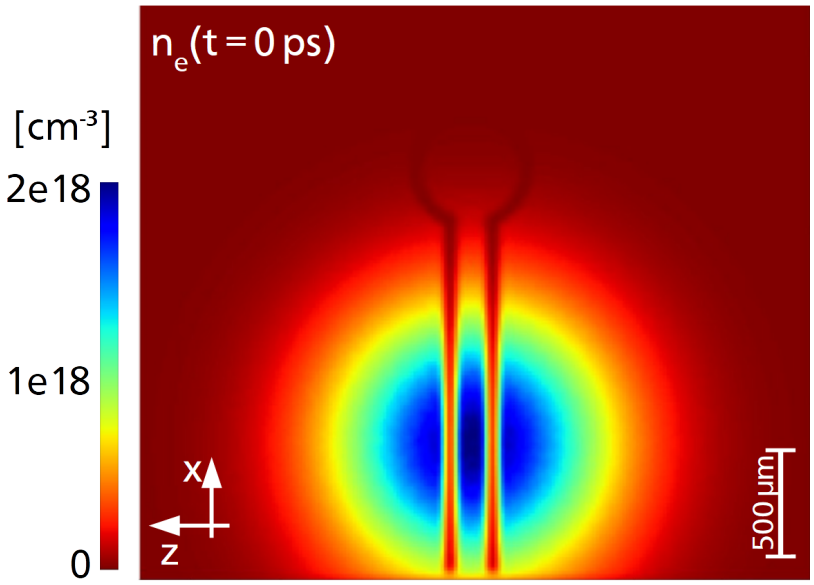

Figure 5.27: The initial electron density distribution for PIC simulations. It is compensated by the initial proton density to local charge equilibrium.

density amplitude corresponding to a B-field of 500 T in the centre of the coil, see fig. 5.28. Effects induced by the rising B-field are neglected, therefore also the horizontal stalk is omitted.

Defining the B-field based on a current distribution does not yield satisfactory results for the Ω-loop geometry due to the finite grid in PIC simulations. There, the divergence of the current density can not be zero for a curved wire and following continuity equation, the charge density changes in time. As a result, the E-field grows in time. In order to implement a pure B-field, a pre-processing is necessary. Thus, the vectorized piece-wise current profile is set-up independently and a short PIC run is performed with it. Then, the generated 3D B-field is saved. Further simulations load the normalized B-field an re-scale it to an amplitude of 500 T in the coil centre. Even though the simulation is collision-less, no particles are expected to enter the space occupied by the conductor due to the high B-field of kT scale on it's boundaries, thus the presence of the conductor is not essential to simulations.

In a 3D Cartesian geometry the simulation box sizes $(L_x, L_y, L_z) = (3840, 2048, 3072)$ µm. Particles that reach the boundaries are removed from the simulation with the Silver Muller boundary condition. The spatial resolution is 10 µm, the time step is 12.5 fs. The set of numerical diagnostics comprises plotter for both charge density distributions and all components of EM in the main Cartesian planes, as well as the total charge that remains within the boundary of the simulation. Results from different time steps are plotted in fig. 5.29, depicting electron number density distribution n_e, ion number density distribution n_p and charge density distribution ρ in the coil plane and showing the transverse E-field E_y in the horizontal plane through the coil centre.

One notes that the distributions of negative and positive charges resemble for all time steps, with similar amplitudes. Possibly, electrons are being trapped in the B-field and build up an E-field that moves ions. The overall charge density allows to perceive the regions of charge imbalance located in vicinity of the conductor. With the Lorentz force depending on the sign of charges, ions and electrons are dominating opposed sides in the loop. Electrons cling close to the conductor on the inside of the loop, filling it for 200 ps after the simulation started. A positive charge density is comparably more diluted. In turn, the transverse E-field shows

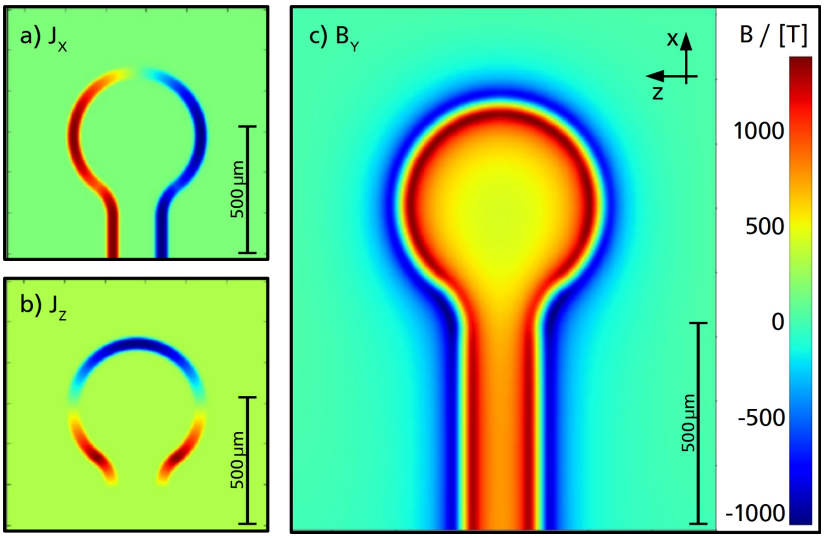

Figure 5.28: The real sized B-field in a SMILEI 3D PIC simulation box is modelled with uniform current density distributions (a,b) resulting a pre-calculation. The PIC calculated field (c) is set up to 500 T in the coil centre, and injected statically into the main simulations.

electrons to be seed to stronger fields than the positive space charge. For late times, the simulation shows edge effects that are pronounced in a rising maximum charge density for positive and negative charges and that are especially visible with the rising amplitude of the E-field in narrow sections close to the boundary. Problems with the boundary may arise due to the zero order of the Silver Muller boundary conditions.

For all simulation times, the sign of the transverse field reveals an attraction towards the coil plane for ion deflectometry with a main propagation following the intersection of horizontal plane and coil plane in positive z direction. The E-field amplitudes of several $\mathrm{GV\,m^{-1}}$ are able to compensate for B-fields of $B_\phi \leq E_r/v_\mathrm{i} \approx 1 \cdot 10^9\,\mathrm{V\,m^{-1}} \,/\, 10\,\mu\mathrm{m\,ps^{-1}} = 100\,\mathrm{T}$. Thus, present transverse E-fields are able to explain shielding effects. The dense accumulation of space charge in vicinity of the conductor can efficiently bias ion deflectometry of B-fields. The delayed onset of shielding effects can be explained with the time needed for the plasma to expand until reaching the Ω-coil.

There are three major differences between simulation and experimental conditions. First, the plasma is artificially set into motion to shorten simulation times, which makes a comparison to experimental results on an absolute timescale impossible. For real experimental conditions, plasma expansion is expected to reach the coil later. Second, due to the simplified target geometry and the static B-field, the influence of the horizontal target stalk is neglected. Its presence may influence the capturing efficiency of electrons and its timescale. Third, the plasma is modelled as density cloud whereas the laser-plasma streams steadily and on longer timescales in experimental conditions. The short lifetime of the negative space charge density facing the proton deflectometry source might be much longer when alimented constantly.

The total charge balance of the simulation is plotted in fig. 5.30. Initially, 45 nC of charge in the simulation box are due to a fraction of hot electrons that escaped the potential barrier. The expanding and propagating plasma maintains this charge until it reaches the upper boundary of the simulation box at 200 ps. During the plasma cloud leaves the simulation box, the charging of the simulated space drops to negative values. This further indicates, that predominantly electrons are trapped in the vicinity of the conductor and that no ion population neutralizes their space charge. The remaining charge decreases after a peak charging with

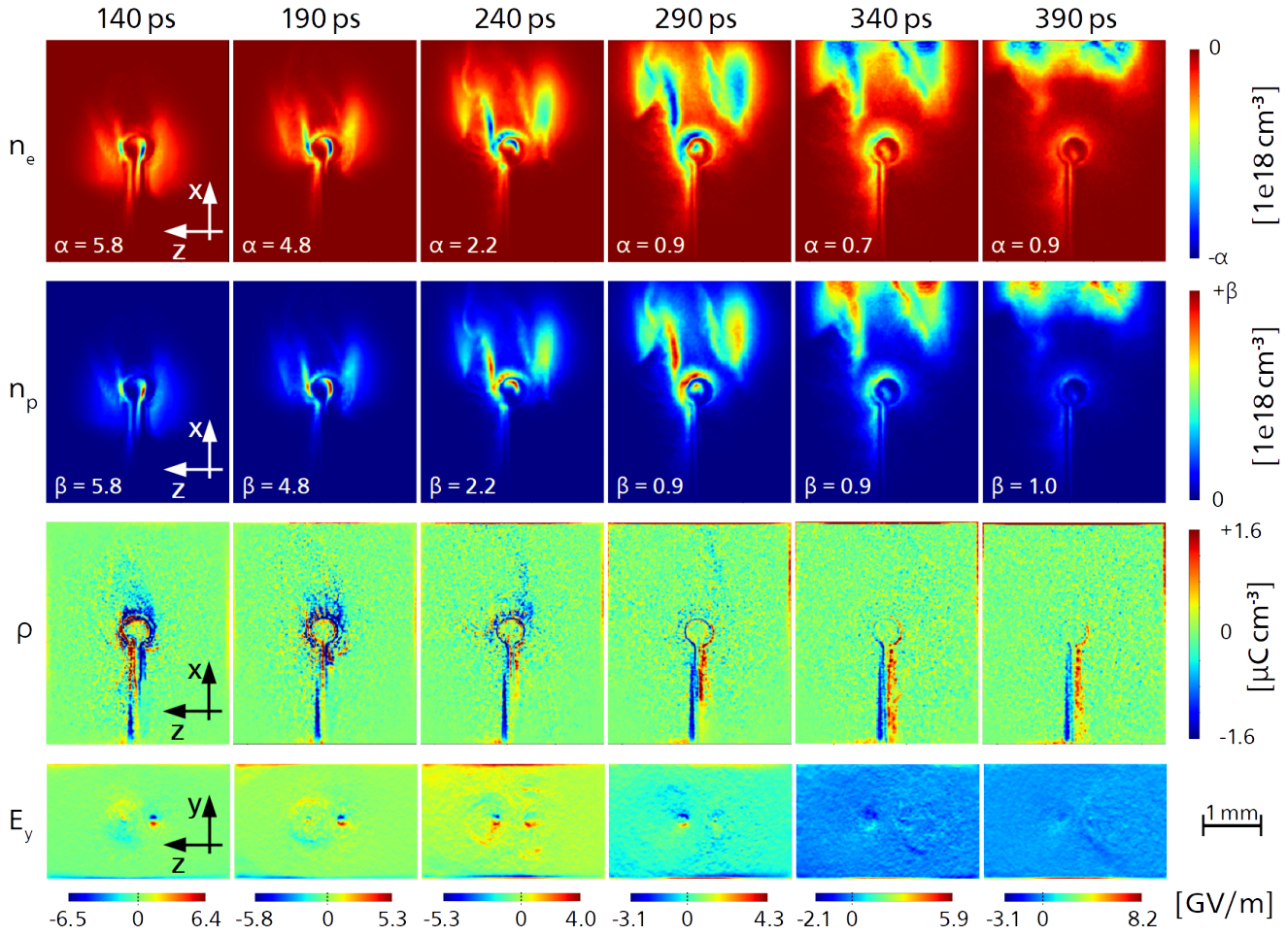

Figure 5.29: Temporal evolution of the electron number density distribution n_e, ion number density distribution n_p and charge density distribution ρ in the coil plane, as well as the transverse E-field E_y in the horizontal plane through the coil centre. The spatial scale of all plots is equal, magnitudes can be understood with the corresponding colour bar. Only a tiny fraction of electrons is deviated, but is source to residual space charge dynamics inducing strong electric fields.

≈ -40 nC is reached, due to a slow diffusion of electrons. The decay to zero happens on longer timescales than simulated.

In summary, it is possible that fast electrons from the driver laser interaction arrive in the vicinity of the coil on timescales of hundreds of ps. Then electrons are trapped on small Larmor radii, accumulating an asymmetric toroidal charge distribution and induce an E-field which shields the B-field. Fields are dynamically evolving but with their timescale quasi-static for probing MeV protons. PIC simulations presented in this work are preliminary due to the artificial motion of the plasma cloud, which increases the energy of ions to values that are unphysical: future simulations should abandon this initial condition at the expense of calculation time. Then also the dynamic character of the magnetic field should be taken into account, with electric field effects from the temporal derivative of the vector potential.

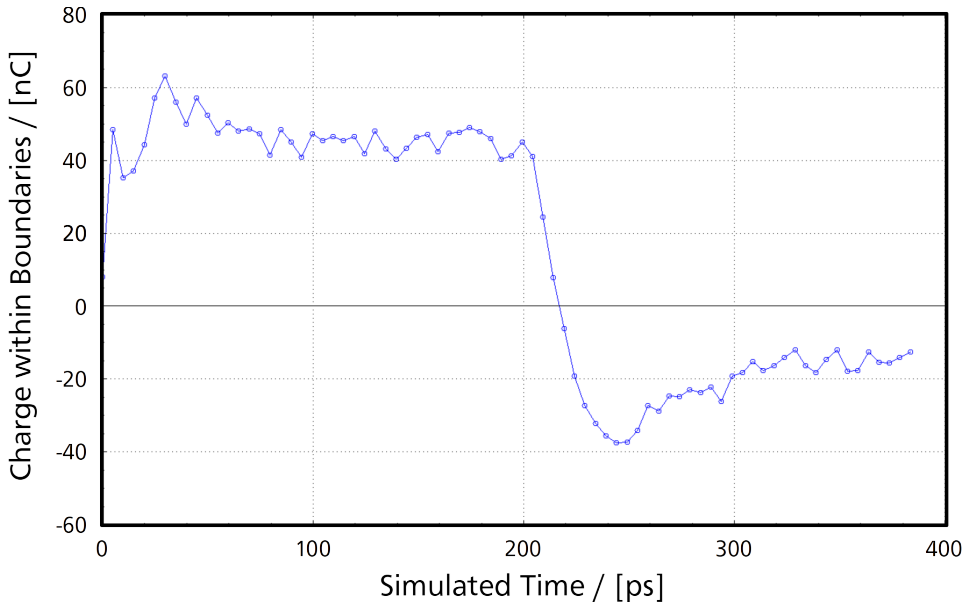

Figure 5.30: Temporal evolution of the charge balance within the boundaries of the simulation box, unravelling a slowly decaying net-negative charge imbalance for times after the plasma cloud passes the boundary.

Shielding Effects by a Toroidal Space Charge Distribution

As seen with the previous section, the accumulation of negative space charge yields E-fields that superpose with B-fields, able to yield partial compensation of magnetic focusing effects by an electric force. First interpretation of this shielding effect focused on a spherical charge distribution either in the centre of the coil or between the Ω-legs, but experimental proton deflectograms were only roughly reproduced [SBGE+18]. This work widens the scope to toroidal distributions, which is made possible with an implementation of a fast analytical E-field solver for toroidal potentials to PAFIN.

Toroidal and spherical charge distributions are simulated with their analytical E-field in the ROI in vicinity of the coil, compare fig. 5.31 (a). Charged spheres are positioned in the coil centre fig. 5.31 (b) and beneath the Ω-legs fig. 5.31 (c). The toroidal charge distribution fills the space around the coiling wire fig. 5.31 (d), but is continuous between the legs. Experimental data for early probing in fig. 5.31 (e) and late probing in fig. 5.31 (f) are compared to the synthetic distortion of deflectograms by toroidal and spherical charge distributions respectively. Depicted are best fitting bulb shapes for the experimentally obtained bulb width, under variation of coiling current and integral charge Q in the charge distributions. A larger part of the simulated data set is depicted in detail in table 8.1.

The toroid has a main-radius equal to the coil radius and lies in superposition with the coil-wire. The small toroid radius is 35 µm, an exemplary dimensioning motivated by the heuristic charging studies here-before. The direct comparison of bulbs shows that deflections with toroidal charge distribution appear similar to experimental results for higher amplitudes of coiling currents, shielded off by higher amounts of total charge than it is the case for spherical distributions. Especially the asymmetry that is imprinted in the bulb shape for late probing is only reproduced by the toroidal charge distribution. However, the trend of decreasing currents cannot be reversed to a trend of increasing currents by the toroidal charge distribution. For late times, some experimental caustics resemble simulated deflections imposed by charge between the Ω-legs, pointing to a

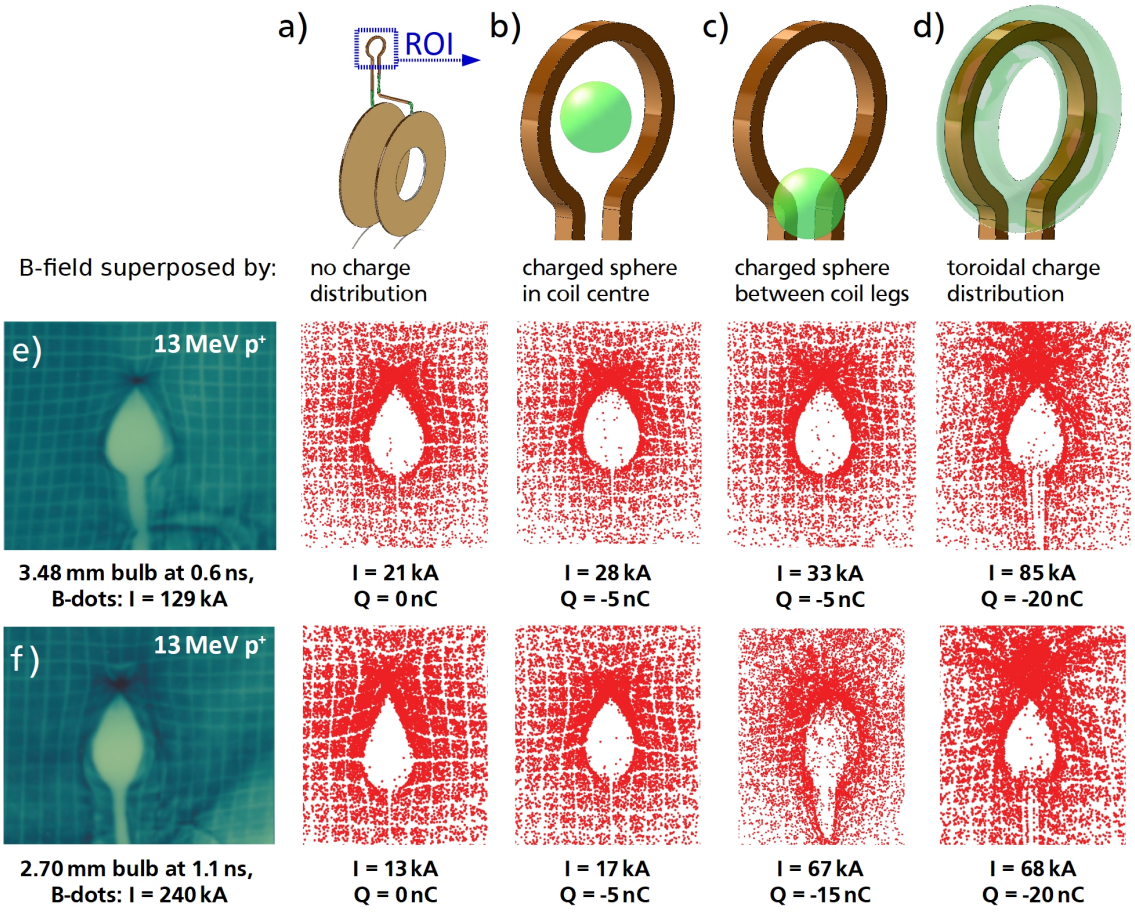

Figure 5.31: Side-on synthetic proton deflectometry of the coil's B-field in column a) compared to experimental data in row e) for early probing and row f) for late probing. Here, protons of $13\,\mathrm{MeV}$ energy cross the vicinity of the coil perpendicularly to the coil axis. In columns (b) – (d) results with different superposed charge distributions are compared to the experimental data: for a uniformly charged sphere with a radius of $250\,\mu\mathrm{m}$ in b) the coil centre and c) in the Ω-opening gap $250\,\mu\mathrm{m}$ underneath the coil centre; both are compared to d) a uniformly charged toroid of main-radius $275\,\mu\mathrm{m}$ and small-radius $35\,\mu\mathrm{m}$. The toroid allows best reproduction of bulb size and shape at the same time for both probing times, and for elevated amounts of charge. To appreciate distances better, note that the non-perturbed mesh period is $\approx 106\,\mu\mathrm{m}$ in the coil plane and projects to $1\,\mathrm{mm}$ on the RCF plane.

possible accumulation of more charge in the dense field between the legs. Then, the resulting distribution would contain more integral charge and eventually allow for higher currents to be shielded.

Note that the deformations in the mesh far from the coil are best reproduced without additional charge, argument for a plasma filling, where the potential is acting over smaller distances due to Debye shielding.

It is likely, that a toroidal charge distribution in combination with an additional amount of charge in the vicinity of the Ω-legs is responsible for shielding the B-field. With two charge distributions and one B-field, there are many possible combinations for matches of charge and current, in the range from fits with spheres to fits with a toroid. Unlike B-dot-probe results, this analysis does not evidence currents of the order of hundreds of kA. This is motivation for further experimental studies to determine the exact nature of the coil filling, *e.g.* by means of interferometry.

The perturbation by charge distributions in the vicinity of the coil is to be controlled prior to the application of ultra-strong B-fields to ion beam lensing in free space. For applications too, it is of paramount importance to shield the coil from the laser plasma interaction, to decrease any amount of plasma propagating towards the coil to avoid shortening or ablation.

5.2.1.2 Suppression of Space Charge Effects in Vicinity of the Coil

Shielding can be achieved by placing auxiliary obstacles between the driver laser interaction region and the coil region of the target. A 50 µm thick Tantalum shielding was investigated successfully in experiments at the GEKKO-LFEX laser facility (ILE in Osaka, Japan). Two co-axial coils were used to build up a 600 T B-field in Helmholtz geometry, each driven with one GEKKO XII beam with $540(100)$ J within 1.3 ns focused down to $21(4) \cdot 10^{15}\,\mathrm{W\,cm^{-2}}$ [Law+16]. B-fields were consistently measured in alternating shots with field probes and proton deflectometry driven by the LFEX laser.

Modification of the target geometry is another strategy to shield the coil efficiently. Placing the coil plane behind the capacitor back-plate blocks the direct line of sight between coil and ns-pulse interaction region. Standard Double Plate Ω-coil Targets fig. 5.32 (a) and modified Double Plate Ω-coil Targets fig. 5.32 (b) are investigated at the LULI pico2000 laser facility. Driver pulse energies range from 500 J to 600 J, delivered within a 1 ns square top profile and focused down to $10^{17}\,\mathrm{W\,cm^{-2}}$. Proton deflectometry is driven based on TNSA by an auxiliary ps driver at 50 J focused to $10^{19}\,\mathrm{W\,cm^{-2}}$. Both Ω coils have 250 µm centre radius and a $^{2}/_{5}\pi$ omega opening angle with 190 µm centre leg distance. Targets are manufactured from Copper (Cu) foils of 50 µm thickness and all wire sections have squared profiles with 50 µm sides. The driver laser enters through the centred 1.3 mm diameter hole in the front plate to drive the back plate. Both plates have a 3 mm diameter and a 950 µm spacing between them, the lateral distance of coil centre and plate centre is always 3 mm. In modified Double Plate Ω-coil Targets, the coil centre located 420 µm beyond the back plate of the laser driven capacitor section.

Note that the B-field polarity of both targets is opposite as the plates are connected to the respectively other Ω-leg. Furthermore, the self inductance of the target changes from 7 nH to 15.4 nH for longer wire sections and more curved parts, calculated with a finite element method [Den12].

The experimentally observed bulb widths for different probing times are reproduced with PAFIN simulations to deduce the current flowing in the conductor, see fig. 5.32 (c). Best fitting currents are converted to B-field energy and weighted by the respective driver laser energy for a better comparability of results, see fig. 5.32 (d). Here, the laser pulse energy is the integrated pulse energy until the time of measurement. For early times, and for both target types, the overall energy conversion efficiency is of the order of 1.5 %. This is well below

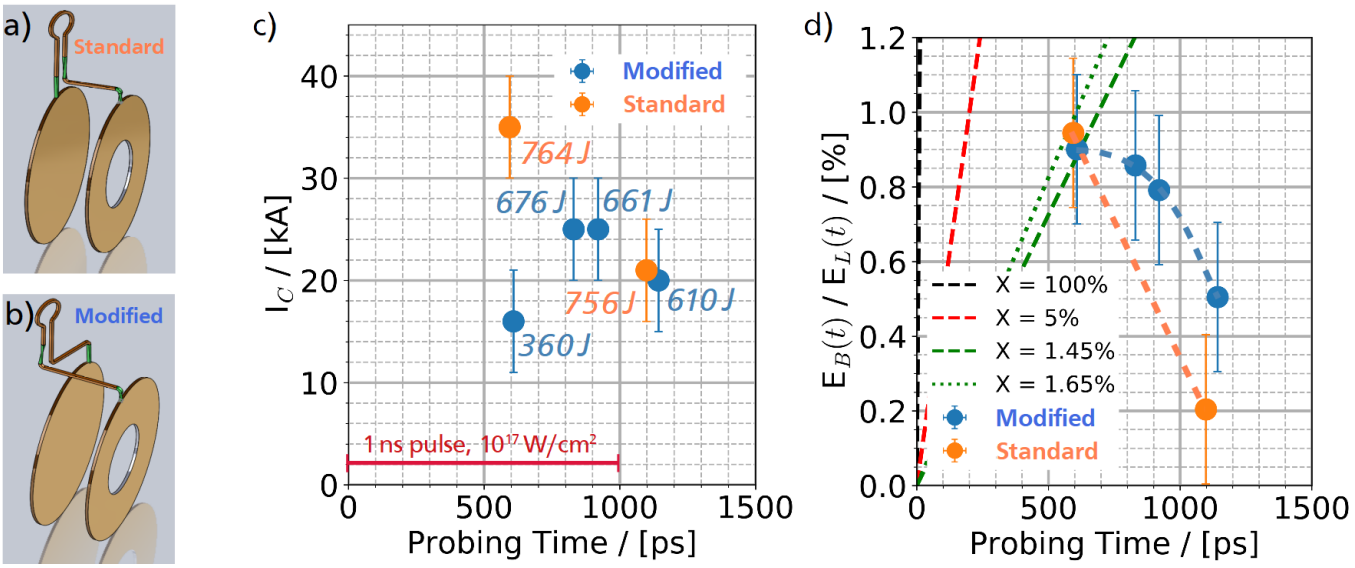

Figure 5.32: (a) Standard Double Plate Ω-coil Target geometry comprising Ω-coil section, wiring and capacitor compared to (b) modified Double Plate Ω-coil Target with the coil centre located 420 µm beyond the back plate of the laser driven capacitor section. (c) Bets fitting currents for experimental deflectometry bulbs that are synthetically reproduced by a B-field only. (d) Deduced B-fields for both target types are compared via the energy fraction converted from laser energy into B-field energy. Dotted lines are meant to guide the eye and do not represent a physical fit. The parameter X names the time dependent fraction of laser energy to B-field energy.

8.3(15) % expected for Cu targets from B-dot-probe results measured in previous experiments [San+15]. Proton deflectometry measures decreasing B-field amplitudes for late probing but still during laser drive, comparable to previous results, opening up the possibility that earlier probing would have revealed fields of higher conversion efficiency. With respect to previous experiments, the front hole diameter became shrinked from $1.750 \cdot 10^3$ µm to $1.300 \cdot 10^3$ µm. Such change may influence the plasma dynamics between the plates and thus the current generating mechanism, albeit previous work did not find such correlation [San+15].

For the modified target geometry, the interfered field strength solely based on magnetic force decreases less and later during the target drive. The shielding effects are partially suppressed, but some charges still may be arriving at the displaced coil location.

Modified targets might enhance the B-field effect on charged particle beams, paving the ground for further investigations of clean ion beam lensing with the Double Plate Ω-coil Target platform. They are advantageous compared to solutions comprising a shielding: (a) the set up requires alignment of one element less and a free standing Double Plate Ω-coil Target could be even suitable for low repetition rate experiments using target wheels, and (b) the removal of shielding removes a risk of short cuts between stalk parts of the target. Short cuts may be triggered either by ablation or photo-ionization of the shielding. X-ray heating produces both, a plasma that can expand towards the legs and a potential difference to the Double Plate Ω-coil Target. For dense plasma filling the legs, current will rather flow through the plasma with very low resistance than through the conductor. Electrical arcs occur for any imperfections in the shielding if it attains a potential difference to the Double Plate Ω-coil Target. Efficient X-ray heating and the production of dense plasma at the shielding surface are observed in experiments.

5.2.2 Current Dynamics in Ω-Coil Targets Driven by Nanosecond Laser Pulses

The full picture of mechanisms at play that are responsible for the conversion of laser pulse energy into the coil's B-field energy are not yet fully understood. The rising return current in the consumer loop with Ω-coil can be modeled as induced by the laser pulse [See83], generated by space charge effects arising with the hot electron dynamics in the laser-plasma [Dai+86; Cou+05], or depending on the full laser-plasma dynamics including space charge effects and self-magnetization [Tik+17; Wil+20]. Note that the platform's name Capacitor Coil Target suggests wrongly a general importance of capacitive effects [Wil+20].

In a laser driven capacitor-coil system [See83; Dai+86], coil current I_C and capacitor voltage V_C are related by

$$V_\mathrm{C}(t) = L_\mathrm{C}(t) \cdot \mathrm{d}_t I_\mathrm{C}(t) + R_\mathrm{C}(t) \cdot I_\mathrm{C}(t) \qquad \text{(charging while laser is on)} \tag{5.13}$$

$$0 = L_\mathrm{C}(t) \cdot \mathrm{d}_t^2 I_\mathrm{C}(t) + R_\mathrm{C}(t)\, \mathrm{d}_t I_\mathrm{C}(t) + \frac{I_\mathrm{C}(t)}{C_\mathrm{C}(t)} \qquad \text{(after laser switches off)} \tag{5.14}$$

simplified to a lumped element circuit with inductance L_C, resistance R_C and capacitance C_C. Modelling approaches differ by consideration of the time dependent circuit parameters and the driving mechanisms that yield voltage build up. This section first introduces the main concepts of modelling approaches and then proceeds with comparison to experimental data.

5.2.2.1 Capacitor-Coil Modelling

The charging of the capacitor is due to laser-heated electrons escaping from the cathode, and eventually collected by the anode. This dynamics resembles a thermionic diode, the voltage source is a plasma diode. The direct diode current I_D can be approximated with

$$I_\mathrm{D} = (q_\mathrm{e} n_\mathrm{h}) \cdot \left(\pi r_\mathrm{h}^2 \Delta\Theta\right) \cdot \int_{q_\mathrm{e} V_\mathrm{C}}^{\infty} v(\epsilon) f(\epsilon)\, \mathrm{d}\epsilon \quad , \tag{5.15}$$

with a hot electron density n_h and energy distribution function $f_\mathrm{h}(E)$, where r_h is the radius of the emission zone and $\Delta\Theta$ is the solid angle of hot electron emission. q_e denotes the elementary charge. Integration is performed over all kinetic energies ϵ more important than the potential barrier between anode and cathode, $v(\epsilon)$ denotes the corresponding electron velocity. Furthermore assuming the cathode potential to be zero, the diode tension evaluates with

$$C_\mathrm{D} V_\mathrm{C} = \int_{t_0}^{t} I_\mathrm{D}(\tau)\, \mathrm{d}\tau \approx \tau_\mathrm{L} \cdot \langle I_\mathrm{D} \rangle \quad , \tag{5.16}$$

where the capacitance is set static. Electron heating is mostly due to resonance absorption at the target surface for our intensity regime [Dai+86]. The heating time is the laser pulse duration τ_L, which allows us to simplify the integration in eq. (5.16) with a product of laser pulse duration and time averaged current $\langle I_\mathrm{D} \rangle$. Result is an expression for the gap voltage of the diode, thus the set of equations is closed.

5.2.2.2 Enhanced Diode Modelling

The capacitor-coil modelling limits the diode current only by space charge effects, disregarding plasma dynamics. The laser driven electron current $\vec{J}$ in the laser-plasma induces a B-field $\vec{B}$

$$\vec{\nabla} \times \vec{B} = \mu_0 \vec{J} \quad , \tag{5.17}$$

and electrons are pulled together by the resulting Lorentz force until the magnetic pressure gradient is in balance with the thermal pressure gradient. Ions follow and the plasma column in the diode gap is pinching. Setting equal the spatial width of the diode gap D_D with the collapse point of the plasma, one derives the maximum plasma current the diode can transport [Tik+17; Wil+20]

$$I_\mathrm{D}(t) \leq \frac{V_\mathrm{D}(t)}{Z_\mathrm{D}} \quad , \tag{5.18}$$

with the effective internal diode impedance

$$Z_\mathrm{D} = Z_0 \lambda_\mathrm{De} \cdot \frac{D_\mathrm{D}}{(r(t))^2} \quad , \tag{5.19}$$

where $r(t)$ designates the radius of the current filament, $Z_0 = \sqrt{\mu_0/\epsilon_0} = 377\,\Omega$ the vacuum impedance, and $\lambda_\mathrm{De} = v_\mathrm{te}/\omega_\mathrm{pe} = \sqrt{\epsilon_0 k_\mathrm{B} T_\mathrm{e}/n_\mathrm{e} q_\mathrm{e}^2}$ is the electron Debye length. Alternatively presuming the plasma inductance to be much smaller than the plasma resistivity, the impedance can be approximated with the plasma resistivity [Wil+20]

$$Z_\mathrm{D} \approx R_\mathrm{p} = \eta_\perp \cdot \frac{D_\mathrm{D}}{\pi \cdot (r(t))^2} \quad , \tag{5.20}$$

with the transverse Spitzer resistivity

$$\eta_\perp = \frac{Z_\mathrm{pi} \cdot \ln[\Lambda_\mathrm{C}]}{T_\mathrm{e}^{3/2}} \cdot 10.3 \cdot 10^{-3}\,\Omega\,\mathrm{cm} \quad , \tag{5.21}$$

where Z_pi is the charge state of the ions in the plasma and $\ln[\Lambda_\mathrm{C}]$ is the coulomb logarithm, the electron temperature is in eV.

The equilibrium voltage of the diode was recently found to be directly proportional to the laser-driven Maxwellian plasma electron temperature $V \approx k_\mathrm{B} T_\mathrm{e}/q_\mathrm{e}$ [Wil+20]. The governing equations are rewritten as

$$k_\mathrm{B} T_\mathrm{e}/q_\mathrm{e} = L_\mathrm{C}(t) \cdot \mathrm{d}_t I_\mathrm{C}(t) + (R_\mathrm{C}(t) + Z_\mathrm{D}(t)) \cdot I_\mathrm{C}(t) \qquad \text{(charging while laser is on)} \tag{5.22}$$

$$0 = L_\mathrm{C}(t) \cdot \mathrm{d}_t^2 I_\mathrm{C}(t) + R_\mathrm{C}(t)\, \mathrm{d}_t I_\mathrm{C}(t) + \frac{I_\mathrm{C}(t)}{C_\mathrm{C}(t)} \qquad \text{(after laser switches off)} \quad . \tag{5.23}$$

5.2.2.3 Simultaneous Measurement of Coiling Current and Plasma Current

Models are compared hereinafter with experiments aiming at simultaneous measurement of the coiling current in the Ω-loop on one hand side and the magnitude and spatial distribution of the diode current on the other hand side. The ongoing development of the set of diagnostics [Pis+19] may pave the ground towards integrated experiments, also deploying direct voltage measurements of the gap voltage, *e.g.* demonstrated in [Wil+20].

Double Plate Ω-coil Target drive for the experiment at the PALS (Prague Asterix Laser System) facility (Praha, CZ) is realized with a Gaussian laser pulse of 350 ps FWHM containing 250 J to 500 J that is focused down to FWHM foci of 100 µm to reach intensities of the order of several $10 \cdot 10^{15}\,\mathrm{W\,cm^{-2}}$. The driver laser wavelength is $1.315 \cdot 10^{3}$ nm. Three distinct studies explore both the standard and a modified Double Plate Ω-coil Target, under variation of the conductor geometry and the capacitor gap width.

Experimental diagnosis of currents is performed via measurement of induced B-fields. A TGG crystal is placed in vicinity of the Ω-coil for polarimetry based on Faraday rotation, and the laser plasma is diagnosed with complex interferometry. The optical scheme of the three channel polaro-interferometric system is depicted in fig. 5.33. The probe laser pulse passes a linear polarizer, back-lights both regions of interest and then trespasses an analyser. The $L_{\mathrm{CRY}} = 500\,\mu\mathrm{m}$ thick TGG crystal is positioned co-planar with the coil, either facing analyser or polarizer. Its Verdet constant is $-60\,\mathrm{rad\,T^{-1}\,m^{-1}}$. The pulse is imaged with a telescope objective into a CCD. For the interferometric measurement of the plasma density, a wedge is inserted in the beam yielding interfringes. Special care is taken to ensure that the interfering light stems from sections of the probe pulse far from the region of interest around the target.

In order to appreciate the evolution of currents within one driver shot, the 40 fs long Ti:Sa probe beam pulse is split three channels that intersect at the target position under a small angle of 5° in one vertical plane. The pulses are partitioned to contain each the order of 10 mJ and delayed with respect to each other to probe the target within one shot at three different times. The respective probing time is measured on a shot-to-shot basis with a precision of the order of ± 10 ps by a fast EOT photo-detector recorded on a 12 GHz oscilloscope.

First Study: Direct Current in Standard Double Plate Ω-coil Targets

The standard Double Plate Ω-coil Target with 3 mm diameter capacitor plates and a 500 µm diameter Ω-loop is equal to its version discussed in the previous section, despite for the hole in the front plate, here of 1 mm diameter, and the gap width, which becomes varied. The small polarizer-analyser pass angle is set to $\beta = 2°$, letting only the probing intensity fraction of $\sin[\beta]$ pass. Between laser interaction region and crystal, a 1 mm lead shielding with 75 µm thickness is introduced, see fig. 5.34. The geometrical details of the shielding, especially the slit cut-out for the coil and the distance of coil plane and crystal front surface are subject to change on a shot-to-shot basis.

The gap in the 7 mm times 13 mm large shielding foil is cut to 650 µm width, enough spacing to avoid shortening between the coil legs and the shielding. The gap slit is parallel to the plate planes and the shielding clamps the TGG crystal in position. The gap is aligned to end just before the crystal. The coil centre is positioned vertically 3 mm above the laser interaction point on the capacitor plate. Therefore the shielding does not protect the crystal from plasma emission in gracing incidence, stemming from half of the plasma.

The distance between coil plane and crystal surface was set to 35 µm. Reference and shot data for early timing are compared in fig. 5.35. The darkening in vicinity of the coil is induced by Faraday rotation and due to a reduced intensity projection with respect to the analyser. The clockwise rotation of the polarization

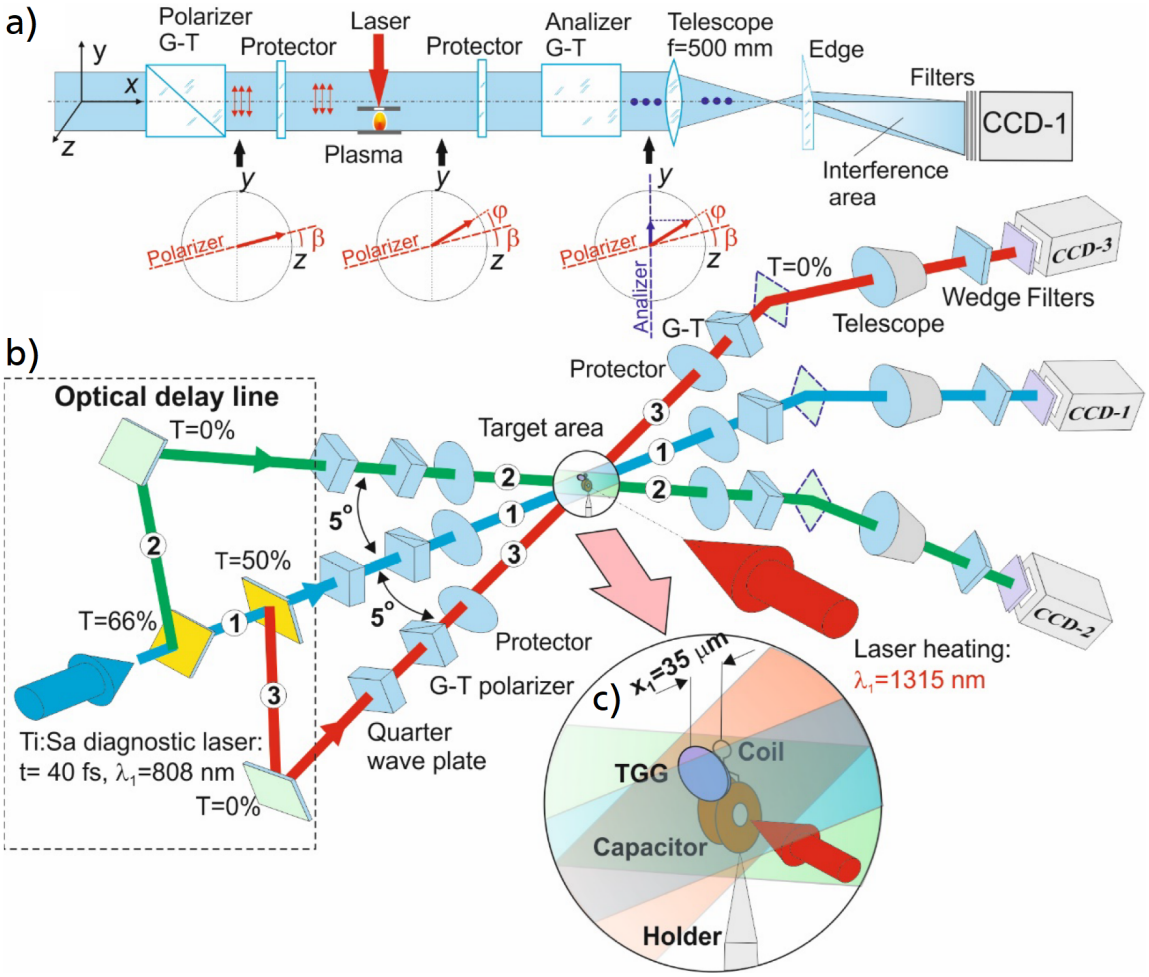

Figure 5.33: Three frame polaro-interferometric system at PALS, combining polarimetry and complex interferometry to determine B-fields arising in vicinity of the coil and in the plasma for a ns-laser driven Double Plate Ω-coil Target. (a) The optical scheme of one single channel, note that the TGG crystal for polarimetry of the B-field in vicinity of the Ω-coil does only fill a small part of the full probe beam size. (b) The three channels separated in space and time cross under small angles at the target position. (c) Zoom into the region of interest around the Double Plate Ω-coil Target, with indication of the driving laser pulse entering the capacitor-like plate assembly through a small hole in one of the plates. Note that the TGG crystal is positioned here before the coil, with respect to the probe beam propagation direction. Figure from [Pis+19].

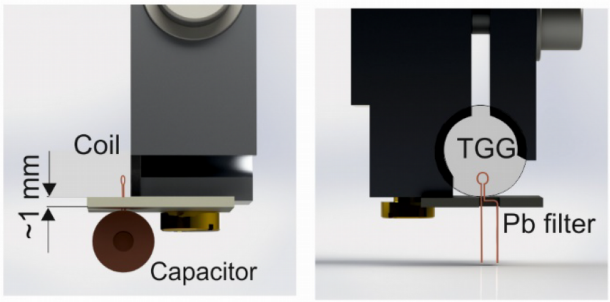

Figure 5.34: Side view of the TGG crystal mount (left) and view from the detector side of the imaging system (right). The TGG crystal and additional shielding are positioned independently from the Double Plate Ω-coil Target.

that is necessary to obtain such reduced projection is consistent with anti-parallel orientation of B-field and probe-beam propagation direction within the coil. Outside the coil, the intensity of the pulse increases consistently, but only to a low extend that is even comparable to shot to shot fluctuations in the probe beam intensity. Note that reference and shot are obtained in two independent probe beam shots.

The current-normalized integrated B-field over the crystal depth evaluates to the order of 200 T µm kA^{-1}, see fig. 5.35 (d). With a large Verdet constant of 60 rad T^{-1} m, Faraday rotation is of the order of 12 mrad kA^{-1}. Currents of several hundred kA may therefore yield ambiguous results, but small currents can be well detected.

With reference to possible ambiguities, we deduce the first four possible Faraday rotation angles of darkened and brightened regions through the crystal, respectively inside and outside of the Ω-loop. As brightening and darkening stem from the very same current distribution, we relate possible ranges of coiling current that fit both. For data analysis this steps, a numerical routine became developed, see section 7.6. The results for the first frames of three independent driver shots are depicted in fig. 5.36. The shots deploy three comparable targets, which only differ with the capacitor gap width. For shots 53901, 53095 and 53096 the gaps measure 920 µm, 1.080 mm and 1.130 mm respectively.

Figure 5.36 (a) compares the ambiguous data to the qualitative evolution of the Gaussian driver laser pulse. Figure 5.36 (b) shows the fraction of laser pulse energy converted to B-field energy. In a first step, an eventual current build up time delay is not considered and the energy conversion is presumed instantaneous. Fits show, the lowest possible intervals are best fitting with a conversion efficiency of 0.32 % to 0.96 %, which is in agreement with the order of magnitude found in the previous section and in other experiments [San+15]. The next best match is for a high conversion efficiency of 29 % to 75 %.

Results obtained for later probing are possibly biased by a darkening of the TGG crystal due to the irradiation of the crystal with hard X-rays. Those later probing times coincide with the arrival of the main driver pulse peak on the target. In the set-up with a polarizer-analyser pair surrounding the crystal, both de-polarization or changes in the absorbance may be reasons. A bright signal level in the vicinity of the coil at late probing times, when the crystal appears blackened else, points to depolarization rather than absorption as major cause. De-polarization occurs for heated crystals [YF13; Sle+15] majorly due to changes in the refractive index with temperature [Yas+13]. It is known that the Verdet constant is temperature dependent [Sta+14], and analysis of data where darkening occurs does not seem possible without further investigation of the crystal properties under high doses of hard X-rays.

With a conversion efficiency of $640(32) \cdot 10^{-3}$ %, the coil current is expected to reach a maximum of $28(10)$ kA, for an average driver pulse energy of 220 J and a consumer loop impedance of $7(1)$ nH.

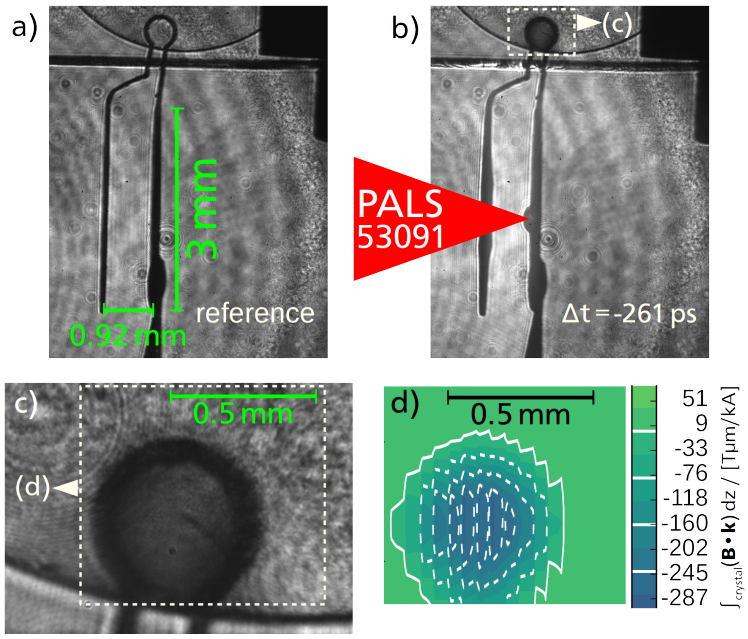

Figure 5.35: (a) Reference image of the first channel, prior to the main driver laser shot PALS #53091: the Double Plate Ω-coil Target is mounted on a insulating glass needle such as the TGG crystal intersects the probe beam path in vicinity of the Ω-coil, a lead shielding partially protects the crystal. (b) The driven Double Plate Ω-coil Target probed at $-261\,\mathrm{ps}$ with respect to the peak of the $350\,\mathrm{ps}$ FWHM Gaussian main driver pulse. The plasma plume is visible as dark region, ejected from the right hand side capacitor plate. (c) The inner of the coil appears visibly darker than in the reference image. (d) Compared is a numerical solution for the integrated field of the conductor, which is proportional to the Faraday rotation angle and therewith the change in intensity. The field inside the coil yields rotations 25 times larger than outside the coil, which can explain why brightening is not observed.

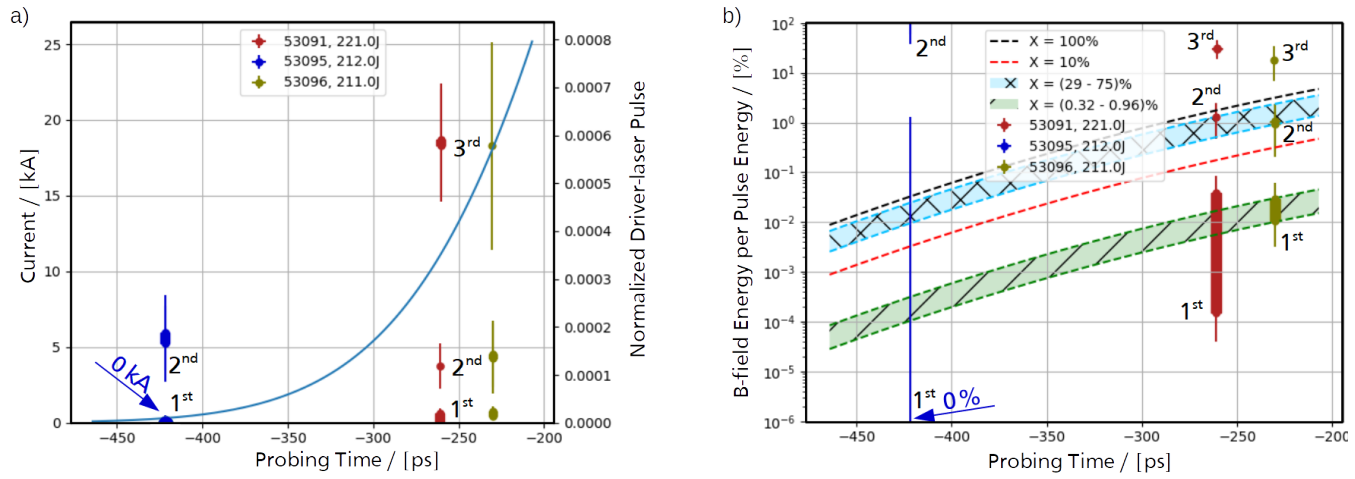

Figure 5.36: (a) The current in the conductor interfered by Faraday rotation from the respective 1st, 2nd and 3rd projection is qualitatively compared to the rising Gaussian driver laser pulse. (b) Ratio of B-field energy and laser pulse energy, with an estimated target inductance of 7 nH. The Gaussian driver laser pulse is re-normalized to fit the evolution indicated by data points. The quantity X in the legend denotes the conversion efficiency from laser energy to B-field energy.

The complex interferogram of the capacitor part of the target yields a measurement of the SMF in the plasma. The analysis procedure is schematized in fig. 5.37. The laser coming from the right hand side drives a plasma into the capacitor gap, see fig. 5.37 (a). The plasma column retards the EM wave of the probe laser beam and resulting phase shifts produce the visible interferogram. The interfringe space appears to be brighter in the upper half of the plasma column in the zy-plane if compared to the bottom half. This indicates the rotation of the polarization due to magneto optic effects. The Fast Fourier Transform (FFT) of the polari-interferogram fig. 5.37 (b) gives access to the amplitude distribution with the central lobe and the phase shift with the side lobe. Both, phase shift fig. 5.37 (c) and the rotation of polarization fig. 5.37 (d) are obtained following the analysis procedures described in section 4.2.2 and section 4.2.3. Both are essential for calculation of electron density and SMF, see section 4.2.4.

Essential presumption for calculation of the azimuthal SMF is a zero B-field for regions where the plasma density measurement is within the noise level. Figure 5.38 shows plasma density, SMF, positive axial current density and the radially integrated direct current. Note that high density plasma does not fill the full capacitor gap.

The current density follows from Maxwell's equation in cylindrical coordinates,

$$\vec{j}(z,r) = \mu_0^{-1} \cdot [(-\partial_z B_\phi(z,r))\,\vec{e}_r + (r\partial_r(r \cdot B_\phi(z,r)))\,\vec{e}_z] \quad , \tag{5.24}$$

which swings to negative axial values for $\partial_r(r \cdot B_\phi(z,r)) < 0$, at the radial position where the radial gradient is larger than the normalized field – which occurs for cases where the field amplitude decays radially faster than $1/r$. Experimental results show azimuthal peaks of ≈ 3 MG at radial positions of 25 µm, decaying to tens of kG over tens of µm, thus evidencing negative axial return current in the plasma. Figure 5.38 (c) shows the positive range of the axial current density, responsible for the direct current in the gap. The radius of the current filament is $26(11)$ µm.

The integrated direct current in fig. 5.38 (d) is calculated as the radially space-integrated forward directed axial component of the current density. The orders of magnitude agree for direct current and looping current

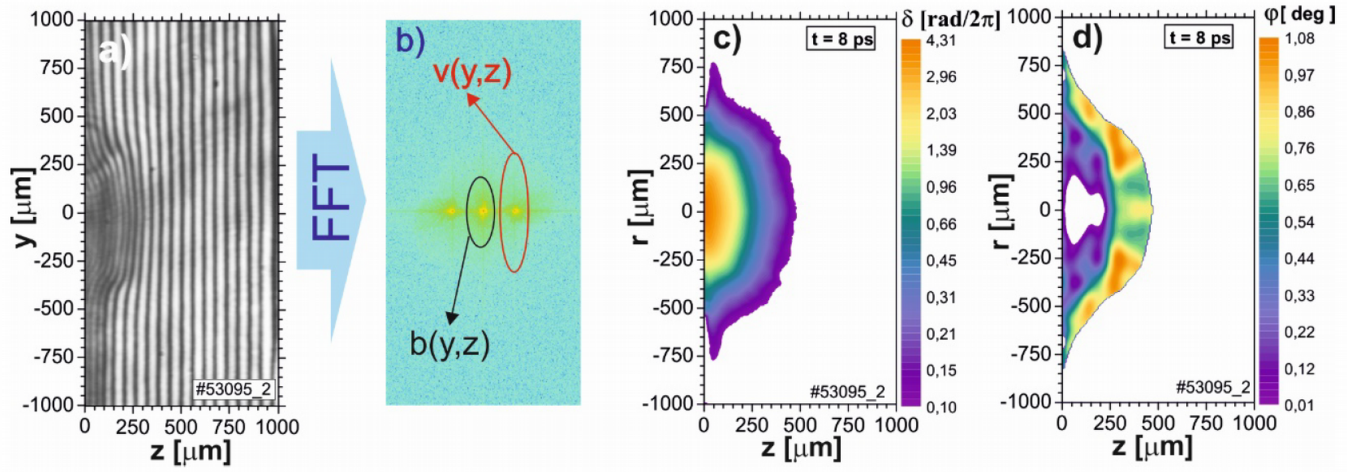

Figure 5.37: (a) The complex interferogram, and (b) the corresponding Fourier spectrum are used to derive (c) phase distribution and (d) the Faraday rotation angle distribution. Figure extracted from [Pis+19].

in the conductor, with a mean direct current of $50(20)$ kA at $8(2)$ ps after arrival of the laser pulse peak for shot 53095. The extrapolated value of the looping current for this time is $20(7)$ kA, based on a constant conversion efficiency of $640(32) \cdot 10^{-3}$ %. Only with a constant conversion efficiency of about 4 %, direct current and looping current would attain the exact same value.

Second Study: Direct Current in Inverted Standard Double Plate Ω-coil Targets

Measurements in the first study only allow perception of low B-field amplitudes for early times, before the crystal is perturbed by plasma emission. In an attempt to measure B-fields for later time, the very same type of target is used inverted for this second study, in such a way the laser impacts on the outer side of the closed plate instead of on its inner side. Despite, the experimental parameters are alike the first study, *e.g.* laser shot #53105 with a driver laser pulse energy of 231 J aims at a Double Plate Ω-coil Target with gap width of 990 µm. The plasma emission is effectively shielded off the TGG crystal in vicinity of the Ω-coil by the interaction plate itself, see in fig. 5.39.

The brightening of the inner section of the coil is expected for inversion with results from the first study and consistent with a current flowing from interaction plate towards the coil. The rotation of polarization is continuously increasing for ramping up path-integrated B-fields. The Ω-coil's field has the highest integrated values on the coil axis, dropping to zero radially, and further only slightly swinging to negative values outside the coil radius. The later negative swing, which must be visible as darkening of the crystal in the inverted experimental configuration, is not observed. This is most likely due to the high noise level but could also indicate depolarization effects due to a mutually heating up crystal.

Late times show signatures of strong coiling currents, see fig. 5.40 for 461 ps after passage of the driver pulse peak where the driver can be considered as switched off. Towards conductor rods, the brightness increases from the unperturbed intensity level. Inside the coil, the brightness decreases towards the centre and reaches a level underneath the unperturbed level, before rising again in vicinity of the very centre. This indicates a rotation of polarization in a range from $(\pi - 2\beta)$ to (π).

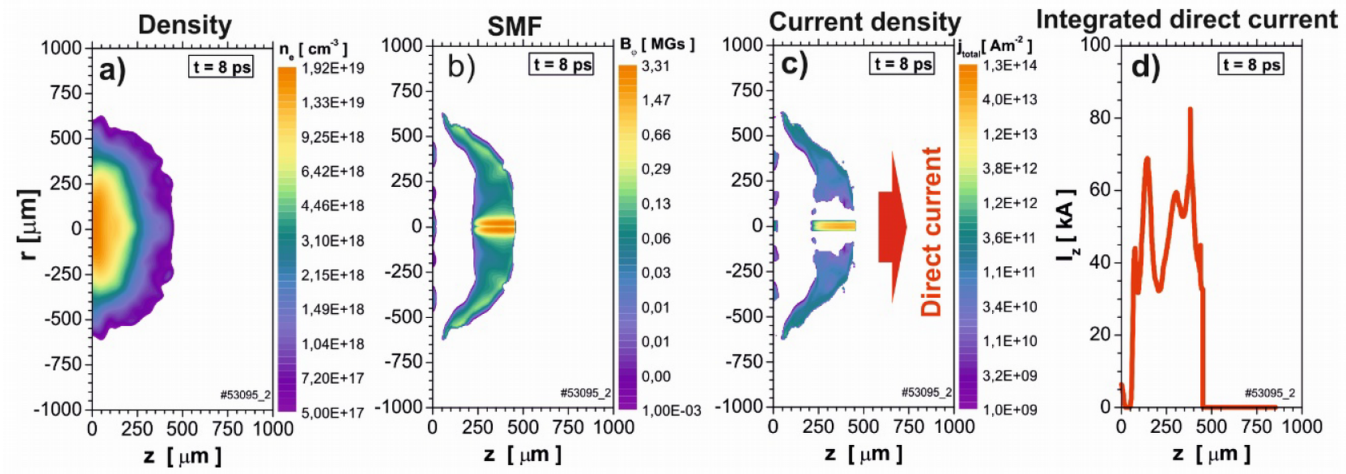

Figure 5.38: Calculated distributions: (a) electron density, (b) absolute azimuthal SMF, (c) current density-direct and (d) integrated direct current. Figure extracted from [Pis+19].

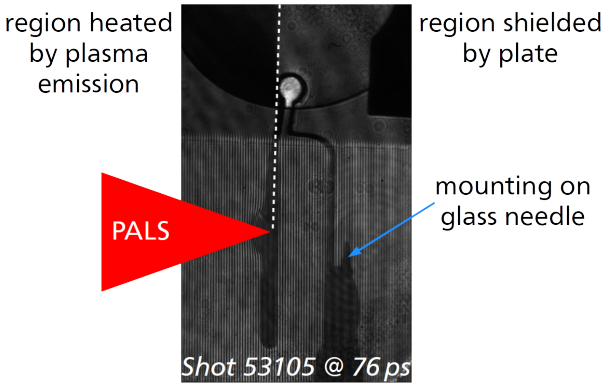

Figure 5.39: The PALS laser hits the vertically flipped target, in such a way that the interaction plate shields off the TGG in vicinity of the coil efficiently from emission stemming from the laser driven plasma.

The expected rotating force on the coil axis is $287\,\mathrm{T\,\mu m\,kA^{-1}}$, compare fig. 5.35. Thus these angles of rotation are reached for $-(\pi - 2\beta)\mathrm{rad}/60\,\mathrm{T\,m}/287\,\mathrm{T\,\mu m\,kA^{-1}} = -178.4\,\mathrm{kA}$ and $-182.4\,\mathrm{kA}$ respectively.

Note that the dips to darker values do not decrease down to values encountered behind the conductor rod, thus are of intensities higher than the background intensity. Interference effects stemming from the coil shape are visible and may alter the brightness level in the centre.

Data of all shots in this configuration is compared in fig. 5.41. Only shot #53105 shows a clear evolution, the other shots might be not conclusive due to the high noise level in the measurements, especially for shots #53104 and #53115. Shot #53105 shows qualitative agreement with the evolution of the laser pulse energy deposition, and quantitative agreement in all frames for a total conversion efficiency from laser pulse energy to B-field energy ranging from 10 % to 60 % in the margins of error, see fig. 5.41 (b). This is in agreement with the highest possible interval from 29 % to 75 % fitting data from the first study. The higher end of this interval of conversion efficiency is nevertheless not realistic. The magnetic field is not the only effect on the crystal. It is likely that the crystal was suffering from irradiation or the interaction with charged particles. Those two influences were not quantified but the partial blinding of the crystal that is visible with fig. 5.40 (c) can indeed be an indication of such disturbance. Lower conversion efficiencies do not fit the third frame of

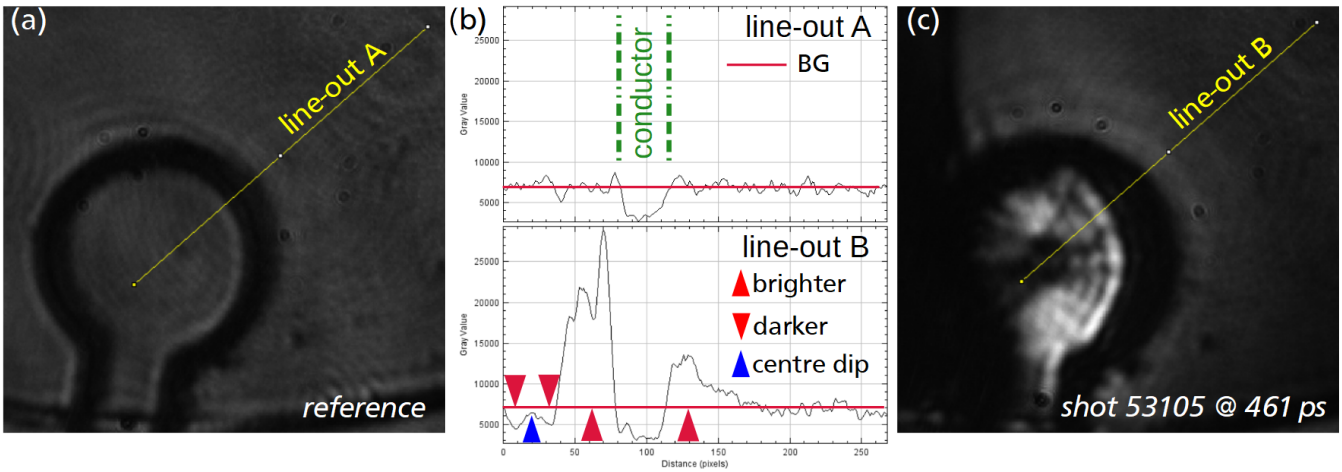

Figure 5.40: (a) Probe laser reference and (c) on-shot Faraday rotation measurement for the vertically flipped target. Indicated line-outs are compared in (b), revealing a likely rotation of the polarization up to the 2nd or 3rd projection.

shot #53105 well – a good fit requires a conversion efficiency as high as 50 %. Illustrated as green interval is the the best fit found in the previous study, which notably only fits the respective first and second frame of shot #53105. With only one shot the dynamics is badly resolved, and further studies are needed to investigate the influence of irradiation on the crystals.

The Complex Interferogram for shot #53105 shows clear signatures of phase rotation and phase shift for two frames yielding plasma density and SMF distribution, see fig. 5.42 and fig. 5.43. The plasma electron density of the order of several $10^{19}\,\mathrm{cm}^{-3}$ and B-fields of several MG agree with the first study, but the B-field is pronounced in a slimmer sheath of the plasma corona. The toroidal field close to the laser axis is restraint to the front of the expanding plasma. For an early probing time of $-354\,\mathrm{ps}$, fig. 5.42 (a) shows that the plasma at a detection threshold of $10^{18}\,\mathrm{cm}^{-3}$ expanded $220(10)\,\mu\mathrm{m}$ from the interaction plate, then reaching $500(10)\,\mu\mathrm{m}$ for 76 ps, see fig. 5.42 (b). The plasma expansion starts well before the main pulse arrives on the target, which might be due to pre-pulses.

The integrated direct current and the corresponding return current are deduced from the SMF following eq. (5.24). Figure 5.42 (c) and fig. 5.43 (c) show both currents, illustrating their equality which is intrinsic to the analysis and follows from the presumed charge neutrality of the plasma. At early probing time, the average direct current of $37(10)\,\mathrm{kA}$ is much larger than the measured current in the conductor of $4(4)\,\mathrm{kA}$. Late times show the average direct current of $72(20)\,\mathrm{kA}$ that is above what would be expected from conversion efficiencies of several percent.

The delayed rise of the coil current is an indication that the inductivity of the target imposes longer timescales than triggered by the laser-driven mechanisms. While the laser is on, eq. (5.13) lets one estimate a characteristic rise time of the lumped circuit $\tau_{1/\mathrm{e}} = L_\mathrm{C}/R_\mathrm{C}$ ranging from 79 ns to 233 ns for an inductivity of $5(2)\,\mathrm{nH}$ and the initial wire resistance of $33(4)\,\mathrm{m\Omega}$ for the cold target. The additional resistance of the Cu plates, the skin effect and Joule heating of the conductor can decrease this time. Joule heating was found to heat Cu targets to the evaporation point [Tik+17], which is at $240 \cdot 10^{-3}\,\mathrm{eV}$. With equal electron and ion temperatures, one calculates a resistivity of $74\,\mathrm{n\Omega\,m}$ at the evaporation point, see fig. 5.44. Taking into account an early-on current-carrying plasma expansion from ≈800 ps before the scheduled impact of the maximum intensity, the observed $1/\mathrm{e}$ rise time approximates to 900 ps. Estimating the full rise time to be of the order of 1.5 ns, the

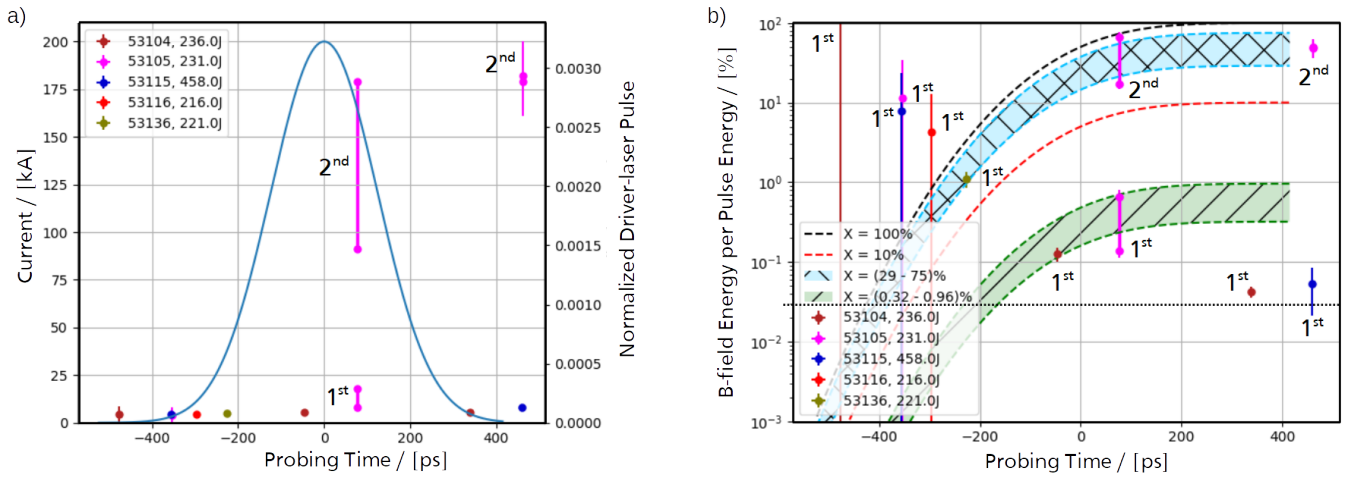

Figure 5.41: (a) The current in the conductor interfered by Faraday rotation is qualitatively compared to the Gaussian driver laser pulse. (b) Ratio of B-field energy and laser pulse energy, with an estimated target inductance of 7 nH. The integrated energy deposition by the Gaussian driver laser pulse is re-normalized to fit the evolution indicated by data points. The quantity X in the legend denotes the conversion efficiency from laser energy to B-field energy. If rotation angles other than for the 1st projection are used to derive currents for one shot, a counter for the respective projection is indicated.

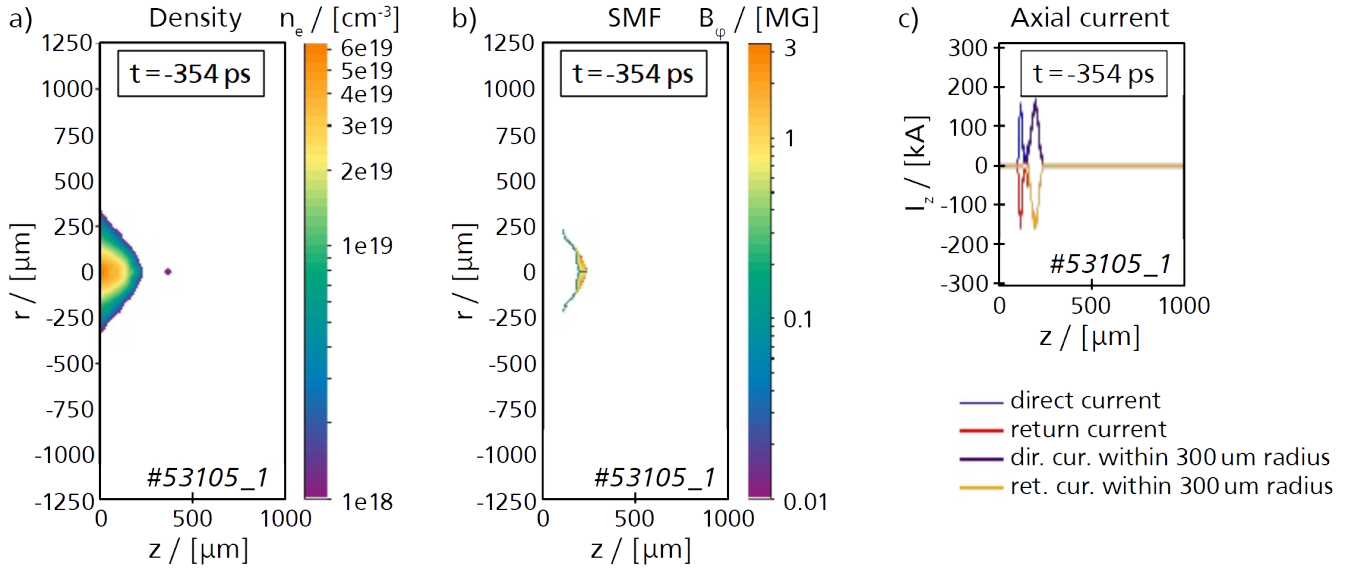

Figure 5.42: Calculated distributions: (a) electron density, (b) absolute azimuthal SMF and (c) integrated axial current. Highlighted in (c) are direct and return current resulting integration within a cylinder of 300 µm radius around the laser axis, superposing perfectly the complete integral in vicinity of the front of the plasma plume and zero towards the interaction disk.

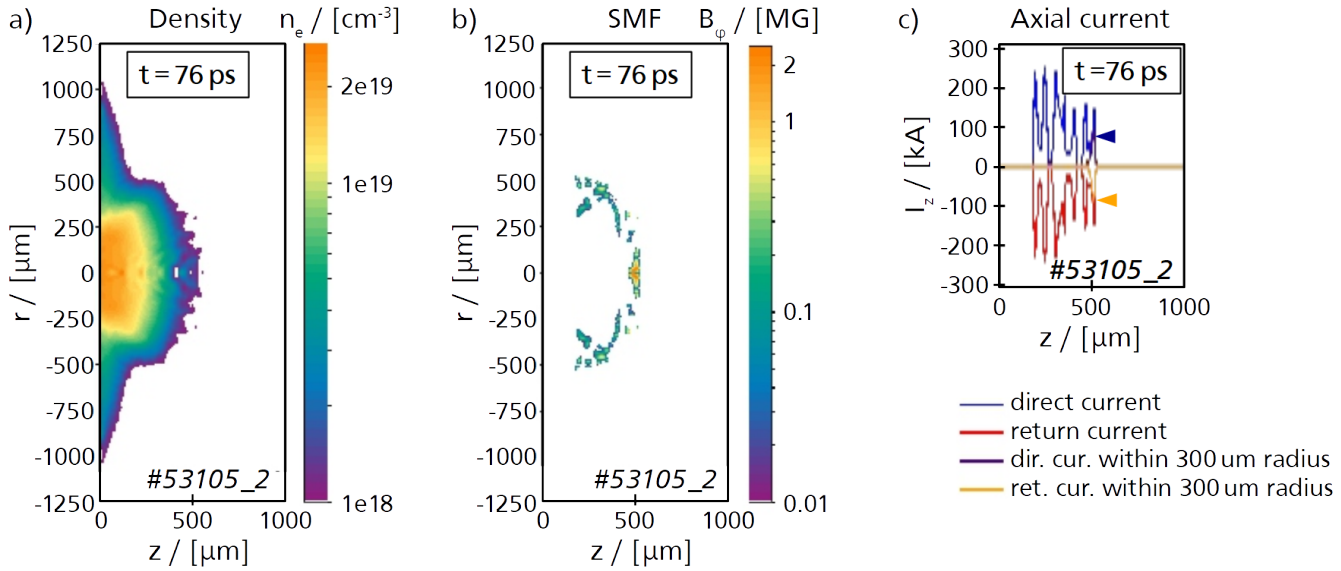

Figure 5.43: Derived distributions of (a) electron density, (b) absolute azimuthal SMF and (c) integrated axial current. Indicated in (c) are the maximum amplitude of direct and return current resulting integration within a cylinder of 300 µm radius around the laser axis. The arrow shows the amplitude of the time average.

skin depth $\delta = \sqrt{2\rho/\mu_0\omega}$ results to 10 µm. The wire resistance then calculates to the order of 400 mΩ, which is $14\times$ lower than required to explain the observed short $\tau_{1/e}$ rise time.

Heating the target to a resistivity of $1.71(74)$ µΩ m allowed to reproduce the observed rise time, but it required a target electron temperature yielding the peak of the resistivity evolution, ranging from 13 eV to 54 eV, see fig. 5.44. Such values might be attained my means of X-ray heating. A time resolved experimental measurement of target surface temperature and density is of interest for further experimental campaigns.

Third Study: The Interaction at Higher Laser Pulse Energy with Modified Double Plate Ω-coil Targets

The direct comparability of results in the second study to modelling of the Double Plate Ω-coil Target platform is challenging due to the absence of a second plate. Further studies focus at the original platform driven with a higher laser pulse energy of ≈500 J and at later probing times, thus necessitating a modified Double Plate Ω-coil Target and modified crystal mounting for a better shielding of the TGG crystal. The capacitor section is similar with with 3 mm diameter plates, but gaps are of width of 1.25 mmand the hole in the front plate is made larger to avoid laser-clipping. It has a diameter of 1.7 mm. The 500 µm diameter Ω-loop is horizontally oriented and located 1.5 mm behind the back plate and 2.4 mm above the driver laser axis, see fig. 5.45.

Expecting coiling currents of the order of tens to hundreds of kA, the suitable coil-centre to crystal-surface distance is found to be $z_{\mathrm{CRY}} = 625$ µm by equating eq. (4.31) and eq. (4.33). This large distance renders measurements of low field amplitudes difficult and clearly aims at the maximum field amplitudes occurring for late times. Other than in both previous studies, the crystal is positioned in front of the coil plane, with respect to the propagation direction of the probe beam.

Coiling currents interfered from the first possible Faraday rotation angle are compared to the temporal evolution of the driver laser pulse in fig. 5.46. In three shots, referred to as #54657, #54662 and #54664,

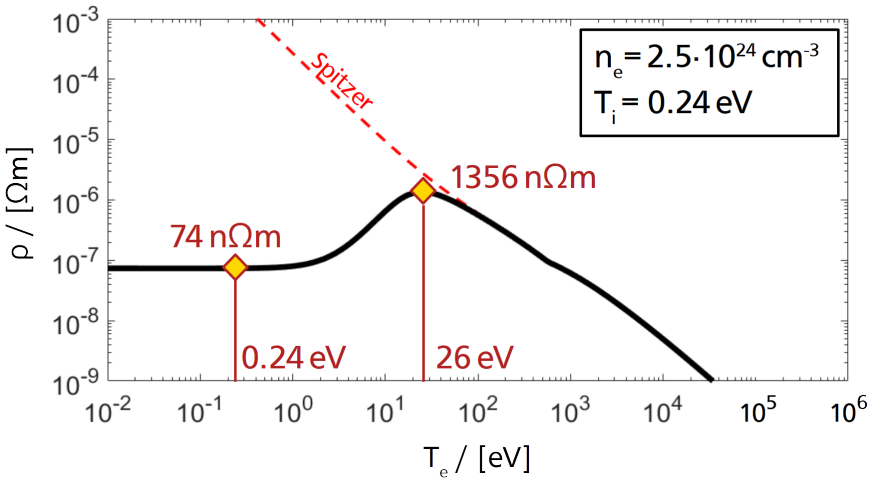

Figure 5.44: Resistivity calculated for solid density Cu with background ions at the boiling point for different electronic temperatures. The black solid line illustrates the Eidmann-Chimier resistivity for solid density Cu [CTH07], the dashed line indicates the Spitzer resistivity for this case. The higher resistivity for warm targets could explain the fast rise of coiling currents.

Faraday rotation appears clearly in vicinity to the conductor. Results for shot 54657 is derived from noisy data and could be misleading. In two other shots, #54663 and #54674, the probe laser intensity in vicinity of the crystal boundary changes in magnitude as it does in vicinity of the conductor. It is not clear why this arises and results of the later shots must be interpreted with great care. For all shots, the current does not swing to negative values after the laser drive is off, but decays slowly, see fig. 5.46 (a). With the results from shots #54662, #54663, #54664 and #54674, one notes a steep rise for the coiling current during ≈200 ps and a slow decay that is not resolved by the ns-scale scan of probing time.

In detail, for shot #54657, the polarizer-analyser angle is $\beta = 3°$ for all frames. Interferograms show the three distinct probing times −610 ps, −330 ps and 100 ps with respect to the driver laser pulse peak impact time. The intensity of transmitted light increases comparing the earliest probing time with both later times. This is consistent with a positive rotation of the polarization due to an increasing B-field amplitude. The positive rotation indicates anti-parallel configuration of wave vector and B-field. Anti-parallel fields are issued from positive currents directed from back- to front plate of the Double Plate Ω-coil Target. Analysis with proCOIN_FR yields coiling currents of 0 kA, 121 kA to 153 kA and 84 kA to 132 kA for the respective first, second and third frame. For shot #54662, $\beta = 30°$ is set for the intermediate and $\beta = 3°$ for first and last time frames. The three distinct probing times are −146 ps, 134 ps and 564 ps. The coiling current is 135 kA for the last frame. Here, the intermediate frames are of too poor quality for analysis. On shot #54663, polarizer-analyser angles remain unchanged from shot #54662 and probing times change to −359 ps, −79 ps and 251 ps. The coiling current of 137 kA is interfered for probing at 251 ps. For shot #54664, the polarizer-analyser angle is $\beta = 3°$ for all frames. Coiling currents of 0 kA and 142 kA are determined for first and second frame acquired at −395 ps and −115 ps respectively. Shot #54674 shows significant rotation angles. The polarizer-analyser angle changes to $\beta = 3°$, 2° and −3° for the three channels respectively. Probing times are −473 ps, −193 ps and 237 ps, showing coiling currents of 0 kA, 107 kA to 308 kA and 135 kA to 322 kA. The target for this shot was deformed, the capacitor plates were inclined with respect to each other. The plate distance on the laser axis passing centred through the front disk is $1.029(10) \cdot 10^3$ µm, the vertical plate inclination angle 9.0(3)°.

The conversion efficiency of laser energy to B-field energy is plotted in fig. 5.46 (b), where the inductance of

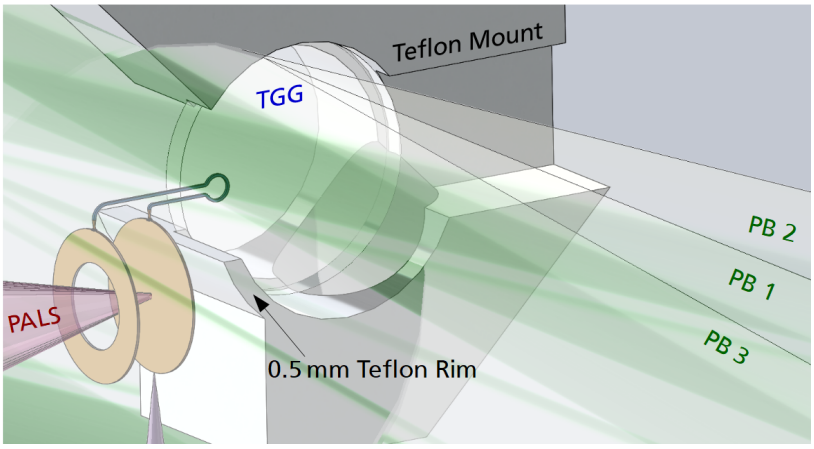

Figure 5.45: Modified Double Plate Ω-coil Target driven by the main ns-pulse at PALS, diagnosed by a three-frame polari-interferometer based on an auxiliary fs-pulse that is probing the laser-plasma and the magnetized TGG crystal.

the consumer loop is analytically calculated and presumed constant with $5(2)$ nH. Note that here the first possible angle of Faraday rotation is the only that yields B-fields containing less energy than the laser pulse, thus which are feasible. After passage of the maximum intensity of the laser drive, the conversion efficiency of all shots fits best to $8.8(2)$ %. There-before, the steep ramp up of the current indicates better conversion efficiency for early times. Best fitting ranges of previous studies are compared in the same graph. The high efficiency branch found in the first study is centred with the best fit found in the second study and intersects with most early measurements in the margin of uncertainty for this study.

For the same shots, Complex Interferograms qualitatively indicate B-fields by showing asymmetric rotation of polarization underneath and above the driven plasma plume, but Complex Interferometry for this study yield noisy bad quality images and the measurements are to be understood indicative. Two typical shots for their B-field structure are shown with fig. 5.47 and fig. 5.48. Shot #54674 in fig. 5.48 is considerably different to data in the first study, with a strong B-field present in the corona and no visible toroidal field. Shot #54657 in fig. 5.47 is characterized with field fluctuations in the corona and a toroidal signature for later frames. Both field structures show amplitudes ≈30 % higher as observed before. The spatial distribution of the electron density also is considerably different. Lobes appear, eventually pointing to the solid part of the front plate. This difference mat arise due to a different intensity distribution in the focal spot, due to missalignements or objects in the beamline. The inner of the cone of dense plasma is filled with oscillations on the laser axis. Note that the laser pulse spatially fills the capacitor gap for early times, then interfering with its reflection and eventually yielding plasma resonances with the standing EM wave. One further notes plasma stemming from the front plate for latest probing times, eventually ablating from the X-ray heated inner surface. Back- and front-plate plasma connect for times of ≈100 ps.

As for the second study, rise times of coiling currents are short with respect to the lumped RL-parameters of the circuit defined by the target. For shot #54657, the detection of plasma above the sensitivity threshold of the interferometer allows to crudely interfere that the dynamics starts at ≈ -890 ps – in particular the plasma expanded to $296(37)$ µm from the target surface for -610 ps and to $593(37)$ µm for -330 ps. This is consistent with the second study and points to a possible systematic error for the determination of the probing time.

Later times, for which the capacitor is filled with dense plasma, show a stabilized energy conversion efficiency.

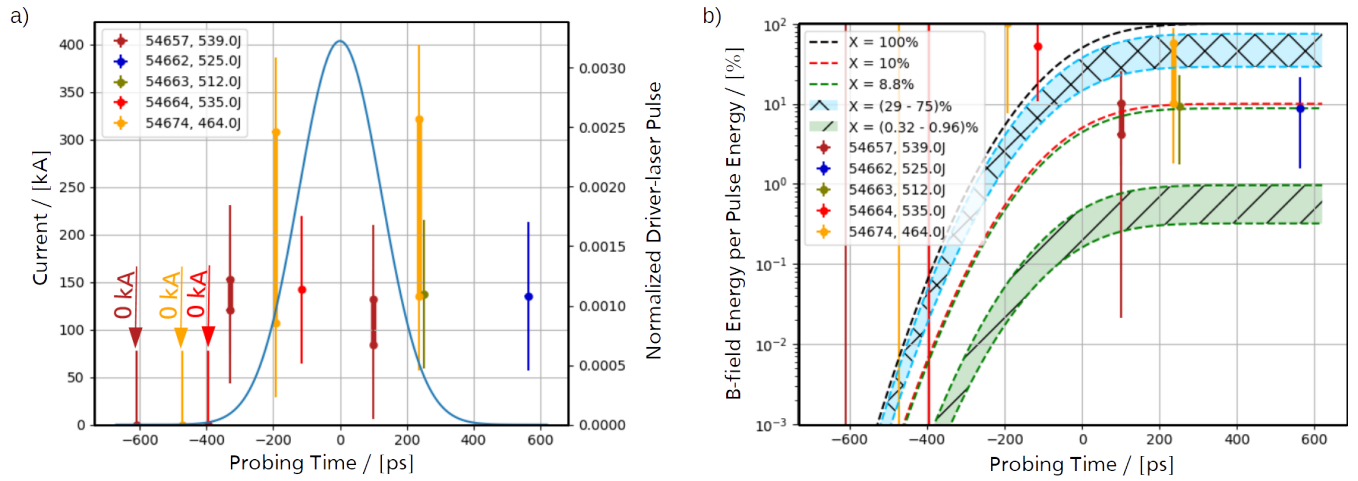

Figure 5.46: (a) Coiling current in the Ω-coil for distinct shots determined by Faraday rotation, superposed to the qualitative temporal evolution of the driver laser pulse. (b) The conversion efficiency X from laser energy to B-field energy, when presuming the geometrical inductivity of $5(2)$ nH.

Earlier times at which plasma is not filling the gap show currents corresponding to very high conversion efficiency. If one compares this to results of previous studies, presuming in analogy an initially constant $52(23)$ % conversion efficiency, the stabilization level of $8.8(2)$ % total efficiency is reached at $-109(42)$ ps. The measured gap fill time does not coincide with the deduced stabilization time.

5.2.2.4 Comparison of Experimental Results and Modelling

Highest currents are plausible for shots of the third study with modified target geometry and high laser pulse energy, reaching $135(78)$ kA for most shots and up to $228(171)$ kA for one shot, see fig. 5.46 (a). Nevertheless, shots on inverted targets in the second study yield non negligible currents of the same order with $180(18)$ kA, here for a low energy shot, see fig. 5.41 (a). The rise times of currents is shorter for high energy shots on the modified target when compared to low energy shots on the standard target.

Further comparing results via the conversion efficiency of laser energy to B-field energy allows normalization to driver laser energy and target inductance. A high conversion efficiency can explain high currents for shots on inverted targets at all times, see fig. 5.41 (b). On the contrary, results for standard targets indicate low conversion efficiency of ≈1 % for earliest times in fig. 5.36 (b), followed by a steep increase in current and a final agreement with several % of total conversion efficiency, see fig. 5.46 (b). The conversion efficiency discussed here relies in absolute value on a numerically deduced target impedance, therefore it yields comparable results but the absolute value may be an over-estimate. The temporal evolution of the absorption of laser energy is crucial for such comparisions – future experiments must measure it to better determine (a) absolute laser timing, (b) pulse shape and (c) different heating regimes during intensity ramp-up.

Concerning the first modelling hypothesis, that the laser heating is directly driving the coiling current, one sees that a proportional conversion from laser energy to field energy in a steady state assumption does not fit the temporal evolution of experimental results. The first study evidences an initially low best fitting $640(32) \cdot 10^{-3}$ % conversion efficiency, pointing together with the third study to a very steep increase in current after -200 ps that evolves de-phased with laser energy deposition. This indicates that lumped circuit

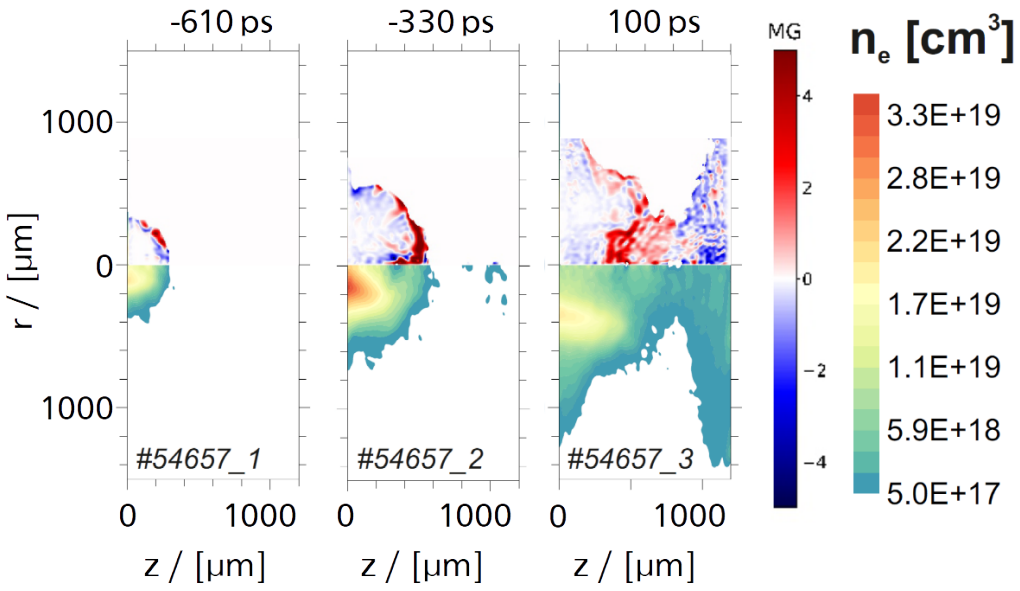

Figure 5.47: Complex Interferometry for PALS shot #54657 yields measurement of SMF (top sections) and electron density (bottom section) for each frame of the three-channels, probing times correspond to the delay with respect to the peak arrival time of the driver pulse.

modelling can be based on a voltage source. Further, the second study shows no direct correlation between laser driven direct current and coiling current.

The remainder of this section pursuits the approaches of capacitor-coil modelling and enhanced diode modelling. B-fields have high amplitudes even after the driver laser is off, and visually no fast decay. This long persistence of B-fields is also seen by other experiments with target geometry resembling the second study, shot at the very same laser system [Kum+20]. For a lumped RLC circuit model, a quarter period corresponds to $\tau_{\mathrm{LC}/4} = 2\pi\sqrt{L_\mathrm{C} C_\mathrm{C}}/4$. For the targets discussed here-before, with $L_\mathrm{C} = 5(2)$ nH and $C_\mathrm{C} \approx 100$ fF in vacuum, it follows $\tau_{\mathrm{LC}/4} \approx 35$ ps. Such high frequency oscillations are not observed. Either the target capacitance is higher or the influence of the capacitance is negligible. In case of an over-damped evolution with a negligible influence of the capacitance, the coil current relaxes with $I_\mathrm{C}(t) \propto \exp\left[-(t-t_0)/\tau_\mathrm{RL}\right])$ where $\tau_\mathrm{RL} = 2L_\mathrm{C}/R_\mathrm{C}$. The data set does not hold enough points in the tail for a fit. Analytical calculation yields for cold Cu $R_\mathrm{C} \approx 30\,\mathrm{m\Omega}$, thus $\tau_\mathrm{RL} \approx 300$ ns. This time is expected to be shorter due to a rising resistivity with ohmic heating during current flow, but its order of magnitude agrees to an un-noticeable decay over hundreds of ps.

The first study holds the best quality complex interferograms, showing a direct current in the plasma that integrates to 50(20) kA at a relative timing of 8(2) ps, to which the gap is not yet filled with dense plasma. With measured electron densities of the order of $10^{18}\,\mathrm{cm}^{-3}$ and typical hot electron temperatures of $T_\mathrm{h} = 40$ keV (for details on the methodology see [Kru+21]), discussed experiments are in a regime of low densities and high temperature that allows us to assume a Maxwellian distribution for the hot electrons in the frame of the capacitor-coil modelling approach. With a half-spherical emission to $\Delta\Theta = \pi$, the direct diode current results from eq. (5.15) to

$$I_\mathrm{D} = q_\mathrm{e}\pi r_\mathrm{h}^2 n_\mathrm{h} (2\pi)^{3/2} \left(\frac{k_\mathrm{B}T_\mathrm{h}}{m_\mathrm{e}}\right)^{1/2} \left(\frac{q_\mathrm{e}V_\mathrm{C}}{k_\mathrm{B}T_\mathrm{h}} + 1\right) \exp\left[-\frac{q_\mathrm{e}V_\mathrm{C}}{k_\mathrm{B}T_\mathrm{h}}\right] \quad , \tag{5.25}$$

where k_B is the Boltzmann constant and m_e the electron mass. In the limit of a static electron distribution and

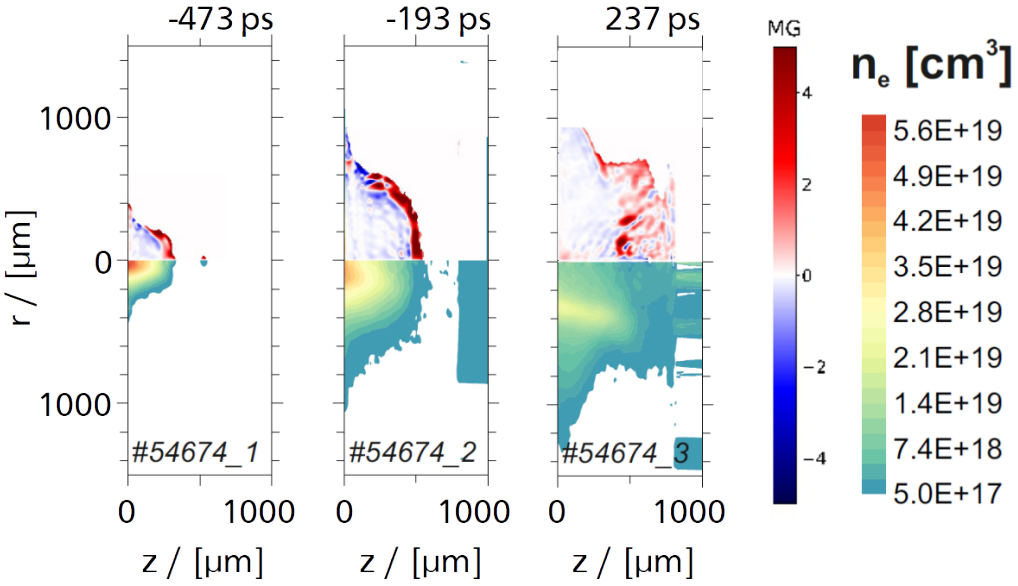

Figure 5.48: Complex interferometry for PALS shot #54674 yields measurement of SMF (top sections) and electron density (bottom section) for each frame of the three-channel s, probing times correspond to the delay with respect to the peak arrival time of the driver pulse.

presuming $q_\mathrm{e}V_\mathrm{C} \gg k_\mathrm{B}T_\mathrm{h}$, we inject the averaged eq. (5.16) into eq. (5.25) and obtain

$$q_\mathrm{e}V_\mathrm{C} \approx k_\mathrm{B}T_\mathrm{h} \cdot \ln\left[\left(q_\mathrm{e}r_\mathrm{h}\right)^2 n_\mathrm{h} C_\mathrm{D}^{-1} \tau_\mathrm{L} \left(2\pi\right)^{3/2} \left(m_\mathrm{e}k_\mathrm{B}T_\mathrm{h}\right)^{-1/2}\right] \quad . \tag{5.26}$$

For shot 53095, measured values for n_h range from $1 \cdot 10^{18}\,\mathrm{cm}^{-3}$ to $10 \cdot 10^{18}\,\mathrm{cm}^{-3}$ and the heated region has a radius of approximately 500 µm. With a comparatively small capacity of the capacitor-like target part of 97.9 fF, the ratio of diode tension and electron temperature $^{q_\mathrm{e}V_\mathrm{C}}/_{k_\mathrm{B}T_\mathrm{h}}$ following eq. (5.26) attians the order of

$$\frac{q_\mathrm{e}V_\mathrm{C}}{k_\mathrm{B}T_\mathrm{h}} \approx \Gamma + \ln\left[\frac{k_\mathrm{B}T_\mathrm{h}}{1\,\mathrm{keV}}\right] \quad . \tag{5.27}$$

We obtain Γ in a range from 17.2 to 19.5 for the given range of number densities, such as the relation agrees weakly with the initial presumption $q_\mathrm{e}V_\mathrm{C} \gg k_\mathrm{B}T_\mathrm{h}$ for electron temperatures of several keV. For hot electron temperatures of several tens of keV, the ratio therefore scales from 17 to 25. Such high ratio implies a low direct current. Assuming the higher electron number density within the measured range yields $\Gamma = 19.5$, and it follows $I_\mathrm{D} \approx 20.5 \cdot \exp\left[-19.5\right] \cdot 83.66\,\mathrm{MA} \approx 3\,\mathrm{kA}$. This is in contradiction to the experimental measurements of several tens of kA for the direct current in the gap.

Following eq. (5.27), a hot electron temperature of 40 keV leads to the diode tension of 928 keV. The coiling current can be estimated via solution of eq. (5.13). For the experimental case with a resistance of 34 mΩ and an inductance of 7 nH, the diode tension induces a current of approximately 27 MA. The rise time of the current is much longer than the laser pulse duration with $\tau_{1/\mathrm{e}} = L/R \approx 200\,\mathrm{ns}$, thus $\mathrm{d}_t I \approx V_C/L$ and for ns-laser pulses $I_\mathrm{max} \approx \tau_L \cdot V_C/L \approx 46\,\mathrm{kA}$. The comparison of the direct current to the coiling current reveals two general problems of the capacitor model. First, the coiling current is one order of magnitude higher than the direct current, which produces a charge imbalance. Second, the a strong coiling current induces B-fields

with energies $L_C I_{max}^2/2 \approx 14.8\,\mathrm{J}$ well above the total electrostatic energy stored in the capacitor $C_D V_C^2/2 \approx 19\,\mu\mathrm{J}$. The capacitor can not aliment the consumer loop with such strong current.

Addressing the energy imbalance, the electrostatic energy may be higher if screened by a dense plasma filling the capacitor [Goy+17]. On the contrary, one experimentally finds low density plasma filling in the capacitor for times with already large current amplitude.

Addressing the charge imbalance, the system can be described as working in a quasi-steady regime [Fik+16]. There, a continuous current flow through diode and wire section is alimented by the laser energy, and no mismatch arises due to separate considerations of both sections. Such current source model does not agree to the experimentally observed de-phased direct current and coiling current.

Both corrections have been refined in the enhanced diode modelling approach [Tik+17; Wil+20], taking also into account the dynamics and differing regimes in the plasma expansion from the cathode as well as the ohmic heating of the external circuit and the magnetization of the laser driven plasma. First one calculates the diode impedance and the current-limit for pinching, and then one applies the lumped circuit equations for calculation of the current evolution. In the third study, hot electron temperatures reach 40 keV, plasma densities range from $1 \cdot 10^{18}\,\mathrm{cm}^{-3}$ to $100 \cdot 10^{18}\,\mathrm{cm}^{-3}$ in vicinity of a current filament of ≈50 µm radius and the diode gap width measures 1 mm. The diode impedance for calculation of the pinching limit results from eq. (5.19) to Z_D ranging from $22\,\Omega$ to $244\,\Omega$. The maximum current in the filament calculates to $I_{C,max} = k_B T_e / q_e Z_D$, ranging from 164 A to $1.818 \cdot 10^3$ A. In analogy one calculates for parameters of the first study Z_D ranging from $262\,\Omega$ to $829\,\Omega$ and thus $I_{C,max}$ ranging from 48 A to 153 A. This under-estimates can be related to the simplifying nature of the potential well in the model – it is only equalized to the hot electron temperature – or an overestimate for the diode impedance.

If the full plasma column is responsible for direct currents rather than only the filament close to the axis, the impedance drops and higher currents are allowed. For the first study the quasi-planar section of the column has a radius of ≈250 µm, then Z_D ranges from $900 \cdot 10^{-3}\,\Omega$ to $8.9\,\Omega$ and $I_{C,max}$ results ranging from 4 kA to 44 kA. For the third study the dense section of the column has a radius of ≈500 µm, then $I_{C,max}$ ranges from 18 kA to 57 kA. Here, Z_D is ranging from $700 \cdot 10^{-3}\,\Omega$ to $2.2\,\Omega$. Both intervals of the calculated maximum coiling current are in a good agreement with respective experimental results.

The evolution of the coiling current follows with eq. (5.22). The characteristic time of the lumped circuit $\tau_{1/e} = L_C/(Z_D + R_C) \approx L_C/Z_D$ is ranging from $500 \cdot 10^{-3}$ ps to 10 ps. This fast rise of currents agrees with the scale of observed values. Note that steeper rising edges are related to higher electron densities and lower hot electron temperatures. One further calculates $I_{C,sat} = k_B T_e (1 - \exp[-\tau_L/\tau_{1/e}])/q_e Z_D$ which gives a range from 3 kA to 43 kA for the first study and from 15 kA to 54 kA for the third. Both are expectedly close to their maximum values.

The overall comparison shows best agreement of experimental results with enhanced diode model. Hot dense plasma of large extend in the diode gap yields highest conversion efficiency of laser energy to B-field energy. For a full comparison of the experimental data with the model, this studies lack a complete set of electron- and ion spectra. This is motivation for further experiments. The high currents detected for inverted targets motivates further modelling of the diode dynamics.

Long laser pulses of hundreds of ps to tens of ns with pulse energies ranging in the hundreds of J are capable of driving hot dense plasma in the diode gap, maintaining a gap voltage that is alimenting the coil as source of kA currents for long ns lifetime. The next section will focus on short laser pulses at higher intensities which induce transient currents by target discharge.

5.2.3 Transient EM Fields and Pulsed Discharge Currents

Thus far strongest B-fields generated on earth and the most powerful pulsed EM fields are born in relativistic laser-plasma interaction. Reported are B-fields of 34 kT [Tat+02; San+02] inside the laser-plasma, emission of pulsed EM radiation ranging up to hundreds of $\mathrm{kV\,m^{-1}}$ [Con+20], and giant E-fields with hundreds of $\mathrm{GV\,m^{-1}}$ within a µm-scale potential gradient length [Rom+05]. The laser interaction triggers intense broadband electromagnetic pulses (EMPs) ranging from radio frequencies [J.S+77] to X-rays [C C+09]. The dynamics is rooted in the rapid laser heating of electrons, depending on the evolution of the laser intensity and target surface, with equilibration times longer than the driver pulse duration [Nil+12]. The observable fields are induced by resulting EM potential dynamics with large gradients, ultra-strong electron currents and successive target discharge by escaping relativistic electrons [J.-+14; Poy+18; Gal+20].

The aspect of relativistic laser-plasma interaction important for this work is an efficient target discharge due to relativistic electrons that overcome the potential barrier and escape [A. +15a; Bru87; SW97; Wil+92; AJ98]. Firstly, the EM potential dynamics in the target skin depth [S.P+00; K. +09] is seed of mono-peak electromagnetic discharge pulses (EMDPs) traveling along the target surface [S. +15] guided by the target geometry [H. +16]. The laser-generation of EMDP of tens of ps FWHM and rise times of ≈10 ps has been studied for a wide range of laser parameters. EMDP up to amplitudes of tens of $\mathrm{GV\,m^{-1}}$ and tens of T are triggered by laser pulses focused at intensities from $10^{18}\,\mathrm{W\,cm^{-2}}$ to $10^{19}\,\mathrm{W\,cm^{-2}}$ with a pulse duration from the tens of fs to several ps and driver pulse energies from 70 mJ to 50 J [K. +09; S. +15; H. +16; M. +17a].

Second consequence of the rapid target discharge is the generation of a strong return current from the ground, itself seed to some part of the emitted EM spectrum referred to as Giant Electro-Magnetic Pulses (GEMP) [J.-+14; Bra+18]. Modelling this current dynamics based on a lumped-element RLC circuit yields periodicity of hundreds of ps for mm sized metallic laser-interaction targets conductively connected to coil features of several hundred µm radius.

Pulsed B-fields of tens of ps lifetime can be applied to charged particle beam lensing, with low risk of accumulation of charges on the short timescale of efficient operation, soon after the laser-plasma interaction took place. Such B-fields are quasi-static for high energy ions of $60\,\mathrm{MeV\,u^{-1}}$, following eq. (5.8). Further advantageous are steep temporal gradients which possibly allow for chromatic tailoring of spectrally broad ion beams.

This work presents a laser-driven, open-geometry platform for generation of a guided EMDP emanating from the laser-interaction region, that precedes a neutralizing pulse discharge current from the ground, both transporting kA-range currents. Both transient currents are separated experimentally for the first time, within their evolution on the timescale of hundreds of ps. In literature, comparable laser driven platforms are reported for the generation of pulsed B-fields [Zhu+18], and the tailoring of laser-driven particle beams [S. +16], but with no separation or identification of both transient currents.

5.2.3.1 Experimental Platform

This work explores transient fields arising around various types of Disk Coil Targets (DCT). The experiment was carried out at the PHELIX system at Helmholtz Centre for Heavy Ion Research (GSI) [M. +17b], a Nd:glass laser system with a 1.053 µm wavelength [Bag+10]. Target discharge is driven by laser pulses of 500 fs duration, 50 J energy and intensities of $5 \cdot 10^{18}\,\mathrm{W\,cm^{-2}}$. The discharge targets are laser-cut in one piece from 50 µm thick flat Cu foils. All types of the four different discharge targets comprise an interaction disk and a loop-feature in a 50 µm squared wire section: depicted in fig. 5.49 (a) Disk Loop Targets (DLT) with a

helix-shaped loop, and (b) Disk Ω-Coil Targets (DCT) as well as (c) Double-Plate Coil Targets (DPCT) with a Ω-shaped loop. Double-Plate Coil Targets correspond to the Double Plate Ω-coil Target discussed in previous sections of this work, omitting the fact that capacitive effects can not be supposed important *a priori*. This geometry is simplified for the derived fourth target type: (d) DPCT-f lack the front plate, resulting in an open ended wire on one side of the loop. The interaction disk of Disk Loop Target and Disk Ω-Coil Target has a diameter of 2 mm, Double-Plate Coil Targets and their derivation DPCT-f with one plate only have 3 mm diameter disks.

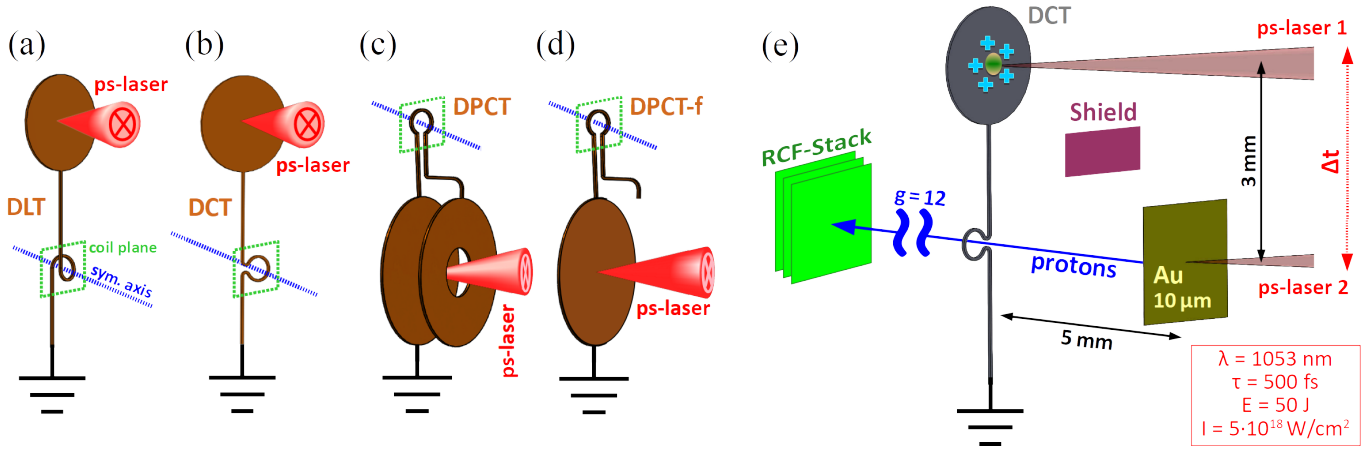

Figure 5.49: Discharge targets are laser-cut in one piece from 50 µm thick flat Cu foils. All types comprise a interaction disk and a loop-feature in their 50 µm squared grounding stalk: (a) Disk Loop Targets (DLT) with a helix-shaped loop, and (b) Disk Ω-Coil Targets (DCT) as well as (c) Double-Plate Coil Targets (DPCT) with a Ω-shaped loop and (d) Double-Plate Coil Targets without front plate (DPCT-f) with a Ω-shaped loop. (e) The experimental proton-deflectometry set-up relies on two equal ps-laser pulses with adjustable delay Δt. ps-pulse #1 induces target discharge on the interaction disk and ps-pulse #2 drives a TNSA proton beam from a 10 µm thick Au foil that probes the loop feature and gets imaged via a stack of RCF. A 100 µm Tantalum shield blocks the direct line of sight between both laser interaction regions.

The discharge ps time- and mm spatial-scales are captured by ion beam deflectometry deploying a TNSA generated proton beam, accelerated by using a second PHELIX beam portion similar to the discharge target driver, with an adjustable temporal delay, see Figure 5.49 (e).

5.2.3.2 Generation and Characterization of Transient EM Fields

The EM discharge pulse can be modeled by a propagating charge distribution, inducing magnetic and E-fields [S. +16]. It became employed in a solenoid geometry for guiding a TNSA particle beam generated in the same interaction process [S. +16; Bar+20]. Though these first particle-beam lensing experiments have considerably advanced our knowledge, the physical mechanisms responsible for the formation and propagation of the EM discharge pulse are not entirely understood.

The remainder of this section firstly shows experimental results, that are then interpreted in a heuristic manner. Secondly, PIC simulations are presented that support basic assumptions made for the heuristic analysis and allow further insights in the discharge pulse dynamics. The EM discharge pulse is separated from EMP

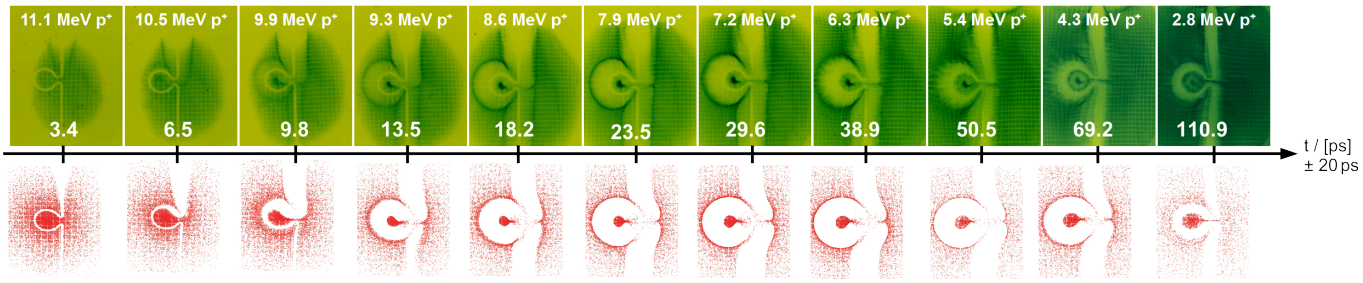

Figure 5.50: RCF proton imprints for different probing times within one shot (top) - the corresponding synthetic images are obtained by coupled dynamic target discharge pulse and test-particle simulations (bottom). The laser pulse impacts in the target above the field of view, we see the discharge pulse coming from the top and following the target geometry. The un-driven Ω-Coil in the upper left RCF has a diameter of 500 µm and all images have the same spatial scale. For late times, features like a ring-shaped caustic inside the coil and filaments are visible in the data.

and relativistic electrons. Thirdly presented are approaches to a heuristic modelling of the discharge pulse amplitude and an analytical formulation of the discharge pulse dispersion.

Results and Interpretation

Deflectometry results from one single sample shot with a Disk Ω-Coil Target are shown in fig. 5.50. Results are similar with all target types. For early times the target appears to be unaltered: deflections of protons then result from scattering in the solid density wire. Strong deflections away from the target rod with sharp caustics appear a few ps after driving the discharge target. The deflections decrease exponentially back to zero after a peak value is reached - they are not due to a thermally expanding target but rather to an EM effect. The wavefront propagation of an EM discharge pulse along the target wire is clearly evidenced though this sequence of images.

The data shows that even the demonstrated platform of simple geometry is straight forward applicable to energy selective tailoring of laser-accelerated particle beams. For this very shot, 8.6 MeV and 9.3 MeV protons are affected by the peak amplitude of the propagating pulse. For both energies, we observe the most intense and smallest spots on RCF that issue from protons passing along the symmetry axis through the loop. Changes of proton beam emittance mostly arise due to a loss of a fraction of the particle beam that is due to the strong EM forces, and post-acceleration effects. A determination of the beam emittance after passage of the loop is difficult in one only shot: it would require knowledge about the particle phase-space measured at three consecutive distances. Due to the presence of the RCF stack, the energy resolved spatial shape of the beam can only be determined at one position per shot. Note that identical reference shots with un-driven discharge targets require a perfect shot-to-shot reproducibility yet not feasible at high power laser facilities. A rudimentary emittance estimate is now done with a series of two distinct laser shots. Accordingly, one needs to presume either beam focusing prior to the RCF or a change in divergence only, which may lead to a focus beyond the RCF position. In cases where 6.3 MeV protons are affected by the discharge's peak, presuming a reduction of beam divergence, the beam emittance shrinks by a factor ≈ 3 compared to cases without driving the coil: from initially $1.59(5)$ mm mrad to $500(1) \cdot 10^{-3}$ mm mrad.

Seven shots allowed to see the wavefront propagation imprinted on consecutive RCF. The measured mean group velocity v_g of the wavefront along the Cu-target rod is $(0.82 \pm 0.06) \cdot c$, with the minimum value

Table 5.1: Group velocity of the wave front along straight sections of the Cu wire in units of the speed of light c. Laser parameters and target material were not intentionally varied. For two shots error bars are adapted to the interpretation of a causal wave propagation, the uncertainty of the original measurement overlaps with values that overpass the speed of light. Shot #25 allows observation of the wave front in two consecutive pairs of RCF, yielding two measurements that agree within the margin of their uncertainty.

Shot #	Discharge-Target Driver Energy	Target Type	Group Velocity v_g
11	51.5 J	DPCT	$(0.77 \pm 0.10) \cdot c$
21	51.5 J	DPCT-f	$(0.82 \pm 0.05) \cdot c$
22	47 J	DCT	$(0.82 \pm 0.18) \cdot c$
37	53.5 J	DCT	$(0.78 \pm 0.20) \cdot c$
41	41.4 J	DCT	$(0.95\ ^{+0.05}_{-0.10}) \cdot c$
25	44.3 J	DLT	$(0.80 \pm 0.08) \cdot c$
25	44.3 J	DLT	$(0.78 \pm 0.09) \cdot c$
39	51 J	DLT	$(0.81\ ^{+0.19}_{-0.25}) \cdot c$

$(0.77 \pm 0.10) \cdot c$ and the maximum value $(0.95\ ^{+0.05}_{-0.10}) \cdot c$. All measurements are given in Table 5.1. Note, the variation may be due to differences in the effective laser pulse power on target from shot to shot but also for variations in surface quality from target to target issuing from the laser cutting. Note also, that the driver energy is deduced from measurements before pulse amplification and not checked on a shot to shot basis.

Quantitative analysis firstly aims at an approximation of the electric component of the discharge pulse. In literature, most simplified modelling considers the discharge pulse to be a moving linear charge-density distribution $\lambda(\vec{x}, t)$. Following this assumption, one presumes that the E-field has a stronger influence than the B-field on radial deflections of probing protons along the straight target rod, for the accessed TNSA proton energy range of 1 MeV to 20 MeV, well below relativistic values. The proton deflection angle results of an acceleration perpendicular to the directrix of the hyperbolic particle orbit, see fig. 5.51. As first approximation, one neglects changes in the velocity component parallel to the directrix. Secondly, one sets equal the norm of in- and outgoing velocity vector for trajectories from negative and positive infinity. In the limit of small deflection angles Θ, we derive

$$\lambda \approx \frac{4\pi\epsilon_0}{q_\mathrm{p}} \cdot \frac{\gamma_\mathrm{p} m_\mathrm{p} v_\mathrm{p}^2}{2} \cdot \frac{\Theta}{\pi} \tag{5.28}$$

with m_p, q_p and v_p being the probing proton mass, charge and velocity respectively, ϵ_0 is the vacuum permitivity and γ_p the Lorentz factor. With observed deflections of the order of 3° for protons of 10 MeV, we obtain the order of 20 nC mm^{-1}.

Accordingly, fig. 5.52 shows the temporal evolution of the change of proton kinetic energy perpendicular to the TNSA axis and the deduced evolution of the charge distribution. The temporal axis is given with respect to target drive, and individual measurements are compared using their respective arrival time at the Ω-coil.

The peak of $\approx$25 nC mm^{-1} rises during 10 ps and has a FWHM of 50 ps. The smooth peak is followed by an exponential decay. A modified Weibull function with purely exponential tail fits this evolution, reading

$$f(t) = \frac{Q_0}{k + \mathrm{e} - 1} \cdot \begin{cases} 0 & \text{if } v_\mathrm{g} t \leq 0 \\ \frac{k}{\sigma} \left(\frac{v_\mathrm{g} t}{\sigma}\right)^{k-1} \exp\left[1 - \left(\frac{v_\mathrm{g} t}{\sigma}\right)^{k}\right] & \text{if } v_\mathrm{g} t \leq \sigma \\ \frac{k}{\sigma} \exp\left[1 - \left(\frac{v_\mathrm{g} t}{\sigma}\right)\right] & \text{if } v_\mathrm{g} t > \sigma \end{cases} , \tag{5.29}$$

where Q_0 denotes the normalization factor of the function representing the total target discharge and e is Euler's number, exp [1]. The form parameters fits to $k = (1.25 \pm 0.02)$ and the characteristic pulse length to $\sigma = 10.1(3)$ mm, with $v_\mathrm{g} = 0.82 \cdot c$. Integration of the fitting curve yields an equivalent total target discharge of $Q_0 = 342(5)$ nC.

The deduced evolution is tested with synthetic deflectometry based on dynamic test-particle transport- and EM field simulations with PAFIN, see section 7.2. Note that an earlier analysis of the discharge stream around the omega shaped part of the target rod [M. 16] pointed out that a charge density on the wire alone, creating electrostatic fields, is not accurately reproducing the experimental proton-deflections. The current density of an EM mode is derived from the measured group velocity and the fit of the discharge pulse via solution of the 1D continuity equation, assuming a constant group velocity v_g,

$$I(x,t) = v_\mathrm{g} \cdot \lambda(x,t) \quad . \tag{5.30}$$

The discharge current $I(x,t)$ induces a B-field which co-propagates with the E-field. No influence of neither $\partial\vec{E}/\partial t$ nor the temporal change of the vector potential are taken into account. Simulations do not consider the retarded character of fields for their large ps lifetime on the timescale of probing projectiles.

The dynamic simulations maintain the fitted pulse shape, but re-normalize it to different total charges Q_0. The best fitting simulation results in the bottom row of fig. 5.50 are compared to their exact experimental counterparts in the top row. Note the perfect agreement of asymmetric features of focused particles in the coil centre for early probing times for $Q_0 = 300$ nC. The dynamic simulations are in a very good agreement with space- and time-scales of the experimental data, particularly the deflections around the straight part of the wire. Some small deviation of simulated deflectograms and experimental results arise in vicinity of the Ω-legs of the coil. The neglect of $\partial\vec{E}/\partial t$ and the retarded character of fields may contribute to the mismatch. The re-normalized peak is compared to the original fit in fig. 5.52 as the red curve.

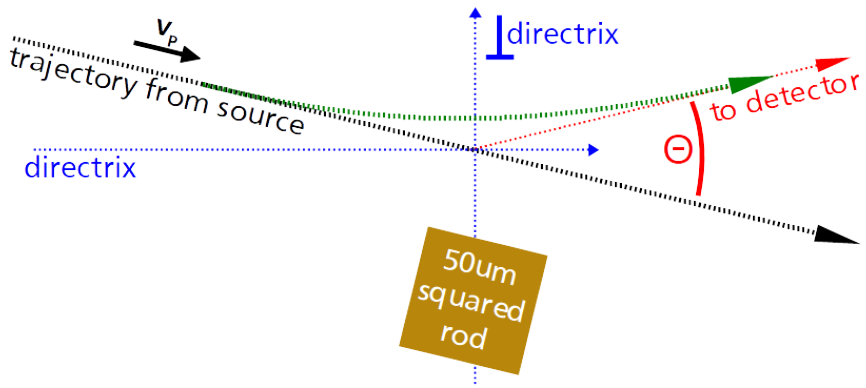

Figure 5.51: The geometry of the probing particle deflection around the target rod.

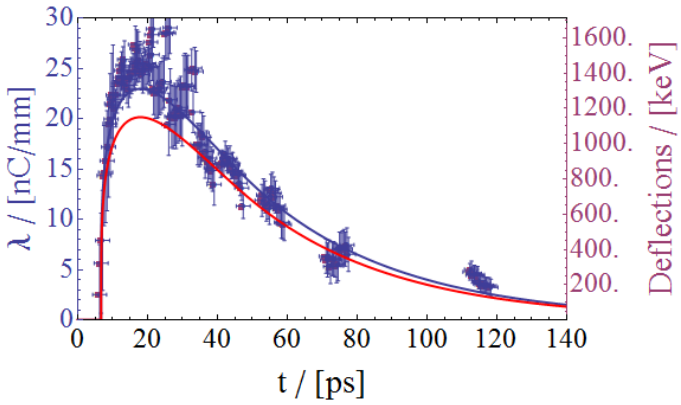

Figure 5.52: Evolution of the discharge pulse extracted upon electro-static assumptions from deflectometry data in fig. 5.50 (using eq. (5.28)) around straight wire sections of a Disk Ω-Coil Target. The relative timing is evaluated with respect to the arrival time at the Ω-Coil. The gain of proton kinetic energy perpendicular to the TNSA axis is indicated on the plot's right hand side. $t = 0\,\mathrm{ps}$ corresponds to the driver laser impact, the temporal uncertainty comprises the range of proton energies imprinted within one active layer and the time the probing protons are in vicinity of the deflecting charge distribution, which is assumed to be of the order of the void around the wire. The data points correspond to measured deflections. The blue curve represents a fit with eq. (5.29) and integrated charge of $342(5)\,\mathrm{nC}$. The red curve corresponds to the renormalized fit with an integrated charge of $300\,\mathrm{nC}$, this peak corresponds to the dynamically deconvoluted discharge peak.

The full field maps show that the streaming EM pulses have amplitudes of tens of $\mathrm{GV\,m^{-1}}$ and tens of T. In order to understand the influence of such low amplitude B-field of several T in respect to electrostatic effects on TNSA protons of several MeV, one follows protons traversing the loop on the symmetry axis. Projectiles run up the potential well ahead of the coil and decelerate. Equating the potential of an uniformly charged ring and the proton kinetic energy yields an analytical estimate of the upper limit for the deceleration prior to the target,

$$\Delta v_{\parallel\mathrm{TNSA}} \leq \sqrt{\frac{q_\mathrm{p}\lambda}{m_\mathrm{p}\epsilon_0}} \approx 3.3 \cdot \sqrt{\lambda_{\mathrm{nC\,mm^{-1}}}} \quad [\mathrm{\mu m\,ps^{-1}}] \quad . \tag{5.31}$$

Amplitudes of $\lambda = 20\,\mathrm{nC\,mm^{-1}}$ lead to deceleration by $\Delta v_{\parallel\mathrm{TNSA}} \approx 15\,\mathrm{\mu m\,ps^{-1}}$, the speed of 1.1 MeV protons. Protons of several MeV kinetic energy have velocities of several $10\,\mathrm{\mu m\,ps^{-1}}$ – thus the relative change in velocity is non-negligible.

The electric component of the pulse is responsible for axial deceleration of ions prior to their transit through the coil - the magnetic component thereby has a stronger focusing power on ions passing the field's maximum in vicinity of the coil. After transit of the coil plane, the E-field leads to a re-acceleration maintaining the in- and out-going kinetic energy of particles approximately equal. The charge density peak is asymmetric and decelerating and accelerating potential vary. In simulations, the difference of particle energies before and after passing the coil is of the order of hundreds of keV.

Access to the full phase space of the probing particles gives further insight in the dynamic processes in vicinity of the conductor rod. Before passing the wire, the particle decelerates in the direction parallel to the directrix of the hyperbolic particle orbit. This violates the first assumption made to derive the charge density. Such

decrease in velocity leads, following the analysis with eq. (5.28), to an overestimation of the linear charge distribution by a factor of up to

$$\frac{\lambda\left(v_{\parallel\mathrm{TNSA}}\right)}{\lambda\left(v_{\parallel\mathrm{TNSA}}-\Delta v_{\parallel\mathrm{TNSA}}\right)}=\frac{v_{\parallel\mathrm{TNSA}}^{2}}{\left(v_{\parallel\mathrm{TNSA}}-\Delta v_{\parallel\mathrm{TNSA}}\right)^{2}}. \tag{5.32}$$

The ratio of the total discharge value derived with first electrostatic assumptions and the re-normalized charge of the best-fitting dynamic simulation is 1.14 ± 0.18. For probing protons of 8.8 MeV, this ratio corresponds to $\Delta v_{\parallel\mathrm{TNSA}} \approx 2.6\,\mu\mathrm{m\,ps}^{-1}$ following eq. (5.32) – equal to a deceleration to 7.7 MeV. This agrees with the dynamic simulations that show that the change of kinetic energy reaches the order of 1 MeV.

Temporal Resolution of the Diagnostics

Proton deflectometry results must be regarded with great caution for the temporal resolution of the diagnostics. The interaction of pulse and particle beam starts with particles that already passed the wire and evolves on smaller timescales than the particle transit time. Presuming the validity of the fit function eq. (5.29) with $\lambda(t) = f(t)$, the peak of the pulse is attained for

$$\tau_{\mathrm{rise}}=\sqrt[k]{\frac{k-1}{k}}\cdot\frac{\sigma}{v_{\mathrm{g}}}\overset{\mathrm{exp}}{=}11.3(12)\,\mathrm{ps}\gg\tau_{\mathrm{L}} \tag{5.33}$$

with rise time τ_{rise}. As seen in fig. 5.52, the discharge pulse rises for about $22\times$ the laser pulse duration. This result may be due to the temporal resolution of charged particle beam deflectometry in the low-MeV u^{-1} projectile energy range, but also indication of a target discharge in the explosive regime on timescales longer than the laser drive [Poy+18]. A later section refers to the charging dynamics, the following estimates concern the temporal resolution of the diagnostics.

The discharge pulse travels with about $250\,\mu\mathrm{m\,ps}^{-1}$ which is approximately 5 – $25\times$ faster than the probing protons at $10\,\mu\mathrm{m\,ps}^{-1}$ for 1 MeV kinetic energy and up to $60\,\mu\mathrm{m\,ps}^{-1}$ for 20 MeV. During the steep first 4 ps of the full 11 ps rising edge, the protons propagate 40 µm to 240 µm. Dynamic simulations show that the propagating EM fields affect protons passing as far as approximately 250 µm distance from the wire. We estimate that protons are subdue to interaction on trajectories shorter than 500 µm and see that the fastest protons need twice the duration of the steep rising edge to travel through the hyperbolic orbit in vicinity of the target. Deflectometry results on these timescales are strongly convoluted. The pulse may have a shorter rise time with steep spatial gradients of the potential yielding three dimensional deflections that are not covered by the analysis according to eq. (5.28).

This ambiguity on the leading edge of the discharge pulse motivates further investigation with a better temporal resolution for the peak, *e.g.* by the use of short laser-pulse probing for future experiments based on electro- and magneto-optic effects in thin film crystals [Wil+02; Bis+17].

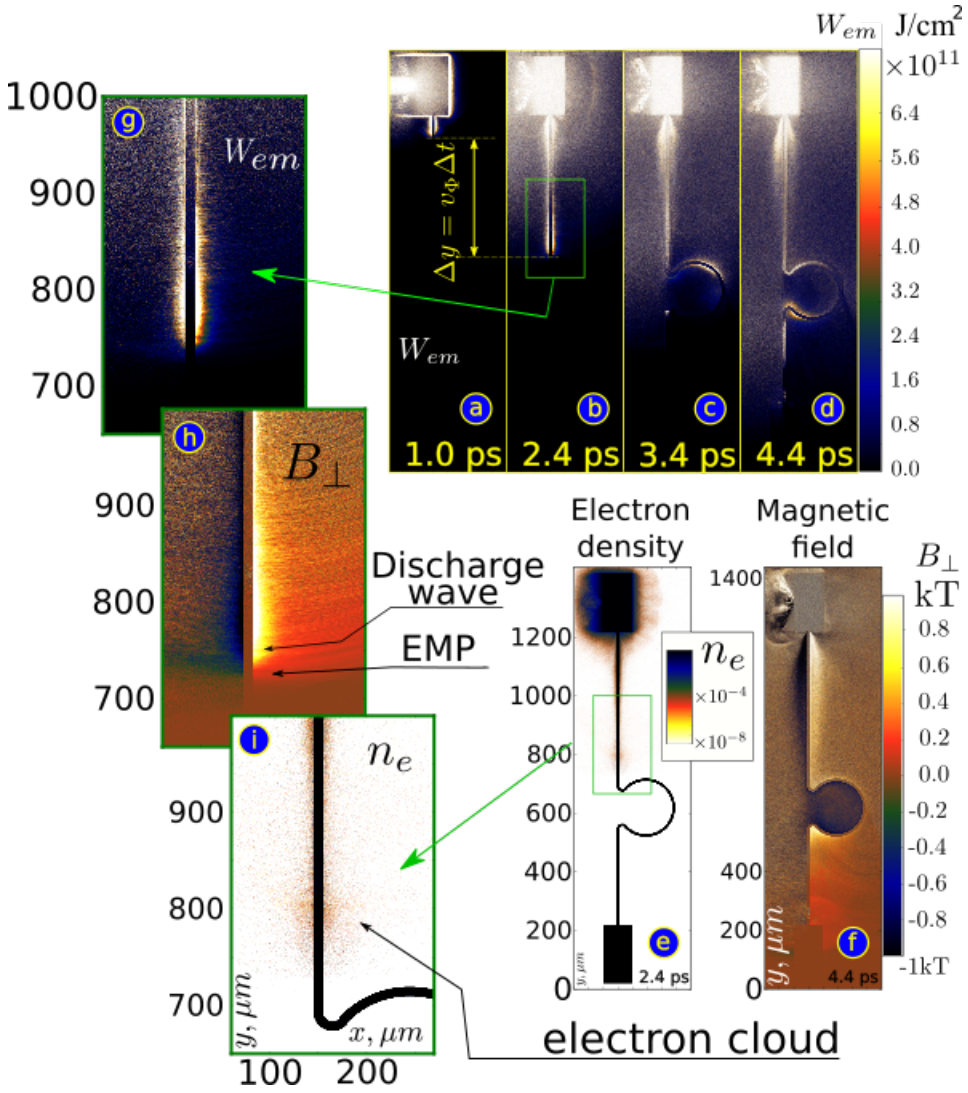

Figure 5.53: Down-scaled 2D PIC simulations of the laser driven discharge on Disk Ω-Coil Targets show target bound discharge pulse, EMP in free space and an accelerated electron cloud following the discharge peak along the target wire. Panels (a – d,g) show the EM energy-density in units of the 2D simulation, (f,h) the B-field strength perpendicular to the simulation plane and (e,i) the electron density in units of $10n_c$. (g,h) highlight the spatially pulsed character of the discharge wave and (i) shows the accelerated electron cloud.

Particle in Cell Simulations

With the evidence of pulsed electric and B-field components streaming along the target rod, 2D PIC simulations of the laser-target interaction with PICLS [Mis+13] are performed for a deeper understanding of the nature of the discharge pulse. The simulations resolve the successive propagation of EM waves and accelerated particle species. First, five times down-scaled simulations capture the whole target geometry and distinguish between transient EM effects: the propagation of fast electrons, EMP emission and guided EM discharge pulse. In a second step, real-scale 2D PIC simulations are used to study the generation of hot electron current and return current as well as associated EM fields.

The down-scaled simulations (all sizes except the coil diameter) employ a driver laser pulse at the intensity of $10^{19}\,\mathrm{W\,cm^{-2}}$ comparable to the experiment but with $800 \cdot 10^{-3}$ µm wavelength and a pulse duration of 1.33 ps. The pulse interacts with the target in normal incidence with a 16 µm FWHM focal spot. Its E-field oscillates in the simulation plane. The spatial and temporal profiles are flat top with Gaussian edges. The target plasma is composed of Hydrogen (H) ions and electrons with a initially uniform $10n_c$ density. The initial electronic and hydrogen temperatures are set to zero. The spatial step in both dimensions is 40 nm. The time step is $100 \cdot 10^{-3}$ fs. The boundary conditions used are absorbing in both dimensions. Binary collisions and field ionization are not taken into account.

The resulting EM energy-density $w_{\mathrm{em}} = B_\perp^2/2\mu_0 + \epsilon_0 E_\parallel^2/2$ is given in Figure 5.53 (a – d,g) for different times. The driver laser pulse is injected at the left side of the simulation box. We see a discharge pulse bound to the target geometry at a high energy density, of several $10^{11}\,\mathrm{J\,cm^{-2}}$, and propagating at the velocity $0.964c$, close to the speed of light. Its spatially pulsed character is highlighted by a zoom in Figure 5.53 (g). The B-field amplitude perpendicular to the simulation plane is given for the same time in Figure 5.53 (h). A spherical EMP in free space, that emanates from the interaction region with the velocity of light, distinguishes from the guided EM discharge pulse, that is slightly slower. For late times of 4.4 ps depicted in Figure 5.53 (f), we see strong B-fields in the vicinity of the laser-plasma interaction region. This indicates a return current building up.

The electron density 2.4 ps after the interaction started is shown in Figure 5.53 (e), and detailed in Figure 5.53 (i). Aside the plasma expansion in the hot interaction region, we identify a population of electrons that co-propagates with the discharge pulse.

The E-field streaming along the target has a mono-mode characteristic in comparison to the fast oscillating EMP. The amplitude of the radial E-field at straight wire sections is $100\,\mathrm{GV\,m^{-1}}$ in the simulation, scaling to $20\,\mathrm{GV\,m^{-1}}$ in the experimental frame. The simulated amplitude of the B-field component around the target rod is 500 T, in the coil's centre it decreases to 100 T. Scaling to the experimental coil-size leads to ≈20 T in the coil center. Both components agree in field strength with the values in the previous section heuristically deduced from experimental data. The PIC simulations confirm a very strong radial E-field, and a weak azimuthal magnetic field. The electric fled dominates the Lorenz force around straight wire sections. Accordingly our initial assumption that there is mainly an E-field effect is justified.

More detailed 2D PIC simulations are used to study the generation of hot electron current and return current as well as associated EM fields on real-scale 50 µm thick foils. Here, we solely simulate the laser-target interaction region and a successive straight conductor section. The incident laser pulse with 1 µm wavelength and a pulse duration of 100 fs has a maximum intensity of $10^{19}\,\mathrm{W\,cm^{-2}}$ within the 3.5 µm FWHM of the focal spot. The pulse interacts with the target in normal incidence. Its E-field is in the simulation plane. The spatial and temporal profiles are truncated Gaussians. The target plasma is composed of Al ions and electrons with a $700n_c$ maximum density. A 1 µm longitudinal scale-length exponential pre-plasma is present in front of

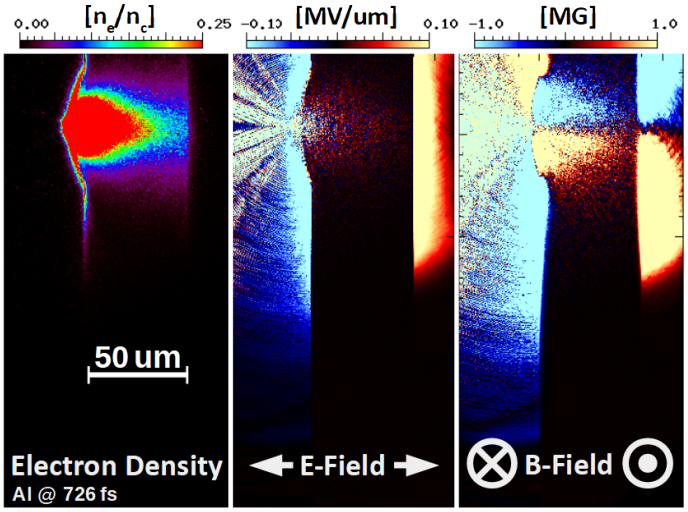

Figure 5.54: Real-scale 2D PIC simulations showing the electron energy density, instantaneous E_x E-field, with horizontal axis x and instantaneous B_z magnetic field, with z the axis pointing out of the image plane, 726 fs after the beginning of the simulation.

the target with a Gaussian transverse profile and a total length of $\Delta y = 10\,\mu\text{m}$. The initial electronic and aluminum temperatures are set to zero. The spatial step in both dimensions is 20 nm and there are 2 Al ions and 26 electrons per cell. The time step is $66 \cdot 10^{-3}$ fs. The boundary conditions used are absorbing in both dimensions. Field ionization using the ADK formula [PPT66; MNV86] is taken into account as well as impact ionization. Binary collisions are also taken into account.

Instantaneous magnetic and E-fields as well as the electron density are shown in fig. 5.54, 726 fs after the beginning of the simulation. The laser pulse is injected at the left side of the simulation box. The maximum of the laser pulse enters the plasma after 330 fs. We observe an azimuthal B-field B_z of the order of 100 T appearing inside the target as well as in the vicinity of the target rod, see fig. 5.54.The B-field inside the target is typical for laser-accelerated electrons. Even though there are electrons down-streaming the target from the laser-interaction surface, the orientation of the surface B-field is clearly indicating a positive charge density propagation. The E_x E-field in fig. 5.54 has a peak amplitude of several $100\,\text{GV}\,\text{m}^{-1}$, and its sign agrees with a positively charged target.

The simulation reveals different EM waves originating from the interaction region at both surfaces of the target: a spherical EMP in free space is visible on the front side, propagating with the velocity of light and a discharge pulse propagates along front and rear target surfaces. The different progress at front and rear surface can be explained by the delayed build up of the potential at the target rear side. From the time evolution of the B_z and E_x fields along the target surface, the velocity of the downward propagating EM mode on the front surface is measured to be $0.87c$. This is in good agreement with the experimental values, regarding both Cu and Al as similar perfect conductors.

One notes that the surface B-field is present in depth not indicating any E-field, which hints the build up of strong a return current in the target skin depth. This is most pronounced in vicinity of the laser heated region in areas where the target is cold, and decreases towards the wavefront of the EM mode. The steep rising edge of the amplitude of the B-field field in vicinity of the wavefront on the conductor front surface has a rise time of $144(48)$ fs, the order of the driver laser pulse duration in the simulation. This corresponds to a current induced by direct target discharge via ultra-relativistic electrons. The thereafter building up return current is

due to relativistic electrons, escaping the target on a longer timescale after scattering events inside the target. Further, the E-field at the target rear reaches highest values around the wavefront of the EM mode, dipping towards the laser axis. Also there, return currents towards the axis inside the target are indicated by B-fields. The dip in the underlying potential is likely due to axial and radial neutralization current dynamics.

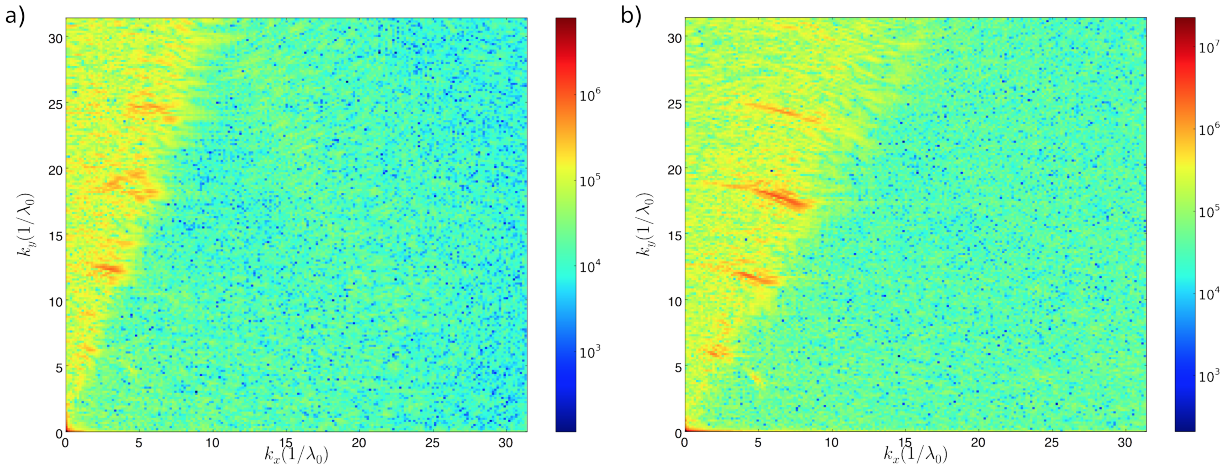

Figure 5.55: 2D Fourier transformation of the B-field maps in squared slices of $40\,\mu$m width and height adjacent to the target front surface (a) close to the interaction region and thus related to late times, and (b) far from the interaction region and thus related to earlier times.

The instantaneous B-field after 726 fs has been analysed in two squared slices of $40\,\mu$m width and height corresponding to regions on the target front surface: the first starting 64 µm underneath the laser axis, and the second at 104 µm. The spatial separation ensures that these two regions will contain EM fields and particles emitted at different stages of the laser-plasma interaction, the first region at early times and the second region at late times. Results of 2D Fourier transformation of the B-field maps in fig. 5.55 show that certain harmonics of the laser frequency dominate the signal, with a contrast of about 80 % in respect to the rest of the quasi-continuous signal. This continuous baseline has itself a 80 % contrast in respect to the background. The closer region has a signature with a dominant second harmonic, whereas the far region shows more signal in the third harmonic.

Summary of Evidence from Data and Simulations

Experimental results are successfully reproduced by heuristically modelling the discharge pulse as moving charge density distribution, taking into account B-fields. The group velocity of the pulse is lower than the speed of light, with experimental results being in qualitative agreement with collisional PIC simulations. Data suggests that the rise time of the EM discharge pulse is of the order of ten ps. PIC simulations show in detail that the rise time of the transient wavefront is on the order of the driver laser pulse duration, but also that the potential dynamics evolves on longer timescales than simulated, and therefore the return current dynamics.

The inferred dynamics of the guided EM discharge pulse, with clear evidence of a spatial EM pulse with a mostly mono-mode transverse E-field structure, motivates modeling efforts in order to conduct studies that do not require costly PIC simulations.

5.2.3.3 Modelling of the Electromagnetic Discharge Pulse

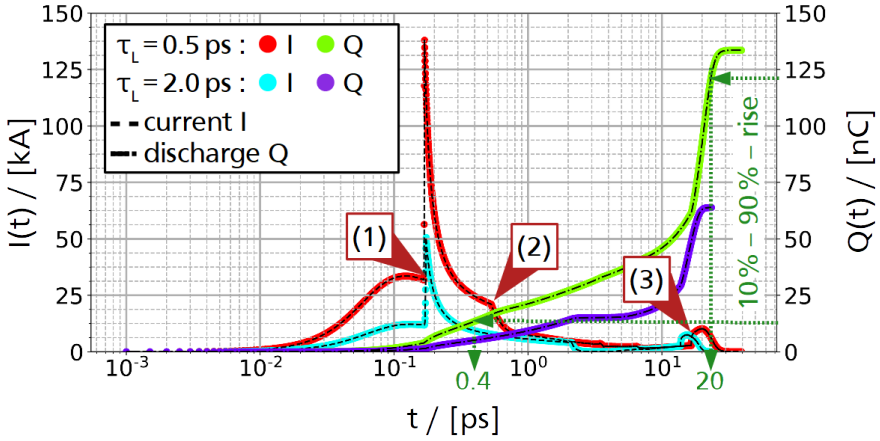

Figure 5.56: Target discharge current I (red, cyan) and total target charging Q (green, violet) simulated with ChoCoLaT2 for the experimental laser parameters but two distinct pulse durations of $500 \cdot 10^{-3}$ ps and 2 ps and 50 % absorption efficiency. Indicated are times corresponding to (1) the apparition of the target rear side current due to electrons that traversed the target, (2) the laser pulse end and (3) the moment when the average Debye length of the initially exponential hot electron distribution in the target becomes larger than the target thickness, due to collisional cooling and ejection of most energetic electrons.

A first detailed attempt to model target charging in short laser pulse interactions [A. +15b; Poy+18] allows to predict the expected discharge current due to relativistic electrons. The numerical code ChoCoLaT2 simulates laser electron heating on a thin disk target and successive electron escape mitigated by the target potential, based on the driver laser parameters and the interaction geometry. It takes into account the collisional cooling of electrons within cold solid density targets. The energy and time depended hot electron distribution function $f(E,t)$ describes electrons inside the target and evolves with

$$\partial_t f(E,t) = \frac{h_\mathrm{L}(E)\Theta(\tau_\mathrm{L}-t)}{\tau_\mathrm{L}} - \frac{f(E,t)}{\tau_\mathrm{ee}(E)} - g(E,t) \tag{5.34}$$

$$h_\mathrm{L}(E) \stackrel{!}{=} \frac{N_0}{T_0}\exp\left[-E/T_0\right] \tag{5.35}$$

$$N_0 \stackrel{!}{=} \int f(E,0)\,\mathrm{d}E \tag{5.36}$$

where $h_\mathrm{L}(E)$ is a constant exponential source of hot electrons, $\Theta(t)$ the Heaviside function limiting electron heating to the laser duration, $\tau_\mathrm{ee}(E)$ the energy dependent cooling time and $g(E,t)$ the rate of electron ejection from the target. The initial hot electron temperature T_0 depends on laser wavelength and pulse intensity [FMF85; Beg+97; Wil+92]; and N_0 is re-normalized to the energy balance $N_0 T_0 = \eta E_\mathrm{L}$ between the total energy of hot electrons in the target and the absorbed laser energy.

With the experimental interaction parameters and a laser absorption between 30 % and 50 %, ChoCoLaT2 simulations result in a target discharge of $Q_0 = 150(20)$ nC. This is of the same order of magnitude as experimental results. Taking into account that ChoCoLaT systematically underestimates target discharge by a factor of 2 to 3 [Poy+18], the agreement is fairly good. Based on such simulation of the target discharge

dynamics, the following section presents heuristic estimates for the EM discharge pulse amplitude in the conductor rod. The starting points of two approaches are respectively (i) the maximum current density and (ii) the maximum charge density produced in vicinity of the interaction region. The attainable maxima will be related to the target geometry in order to find an estimate for the discharge-pulse peak maximum along wire sections.

Furthermore, the discharge wave dispersion is explored for a better understanding of the group velocity difference to the speed of light.

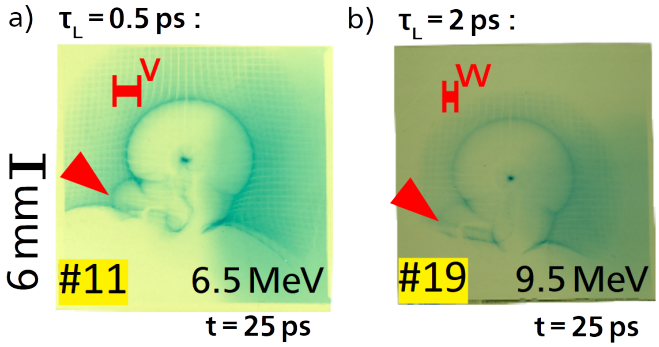

Figure 5.57: Deflectometry results of driven Double-Plate Coil Targets from two independent shots employing (a) a short driver laser pulse length of $500 \cdot 10^{-3}$ ps compared to (b) a long driver laser pulse length of 2 ps with fixed focal spot size. The PHELIX energy for shot #11 is 51.5 J and for #19 it is 49.7 J. The deflections (v) and (w) around the vertical stalk (indicated with a red arrow) to the front plate of the Double-Plate Coil Target geometry indicate pulse amplitudes of $\lambda_v \approx 18(6)\,\mathrm{nC\,mm^{-1}}$ and $\lambda_w \approx 15(5)\,\mathrm{nC\,mm^{-1}}$.

5.2.4 Peak Amplitudes

ChoCoLaT2 simulations show that the target discharge evolves on longer timescales τ_Q than the laser drive, which is related to the hot electron cooling. Results of target discharge simulations in fig. 5.56 show a 10 %-90 % rise time of 20 ps, which is the order of the experimentally observed 11 ps. The discharge dynamics show piece-wise logarithmic growth, with two intervals of $\Delta Q_1/Q_0 \approx 40$ % and $\Delta Q_2/Q_0 \approx 60$ %.

A first modelling approach derives the discharge pulse amplitude in the limit of a steady state target discharge. A second approach follows, where the rapidly induced surface charge density is seed to a pulse of coupled polarization and surface waves, as it was recently discussed in [Bra+20b; BKB20]. Both approaches are compared to experimental results of discharge pulse amplitudes obtained under variation of the driver laser pulse length, shown with fig. 5.57. Experimentally, the discharge pulse amplitude decreases only slightly to (83^{+13}_{-42}) % for shots performed with longer laser pulse duration of $\tau_L = 2$ ps. Note that in this shots with Double Plate Ω-coil Targets, the pulse reaches the front plate after 16(2) ps, and the probing time of 25 ps therefore images the vicinity of the pulse peak on the stalk section.

Following the ChoCoLaT2 modelling, with the longer pulse length decreasing the laser intensity, the initial hot electron temperature decreases and thus the amount of ejected charge. Relevant for the first approach, the simulated target discharge currents show a decrease of the amplitude down to (37 ± 8) % for a longer laser pulse duration, this agrees in the margins of the respective uncertainties with the measured values.

Regarding the second approach, the simulated total target discharge shows a decrease of the amplitude down to (47 ± 7) % for a longer laser pulse duration, which also is in fair agreement with the measurement.

In the first heuristic approach, one presumes the target discharge rate $[\partial_t Q]^{\text{ChoCoLaT}} = [I]^{\text{ChoCoLaT}}$ as direct source to the current carried by the discharge pulse. As primary consequence, the discharge pulse rise time can be directly related to the rise time of the target discharge. The radial current density on the disk approximates to

$$j_r(r,t) = \frac{r \int_0^r [I]^{\text{ChoCoLaT}}(R,t)\,\mathrm{d}R}{\pi \mathfrak{D}^2 \cdot \delta_z}, \tag{5.37}$$

with skin depth δ_z. For uniform target discharge affecting a cylindrical region with radius $\mathfrak{D}$, hence with $[I]^{\text{ChoCoLaT}}(r,t) = I_0(t) \cdot \Theta[\mathfrak{D} - r]$, eq. (5.37) simplifies to

$$j_r(r,t) = -\frac{I_0(t)}{\pi \mathfrak{D}^2 \cdot \delta_z} \cdot \max\left[0; \min\left[\frac{r}{2}; \mathfrak{D} - \frac{r}{2}\right]\right], \tag{5.38}$$

where $\Theta[x]$ is the Heaviside function. The maximum current density is located at the edge of the cylinder and calculates to

$$j_r(\mathfrak{D},t) = -\frac{I_0(t)}{2\pi \mathfrak{D} \cdot \delta_z} \leq \frac{[I_{\text{max}}]^{\text{ChoCoLaT}}}{2\pi \mathfrak{D} \cdot \delta_z} \tag{5.39}$$

with a maximum target discharge current $[I_{\text{max}}]^{\text{ChoCoLaT}}$. One notes a inverse proportionality to the radius $\mathfrak{D}$.

The second heuristic approach does not take into account the detailed discharge current dynamics but focuses on a building up charge density on the target surface. This charge density is distributed in the interaction region and a adjacent belt area within the light cone along the conductor surface. In order to simplify the dynamic problem, one assumes that the target gets charged to the total target discharge Q_0 essentially for a duration τ_{Q}. Dividing this charging time in $N \in \mathfrak{N}_+^0$ iterations, the laser-target interaction leads to a zone with a net loss of electrons $\delta Q_i(t)$ per timestep $\tau_i = \tau_{\text{Q}}/N$. Further one assumes this region to be a disk with radius $\mathfrak{D}$, and that from there the potential expands over the target surface with a constant group velocity v_{g}. In this scheme the charge density within the boundary $\mathfrak{D}$ is uniform and at the maximum amplitude during charging. Only taking into account radial forward propagation, one obtains a recursion relation in which the full charge density $\sigma(r,t)$ on the disk is re-normalized to the expanded surface in each time step. The charge integrates to

$$\begin{aligned}
\Sigma(\mathfrak{D},i) &:= \int_0^{\mathfrak{D}} \sigma(r,t(i))\,\mathrm{d}S \\
\Sigma(\mathfrak{D},i=0) &:= 0 \\
\Sigma(\mathfrak{D},i+1) &:= \left(1 - \frac{\left(\mathfrak{D} + v_{\text{g}}\tau_i\right)^2 - \mathfrak{D}^2}{\left(\mathfrak{D} + v_{\text{g}}\tau_i\right)^2}\right) \Sigma(\mathfrak{D},i) + \delta Q_i \\
\Leftrightarrow \Sigma(\mathfrak{D},i+1) &= \frac{\Sigma(\mathfrak{D},i)}{\left(1 + v_{\text{g}}\tau_i/\mathfrak{D}\right)^2} + \delta Q_i \quad .
\end{aligned} \tag{5.40}$$

This is well known as the Tower of Hanoi recursion type and can be solved to

$$
\begin{aligned}
d :=& \frac{1}{\left(1 + v_g \tau_i / \mathfrak{D}\right)^2} \\
\Sigma\left(\mathfrak{D}, i > 0\right) =& d^i \cdot \Sigma\left(\mathfrak{D}, i = 0\right) + \cdot \sum_{n=0}^{i-1} d^n \delta Q_{i-1-n}, \\
\Leftrightarrow \Sigma\left(\mathfrak{D}, i > 0\right) =& \sum_{n=0}^{i-1} d^n \delta Q_{i-1-n},
\end{aligned}
\tag{5.41}
$$

with a solution for the limit superior of an infinite amount of time steps with constant discharge rate. We have in other words, a solution for steady state target discharge, reading

$$
\begin{aligned}
\lim_{N \to \infty} \Sigma\left(\mathfrak{D}, N\right) \leq & \frac{Q_0 \cdot \mathfrak{D}}{v_g \tau_Q} \left(1 - \exp\left[-\frac{v_g \tau_Q}{\mathfrak{D}}\right]\right) \\
=: & Q_{\max}.
\end{aligned}
\tag{5.42}
$$

In this crude estimate, the dimensionless ratio $v_g \tau_Q / \mathfrak{D}$ governs the limiting maximum of the charge for comparable discharge dynamics. In contrast to the first heuristic approach, the maximum decreases if only $\mathfrak{D}$ shrinks.

5.2.5 Influence of Target Dimensioning

The peak amplitudes for the discharge pulse can be related to the observable amplitudes far from the interaction region by taking into account the geometrical coupling of interaction region and target stalk, see fig. 5.58.

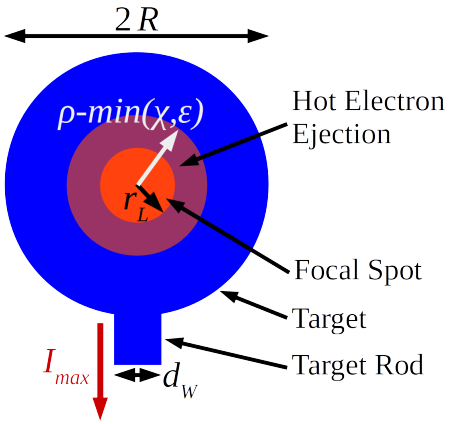

Figure 5.58: Discharge Disk of thickness ϵ and radius R, also indicated are the laser accelerated electrons' range, ρ, and the range until their first collision with an ion is represented by the depth, χ.

The laser intensity determines the hot electron temperature and with the target material one determines the electrons' range, ρ, and the range until their first collision with an ion, χ. For disk targets of thickness ϵ and radius R, charge limited are cases of compact targets where $R < \max\left[r_L + v_g \tau_L, \rho - \min\left[\chi, \epsilon\right]\right]$. Compact targets show dynamics on shorter timescales than discussed here. The radius $\mathfrak{D}$ is set to the focal spot radius $r_L \approx 25\,\mu\text{m}$, as electrons are mostly leaving this region. For the experimental case and at maximum absorption

efficiency, one determines $T_\mathrm{h} \approx 650\,\mathrm{keV}$ via the ponderomotive scaling of the hot electron temperature [Wil+92; MV+96], and with Cu targets $\rho - \epsilon \approx 365\,\mu\mathrm{m} > 148\,\mu\mathrm{m} \approx r_L + v_\mathrm{g}\tau_L$. The here discussed targets are not compact with $R > \rho - \epsilon$.

Following the first heuristic modelling approach, one obtains a maximum amplitude I_max for currents flowing through an attached rod with exit width $d_W << R$, see fig. 5.58. From eq. (5.39) follows for the exact moment when the discharge pulse reaches the disk boundary

$$\begin{aligned} I_\mathrm{max} &= \frac{d_W}{2\pi R} \cdot [I_\mathrm{max}]^\mathrm{ChoCoLaT} \\ \lambda_\mathrm{max} &= \frac{I_\mathrm{max}}{v_\mathrm{g}} \quad . \end{aligned} \tag{5.43}$$

The measured group velocity is now used to obtain $\lambda_\mathrm{max} \approx 4.3\,\mathrm{nC\,mm^{-1}}$ for $\tau_\mathrm{L} = 500 \cdot 10^{-3}\,\mathrm{ps}$. Note that the simulated total target discharge is a factor of 2.3 smaller than the experimental value. Scaling the current with this factor yields the estimate of $\approx$10 $\mathrm{nC\,mm^{-1}}$ for the discharge pulse peak. This value agrees only with the order of magnitude.

Following the second approach from eq. (5.42) results $Q^0_\mathrm{max}(\tau_\mathrm{Q})$ with

$$\Rightarrow Q^0_\mathrm{max}(\tau_\mathrm{Q}) := \lim_{N\to\infty} \Sigma\,(r_L, N) \quad . \tag{5.44}$$

Two scenarios for the potential evolution can be contrasted, (a) either a diffusive peak expansion with flattening of the charge density over time or (b) the formation of a pulsed peak that maintains the same amplitude. When the potential reaches the borders of the target, for (a) it will start to equalize over the full target disk, only spreading further along the grounding wire, and for (b) the peak will partially reflect, only coupling to the wire in its vicinity. Both cases can be distinguished by the resulting peak amplitude coupled into the target wire. One takes into account for (a) a renormalization of the maximum charge density with respect to the full surface of the disk, and (b) a peak of initial radius r_L. It follows

$$\begin{aligned} \lambda^\mathrm{a}_\mathrm{max} =& \frac{d_W}{\pi R^2} \cdot Q^0_\mathrm{max}(\tau_\mathrm{Q}), \\ \lambda^\mathrm{b}_\mathrm{max} =& \frac{d_W}{\pi\,(2\mathfrak{D}R - \mathfrak{D}^2)} \cdot Q^0_\mathrm{max}(\tau_\mathrm{Q}), \\ I_\mathrm{max} =& v_\mathrm{g} \cdot \lambda_\mathrm{max} \quad . \end{aligned} \tag{5.45}$$

The maximum size of the region affected by potential dynamics calculates to $\mathfrak{D} = r_\mathrm{L} + c\tau_\mathrm{Q}$. One sets $Q_0 \approx 300\,\mathrm{nC}$ in order to obtain the discharge time τ_Q which is necessary for $\lambda^\mathrm{a}_\mathrm{max}$ and $\lambda^\mathrm{b}_\mathrm{max}$ to attain the experimentally observed $20\,\mathrm{nC\,mm^{-1}}$, with $R = 1\,\mathrm{mm}$ and $d_W = 50\,\mu\mathrm{m}$. For (a) one obtains no possible solution. Case (b) requires a discharge time of 6.3 ps, which is consistent with the experimental rise time and points to a pulse in space and time.

As a summary, rise time and peak amplitude derived from both modelling approaches are compared to experimental values in table 5.2. The rough agreement of both modelling approaches is motivation for further studies to investigate how the discharge pulse comes into live.

Table 5.2: Comparison of figures of merit (rise time, peak amplitude and amplitude ratio for shots with longer and shorter driver laser pulse) derived by two modelling approaches and experimental data.

Derived from:	Rise Time:	Peak Amplitude:	$\lambda(\tau_\mathrm{L} = 2\,\mathrm{ps}\,)/\lambda(\tau_\mathrm{L} = 500\,\mathrm{fs}\,)$:
Experiment	11.3(12) ps	$20\,\mathrm{nC\,mm^{-1}}$	(83^{+13}_{-42}) %
1st Approach	200 fs	$10\,\mathrm{nC\,mm^{-1}}$	(37 ± 8) %
2nd Approach	6.3 ps	$20\,\mathrm{nC\,mm^{-1}}$	(47 ± 7) %

5.2.6 Discharge Wave Dispersion

Besides the amplitude, the main observed feature of the discharge wave propagation is the velocity of its wavefront, with experimental data in table 5.1. The following approach was developed in the framework of this dissertation by a large collaboration [EBGK+21]. In our modelling approach, the wire is described as a plasma cylinder with radius a, temperature T_e and electron density n_e. The propagation is considered in a far-distant wave zone using Maxwell equations in the cylindrical coordinate system (r, θ, z) with unit vectors $\vec{e}_r, \vec{e}_\theta, \vec{e}_z$, both inside and outside the plasma cylinder

$$\begin{cases} \left[\partial_z E_r(r,z,t) - \partial_r E_z(r,z,t)\right]\vec{e}_\theta = -\frac{1}{c}\partial_t \vec{B}(r,z,t), \\ \frac{1}{r}\partial_r\left[rB_\theta(r,z,t)\right]\vec{e}_z - \partial_z B_\theta(r,z,t)\vec{e}_r = \frac{1}{c}\partial_t \vec{D}(r,z,t), \\ \frac{1}{r}\partial_r\left[rD_r(r,z,t)\right] + \partial_z D_z(r,z,t) = 0. \end{cases} \tag{5.46}$$

Plasma properties are defined by the dielectric tensor, which non-zero components, in the simple case of Maxwellian collisionless plasma, read [LP81]

$$\varepsilon_{rr}(\omega,k) = 1 - \frac{\omega_e^2}{\omega^2} F\left(\frac{\omega}{\sqrt{2}kv_T}\right), \tag{5.47}$$

$$\varepsilon_{zz}(\omega,k) = 1 + \frac{\omega_e^2}{(kv_T)^2}\left[1 + F\left(\frac{\omega}{\sqrt{2}kv_T}\right)\right], \tag{5.48}$$

where

$$F(x) = \frac{x}{\sqrt{\pi}} \lim_{\delta\to 0} \int_{-\infty}^{\infty} \frac{e^{-z^2}}{z - x - i\delta} dz, \tag{5.49}$$

and $\omega_e = \sqrt{4\pi n_e e^2/m_e}$ is the electron plasma frequency, $v_T = \sqrt{T_e/m_e}$ is the thermal electron velocity, m_e is the electron mass.

To obtain the dispersion relation, the field components are transformed into their Fourier transform components,

$$\{E,B,D\}_i(r,z,t) = \int \{E,B,D\}_i(r,k,\omega)\cdot \mathrm{e}^{-i(\omega t + kz)} dk d\omega, \tag{5.50}$$

and substituted to (5.46), which provides a set of the second-order differential equations for cylindrical functions. The solutions should be finite at $r \to 0$ and $r \to \infty$, and also they must be joined at the edge of the

plasma cylinder $r = a$.

$$\begin{cases} E_r^{(out)}(r,k,\omega) = AH_1^1(\chi r), \\ E_z^{(out)}(r,k,\omega) = -A\frac{i\chi}{k}H_0^1(\chi r), \\ B^{(out)}(r,k,\omega) = A\frac{\omega}{ck}H_1^1(\chi r), \\ E_r^{(in)}(r,k,\omega) = BJ_1(\xi r), \\ E_z^{(in)}(r,k,\omega) = -B\frac{i\xi}{k}J_0(\xi r), \\ B^{(in)}(r,k,\omega) = B\frac{\varepsilon\omega}{ck}J_1(\xi r), \end{cases} \tag{5.51}$$

where A, B are constants, $\chi^2 \equiv (\frac{\omega^2}{c^2} - k^2)$, $\xi^2 \equiv (\varepsilon\frac{\omega^2}{c^2} - k^2)$, H_k^i is Hankel function of the kind i and the order k, J_k is the Bessel function of the order k, $\varepsilon(\omega, k)$ is the dielectric function. The consistency of all these conditions provides the dispersion relation

$$\frac{K_0(\alpha ka)}{K_1(\alpha ka)} = -\frac{\left(\frac{1}{\varepsilon_{rr}(\omega,k)} - \frac{\omega^2}{k^2c^2}\right)}{\alpha\beta}\frac{I_0(\beta ka)}{I_1(\beta ka)}, \tag{5.52}$$

where $\alpha \equiv \pm\sqrt{1 - \frac{\omega^2}{(kc)^2}}$, $\beta \equiv \pm\sqrt{\frac{\varepsilon_{zz}(\omega,k)}{\varepsilon_{rr}(\omega,k)} - \varepsilon_{zz}\frac{\omega^2}{(kc)^2}}$, $I_i(x)$ and $K_i(x)$ are i-th order modified Bessel functions of the first and the second kind respectively.

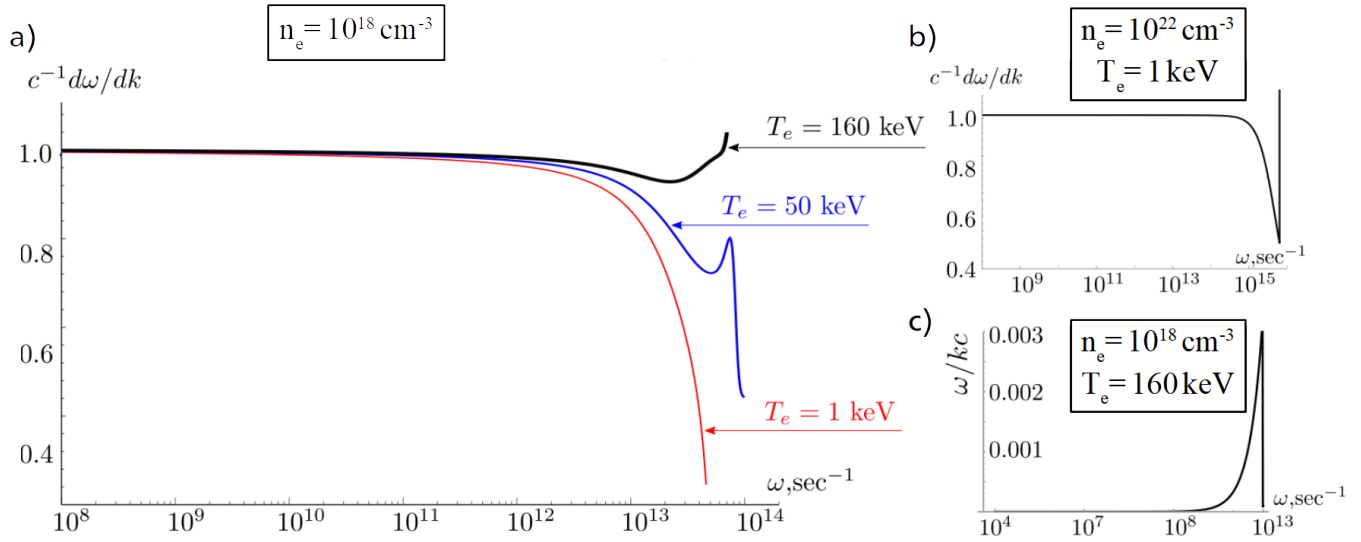

Figure 5.59: (a) Group velocity, calculated numerically from the dispersion relation (5.52), for $n_e = 10^{18}\,\mathrm{cm}^{-3}$ and $T_e = 1\,\mathrm{keV}$ (red, lower curve), $T_e = 50\,\mathrm{keV}$ (blue, middle curve), and $T_e = 160\,\mathrm{keV}$ (black, upper curve). (b) shows the numerical solution for the group velocity for $n_e = 10^{22}\,\mathrm{cm}^{-3}$ and $T_e = 1\,\mathrm{keV}$. (c) shows the phase velocity for the lower branch of the dispersion relation (5.52) for $n_e = 10^{18}\,\mathrm{cm}^{-3}$ and $T_e = 160\,\mathrm{keV}$.

From the PIC simulations we may conclude, that the considered cylindrical plasma is hot, and its initially sharp edges diffuse on the scale of the Debye length. It is possible to make only qualitative conclusions from the model dispersion equation (5.52), using the effective electron plasma density of the hot layer around the original solid-density cold wire. According to the PIC simulations in Fig. 5.53 the effective electron density is of the order of $n_e \sim 10^{18}\,\mathrm{cm}^{-3}$. Assuming the main frequency of the leading edge of the discharge wave to be of the order of the inverse laser pulse duration $\omega \sim 2\pi/\tau_L$, $\tau_L = 500 \cdot 10^{-3}\,\mathrm{ps}$, that is $\omega \approx 12 \cdot 10^{12}\,\mathrm{s}^{-1}$, we find that the plasma frequency for this effective electron density is somewhat higher $\omega_e \approx 56 \cdot 10^{12}\,\mathrm{s}^{-1}$. The

difference between these two frequencies is an important parameter: as we can see in Figure 5.59 (a), the group velocity in the domain $\omega \sim 10^{13}\,\mathrm{s}^{-1}$ is close to the light velocity in case of $n_e = 10^{18}\,\mathrm{cm}^{-3}$.

Another important parameter in the model is the plasma temperature. It actually defines the rate of collisionless Landau damping, which is growing up with plasma temperature as more resonant particles are present in the system. In Fig 5.59 (a) three curves show the group velocity, numerically calculated from Eq. (5.52) for three plasma temperatures. For a relatively low temperature $T_e = 1\,\mathrm{keV}$ (red curve), the resonance at plasma frequency $\omega = \omega_e$ is very sharp, and the group velocity goes down quite deeply, to $\omega/(kc) \sim 0.6$. Increasing of the temperature results in smoothing of this discontinuity, as illustrated by the blue curve for $T_e = 50\,\mathrm{keV}$. For the parameters of the actual experiment, however, the scale of the hot electron energies in PIC simulations is about hundred keV. For this situation, the curve becomes very flat, decreasing at it most to $\omega/(kc) \sim 0.8...0.9$ (black curve), consistent with the experimental observation within error bars. Note that experimental results also could be explained by lower temperature plasma with higher electron density, see fig. 5.59 (b). The lower the electron density is, the lower is the group velocity for a given frequency. This result may be also readily obtained, if one considers just the propagation of the wave along a cold Cu wire [BT64].

In summary, the highly nonlinear dependence of the group velocity is defined by the two main parameters effective plasma density and temperature, both sensitive to the irradiation conditions. This may give rise to the variation of the experimentally observed values of the phase velocity, and motivates further experimental studies. Landau damping is the only absorption mechanism in the considered model, which makes the wave to be not purely transverse. This effect may contribute to effective electron acceleration along the wire [P. +07; KBB18], as seen in fig. 5.53 (i).

5.2.6.1 Dynamics after the Discharge Pulse

Analysis of the proton-imprints in fig. 5.60 and fig. 5.61 allows to detail on the evolution of the EM effects for later times. Following the full evolution for DPCT geometry in fig. 5.60 (a), the long tail of the discharge pulse continues weakly squeezing the charged particle beam in proximity of the loop, but two striking changes arise: the appearance of a 'sun-rayed' pattern of caustics in vicinity of the coil and a doughnut shaped caustic inside the coil. Besides these two characteristic caustics, deflections around the coil diagnose the rise of the return current.

Characteristic Caustics

A 'sun-rayed' pattern of proton density minima is visible on RCF imprints. It appears inside and around the coil and the stripes appear perpendicular to the conductor surface. This pattern is shown in Figure 5.60 (b), the perpendicularity is especially pronounced in the Ω-leg part for shot #32 with a DPCT. The appearance of such caustics is observed in all shots, $33(11)\,\mathrm{ps}$ after the passage of the pulse peak on the coil. The deflection pattern remains stationary, caustics change contrast but not their location with respect to the conductor. The hydrodynamics of a wire plasma is too slow at the estimated heating rate to form a modulated plasma density at the observed distance around the wire. The observed ray-like structure is likely to be defined by a modulation of the potential on the conductor or in direct vicinity of the target.

Variations in the potential might be caused by the rising return current, as studied in [A. +15a], appendix D. That paper describes such fluctuations, without taking into account the retarded character of the evolving fields. Assuming a constant propagation speed of the pulse with $(0.82 \pm 0.06) \cdot c$ and a spread of retarded feedback with c, one obtains an estimated time-of-travel from interaction region to grounding and back to the

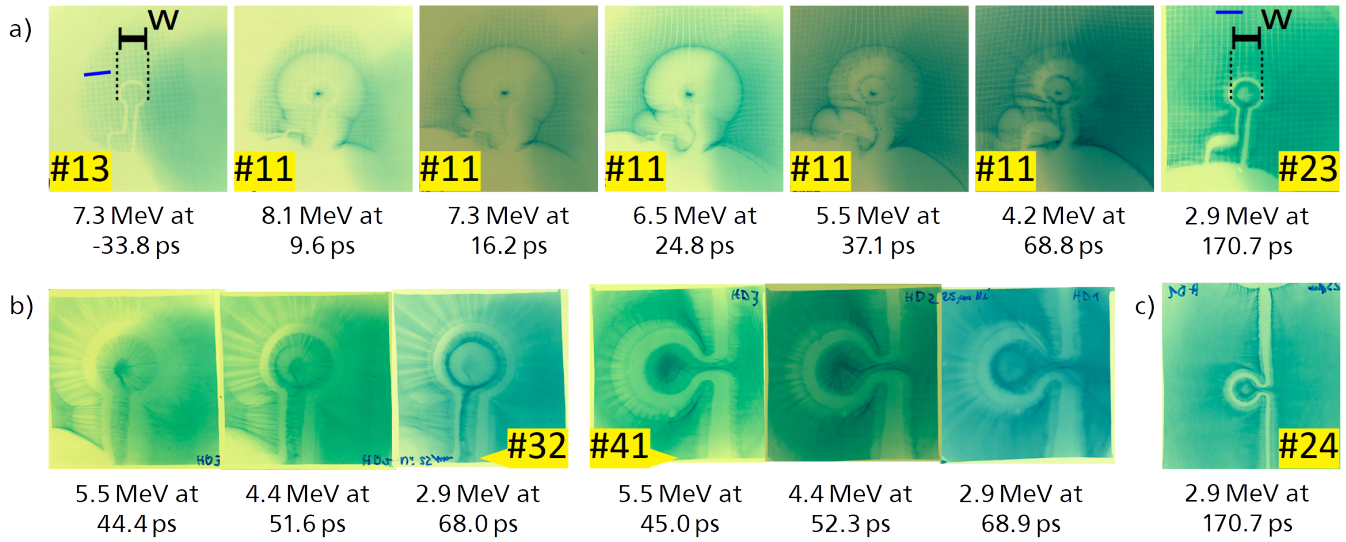

Figure 5.60: Typical evolution of deflections imaged on RCF, (a) here for Double-Plate Coil Target geometry. Comparing an early imprint for shot #13 and a late imprint for shot #23 with the magnification corrected scale-bar (w), we see that the coil diameter increased by the order of two conductor widths, this is $100\,\mu\mathrm{m}$. (b) For the exponentially decaying discharge pulse amplitude after passage of the peak at $\approx 12\,\mathrm{ps}$, the intense imprint in the coil centre issued from the dense beam faints. While there a ring shaped caustic appears, concentric with the coil. Both shots #32 and #41 were performed with a increased magnification by approaching the TNSA source to $1.99\,\mathrm{mm}$ and $2.01\,\mathrm{mm}$ from the coil plane respectively. Double-Plate Coil Target deflectograms (shot #32) agree with the ones obtained for Ω-Coil Target geometry (shot #41), (c) also for latest probing times (shot #24). The centre void within the ring shaped caustic lasts for our latest observations. Note the coil shadow in each imprint, the coil diameter is $500\,\mu\mathrm{m}$ in the coil plane, blue bars in (a) indicate the distance of $6.5\,\mathrm{mm}$ in the detector plane. The timing reference is the driver laser impact, proton energies are given, and probing times account for the time of flight from source foil to coil plane.

coil of $30.8(40)\,\mathrm{ps}$. Considering the target mounting with a conductive glue drop of $\approx 1\,\mathrm{mm}$ diameter that holds the target on the grounding needle, time-of-travel and birth time of the caustic pattern overlap in the range of their uncertainty.

Another possible explanation for the rayed pattern would be a modulation of the discharge wave itself. According to the model presented in the previous section for the discharge wave dispersion, the phase velocity of a short scale modulation of a Sommerfeld-like propagating wave appears to be very low, compare fig. 5.59 (c). Accordingly, the ray-pattern would be almost constant during the observation time. In this case, consider a low-velocity branch of the solutions of Eq. (5.52). In the limits $\omega \to 0$, $\omega/(kc) \to 0$, the dispersion relation gives in the main order

$$(ka)^2 \left(\gamma + \ln\frac{2}{ka}\right) \pm 2\left(\frac{kv_T}{\omega_e}\right)^2 \approx 0, \tag{5.53}$$

where $\gamma \approx 0.577$ is the Euler-Mascheroni constant. The constant value of the wave number $k \approx 1.12a^{-1}$, defined from Eq. (5.53), of the order of the inverse cylinder radius, corresponds to the low-velocity branch of the discharge wave. It may be excited if a seed perturbation, *e.g.* from the surface wire structure, is applied

along the plasma cylinder. Comparing the spatial ∼50 µm and temporal ∼30 ps scales of the fine ray-like structure in fig. 5.60, this solution provides its qualitative description.

During the emergence of the ray-pattern, fig. 5.60 (b), the contrast of the beam on the coil axis becomes weaker, then progressively a ring-shaped sharp cusp appears with increasing contrast. The ring is concentric with the coil and clings close to the conductor on the inner side. For even later probing, no more protons reach the RCF on the coil axis, a clear void forms, see fig. 5.60 (c). Void and ring are visible for the latest observation times, at ≈171 ps after the laser-interaction. The ray pattern is barely visible already after ≈70 ps. The ring stays very clear. The evolution from focus point towards a strong ring-like deflection arises independently of the target geometry. Possibly, electrons coming from the laser interaction region get trapped in the vicinity of the coil and perturb proton deflectometry results.

After the passage of the full discharge wave, the proton image of the target appears nearly un-altered. Only for some shots, target rods are up to twice as large compared to images of the yet undriven target. The initially straight rod shows small surface modulations. Eventually ohmic heating [Tik+17] led to a slight expansion of the target wire with a velocity of $\approx 500(3) \cdot 10^{-3}\,\mu\mathrm{m\,ps^{-1}}$, or deflections are imposed by a slightly charged target with hundreds of $\mathrm{pC\,mm^{-1}}$.

Magnetic Field Induced by a Neutralizing Pulsed Discharge Current

Where early probing times <60 ps indicate B-fields induced by the displacement current of the discharge pulse, late probing times unravel a superposed charge-neutral return current. The B-field signature appears clearly in shots where the probe beam main propagation direction is set perpendicular to the axis of the omega-shaped coil (see fig. 5.61). In such configuration, E-fields deflect symmetrically all protons passing above or below the coil's symmetry axis, as shown in the first panels of fig. 5.61 (a) and (b) respectively for the Ω-Coil or the Ω-legs facing the proton beam source. With probing times around 60 ps, one starts observing an asymmetry comparing both orientations, shown in the following images of fig. 5.61 (a) and (b). Bulb shaped caustics result from an attraction to wire sections co-linear with the particle propagation on one side of the coil and a repelling force on the opposed side of the coil. Such asymmetric force can be the Lorentz force of a magnetic field induced by a coiling current. The inversion of the bulb's polarity, when flipping vertically the target by 180°, is a signature of B-fields of opposing sign for both orientations. This bulb shaped caustics are a clear indication of strong return currents, as seen in previous sections of this work.

Note, that shot #27 in fig. 5.61 (b) witnesses a sudden change from symmetric to asymmetric deflections for probing at $t = 61.2$ ps, a weak symmetric caustic is superposed by a strong asymmetric caustic. The field configuration may have changed rapidly during the passage of the probing particles.

The rise of a return current during the discharge wave decay is consistent with the target geometry. The discharge pulse reaches the grounding glue drop at $t = 24(4)$ ps, then spreading over a large area and dropping in charge density, accordingly. Electrons from the target holder are eventually causing a return current to rise. This return current could reach the coil already at $t = 30.8(40)$ ps.

The bulb imprint on deflectograms does not change its polarity between passage of the discharge pulse and late times. This observation supports the rise of a negative return current coming from the grounding rather than a second passage of an important reflected pulse portion. There is no change in polarity during the full observation time of ≈200 ps.

Dynamic simulations with PAFIN reproduce the deflections for early times employing a linearly rising return current with $\mathrm{d}_t I = 20\,\mathrm{kA\,ns^{-1}}$. The simulations take into account the wave character of the current in the

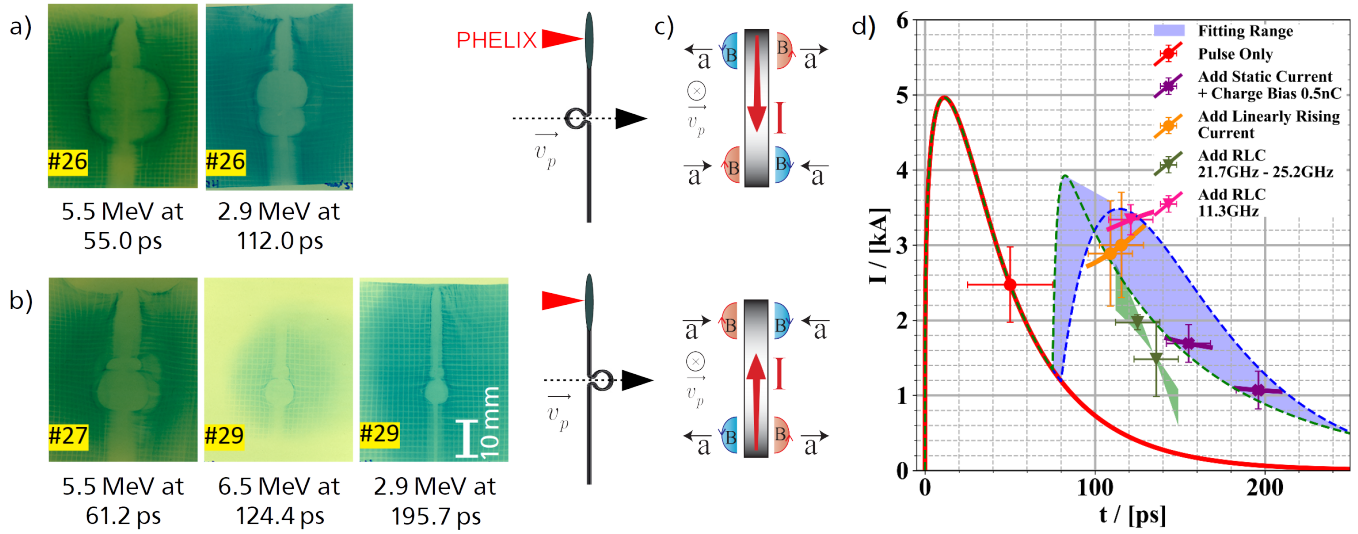

Figure 5.61: B-field evolution imaged in typical deflections on RCF, for flat Ω-Coil Target geometry. Deflections are obtained in side-on deflectometry, where coil axis and probing axis are perpendicular, resulting in (a) Ω-Coils and (b) Ω-legs facing the proton source side. Due to (c) the Lorentz force in top- and bottom-sections of the coil, the characteristic bulb shape changes depending on which side of the loop faces the proton source. The direction of current is indicated for the side facing the source. The Lorenz force changes direction according to the current flow and the acceleration a acting on protons accordingly. Through (a–c) top and bottom rows represent one versus the other orientation. (d) Return current amplitudes are obtained from the data utilizing synthetic deflectometry simulations, studying current amplitude and temporal evolution. Early deflectographs can be reproduced with the discharge pulse alone (red curve and point), then a mismatch arises that is resolved presuming static- (purple), linear- (orange) and sinusoidal currents (green and pink). Data points correspond to the best fitting amplitude within a temporal evolution plotted by a line or interval in the same color. The later temporal evolution is plotted for the time of the passage of the probing proton in vicinity of the coil. Fits to model eq. (5.56) yield various results depending weather early or late data is targeted with the respective slope. The timing reference is the driver laser impact, proton energies are given.

vicinity of the coil. Bulb sizes indicate currents of several kA, shown in fig. 5.61 (d). Deflectrogrpahs of latest probing times can be well reproduced with the B-field of a quasi-static current in the target superposed to the E-field of a charge density bias on the wire that has the order of $500 \cdot 10^{-3}\,\mathrm{nC\,mm^{-1}}$. This order of magnitude for a residual charge density is consistent with the deflections observed around straight sections of the target rod, discussed in the previous section. Integrated over the full target surface, the total residual target charging is estimated to be ≈20 nC.

Linearly evolving or quasi-static return currents do not yield good agreement between experimental data and synthetic deflectographs for probig times of 100 ps to 140 ps. This hints a transient current dynamics. The return current I_{rc} forms due to the residual potential on the target. Assuming a lumped element RLC-circuit with the same current in the full wire part of the target, the governing equation is

$$\begin{aligned}\omega_{\mathrm{LC}} &= \frac{1}{\sqrt{LC}},\\ \delta_{\mathrm{RL}} &= \frac{R}{2L},\\ 0 &= \partial_t^2 I_{\mathrm{rc}}(t) + 2\delta_{\mathrm{RL}}\partial_t I_{\mathrm{rc}}(t) + \omega_{\mathrm{LC}}^2 I_{\mathrm{rc}}(t).\end{aligned} \tag{5.54}$$

A flat Cu Ω-Coil Target is modeled according to its geometrical properties with a inductance of $L = 7.25\,\mathrm{nH}$, a resistivity of $\rho = 16.8\,\mathrm{n\Omega\,m}$ and a capacity of $C_1 = 222.5\,\mathrm{fF}$. In the extreme case of an oxidized target consisting of CuO, assuming the same resistivity but at higher permitivity of $\epsilon_{\mathrm{rm}} = 18.1$, $C_2 = 1.28\,\mathrm{pF}$.

Taking into account the skin depth [Joh63], one obtains $\omega_{\mathrm{RLC}} = 25.15\,\mathrm{GHz}$ and $\delta_{\mathrm{RL}} = 34.43\,\mathrm{MHz}$. For a fully oxided CuO target one calculates $\omega_{\mathrm{RLC}} = 5.91\,\mathrm{GHz}$ and $\delta_{\mathrm{RL}} = 16.96\,\mathrm{MHz}$. For both cases this represents an under-damped oscillation with $\omega_{\mathrm{LC}} >> \delta_{\mathrm{RL}}$. The damping factor indicates a ns-scale current dynamics. Therefore we would expect an oscillation with frequency ω_{RLC} with periods ranging from ≈250 ps to ≈1 ns depending on the degree of oxidation. PAFIN simulations in this frequency range reproduce particular proton imprints, see fig. 5.61(d), but there is no possible fitting for all data points. Overall, one observes instead a pulsed character of the current, with no swing to negative values.

It is $\omega_{\mathrm{LC}} << \delta_{\mathrm{RL}}$, which suits the over-damped regime of the RLC system. Thus, a more accurate modeling is undertaken with the solution of a Pulse Discharge Current (PDC), with

$$\begin{aligned}I_{\mathrm{PDC}}(t) &= \frac{Q_0}{\alpha^{-1} - \beta^{-1}} \cdot \left(\exp\left[-\alpha t\right] - \exp\left[-\beta t\right]\right)\\ \alpha &= \delta_{\mathrm{RL}} \pm \sqrt{\delta_{\mathrm{RL}}^2 - \omega_{\mathrm{LC}}^4}\\ \beta &= 2\delta_{\mathrm{RL}} - \alpha\end{aligned} \tag{5.55}$$

The model fits to the data in a wide range of parameters, as illustrated in fig. 5.61(d). The range where valid fit functions can be produced is indicated as blue area. The parameter α ranges from ≈25 GHz to ≈420 GHz and β then results inversely proportional with values from 25 GHz to 10 GHz. As the shape of the target visibly does not change with probing time, one may assume a constant inductance. Knowing L, α and β in the PDC allows us to un-ambiguously calculate ranges for R and C, with

$$\begin{aligned}R &= L \cdot (\alpha + \beta)\\ C &= (L\alpha\beta)^{-1}.\end{aligned} \tag{5.56}$$

The resistance ranges from $3.118 \cdot 10^3\,\Omega$ to $363\,\Omega$ and the capacitance from 220.7 fF to 32.84 fF. The later suits well the capacity of a pure Cu target, thus there may be a better agreement for the higher end of the fitting interval. This, corresponding to parameters yielding the resistance value of 363 , indicates resistance three orders of magnitude above the case of cold Cu where $R \approx 5\,\Omega$ for the frequency range of tens of GHz.

This decrease of conductivity can be a further indication that the target is heated. A large decrease in conductivity $\sigma = q_{\mathrm{e}}^2 n_{\mathrm{e}}/m_{\mathrm{e}}\nu_{\mathrm{e}}(T_{\mathrm{e}})$ can be reasoned by the temperature depended electron collision frequency [CTH07] and mutually low electron densities. For an electron density of of $n_{\mathrm{e}} = 10^{18}\,\mathrm{cm}^{-3}$ as seen in PIC simulations, and electron temperatures of ≈1 keV reasonable to explain the group velocity of the pulse, the resistivity can increase to values that explain the large resistance, see fig. 5.62. E.g., an increase by a factor of 726 is calculated for a low temperature of 40 eV.

Note that surface plasma may change both the inductivity and capacitance of the conductor. This underlines the importance of further studies aiming at experimental determination of the physical properties of the conductor.

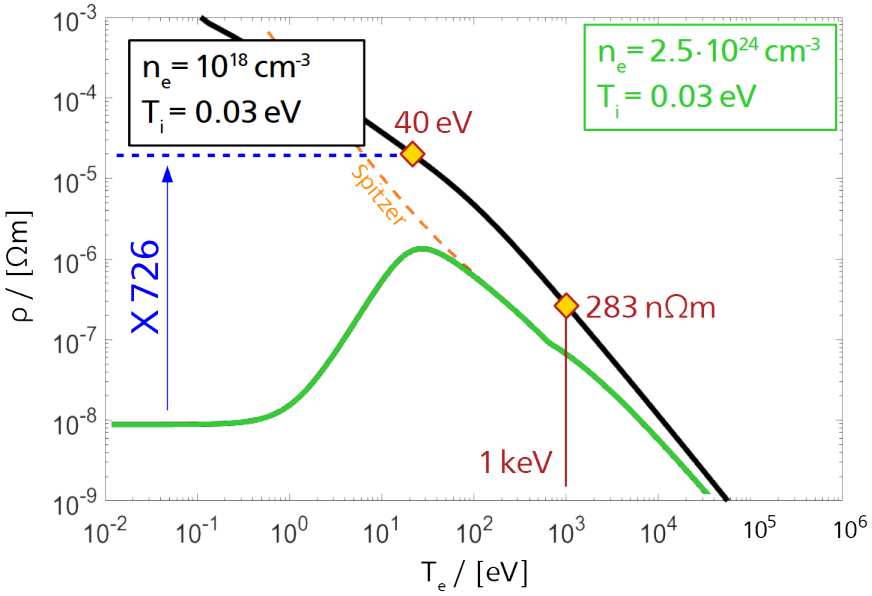

Figure 5.62: Resistivity calculated for Cu with cold background ions at different electronic densities. The green solid line illustrates the resistivity of solid density Cu, the dashed line indicates the Spitzer resistivity for this case. The black solid line depicts the Eidmann-Chimier resistivity for Cu at a density value discussed to explain the discharge wave dispersion.

5.2.6.2 Conclusion on Transient Fields

The E-field component dominates the lensing characteristics of the transient EM platform shortly after the laser drive, succeeded by a strong B-field induced by a pulse discharge current, which is charge-neutral in contrast to the earlier transient discharge pulse. It is shown that the target temperature is a important control parameter of the discharge pulse dispersion and the return current dynamics. The high branch of the dispersion relation is responsible for a group velocity different from the speed of light. Solutions on the low branch of the dispersion relation agree with modulations of the target potential in their spatial dimensions and temporal growth rate. The return current dynamics is due to the temperature and density depended conductivity.

The pulsed kA-currents evolve on the timescales of tens of 10 ps along the target geometry, promising for future application as chromatic magnetic lenses. Further interesting are the low frequency modulations of the target potential and their eventual applicability to ion beam tailoring. Even if for this experiment, the seed of the potential modulation is not being controlled, their imprint on the MeV protons is clearly visible.

5.2.7 Summary on Magnetic Lenses

Quasi-static ultra-strong B-fields produced by ns-pulse driven Ω-coil targets are based on not yet fully understood current generating mechanisms. This work supports evidence in favour of the enhanced Diode

modelling approach [Tik+17]. The current is naturally proportional to the diode tension divided by the diode impedance. The tension is directly proportional to the hot electron temperature, which mainly ensues from the laser irradiance. Therefore beneficial are laser pulses at high intensities and with large wavelengths. The impedance scales with the electron Debye length and the ratio of gap width and the front surface of the expanding plasma column. High currents are best induced by driving plasma of high temperature and high density that expand in large columns. The comparison of model and experimental results shows that a large part of the expanding plasma column must be responsible for the experimentally observed current. The rise time of currents scales with the ratio of inductance and impedance. In order to reach maximum currents, the driver laser must maintain the gap voltage during the full rise time. Long laser pulses are needed to access a quasi stationary regime. The repetition rate of state-of-the art laser systems in this regime is currently limited to tens of minutes [Bau95; Web+17], allowing for experiments or applications that do not require quasi-continuous beam currents.

Further, two fundamental problems of the platform were addressed with a modified target geometry. Notably the accumulation of charges in vicinity of the coil and the irradiation of the coil region by X-rays when deploying Ω-coils situated directly above the ns-laser driven plasma. The E-field of space charge compensates the magnetic force and inhibits ion-beam lensing, X-rays efficiently heat conductor and eventual secondary samples. Understanding the evolution and structure of E-fields and tweaking the target geometry makes it possible to mitigate shielding and heating, and to apply the ultra-strong B-fields to magnetize secondary samples, which will be discussed in further sections of this work.

The shielding effects can be best modelled with a toroidal potential that superposes the magnetic field. Its origin is related to the plasma dynamics. The B-field impairs the electron motion from the plasma expansion and local net positive and negative space charge densities induce E-fields. Due to the Lorentz force, up-streaming electrons gyrate clockwise with respect to the axial B-field in the Ω-coil. Thus, electrons tend to stream towards the conductor of anti-parallel current density and are being repelled from conductor sections carrying a parallel current density. In schemes of axis-perpendicular deflectometry, the resulting potential attracts ions on one side of the loop and repels them from the other. For deflectographs this work, deflectometry protons encounter first the positive potential and then the negative potential. This favours a net compensation of electric and magnetic deflections.

Future studies must comprise expensive PIC simulations with a plasma expansion strictly comparable to the experimental studies. Aim will be to analyse the space charge dynamics in vicinity of the conductor, notably if space charges neutralize for late times due to the counter-streaming positive and negative density, or to which extend the charge separation launches plasma waves.

Geometries of the platform that are different to the standard version prove efficient in generating high amplitude currents, such as a reverted Double Plate Ω-coil Target investigated in this work and a target comprising one only plate reported with [Kum+20]. Such geometries are appealing because they allow to well separate loop and laser-plasma, without drastic increase of the target inductivity which is mostly related to long sections of parallel conductors, such as present in a Ω-coil.

Transient EM lenses are promising for tailoring of laser accelerated particle beams, but much open questions must be addressed for their further modelling. Target drive is efficient by ultra-short intense laser pulses, optimizing the discharge by relativistic electrons. The platform is potentially suited for HRR applications, relying on state-of-the-art HRR laser systems [Web+17]. Direct applications are feasible if target manufacturing is automatized and brought next to the interaction chamber. A major advantage of the platform is its performance also in a flat target geometry, allowing production in large quantities and automatized mounting. Principally, from laser cutting to gluing on a endless tape, the full mounting can be performed under vacuum.

The transient fields have applications beyond lensing, notably the modification of the particle spectrum by post-acceleration, which will be discussed in further sections of this work.

5.3 Electromagnetic Lensing Applied to Ion Beam Sources

The UNILAC at GSI [Bar+17a] as typical example of a standard linear accelerator operates at 108 MHz and delivers ion beams with $100 \cdot 10^3$ ions in micro-bunches of temporal bunch width ranging from 3 ns to 4 ns. The beam in such a machine is split in macro-bunches, which are here micro-bunch trains with a period of 9.2 ns. The beam current averages to 4.0 µA to 5.3 µA for proton beams, and to 397 µA [Bar+17b] for uranium beams at 1.4 MeV u^{-1}. The design values of future accelerators are much higher, the planned linear proton accelerator for FAIR [SF06] will operate at 325 MHz aiming at ion beams with $7 \cdot 10^{12}$ protons in 36 µs macro-bunches, which corresponds to a beam current of 31.15 mA.

This high beam currents are realized with ion numbers comparable to laser accelerated particle beams, but beams of standard accelerators are perfectly monochromatic and have a low emittance. The downside of standard accelerators is their energy intensive operation and large spatial size, modern state-of-the-art HRR ready laser systems [Web+17] are more compact, and future dedicated beamlines might show an increased efficiency. Application of magnetic lenses to a laser accelerated beam conserves the beams emittance, and chromatic lensing decreases the beam current by orders of magnitude. This section discusses possibilities of either modifying the laser-accelerated particle beam at birth, or narrowing the beam's phase space by post acceleration events.

5.3.1 Target Normal Sheath Acceleration from Magnetized Samples

With benefit from the modified target geometry that ensures a better protection of the volume in vicinity of the Ω-coil, experimental demonstration of TNSA from a magnetized secondary sample that is injected in the coil's centre is possible, building upon previous studies that show the collimating effects on laser-heated electron beams in magnetized solid samples [BG+18]. This section shows that the sheath field accelerated ion beam with B-field switched on is brighter but shows a lower cut-off energy compared to the reference shot without magnetic field.

The sheath field formation is directly affected by the emission characteristics of relativistic electrons. The trajectories of the laser heated electrons inside the sample define the initial extend and homogeneity of the sheath. The evolution of the sheath then is due to target geometry and externally applied forces. Ions are accelerated perpendicularly to resulting equipotential lines in the sheath. Control of the sheath field allows control of the particle beam emittance.

Laser heated electron beams that propagate inside a magnetized target after generation are more collimated compared to cases without field [M. 17]. For B-field amplitudes B_0 from 0 T to 600 T, the transverse spatial distribution of the relativistic electron beam (REB) leaving the target rear side are depicted in fig. 5.63. The transition from beam smoothing to radial confinement is due to the shrinking electron gyroradius inside the sample for rising field amplitudes. REB energy densities at B-field amplitudes of 600 T are one order of magnitude higher than without magnetic field. With growing REB flux, the sheath field amplitude and therewith the maximum accelerated ion beam energy is expected to rise. The FWHM of REBs decreases conciderably with rising B-field amplitude, yielding large transverse gradients in the sheath field. Note that the impact of changing gradients in the sheath on the ion beam divergence is reported for TNSA, varying the

target thickness of thin foils [RS16]. Thick targets that scatter the electron beams to a broad beam develop flat sheaths that accelerate low-divergence ion beams. Thin targets with larger transverse gradients in the sheath emmit ion beams with large divergence angles. Collimated REBs are at risk to generate sheaths that yield more divergent ion beams.

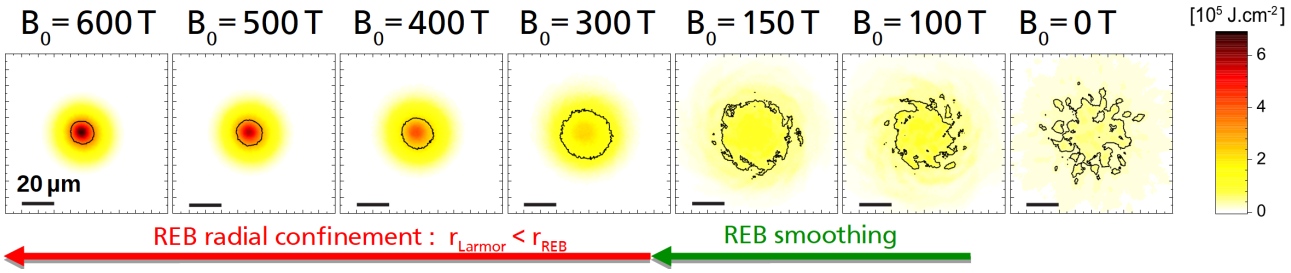

Figure 5.63: Simulated REB energy-density flux at the rear surface of 60 µm thick Hydrocarbon (CH) targets in function of the target magnetization. B_0 denotes the field strength in the target centre, corresponding to the coil center. Note that coil lines, laser axis and target normal are co-linear. The transition from a broad electron emission due to scattering and filamentation inside the target to a spot-like emission corresponds to the shrinking Larmor radius of relativistic electrons. For details on simulations, see [BG+18].

The higher is the electron energy, the earlier the electrons leave the target rear due to the lateral velocity component and the larger is the gyrordius due to the transverse velocity. Sheaths with smallest transverse gradients during one acceleration cycle arise thus at early times, accelerating ions of highest energies with their largest lateral gradients. Lower ion energies encounter sheaths of larger transverse gradients and may have a larger beam divergence. Nevertheless, B-fields of the order of hundreds of T are capable of MeV ion beam lensing [M. 16], thus reducing the ion beam divergence during acceleration. Overall, magnetization is expected to increase the ion beam cut-off energy and may decrease the beam divergence.

Flatmost sheath potentials are to be expected when the target radius gets larger than the Larmor radius of the extremities of the relativistic electron beam $r_\mathrm{T} B_0 \geq m_\mathrm{e} c/q_\mathrm{e} \approx 1.7045 \cdot 10^3\,\mathrm{T\,\mu m}$. Then, no relativistic electron escapes the transverse target sides. For a target radius of 90 µm this radial confinement of the relativistic electrons occurs for fields larger than 18 T. For higher field amplitudes, the REB becomes radially confined within its initial waist of the order of the laser focal spot size if $r_\mathrm{L} B_0 \geq 1.7045 \cdot 10^3\,\mathrm{T\,\mu m}$. For focus radii of the order of 5 µm this requires B-fields larger than 341 T. Thus, B-fields generated with the long-pulse driven Ω-coil target platform are in a range suited for REB tailoring.

5.3.1.1 Experimental Platform

Targets and experimental set-up of the campaign at the LULI pico2000 laser facility are depicted in fig. 5.64. Ion acceleration is based on laser-driven electron heating on the front centre of a 50 µm thick disk target made from poly(pyromellitimide-1,4-diphenyl ether) (Kapton). The disk has a radius of 90 µm and is glued with UV light activated glue to a glass needle, see fig. 5.64 (e–f). The 1 ps heater beam with $30(1)$ J on target is focused to $10^{19}\,\mathrm{W\,cm^{-2}}$ on the target centre in normal incidence. The contrast of the laser pulse is depicted in fig. 5.64 (d). The ASE contrast is 10^{-5} up to 75 ps before the main pulse peak, ramping up to 10^{-3} at 3.5 ps before the main peak.

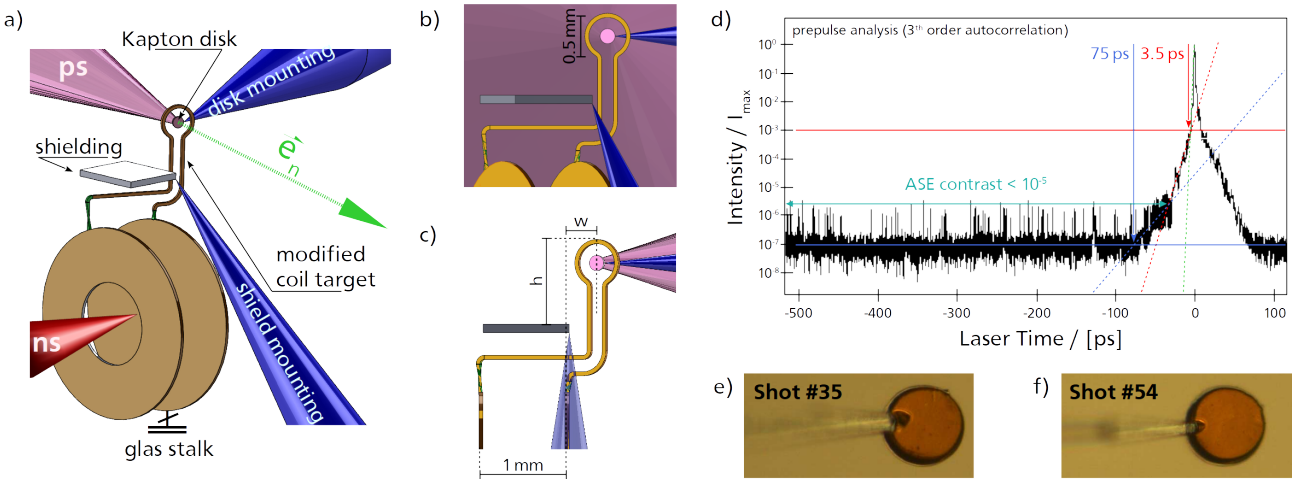

Figure 5.64: (a–c) Experimental set-up and targetry for ps-laser driven ion acceleration from a magnetized Kapton disk target with the modified Ω-coil target as B-field generator. The coil centre is shifted by $w = 320\,\mu\text{m}$ behind the interaction disk, which then blocks the direct line of sight to the laser-plasma on the coil target. An additional $100\,\mu\text{m}$ Tantalum shielding reduces the plasma flow towards the coil. (d) The laser contrast of the $1\,\text{ps}$ FWHM pulse peak for electron heating into the Kapton target is $1 \cdot 10^{-3}$ at $3.5\,\text{ps}$ before maximum, measured with a 3rd order autocorrelator system. The ASE contrast up to $40\,\text{ps}$ before impact is $10 \cdot 10^{-6}$, rising from a constant level of $100 \cdot 10^{-9}$ until $-75\,\text{ps}$. (e–f) $180\,\mu\text{m}$ diameter Kapton disks are mounted with UV light activated glue onto glas needles, depicted in a view from the laser side.

Magetic fields are generated with a modified Ω-coil target driven by a 1 ns flat-top laser pulse containing 627 J at a wavelength of $1.057 \cdot 10^3$ nm tightly focused to $120(1) \cdot 10^{15}\,\text{W cm}^{-2}$. The laser pulse rise time is ≈ 100 ps. The coil is co-axially aligned to the disk target, see fig. 5.64 (b). Ω-coils have a central diameter of 500 µm and a squared conductor rod with sides of 50 µm length. The Ω opening angle is $^2/_5\pi$, with coil ends joining the parallel legs which are at a centre distance of 190 µm. All curvatures are at constant radii. The full coil target comprising Ω-coil section, interaction disk and a parallel holed front plate is laser cut from one piece and hand fold. The hole in the front plate has a diameter of 1.3 mm, disks have a diameter of 3 mm and a distance of ≈1 mm. The coil centre is located 320 µm beyond the interaction plate.

The delay between the onset of the coil target drive and the disk target drive is set to 700 ps. A lower limit is motivated by the magnetization time of the $2L = 50\,\mu\text{m}$ thick disk target that is of the order of $\tau_{\text{diff}} \approx \mu_0 \mu_r L^2/\rho \approx 500\,\text{ps}$, approximated with the magnetic diffusion time and a resistivity of $5 \cdot 10^{-6}\,\Omega\,\text{m}$.

The experimental environment is violent, with plasma emission heating efficiently material in vicinity of the driven plasma. An additional Tantalum shielding of 100 µm thickness is positioned $h = 450\,\mu\text{m}$ underneath the horizontal coil centre plane with the long side parallel to the target plates, centred with the gap between both plates. It is 1 mm wide and 1.2 mm long. Expansion of the shielding on the side facing the ns-laser interaction illustrates the effects of plasma emission, shown with fig. 5.65 (a). Time resolved images of the target assembly backlighted by an auxillary optical probe are obtained by Gated Optical Imaging (GOI) with 80 ps gate. The backlighter beam is a Gaussian 8 ns FWHM laser pulse of 532 nm wavenlength, containing several tens of mJ. GOI, probing beam and driver laser system do have temporal jitters of several ps. Highlighted with fig. 5.65 (b), the target stalk which is bridging the gap between both plates does show more pronounced expansion on the side facing the plasma. The other side and all other conductor sections are only slightly expanded, most likely due to ohmic heating.

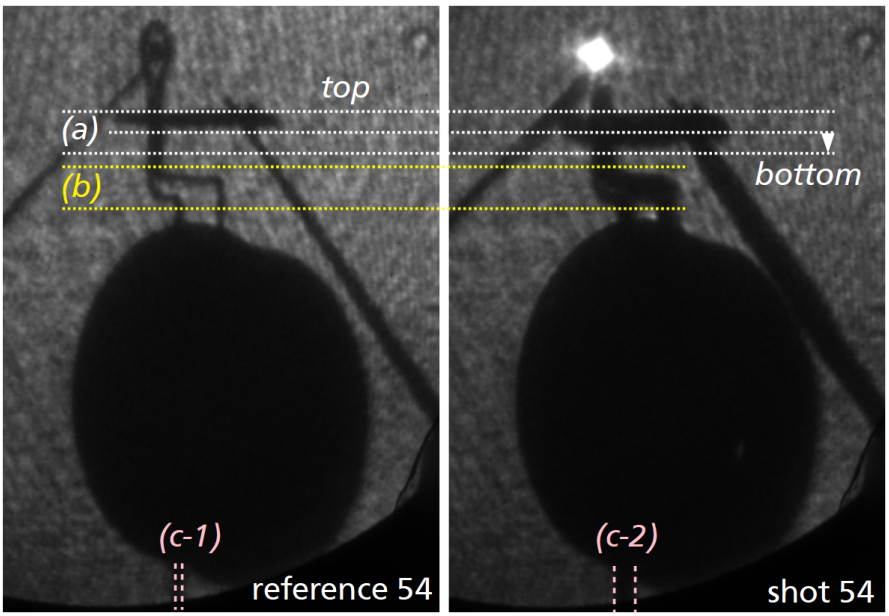

Figure 5.65: (a) The Tantalum shielding is heated by the plasma emission from the bottom and expands into free space for shot #54. (b) The target stalk which is bridging the gap between both plates does show more pronounced expansion on the side facing the plasma, and (c) the target mounting glass needle also shows expansion. The on-shot GOI image is acquired at $-40(200)$ ps (jitter) before the ps-driver shot, with 80 ps gate.

From the driver energy of 627 J one interferes a coiling current of 37^{+17}_{-8} kA at 700 ps supposing the inductance of 10(5) nH. This estimate uses a conversion efficiency from laser energy to B-field energy of 1.55(10) % derived from a study here-before, see fig. 5.32. Such low B-field amplitude is expected to show only a small impact on the electron transport [BG+18] and ion beam collimation [M. 16]. Note that proton deflectometry results may lead to an underestimate of the B-field strength, for reasons of imperfect shielding from space-charge accumulations discussed in a previous section. Independent B-dot-probe measurements point to hundreds of kA for comparable shots and therefore conversion efficiencies of the order of 5%, comparable to results of an earlier campaign at the same installation with a similar set-up [San+15]. Therewith resulting ≈80 kA of coiling current induces fields of ≈200 T, just below the limit for a radial confinement of the relativistic electron beam.

5.3.1.2 Radio-Chromic Film Results and Interpretation

Ion beam imprints are recorded on stacks of RCF positioned at 48(2) mm in laser forward direction from the Kapton disk. The stack is shielded from low energy radiation and target debris by a 10 µm thick Al foil. Raw data of reference shot #35 and shot #54, where the coil target is driven by the ns-pulse, is depicted in fig. 5.66. Results of shot #35 without driven coil show a smoother beam than results for shot #54. With no intentional pre-heating of the Kapton disk, protons from the contamination layer are expected to be majorly accelerated and up to highest velocities for their highest charge to mass ratio. Indicated are the proton energies corresponding to the range of the respective active layer within the stack, calculated with the code PySTarT. The maximum proton energy $U_{Z=1}$ in the reference shot is 15.4(6) MeV, and 11.5(5) MeV for the shot intended in magnetized conditions. A bold estimate for the expected carbon energy $U_{Z=6} \approx 90$ MeV in

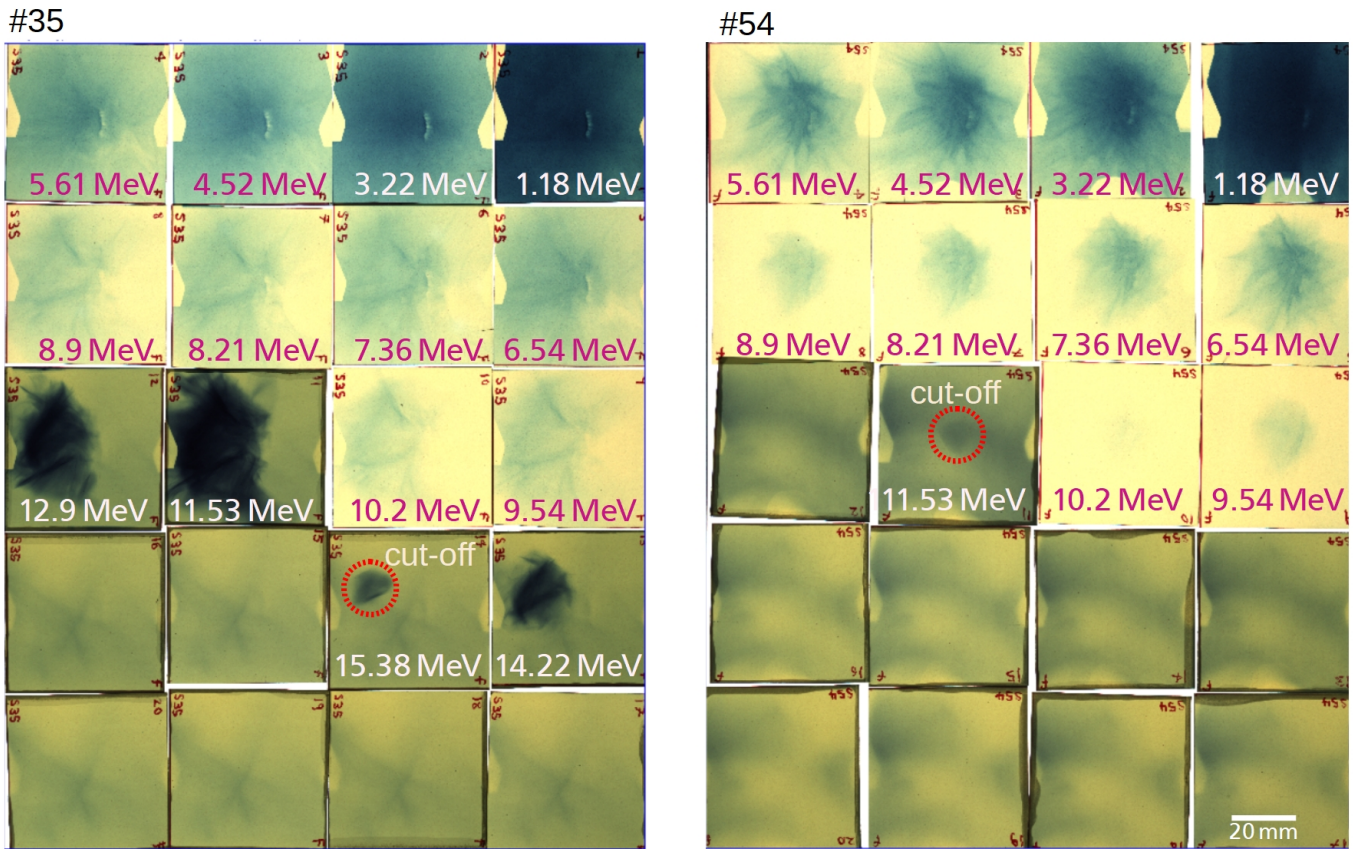

Figure 5.66: Proton beam imprints on stacks of $10\times$ HD-V2 followed by $10\times$ EBT-3 RCF that are shielded by $10\,\mu m$ of Al foil for (left) the reference shot with Kapton disk drive only and (right) the shot with additionally driven coil target. Proton projectile energies imprinting their respective maximum of energy in the active layers are indicated.

the reference shot follows $U_Z \leq Z \cdot U_{Z=1}$, derived by setting constant the accelerating potential for all species. This is an upper estimate as the energy should be smaller due to the partial compensation of the accelerating field by lighter ions that advance with higher velocity. Such carbon ions have small ranges that yield imprints only on the first two layers in the stack. Both first layers are exposed to doses higher than the calibrated dose range, therefore a quantitative analysis trying to separate both ion species is not attempt.

The reference beam shows a shifting beam centre, typical for the transition between different ion acceleration mechanisms [Wag+15]. For low ion energies, the beam follows the aligned laser axis, for high ion energies, the beam appears deviated to the upper left. For early times of acceleration, corresponding to high ion energies, the TNSA mechanism accelerates ions in target normal direction. For later times, regarding the Hydrocarbon (CH) target thickness of $50\,\mu m$, a change to the BOA mechanism is unlikely [Yin+11]. BOA is predicted to appear for targets of only some µm thickness. Key to the changing acceleration direction might be the evolution of the TNSA sheath field, *e.g.* with quasi-spherical equipotential levels for late times as consequence of the limited target surface with higher charging of edges influencing the potential distribution.

For the shot with driven coil target, the observed filamanetation of the beam and the lower cut-off energy point to target pre-heating. A still imperfect shielding of the coil region from the laser-plasma interaction probably results in a degradation of the Kapton disk by high energy photons and electrons. It is known that

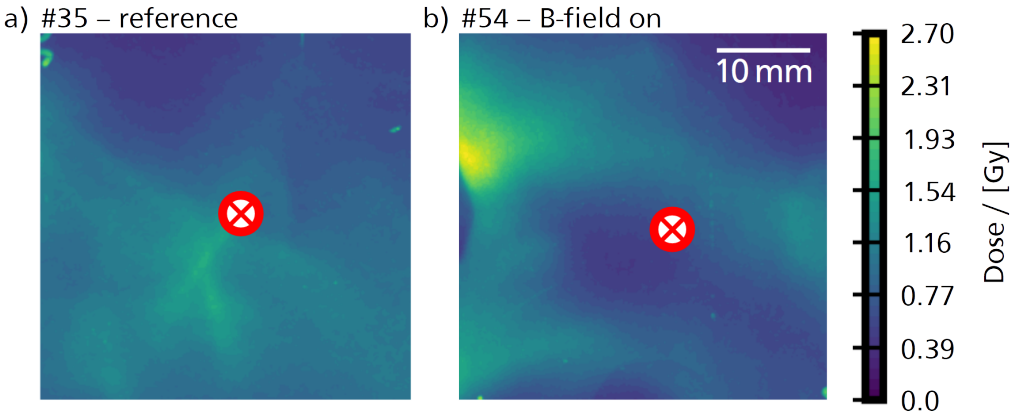

Figure 5.67: Comparison of the background signal recorded on the 15th layer RCF stacks of the same configuration for shots (a) #35 without B-field and (b) #54 with magnetic field. The pre-aligned laser axis is indicated with a red cross. Note that the alignment uncertainty of the stack was high and the laser axis must be expected within two diameters of the mark. The magnetic field may cause a residual angular momentum which can explain the dipping dose in vicinity of the axis.

the target rear side parameters are crucial for beam quality and cut-off energy [Rot+02]. Filamentation of the beam is observed for roughened rear surfaces. Further, a target rear with steep density gradient yields highest cut-off energies. The accelerating sheath field strength is proportional to $k_\mathrm{B}T_\mathrm{h,e}/q_\mathrm{e}\lambda_{D,max(i,e)}$, with $T_\mathrm{h,e}$ the hot electron temperature accelerated at the front side, and $\lambda_{D,max(i,e)}$ the maximum of hot-electron Debye length or ion scale length at the rear side. Heating of the target results in a broadening of the sheath due to pre-heated plasma, thus a lowering of accelerating fields, and therewith a lower cut-off energy.

Besides a lower cut-off energy for the shot with driven coil target, dose imprints of high energy electrons and photons vary in structure and amplitude. The background signal above the cut-off energy for the detected ion beams is depicted in fig. 5.67, compared via the respective 15th layer of the RCF stack in the very same configuration. The deposited dose for the shot with driven coil has a higher maximum value. For shots without coil drive, the dose is essentially dropping concentrically from a filamented maximum value in laser forward direction. For shots with magnetic field, the dose map shows a complex structure, with a void in the centre and a maximum off-centre to the upper left. Filamented maximum and void are slightly off the laser axis, hinting a possible systematic misalignment of the coil axis and therewith the target normal. The void surrounded by an elliptical local maximum can be explained in analogy to the lensing effects of a coil's magnetic field. The forward propagation of charged projectiles yields an angular acceleration due to radial components of diverging field lines. A beam trespassing the coil from negative to positive infinity experiences acceleration up to the coil plane and successive deceleration. The electron beam escapes from the Kapton target in the coil plane with no compensation of gained angular velocity. This field geometry may lead to a conical beam.

The ring-shaped local maximum surrounding the void shows a 12° divergence angle with respect to the centre axis. It has an opening gap to the lower right side to which opposed is located the global maximum. This characteristic symmetry may be the imprint of the Ω-opening, where a horizontal geometry of the field lines breaks the radial symmetry of the field. Electrons propagating at the speed of light are expected to gain azimuthal velocity exciting the coil's magnetic field, yielding counter clockweise rotation of the beam. The first possible roation angle that leads to observed imprint is 30°. Such can be caused by B-fields of the order of 200 T, estimated in the limit of a solenoid B-field with a delta spiked azimuthal B-field [Kum09] with

electrons propagating at the speed of light with a gamma of 10 and a maximum radial B-field located at the FWHM of the coil's B-field. REB tailoring inside the target is at the limit of radial confinement for such field strength of 200 T, thus small effects on the accelerated ion beam are expected.

5.3.1.3 Ion Beam Tailoring

Typical ion number density maps are depicted in fig. 5.68 comparing representative layers for reference and magnetized TNSA. Maps are obtained with decon_RCF presuming proton projectiles. The position for the pre-aligned laser axis (L) and the position of the beam centre of mass for both first active layer imprints (B) is indicated. Converted raw data is shown in each top left panel, which then is smoothed with a Gaussian kernel of standard deviation 2.5 mm resulting in the respective top right map, and fitted to a 2D Gauss distribution depicted in the bottom right. Smoothing renders the strongly filamented beam for acceleration in magnetized conditions comparable to the smooth reference beam. In each bottom left map, the raw number density is overlaid by two circles around the laser axis representing both 10° and 20° beam opening angles. As first observation, slimmer opening angles and higher peak intensities are noted for beams accelerated in magnetized conditions. Second, the centre of mass of the ion beam does not correspond to the aligned laser axis. During the reference shot it shows an evolution towards higher angles for higher energies, and only a small offset in magnetized conditions. 2D Gaussian fits are used in the following to retrieve integral particle numbers and beam opening angles.

The total proton number per unit energy of 1 MeV is calculated as integral over the full beam. In the reference shot aiming at TNSA as driving mechanism, the particle number density shows the order of several $100 \cdot 10^9\,\mathrm{MeV}^{-1}$ for lowest proton energies and several $1 \cdot 10^9\,\mathrm{MeV}^{-1}$ before cut-off, see fig. 5.69 (a). The slope of the reference shot fits to the isothermal expansion model as described in [RS16], see the panel in fig. 5.69 (a). A fit to the full spectrum yields a beam parameter $Zk_\mathrm{B}T_\mathrm{h,e} = 290(10)\,\mathrm{keV}$ and a total particle number of $7.0(8) \cdot 10^{12}$ in the beam. The number of high energy ions is larger than predicted, low energy ion numbers fit well. Admitting a possible overestimation of protons for low energies due to the neglect of carbon species in the beam and a bias of low energy electrons imprinting first two layers, the high energy tail of the beam is fitted with better agreement to a beam parameter of $Zk_\mathrm{B}T_\mathrm{h,e} = 1.5(1)\,\mathrm{MeV}$ and a total particle number of $540(7) \cdot 10^9$ in the beam. Note, a beam parameter of 2 MeV for a laser pulse energy of 30 J is required for generation of 15 MeV protons, according to the estimate by Passoni and Lontano [MM08]. Thus, a hot electron temperature of 1.5 MeV is reasonable.

Without attention to the first two layers, a key differences of the magnetized shot with respect to the reference shot is a convex rather than concave spectral shape. The convex shape of the spectrum is manifest of the B-field not only tailoring the REB but also guiding the ion beam. Further, the energy resolved FWHM beam opening angle is depicted in fig. 5.69 (b). Neglecting the first two energies recorded on the first two layers, the relation between beam opening angle and energy is approximately linear. This points to a transverse hyperbolic shape of the sheath field [Car+07] different to typical TNSA sheaths that are Gaussian. Note that this may be due to the small diameter of the interaction disk, where the expanding potential reaches the edges already during laser drive and on timescales comparable to the timescales of the ion acceleration itself [Lim+08]. The sheath is expanding with a velocity close to the velocity of light, then reaching the target edges after $300 \cdot 10^{-3}$ ps. The target stalk is from glass, but also irradiated by the plasma emission. Surface ionization eventually renders it conductive enabling a return current to rise. The interplay between edge effects, return currents and target discharge impacts on the target potential. This is a clear motivation for future experiments to monitor the sheath, *e.g.* by optical probing [J+10].

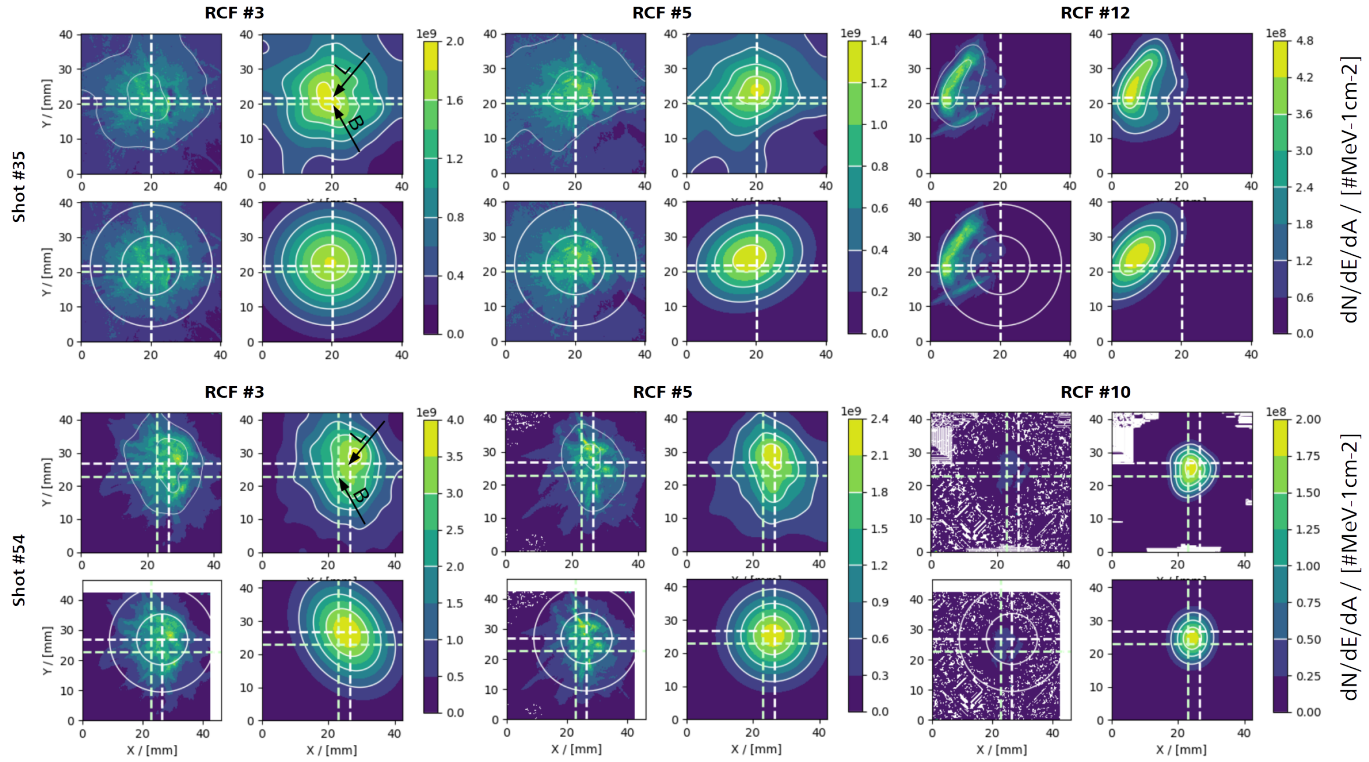

Figure 5.68: Selection of typical imprints on RCF measured with the red colour channel and converted to proton number density maps, each with (top left panel) the converted raw data, (top right panel) the converted raw data smoothed with a Gaussian kernel, (bottom left panel) the converted raw data superposed with two circles representing beam half-opening-angles of 10° and 20° respectively, and (bottom right panel) a 2D Gaussian fit to the smoothed distribution.

The magnetized sample represents a more intense ion source. The beam opening angle in magnetized conditions is systematically lower than the reference shot, highlighted for intermediate proton energies recorded on the red colour channel with the panel in fig. 5.69 (b). Also, the maximum intensity is thoroughly higher, see fig. 5.69 (c). The filamentation of the beam in magnetized conditions results in local extremes that overpass the Gaussian fit amplitude by factors larger than two, illustrated with star shaped markers for the red colour channel. The exact particle number density spectrum for all projectiles within an opening angle of 10° is shown in fig. 5.69 (d). Magnetized ion acceleration yields higher particle numbers within smaller opening angles for low ion energies up to approximately 8 MeV.

5.3.1.4 Enhanced Ion Beams by Magnetized Target Normal Sheath Acceleration

The magnetization of the sample with a ultra-strong B-field of the order of 200 T is likely, consistent with a typical energy conversion efficiency of the platform and the measured electron beam imprint on RCF. Such B-fields are expected to confine the REB in-efficiently, and only slightly affect ion acceleration. Indeed, the proton beam born at the rear of the magnetized sample has a slightly lower opening angle and higher number density amplitude than the comparable reference shot. The beam intensity in magnetized conditions rises at maximum to 150 % of the reference case. While the reference shot shows an energy depended main

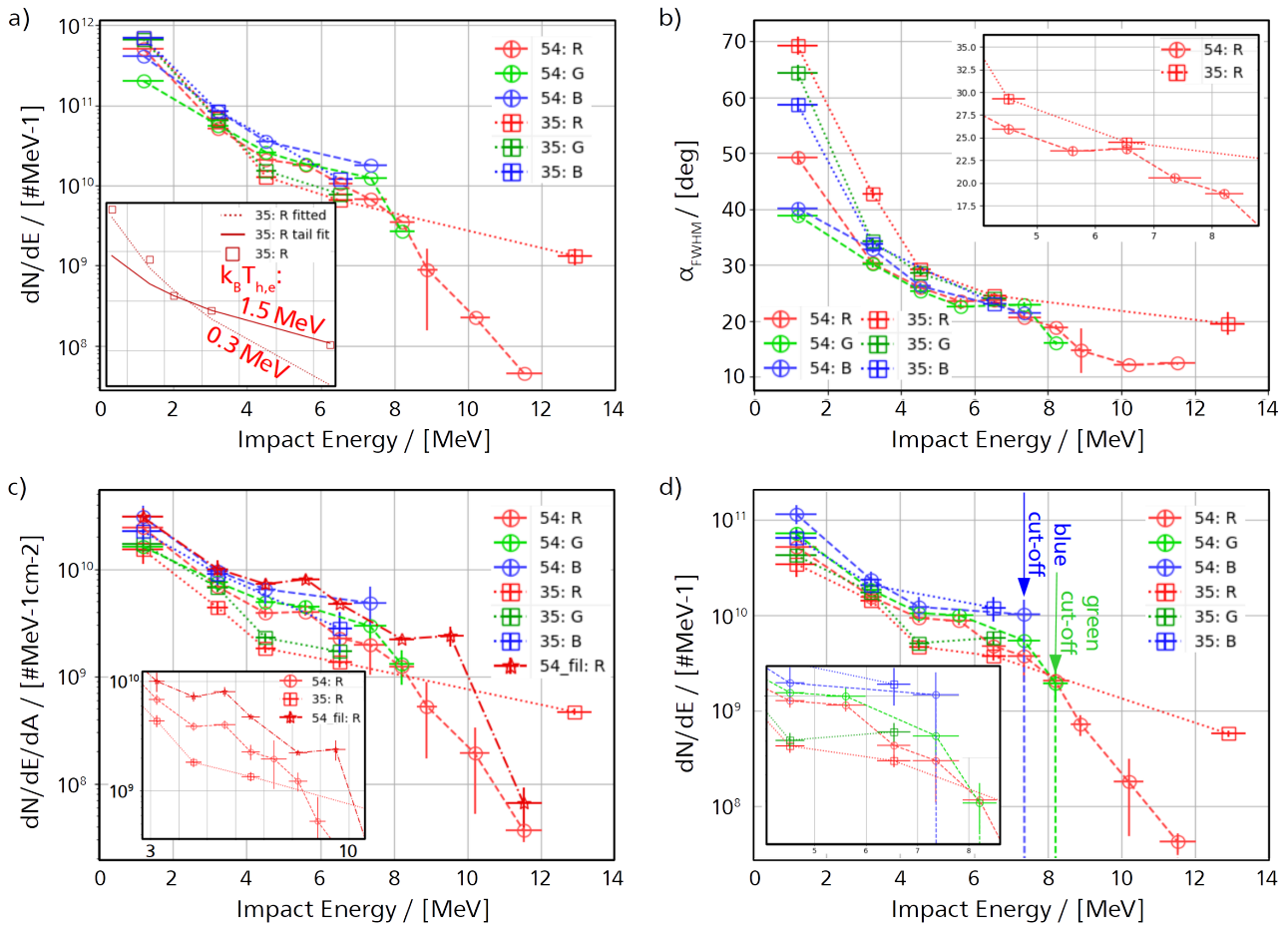

Figure 5.69: Comparison of TNSA in reference shot #35 and magnetized TNSA in shot #54 via (a) the total proton number per unit energy of $1\,\mathrm{MeV}$ that is calculated as integral over the fit of the full beam, (b) the beam opening angle from the maximum of both fitted elliptic axes, (c) the maximum beam intensity from smoothed converted data – where the data series 54_fil compares the maximum beam intensity in the brightest filament from the original converted data, and (d) the beam integral from converted data within $10°$ opening angle around the mean beam centre on both first layers in the stack. The inset panels highlight details, with (a) a fit to the isothermal expansion model, (b) measurements of the least biased red colour channel from $4\,\mathrm{MeV}$ to $9\,\mathrm{MeV}$, (c) *idem* from $3\,\mathrm{MeV}$ to $10\,\mathrm{MeV}$, and (d) all colour channels in detail from $4\,\mathrm{MeV}$ to $9\,\mathrm{MeV}$. Magnetized TNSA delivers a brighter proton beam for the intermediate energy range, with slightly higher beam current and noticeably higher maximum intensity.

propagation axis, the shot in magnetized conditions shows overall the same propagation direction for all energies.

Maps of plasma parameters in vicinity of the accelerating sheath in a regime relevant to this work are available with recent numerical studies [Wei+20]. Qualitatively, density decreases faster than temperature rises for increasing distance to the target surface, and the sheath naturally divides in two sections: A high density and low temperature section close to the initial target rear surface is mostly cylindrical symmetric with the target normal, and a low density high temperature section at larger distance comprising electrons of large orbits and escaping electrons is oriented with the magnetic field. This can be explained by a pressure balance, a plasma is magnetically confined if the magnetic pressure $B_0^2/2\mu_0$ is much larger than the plasma pressure $nk_\mathrm{B}T$. Magnetic pressure dominates the dynamics of low density sections and plasma pressure makes the influence of B-fields less important in dense sections. Simulations show that high energy ions are consequently accelerated in direction of the field lines and low ion energies symmetrically to the target normal. TNSA from magnetized samples for ultra high B-fields of the kT also is referred to as Magnetized Electron Sheath Acceleration for the change of mean ion propagation direction from target normal towards the B-field orientation. This is consistent with the uniformly directed nature of the beam in the discussed experiment, where target normal and B-field are co-linear.

First experimental results put in evidence enhanced emittance for magnetized TNSA, together with theoretical insights they are motivation for further studies with an experimental geometry that does shield the coil region more efficiently.

5.3.1.5 Enhanced Relativistic Electron Beams by Magnetization

Even though the ion yield and the cut-off energy decrease with increasing magnetization time, the relativistic electron beam is expected to intensify, especially since preplasma benefits the energy coupling. With the measurement data from RCF stacks, one can examine the relativistic electron beam for signs of magnetization. As discussed in section 5.3.1.2 and highlighted in fig. 5.67, samples that are visually aligned in the coil centre do produce hollow doughnut shaped relativistic electron beams for late times.

Figure 5.70 illustrates the dose deposited in the 15th layer for all laser-shots with the same set-up, with identical stacks that embody $10\times$ HD-V2 followed by $10\times$ EBT-3 RCF, shielded by 10 µm of Al foil. Note, that the bright feature for shot #33 stems from ions and that fig. 5.70 (a) groups results for 25 µm thick CH samples and fig. 5.70 (b) for 25 µm thick CH samples.

For both types, the dose deposited by relativistic electron beams increases with later times when one expects a rising degree of magnetization in the sample. For this late times, bright features are visible in the dose imprints for targets which were drifting slightly off the coil centre during vacuum pump down. They form stripes that might be related to the different residual radial momenta that result after the exit of the B-field for different parts of their spectrum. The transition from early times with incomplete magnetization of the target to late time with completely magnetized samples is hinted in fig. 5.70 (a). Where launching times up to 300 ps show a broad relativistic electron beam filling the full frame, features with narrow opening angle or hollow beams are visible from 500 ps.

The releativistic electron beam features agree qualitatively with the presence of a strong magnetic field. For quantitative analysis, future experiments must measure their angularly resolved spectrum.

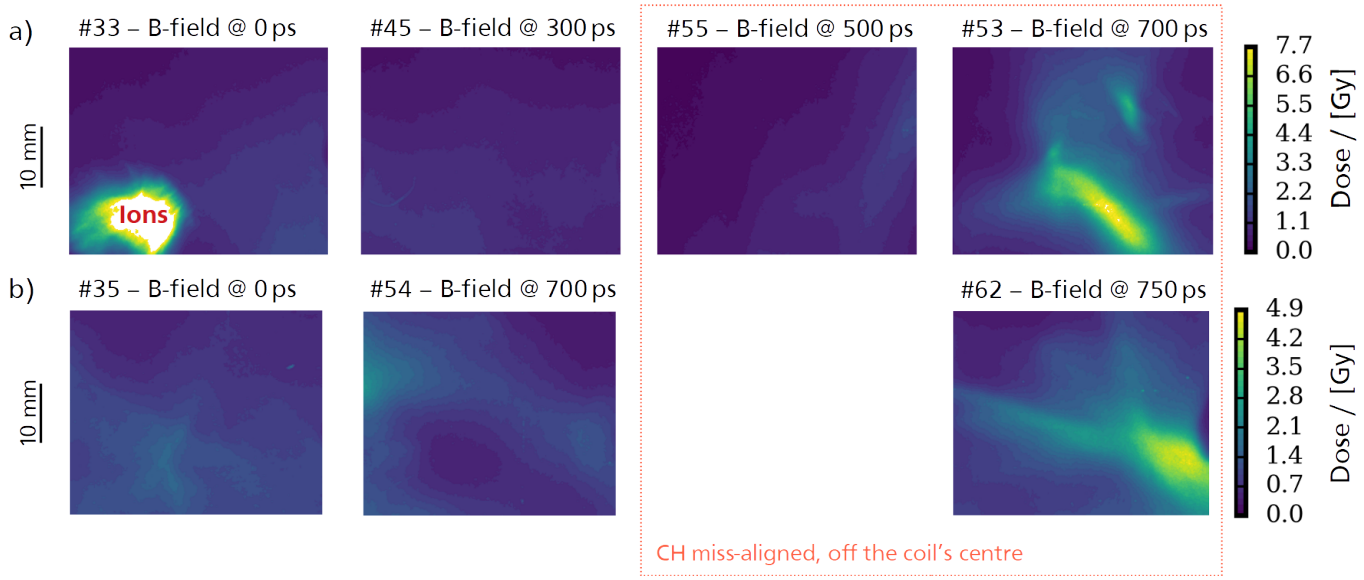

Figure 5.70: The relativistic electron beam imaged by the respective 15th layer in each of the shots. The timing between ns-laser driving the B-field and ps-laser driving the ion acceleration was varied from shot-to-shot (a) for 25 µm thick CH targets and (b) for 50 µm thick CH targets. Ion beam features are indicated as such if present.

5.3.2 Transient EM Fields as Ultra-fast Spectral Compressors

Laser accelerated ion beams have a large spectral extend that yields non-negligible drift broadening, thus reducing the beam current. The initial temporal bunch length extends with increasing distance to the source from typical initial values of $\tau_{\mathrm{acc}} \approx 1$ ps to

$$\tau_{\mathrm{drift}} = \tau_{\mathrm{acc}} + (A_{\mathrm{i}})^{1/2} \cdot \left(E_{\mathrm{min}}^{-1/2} - E_{\mathrm{max}}^{-1/2} \right) \cdot 720\,\mathrm{ps} \quad , \tag{5.57}$$

where τ_{drift} denotes the temporal width of a beam with projectile energies ranging from a minimum E_{min} to a maximum E_{max} kinetic energy at a given drift position s_{bl}. Units are u for projectile mass A_{i}, cm for distances and MeV for projectile energies. The drift broadening reaches 2.3 ns after a m-scale drift space for a TNSA proton beam in a spectral bin of 9 MeV to 11 MeV. Note, that the lateral drift width of such an energy bin centred at s_{bl} is

$$\Delta s_{\mathrm{lat}} = 2 s_{\mathrm{bl}} \cdot \frac{E_{\mathrm{max}}^{1/2} - E_{\mathrm{min}}^{1/2}}{E_{\mathrm{max}}^{1/2} + E_{\mathrm{min}}^{1/2}} \quad . \tag{5.58}$$

Here, $\Delta s_{\mathrm{lat}} \approx 10$ cm at 1 m from the source.

Pulsed EM fields of MV m^{-1} and tens of mT in the radio frequency (RF) domain are widely used for charged particle beam tailoring, notably for energy- and temporal-compression by rotation of the longitudinal phase space. Spatial energy compression is archived by flattening the phase space ellipse in vicinity of a centre

energy, resulting in larger co-propagating ion number densities. The spatial extend of the flat ellipse is the spatial bunch length. Temporal compression results over-rotation of the phase space ellipse, accelerating ions in the beam tail to energies above the bunch centre energy and decelerating ions in the beam head to lower energies. The beam will compress laterally with time of flight with a minimum width at the lateral drift focus.

Low velocity RF cavities can be applied to slow laser accelerated MeV ion beams [Ike+09; Nis+09]. Predictions claim possible intensification of beam currents by a factor of hundred in a small spectral width [Jia+12]. Recent experiments deploying solenoid magnets for beam focusing and a RF cavity demonstrated energy-compression to $350 \cdot 10^6$ protons of $8.5(2)$ MeV [Bus+14a] and temporal compression down to $458(40)$ ps at the lateral drift phase focus several m from the proton source [Bus+15]. Current experimental studies of the Laser Ion Generation, Handling and Transport (LIGHT) collaboration [Bus+14b] aim at injecting an additional solenoid into the beamline for down-focusing of laser accelerated proton beams, with perspective to record intensities of $780 \cdot 10^3\,\mathrm{ps}^{-1}$ corresponding to beam currents of 124 mA at several m distance form the source [Jah+19].

Further optimization aims at higher beam currents, notably by reducing the lateral drift width of energy-compressed beams or the temporal drift focus towards the small initial bunch length. A limiting factor is the spectral acceptance of cavity systems. For both types of compression, increasing the potential gradients at play allows for broader spectral acceptance and therewith a higher ion number density in the tailored beam bunch. Accelerating fields are limited by the critical B-field of superconducting cavity material, *e.g.* highest E-fields of $45\,\mathrm{MV\,m}^{-1}$ are accompanied by limiting B-fields of 190 mT at 2 K for niobium [Lil+04]. This work aims at further exploration of mm scaled laser driven EM devices that make use of stronger pulsed transient EM fields presented here-before, with electric components of tens of $\mathrm{GV\,m}^{-1}$ and magnetic components of tens of T. Such a platform can be introduced in proximity to the laser-plasma ion source, targeting early on energy-compression within small lateral drift width. The next sections demonstrate first a pre-compressor for application in the framework of LIGHT [Bus+14b], and second numerical estimates for an enhanced proton beam source at ELI-BEAMLINES (Praha, CZ).

5.3.2.1 Origami Micro-Compressor for Laser Ion Generation, Handling and Transport

The LIGHT project aims at combining laser-particle acceleration and standard accelerator technology for beam tailoring. In its current set-up, the LIGHT beamline Z6–Z4 at GSI comprises a TNSA particle source followed by a first pulsed high-field solenoid magnet for beam collimation, a cavity for phase rotation and a second solenoid magnet for down-focusing, see fig. 5.71 (a). This work introduces a micro post-accelerator as pre-compressor between source and first magnet, aiming at increasing the number of particles being collimated by the solenoid lens, see fig. 5.71 (b). In a first step, the micro-compressor is characterized experimentally, in a second step it is applied in the full beamline and compared to normal operation without micro-compressor.

The fields for post-acceleration are induced by the self-generated EM discharge pulse, motivated from the great success of its application to TNSA proton beam lensing [S. +16; Kar+16]. The discharge pulse emanates from the laser interaction region and couples in two attached wires. The wires guide the EM discharge pulse to two co-axial coils, one of which is conductively connected to the ground and one of which is terminated with an open end. In a timeline, fields in vicinity of the grounded coil are induced first by the traversing discharge pulse, secondly by the successively rising return current and thirdly by a partial reflection of the pulse due to the impedance miss-match at the target mounting. The later will be negligible for this work as the target was conductively mounted. The fields around the open-ended coil stem from firstly the passage of the discharge pulse and secondly from the fully reflected pulse.

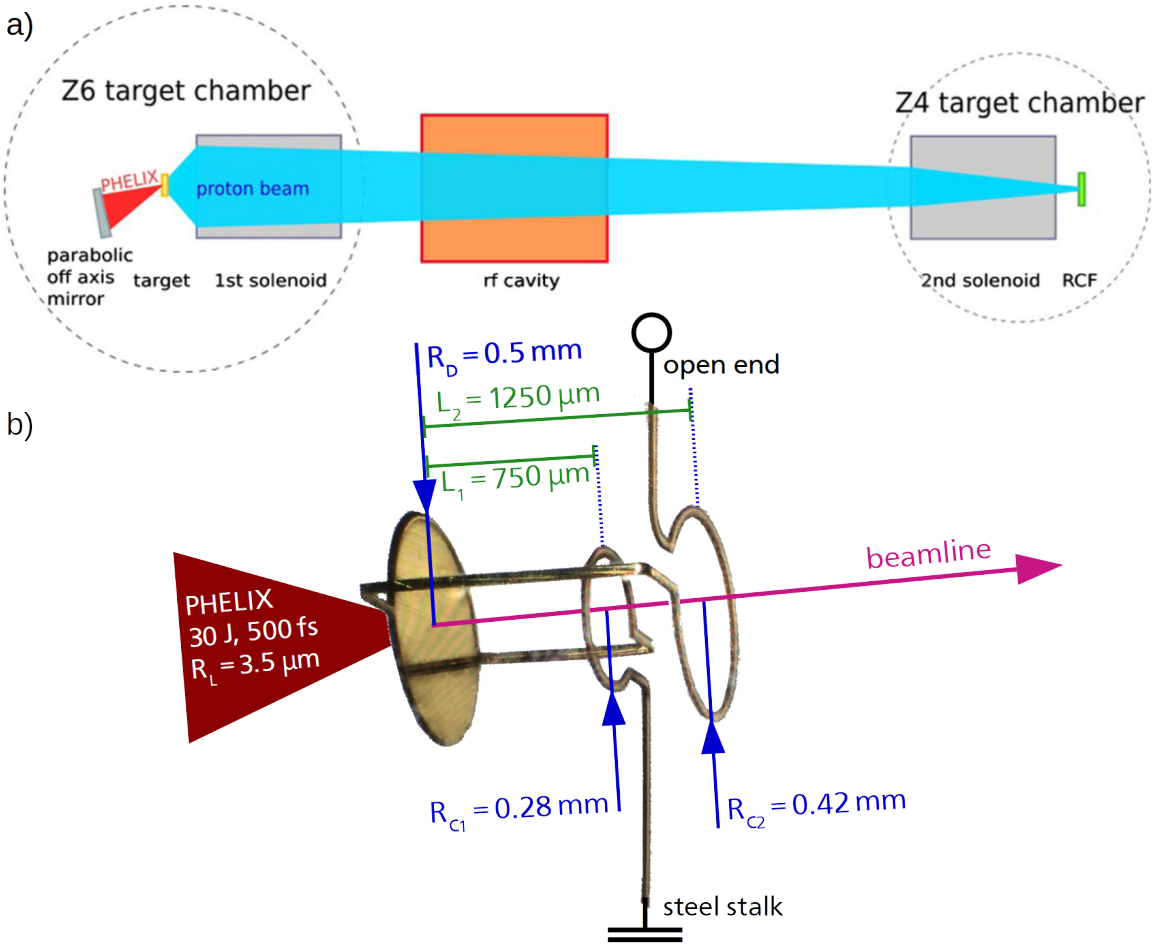

Figure 5.71: LIGHT beamline as of 2020. (a) The PHELIX system is compressed to several hundreds of fs and drives a TNSA source inside the Z6 target chamber. The ion beam is accelerated into a first solenoid magnet for collimation towards a RF cavity. Ions successively arriving in the Z4 target chamber are down-focused to high intensity by a second solenoid magnet. Beam diagnostics such as RCF, magnetic spectrometers and ToF detectors are positioned in vicinity of the beam focus. (b) Microscope picture of the modified TNSA target with two coils, one between interaction disk and grounding, and one towards an open wire ending. Figure (a) extracted from [Jah+19].

The TNSA ion beam is generated at the rear of the interaction disk, on the double-coil axis. Note that the disk normal and coils' axes are co-linear. Tuning of the target geometry allows to chromatically tailor the ion beam, notably by adjusting the length of the wire sections between interaction disk and coils as well as the length of wires to grounding and open end. For ideal micro-compressor operation, ions of the centre-energy chosen for beam transport must arrive at the first coil during decay of the repelling E-field. Faster ions experience stronger deceleration and the spectrum compresses towards the centre-energy. Such decaying fields are observed after the passage of the discharge pulse peak through the Ω-coil. Further, ions of the centre-energy must have passed the coil plane for times when the partial reflection of the discharge pulse is expected to arrive in the coil, then pushing the respective slower ions towards the centre-energy. The rise of the return current potentially yields a reduction of the beam opening angle by induced magnetic lensing, in addition to the electric lensing from the positively charged coil. At the second coil, similar constraints apply, but with a strong reflected pulse due to the open wire ending and no return current. The open end has a length that ensures arrival of the reflected pulse after passage of the centre-energy.

This work aims at exploration of three aspects with this simplified Helmholtz-coil geometry: the collimative effects of the EM lens, acceleration imposed by the E-field component traveling along the flat Ω-coils, and magnetic lensing with the field induced by the return current. The remainder of this section is organized as follows: firstly experimental results are presented, and secondly results from standard operation of the LIGHT beamline and operation with pre-compressor are compared.

The PHELIX system drives the TNSA source with a pulse of $60 \cdot 10^{18}\,\mathrm{W\,cm^{-2}}$ during $500(2) \cdot 10^{-3}$ ps focused to 3.5 µm FWHM. Standard TNSA targets at the LIGHT beamline are 10 µm thick large mm-scale flat gold foils. For reasons of mechanical stability, micro-compressor TNSA targets are 20 µm flat disks of 1 mm diameter, the 50 µm wide rectangular wiring is shielded off the laser plasma by the interaction disk itself. Therefore no heating is expected and the group velocity of the discharge pulse is assumed to be equal to the speed of light.

At Z6, the first solenoid captures typically up to one third of the accelerated TNSA protons in an energy range with central energy of 8.5 MeV and 20 % spread [Kum09; Bus+13]. The here discussed campaign aims at transport of protons of ≈8 MeV. In order to measure the impact of the micro-compressor on the TNSA beam, a stack of RCF is attached to the entrance of the first solenoid in order to retrieve changes to the spatial and spectral proton number density distribution. The RCF for 4.1 MeV, 8.8 MeV, 13.5 MeV and 19.5 MeV contain snapshots of the different stages of operation of the dynamic platform, depicted in fig. 5.72. RAW data, dose converted data and deconvoluted number density distribution for all layers of the relevant shot and reference shot can be found in the appendix with fig. 8.3 and following.

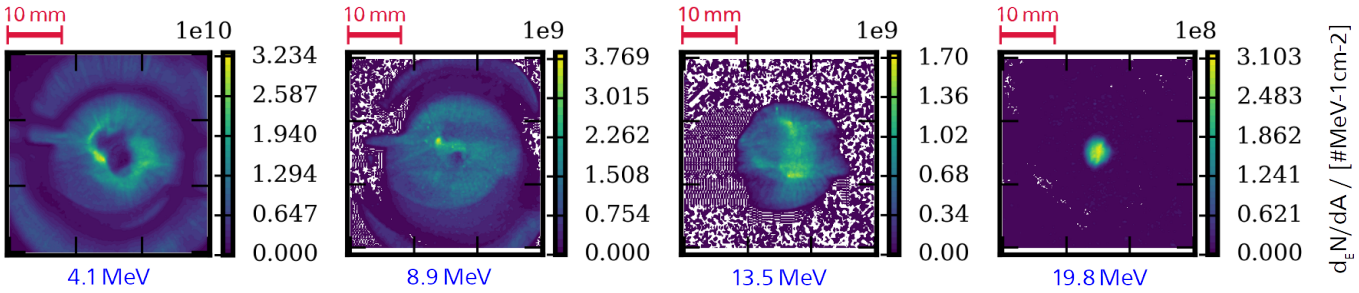

Figure 5.72: 2D maps of proton number density per unit energy of 1 MeV, obtained from the red channel of RCF positioned at the entrance of the first solenoid. The peak energy deposition within the respective active layer occurs for the indicated proton energy.

All RCF of one stack are used for deconvolution of the spatially resolved proton sprectrum with decon_RCF,

presuming the first layer after cut-off to represent the background dose. Shot #61 with micro-compressor is measured with a stack of 14× HD-V2 of batch #11171501 followed by 7× EBT-3 of batch #07291902 which is shielded by 12.5 µm of Al and 50 µm of Cu, and reference shot #01 deploys a more complex stack with 12.5 µm of Al plus 150 µm of Cu plus 2× HD-V2 plus 150 µm of Cu plus 1× HD-V2 plus 150 µm of Cu plus 1× HD-V2 plus 150 µm of Cu plus 1× EBT-3 plus 150 µm of Cu plus 1× EBT-3 plus 150 µm of Cu plus 1× EBT-3, using the same batches for each type of RCF. The respective calibration data can be found in the appendix with fig. 8.1 and fig. 8.2. All data from reference and shot can be also found there from fig. 8.23 and fig. 8.3 to following.

The spectra for both shots are depicted in fig. 5.73, the absolute particle number per unit energy of 1 MeV is comparable. One notes the slightly lower cut-off energy for the micro-cavity source, but more importantly a up to 50 % reduced FWHM opening angle. The beam has higher amplitude particle number density distributions in space. The TNSA spectrum obtained with the reference shot is similar to spectra habitually reported for this beamline [Bus+15], with a cut-off energy of 22.6(4) MeV and a convex distribution for the FWHM opening angle that ranges with rising energy from 40° to 15°, see fig. 5.73 (d).

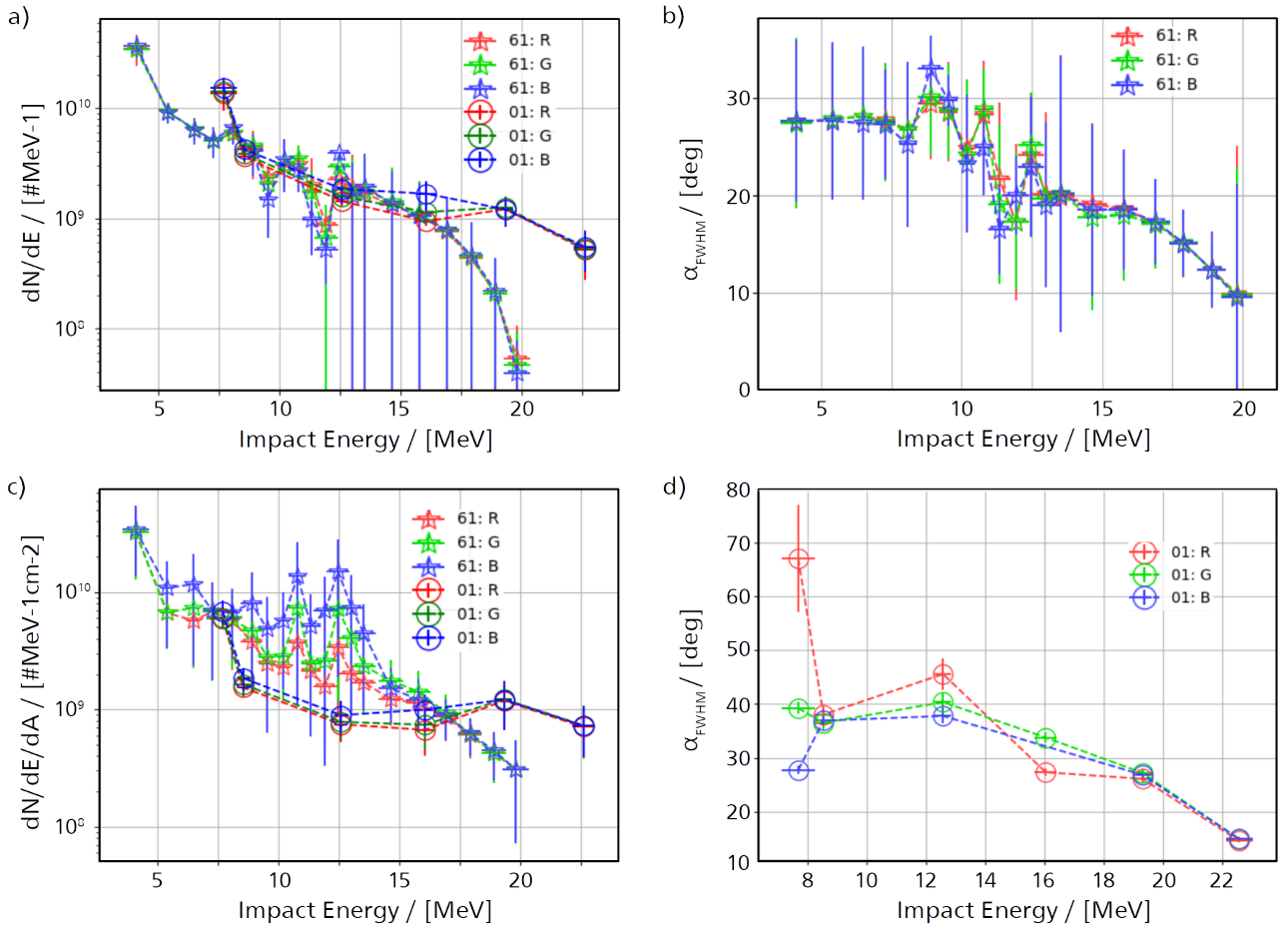

Figure 5.73: Comparison of TNSA and compressed TNSA via (a) the total proton number per unit energy of 1 MeV that is calculated as integral over the acceptance angle of the first solenoid, notably 30°, (b) the FWHM beam opening angle of the full guided beam, (c) the maximum beam intensity from converted data for both full beams, and (d) the FWHM beam opening angle of the full reference beam.

In detail, the fastest protons of 19.5 MeV encounter decelerating fields induced by the rising edge of the discharge pulse on their approach to the first coil, and pass at the same time when the discharge pulse peak fills the coil completely. Thus, their opening angle is reduced by the radial electric field. Further, those protons are expected to experience a slight net acceleration forward and to the right, with respect to their initial mean propagation direction. This deviation is visible on RCF imprints. Afterwards, lower energy protons become deflected towards the beam-axis, indicating a flat tail of the discharge pulse which induces mostly radially uniform fields. Due to such tail, protons experience laterally higher decelerating fields than accelerating fields.

For protons from 8.8 MeV to 13.5 MeV the beam is heavily distorted, showing imprints of the reflection of the discharge pulse traveling through the second coil. The reflection carries a current opposing the tail current, thus the B-field re-organizes during the passage of this spectral band, resulting in an opposition of both axial fields with thus strong radial component between both coils. For imprints of protons of 8.8 MeV, RCFs start showing the evolution of two voids, one on each coil centre. Note that protons of 8.8 MeV traverse the central plane of the second coil approximately when the reflection of the discharge pulse fills the coil completely, thus yielding a inversion of the field that leaves this protons with residual azimuthal momentum resulting in a radial drift away from the B-field axis.

For protons with energies lower than 7.3 MeV, the voids are also pronounced in a loss of absolute particle number density with respect to the reference shot. Such protons pass the first coil after the strong return current can start inducing a strong magnetic field, therefore they encounter the strong radial fields building up between both coils. Note that the rise of the return current from the ground is induced by the retarded potential expanding through free space rather than due to the arrival of the discharge pulse on the glue drop. With a singular strong azimuthal push that is not compensated for by the fields around the second coil, the protons drift off the axis of the strong radial fields. In conclusion, both voids correspond respectively to the B-field axis of the second coil and to the axis of the radial field between both coils.

Overall, guided TNSA yields a lower divergence angle of the proton beam and slightly higher beam intensity when compared to standard TNSA around 8 MeV. Thus, even though the absolute particle number arriving in the first solenoid is comparable for both cases, more protons enter with low divergence angle with pre-compressor.

The throughput of the beamline with and without micro-cavity is compared in fig. 5.74 with two independent shots. The total proton number in the focus of the second solenoid for 7.7 MeV is comparable for both cases, but the peak fluence is much larger employing the compressor. This reflects the overall conservation of proton number arriving in the acceptance angle of the first solenoid, but with more protons entering with smaller angle from the axis. Note the double peak structure for the result with micro-compressor that likely arises due to a on-shot miss-alignement of the Helmholtz-coil axis. Even though the R&D on targetry is ready for perfect targets, vacuum alignment systems could be improved.

The platform can be further optimized for the use at the LIGHT beamline by rewiring the second coil, aiming at the same longitudinal B-field orientation for both coils for times when the reflected discharge pulse dominates the dynamics around the second coil. Then, magnetic lensing may further enhance the collimating effects on the beam. The spatial compression of the beam is successfully demonstrated, but the spectral compression does not take place efficiently in this simple target geometry. The following section will examine a geometry that is also compact but more complex and that has more influence on the spectrum.

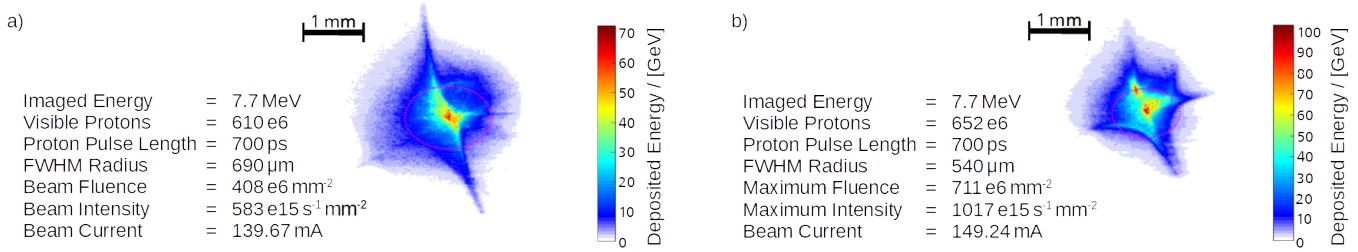

Figure 5.74: (a) The focal spot of the solenoid at Z4 for standard operation of the LIGHT beamline, in units of deposited energy. (b) The focal spot for a shot with micro-compressor as particle source, with exact same tuning of the beamline. One notes a higher peak fluence at about the same beam current when deploying the micro-compressor.

5.3.2.2 Numerical Study for a Conic Helical Compressor

In order to deploy the EMDP in complex targets for spatial and spectral ion beam tailoring, knowledge of the spatial and temporal pulse shape is of major importance. The pulse may be adequately modeled as Sommerfeld Wave [S. +15] or with a charge density distribution following the geometry of wire sections of the target [S. +16] – by also taking into account the displacement current as discussed herebefore. Note that a theoretical model for the exact pulse shape is not available yet, authors employ fits to experimental data or costly Particle In Cell (PIC) simulations. Three detailed experimental observations deploying simple target geometries report on rise times of ≈10 ps for various driver laser systems and differing geometries for the laser-interaction region on the target: first a Ti:Sa laser system with a laser pulse of 150 fs duration and 70 mJ energy that is focused at 10^{18} W cm^{-2} directly on the target wire [S. +15], second the ARCTURUS laser system at Heinrich-Heine Univ. with 30 fs pulse duration and 3 J energy that is focused at 10^{20} W cm^{-2} on a squared plate with 2.3 mm sides conductively connected to the target wire [S. +16; Had+20] and thirdly, discussed with this work, the PHELIX system at GSI with 500 fs duration and 50 J energy that is focused at 10^{19} W cm^{-2} on a 2 mm diameter disk laser-cut from a foil with the target wire. The FWHM of pulses is 10 ps, 15 ps and 50 ps and the integral charge 16 nC, 60 nC and 300 nC respectively.

Experimental results [Akt+19] in the regime of relativistic laser-target-interaction indicate that the EMDP maximum amplitude scales with the laser parameters following the ponderomotive scaling of the hot electron temperature [Wil+92; MV+96]. For constant laser intensity, one observes a monotonously increasing EMDP amplitude for larger focal radii, but a peaked maximum with following monotonous falling edge for a variation of the pulse duration. Albeit this is qualitatively consistent with target charging simulations, no bench-marked modelling of the discharge pulse is available solely based on the interaction parameters. Note, to avoid assumptions on the EMDP shape and amplitude one may determine it in a single shot geometry [H. +16] prior to application, as motivated with excellent results of the strategy in [S. +16]. For this generalizing study, the EMDP is modeled according to the fit function found earlier in this work, see eq. (5.29), which reads

$$\lambda(t) = \frac{Q_0}{k + \mathrm{e} - 1} \cdot \begin{cases} 0 & \text{if } x \leq 0 \\ \frac{k}{\sigma} \left(\frac{v_g t}{\sigma}\right)^{k-1} \exp\left[1 - \left(\frac{v_g t}{\sigma}\right)^{k}\right] & \text{if } v_g t \leq \sigma \\ \frac{k}{\sigma} \exp\left[1 - \left(\frac{v_g t}{\sigma}\right)\right] & \text{if } v_g t > \sigma \end{cases}, \tag{5.59}$$

where Q_0, v_g, k and σ denote the total target discharge, the group velocity of the pulse, the form parameter and the characteristic pulse length. Experimentally obtained data can be fitted by this formula for different laser-target interaction conditions and conductor geometries. Hereinafter provided simple estimates aim at the study of a pulse with a minimum possible pulse length, and thus maximum possible intensity. Such a well pronounced peak can be of interest in chromatic charged particle beam lensing applications whereas a flat peak is more suitable for applications to a broad energy spectrum.

The peak of the pulse is attained for

$$t = \sqrt[k]{\frac{k-1}{k}} \cdot \frac{\sigma}{v_g} := \tau_L + \delta\tau \quad , \tag{5.60}$$

here assumed equal to the laser pulse length τ_L plus a extended target discharge time $\delta\tau$ depending on the cooling of the hot electron distribution. For the following, the group velocity of the pulse is set to the speed of light $v_g := c$. Therefore, the maximum of the linear charge density is given as

$$\lambda_{max} = \frac{Q_0}{v_g \cdot (\tau_L + \delta\tau)} \cdot \frac{k-1}{k+e-1} \cdot \exp\left[\frac{1}{k}\right]. \tag{5.61}$$

Aim is to maximize the discharge peak amplitude while minimizing the characteristic pulse length. Note that only $k \geq 1$ allows for a maximum in the model function and $k > 1$ for a finite gradient in the rising edge. For $k \approx 1$, eq. (5.61) simplifies to $\lambda_{max} \approx Q_0(k-1)/v_g(\tau_L + \delta\tau)$ and eq. (5.60) to $\sigma \approx v_g(\tau_L + \delta\tau)k/(k-1)$. In this limit, one approximates the characteristic pulse length to

$$\Rightarrow \sigma_{O(1)} = v_g \cdot (\tau_L + \delta\tau) + \frac{Q_0}{\lambda_{max}}. \tag{5.62}$$

Further one presumes $\delta\tau \to 0$ for simplification, which will further maximize the discharge pulse amplitude, at risk to overestimate the field strength. Holding constant the ratio $Q_0/v_g\tau_L$ in eq. (5.61) yields a constant discharge pulse peak, which is feasible for short pulse duration where the total target discharge increases with increasing pulse duration, see [Akt+19]. Then reducing the laser pulse duration yields for eq. (5.62) shorter discharge pulses. Another approach to higher pulse amplitudes and lower pulse duration is the decrease of the group velocity, which is possible by pre-heating of the target as seen in section 5.2.3.3.

Note that this set of equations represents only a rough estimate that may motivate further studies on how the pulse shape is influenced by discharge dynamics and target geometry, *e.g.* numerically by target discharge simulations coupled to a Maxwell solver or following recently discussed analytical modelling [Bra+20b; BKB20]. For applications, it may be essential to produce an EMDP with fixed design parameters, and thus find exact relations.

Applying ChoCoLat, allows quick parametric studies to find a rough estimate of the total target discharge by intense laser interaction on solid targets. Figure 5.75 illustrates two examples of parametric studies with ChoCoLat focusing at the parameter range of two existing large scale laser facilities. The capability of solid target discharge at the PHELIX system at GSI is compared with the soon to be operational L4 beam at ELI-Beamlines. Contours correspond to iso-lines of equal target discharge mapped over the parameter space of focal spot size and laser pulse duration. Both numerical studies are set up around a realistic optimum maximum intensity, represented by the intersection of dashed lines. The laser absorption is set to 50 %. Note

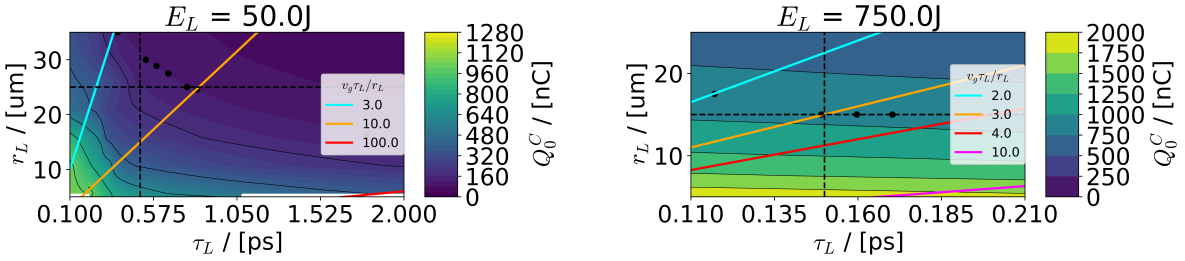

Figure 5.75: Simulated total target discharge mapped for the parameter space $(\tau_\mathrm{L}, r_\mathrm{L})$ of laser pulse duration and FWHM Gaussian focal spot radius in case of a $\lambda_\mathrm{L} = 1\,\mu$m laser for a given amount of absorbed laser energy E_L. Dashed lines indicate parameters comparable to (left) PHELIX system at GSI with black points representing simulations yielding discharges of 120 nC, and (right) L4 at ELI-Beamlines with black points representing simulations yielding discharges of 850 nC.

that the discharge estimated by the numerical study systematically underestimates the true target discharge value by a factor of $2-3$ [Poy+18].

As discussed in section 5.2.3.3, according to a first modelling approach the discharge current directly translates into a radial return current. A discharge driven in the centre of a disk of radius R allows for a maximum discharge peak of

$$\lambda_\mathrm{max} = \frac{d_W}{2\pi R} \cdot \frac{[I_\mathrm{max}]^\mathrm{ChoCoLaT}}{v_\mathrm{g}} \quad , \tag{5.63}$$

streaming along an attached wire of diameter d_W. A second model starts from the potential building up due to the target discharge and allows for a maximum discharge peak of

$$\lambda_\mathrm{max} = \frac{d_W}{\pi R^2} \cdot \frac{[Q_\mathrm{max}]^\mathrm{ChoCoLaT} \cdot r_\mathrm{L}}{v_\mathrm{g} \cdot (\tau_\mathrm{L} + \delta\tau)} \left(1 - \exp\left[-\frac{v_\mathrm{g} \cdot (\tau_\mathrm{L} + \delta\tau)}{r_\mathrm{L}}\right]\right) \quad , \tag{5.64}$$

presuming the discharged region to be equal to the laser focal spot.

Constant ratios of $v_\mathrm{g}\tau_\mathrm{L}/r_\mathrm{L}$, plotted as solid lines in fig. 5.75. Their intersections with one respective iso-line representing equal target discharge lead to constant EMDP peak amplitude according to the second modelling approach. The peak amplitude varies less with varying laser parameters for small angle intersections.

The PHELIX system delivers up to 100 J in a $\lambda_\mathrm{L} = 1.053$ µm pulse of variable duration τ_L from $500 \cdot 10^{-3}$ ps to 2 ps that can be focused to focal spots with radius r_L ranging from 3 µm to 25 µm using varying focusing optics. L4 is designed to operate with central wavelength of 1.060 µm with a pulse length ranging $120 \cdot 10^{-3}$ ps to 100 ps at energies up to $1.500 \cdot 10^3$ J. Assuming a comparable range of short focal length, L4 proves to be more efficient in discharging targets due to the high intensities that can be archived in a range of short pulse duration. Both models agree, that the parameter space spanned by the L4 beam allows for more reproducible discharge peaks when fixing the laser focal spot size and varying the laser pulse duration.

Helical coil targets, illustrated in fig. 5.77, prove efficiency in experimental demonstrations with a simple spiral geometry [S. +16; Had+20; Bar+20]. The EMDP propagates with a forward velocity solely depended on the ratio of radius and pitch. Constant chromatic acceleration was investigated recently [Had+20] and

archived matching the pitch dynamically to the ion acceleration. This work further studies the effect of the EMDP on a broad TNSA ion beam spectrum, employing the discharge pulse in geometries with variation of pitch, radius and the number of coiling turns j. With in addition n independent helical coils connected to the interaction disc, one expects no changes to the discharge peak but only modifications of it's exponential tail - which is neglected hereinafter as major forces onto the particles emerge from the peak and as the presumption of $k \approx 1$ already covers the steepest decay.

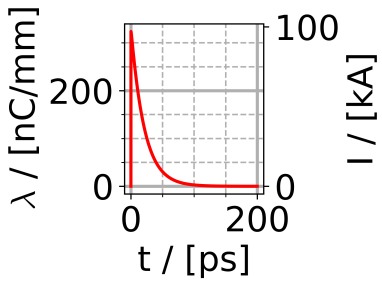

Figure 5.76: Heuristically deduced discharge peak induced by a L4 class laser on a dispersion free gold target with a target disk diameter set to 370 µm and an exit rod of 20 µm width.

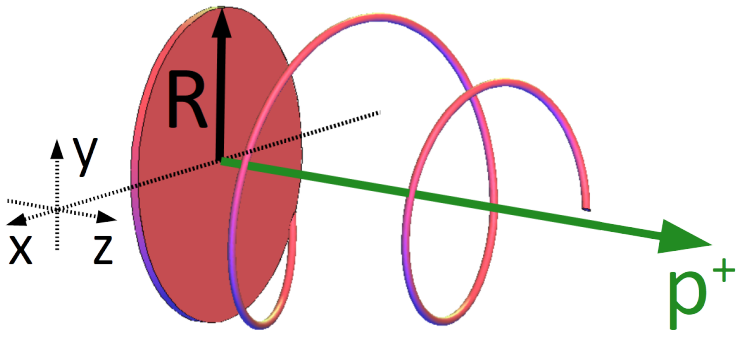

Figure 5.77: Target comprising helical coil and interaction disk: the laser hits the target on the side facing $-z$. EMDP and TNSA are driven by the very same interaction. We vary the number of 2π-turns per helical coil and the amount of independent coils connected to the same interaction disk.

The L4 laser interaction is studied with a solid gold target, set to absorb 750 J of the pulse energy, applying a pulse compressed to 150 fs focused in a 15 µm radius focal spot. The interaction with a 20 µm thick disk target at $700 \cdot 10^{18}\,\mathrm{W\,cm^{-2}}$ leads to a total target discharge of $2.1(4)$ µC and corresponds to the parameter space mapped in fig. 5.75. The target disk diameter R is set to 370 µm the exit rod width d_w measures 20 µm. With the empirical estimate following eq. (5.64) which is in a better accord with results obtained in this work, the discharge peak λ_max then reaches $315(60)\,\mathrm{nC\,mm^{-1}}$. With form parameter $k \approx 1$, eq. (5.62) points to a pulse length of $\sigma = 6.7(12)$ mm.

The pulse for the following numerical study has a peak of $\lambda_\mathrm{max} = 315\,\mathrm{nC\,mm^{-1}}$, $\sigma = 6.25$ mm and $k = 1$, illustrated in fig. 5.76. The resulting peak with FWHM of 30 ps has a spiked slope that reaches displacement currents of ≈100 kA.

In order to estimate the TNSA particle spectrum that can be archived with the L4 laser parameters, first the ponderomotive scaling points one to the hot electron energy of 8.17 MeV. Then the maximum energy for TNSA protons can be derived according to a quasi-static model of Passoni and Lontano [MM08], which is supported by experimental data only up to 500 J and $300 \cdot 10^{18}\,\mathrm{W\,cm^{-2}}$: the cut off energy calculates to 82.4 MeV. Thus, the analysis focuses on protons with an energy between 1 MeV and 82 MeV.

A helical coil with axis z, helicity s, pitch p and radius r is defined with $r \exp\left[\mathrm{i} \cdot (sz/p) \cdot 2\pi\right]$, where x and y coordinates are real and imaginary part respectively. Here, in a helical coil of axial length h, both the radius and the pitch are varied in a heuristic manner. The radius is step-wise linearly decreasing with a sequence of two slopes m_1 and m_2 that are defined with respect to the axial coordinate. The pitch linearly increases with slope m_3 with respect to the number of completed turns of 2π. Each turn is divided in $N = 100$ vectors and the coordinates of the target geometry are described with

$$
\begin{aligned}
\vec{r} &= \begin{pmatrix} -r\left(Z(\theta)\right) \cdot \cos\left[\theta + \theta_0\right] \\ -r\left(Z(\theta)\right) \cdot \sin\left[\theta + \theta_0\right] \\ Z(\theta) \end{pmatrix} \\
\text{with } r(Z) &= \begin{cases} R + m_1 \cdot Z & \text{if } Z \leq l_0 \\ R + m_1 \cdot l_0 + m_2 \cdot (Z - l_0) & \text{if } Z > l_0 \end{cases} \\
Z(\theta) &= \frac{h}{j \cdot (1 + m_3)} \cdot \frac{\theta}{2\pi} \cdot \left(1 + \frac{\theta}{2\pi} \cdot m_3\right) \\
&\quad + h \cdot \left(\frac{i}{j} - \frac{1}{2}\right) \ \forall i \in [1; j] \cap \mathbb{N} \\
\theta &= \frac{o \cdot 2\pi}{N} + \Delta\theta \ \forall o \in [1; N] \cap \mathbb{N} \\
\Delta\theta &= \frac{u \cdot 2\pi}{n} \ \forall u \in [1; n] \cap \mathbb{N}
\end{aligned}
\tag{5.65}
$$

where l_0 denotes the point where the slope of the radial coordinate changes. Now, the total length of the helical coil along the z-axis is set to $h = 1$ mm and further chosen are $l_0 = 400 \cdot 10^{-3}$ mm, $m_1 = -0.5$, $m_2 = -0.1$ and $m_3 = 0.5$.

With this choice of parameters, the velocity of the discharge pulse in direction of the mean particle beam propagation is increased with time, in order to follow the particles accelerated by the discharge pulse. This allows for a push of low energy particles to higher energies in an environment of close to quasi-constant acceleration. The decrease in helical radius is beneficial for the reduction of the particle beam divergence due to the converging conical guidance.

The influence of the EMDP on a charged particle beam is investigated by step-wise particle transport simulations using the PAFIN code. A proton beam propagates through the target geometry along its symmetry axis. In the course of this study, a variation of the number of turns per helix j and the number of independent helical coils n aims at maximization of the particle yield close to the main propagation axis and furthermore on an efficient post-acceleration of the low energy part of the beam spectrum. The later is beneficial firstly as the proton number at high energies can be efficiently increased by pushing the low energy part of the exponentially decreasing TNSA spectrum, and secondly as pushed ions will overtake their initially high energetic counterparts yielding a temporal compression of the particle beam.

For first insights, a flat-top particle spectrum is deployed, the initial divergence distribution is Gaussian with a RMS width of $400 \cdot 10^{-3}$ rad and the particle beam is symmetrically distributed around the z-axis. With $n \geq 3$ independent helical coils, the total amount of particles within a beam divergence angle of 45 mrad roughly doubles compared to the initial particle beam distribution. Similar results are obtained under variation of the number of turns j. This outcome is due to the symmetric push on the particle beam in such cases. With $n = 1$, the asymmetry of the EMDP itself and the inclination of the coil winding result in a non-vanishing radial component on the particle beam axis and therefore in asymmetric push. With $n = 2$, this asymmetries are compensated but the strong fields' radial components cancel each other only in a rotating plane with radial outward acceleration on particles slightly off-axis. For $n \geq 3$, the push yields inward acceleration within a radius $r_{\text{inw}} = r\sqrt{3/4}$.

The RLC-return current is enabled to run through all strings of the target, implicitly presuming that all strings are attached to a ring- or cone-shaped mounting that is conductively connected to the ground. A cold target of described dimensions has the resistivity of $24.4 \cdot 10^{-9}\,\Omega\,\text{m}$ and an inductance of the order of 10 nH per

helical coil. Result are long damping times and therefore an under-damped oscillation. The capacitance of the disk is $C \approx 26$ fF yielding eigenfrequencies of tens of GHz. In simulations, the return current is set to rise from the mounting structure only after the EMDP reaches it.

Figure 5.78 compares the modification of the particle beam spectrum due to variation of the number of turns j for the case with $n = 3$ helical coils, reducing the complexity of the target to a minimum. All projectiles are post accelerated. For $j = 1$ turn, the discharge pulse co-propagates with higher particle velocities than for $j = 2$ turns and influences most efficiently a part of the particle beam at higher energies. The most affected energy shifts towards lower energies with an increasing number of turns j, as the EMDP is then co-propagating with a lower speed in z-direction. The acceleration of protons originally born with low kinetic energies to energies higher than that of protons that are spatially in front of them is a clear signature of an over-rotated phase space ellipse, which yields the production of drift focusing. One clearly sees that the pulse amplitude is not sufficiently high to lead to a temporal compression of the beam at high energies with $j = 1$ turn, yet the phase space is flattened and spatial energy compression archived.

With $n = 3$ independent coils of which each has $j = 1$ turn, an RLC return current rises after 27.86 ps that has a decay constant of 53.13 MHz and a main frequency of 89.27 GHz. Note that the rising return current will only have an influence on protons with energy $<$6.8 MeV. Maintaining the number of coils $n = 3$ but increasing the number of turns to $j = 2$, the RLC return current rises after 51.23 ps with a decay constant of 52.41 MHz and a main frequency of 66.12 GHz. This return current influences even lower proton energies of $<$1.7 MeV. In both cases, the return current can not lead to qualitative changes in the spectral response, neither to particle numbers reaching the end of the coil within any ROI. The peak amplitude of the return current for $j = 1$ turn and $n = 3$ coils is 225 kA, reached after 45 ps and in case of $j = 2$ turns and $n = 3$ coils the amplitude reaches $>$150 kA after 75 ps. The high return current can only be applied if a particle beam is independently driven to pass the target geometry for late times of the dynamic current evolution, as proposed for a Helmholtz coil geometry by Kar et al.

In order to better illustrate the benefit of post-acceleration, the discharge pulse is applied to a TNSA-like particle spectrum in a case with $j = 2$ turns of $n = 3$ independent helical coils. The initial spectral slope is set to correspond to a hot electron temperature of 8.17 MeV as motivated above, and the particle beam energy distribution is modelled with the isothermal expansion model as described in [RS16]. Results are depicted in fig. 5.78 (e-f) and detailed in fig. 5.79. The post acceleration effect increases the amount of particles at intermediate energies by up to an order of magnitude. Protons of initial energies ranging from approximately 5 MeV to 15 MeV are post accelerated to approximately 40 MeV to 50 MeV, with a clear number-density enhancement up to 70 MeV. Note that every change in target geometry will result in the discharge pulse efficiently accelerating an individual dedicated particle energy. Note also, that the violent fields of the discharge pulse are a threat to low energy particles propagating behind the discharge pulse peak: they get decelerated and increase their divergence.

With all presumptions aiming at a maximum EMDP amplitude, numerical results are probably over-estimating future experimental outcomes. Nevertheless, the manifold of tuning parameters related to target discharge and target geometry are promising for tailor-made micro-compressor platforms aiming at applications ranging from ion fast ignition to enhanced plasma accelerators.

5.3.3 Summary of Results

This work follows two strategies to apply EM lensing to laser driven ion sources: first applying the fields during the acceleration mechanism takes place, or second by tailoring beams early after formation. Following the first

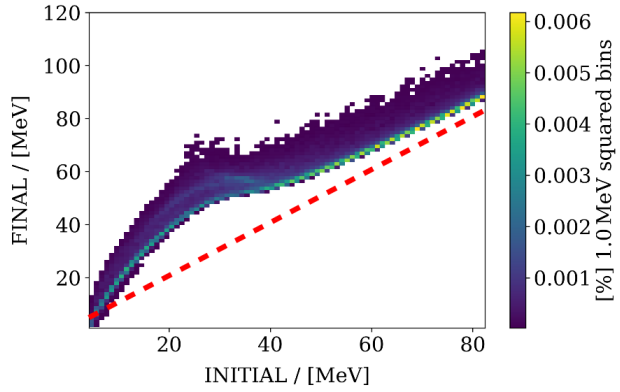

(a) Full Beam for $n = 3$, $j = 1$ with RLC-Current and flat-top particle spectrum

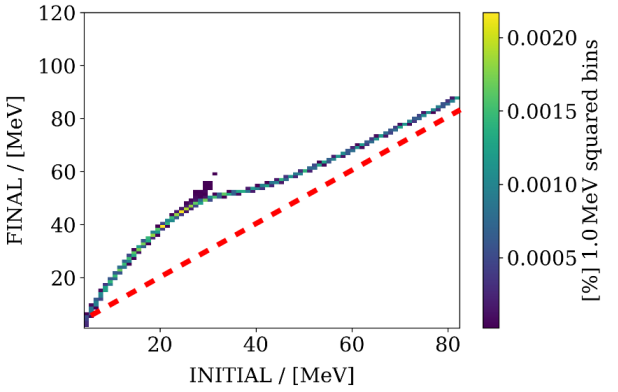

(b) 45 mrad ROI for $n = 3$, $j = 1$ with flat-top particle spectrum

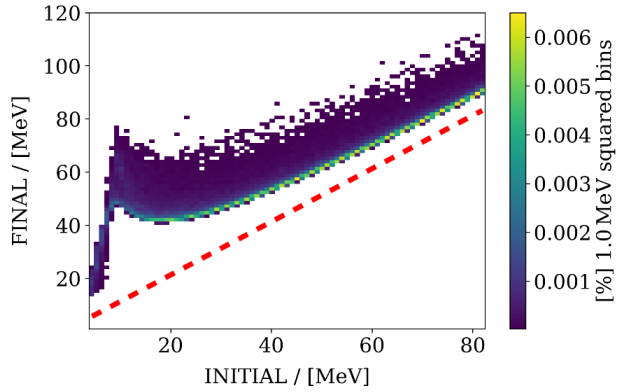

(c) Full Beam for $n = 3$, $j = 2$ with flat-top particle spectrum

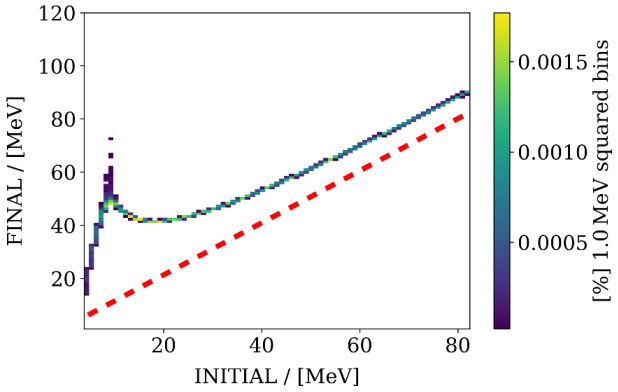

(d) 45 mrad ROI for $n = 3$, $j = 2$ with flat-top particle spectrum

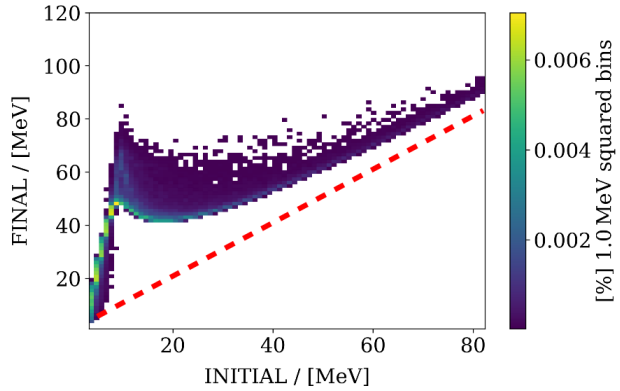

(e) Full Beam for $n = 3$, $j = 2$ with TNSA-like particle spectrum

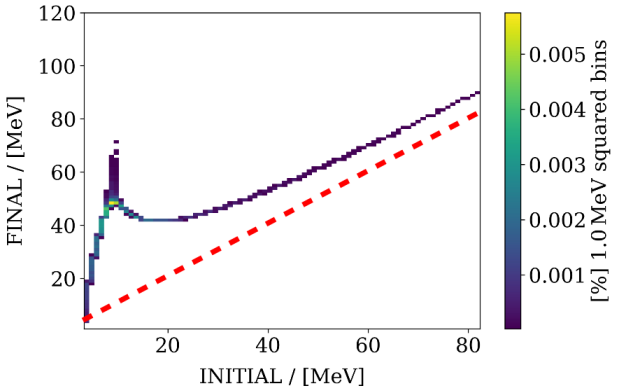

(f) 45 mrad ROI for $n = 3$, $j = 2$ with TNSA-like particle spectrum

Figure 5.78: The particle beam is tailored by an EMDP propagating in helical coil configuration, with variation of the number of independent helical coils n and their respective number j of full 2π turns. Pairs (a,b), (c,d) and (e,f) contrast the full particle beam spectra (respective left) with smearing for large divergence angles due to post acceleration effects and (respective right) for the fraction of particles that forward propagate within a divergence of half-angle 45 mrad. A red dashed line represents the linear relation of an unchanged kinetic energy: post-acceleration is observed for the whole particle beam, only asymptotically fainting for high particle energies. A clear peak unravels the possibility for ToF compression and energy compression. The colour scale is normalized to the total amount of input particles. The initial particle beam spectrum is flat-top for cases (a-d) and TNSA-like for (e-f).

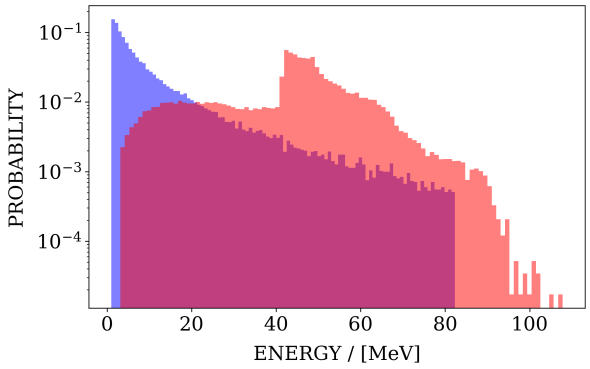

Figure 5.79: The effect of the discharge pulse to a TNSA-like particle beam spectrum: initial particle beam energy distribution in blue, the spectrum at the exit of the simulation box at the end of the target in red. The EMDP spirals within $j = 2$ turns of $n = 3$ independent helical coils, yielding formation of a spectral peak around $50\,\mathrm{MeV}$.

strategy, magnetized TNSA produces brighter ion beams and denser relativistic electron beams, see fig. 5.69 and fig. 5.70 respectively. The magnetization of the solid target for TNSA is based on the ultra-strong B-field of 200 T generated by plasma dynamics on a Double Plate Ω-coil Target driven by an intense ns laser pulse. Besides the emittance bettering for generated ion beams, results that show enhanced relativistic electron beams are promising, *e.g.* for future secondary electron sources or electron beam driven X-ray sources.

In the framework of the second strategy the functionality of a plasma accelerator enhanced by a Helmholtz-coil micro-compressor is demonstrated experimentally, doubling the maximum achievable intensity of the integrated beamline, see fig. 5.74. EM fields carrying several T and $\mathrm{GV\,m^{-1}}$ are induced by the EM discharge pulse that is driven during solid target discharge by ultra-intense sub-ps laser pulses. Tuning of the platform is possible with respect to three mechanisms at play: the EM discharge pulseitself, the induced return current and eventually reflections of the EM discharge pulse. Results are promising for future all-optical platforms capable of spacial and spectral charged particle beam tailoring. The small scales of the platform have two major advantages: the ToF broadening of the beam is easy to revert by phase space rotation and it can be readily implemented in compact HED plasma physics experiments.

A numerical case study illustrates the efficient particle beam tailoring capabilities of EM discharge pulses propagating along conic helical coil targets of advanced symmetry, with multiple independent coils each of several 2π-turns that are connected to the same laser interaction region, see fig. 5.77. Three independent coils are sufficient not to distort the particle beam regarding the angular distribution, minimizing the complexity of the target. Variation of radius and pitch along the particle beam propagation axis allows to follow post-accelerated particles for efficient spectral shaping. TNSA-like proton spectra of initial energies ranging from approximately 5 MeV to 15 MeV are post accelerated to approximately 40 MeV to 50 MeV, see fig. 5.79. Thus, low energetic particles are driven to energies that allow them to overtake parts of the beam at initially higher energies. The resulting compression by time-of-flight can be controlled with the target geometry and the EM discharge pulse parameters. As a perfect target geometry is crucial for studies and applications, target manufacturing techniques have to be developed, with possible benefit from advanced state-of-the-art 3D printing techniques.

6 Conclusions and Outlook

This work discusses the generation of ion beams with a high particle flux and optimal emittance, and also techniques that enable high-repetition rate particle beam generation with bunches at high current densities. New aspects promoted by this work comprise (6.1) an extension to the protocol for spectrometry of ions with SSTD that decrease ambiguity in analysis results; (6.2.1) the experimental acceleration of ions up to intermediate-high energies of tens of MeV by a compact laser-driven system, that can be made ready for HRR operation; (6.2.2) the first successful experimental evidence for an emittance improvement of TNSA ion beams accelerated from magnetized thick solid samples; (6.3.1) the solution to the open question of the origin of charges, which electrically shield laser-driven quasi-static magnetic lenses for ion beam tailoring; and (6.3.2) the investigation of a EM micro-compressor of simple geometry for laser-accelerated ion beams. Further experimental data is presented to feed the scientific debate about (6.4.1) the current inducing mechanisms of long-pulse laser-driven magnetic lenses; and (6.4.2) the discharge pulse for EM lensing, induced by short-pulse laser-driven target discharge.

A use-case scenario that covers many aspects of this work is outlined (6.5) and an outlook (6.6) is given to plausible future work on ion beam tailoring with Ω-coil targets.

6.1 Extended Diagnostic Capabilities of Solid State Track Detectors

In literature, SSTD such as CR-39 are presented as a well understood diagnostics for the determination of absolute ion numbers. Some authors retrieve the energy of impacting projectiles by collecting information on either the diameter or the depth of etched tracks, leaving room for ambiguity concerning the impacting species. The later is mostly resolved by additional spectrometry, then omitting the spatial resolution. In this work, CR-39 are deployed to detect spatial and spectral features of ion beams at the same time (section 5.1.2.2). In particular, it is demonstrated that CR-39 nuclear track detectors are applicable as energy-mass-spectrometer by extension of the standard analysis protocol to comprise both, measurement of track length and diameter, see section 4.3.2.4 and section 5.1.2.2. A future development of the diagnostic has to go hand in hand with the elaboration of automatized data analysis techniques [Rus+91], promising the possibility of efficient use of the detector. Research and development must focus on technical aspects to automatize calibration and analysis of CR39 according to the extended protocol. The diagnostic can be deployed as low-repetition rate high-quality back-up.

6.2 Further Steps in Laser-driven Ion Acceleration

The well studied laser-driven TNSA approach to ion beam generation produces beams of broad exponential spectrum and large opening angle. It is mostly conducted relying on solid targets, which are repetition rate

limited. Here, the micro bunch repetition rate depends on the achievable frequency of target replacement, in principle possible with target wheels or tape targets to the order of 10 Hz. The repetition rate between macro-bunches depends on the alignment time of one target system, of the order of tens of min. The macro-bunch repetition rate might be improved by recent efforts in automation based on computer algorithms. Such repetition rates are suited only for application in fundamental research, where detector read out times are often of the order of several seconds to minutes.

6.2.1 High Repetition Rate Ion Sources

Carefully designed near-critical density gas jets prove to be efficient targets for reproducible generation of beams of ionizing radiation, see section 5.1.2.1 and section 5.1.2.2. The reproducibility observed in this work is limited to one series of shots, and not a day-to-day stability of results. This work demonstrates laser driven ion acceleration from a supersonic gas jet, a low-debris and HRR ready target. The operation repetition rate is mostly limited by the pumping power of the chamber vacuum systems and the damage to the gas jet nozzle.

The acceleration of Helium ions to up to tens of MeV can be driven by a 30 fs, 3 J, $120 \cdot 10^{18}$ W cm^{-2} Ti:Sa laser pulse from a pure near-critical density supersonic gas jet at atomic densities of several 10^{20} cm^{-3}. In addition, passive dose detectors show laser-forward directed imprints of doses of tens of Gy, which could not be related to detected alpha particles. Next experimental studies must investigate if these directed beams are due to electrons, to photons or at least partially to ions, principally bringing together the determination of occurrence from ToF results and the spatial distribution from RCF. This is possible by exhaustive studies based on CR-39 or arrays of EM charged particle spectrometers. Then, the emittance characteristics of the ion beam must be examined, *e.g.* by tracing images of meshes introduced in the beamline. Further, PIC simulations can be undertaken to reproduce experimental results, in order to determine whether CSA or TNSA is the accelerating mechanism at play. Results presented in this work agree qualitatively with predictions made for CSA ion beams accelerated from plasma spheres that have a radially decreasing density, see section 3.4.2.2. This motivates further investigation regarding plasma cylinders, that result more likely from interactions where the Rayleigh length is much larger than the focal spot radius.

The similarities to the model predictions (section 3.4.2.2) allow qualitative predictions for future experiments. The smaller the ratio of hot electron temperature T_0 and the product of electron density n_e and the radius R_0 of the pre-heated plasma $T_0/n_\mathrm{e}R_0^2$, the better is the contrast of the spectral peak with respect to the overall spectrum. Further, the larger the product $Z_\mathrm{i}n_\mathrm{e}R_0^2$, where Z_i is the charge state of the plasma, the larger is the cut-off energy and the overall number of accelerated ions. Last, by keeping the product T_0Z_i constant, the position of the spectral peak remains approximately constant. To accelerate from Hydrogen jets similar spectra as observed from Helium jets, higher electron temperatures and thus a higher power driver laser is required, as well as gas profiles of higher electron density. Then, larger pulse energies are crucial to energize a larger system.

If broad and forward directed features detected in RCF results proof to be due to the detected alpha particles with energies above 40 MeV, then the source would have a direct oncologic applicability for isotope production in alpha-therapy. The cross section for Astatine-211 isotope production from Bismuth-209 by bombardment with alpha particles, see fig. 6.1, is important for alpha particle energies above 20 MeV. Note, that the cross section for Astatine-210 isotope production from Bismuth-209 starts to be relevant above 28.3 MeV [Her+05; AMB19], itself decaying to long-living Polonium-210 which is not directly suited [Had19] but under evaluation [Ike+18] for alpha therapy.

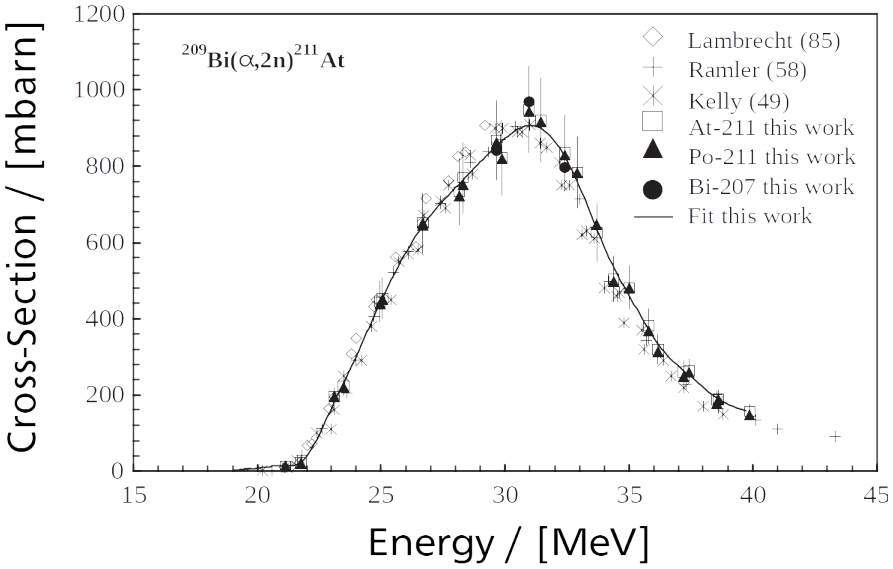

Figure 6.1: Cross-section for the ^{209}Bi$(\alpha, 2n)^{211}$At reaction, where (A) is the graph for the experimental cross-section, (B) and (C) are results of theoretical calculations, extracted from [Her+05].

Attributing the full dose that is detected on RCF to alpha-particles, the measured ion number density reaches $\approx 200 \cdot 10^6\,\mathrm{MeV}^{-1}$ in the energy range of interest. Integrated over the interval from 20 MeV to 28.3 MeV, this results to a time averaged and repetition rate normalized beam current of $10\,\mathrm{pA\,Hz}^{-1}$. A state of the art cyclotron facility can reach alpha particle beam currents of 35 µA [Had+11] for such energies. For a laser system to be able to compete, the repetition rate should exceed 1 MHz, which is out of the scope of state of the art technology. This is clear motivation to further investigate the acceleration mechanisms at play and optimize the yield of accelerated particles.

Such low beam currents might be of interest in radio-chemistry experiments. Radiolysis, the breaking of chemical bonds by radiation, is conducted with alpha projectiles with tens of MeV [SB87] and beam currents of 10 nA to 100 nA. Further optimization of the platform towards a higher ion yield is of interest regarding the production of short ion bunches for ps-pulse radiolysis research [Bal08]. Single shots with high brilliance sources are ideal for not time averaged observations, promising for unprecedented insights [BZN+20].

These possible applications underline the necessity for further target and diagnostics development in order to follow the HRR of the new generation of Ti:Sa systems at 1 Hz to 10 Hz, important to achieve a high average particle flux which in turn is necessary for applications and experiments that require a lot of shots for statistical evaluations. Challenging aspect is the acceleration from hot, dense, plasma, which is not only emitting high energy EM radiation, photons, electrons and ions during interaction but also causing thermal effects and induced discharge currents on timescales longer than the laser duration. This effects create a violent destructive environment for the shock nozzles, with optimum gas density profiles in sub-mm distances from the nozzle surface. With fig. 6.2, see nozzles used in this work after the experiment imaged with an optical microscope. Compared are damaged nozzles and a new nozzle with regard to their different surface and the quality of the exit rim.

The advent of sub-µm high precision 3D printing of mesostructure ceramics [Jon+19] may be beneficial to mass-produce more robust and more precisely tailored shock nozzles. This is advantageous for experimental studies of the platform that aim at parametric studies. For applications, 3D printing entails reproducibility, but efforts towards automatized nozzle exchange systems and good vacuum systems remain non-trivial technical

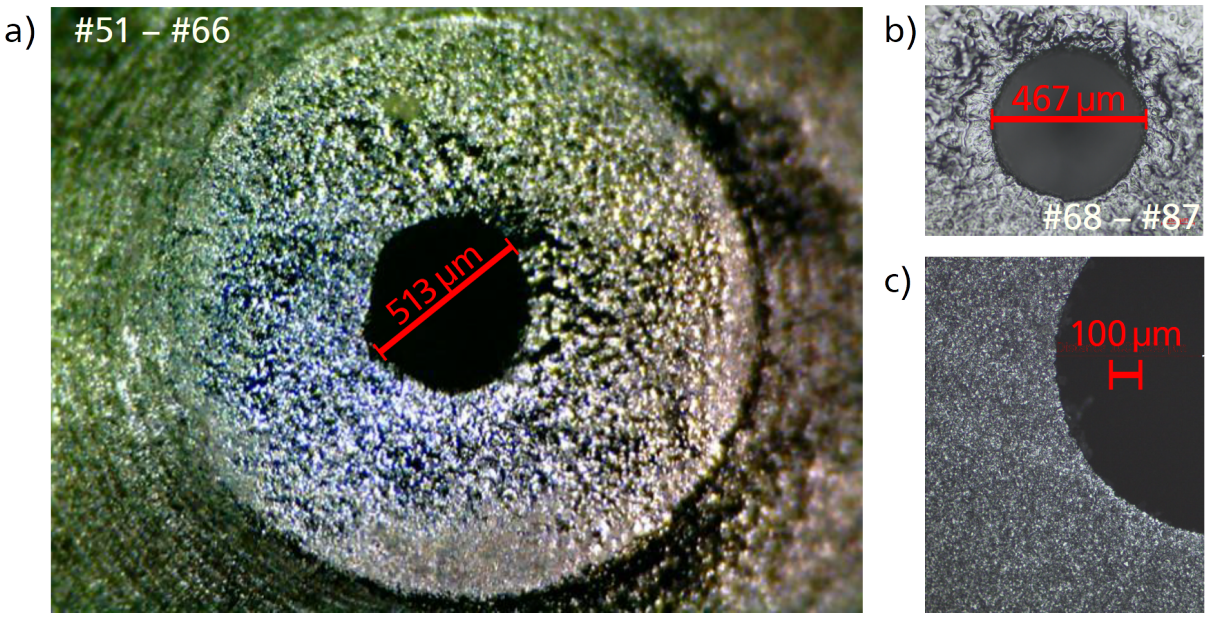

Figure 6.2: For reasons of irradiation or strong return currents, shock nozzle likely suffer from melting-condensation cycles on a shot-to-shot basis. The shock nozzle used for shots (a) #51 to #66 and (b) #68 to #87 in section 5.1 with clear damages to the respective rim, for which perfect cylindrical symmetry is essential for the quality of shock formation. (c) Is a typical nozzle surface with perfect and circular rim-to-surface edge. Note the difference between the surface quality of used and new nozzles: used nozzles show bubble like structures that mat arise due to melting and re-condensation.

challenges. On the diagnostics side, a HRR ready spectrometer must be able to scan a range of solid angles, *e.g.* based on a B-field for mono-molecular gas jets in a compact price-efficient design [Mor+18b; Pal18; Mor+18a].

With perspective to proton-boron fast ignition, studies with Hydrogen jets are essential. Exploratory experiments aiming at the generation of proton beams are hindered by the danger related to gaseous Hydrogen [Por+37]. Note that recent studies with liquid jet targets successfully generated and studied TNSA at HRR with performant diagnostics [Mor+18b; Pal18; Mor+18a], offering another promising route hence with high debris for the high flux of molecules.

6.2.2 Magnetized Target Normal Sheath Acceleration

Besides HRR operability, the reduction of emittance or the reduction of opening angle of laser-accelerated ion beams at birth is further of interest to minimize the attainable focus size of charged particle beams and maximize the coupling efficiency into possible beam transport. Magnetized TNSA improves on the emittance of the accelerated ion beam, yielding narrower opening angles due to the restructured sheath field, and leads to higher ion numbers for the enhanced REB transport through the target. This work demonstrates TNSA from magnetized solid samples, see section 5.3.1.3. The beam intensity is improved to ≈150 % with respect to a un-magnetized reference.

Such source is aiming at low repetition rate research applications. Required for use are technological advances in targetry, such as large-scale production, exchange systems, process automation, debris control and debris removal systems.

Magnetization of sub-mm samples is archived in fields induced by currents running through Ω-loops, alimented by ns-laser driven diodes, also applicable to ion beam tailoring in free space.

6.3 Charged Particle Beam Tailoring

For the efficient collimation of laser-generated ion beams with large divergence or for down-focusing of beams to high energy density, EM lensing is necessary. The transport of laser-driven ion beams to distant applications is possible by standard accelerator technology, but the efficient collection of beams with large divergence very close to the source remains challenging. For compact beam transport within distances not larger than the usual sub-mm sizes of laser-plasma experiments, the needed ultra-strong magnetic fields exceed the possibilities of large-scale accelerator transport elements such as solenoids and quadrupole magnets.

6.3.1 Shielding Effects in ns-laser Driven Magnetic Lenses

B-fields of Ω-coil targets are promising tools for their ultra-strong laser-driven currents ranging up to several hundred kA. When driven by a ns-laser, the induced B-fields risk to be shielded by electrons that accumulate on small Larmor radii in vicinity of conducting rods. This work finds the perturbation stated in earlier work [San+15; SBGE+18] to be likely caused by the plasma dynamics underlying the current. The thermally expanding plasma is polarized by the ultra-strong B-fields in vicinity of the conductor and electrons are being caught on their Larmor orbits on long timescales. A perfect toroidal distribution gives good agreement with experimental results in heuristic particle transport simulations, but detailed PIC simulations indicate an asymmetry in the potential distribution. The exact spatial distribution might be resolved in future experiments by axial probing. Increasing the complexity of capacitor coil targets betters only slightly the decrease of shielding effects, despite tremendously lowering the B-field amplitude due to a – by factors – higher inductance of the target.

Further work could try to tailor the plasma expansion in order to protect the coil from shielding effects and heating, *e.g.* by introducing obstacles or field inducing features that confine the plasma to a distinct expansion. One also may envisage to change the target design of the magnetic lenses to yield a minimum inductance and a maximum shielding from plasma effects, such as illustrated in fig. 6.3. Here, the front plate of the standard capacitor coil target is exchanged with a cylinder. Such modification means a major change to the plasma dynamics. New target geometries must be evaluated with respect to their performance as plasma diode.

One may well also only use a single plate design, which was mimiked in this work by a inverted capacitor coil target and independently proven operational in [Kum+20]. The inverted target performed comparable to standard capacitor coil shots with the same laser in the same campaign. Both are able to reach currents above 100 kA.

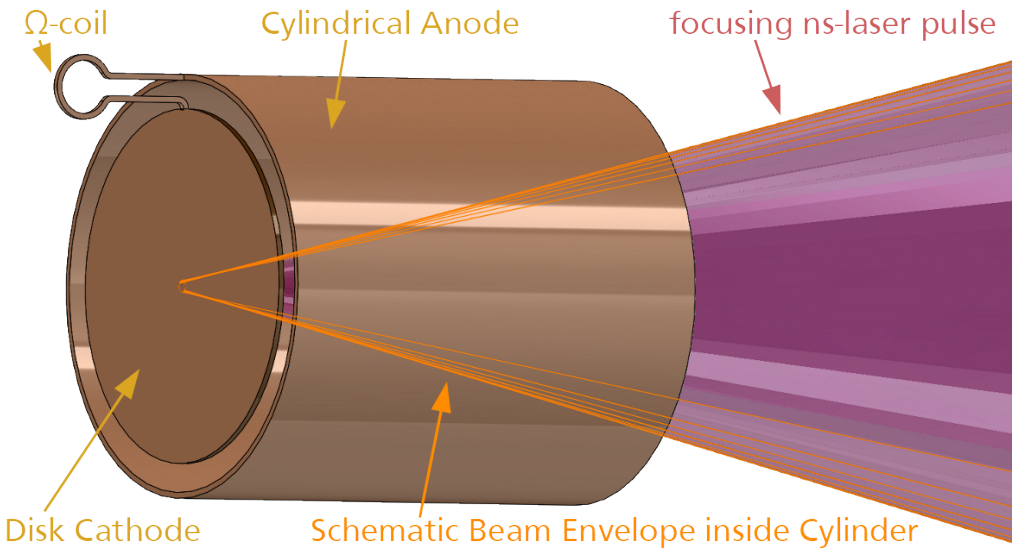

Figure 6.3: Halfraum Ω-coil target with a laser-driver entering from the right in normal incidence to the cathode plate. The target could be mounted non-conductively at the cathode.

6.3.2 Micro-Compression after Target Normal Sheath Acceleration

The fields of the transient discharge pulse induced by ultra-relativistic laser-target interaction are strong enought to guide TNSA beams even in targets of simple geometry. This work shows that this fields of tens of ps lifetime and amplitudes of multiple $\mathrm{GV\,m^{-1}}$ and several Tesla guided by simple flat Ω-coil targets can be applied to chromatic charged particle beam tailoring, see section 5.2.3.2 for protons in the range of 10 MeV. Using a dual laser set-up, energy-selection of the particles with reduced opening angle is possible by tuning the delay between the laser pulse driving the coil and the one generating the proton beam.

The return current in such a platform is being detected as Pulse Discharge Current which evolves on a timescale of tens of ps with amplitudes of several kA. EM field platforms with strong magnetic component driven by short pulses overcome the drawbacks of the X-ray bathing of secondary samples on the time scale of ns and last sufficiently long for steady guidance of high energy ions. Moreover, they are well suited for the many new research facilities that dispose of Ti:Sa PW class HRR laser systems, aiming at a B-field platform for experiments at an intermediate repetition rate.

Further, micro-compression is elaborated for the use-case scenario of an improved coupling of TNSA beams into standard accelerator beamlines. The spectral and spatial shaping of laser-driven proton beams is a hot topic in the accelerator community, using pulsed high-field magnet beamline [Bra+20a]. For an enhanced effect and aiming at spectral compression, the discharge pulse is split in two portions and guided through a double-loop Helmholz coil-pair, see section 5.3.2.1. The target is build in order to accelerate the self-generated ion beam into the coils' symmetry axis and with attention to the timing of the passage of ion beam and both pulse portions through the respective coil. This form of micro-compressor is improving the ion beam number density per unit area by a factor of two. Recently, is was reported that more complex targets are able to improve the brightness of the beam by orders of magnitude [S. +16].

Future work could investigate precisely tailored complex geometries, as motivated in section 5.3.2.2. EMDP can be deployed for ToF compression, energy compression and it may be possible to set up experiments with elaborate temporal-pulse shaping for ion beams intended to heat secondary samples. The simulated shaping

of TNSA spectra to incorporate pronounced broad peaks around centre-energies of several tens of MeV is promising for applications in proton-triggered isotope-production for medical applications, see [ARR21].

6.4 Theoretical Modelling of All-Optical Platforms for Ion Beam Transport

The applicability of laser-driven beam transport elements is promising for future applications ranging from hadron-therapy to fast ignition, hence it is of great interest to fully understand the origin of laser-driven currents and the limiting mechanisms at play.

6.4.1 Diode Model

Further evidence is presented in favour of the Diode model for ns-laser driven coil target, albeit the ramp up phase of the coil current is not well resolved in the study with Faraday rotation measurements, see section 5.2.2.3. Further, the complex-interferometry results are of only poor quality. The experiment presented in this work must be repeated with a focus on the ramp up phase of the coiling current. Moreover, the current decay was not resolved with enough data points, it is important to observe coiling currents for longer delays to the driver-off time, in order to discriminate different oscillatory regimes of the circuit and to determine characteristic circuit parameters.

6.4.2 Discharge Pulse Model and Return Current Dynamics

Further insights are given into the dynamics of EM discharge pulses, regarding generation and propagation. This work covers relativistic intensity ps-laser driven discharge pulses and return currents and gives insights into the pulse regime between ultra-short fs pulses and long ns pulses. The birth of the EM discharge pulse could be explained with a pulsed potential that is excited by the laser-driven ultra-relativistic electrons when leaving the target, see section 5.2.3.3. The heuristic modelling of the discharge pulse peak yields results that agree for the order of magnitude with experimental data, but this is not sufficient for development of reliable ion beam tailoring platforms. A more physical modelling must solve the Maxwell equations in cylindrical coordinates on the interaction disk in order to take into account a spatial and temporal dependence of the current dynamics on the target due to the rising potential, and the coupling dynamics into the stalk. Especially, results of PIC simulations suggest a non negligible current dynamics in the skin depth of the target.

Theoretical modelling finds, that the highly non-linear dependence of the group velocity of the pulse is defined by two main parameters: effective plasma density and temperature. This is motivating studies towards controlled dispersion, *e.g.* by controlled irradiation. Here-before measured were fast group velocities close to the speed of light for clean targets that were on no line-of-sight of laser-plasma, and speeds down to 70 % of the speed of light are measured for targets with surface defects that exposed conducting parts of the target to irradiation stemming from the laser-plasma.

The discharge pulse rise time is a key parameter that influences the pulse intensity. The proton deflectometry diagnostic deployed in this work may have limited the measured rising edge to its intrinsic temporal resolution. In future important are optical measurement of fields of discharge pulses to remove ambiguities and to be able to conduct a precise parametric modelling of the phenomenon.

The transition between EM discharge pulse and pulse discharge current is for the first time experimentally resolved. In literature, comparable laser driven platforms are reported for the generation of pulsed B-fields [Zhu+18], and the tailoring of laser-driven particle beams [S. +16], but with no separation or identification of both transient currents. Note that a parametric study of the discharge pulse parameters has been carried out recently [Akt+19] investigating charge density maximum and integral charge as a function of laser pulse duration, pulse energy and pulse intensity. A partial characterization of the Pulsed Discharge Current has been carried out as well in [Wan+14], also demonstrating neutral kA currents.

Nevertheless, the rising edge of the pulse discharge current is not well resolved in this work, but of utter importance for a conclusive determination of the related pulse discharge current dynamics. Measurement is possible by polarimetry, as done for the long pulse driven platform in the course of this work. Complex interferometry could be valuable for simultaneous characterization of the plasma dynamics in vicinity of the target. A smooth transition would correspond to an evolution due to conductivity expected for hot surface plasma – a hypothesis that must be checked also by time resolved temperature measurements, *e.g.* by means of the detection of atomic relaxation spectra.

6.5 Synthesis

This work describes the path to laser-driven ion beam generation and direct applications of generated ion beams, but explored phenomena related to target discharge and magnetization open up new perspectives. First, future integrated studies could deploy a laser driven hydrogen jet for proton beam generation, aiming at proton-boron fast ignition with a focused proton beam impacting in proton boron fuel. Compression and beam transport can be adjusted to deliver a tailor made ion spectrum, which is suited for the specific ignition application [Rot+01b]. Specifically, the elaborate experimental set-up could comprise a metallic pick-up arm in vicinity of the plasma channel, apt to guide the return current dynamics. Return currents can be guided up to the cm-scale distances, looping in Helmholtz geometry around the beam axis for lensing, or in helical coils for micro-compression.

Second, beam transport for distant HEDP experiments, possibly by standard accelerator technology such as HF cavities and solenoid magnets, can be improved towards higher energy densities in smaller focal spots when deploying ultra-strong magnetic fields of Ω-coil targets for down-focusing.

6.6 Extrapolation of Results

Many questions that arose in the course of this work remain open, this section will detail on further research opportunities regarding Ω-loop targets.

Ultra strong laser driven magnetic lenses are subdue to perturbations by space charge effects, the lensing in the vicinity of coil features is partially compensated by E-fields. Besides shielding by obstacles or plasma tailoring, discussed herebefore, a conductive sample in the coil centre would shield off the electric potential and reduce the effect of E-fields on lensed particle beams. Ferromagnets or weak ferrimagnets allow for a net magnetization of the material parallel to the externally applied magnetic field. One must beware of the saturation of the magnetization, which does not allow to scale up ultra-strong B-fields largely. Ferromagnets and ferrimagnets retain their magnetization even after the external field has been removed and may be interesting materials for HRR applications, *e.g.* if meshes manufactured of this materials are used as micro-lensing arrays.

For cases which do not require shielding, compound crystals allow for high-amplitude magnetization. In addition, crystals show magnetization along crystallographic axis, where one expects ion channelling. Studies show capabilities of magnetization up to the 120 T [Kat+95] and recently discussed are compounds of $(\mathrm{Nd,Dy})_2\,\mathrm{Fe}_{14}\mathrm{B}$ potentially suitable for high temperature environments [Kos+20].

Magnetization of secondary plastic samples with Double Plate Ω-coil Target was demonstrated [BG+18]. Dielectric samples of 60 µm thickness were magnetised under 1 ns. Ferromagnetic pure iron has a low resistivity with $\rho = 1.105 \cdot 10^{-3}\,\Omega\,\mathrm{m}$ and relative magnetic permeability of $\mu_\mathrm{r} \approx 200$ – the magnetic diffusion time through L =60 µm calculates to

$$\tau_\mathrm{diff} = \frac{\mu_0 \mu_r L^2}{\rho} \approx 1\ \mathrm{ns} \quad . \tag{6.1}$$

One must be careful with the stopping power on ion beams that traverse the magnetized sample. Iron with a density of $7.87\,\mathrm{g\,cm^{-3}}$ stops traversing particles significantly. Natural maghemite has a lower density of $4.9\,\mathrm{g\,cm^{-3}}$ and a high relative magnetic permeability in a range from $2 \cdot 10^6$ to $2.5 \cdot 10^6$ in cold state with a peaked increase towards the Curie temperature of 948 K, after which it approaches quickly unity [GY16]. The material is weakly ferrimagnetic and a semiconductor with chemical form $\gamma - \mathrm{Fe_2O_3}$. The material is widely available due to its industrial use for the production of recording tapes. Its resistivity ranges between $100 \cdot 10^{-6}\,\Omega\,\mathrm{m}$ to $1 \cdot 10^6\,\Omega\,\mathrm{m}$ and diffusion times depend largely on the actual sample with a range from several ten fs to hundreds of ms for samples of tens of µm thickness. Besides the benefit of increased magnetization compared to pure iron, meghemite will be reacting to external toroidal potentials with a certain degree of radial polarization that yields an additional focusing effect on charged particle beams passing through its centre.

Magnetized samples have a higher magnetic flux density and may be interesting tools to yield residual angular momentum in charged particle beams if injected into the trajectory after passage of the coil. This motivates investigation of magnetization in laser driven B-fields, on demagnetization under the influence of ionizing radiation and the optimum material regarding particle stopping and scattering. A resulting doughnut particle beam with intensity minimum in its centre may be usefull for cylindrical heating of secondary samples around a unaltered core section.

Magnetism in combination with ultra-strong or transient fields is an interesting field of research that was not yet covered to our best knowledge. It offers possible applications, but also a field of study in material sciences. Especially the advent of research on nano-materials can benefit from studies in intermediate to high amplitude field environments in the high frequency domain. Electrostatic and magnetic properties of materials in function of crystal grain size, spin organization and frequency dependence can be studied employing short or long pulse driven coil targets. As example for the current state of art, materials are studied in the RF regime up to 100 MHz with fields of the order of one T [Yun+14].

Another field of interest is achromatic lensing of charged particle beams. Shaping of discharge pulse and return current in coil targets was not yet performed, which is of great interest during the downramp of the magnetic field. Adaptive current design would allow for the focus of high field amplitudes acting on high energy ions at early times to overlap with the focus for low field amplitudes at late times acting on slower ions, then potentially increasing the focused energy density by taking advantage of broad beam spectra issued by laser-plasma acceleration of ions – yielding a better control of the heating of secondary samples, *e.g.* for generation of warm dense matter.

7 Deliverables

This chapter brings together all the individually mentioned calibration data and software throughout this work. First, batch calibrations for radio-chromic films are given. Secondly, all programmes and scripts are introduced, with details on installation, program flow and possible development perspectives.

7.1 Batch Calibration for Radio-Chromic Films

Hereinafter presented in compact form are all RCF batch calibrations performed in the course of this work at the MAU in Institut Bergonie, Bordeaux, France. Scans with the EPSONEXPRESSION 11000 XL were performed using the `Silverfast 8.8` scanner software, with settings shown in section 8.2. For more details see section 4.3.1.2 and section 4.3.1.4. Each calibration fit is denoted by the film type and the batch number.

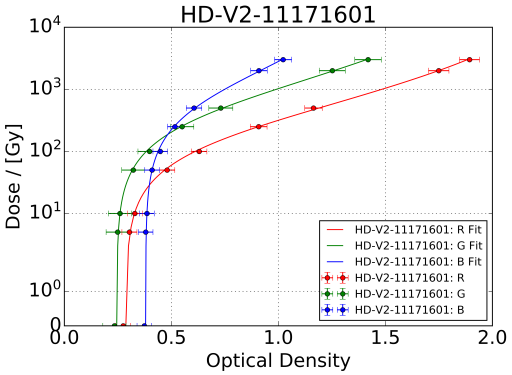

(a) data and fit for all channels

```
HD-V2-11171601 Ch:R
 A = 2.3678 +/- 0.093
 k = 248.8 +/- 32.8
 OD_0 = 0.2874 +/- 0.0202

HD-V2-11171601 Ch:G
 A = 2.164 +/- 0.247
 k = 611.0 +/- 190.0
 OD_0 = 0.2448 +/- 0.0285

HD-V2-11171601 Ch:B
 A = 1.38 +/- 0.255
 k = 957.0 +/- 410.0
 OD_0 = 0.3798 +/- 0.0174
```

(b) fit reports for all colour channels

Figure 7.1: Fit of the universal dose response model to calibration data for HD-V2-11171601.

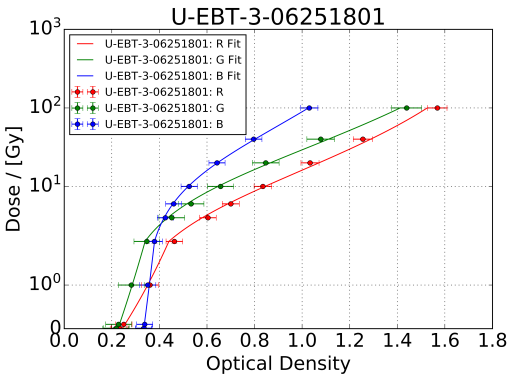

(a) data and fit for all channels

```
U-EBT-3-06251801 Ch:R
 A = 1.8316 +/- 0.0774
 k = 6.735 +/- 0.919
 OD_0 = 0.2435 +/- 0.0186

U-EBT-3-06251801 Ch:G
 A = 1.965 +/- 0.182
 k = 13.59 +/- 3.4
 OD_0 = 0.2258 +/- 0.0267

U-EBT-3-06251801 Ch:B
 A = 1.378 +/- 0.176
 k = 25.23 +/- 7.47
 OD_0 = 0.3344 +/- 0.0157
```

(b) fit reports for all colour channels

Figure 7.2: Fit of the universal dose response model to calibration data for U-EBT-3-06251801.

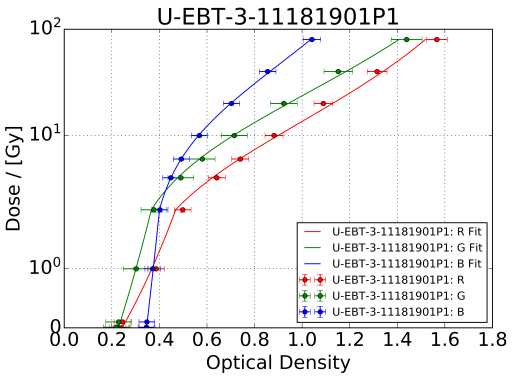

(a) data and fit for all channels

```
U-EBT-3-11181901P1 Ch:R
 A = 1.8402 +/- 0.0802
 k = 5.727 +/- 0.799
 OD_0 = 0.2432 +/- 0.0189

U-EBT-3-11181901P1 Ch:G
 A = 1.955 +/- 0.179
 k = 10.91 +/- 2.73
 OD_0 = 0.2279 +/- 0.0275

U-EBT-3-11181901P1 Ch:B
 A = 1.384 +/- 0.18
 k = 20.66 +/- 6.17
 OD_0 = 0.3458 +/- 0.0159
```

(b) fit reports for all colour channels

Figure 7.3: Fit of the universal dose response model to calibration data for U-EBT-3-11181901P1.

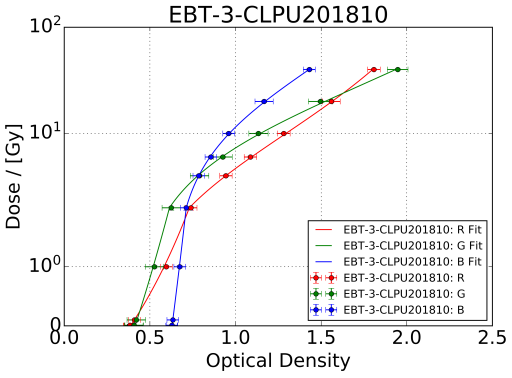

(a) data and fit for all channels

```
EBT-3-CLPU201810 Ch:R
 A = 2.2052 +/- 0.0944
 k = 4.219 +/- 0.535
 OD_0 = 0.3872 +/- 0.0196

EBT-3-CLPU201810 Ch:G
 A = 3.327 +/- 0.359
 k = 13.06 +/- 3.0
 OD_0 = 0.414 +/- 0.0279

EBT-3-CLPU201810 Ch:B
 A = 2.178 +/- 0.377
 k = 21.52 +/- 6.96
 OD_0 = 0.6296 +/- 0.017
```

(b) fit reports for all colour channels

Figure 7.4: Fit of the universal dose response model to calibration data for EBT-3-CLPU201810.

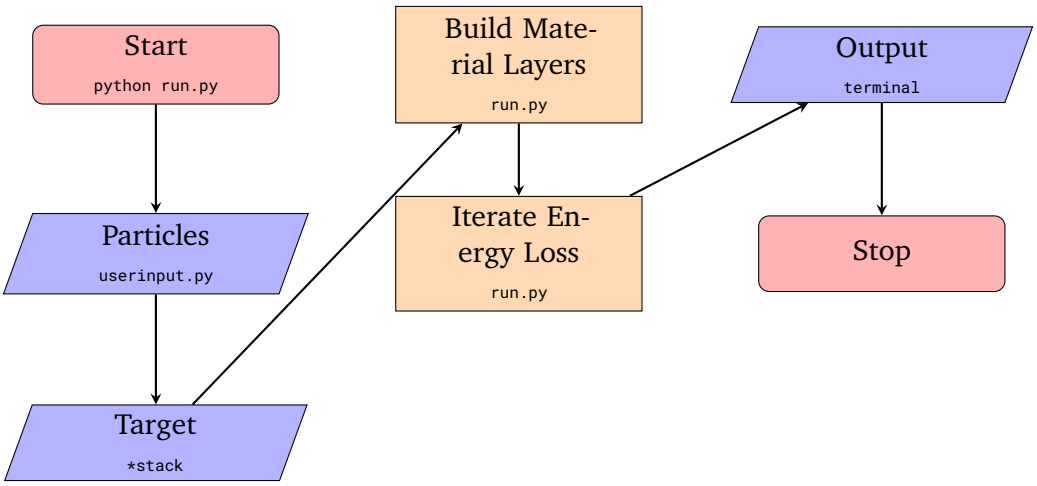

Figure 7.5: pyPEST run

7.2 Particle Field Interaction Simulation Code

The PAFIN code [M. 15; M. 16] calculates the trajectories of charged particles in EM fields. After generation of a particle beam with any given phase space, either iterative step-wise transport or small angle projection of charged particles is coupled to a Lorenz force solver. The code processes any combination of magnetic- and E-fields with the possibility of defining current density and charge density distribution, and it allows implementation of analytical solutions for fields as time-varying functions.

PAFIN became equipped with a structure-preserving second-order integration of relativistic charged particle trajectories in EM fields, introduced by [HC17]. The method takes more care of the evaluation of the Lorentz factor than the widely employed relativistic Boris Push [Bor70; BL91]. Note that formular (19) in [HC17] misses a c^2 on the left hand side of the equation. For the transport scheme in PAFIN, the final result equation (20) in [HC17] is corrected accordingly in the last term to $\|\vec{\beta} \cdot \vec{u}\|^2 \cdot c^{-2}$ instead of $\|\vec{\beta} \cdot (\vec{u})^2\|$.

PAFIN allows implementation of analythical solutions for fields as functions or the use of externally generated meshed fields. The code contains a non-trivial implementation of toroidal potentials. The exact solution for an E-field based on an a toroidal potential [HA04] allows quick calculation of E-field components using toroidal harmonics. Calculation of the later is numerically realized refering to the commonly available soubroutine `dthor_3` [SG00]. For use, the licenced subroutines `dtor3_2.f`, `Rout.f` and `adrout.f` [GS01] are to be downloaded and placed in the same directory as the PAFIN root.

7.3 pyPEST

Pythonic Photon and Electron Stopping (pyPEST) launches electrons of given input energy through a stack of target material and prompts the expected linear range as well as the LET following the trajectory. The angular scattering by collisions is ignored in this first version of the code able to find a maximum range only. The stopping power is calculated from tables, published with [McL+91a; McL+91b; Ber+93]. The flow chart of the script is presented with fig. 7.5.

pyPEST is a collaborative GIT project that requires python 3.6. An uncomplicated download is possible via `git clone`. Here we base the example on the CELIA gitLAB-platform accessible via CELIA VPN,

```
git clone http://MEmx@192.168.2.202/MEmx/pyPEST.git
cd pyPEST
```

Listing 7.1: Download

and then the set-up for the full working environment is proposed within a Anaconda 3 environment,

```
conda env create -f pyPEST.yml
conda activate pyPEST
```

Listing 7.2: Set-up commands

which leads us to a first execution via

```
python run.py
```

Listing 7.3: First execution

The code is not suitable for a quantitative assessment of dose deposition, but only for maximum range estimates.

7.4 Pythonic Stopping and Track Analysis for Particle Detectors by Transport of Ions in Matter

PySTarT is a collection of scripts to pilot the Monte Carlo ion transport code SRIM and analyse its output regarding target damage and ion ranges. The flow chart of the script is presented with fig. 7.6.

7.4.1 Runtime Environment

PySTarT is a collaborative GIT project that requires python 2.7 and SRIM [Zie]. An uncomplicated download procedure is proposed based on a `git clone` and the set-up for the full working environment is proposed within a Anaconda 3 environment.

7.4.1.1 Set-Up

The download of the PySTarT code is possible via any trusted source, hereinafter we base the example on the CELIA gitLAB-platform accessible via CELIA VPN. In a Windows operating system, open `GIT bash`, in Linux open a terminal, and navigate to the folder you want to work in. Then execute

```
git clone http://MEmx@192.168.2.202/MEmx/pystart.git
cd pystart
```

Listing 7.4: Download

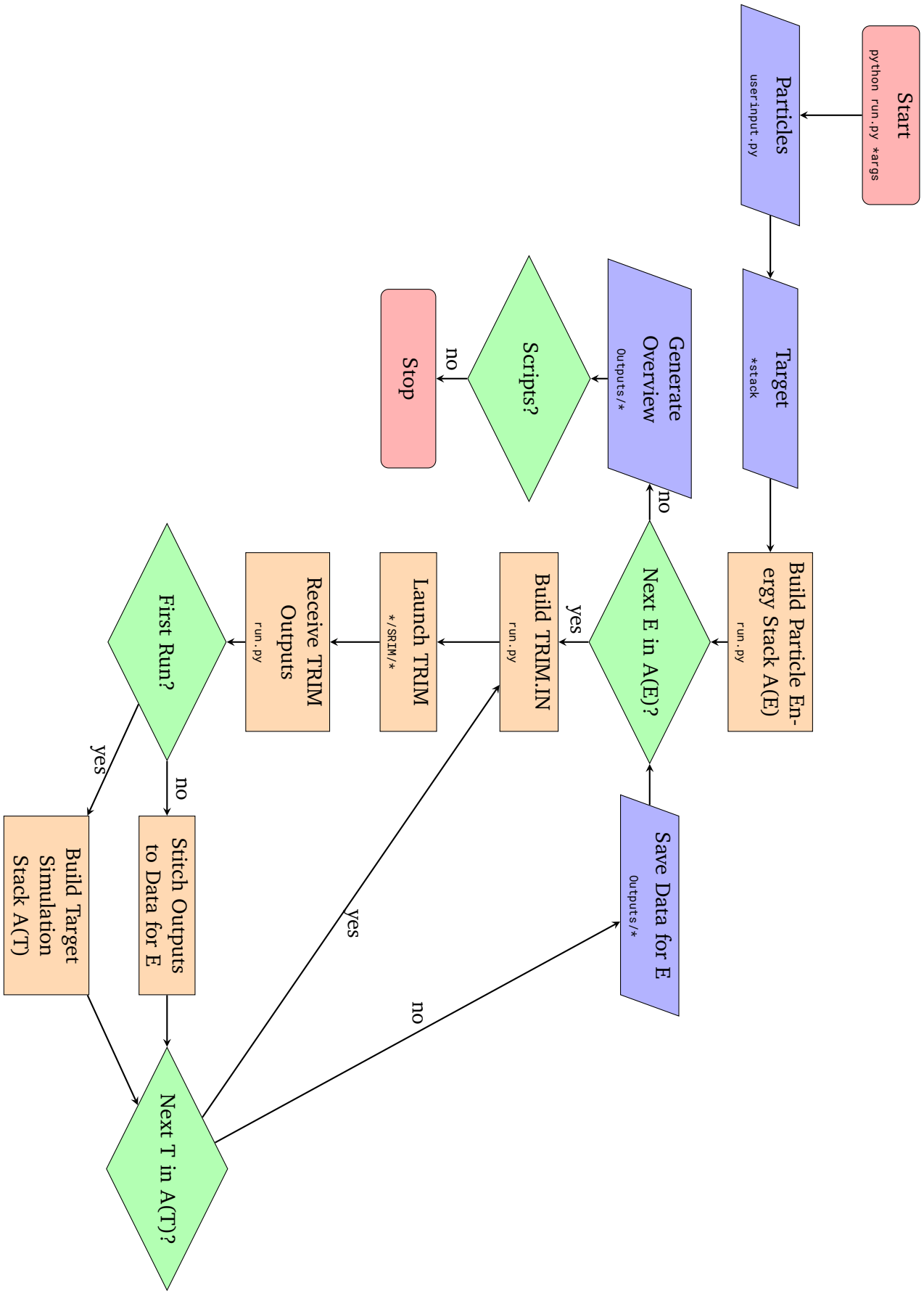

Figure 7.6: PySTarT run

You may now enter into the file `userinput.py` and change the operating system parameter `chos` to fit your system.

In a Windows operating system, open `Anaconda navigator`, navigate to `Environments` and click on the play button behind `base` to launch the `Anaconda prompt`. In Linux, a terminal. Then install some packages,

```
conda create -n PySTarT python=2.7 anaconda
conda activate PySTarT
conda install -n PySTarT numpy matplotlib scipy pandas
conda install -n PySTarT -c conda-forge xvfbwrapper
```

Listing 7.5: Set-up commands

If work independent from Anaconda is wished, please find the details of used packages in `requirements.txt`.

The correct binding of SRIM is non-trivial. With a Windows operating system,

- if SRIM was already installed on your computer, skip this steps.
- if you install SRIM for the first time, please download the 2008 version of SRIM and install it. You may find a suitable installation on `http://www.srim.org`. This will correctly install all the packages and link all the dependancies properly. The location of the SRIM directory might be anywhere, according to your system environment. The most convenient for you would be if you installed SRIM into the PySTarT directory, into a folder `/SRIM`.
- in a second stage, or if you only have the 2008 version installed, you shalt download and install the very last version of SRIM. To upgrade to the 2013 release, you may just unpack the files into the SRIM directorry and then run both `SRIM/SRIM-Setup/SRIM-AutoSetup/SRIM AutoSetup.exe` and `SRIM/SRIM-Setup/_SRIM-Setup (Right-Click).bat`.
- ensure the correct installation of the font `SRIM/SRIM-Setup/Linedraw` in `C:/Windows/fonts`.
- ensure the correct registration of all .dll and .ocx files by manually running `Regsvr32` in a cmd-prompt active in `SRIM/SRIM-Setup`:

```
Regsvr32 ComCtl32.ocx
Regsvr32 ComDlg32.ocx
Regsvr32 MSFlxGrd.ocx
Regsvr32 RichTx32.ocx
Regsvr32 TabCtl32.ocx
```

Listing 7.6: Regsvr32

If any of this is not respected, none of what follows will work. Another funny thing about SRIM is a very likely region-setting bug, see fig. 7.7 of `TIN.exe` - the interface between SRIM and Transport of Ions in Matter (TRIM). To avoid any runtime-error, make sure that the language setting of the computer is coherent with the region setting and your actual geolocation. Also, in order to avoid runtime-errors, make sure that your user has read and write privileges in the full `SRIM` folder - and all of its sub-folders, for all of the files.

Finally, make PySTarT familiar with the location of the SRIM directory by changing the `special_srim_folder` parameter in `userinput.py`. The root directory of PySTarT is supposed to hold SRIM and the scripts in distinct folders. SRIM output and output of the pilot are stored into the `SRIM Outputs` directory that is supposed to be part of the SRIM directory, any other script output is stored into the PySTarT script directory or sub-directories.

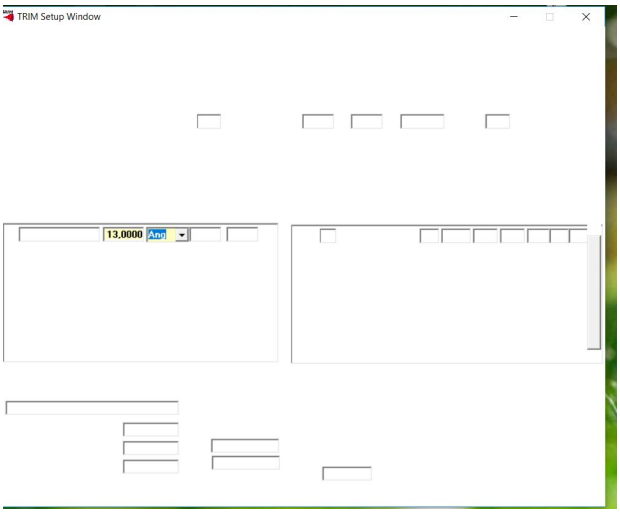

Figure 7.7: SRIM region-setting bug issued by `TIN.exe`.

For Linux operating systems, the installation of SRIM is not necessary The directory `SRIM_UBU/` contains SRIM for Linux users already. You should only ensure that WINE is installed and running. If WINE is not installed on the system, issues with the visual basic implementation are likely if old ubuntu or wine versions are used on new machines. Therefore two distinct procedures to install WINE are discussed hereinafter. Make finally sure that the location of the SRIM directory stored in `userinput.py` with the `special_srim_folder` parameter is correct in your version of PySTarT.

A) via PLAYONLINUX

Open a terminal and go to the correct environment and then perform

```
conda install -n PySTarT -c conda-forge wxPython
sudo apt-get update
sudo apt-get install playonlinux
```

Listing 7.7: Regsvr32

PLAYONLINUX will install WINE automatically as dependency. For a correct use of playonlinux, you need to take into account a detail of using it inside anaconda environments: it will try to boot with the normal `python` - in order to use the `python` inside the `Anaconda` environment edit the file `/usr/share/playonlinux/bash/find_pyt` (you might need root-privileges). Replace the lines

```
# list of interpreter names to try, in order
next_python "python"
next_python "python2.7"
next_python "python2.6"
next_python "python2"
next_python "none"
```

Listing 7.8: Old lines in find_python

with the following lines

```
# list of interpreter names to try, in order
next_python "/opt/Anaconda3/envs/PySTarT/bin/python"
```

```
next_python "none"
```

Listing 7.9: New lines in find_python

and then execute inside a terminal

```
playonlinux
```

Listing 7.10: Execute playonlinux

Further steps after installation of playonlinux are not necessary for the use of PySTarT, the automatic installation of WINE is the essential part.

B) via Terminal Input

If you wish to install wine manually, try

```
cd ../folderwithfiles
dpkg --add-architecture i386
wget -nc https://dl.winehq.org/wine-builds/winehq.key
apt-key add winehq.key
apt-add-repository 'deb http://dl.winehq.org/wine-builds/ubuntu/ xenial main'
apt-get update && apt-get install -y winehq-stable
export WINEARCH=win32
export WINEPREFIX=~/.wine
wine winecfg
wget  https://raw.githubusercontent.com/Winetricks/winetricks/master/src/winetricks
chmod +x winetricks
sh winetricks vb5run vb6run vcrun6 comdlg32ocx msflxgrd
```

Listing 7.11: Manual installation of WINE

7.4.2 Test Run

The code sets up a test automatically, just execute

```
python run.py
```

Listing 7.12: Execute playonlinux

A lack of permission represends a known error and is expressed with a message comparable to fig. 7.8.

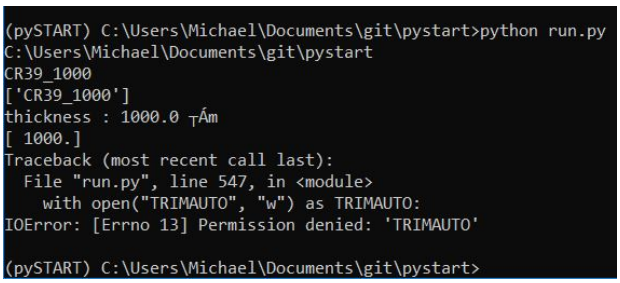

Figure 7.8: SRIM has no permission to work on files in its folder.

For Linux systems, the first run of wine can lead to the following fatal error

```
Call OS with wine TRIM.exe
wine: created the configuration directory '/home/user/.wine'
0012:err:ole:marshal_object couldn't get IPSFactory buffer for interface {000001
31-0000-0000-c000-000000000046}
0012:err:ole:marshal_object couldn't get IPSFactory buffer for interface {6d5140
c1-7436-11ce-8034-00aa006009fa}
0012:err:ole:StdMarshalImpl_MarshalInterface Failed to create ifstub, hres=0x800
04002
0012:err:ole:CoMarshalInterface Failed to marshal the interface {6d5140c1-7436-11ce-8034-00
    aa006009fa}, 80004002
0012:err:ole:get_local_server_stream Failed: 80004002
0014:err:ole:marshal_object couldn't get IPSFactory buffer for interface {00000131-0000-0000-
    c000-000000000046}
0014:err:ole:marshal_object couldn't get IPSFactory buffer for interface {6d5140c1-7436-11ce
    -8034-00aa006009fa}
0014:err:ole:StdMarshalImpl_MarshalInterface Failed to create ifstub, hres=0x80004002
0014:err:ole:CoMarshalInterface Failed to marshal the interface {6d5140c1-7436-11ce-8034-00
    aa006009fa}, 80004002
0014:err:ole:get_local_server_stream Failed: 80004002
Could not load wine-gecko. HTML rendering will be disabled.
Could not load wine-gecko. HTML rendering will be disabled.
wine: configuration in '/home/user/.wine' has been updated.
0009:err:module:import_dll Library MSVBVM50.DLL (which is needed by L"Z:\\home\\user\\GIT\\
    pystart\\SRIM_UBU\\TRIM.exe") not found
0009:err:module:attach_dlls Importing dlls for L"Z:\\home\\user\\GIT\\pystart\\SRIM_UBU\\TRIM.
    exe" failed, status c0000135
```

Listing 7.13: Fatal error for a first WINE execution

All of which is normal set-up procedure, despite the part

```
0009:err:module:import_dll Library MSVBVM50.DLL (which is needed by L"Z:\\home\\user\\GIT\\
    pystart\\SRIM_UBU\\TRIM.exe") not found
0009:err:module:attach_dlls Importing dlls for L"Z:\\home\\user\\GIT\\pystart\\SRIM_UBU\\TRIM.
    exe" failed, status c0000135
```

Listing 7.14: Spot a the bug for the first WINE execution

You may solve the issue with the missing visual basic .dll files by

```
cd ../folderwithfiles
wget  https://raw.githubusercontent.com/Winetricks/winetricks/master/src/winetricks
chmod +x winetricks
sh winetricks vb5run vb6run vcrun6 comclt32 comclt32ocx comdlg32ocx msflxgrd
```

Listing 7.15: Add missing DLL prior to second WINE execution

Possibly, winetricks will not find the package `comclt32` (or/and others), then execute the GUI

```
sh winetricks
```

Listing 7.16: Add missing DLL prior to second WINE execution

and navigate to `Select the default wineprefix` ⇒ `Install a Windows DLL or component` in order to activate the checkboxes for `vb5run`, `vb6run`, `vcrun6`, `comclt32`, `comclt32ocx`, `comdlg32ocx` and `msflxgrd`.

7.4.3 Caclulations for Stacks of Radio-Chromic Films

We create a file `stack.ltr` within the PySTarT root directory in order to specify the following stack of RCF as its file-content

```
Al_10 1
HD 10
MD 3
EBT 20
Mylar_1000 1
```

Listing 7.17: PySTarT RCF Stack for Testing RCF Shielding

In PySTarT, RCF names point to the latest models of each film type: HD $\rightarrow$ HD-V2, MD $\rightarrow$ MD-V3 and EBT $\rightarrow$ EBT-3 as well as UEBT $\rightarrow$ U-EBT-3. This can be changed (currently only by changing material parameters and spatial dimensions) in `userinput.py` following information in table 8.2. The last layer is set in order to avoid particles trespassing the stack if we overestimate the stopping power prior to a first run. We set the particle species to be protons via $Z = 1$ and select the projectile energy range 500 keV to $35.000 \cdot 10^3$ keV. The finer the steps raster this range, the more single simulations will be launched. We select a step size of 500 keV. The spatial resolution of the bins employed by SRIM is set to 2 µm. The higher this resolution, the more SRIM calculations will be stitched together for one single projectile energy.

PySTarT accepts optional input parameters. A location pointer can be defined which should contain the path to the root of PySTarT if executed from a shell active in a distant directory, default is `None`. A name of a specific stack file can be given, as string of the relative path seen from the root directory of PyStarT, default is `stack.txt`. Last, post processors can be disabled by running a silent mode, default is `False`. Now run PySTarT with disabled location pointer, indication of the stack's path and disabled silent mode

```
python run.py None stack.ltr False
```

Listing 7.18: Execute PySTarT

Results derived from the target ionization are given in the following table table 7.1, where d_{alc} denotes the active layer centre position and E_{alc} its range corresponding energy. The later is compared to the linearly extrapolated energy E_{A} centred between the lowest E_{L} and highest E_{H} Bragg-peak energy within each active layer. We do see that there is a small difference between the energy at the centre position of the active layer and the centre of the spectrum with range within the active layer.

The ion energy deposition in active layers principally raises for ions with impact energies from E_{L} to E_{H}. For plastic material and µm distances under regard, the decrease of the Bragg-peak with increasing energy is less important than the build up of the integrated LET with penetration depth into the active layer. Hence, the energy most importantly imaged within an active layer corresponds rather to E_{H}. For ion ranges overpassing the active layer, the integral deposited energy in the active layer decreases as expected from the Bragg curve. For a correct uncertainty estimate towards higher ion impact energies also taking into account filters in vicinity of the active layer, a run of decon_RCF yields the exact energy deposition.

Table 7.1: Stacked RCF behind 10 µm Al shielding.

Stack with 10 µm Al $+10\times$HD-V2 $+3\times$MD-V3 $+20\times$EBT-3							
#	Type	d_{alc} /[mm]	E_{alc} /[mm]	E_{A} /[MeV]	E_{L} /[MeV]	E_{H} /[MeV]	v_{A} /[µm ps^{-1}]

1	HD	16.00(600)e−3	1.042(722)	959(679)e−3	759(722)e−3	1.16(115)	13.6
2	HD	125.00(600)e−3	3.13(304)	3.13(223)	3.04(304)	3.21(327)	24.5
3	HD	234.00(600)e−3	4.47(444)	4.47(317)	4.41(444)	4.53(454)	29.3
4	HD	343.00(600)e−3	5.56(555)	5.56(395)	5.50(555)	5.61(564)	32.6
5	HD	452.00(600)e−3	6.50(649)	6.50(463)	6.45(649)	6.55(659)	35.2
6	HD	561.00(600)e−3	7.34(740)	7.33(525)	7.29(740)	7.37(744)	37.4
7	HD	670.00(600)e−3	8.10(813)	8.10(576)	8.06(813)	8.14(815)	39.3
8	HD	779.00(600)e−3	8.82(886)	8.82(627)	8.78(888)	8.86(886)	41.0
9	HD	888.00(600)e−3	9.48(955)	9.49(676)	9.45(956)	9.52(955)	42.5
10	HD	997.00(600)e−3	10.1(102)	10.12(719)	10.1(102)	10.2(102)	43.8
11	MD	1.230 00(500)	11.4(115)	11.39(814)	11.4(116)	11.4(115)	46.5
12	MD	1.490 00(500)	12.7(128)	12.70(910)	12.7(129)	12.7(128)	49.0
13	MD	1.750 00(500)	13.9(140)	13.88(988)	13.9(140)	13.9(140)	51.2
14	EBT	2.0190(140)	15.0(151)	15.0(107)	15.0(151)	15.1(151)	53.2
15	EBT	2.2970(140)	16.2(162)	16.2(115)	16.1(162)	16.2(163)	55.1
16	EBT	2.5750(140)	17.2(173)	17.2(123)	17.2(174)	17.3(173)	56.9
17	EBT	2.8530(140)	18.2(183)	18.2(130)	18.2(184)	18.3(183)	58.5
18	EBT	3.1310(140)	19.2(193)	19.2(137)	19.2(193)	19.3(193)	60.0
19	EBT	3.4090(140)	20.1(202)	20.1(143)	20.1(203)	20.2(202)	61.3
20	EBT	3.6870(140)	21.0(212)	21.0(150)	21.0(212)	21.1(212)	62.7
21	EBT	3.9650(140)	21.9(220)	21.9(156)	21.9(221)	21.9(220)	63.9
22	EBT	4.2430(140)	22.7(229)	22.7(162)	22.7(230)	22.8(229)	65.1
23	EBT	4.5210(140)	23.6(237)	23.6(168)	23.5(237)	23.6(237)	66.2
24	EBT	4.7990(140)	24.3(245)	24.3(173)	24.3(245)	24.4(245)	67.2
25	EBT	5.0770(140)	25.1(252)	25.1(179)	25.1(253)	25.2(252)	68.2
26	EBT	5.3550(140)	25.9(260)	25.9(184)	25.8(260)	25.9(260)	69.2
27	EBT	5.6330(140)	26.6(268)	26.6(190)	26.6(269)	26.6(268)	70.2
28	EBT	5.9110(140)	27.3(275)	27.3(195)	27.3(276)	27.4(275)	71.1
29	EBT	6.1890(140)	28.0(282)	28.0(199)	28.0(282)	28.1(282)	71.9
30	EBT	6.4670(140)	28.7(289)	28.7(205)	28.7(291)	28.8(289)	72.8

31	EBT	6.7450(140)	29.4(296)	29.4(209)	29.4(297)	29.4(296)	73.6
32	EBT	7.0230(140)	30.1(303)	30.1(214)	30.0(303)	30.1(303)	74.4
33	EBT	7.3010(140)	30.7(309)	30.7(219)	30.7(310)	30.7(309)	75.1

We reckon that this particular stack can be improved depending on possible applications. If the spectrum of a presumably exponentially decaying TNSA proton beam with energy range up to MeV must be determined, this stack is well suited. For charged particle beam deflectometry of slow processes, we would introduce filters between earlier layers towards the end of the stack for separation of high energies. For fast processes, we would introduce a thick shielding in front of the stack to directly access the thin bands of energy for high projectile energies with small separation.

Besides output of material ionization, atom recoils, phonons and created vacancies, PySTarT post processes data with scripts aiming at plotting range data for RCF and simulating the growth of etch pits for CR-39 according to section 4.3.2.6.

7.4.4 Perspectives

PySTarT comprises a post-processor for CR-39 that bursts the scope of a simple SRIM pilot. Aim is to derive a stand-alone CR-39 analysis routine, pretty much as decon_RCF, see section 7.5, is a RCF analysis routine.

7.5 decon_RCF

Hereinafter we present the implementation of a script that is able to convert RCF scan images to number density maps, following section 4.3.1. If using stacks, it is of paramount importance that RCF imprints are aligned prior to any further post-processing. It must be ensured that one position on the film plane corresponds to the same pixel position in every film of the scanned stack. On top of what is described in section 4.3.1.2 and section 4.3.1.4, the analysis software embodies direct calibration curves from scanner grayscale values to dose values for several batches scanned with the EPSON EXPRESSION 11000XL flat-bed scanner. Such curves are advantageous, as they eliminate accumulated uncertainty of two fitting procedures: grayscale to OD and OD to dose. The flow chart of the script is presented with fig. 7.9.

7.5.1 Runtime Environment

decon_RCF is a collaborative GIT project that requires python python 3.7 and PySTarT, section 7.4. An uncomplicated download procedure is proposed based on a `git clone` and the set-up for the full working environment is proposed within a Anaconda 3 environment.

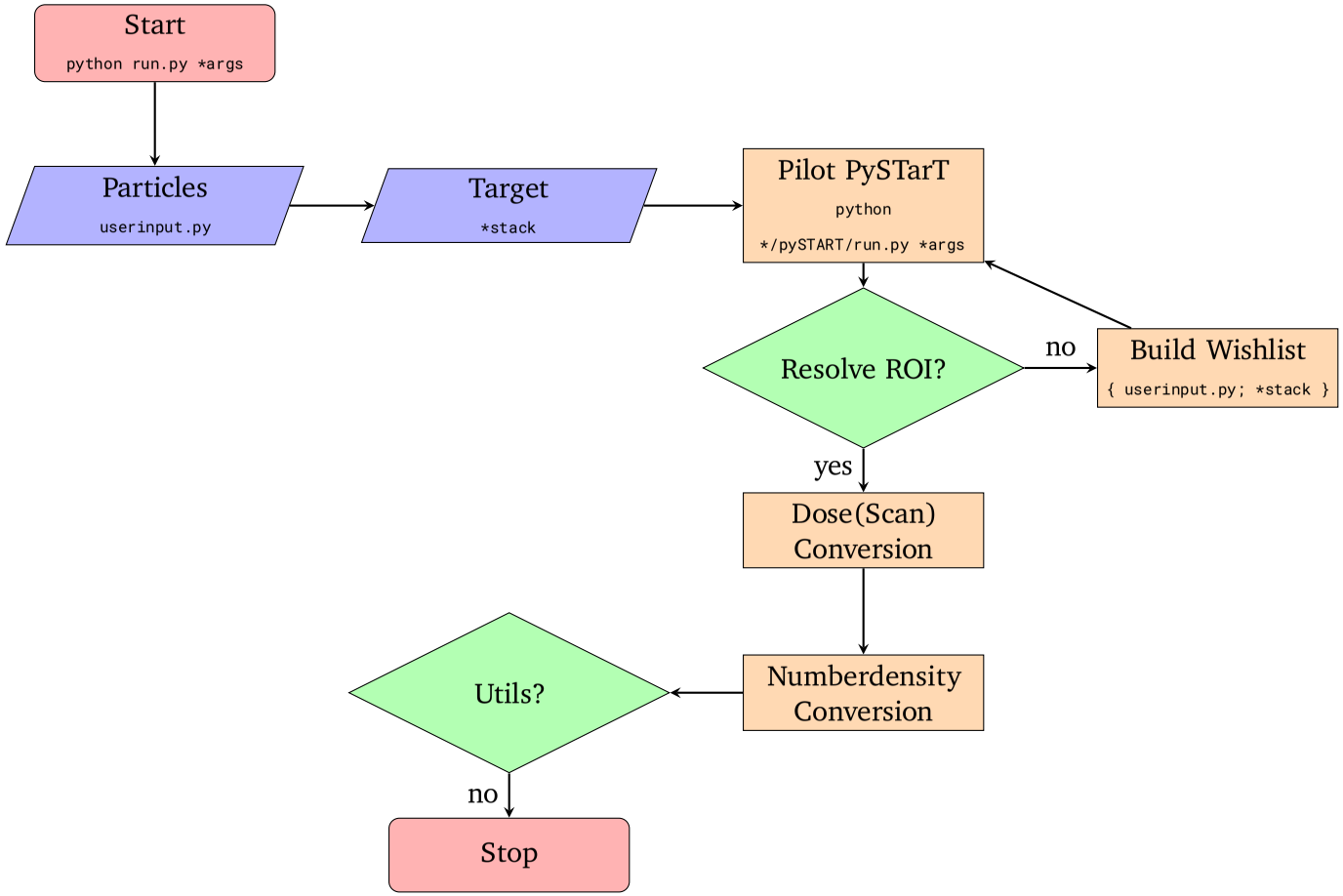

Figure 7.9: decon_RCF run

7.5.1.1 Set-Up

The download of decon_RCF is possible via any trusted source, hereinafter we base the example on the CELIA gitLAB-platform accessible via CELIA VPN. In a Windows operating system, open `GIT bash`, in Linux open a terminal, and navigate to the folder you want to work in. Then execute

```
git clone http://MEmx@192.168.2.202/MEmx/decon_rcf.git
cd decon_rcf
```

Listing 7.19: Download

In a Windows operating system, open `Anaconda navigator`, navigate to `Environments` and click on the play button behind `base` to launch the `Anaconda prompt`. In Linux, a terminal. Then install some packages,

```
conda env create -f decon_rcf.yml
conda activate decon_rcf
```

Listing 7.20: Set-up commands

If work independent from Anaconda is wished, please find the details of used packages in `requirements.txt`.

7.5.2 Test Run

The first two runs shalt be tests to ensure that the environment works fine. The first test is

```
python run.py
```

Listing 7.21: First execution

and the second test has to be, for Windows,

```
python run.py TEST\\DATA\\COMPLEX\\stack.txt TEST\\DATA\\COMPLEX\\background.txt
```

Listing 7.22: Second test execution in WIN

and for Linux,

```
python run.py TEST/DATA/COMPLEX/stack.txt TEST/DATA/COMPLEX/background.txt
```

Listing 7.23: Second test execution in LIN

The code is ready to be used if no errors are issued. The python module `subprocess.py` may not be able to launch a SRIM instance due to a not fail-save implementation of the `_winapi.CreateProcess()` function. If you encounter an `Error [2]` after the call to PySTarT, as in

```
  File "C:\ProgramData\Anaconda3\envs\decon_rcf\lib\subprocess.py", line 957, in
    _execute_child
    startupinfo)
FileNotFoundError: [WinError 2] The system cannot find the file specified
```

Listing 7.24: First run error

A quick fix is to replace the variable paths in this functions with three hard coded paths. First, we insert the actual path to your `Anaconda python.exe` for the PySTarT environment, and second, the actual path for the PySTarT `run.py` file, and at third position the actual path to the working directory of PySTarT. Therefore,

- go to the `subprocess.py` file, line 949 (*e.g.* placed in `C:/ProgramData/Anaconda3/envs/decon_rcf/Li`
- add the following two lines after `try:`

```
try:
    args = 'C:\\ProgramData\\Anaconda3\\envs\\PySTarT\\python.exe C:\\Users\\USER\\Documents\\
    git\\pystart\\run.py'

    cwd = 'C:\\Users\\USER\\Documents\\git\\pystart'

    hp, ht, pid, tid = _winapi.CreateProcess(executable, args,

                                             # no special security
                                             None, None,
                                             int(not close_fds),

                                             creationflags,

                                             env,

                                             cwd,

                                             startupinfo)

finally:
```

Listing 7.25: Change _winapi.CreateProcess()

7.5.3 Example Analysis

The test run concerns analysis of data presented in section 5.1.2.

decon_RCF is set up to simulate a stack of 10 µm Al foil followed by 3 × U-EBT-3 (batch 06251801).The stopping power calculation within this stack is handled by SRIM with a spatial resolution better than 1 µm in a full TRIM simulation. We presume a 0°, thus normal, impact into the stack. TRIM issues the stopping power evolution for distinct energies with adjustable binning - we calculate alpha particle stopping for impact energies from $200 \cdot 10^{-3}$ MeV to 30.2 MeV, see fig. 7.10.

Clearly visible is the Bragg-peak at the end of the penetration range of the impacting ions. The higher the impact energy, the deeper the ion penetrates and the lower is its energy deposition in the first layers. For a good energy resolution of the simulation, the calculation meshes energy bins densely in proximity of active layers. For practical reasons, we chose the Bragg-peak, and both, rising and falling FWHM position, as three different marker positions of the stopping curve. For the RCF, we chose entrance and exit points of active layers as ROI. The simulation terminates only after it produced each type of marker position in front of and after each ROI. We choose the spatial resolution of the simulation to also define the maximum tolerated for ROI to marker distance.

The code automatically presumes the spectrum to reach a maximum value at the energy with range just after the last given active layer. In order to set the detection range to the first active layer after the cut-off energy, the background layer must be included in the stack. This was done for all analysis of this work to comply with the un-interpreted physical information, rather than guessing an arbitrary cut-off between last layer with imprint and first layer without.

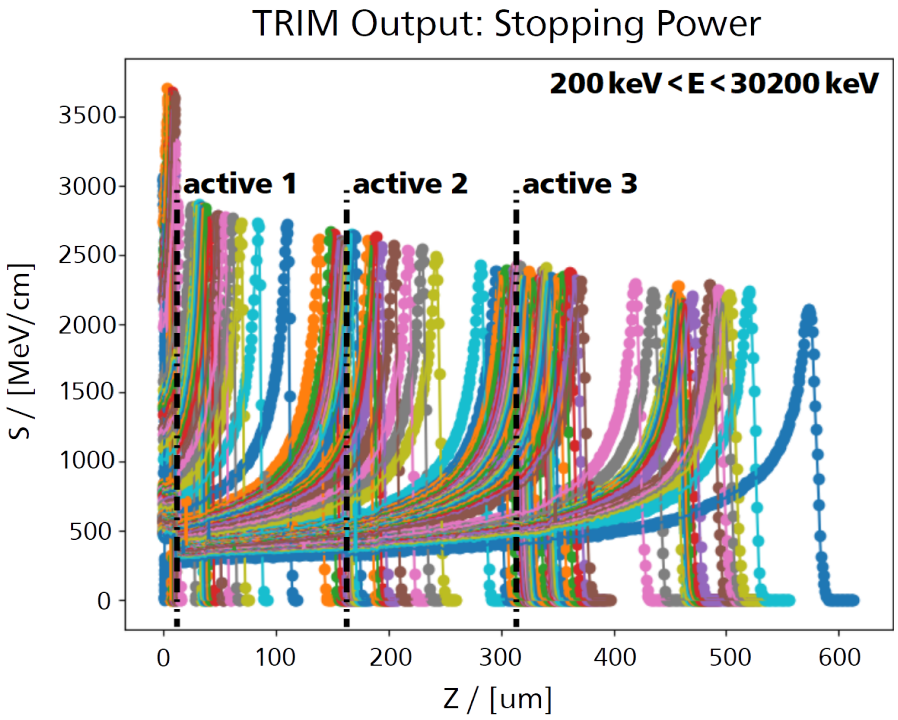

Figure 7.10: RCF stack of shots #79, #85 and #87 with indication of the first four layers, on which analysis focuses. The 3 × U-EBT-3 were protected by a 10 µm Al foil and lower film numbers face the experiment. The stopping power per impact energy is plotted for He ions with respect to the penetration depth into the stack. The active layer positions of RCF are indicated by dashed lines.

Space integration of the ion stopping power in the bonds of each active layer yields a view on the relative contribution of individual ion impact energies to the total energy deposition per layer, see fig. 7.11.

The ion energies that do dominate the deconvolved answer of a certain layer are not equal to the ion energies with Bragg peak in the centre of this active layer. The He-ion energies with a peak for the deposited energy are 6.33(226) MeV for the first layer, 16.06(120) MeV for the second layer and 22.39(93) MeV for the third layer. For the first layer, the discrepancy between the energy with peaked energy deposition and centred Bragg-peak position is of the order of 3 MeV. This can be explained by the slim Bragg-peak for low ion energies that is thinner than the active layer width. For energies of which the Bragg peak reaches the end of the active layer, the energy deposition is maximum compared to all other energies.

7.5.4 Perspectives

- Currently the code approximates all projectile trajectories parallel. We aim at implementation of the source distance and the impact pixel. The code must evaluate all angles for a user-input binning between maximum and minimum deviation from perpendicular impact. The last layer of a stack is relevant to evaluate this maximum angles - all border regions of earlier films that are outside the solid angle of the trajectories connecting source and borders of last film are discarded. Then the code must calculate the stopping power for the bin-trajectories (SRIM accepts impact angles) . The calculation will be bin-times longer. We transform the

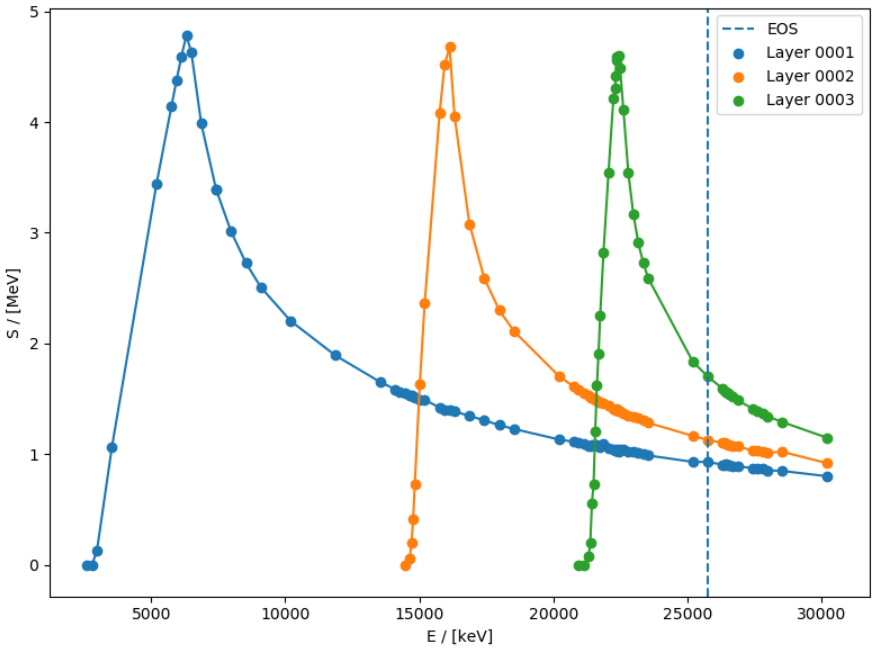

Figure 7.11: The deposited energy per impact energy is plotted for He ions. It is result of integration of stopping power in depth for each active layer in the RCF stack of shots #79, #85 and #87. The 3 $\times$ U-EBT-3 have rather thick active layers wich leads to a domination of the imprint by a high energy contribution for early layers. The first energy traversing the stack is indicated by a dashed line.

2D map (x,y) into a map (a_x,a_y) of angles from the particle source for each pixel. This maps can then be deconvoluted by (linear) approximation of deposited energy between two known bins.

- Basic presumption for the current version of the code is a flat spectrum between two layers. This has a major influence on the results as we pre-define the form of the spectrum, which is a huge bias due to the limited amount of samples we have. It must be goal to allow pre-definition of a spectral shape or multiple spectral shapes for fitting.

7.6 proCOIN_FR

This short section is devoted to a development environment for a script that can be used to analyse complex interferograms and polarimetry based on Faraday rotation. The current version of the program is able to evaluate polarimetry.

7.6.1 Runtime Environment

proCOIN_FR is a collaborative GIT project that requires python python 3.7. An uncomplicated download procedure is proposed based on a `git clone` and the set-up for the full working environment is proposed within a Anaconda 3 environment.

The download of proCOIN_FR is possible via any trusted source, hereinafter we base the example on the CELIA gitLAB-platform accessible via CELIA VPN. In a Windows operating system, open `GIT bash`, in Linux open a terminal, and navigate to the folder you want to work in. Then execute

```
git clone http://MEmx@192.168.2.202/MEmx/matlab-script.git
cd matlab-script/pythonic
```

Listing 7.26: Download

In a Windows operating system, open `Anaconda navigator`, navigate to `Environments` and click on the play button behind `base` to launch the `Anaconda prompt`. In Linux open a terminal. Then install some packages,

```
conda env create -f proCOIN_FR.yml
conda activate proCOIN_FR
```

Listing 7.27: Set-up commands

7.6.2 Input

An example for a general input file is available in `input.txt`. The comma separated columns are

```
#ID,is_camref_or_laserref_or_data,absolute_path_to_image
```

Listing 7.28: Columns in input.txt

where the user defined `#ID` groups references and data that correspond to each other. Reference types or data is defined via `is_camref_or_laserref_or_data` which is either set to `camref`, `laserref` or `data`. The field `absolute_path_to_image` defines the source-file which is either referenced absolute, relative from the execution directory, or relative from the script file directory (searched in this order).

Additional information concerning the experiment can be defined in a file similar to `experiment.txt`. The comma separated columns are

```
#ID,is_shot_number,is_time_to_T0_in_fs,timing_uncertainty_in_fs,with_driver_energy_in_J,
    energy_uncertainty_in_J
```

Listing 7.29: Columns in experiment.txt

where the user defined `#ID` is used to inter-reference data and information. `is_shot_number` is the laser shot number, `is_time_to_T0_in_fs` is the timing in fs, `timing_uncertainty_in_fs` is the timing uncertainty in fs, `with_drive_energy_in_J` is the driver energy in J and `energy_uncertainty_in_J` is the energy uncertainty in J

Further additional information for plotting can be defined in a file similar to `plotter.txt` The comma separated columns are

```
#ID,concider_rotational_possibilities_in_int
```

Listing 7.30: Columns in plotter.txt

where the user defined `#ID` is used to inter-reference data and information. `concider_rotational_possibilitie` defines how many rotational possibilities are calculated for Faraday rotation.

The execute command is

```
python main.py input.txt **kwargs(experiment.txt = (None,string), plotter.txt = (None,string))
```

Listing 7.31: Execution

7.6.3 Runtime

First, background in `camref` is subtracted from both `laserref` and `data`. Then, possible Faraday rotation angles are deduced following [Pis+19].

Bibliography

[A. +15a] A. Poyé et al. In: *Physical Review E* 92(4-1) (2015), p. 043107.

[A. +15b] A. Poyé et al. "ChoCoLaT". In: *CELIA Program Library* (2015). researchgate.net/publication/284609502_ChoCoLaT.

[AJ98] A. Pukhov and J. Meyer-ter-Vehn. In: *Phys. Plasmas* 5 (1998), p. 1880.

[Adm] U.S. Energy Information Administration. *International Energy Outlook 2019 with projections to 2050*. Resume of IEO 2020 issued by IEA. URL: https://www.eia.gov/outlooks/ieo/pdf/ieo2019.pdf.

[Akt+19] E. Aktan et al. "Parametric study of a high amplitude electromagnetic pulse driven by an intense laser". In: *Physics of Plasmas* 26.7 (2019), p. 070701. DOI: 10.1063/1.5094871.

[Alb+20] F. Albert et al. "2020 Roadmap on Plasma Accelerators". In: *New Journal of Physics* (2020). URL: http://iopscience.iop.org/article/10.1088/1367-2630/abcc62.

[AB79] Yu. M. Aliev and V. M. Bychenkov. "Parametric generation of magnetic fields by action of strong radiation on plasma". In: *J. Exp. Theor. Phys.* 49 (1979), p. 805.

[Ami+98] F. Amiranoff et al. "Observation of Laser Wakefield Acceleration of Electrons". In: *Phys. Rev. Lett.* 81 (5 1998), pp. 995–998. DOI: 10.1103/PhysRevLett.81.995. URL: https://link.aps.org/doi/10.1103/PhysRevLett.81.995.

[And+69] H. H. Andersen et al. "An experimental investigation of charge-dependent deviations from the Bethe stopping power formula". In: *Nuclear Physics A* 125.1 (1969), pp. 171 –175. ISSN: 0375-9474. DOI: 10.1016/0375-9474(69)90836-7. URL: http://www.sciencedirect.com/science/article/pii/0375947469908367.

[And+77a] H. H. Andersen et al. "Experimental investigation of higher-order Z1 corrections to the Bethe stopping-power formula". In: *Nuclear Instruments and Methods* 140.3 (1977), pp. 537 –540. ISSN: 0029-554X. DOI: 10.1016/0029-554X(77)90373-1. URL: http://www.sciencedirect.com/science/article/pii/0029554X77903731.

[And+77b] H. H. Andersen et al. "Stopping power of Al, Cu, Ag, and Au for MeV hydrogen, helium, and lithium ions. Z_1^3 and Z_1^4 proportional deviations from the Bethe formula". In: *Phys. Rev. A* 16 (5 1977), pp. 1929–1940. DOI: 10.1103/PhysRevA.16.1929. URL: https://link.aps.org/doi/10.1103/PhysRevA.16.1929.

[AKS70] N. E. Andreev, A. Yu. Kirii, and V. P. Silin. "On the theory of parametric resonnance in a plasma situated in a powerful high-frequency electric field". In: *Radiofizika* 13.9 (1970), pp. 1321–1324. DOI: https://link.springer.com/content/pdf/10.1007/BF01032764.pdf.

[ARR21] ARRONAX. *Arronax priorities*. website. 2021. URL: https://web.archive.org/web/20210123180810/https://www.arronax-nantes.fr/en/production-of-radionuclides/.

[AMB19] Y. H. Asres, M. Mathuthu, and E. Y. Beyene. “The study of alpha particle induced reactions on bismuth-209 isotopes using computer code COMPLET”. In: *Journal of Physics Communications* 3.11 (2019), p. 115006. DOI: 10.1088/2399-6528/ab51c9.

[AV04] S. Atzeni and J. Meyer ter Vehn. “The Physics of Inertial Fusion: BeamPlasma Interaction, Hydrodynamics, Hot Dense Matter”. In: *Oxford Scholarship Online* (2004). DOI: 10.1093/acprof:oso/9780198562641.001.0001.

[AANAJ12] A. A. Azooz, S. H. Al-Nia´emi, and M. A. Al-Jubbori. “Empirical parameterization of CR-39 longitudinal track depth”. In: *Radiation Measurements* 47.1 (2012), pp. 67 –72. ISSN: 1350-4487. DOI: 10.1016/j.radmeas.2011.10.015. URL: http://www.sciencedirect.com/science/article/pii/S1350448711004951.

[AHAJ13] A. A. Azooz, D. Hermsdorf, and M. A. Al-Jubbori. “New approach of modeling charged particles track development in CR-39 detectors”. In: *Radiation Measurements* 58 (2013), pp. 94 –100. ISSN: 1350-4487. DOI: 10.1016/j.radmeas.2013.08.012. URL: http://www.sciencedirect.com/science/article/pii/S1350448713003405.

[Bag+10] V. Bagnoud et al. “Commissioning and early experiments of the PHELIX facility”. In: *Appl. Phys.* B.100 (2010), pp. 137–150. DOI: 10.1007/s00340-009-3855-7.

[BG+18] M. Bailly-Grandvaux et al. “Guiding of relativistic electron beams in dense matter by laser-driven magnetostatic fields”. In: *Nat Commun* 9.102 (2018). DOI: 10.1038.

[Bal08] G. Baldacchino. “Pulse radiolysis in water with heavy-ion beams. A short review”. In: *Radiation Physics and Chemistry* 77.10 (2008). The International Symposium on Charged Particle and Photon Interaction with Matter - ASR 2007, pp. 1218 –1223. ISSN: 0969-806X. DOI: 10.1016/j.radphyschem.2008.05.033. URL: http://www.sciencedirect.com/science/article/pii/S0969806X08001266.

[Bar+20] M. Bardon et al. “Physics of chromatic focusing, post-acceleration and bunching of laser-driven proton beams in helical coil targets”. In: *Plasma Physics and Controlled Fusion* (2020). URL: http://iopscience.iop.org/10.1088/1361-6587/abbe35.

[Bar64] W. Barkas. “Tables of energy losses and ranges of heavy charged particles”. In: *NTIS* NASA-SP-3013 (1964). National Aeronautics and Space Administration (NASA), Washington, D.C., USA, p. 103.

[Bar56] W. H. Barkas. “Mass-Ratio Method Applied to the Measurement of L-Meson Masses and the Energy Balance in Pion Decay”. In: *Phys. Rev.* 101 (2 1956), pp. 778–795. DOI: 10.1103/PhysRev.101.778. URL: https://link.aps.org/doi/10.1103/PhysRev.101.778.

[Bar63] W. H. Barkas. “Resolution of the Σ^--Mass Anomaly”. In: *Phys. Rev. Lett.* 11 (1 1963), pp. 26–28. DOI: 10.1103/PhysRevLett.11.26. URL: https://link.aps.org/doi/10.1103/PhysRevLett.11.26.

[Bar+17a] W. Barth et al. “A superconducting CW-LINAC for heavy ion acceleration at GSI”. In: *EPJ Web Conf* 138.01026 (2017). XXIII International Baldin Seminar on High Energy Physics Problems Relativistic Nuclear Physics and Quantum Chromodynamics (Baldin ISHEPP XXIII). DOI: 10.1051/epjconf/201713801026.

[Bar+17b] W. Barth et al. “High brilliance uranium beams for the GSI FAIR”. In: *Phys. Rev. Accel. Beams* 20 (5 2017), p. 050101. DOI: 10.1103/PhysRevAccelBeams.20.050101. URL: https://link.aps.org/doi/10.1103/PhysRevAccelBeams.20.050101.

[Bas+87] N. G. Basov et al. “Detection of spontaneous magnetic fields in a laser plasma in the Del’fin-1 device”. In: *JETP Lett.* 45.4 (Feb. 1987), p. 25.

[BT64] V. V. Batygin and I. N. Toptygin. *Problems in electrodynamics*. Academic Press, 1964. URL: https://books.google.ru/books?id=AlKPpwAACAAJ.

[Bau72] R. H. Baughman. "Solid-state polymerization of diacetylenes". In: *Journal of Applied Physics* 43.11 (1972), pp. 4362–4370. DOI: 10.1063/1.1660929.

[Bau95] H. Baumhacker. "Layout and performance of the Asterix IV iodine laser at MPQ, Garching". In: *Appl. Phys.* B.61 (1995), pp. 325–332. DOI: 10.1007/BF01081531.

[Bay19] E. Bayart. "Fast dose fractionation using ultra-short laser accelerated proton pulses can increase cancer cell mortality, which relies on functional PARP1 protein". In: *Scientific Reports* 9.10132 (2019). DOI: 10.1038/s41598-019-46512-1.

[BFD19] E. Bayart, A. Flacco, and O. Delmas. "Fast dose fractionation using ultra-short laser accelerated proton pulses can increase cancer cell mortality, which relies on functional PARP1 protein". In: *Sci Rep* 9.10132 (2019). DOI: 10.1038/s41598-019-46512-1.

[Beg+97] F. N. Beg et al. "A study of picosecond laser-solid interactions up to e19Wcm-2". In: *Physics of Plasmas* 4.2 (1997), pp. 447–457. DOI: 10.1063/1.872103.

[BK03] A. R. Bell and R. J. Kingham. "Resistive Collimation of Electron Beams in Laser-Produced Plasmas". In: *Physical Review Letters* 91.035003 (2003).

[BN69] E.V. Benton and W.D. Nix. "The restricted energy loss criterion for registration of charged particles in plastics". In: *Nuclear Instruments and Methods* 67.2 (1969), pp. 343 –347. ISSN: 0029-554X. DOI: 10.1016/0029-554X(69)90471-6. URL: http://www.sciencedirect.com/science/article/pii/0029554X69904716.

[Ber+93] M. J. Berger et al. *ESTAR, PSTAR, and ASTAR: Computer Programs for Calculating Stopping-Power and Range Tables for Electrons, Protons, and Helium Ions (version 1.2.3)*. NIST online resource, National Institute of Standards and Technology, Gaithersburg, MD, USA. NISTIR 4999. 1993. URL: http://physics.nist.gov/Star.

[Bet30] H. Bethe. "Zur Theorie des Durchgangs schneller Korpuskularstrahlen durch Materie". In: *Annalen der Physik* 397.3 (Jan. 1930). 5, pp. 325–400. DOI: 10.1002/andp.19303970303.

[Bet32] H. Bethe. "Bremsformel für Elektronen relativistischer Geschwindigkeit". In: *Z. Phys.* 76 (1932), p. 293.

[BH34] *On the Stopping of Fast Particles and on the Creation of Positive Electrons*. Vol. 146. A 856. p. 83-112. Royal Society of London. The Royal Society, Aug. 1934. URL: http://www.jstor.org/stable/2935479.

[Bey+17] E. Beyreuther et al. "An optimized small animal tumour model for experimentation with low energy protons". In: *PLOS ONE* 12.5 (May 2017), pp. 1–15. DOI: 10.1371/journal.pone.0177428.

[Bic92] H. Bichsel. "Stopping power and ranges of fast ions in heavy elements". In: *Phys. Rev. A* 46 (9 1992), pp. 5761–5773. DOI: 10.1103/PhysRevA.46.5761. URL: https://link.aps.org/doi/10.1103/PhysRevA.46.5761.

[Bic06] H. Bichsel. In: *Nucl. Instrum. Methods* A562 (2006), p. 154.

[Bic+05] H. Bichsel et al. "PASSAGE OF PARTICLES THROUGH MATTER". In: *LBL Reviews* 27 (2005). URL: https://pdg.lbl.gov/2005/reviews/passagerpp.pdf.

[Bin+19] J. H. Bin et al. "Absolute calibration of GafChromic film for very high flux laser driven ion beams". In: *Review of Scientific Instruments* 90.5 (2019), p. 053301. DOI: 10.1063/1.5086822.

[BL91] C. K. Birdsall and A. B. Langdon. *Plasma Physics via Computer Simulation*. Bristol and Philadelphia: Institute of Physics Publishing, 1991. DOI: 10.1201/9781315275048.

[Bis+17] F. Bisesto et al. "Novel Single-Shot Diagnostics for Electrons from Laser-Plasma Interaction at SPARCLAB". In: *Quantum Beam Sci.* 1 (3 2017), p. 13. DOI: 10.3390/qubs1030013.

[Blo33] F. Bloch. "Zur Bremsung rasch bewegter Teilchen beim Durchgang durch Materie". In: *Annalen der Physik* 408.3 (1933), pp. 285–320. DOI: 10.1002/andp.19334080303. eprint: https://onlinelibrary.wiley.com/doi/pdf/10.1002/andp.19334080303. URL: https://onlinelibrary.wiley.com/doi/abs/10.1002/andp.19334080303.

[Boh13] N. Bohr. "II. On the theory of the decrease of velocity of moving electrified particles on passing through matter". In: *The London, Edinburgh, and Dublin Philosophical Magazine and Journal of Science* 25.145 (1913), pp. 10–31. DOI: 10.1080/14786440108634305.

[BZN+20] P. Boller, A. Zylstra, P. Neumaye, et al. "First on-line detection of radioactive fission isotopes produced by laser-accelerated protons". In: *Sci Rep* 10 (2020), p. 17183. DOI: 10.1038/s41598-020-74045-5.

[Bor+04] M. Borghesi et al. "Multi-MeV Proton Source Investigations in Ultraintense Laser-Foil Interactions". In: *Phys. Rev. Lett.* 92 (5 Feb. 2004), p. 055003. DOI: 10.1103/PhysRevLett.92.055003.

[Bor+06] M. Borghesi et al. "Fast Ion Generation by High-Intensity Laser Irradiation of Solid Targets and Applications". In: *Fusion Science and Technology* 49.412 (2006).

[Bor70] J. Boris. In: *Proceedings of the 4th Conference on the Numerical Simulation of Plasmas* (1970). Naval Research Lab, Washington DC, USA.

[Bra+20a] F.-E. Brack et al. "Spectral and spatial shaping of laser-driven proton beams using a pulsed high-field magnet beamline". In: *Sci Rep* 10.9118 (2020). DOI: 10.1038/s41598-020-65775-7.

[Bra+18] P. Bradford et al. "EMP control and characterization on high-power laser systems". In: *High Power Laser Science and Engineering* 6 (2018), e21. DOI: 10.1017/hpl.2018.21.

[BKB20] A V Brantov, A S Kuratov, and V Yu Bychenkov. "Laser-triggered fast charge-separation field generates a strong surface current and wave". In: *Plasma Physics and Controlled Fusion* 62.9 (2020), p. 094003. DOI: 10.1088/1361-6587/ab9f8f.

[Bra+20b] A. V. Brantov et al. "Ultrafast target charging due to polarization triggered by laser-accelerated electrons". In: *Phys. Rev. E* 102 (2 2020), p. 021202. DOI: 10.1103/PhysRevE.102.021202. URL: https://link.aps.org/doi/10.1103/PhysRevE.102.021202.

[Bro+19] E. S. Brondizio et al., eds. *Global assessment report on biodiversity and ecosystem services of the Intergovernmental Science-Policy Platform on Biodiversity and Ecosystem Services*. IPBES secretariat, 2019. DOI: 10.5281/zenodo.3553579.

[Bru87] R. Brunel. "Not-so-resonant, resonant absorption". In: *Phys. Rev. Lett.* 59 (1 1987), pp. 52–55. DOI: 10.1103/PhysRevLett.59.52. URL: https://link.aps.org/doi/10.1103/PhysRevLett.59.52.

[Bru+20] S. Brunner et al. "Dose-dependent Changes After Proton and Photon Irradiation in a Zebrafish Model". In: *Anticancer Research* 14633 (2020). DOI: 10.21873/anticanres.14633.

[Buk+20] N. D. Bukharskii et al. "On the proton radiography of magnetic fields in targets irradiated by intense picosecond laser pulses". In: *Journal of Physics: Conference Series* 1686 (2020), p. 012004. DOI: 10.1088/1742-6596/1686/1/012004.

[Bul+10] Stepan S. Bulanov et al. “Generation of GeV protons from 1 PW laser interaction with near critical density targets”. In: *Phys. Plasmas* 17.4 (2010), p. 043105. DOI: 10.1063/1.3372840.

[Bus+13] S. Busold et al. “Focusing and transport of high-intensity multi-MeV proton bunches from a compact laser-driven source”. In: *Phys. Rev. ST Accel. Beams* 16 (10 2013), p. 101302. DOI: 10.1103/PhysRevSTAB.16.101302. URL: https://link.aps.org/doi/10.1103/PhysRevSTAB.16.101302.

[Bus+14a] S. Busold et al. “Commissioning of a compact laser-based proton beam line for high intensity bunches around 10 MeV”. In: *Phys. Rev. ST Accel. Beams* 17 (3 2014), p. 031302. DOI: 10.1103/PhysRevSTAB.17.031302. URL: https://link.aps.org/doi/10.1103/PhysRevSTAB.17.031302.

[Bus+14b] S. Busold et al. “Shaping laser accelerated ions for future applications – The LIGHT collaboration”. In: *Nuclear Instruments and Methods in Physics Research Section A: Accelerators, Spectrometers, Detectors and Associated Equipment* 740 (2014). Proceedings of the first European Advanced Accelerator Concepts Workshop 2013, pp. 94 –98. ISSN: 0168-9002. DOI: 10.1016/j.nima.2013.10.025. URL: http://www.sciencedirect.com/science/article/pii/S0168900213013715.

[Bus+15] S. Busold et al. “Towards highest peak intensities for ultra-short MeV-range ion bunches”. In: *Sci Rep* 5 (2015), p. 12459. DOI: 10.1038/srep12459.

[But+03] M. J. Butson et al. “Radiochromic film for medical radiation dosimetry”. In: *Materials Science and Engineering R: Reports* 41.3 (2003), pp. 61–120.

[C C+09] C Courtois et al. In: *Phys. Plasmas* 16 (2009), p. 013105.

[Car+07] D. C. Carroll et al. “Active manipulation of the spatial energy distribution of laser-accelerated proton beams”. In: *Phys. Rev. E* 76 (6 2007), p. 065401. DOI: 10.1103/PhysRevE.76.065401. URL: https://link.aps.org/doi/10.1103/PhysRevE.76.065401.

[CSP78] B. G. Cartwright, E. K. Shirk, and P. B. Price. “A nuclear-track-recording polymer of unique sensitivity and resolution”. In: *Nuclear Instruments and Methods* 153.2 (1978), pp. 457 –460. ISSN: 0029-554X. DOI: 10.1016/0029-554X(78)90989-8. URL: http://www.sciencedirect.com/science/article/pii/0029554X78909898.

[Cay+17] W. Cayzac et al. “Experimental discrimination of ion stopping models near the Bragg peak in highly ionized matter”. In: *Nat Commun* 8 (2017), p. 15693. DOI: 10.1038/ncomms15693.

[Cep10] Cepheiden. “Dose Depth Curves”. In: *Wikimedia Commons*. GNU Free Documentation License, Version 1.2. Wikimedia, 2010. URL: https://commons.wikimedia.org/wiki/File:Dose_Depth_Curves.svg.

[CS88] J. Charvát and F. Spurný. “Etching characteristics of cellulose nitrate and CR-39 after high dose electron irradiation”. In: *International Journal of Radiation Applications and Instrumentation. Part D. Nuclear Tracks and Radiation Measurements* 14.4 (1988), pp. 451 –455. ISSN: 1359-0189. DOI: 10.1016/1359-0189(88)90004-0. URL: http://www.sciencedirect.com/science/article/pii/1359018988900040.

[Cha+73] J. B. Chase et al. “Role of spontaneous magnetic fields in a laser-created deuterium plasma”. In: *The Physics of Fluids* 16.7 (1973), pp. 1142–1148. DOI: 10.1063/1.1694477. eprint: https://aip.scitation.org/doi/pdf/10.1063/1.1694477. URL: https://aip.scitation.org/doi/abs/10.1063/1.1694477.

[Cha+18] J. Chatal et al. “Alphatherapy, the new impetus to targeted radionuclide therapy?” In: *Eur. J. Nucl. Med. Mol. Imaging* 45 (2018), pp. 1362–1363. DOI: 10.1007.

[CDB18] J. Chen, W. X. Ding, and D. L. Brower. “Impact of the Cotton–Mouton effect on Faraday polarimetry measurements using circular polarization”. In: *Plasma Physics and Controlled Fusion* 60.8 (2018), p. 085001. DOI: 10.1088/1361-6587/aac708.

[CAB17] S. N. Chen, P. Antici, and E. Boella. “Acceleration of collimated 45 MeV protons by collisionless shocks driven in low-density, large-scale gradient plasmas by a 10^{20} W/cm^2, 1 μm laser”. In: *Sci. Rep.* 7 (2017), p. 16463. DOI: 10.1038/s41598-017-15449-8.

[Che+17] S. N Chen et al. “Collimated protons accelerated from an overdense gas jet irradiated by a 1 μm wavelength high-intensity short-pulse laser”. In: *Sci. Rep.* 7 (2017), p. 13505. DOI: 10.1038/s41598-017-12910-6.

[CTH07] B. Chimier, V. T. Tikhonchuk, and L. Hallo. “Heating model for metals irradiated by a subpicosecond laser pulse”. In: *Phys. Rev. B* 75 (19 2007), p. 195124. DOI: 10.1103/PhysRevB.75.195124. URL: https://link.aps.org/doi/10.1103/PhysRevB.75.195124.

[Cho+97] C. S. Chong et al. “UV-VIS and FTIR spectral studies of CR-39 plastics irradiated with X-rays”. In: *Radiation Measurements* 28.1 (1997). International Conference on Nuclear Tracks in Solids, pp. 119 –122. ISSN: 1350-4487. DOI: 10.1016/S1350-4487(97)00051-6. URL: http://www.sciencedirect.com/science/article/pii/S1350448797000516.

[Chu+90] R. .D. H. Chu et al. “GafChromic dosimetry media: A new high dose, thin film routine dosimeter and dose mapping tool”. In: *Radiat. Phys. Chem.* 35 (1990), pp. 767–773.

[Cik+14] J. Cikhardt et al. “Measurement of the target current by inductive probe during laser interaction on terawatt laser system PALS”. In: *Review of Scientific Instruments* 85.10 (2014), p. 103507. DOI: 10.1063/1.4898016.

[CF04] A. Climent-Font. “First measurements with the madrid 5MV tandem accelerator”. In: *Nuclear Instruments and Methods in Physics* Research Section B: Beam Interactions with Materials and Atoms.219-220 (2004). Proceedings of the Sixteenth International Conference on Ion Beam Analysis., pp. 400 – 404.

[Col97] K. D. Cole. “Diamagnetism in a plasma”. In: *Physics of Plasmas* 4.6 (1997), pp. 2072–2080. DOI: 10.1063/1.872373.

[Con+20] F. Consoli et al. “Laser produced electromagnetic pulses: generation, detection and mitigation”. In: *High Power Laser Science and Engineering* 8 (2020), e22. DOI: 10.1017/hpl.2020.13.

[COP15] COP21. *Paris Agreement*. United Nations, 2015. URL: https://unfccc.int/sites/default/files/english_paris_agreement.pdf.

[Cou+05] C. Courtois et al. “Creation of a uniform high magnetic-field strength environment for laser-driven experiments”. In: *Journal of Applied Physics* 98.5 (2005), p. 054913. DOI: 10.1063/1.2035896.

[Coz20] L. Cozzi. *Sustainable Recovery World Energy Outlook Special Report*. Ed. by E. Hosker. IEA in collaboration with the International Monetary Fund. International Energy Agency, 2020. URL: https://www.iea.org/reports/sustainable-recovery.

[CS05] K. Creath and J. Schmit. “Phase-Measurement Interferometry”. In: *EMO PMI* (2005). URL: http://www.u.arizona.edu/~kcreath/pdf/pubs/2005_KC_JS_EMO_PMI.pdf.

[Cue+15] J. A. Martín-Viera Cueto et al. “A universal dose–response curve for radiochromic films”. In: *Medical Physics* 42.1 (2015), pp. 221–231. DOI: 10.1118/1.4903301. eprint: https://aapm.onlinelibrary.wiley.com/doi/pdf/10.1118/1.4903301. URL: https://aapm.onlinelibrary.wiley.com/doi/abs/10.1118/1.4903301.

[DNP12a] H. Daido, M. Nishiuchi, and A. S. Pirozhkov. “Review of laser-driven ion sources and their applications”. In: *Reports on Progress in Physics* 75.5 (2012), p. 056401. DOI: 10.1088/0034-4885/75/5/056401.

[Dai+86] H. Daido et al. “Ultrahigh Pulsed Magnetic Field Produced by a CO2 Laser”. In: *Japanese Journal of Applied Physics* 26.Part 1, No. 8 (1986), pp. 1290–1295. DOI: 10.1143/jjap.26.1290.

[DNP12b] Hiroyuki Daido, Mamiko Nishiuchi, and Alexander S Pirozhkov. “Review of laser-driven ion sources and their applications”. In: *Rep. Prog. Phys.* 75.5 (Apr. 2012), p. 056401. DOI: 10.1088/0034-4885/75/5/056401.

[Das17] I. J. Das. *Radiochromic Film: Role and Applications in Radiation Dosimetry*. CRC Press, 2017. ISBN: 1-3051650904.

[Deb+17] A Debayle et al. “Electron heating by intense short-pulse lasers propagating through near-critical plasmas”. In: *New J. Phys.* 19.12 (Dec. 2017), p. 123013. DOI: 10.1088/1367-2630/aa953f.

[Den12] R. Dengler. “Self inductance of a wire loop as a curve integral”. In: (Apr. 2012). arXiv: 1204.1486.

[Der+18] J. Derouillat et al. “Smilei : A collaborative, open-source, multi-purpose particle-in-cell code for plasma simulation”. In: *Computer Physics Communications* 222 (2018), pp. 351 –373. ISSN: 0010-4655. DOI: 10.1016/j.cpc.2017.09.024. URL: http://www.sciencedirect.com/science/article/pii/S0010465517303314.

[DES09] DESA. *World Population Prospects: The 2008 Revision*. UN Department of Economic and Social Affairs Population Division, 2009. URL: https://population.un.org/wpp/.

[DB82] M. Deutsch and I. Beniaminy. “Derivative-free inversion of Abel’s integral equation”. In: *Applied Physics Letters* 41.1 (1982), pp. 27–28. DOI: 10.1063/1.93309.

[DNP90] M. Deutsch, A. Notea, and D. Pal. “Inversion of Abel’s integral equation and its application to NDT by X-ray radiography”. In: *NDT International* 23.1 (1990), pp. 32 –38. ISSN: 0308-9126. DOI: 10.1016/0308-9126(90)91446-Z. URL: http://www.sciencedirect.com/science/article/pii/030891269091446Z.

[Dev+16] S. Devic et al. “Reference radiochromic film dosimetry: Review of technical aspects”. In: *Physica Medica* 32.4 (2016), pp. 541 –556. ISSN: 1120-1797. DOI: 10.1016/j.ejmp.2016.02.008. URL: http://www.sciencedirect.com/science/article/pii/S112017971600510X.

[d'H+10] E d'Humiéres et al. “Investigation of high intensity laser proton acceleration with underdense targets”. In: *J. Phys. Conf. Ser.* 244.4 (Aug. 2010), p. 042023. DOI: 10.1088/1742-6596/244/4/042023.

[d’H+13] E. d’Humières et al. “Optimization of laser-target interaction for proton acceleration”. In: *Phys. Plasmas* 20.2 (2013), p. 023103. DOI: 10.1063/1.4791655.

[Don+03] Q. Dong et al. “Optimization of ion acceleration in the interaction of intense femtosecond laser pulses with ultrathin foils”. In: *Phys. Rev. E* 68 (2 2003), p. 026408. DOI: 10.1103/PhysRevE.68.026408. URL: https://link.aps.org/doi/10.1103/PhysRevE.68.026408.

[DHK02] B. Dörschel, D. Hermsdorf, and K. Kadner. “Studies of experimentally determined etch-rate ratios in CR-39 for ions of different kinds and energies”. In: *Radiation Measurements* 35.3 (2002), pp. 183 –187. ISSN: 1350-4487. DOI: 10.1016/S1350-4487(02)00049-5. URL: http://www.sciencedirect.com/science/article/pii/S1350448702000495.

[D+97a] B. Dörschel et al. “Dependence of the Etch Rate Ratio on the Energy Loss in Proton Irradiated CR-39 Detectors and Recalculation of Etch Pit Parameters”. In: *Radiation Protection Dosimetry* 71.2 (May 1997), pp. 99–106. ISSN: 0144-8420. DOI: 10.1093/oxfordjournals.rpd.a032046. URL: https://academic.oup.com/rpd/article-pdf/71/2/99/9929486/99.pdf.

[D+97b] B. Dörschel et al. “Measurement of Track Parameters and Etch Rates in Proton-Irradiated CR-39 Detectors and Simulation of Neutron Dosemeter Responses”. In: *Radiation Protection Dosimetry* 69.4 (Feb. 1997), pp. 267–274. ISSN: 0144-8420. DOI: 10.1093/oxfordjournals.rpd.a031913. URL: https://academic.oup.com/rpd/article-pdf/69/4/267/9929354/267.pdf.

[D+99] B. Dörschel et al. “Measurement of the track etch rates along proton and alpha particle trajectories in CR-39 and calculation of the detection efficiency”. In: *Radiation Measurements* 31.1 (1999). Proceedings of the 19th International Conference on Nuclear Tracks in Solids, pp. 103 –108. ISSN: 1350-4487. DOI: 10.1016/S1350-4487(99)00117-1. URL: http://www.sciencedirect.com/science/article/pii/S1350448799001171.

[D+02] B. Dörschel et al. “Dependence of the etch rate ratio on the energy loss of light ions in CR-39”. In: *Radiation Measurements* 35.4 (2002), pp. 287 –292. ISSN: 1350-4487. DOI: 10.1016/S1350-4487(02)00056-2. URL: http://www.sciencedirect.com/science/article/pii/S1350448702000562.

[Gca] *Dosimetry Media, Types EBT-2 / EBT-3 / HD-V2 / MD-V2-55 / MD-V3*. Manufacturing White Papers, Gafchromic (2011-2017). Gafchromic Specifications. Ashland. URL: http://gafchromic.com/.

[Dre99] M. S. Dresselhaus. “Solid State Physics Part 2 - Optical Properties of Solids”. Course 6.723 MIT. 1999. URL: https://web.archive.org/web/20150724051216/http://web.mit.edu/course/6/6.732/www/6.732-pt2.pdf.

[Dun74] P. H. Duncan. “Analysis of the Moebius Loop Magnetic Field Sensor”. In: *IEEE Transactions on Electromagnetic Compatibility* EMC-16.2 (1974), pp. 83–89. DOI: 10.1109/TEMC.1974.303336.

[DB87] SAEED A. DURRANI and RICHARD K. BULL. *Solid State Nuclear Track Detection*. Ed. by S. A. Durrani and R. K. Bull. Pergamon, 1987, pp. v –ix. ISBN: 978-0-08-020605-9. DOI: 10.1016/B978-0-08-020605-9.50004-6. URL: http://www.sciencedirect.com/science/article/pii/B9780080206059500046.

[Ehr] M. Ehret. “U-EBT-3 are EBT-3 without front layer”. direct communication with the manufacturer Ashland.

[EBGK+21] M. Ehret, M. Bailly-Grandvaux, Ph. Konreev, et al. *Guided Electromagnetic Discharge Pulses Driven by Short Intense Laser Pulses: Characterization and Modelling*. in preparation. 2021.

[ESLOB+20] M. Ehret, C. Salgado-Lopez, V. Ospina-Bohorquez, et al. *Ion acceleration by an ultrashort laser pulse interacting with a near-critical-density gas jet*. 2020. arXiv: 2012.09455.

[Ehr+19] M. Ehret et al. *Kilotesla plasmoid formation by a trapped relativistic laser beam*. 2019. arXiv: 1908.11430.

[Eic+98] H. Eickhoff et al. "The GSI Cancer Therapy Project". In: *Strahlentherapie und Onkologie* 175.Suppl. 2 (1998). 1. Med-AUSTRON conference, Innsbruck (Austria), 8-11 Oct 1997. URL: https://accelconf.web.cern.ch/pac97/papers/pdf/9B008.PDF.

[Enk84] V. Enkelmann. "Structural Aspects of the Topochemical Polymerization of Diacetylenes". In: *Advances in Polymer Science*. Vol. 63. Springer Berlin Heidelberg, 1984.

[Eri19] G. Ericsson. "Advanced Neutron Spectroscopy in Fusion Research". In: *Journal of Fusion Energy* 38 (2019), pp. 330–355.

[Esa+97] E. Esarey et al. "Self-focusing and guiding of short laser pulses in ionizing gases and plasmas". In: *IEEE Journal of Quantum Electronics* 33.11 (1997), pp. 1879–1914. DOI: 10.1109/3.641305.

[EVK75] K. G. Estabrook, E. J. Valeo, and W. L. Kruer. "Two-dimensional relativistic simulations of resonance absorption". In: *The Physics of Fluids* 18.9 (1975), pp. 1151–1159. DOI: 10.1063/1.861276. eprint: https://aip.scitation.org/doi/pdf/10.1063/1.861276. URL: https://aip.scitation.org/doi/abs/10.1063/1.861276.

[FMF85] R. Fabbro, C. Max, and E. Fabre. "Planar laser-driven ablation: Effect of inhibited electron thermal conduction". In: *The Physics of Fluids* 28.5 (1985), pp. 1463–1481. DOI: 10.1063/1.864982. eprint: https://aip.scitation.org/doi/pdf/10.1063/1.864982. URL: https://aip.scitation.org/doi/abs/10.1063/1.864982.

[Fan63] U. Fano. "Penetration of Protons, Alpha Particles, and Mesons". In: *Annual Review of Nuclear Science* 13.1 (1963), pp. 1–66. DOI: 10.1146/annurev.ns.13.120163.000245.

[Fas08] Fastfission. "Binding energy curve - common isotopes". In: *Wikimedia Commons*. Public Domain. Wikimedia, 2008. URL: https://commons.wikimedia.org/wiki/File:Binding_energy_curve_-_common_isotopes.svg.

[Fau+04] J. Faure et al. "A laser–plasma accelerator producing monoenergetic electron beams". In: *Nature* 531 (2004), pp. 541–544.

[Fav+14] V. Favaudon et al. "Ultrahigh dose-rate FLASH irradiation increases the differential response between normal and tumor tissue in mice". In: *Science Translational Medicine* 6.245 (2014), 245ra93. DOI: 10.1126/scitranslmed.3008973.

[Fen+18] Y. Feng et al. "Spectral calibration of EBT3 and HD-V2 radiochromic film response at high dose using 20 MeV proton beams". In: *Rev. Sci. Instrum.* 89 (2018). AIP PUBLISHING LICENSE 4865891495800. URL: 10.1063/1.4996022.

[Fik+16] G. Fiksel et al. "A simple model for estimating a magnetic field in laser-driven coils". In: *Applied Physics Letters* 109.13 (2016), p. 134103. DOI: 10.1063/1.4963763.

[Fiú+12] Frederico Fiúza et al. "Laser-driven shock acceleration of monoenergetic ion beams". In: *Phys. Rev. Lett.* 109.21 (2012), p. 215001.

[Fle+67a] R. L. Fleischer et al. "Criterion for Registration in Dielectric Track Detectors". In: *Phys. Rev.* 156 (2 1967), pp. 353–355. DOI: 10.1103/PhysRev.156.353. URL: https://link.aps.org/doi/10.1103/PhysRev.156.353.

[Fle+67b] R. L. Fleischer et al. “Criterion for registration in various solid state nuclear track detectors”. In: *Phys. Rev.* 156 (2 1967), pp. 353–355. DOI: 10.1103/PhysRev.156.353. URL: https://link.aps.org/doi/10.1103/PhysRev.156.353.

[Fle+75] R. L. Fleischer et al. “Nuclear Tracks in Solids: Principles and Applications”. In: *Univ. California Press* (1975). DOI: 10.1180/minmag.1978.042.322.40.

[For+77] D. W. Forslund et al. “Theory of Hot-Electron Spectra at High Laser Intensity”. In: *Phys. Rev. Lett.* 39 (5 1977), pp. 284–288. DOI: 10.1103/PhysRevLett.39.284. URL: https://link.aps.org/doi/10.1103/PhysRevLett.39.284.

[Fow+80] P. H. Fowler et al. “TRACK RECORDING PROPERTIES OF THE PLASTIC CR-39 FOR NON-RELATIVISTIC IONS IN THE CHARGE RANGE 6 TO 29”. In: *Solid State Nuclear Track Detectors*. Ed. by H. FRANÇOIS et al. Pergamon, 1980, pp. 239 –244. ISBN: 978-0-08-025029-8. DOI: 10.1016/B978-0-08-025029-8.50033-0. URL: http://www.sciencedirect.com/science/article/pii/B9780080250298500330.

[Fre72] J. P. Freidberg. “Resonant Absorption of Laser Light by Plasma Targets”. In: *Phys. Rev. Lett.* 28 (13 1972), pp. 795–799. DOI: 10.1103/PhysRevLett.28.795. URL: https://link.aps.org/doi/10.1103/PhysRevLett.28.795.

[Fro+91] M. Fromm et al. “A study of CR39 bulk etch properties under various temperature and concentration conditions to modelize the dissolution rate”. In: *International Journal of Radiation Applications and Instrumentation. Part D. Nuclear Tracks and Radiation Measurements* 19.1 (1991), pp. 169 –170. ISSN: 1359-0189. DOI: 10.1016/1359-0189(91)90166-F. URL: http://www.sciencedirect.com/science/article/pii/135901899190166F.

[Fro+07] D. H. Froula et al. “Quenching of the Nonlocal Electron Heat Transport by Large External Magnetic Fields in a Laser-Produced Plasma Measured with Imaging Thomson Scattering”. In: *Phys. Rev. Lett.* 98 (13 2007), p. 135001. DOI: 10.1103/PhysRevLett.98.135001. URL: https://link.aps.org/doi/10.1103/PhysRevLett.98.135001.

[Fuj+13] S. Fujioka et al. “Kilotesla Magnetic Field due to a Capacitor-Coil Target Driven by High Power Laser”. In: *Sci. Rep.* 3.1170 (2013).

[Gal+07] A. L. Galkin et al. “Relativistic motion and radiation of an electron in the field of an intense laser pulse”. In: *Quantum Electronics* 37.10 (2007), pp. 903–909. DOI: 10.1070/qe2007v037n10abeh013626.

[Gal+20] M. Galletti et al. “Direct observation of ultrafast electrons generated by high-intensity laser-matter interaction”. In: *Appl. Phys. Lett.* 116 (2020), p. 064102. DOI: 10.1063/1.5142265.

[Ged+04] C. G. R. Geddes et al. “High-quality electron beams from a laser wakefield accelerator using plasma-channel guiding”. In: *Nature* 531 (2004), pp. 538–541. DOI: 10.1038/nature02900.

[GS01] A. Gil and J. Segura. “DTORH3 2.0: A new version of a computer program for the evaluation of toroidal harmonics. This program can be downloaded from the CPC Program Library under catalogue identifier: http://cpc.cs.qub.ac.uk/summaries/ADOH”. In: *Computer Physics Communications* 139.2 (2001), pp. 186 –191. ISSN: 0010-4655. DOI: 10.1016/S0010-4655(01)00188-6. URL: http://www.sciencedirect.com/science/article/pii/S0010465501001886.

[Gin70] V. L. Ginzburg. *The propagation of electromagnetic waves in plasma*. 2nd ed. Internat. Ser. Mono. Electromagn. Waves. Trans. from the Russian. Oxford: Pergamon, 1970. URL: https://cds.cern.ch/record/103352.

[GMI12] GMIA. *GELATINHANDBOOK*. Ed. by GMIA. GELATIN MANUFACTURERS INSTITUTE OF AMERICA, 2012.

[GT92] A. N. Golovchenko and S. P. Tretyakova. “Registration properties of different types of CR-39 in vacuum conditions of irradiation”. In: *International Journal of Radiation Applications and Instrumentation. Part D. Nuclear Tracks and Radiation Measurements* 20.3 (1992). Special Section Galactic Cosmic Radiation: Constraints on Space Exploration, pp. 521 –523. ISSN: 1359-0189. DOI: 10.1016/1359-0189(92)90040-3. URL: http://www.sciencedirect.com/science/article/pii/1359018992900403.

[Goy+17] C. Goyon et al. “Ultrafast probing of magnetic field growth inside a laser-driven solenoid”. In: *Phys. Rev. E* 95 (3 2017), p. 033208. DOI: 10.1103/PhysRevE.95.033208. URL: https://link.aps.org/doi/10.1103/PhysRevE.95.033208.

[Gre+82] P. T. Green et al. “ON THE OPTIMISATION OF ETCHING CONDITIONS FOR CR39 AND OTHER PLASTIC TRACK DETECTORS”. In: *Solid State Nuclear Track Detectors*. Ed. by P.H. FOWLER and V.M. CLAPHAM. Amsterdam: Pergamon, 1982, pp. 179 –182. ISBN: 978-0-08-026509-4. DOI: 10.1016/B978-0-08-026509-4.50042-8. URL: http://www.sciencedirect.com/science/article/pii/B9780080265094500428.

[GY16] A. Gupta and D. S. Yan. “Chapter 17 - Magnetic and Electrostatic Separation”. In: *Mineral Processing Design and Operations (Second Edition)*. Ed. by Ashok Gupta and Denis Yan. Second Edition. Amsterdam: Elsevier, 2016, pp. 629 –687. ISBN: 978-0-444-63589-1. DOI: 10.1016/B978-0-444-63589-1.00017-4. URL: http://www.sciencedirect.com/science/article/pii/B9780444635891000174.

[H. +16] H. Ahmed et al. In: *Phys. Rev. A* 829 (2016).

[Had19] F. Haddad. “Isotope production for medical applications: what can be done?” In: *21st Colloque Ganil*. 2019. URL: https://21colloqueganil.sciencesconf.org/data/pages/ColloqueGANIL2019_Haddad.pdf.

[Had+11] F. Haddad et al. “The ARRONAX Project”. In: *Current Radiopharmaceuticals* 4.3 (2011), pp. 186–196. ISSN: 1874-4710. URL: https://www.ingentaconnect.com/content/ben/crp/2011/00000004/00000003/art00003.

[Had+20] P. Hadjisolomou et al. “Dynamics of guided post-acceleration of protons in a laser-driven travelling-field accelerator”. In: *Plasma Physics and Controlled Fusion* 62.11 (2020), p. 115023. DOI: 10.1088/1361-6587/abb91a.

[Haj+08] M. Hajek et al. “Convolution of TLD and SSNTD measurements during the BRADOS-1 experiment onboard ISS (2001)”. In: *Radiation Measurements* 43.7 (2008), pp. 1231 –1236. ISSN: 1350-4487. DOI: 10.1016/j.radmeas.2008.04.094. URL: http://www.sciencedirect.com/science/article/pii/S1350448708002539.

[HL18] E. Hecht and K. Lippert. *Optik*. Berlin, Boston: De Gruyter, 2018. ISBN: 978-3-11-052665-3. DOI: 10.1515/9783110526653. URL: https://www.degruyter.com/view/title/525251.

[Heg+03] M. Hegelich et al. “MeV ion jets from short-pulse-laser interaction with thin foils”. In: *Physical Review Letters* 89.085002 (2003).

[Hel+16] M. H. Helle et al. “Laser-Accelerated Ions from a Shock-Compressed Gas Foil”. In: *Phys. Rev. Lett.* 117 (16 Oct. 2016), p. 165001. DOI: 10.1103/PhysRevLett.117.165001. URL: https:/link.aps.org/doi/10.1103/PhysRevLett.117.165001.

[Her+05] A. Hermanne et al. “Experimental study of the cross-sections of alpha-particle induced reactions on 209Bi”. In: *Applied Radiation and Isotopes* 63.1 (2005), pp. 1–9. ISSN: 0969-8043. DOI: 10.1016/j.apradiso.2005.01.015. URL: https://www.sciencedirect.com/science/article/pii/S0969804305000345.

[HA04] J. A. Hernandes and A. K. K. Assis. “Surface charges and external electric field in a toroid carrying a steady current”. en. In: *Brazilian Journal of Physics* 34 (Dec. 2004), pp. 1738 –1744. ISSN: 0103-9733. URL: http://www.scielo.br/scielo.php?script=sci_arttext&pid=S0103-97332004000800041&nrm=iso.

[Hic99] D. G. Hicks. “Charged Particle Spectroscopy: A new window on inertial confinement fusion”. PhD thesis. MIT, 1999.

[HC17] A. V. Higuera and J. R. Cary. “Structure-preserving second-order integration of relativistic charged particle trajectories in electromagnetic fields”. In: *Physics of Plasmas* 24.5 (2017), p. 052104. DOI: 10.1063/1.4979989.

[Hof14] G. Hoffmeister. “Influencing laser-accelerated ions by femtosecond-laser desorption”. PhD thesis. TU Darmstadt, 2014.

[Hoh+12] M. Hohenberger et al. “Inertial confinement fusion implosions with imposed magnetic field compression using the OMEGA Laser”. In: *Physics of Plasmas* 19.5 (2012), p. 056306. DOI: 10.1063/1.3696032.

[Hua+21] M. Huault et al. “Calibration of a time-integrated and 2D spatially resolved proton kinetic energy spectrum diagnostic based on an HD-V2 radiochromic films stack”. In: *RSI* (2021). in preparation.

[Hum89] J. C. Humphreys. “Nist high-dose calibration services”. In: *Nucl. Instruments Methods Phys. Res.* Sec. B: Beam Interactions with Mater.Atoms 40 (1989), pp. 1173–1177.

[Hut02] I. H. Hutchinson. *Principles of Plasma Diagnostics*. 2nd ed. Cambridge University Press, 2002. DOI: 10.1017/CBO9780511613630.

[IAE18] IAEA. *Medical physics staffing needs in diagnostic imaging and radionuclide therapy: an activity based approach*. Tech. rep. International Atomic Energy Agency, 2018. URL: https://www-pub.iaea.org/MTCD/Publications/PDF/PUB1797_web.pdf.

[IEA20a] IEA, ed. *Energy Efficiency 2020*. International Energy Agency, 2020. URL: https://www.iea.org/reports/energy-efficiency-2020.

[IEA20b] IEA, ed. *Energy Technology Perspectives 2020*. International Energy Agency, 2020. URL: https://www.iea.org/reports/energy-technology-perspectives-2020.

[IEA20c] IEA. *World Energy Review 2020*. International Energy Agency, 2020. URL: https://www.iea.org/reports/world-energy-outlook-2020.

[Ike+18] H. Ikeda et al. “Application of astatine-210: Evaluation of astatine distribution and effect of pre-injected iodide in whole body of normal rats”. In: *Applied Radiation and Isotopes* 139 (2018), pp. 251–255. ISSN: 0969-8043. DOI: 10.1016/j.apradiso.2018.05.021. URL: https://www.sciencedirect.com/science/article/pii/S0969804317313660.

[Ike+09] M. Ikegami et al. “Radial focusing and energy compression of a laser-produced proton beam by a synchronous rf field”. In: *Phys. Rev. ST Accel. Beams* 12 (6 2009), p. 063501. DOI: 10.1103/PhysRevSTAB.12.063501. URL: https://link.aps.org/doi/10.1103/PhysRevSTAB.12.063501.

[Ing+18] F. Ingenito et al. In: *EPJ Web of Conferences* 167 (2018), p. 05006.

[IPC14] IPCC. *Climate Change 2014 Synthesis Report*. Intergovernmental Panel on Climate Change, 2014. URL: https://www.ipcc.ch/site/assets/uploads/2018/05/SYR_AR5_FINAL_full_wcover.pdf#page=22.

[ISO13] ISO. *Practice for use of a radiochromic film dosimetry system*. Tech. rep. ISO/ASTM51275, 2013.

[J.-+14] J.-L. Dubois et al. In: *Physical Review E* 89 (2014), p. 013102.

[J+10] O. Jächel et al. "All-optical measurement of the hot electron sheath driving laser ion acceleration from thin foils". In: *New Journal of Physics* 12 (2010), p. 103027. DOI: 10.1088/1367-2630/12/10/103027.

[Jah+19] D. Jahn et al. "Focusing of multi-MeV, subnanosecond proton bunches from a laser-driven source". In: *Phys. Rev. Accel. Beams* 22 (1 2019), p. 011301. DOI: 10.1103/PhysRevAccelBeams.22.011301. URL: https://link.aps.org/doi/10.1103/PhysRevAccelBeams.22.011301.

[Jäk+99] O. Jäkel et al. "Treatment planning for light ions: How to take into account Relative Biological Effectivness (RBE)". In: *Strahlentherapie und Onkologie* 175 (1999), pp. 12–14. DOI: 10.1007/BF03038877.

[Jas32] K. Jaspers. *Die Geistige Situation der Zeit*. Vol. 5. 9. Abdr. 5 Ed. 1999. de Gruyter, 1932.

[JC11] D. Jette and W. Chen. "Creating a spread-out Bragg peak in proton beams". In: *Physics in Medicine and Biology* 56.11 (2011), N131–N138. DOI: 10.1088/0031-9155/56/11/n01.

[Jia+12] T. Jian et al. "Energy spectrum optimization of laser-produced protons by RF cavity". In: *High Power Laser and Particle Beams* 24.120245 (2012), p. 467. DOI: 10.3788/HPLPB20122402.0467.

[Joh63] W. C. Johnson. "Transmission Lines and Networks". In: McGraw-Hill, 1963, p. 58.

[Jon+19] L. Jonušauskas et al. "Mesoscale laser 3D printing". In: *Opt. Express* 27.11 (2019), pp. 15205–15221. DOI: 10.1364/OE.27.015205. URL: http://www.opticsexpress.org/abstract.cfm?URI=oe-27-11-15205.

[J.S+77] J.S. Perlman et al. In: *Appl. Phys. Lett.* 31 (1977), p. 414.

[K. +09] K. Quinn et al. In: *Phys. Rev. Lett.* 102 (2009), p. 194801.

[Kal03] M. Kalal. "Modern Topics in Physics". In: ed. by Z. Kluiber. ARSCI, Praha. 2003. Chap. Complex Interferometry, pp. 267–272. ISBN: 80-86078-28-0.

[Kal15] M. Kalal. "Complex Interferometry: How Far Can You Go?" In: *Physics Procedia* 62 (2015). 3rd International Conference Frontiers in Diagnostic Technologies, ICFDT3 2013, 25-27 November 2013, Laboratori Nazionali di Frascati, Italy, pp. 92 –96. ISSN: 1875-3892. DOI: 10.1016/j.phpro.2015.02.016. URL: http://www.sciencedirect.com/science/article/pii/S1875389215000474.

[Kal+04] M. Kaluza et al. "Influence of the Laser Prepulse on Proton Acceleration in Thin-Foil Experiments". In: *Physical Review Letters* 94.045003 (2004).

[Kar+16] S. Kar et al. "Dynamic control of laser driven proton beams by exploiting self-generated, ultrashort electromagnetic pulses". In: *Physics of Plasmas* 23.5 (2016), p. 055711. DOI: 10.1063/1.4948725.

[Kat+95] H. Kato et al. “Field-induced phase transitions in ferrimagnetic R2Fe14B in ultra-high magnetic fields”. In: *Physica B: Condensed Matter* 211.1 (1995). Research in High Magnetic Fields, pp. 105 –107. ISSN: 0921-4526. DOI: 10.1016/0921-4526(94)00956-V. URL: http://www.sciencedirect.com/science/article/pii/092145269400956V.

[KK68] R. Katz and E. J. Kobetich. “Formation of Etchable Tracks in Dielectrics”. In: *Phys. Rev.* 170 (2 1968), pp. 401–405. DOI: 10.1103/PhysRev.170.401. URL: https://link.aps.org/doi/10.1103/PhysRev.170.401.

[Kim+19] K. J. Kim et al. “Prospective 3He-rich landing sites on the Moon”. In: *Planetary and Space Science* 177 (2019), p. 104686. ISSN: 0032-0633. DOI: https://doi.org/10.1016/j.pss.2019.07.001. URL: https://www.sciencedirect.com/science/article/pii/S0032063318303842.

[Kir11] D. Kirby. “Radiation Dosimetry of conventional and laser-driven particle beams”. Dissertation. The University of Birmingham, 2011.

[KM79] V. V. Korobkin and S. L. Motylev. “On a possibility of using laser radiation for generation of strong magnetic fields”. In: *Sov. Tech. Phys. Lett* 5.474 (1979).

[KS66] V. V. Korobkin and R. V. Serov. “Investigation of the magnetic field of a spark produced by focusing laser radiation”. In: *JETP Lett.* 4.3 (Aug. 1966), pp. 103–106. URL: http://www.jetpletters.ac.ru/ps/1624/article_24843.pdf.

[Kos+20] N. V. Kostyuchenko et al. “High-field magnetization study of (Nd,Dy)2Fe14B: Intrinsic properties and promising compositions”. In: *Intermetallics* 124 (2020), p. 106840. ISSN: 0966-9795. DOI: 10.1016/j.intermet.2020.106840. URL: http://www.sciencedirect.com/science/article/pii/S0966979519306144.

[KE85] W. L. Kruer and K. Estabrook. “JxB heating by very intense laser light”. In: *The Physics of Fluids* 28.1 (1985), pp. 430–432. DOI: 10.1063/1.865171. eprint: https://aip.scitation.org/doi/pdf/10.1063/1.865171. URL: https://aip.scitation.org/doi/abs/10.1063/1.865171.

[Kru+21] M. Krupka et al. “Design of modular multi-channel electron spectrometers for application in laser matter interaction experiments at Prague Asterix Laser System”. In: *Review of Scientific Instruments* 92.2 (2021), p. 023514. DOI: 10.1063/5.0029849.

[Kum+20] D. Kumar et al. “Magnetic field generation using single-plate targets driven by kJ-ns class laser”. In: *Plasma Physics and Controlled Fusion* (2020). URL: http://iopscience.iop.org/10.1088/1361-6587/abb617.

[Kum09] V. Kumar. “Understanding the focusing of charged particle beams in a solenoid magnetic field”. In: *American Journal of Physics* 77.8 (2009), pp. 737–741. DOI: 10.1119/1.3129242.

[KBB18] A. S. Kuratov, A. V. Brantov, and V. Yu. Bychenkov. “Modeling of Laser Generation and Propagation of Electron Bunch Along Thin Irradiated Wire”. In: *Bulletin of the Lebedev Physics Institute* 45.11 (2018), pp. 346–349. ISSN: 1934-838X. DOI: 10.3103/S1068335618110052.

[Lan28] I. Langmuir. “Oscillations in Ionized Gases”. In: *Proceedings of the National Academy of Science* 14 (1928), pp. 627–637.

[LG+18] J. M. Lárraga-Gutiérrez et al. “Evaluation of a LED-based flatbed document scanner for radiochromic film dosimetry in transmission mode”. In: *Physica Medica* 47 (2018). CC BY-NC-ND license, pp. 86–91. URL: 10.1016/j.ejmp.2018.02.010.

[Law+16] K. F. F. Law et al. “Direct measurement of kilo-tesla level magnetic field generated with laser-driven capacitor-coil target by proton deflectometry”. In: *Applied Physics Letters* 108.9 (2016), p. 091104. DOI: 10.1063/1.4943078.

[Law+20] K. F. F. Law et al. “Relativistic magnetic reconnection in laser laboratory for testing an emission mechanism of hard-state black hole system”. In: *Phys. Rev. E* 102 (3 2020), p. 033202. DOI: 10.1103/PhysRevE.102.033202. URL: https://link.aps.org/doi/10.1103/PhysRevE.102.033202.

[Law57] J. D. Lawson. “Some criteria for a power producing thermonuclear reactor”. In: *Proceedings of the Physical Society (London)* 70 (1957), pp. 6–10.

[LMS03] K. W. D. Ledingham, P. McKenna, and R. P. Singhal. “Applications for Nuclear Phenomena Generated by Ultra-Intense Lasers”. In: *Science* 300.5622 (2003), pp. 1107–1111. ISSN: 0036-8075. DOI: 10.1126/science.1080552. eprint: https://science.sciencemag.org/content/300/5622/1107.full.pdf. URL: https://science.sciencemag.org/content/300/5622/1107.

[Led+14] K. W. D. Ledingham et al. “Towards Laser Driven Hadron Cancer Radiotherapy: A Review of Progress”. In: *Appl. Sci.* 4 (2014), pp. 402–443.

[Lee+14] W. P. Leemans et al. “Multi-GeV Electron Beams from Capillary-Discharge-Guided Subpetawatt Laser Pulses in the Self-Trapping Regime”. In: *Phys. Rev. Lett.* 113 (24 2014), p. 245002. DOI: 10.1103/PhysRevLett.113.245002. URL: https://link.aps.org/doi/10.1103/PhysRevLett.113.245002.

[Lew16] D. Lewis. *GAFCHROMIC DOSIMETRY MEDIA, TYPE MD-V3*. Ashland. Feb. 2016. URL: http://gafchromic.com/.

[Lew10] D. F. Lewis. “Radiochromic Film”. In: *ISP Products Presentation*. Advanced Materials Group. International Specialty Products. 2010. URL: https://web.archive.org/web/*/http://www.elimpex.com/new/products/radiation_therapy/Gafchromic/content/Lewis_Radiochromic_Film_20101020.pdf.

[Li+02] Yuelin Li et al. “Small-angle Thomson scattering of ultrafast laser pulses for bright, sub-100-fs x-ray radiation”. In: *Phys. Rev. ST Accel. Beams* 5 (4 2002), p. 044701. DOI: 10.1103/PhysRevSTAB.5.044701. URL: https://link.aps.org/doi/10.1103/PhysRevSTAB.5.044701.

[Lif+14] A Lifschitz et al. “Ion acceleration in underdense plasmas by ultra-short laser pulses”. In: *New J. Phys.* 16.3 (Mar. 2014), p. 033031. DOI: 10.1088/1367-2630/16/3/033031.

[LP81] E. M. Lifshitz and L. P. Pitaevskii. *Course of Theoretical Physics: Vol 10, Physical Kinetics*. Pergamon press, 1981.

[Lil+04] L. Lilje et al. “Achievement of 35MV/m in the superconducting nine-cell cavities for TESLA”. In: *Nuclear Instruments and Methods in Physics Research Section A: Accelerators, Spectrometers, Detectors and Associated Equipment* 524.1 (2004), pp. 1 –12. ISSN: 0168-9002. DOI: 10.1016/j.nima.2004.01.045. URL: http://www.sciencedirect.com/science/article/pii/S0168900204001391.

[Lim+08] J. Limpouch et al. “Enhanced laser ion acceleration from mass-limited targets”. In: *Laser and Particle Beams* 26.2 (2008), pp. 225–234. DOI: 10.1017/S0263034608000268.

[Liu+16] M. Liu et al. “Collisionless electrostatic shock formation and ion acceleration in intense laser interactions with near critical density plasmas”. In: *Phys. Plasmas* 23.11 (2016), p. 113103. DOI: 10.1063/1.4967946.

[Luh75] N. Luhmann. “Soziologische Aufklärung Band 2”. In: VS Verlag für Sozialwissenschaften, 1975. Chap. Die Weltgesellschaft, p. 77.

[Luh98] N. Luhmann. *Die Gesellschaft der Gesellschaft*. Vol. 1. Suhrkamp-Taschenbuch Wissenschaft 1360 1 and 2. Suhrkamp, 1998.

[M. 17] M. Bailly-Grandvaux. “Laser-driven strong magnetic fields and high discharge currents: measurements and applications to charged particle transport”. PhD thesis. Université de Bordeaux, 2017.

[M. 15] M. Ehret. “Charged particle beam transport in intense electromagnetic fields”. In: *Master Proposal Université de Bordeaux and Technische Universität Darmstadt* (2015). DOI: 10.13140/RG.2.1.3820.0806.

[M. 16] M. Ehret. “TNSA-Proton Beam Guidance with Strong Magnetic Fields Generated by Coil Targets”. In: *Master Thesis Technische Universität Darmstadt* (2016). DOI: 10.13140/RG.2.1.3855.7847.

[M. +17a] M. Ehret et al. “Energy selective focusing of TNSA beams by picosecond-laser driven ultra-fast EM fields”. In: *GSI Scientific Report 2016* GSI-2017-1 (2017), p. 227. DOI: http://dx.doi.org/10.15120/GR-2017-1.

[M. +17b] M. Ehret et al. “Energy selective focusing of TNSA beams by picosecond-laser driven ultra-fast EM fields”. In: *News and Reports from HEDgeHOB* GSI-2017-2 (2017), pp. 19–20.

[MM08] M. Passoni and M. Lontano. “Theory of Light-Ion Acceleration Driven by a Strong Charge Separation”. In: *Physical Review Letters* 101.115001 (2008).

[Mac13] A. Macchi. *A Superintense Laser-Plasma Interaction Theory Primer*. Springer, Dordrecht, 2013. DOI: https://aproxy.ulb.tu-darmstadt.de:2062/10.1007/978-94-007-6125-4.

[MBP13] Andrea Macchi, Marco Borghesi, and Matteo Passoni. “Ion acceleration by superintense laser-plasma interaction”. In: *Rev. Mod. Phys.* 85 (2 May 2013), pp. 751–793. DOI: 10.1103/RevModPhys.85.751.

[Mai60] T. H. Maiman. “Stimulated Optical Emission in Ruby”. In: *Nature* 4736 (1960), pp. 493–494. URL: https://link.springer.com/content/pdf/10.1038/187493a0.pdf.

[Mak+18] M. Makvandi et al. “Alpha-Emitters and Targeted Alpha Therapy in Oncology: from Basic Science to Clinical Investigations”. In: *Targ Ocol* 13 (2018), pp. 189–203. DOI: 10.1007/s11523-018-0550-9.

[Mal+01] A. A. Malek et al. “Mechanistic model for bond scission in a polymeric system by radiation”. In: *Radiation Physics and Chemistry* 60.6 (2001), pp. 603 –607. ISSN: 0969-806X. DOI: 10.1016/S0969-806X(00)00349-2. URL: http://www.sciencedirect.com/science/article/pii/S0969806X00003492.

[MM96] G. Malka and J. L. Miquel. “Experimental Confirmation of Ponderomotive-Force Electrons Produced by an Ultrarelativistic Laser Pulse on a Solid Target”. In: *Physical Review Letters* 77.75 (1996).

[Man+04] S. P. D. Mangle et al. “Monoenergetic beams of relativistic electrons from intense laser–plasma interactions”. In: *Nature* 431 (2004), pp. 535–538. DOI: 10.1038/nature02939.

[MV+96] J. M. Martinez-Val et al. “Fusion burning waves in proton-boron-11 plasmas”. In: *Physics Letters A* 216.1 (1996), pp. 142 –152. ISSN: 0375-9601. DOI: 10.1016/0375-9601(96)00252-6. URL: http://www.sciencedirect.com/science/article/pii/0375960196002526.

[MJ10] M. Martišíková and O. Jäkel. “Dosimetric properties of Gafchromic® EBT films in medical carbon ion beams”. In: *Physics in Medicine and Biology* 55.18 (2010), pp. 5557–5567. DOI: 10.1088/0031-9155/55/18/019.

[Mat+10] Materialscientist et al. “Attenuation Coefficient Iron”. In: *Wikimedia Commons*. GNU-Lizenz für freie Dokumentation, Version 1.2. Wikimedia, 2010. URL: https://de.wikipedia.org/wiki/Datei:Attenuation_Coefficient_Iron.svg.

[MM12] V. I. Matveev and D. N. Makarov. “Bloch correction in the theory of energy losses by fast charged particles”. In: *Tech. Phys.* 57 (2012). original in Zhurnal Tekhnicheskoi Fiziki, 2012, Vol. 82, No. 11, pp. 137–139, pp. 1600–1602. DOI: 10.1134/S1063784212110163.

[Mau87] W. Maurer. *NEUTRON AND GAMMA IRRADIATION EFFECTS ONORGANIC INSULATING MATERIALS FOR FUSIONMAGNETS*. TECDOC 417. International Atomic Energy Agency, Vienna: IAEA, 1987.

[Max+74] C. E. Max et al. “Self-Modulation and Self-Focusing of Electromagnetic Waves in Plasmas”. In: *Phys. Rev. Lett.* 33 (4 1974), pp. 209–212. DOI: 10.1103/PhysRevLett.33.209. URL: https://link.aps.org/doi/10.1103/PhysRevLett.33.209.

[McL96] W. L. McLaughlin. “Novel radiochromic films for clinical dosimetry”. In: *Radiat. protection dosimetry* 66 (1996), pp. 263–268.

[MC65] W. L. McLaughlin and L. Chalkley. “Measurement of radiation dose distributions with photochromic materials”. In: *Radiol.* 84 (1965), pp. 124–125.

[McL+91a] W. L. McLaughlin et al. “Sensitometry of the response of a new radiochromic film dosimeter to gamma radiation and electron beams”. In: *Nuclear Instruments and Methods in Physics Research Section A: Accelerators, Spectrometers, Detectors and Associated Equipment* 302.1 (1991), pp. 165 –176. ISSN: 0168-9002. DOI: 10.1016/0168-9002(91)90506-L. URL: http://www.sciencedirect.com/science/article/pii/016890029190506L.

[McL+91b] W. L. McLaughlin et al. “Sensitometry of the response of a new radiochromic film dosimeter to gamma radiation and electron beams”. In: *Nuclear Instruments and Methods in Physics Research Section A: Accelerators, Spectrometers, Detectors and Associated Equipment* 302.1 (1991), pp. 165 –176. ISSN: 0168-9002. DOI: 10.1016/0168-9002(91)90506-L. URL: http://www.sciencedirect.com/science/article/pii/016890029190506L.

[Mil+18] R. Hernández Millares et al. “A New Promising Approach for Radiochromic Film-Dosimetry at micrometer resolution using a Two Peak Ratio Method by Confocal Raman Spectroscopy”. In: *Transactions of the Korean Nuclear Society Autumn Meeting*. Yeosu, Korea, Oct. 2018.

[Mis+13] R. Mishra et al. “Collisional particle-in-cell modeling for energy transport accompanied by atomic processes in dense plasmas”. In: *Physics of Plasmas* 20.7 (2013), p. 072704. DOI: 10.1063/1.4812701.

[Mol32] C. Moller. In: *Ann. Physik* 14 (1932), p. 531.

[Mon+15] D. S. Montgomery et al. “Use of external magnetic fields in hohlraum plasmas to improve laser-coupling”. In: *Physics of Plasmas* 22.1 (2015), p. 010703. DOI: 10.1063/1.4906055.

[Mor+18a] J. T. Morrison et al. “Corrigendum: MeV proton acceleration at kHz repetition rate from ultra-intense laser liquid interaction (2018 New J. Phys. 20 022001)”. In: *New Journal of Physics* 20.6 (2018), p. 069501. DOI: 10.1088/1367-2630/aac5d1.

[Mor+18b] J. T. Morrison et al. “MeV proton acceleration at kHz repetition rate from ultra-intense laser liquid interaction”. In: *New Journal of Physics* 20.2 (2018), p. 022001. DOI: 10.1088/1367-2630/aaa8d1.

[Mue+91] P. J. Muench et al. “Photon energy dependence of the sensitivity of radiochromic film and comparison with silver halide film and LiF TLDs used for brachytherapy dosimetry”. In: *Med. Phys.* 18 (1991), pp. 769–775.

[Mul20] P. Mulser. *Hot Matter from High-Power Lasers*. 1st. Springer Graduate Texts in Physics. Springer, Berlin, Heidelberg, 2020. DOI: https://aproxy.ulb.tu-darmstadt.de:2062/10.1007/978-3-662-61181-4.

[MNV86] M.V. Ammosov, N.B Delone, and V.P. Krainov. “Tunnel ionization of complex atoms and of atomic ions in an alternating electromagnetic field”. In: *Soviet Physics - JETP* 64(6) (1986), pp. 1191–1194.

[Nak+10] Tatsufumi Nakamura et al. “High-Energy Ions from Near-Critical Density Plasmas via Magnetic Vortex Acceleration”. In: *Phys. Rev. Lett.* 105 (13 Sept. 2010), p. 135002. DOI: 10.1103/PhysRevLett.105.135002.

[Nee+06] D. Neely et al. “Enhanced proton beams from ultrathin targets driven by high contrast laser pulses”. In: *Applied Physics Letters* 89.021502 (2006).

[NS00] W. M. Nevins and R. Swain. “The thermonuclear fusion rate coefficient for p-11B reactions”. In: *Nuclear Fusion* 40.4 (2000), pp. 865–872. DOI: 10.1088/0029-5515/40/4/310.

[NY04] D. Nikezic and K. N. Yu. “Formation and growth of tracks in nuclear track materials”. In: *Materials Science and Engineering: R: Reports* 46.3 (2004), pp. 51 –123. ISSN: 0927-796X. DOI: 10.1016/j.mser.2004.07.003. URL: http://www.sciencedirect.com/science/article/pii/S0927796X04000579.

[NY06] D. Nikezic and K. N. Yu. “Computer program TRACK_TEST for calculating parameters and plotting profiles for etch pits in nuclear track materials”. In: *Computer Physics Communications* 174.2 (2006), pp. 160 –165. ISSN: 0010-4655. DOI: 10.1016/j.cpc.2005.09.011. URL: http://www.sciencedirect.com/science/article/pii/S0010465505005187.

[NY08] D. Nikezic and K. N. Yu. “Computer program TRACK_VISION for simulating optical appearance of etched tracks in CR-39 nuclear track detectors”. In: *Computer Physics Communications* 178 (2008), pp. 591–595. DOI: 10.1016/j.cpc.2005.09.011. URL: http://www.sciencedirect.com/science/article/pii/S0010465505005187.

[Nil+12] P. M. Nilson et al. “Time-Resolved Measurements of Hot-Electron Equilibration Dynamics in High-Intensity Laser Interactions with Thin-Foil Solid Targets”. In: *Phys. Rev. Lett.* 108 (8 2012), p. 085002. DOI: 10.1103/PhysRevLett.108.085002. URL: https://link.aps.org/doi/10.1103/PhysRevLett.108.085002.

[Nis+09] M. Nishiuchi et al. “Focusing and spectral enhancement of a repetition-rated, laser-driven, divergent multi-MeV proton beam using permanent quadrupole magnets”. In: *Applied Physics Letters* 94.6 (2009), p. 061107. DOI: 10.1063/1.3078291.

[Nov+15] A. S. Novo et al. “Physics of collisionless shocks: theory and simulation”. In: *Plasma Physics and Controlled Fusion* 58.1 (2015), p. 014005. DOI: 10.1088/0741-3335/58/1/014005.

[N+09] F. Nürnberg et al. “Radiochromic film imaging spectroscopy of laser-accelerated proton beams”. In: *Rev. Sci. Instrum.* 80.033301 (Mar. 2009). URL: https://dx.doi.org/10.1063/1.3086424.

[Oda+97] K. Oda et al. “Effects of low-LET radiations on CR-39 track detector”. In: *Radiation Measurements* 28.1 (1997). International Conference on Nuclear Tracks in Solids, pp. 85 –88. ISSN: 1350-4487. DOI: 10.1016/S1350-4487(97)00045-0. URL: http://www.sciencedirect.com/science/article/pii/S1350448797000450.

[Oud+16] A. den Ouden et al. “Progress in the Development of the HFML 45 T Hybrid Magnet”. In: *IEEE Transactions on Applied Superconductivity* 26.4 (2016), pp. 1–7. DOI: 10.1109/TASC.2016.2524544.

[P. +07] P. McKenna et al. “Lateral Electron Transport in High-Intensity Laser-Irradiated Foils Diagnosed by Ion Emission”. In: *Phys. Rev. Lett.* 98 (14 2007), p. 145001. DOI: 10.1103/PhysRevLett.98.145001. URL: https://link.aps.org/doi/10.1103/PhysRevLett.98.145001.

[Pal18] Ch. Palmer. “Paving the way for a revolution in high repetition rate laser-driven ion acceleration”. In: *New Journal of Physics* 20.6 (2018), p. 061001. DOI: 10.1088/1367-2630/aac5ce.

[Par78] H. G. Paretzke. “ON PRIMARY DAMAGE AND SECONDARY ELECTRON DAMAGE IN HEAVY ION TRACKS IN PLASTICS”. In: *Solid State Nuclear Track Detectors*. Ed. by F. GRANZER, H. PARETZKE, and E. SCHOPPER. Pergamon, 1978, pp. 87 –98. ISBN: 978-1-4832-8338-8. DOI: 10.1016/B978-1-4832-8338-8.50008-X. URL: http://www.sciencedirect.com/science/article/pii/B978148328338850008X.

[Par+19] J. Park et al. “Ion acceleration in laser generated megatesla magnetic vortex”. In: *Phys. Plasmas* 26.10 (2019), p. 103108. DOI: 10.1063/1.5094045.

[Pas04] C. Pascual. “Experimental determination of stopping forces for ions in matter”. PhD thesis. Universidad Autónoma de Madrid, 2004.

[PL08] M. Passoni and M. Lontano. “Theory of Light-Ion Acceleration Driven by a Strong Charge Separation”. In: *Physical Review Letters* 101.115001 (2008).

[Pas+04] M. Passoni et al. “Charge separation effects in solid targets and ion acceleration with a two-temperature electron distribution”. In: *Physical Review* E.69 (2004), p. 026411.

[Pat+03] P. K. Patel et al. “Isochoric Heating of Solid-Density Matter with an Ultrafast Proton Beam”. In: *Phys. Rev. Lett.* 91 (12 Sept. 2003), p. 125004. DOI: 10.1103/PhysRevLett.91.125004.

[Pea+07] F. Peano et al. “Dynamics and control of the expansion of finite-size plasmas produced in ultraintense laser-matter interactions”. In: *Physics of Plasmas* 14.5 (2007), p. 056704. DOI: 10.1063/1.2436855.

[Pee+20] J. L. Peebles et al. “Axial proton probing of magnetic and electric fields inside laser-driven coils”. In: *Physics of Plasmas* 27.6 (2020), p. 063109. DOI: 10.1063/1.5134786.

[PPT66] A. M. Perelomov, V. S. Popov, and M. V. Terent´ev. “Ionization of atoms in an alternating electric field”. In: *Sov. Phys.* JETP.23 (1966), pp. 924 –934. URL: http://jetp.ac.ru/cgi-bin/dn/e_023_05_0924.pdf.

[Per+13] L. J. Perkins et al. “Two-dimensional simulations of thermonuclear burn in ignition-scale inertial confinement fusion targets under compressed axial magnetic fields”. In: *Physics of Plasmas* 20.7 (2013), p. 072708. DOI: 10.1063/1.4816813.

[Pis+90] T. Pisarczyk et al. “Faraday-rotation method for magnetic-field diagnostics in a laser plasma”. In: *J Russ Laser Research* 11 (1990), pp. 1–32. DOI: 10.1007/BF01124729.

[Pis+15] T. Pisarczyk et al. “Space-time resolved measurements of spontaneous magnetic fields in laser-produced plasma”. In: *Physics of Plasmas* 22.10 (2015), p. 102706. DOI: 10.1063/1.4933364.

[Pis+19] T. Pisarczyk et al. “Elaboration of 3-frame complex interferometry for optimization studies of capacitor-coil optical magnetic field generators”. In: *Journal of Instrumentation* 14.11 (2019), pp. C11024–C11024. DOI: 10.1088/1748-0221/14/11/c11024.

[Pis+20] T. Pisarczyk et al. “Hot electron retention in laser plasma created under terawatt sub-nanosecond irradiation of Cu targets”. In: *Plasma Physics and Controlled Fusion* (2020). URL: http://iopscience.iop.org/10.1088/1361-6587/abb74b.

[Pol+06] B. B. Pollock et al. “High magnetic field generation for laser-plasma experiments”. In: *Review of Scientific Instruments* 77.11 (2006), p. 114703. DOI: 10.1063/1.2356854.

[Por16a] L. Porter. *GAFCHROMIC DOSIMETRY MEDIA, TYPE EBT-3*. Ashland. Feb. 2016. URL: http://gafchromic.com/.

[Por16b] L. Porter. *GAFCHROMIC DOSIMETRY MEDIA, TYPE HD-V2*. Ashland. Feb. 2016. URL: http://gafchromic.com/.

[Por+37] R. B. Porter et al. *Hindenburg Burns in Lakehurst Crash*. The New York Times, Vol. 86, No. 28958. May 1937.

[pow20] nuclear power.net. *The relative importance of various processes of gamma radiation interaction with matter*. online. https://www.nuclear-power.net/wp-content/uploads/2015/03/attenuation.png. 2020. URL: https://www.nuclear-power.net/nuclear-power/reactor-physics/atomic-nuclear-physics/radiation/x-rays-roentgen-radiation/x-ray-attenuation/.

[Poy+18] A. Poyé et al. “Thin target charging in short laser pulse interactions”. In: *Phys. Rev. E* 98 (3 2018), p. 033201. DOI: 10.1103/PhysRevE.98.033201. URL: https://link.aps.org/doi/10.1103/PhysRevE.98.033201.

[Pre+17] I. Prencipe et al. “Targets for high repetition rate laser facilities: needs, challenges and perspectives”. In: *High Power Laser Science and Engineering* 5 (2017), e17. DOI: 10.1017/hpl.2017.18.

[Pri+05] J. Primot et al. “L’analyse de surface d’onde par interférométrie à décalage multilatéral”. French. In: *Photoniques (Orsay)* (2005). ISSN: 1629-4475.

[Pug+16] L. P. Pugachev et al. “Acceleration of electrons under the action of petawatt-class laser pulses onto foam targets”. In: *Nuclear Instruments and Methods in Physics Research Section A: Accelerators, Spectrometers, Detectors and Associated Equipment* 829 (2016). 2nd European Advanced Accelerator Concepts Workshop - EAAC 2015, pp. 88 –93. ISSN: 0168-9002. DOI: 10.1016/j.nima.2016.02.053. URL: http://www.sciencedirect.com/science/article/pii/S0168900216002291.

[PV96] A. Pukhov and J. Meyer-ter Vehn. “Relativistic Magnetic Self-Channeling of Light in Near-Critical Plasma: Three-Dimensional Particle-in-Cell Simulation”. In: *Phys. Rev. Lett.* 76 (21 May 1996), pp. 3975–3978. DOI: 10.1103/PhysRevLett.76.3975.

[Rei08] M. Reiser. *Theory and design of charged particle beams*. 2008. URL: http://dx.doi.org/10.1002/9783527622047.

[Ren17] K. F. Renk. *Basics of Laser Physics*. Vol. 2. Graduate Texts in Physics. Springer Cham, 2017.

[RH+15] J. Rojas-Herrera et al. “Impact of x-ray dose on the response of CR-39 to 1–5.5 MeV alphas”. In: *Review of Scientific Instruments* 86.3 (2015), p. 033501. DOI: 10.1063/1.4913906.

[Rom+05] L. Romagnani et al. “Dynamics of Electric Fields Driving the Laser Acceleration of Multi-MeV Protons”. In: *Phys. Rev. Lett.* 95 (19 2005), p. 195001. DOI: 10.1103/PhysRevLett.95.195001. URL: https://link.aps.org/doi/10.1103/PhysRevLett.95.195001.

[Ros+19] O. N. Rosmej et al. “Interaction of relativistically intense laser pulses with long-scale near critical plasmas for optimization of laser based sources of MeV electrons and gamma-rays”. In: *New Journal of Physics* 21.4 (2019), p. 043044. DOI: 10.1088/1367-2630/ab1047.

[Ros52] B. B. Rossi. *High-energy particles*. New York, NY, USA: Prentice-Hall, 1952.

[RS16] M. Roth and M. Schollmeier. “Ion Acceleration—Target Normal Sheath Acceleration”. In: *CERN Yellow Reports* 1 (2016). Proceedings of the 2014 CAS-CERN Accelerator School: Plasma Wake Acceleration. DOI: 10.5170/CERN-2016-001.231.

[Rot+01a] M. Roth et al. “Fast Ignition by Intense Laser-Accelerated Proton Beams”. In: *Phys. Rev. Lett.* 86 (3 Jan. 2001), pp. 436–439. DOI: 10.1103/PhysRevLett.86.436.

[Rot+01b] M. Roth et al. “Fast Ignition by Intense Laser-Accelerated Proton Beams”. In: *Phys. Rev. Lett.* 86 (3 2001), pp. 436–439. DOI: 10.1103/PhysRevLett.86.436. URL: https://link.aps.org/doi/10.1103/PhysRevLett.86.436.

[Rot+02] M. Roth et al. “Energetic ions generated by laser pulses: A detailed study on target properties”. In: *Phys. Rev. ST Accel. Beams* 5 (6 2002), p. 061301. DOI: 10.1103/PhysRevSTAB.5.061301. URL: https://link.aps.org/doi/10.1103/PhysRevSTAB.5.061301.

[Rud+80] F. H. Ruddy et al. “CR-39 polymer, a promising new solid state track recorder for high energy neutron applications”. In: *IAEA INIS Conference Report* HEDL-SA–2149 (1980). 14 Apr 1980; 22 p; Symposium on neutron cross sections from 10 - 50 MeV; Upton, NY, USA; 12 - 14 May 1980; CONF-800551–20; Available from NTIS., PC A02/MF A01.

[Rus+91] G. Rusch et al. “The Siegen automatic measuring system for track detectors: New developments”. In: *International Journal of Radiation Applications and Instrumentation. Part D. Nuclear Tracks and Radiation Measurements* 19.1 (1991), pp. 261 –266. ISSN: 1359-0189. DOI: 10.1016/1359-0189(91)90188-N. URL: http://www.sciencedirect.com/science/article/pii/135901899190188N.

[S. +16] S. Kar et al. In: *Nat. Comm.* 7 (2016), p. 10792.

[S. +15] S. Tokita et al. In: *SR* 5:8268 (2015).

[Sad+97] M. Sadowski et al. “Comparison of responses of CR-39, PM-355, and CN track detectors to energetic hydrogen-, helium-, nitrogen-, and oxygen-ions”. In: *Radiation Measurements* 28.1 (1997). International Conference on Nuclear Tracks in Solids, pp. 207 –210. ISSN: 1350-4487. DOI: 10.1016/S1350-4487(97)00069-3. URL: http://www.sciencedirect.com/science/article/pii/S1350448797000693.

[SB87] R.D. Saini and P.K. Bhattacharyya. “Radiolytic oxidation of U(IV) sulphate in aqueous solution by alpha particles from cyclotron”. In: *International Journal of Radiation Applications and Instrumentation. Part C. Radiation Physics and Chemistry* 29.5 (1987), pp. 375 –379. ISSN: 1359-0197. DOI: 10.1016/1359-0197(87)90009-9. URL: http://www.sciencedirect.com/science/article/pii/1359019787900099.

[Sal21] M. Salvadori. “Accurate spectra for high energy ions by advanced time-of-flight diamond-detector schemes in experiments with high energy and intensity lasers”. In: *Sci Rep* 11 (2021), p. 3071.

[San+02] A. S. Sandhu et al. “Laser-Generated Ultrashort Multimegagauss Magnetic Pulses in Plasmas”. In: *Phys. Rev. Lett.* 89 (22 2002), p. 225002. DOI: 10.1103/PhysRevLett.89.225002. URL: https://link.aps.org/doi/10.1103/PhysRevLett.89.225002.

[SBGE+18] J. J. Santos, M. Bailly-Grandvaux, M. Ehret, et al. “Laser-driven strong magnetostatic fields with applications to charged beam transport and magnetized high energy-density physics”. In: *Physics of Plasmas* 25.5 (2018), p. 056705. DOI: 10.1063/1.5018735.

[San+15] J. J. Santos et al. “Laser-driven platform for generation and characterization of strong quasi-static magnetic fields”. In: *New Journal of Physics* 17.8 (2015), p. 083051. DOI: 10.1088/1367-2630/17/8/083051.

[SG91] J. A. Sayeg and R. C. Gregory. “A new method for characterizing beta-ray ophthalmic applicator sources”. In: *Med. Phys.* 18 (1991), pp. 453–461.

[Say+88] M. C. Saylor et al. “A thin film recording medium for use in food irradiation”. In: *Radiat. Phys. Chem.* 31 (1988), pp. 529–536.

[SW97] S.C. Wilks and W.L. Kruer. In: *IEEE J. Quantum Electron.* 33 (1997), p. 1954.

[Sch+17] V. A. Schanz et al. “Noise reduction in third order cross-correlation by angle optimization of the interacting beams”. In: *Opt. Express* 25 (2017), pp. 9252–9261.

[Sch14] Schott. *BG38 Data Sheet*. Tech. rep. Schott, 2014. URL: https://web.archive.org/web/20210413154054/https://shop.schott.com/medias/schott-bandpass-bg38-jun-2017-en.pdf?context=bWFzdGVyfHJvb3R8Nzk2NTk2fGFwcGxpY2F0aW9uL3BkZnxoMmMvaGQwLzg4MjAyMzM4NjMxOTgucGRmfDA2NGQ4ZmY2MmUzOGEyZmIyNWM4MzA3MGExMGYyNTgxZGJmZDNmYjBmNmQ3NmNmZTRiMTFmYWJlMDAwNTZkYTM.

[Sch+08] J. Schwartz et al. “High Field Superconducting Solenoids Via High Temperature Superconductors”. In: *IEEE Transactions on Applied Superconductivity* 18.2 (2008), pp. 70–81. DOI: 10.1109/TASC.2008.921363.

[See83] J. F. Seely. “Pulsed megagauss fields produced by laser-driven coils”. In: *Applied Physics* B.31 (1983), pp. 37–43.

[Seg95] S. E. Segre. “Plasma polarimetry for large Cotton–Mouton and Faraday effects”. In: *Physics of Plasmas* 2.8 (1995), pp. 2908–2914. DOI: 10.1063/1.871190.

[SG00] J. Segura and A. Gil. “Evaluation of toroidal harmonics”. In: *Computer Physics Communications* 124.1 (2000), pp. 104 –122. ISSN: 0010-4655. DOI: 10.1016/S0010-4655(99)00428-2. URL: http://www.sciencedirect.com/science/article/pii/S0010465599004282.

[Sei+15] M. Seimetz et al. “Calibration and Performance Tests of Detectors for Laser-Accelerated Protons”. In: *IEEE Transactions on Nuclear Science* 62.6 (2015), pp. 3216–3224.

[Sig06] P. Sigmund. *Particle Penetration and Radiation Effects*. Solid State Sciences 151. Berlin Heidelberg : Springer-Verlag, 2006. ISBN: 3-540-31713-9.

[SS] P. Sigmund and A. Schinner. “Notes on Barkas-Andersen effect”. In: *The European Physical Journal* 318.68 (), p. 10. DOI: 10.1140/epjd/e2014-50461-3.

[Sil+04] Luís O. Silva et al. “Proton Shock Acceleration in Laser-Plasma Interactions”. In: *Phys. Rev. Lett.* 92 (1 Jan. 2004), p. 015002. DOI: 10.1103/PhysRevLett.92.015002.

[Sle+15] O. Slezak et al. “Thermally induced depolarization in terbium gallium garnet ceramics rod with natural convection cooling”. In: *Journal of Optics* 17.6 (2015), p. 065610. DOI: 10.1088/2040-8978/17/6/065610.

[SSP72] R. D. Small, V. A. Sernas, and R. H. Page. “Single Beam Schlieren Interferometer Using a Wollaston Prism”. In: *Appl. Opt.* 11.4 (1972), pp. 858–862. DOI: 10.1364/AO.11.000858. URL: http://ao.osa.org/abstract.cfm?URI=ao-11-4-858.

[Smi+53] F. M. Smith et al. “Measurements of Meson Masses and Related Quantities”. In: *Phys. Rev.* 91 (3 1953), pp. 765–766. DOI: 10.1103/PhysRev.91.765. URL: https://link.aps.org/doi/10.1103/PhysRev.91.765.

[Sna+00] R. A. Snavely et al. “Intense High-Energy Proton Beams from Petawatt-Laser Irradiation of Solids”. In: *Phys. Rev. Lett.* 85 (14 2000), pp. 2945–2948. DOI: 10.1103/PhysRevLett.85.2945. URL: https://link.aps.org/doi/10.1103/PhysRevLett.85.2945.

[Soa06] C. G. Soares. “Radiochromic film dosimetry”. In: *Radiat. Measurements* 41 (2006). The 2nd Summer School on Solid State Dosimetry: Concepts and Trends in Medical Dosimetry, S100–S116. ISSN: 1350-4487. DOI: 10.1016/j.radmeas.2007.01.007. URL: http://www.sciencedirect.com/science/article/pii/S1350448707000121.

[S.P+00] S.P. Hatchett et al. In: *Phys. Plasmas* 7 (2000), p. 2076.

[Spe+01] I. Spencer et al. “Laser generation of proton beams for the production of short-lived positron emitting radioisotopes”. In: *Nucl. Instrum. Methods Phys. Res., Sect. B* 183.3 (2001), pp. 449–458. ISSN: 0168-583X. DOI: 10.1016/S0168-583X(01)00771-6. URL: http://www.sciencedirect.com/science/article/pii/S0168583X01007716.

[SF06] P. Spiller and G. Franchetti. “The FAIR accelerator project at GSI”. In: *Nuclear Instruments and Methods in Physics Research Section A: Accelerators, Spectrometers, Detectors and Associated Equipment* 561.2 (2006). Proceedings of the Workshop on High Intensity Beam Dynamics, pp. 305 –309. ISSN: 0168-9002. DOI: 10.1016/j.nima.2006.01.043. URL: http://www.sciencedirect.com/science/article/pii/S0168900206000507.

[SR75] J. A. Stamper and B. H. Ripin. “Faraday-Rotation Measurements of Megagauss Magnetic Fields in Laser-Produced Plasmas”. In: *Phys. Rev. Lett.* 34 (3 1975), pp. 138–141. DOI: 10.1103/PhysRevLett.34.138. URL: https://link.aps.org/doi/10.1103/PhysRevLett.34.138.

[Sta+71] J. A. Stamper et al. “Spontaneous Magnetic Fields in Laser-Produced Plasmas”. In: *Phys. Rev. Lett.* 26 (17 1971), pp. 1012–1015. DOI: 10.1103/PhysRevLett.26.1012. URL: https://link.aps.org/doi/10.1103/PhysRevLett.26.1012.

[ST] National Institute of Standards and Technology. *STAR*. ESTAR, ASTAR and PSTAR. URL: https://physics.nist.gov/PhysRefData/Star/Text/intro.html.

[Sta+14] A. Starobor et al. “Study of the properties and prospects of Ce:TAG and TGG magnetooptical ceramics for optical isolators for lasers with high average power”. In: *Opt. Mater. Express* 4.10 (2014), pp. 2127–2132. DOI: 10.1364/OME.4.002127. URL: http://www.osapublishing.org/ome/abstract.cfm?URI=ome-4-10-2127.

[SP86] J. Stejny and T. Portwood. “A study of the molecular structure in CR-39”. In: *International Journal of Radiation Applications and Instrumentation. Part D. Nuclear Tracks and Radiation Measurements* 12.1 (1986). Special Volume Solid State Nuclear Track Detectors, pp. 121 –123. ISSN: 1359-0189. DOI: 10.1016/1359-0189(86)90552-2. URL: http://www.sciencedirect.com/science/article/pii/1359018986905522.

[Ste+96] M. A. Stevens et al. “High-resolution dosimetry using radiochromic filmand a document scanner”. In: *Phys. Med. Biol.* 41 (1996), pp. 2357–2365.

[Icra] *Stopping Powers and Ranges for Protons and Alpha Particles*. 49th ed. ICRU. 1993. URL: http://physics.nist.gov/PhysRefData/.

[Icrb] *Stopping Powers for Electrons and Positrons*. 37th ed. ICRU. 1984.

[SM85a] D. Strickland and G. Mourou. “Compression of amplified chirped optical pulses”. In: *Opt. Commun.* 56.3 (1985), pp. 219–221. ISSN: 0030-4018. DOI: 10.1016/0030-4018(85)90120-8. URL: http://www.sciencedirect.com/science/article/pii/0030401885901208.

[SM85b] Donna Strickland and Gerard Mourou. “Compression of amplified chirped optical pulses”. In: *Optics Communications* 56.3 (1985), pp. 219 –221. ISSN: 0030-4018. DOI: 10.1016/0030-4018(85)90120-8. URL: http://www.sciencedirect.com/science/article/pii/0030401885901208.

[Str10] D. Strozzi. *Fusion N-Tau-Product for Deuterium Reactions*. Wikimedia Commons. Licence is https://creativecommons.org/licenses/by-sa/3.0deed.en. 2010. URL: https://commons.wikimedia.org/wiki/File:Fusion_ntau.svg.

[Syl+12a] F. Sylla et al. “Anticorrelation between Ion Acceleration and Nonlinear Coherent Structures from Laser-Underdense Plasma Interaction”. In: *Phys. Rev. Lett.* 108 (11 Mar. 2012), p. 115003. DOI: 10.1103/PhysRevLett.108.115003.

[Syl+12b] F Sylla et al. “Development and characterization of very dense submillimetric gas jets for laser-plasma interaction”. In: *Rev. Sci. Instrum.* 83.3 (2012), p. 033507.

[Syl+13] F. Sylla et al. “Short Intense Laser Pulse Collapse in Near-Critical Plasma”. In: *Phys. Rev. Lett.* 110 (8 Feb. 2013), p. 085001. DOI: 10.1103/PhysRevLett.110.085001.

[Tab+94] M. Tabak et al. “Ignition and high gain with ultrapowerful lasers*”. In: *Physics of Plasmas* 1.5 (1994), pp. 1626–1634. DOI: 10.1063/1.870664.

[Tan+18] M. Tanabashi et al. “Review of Particle Physics”. In: *Phys. Rev. D* 98 (3 2018), p. 030001. DOI: 10.1103/PhysRevD.98.030001. URL: https://link.aps.org/doi/10.1103/PhysRevD.98.030001.

[Tat+02] M. Tatarakis et al. “Measuring huge magnetic fields”. In: *Nature* 415 (2002). (London), p. 280. DOI: 10.1038/415280a.

[Aea] *Techniques for high-dose dosimetry in industry, agriculture and medicine - proceedings of a symposium held in vienna, 9-13 november 1998*. AEA-TECDOC 1070. AEA. INIS Clearinghouse, Nov. 1999.

[TD95] N. X. Thang and T. T. Doan. “Structure effect in response function of CR-39 detector”. In: *Radiation Measurements* 25.1 (1995). Nuclear Tracks in Solids, pp. 185 –187. ISSN: 1350-4487. DOI: 10.1016/1350-4487(95)00071-L. URL: http://www.sciencedirect.com/science/article/pii/135044879500071L.

[Tho+75] J. J. Thomson et al. “Magnetic Fields Due to Resonance Absorption of Laser Light”. In: *Phys. Rev. Lett.* 35 (10 1975), pp. 663–667. DOI: 10.1103/PhysRevLett.35.663. URL: https://link.aps.org/doi/10.1103/PhysRevLett.35.663.

[Tik02] V. T. Tikhonchuk. “Interaction of a beam of fast electrons with solids”. In: *Physics of Plasmas* 9.1416 (2002).

[Tik+17] V. T. Tikhonchuk et al. “Quasistationary magnetic field generation with a laser-driven capacitor-coil assembly”. In: *Phys. Rev. E* 96 (2 2017), p. 023202. DOI: 10.1103/PhysRevE.96.023202. URL: https://link.aps.org/doi/10.1103/PhysRevE.96.023202.

[TNY06] K. C. C. Tse, F. M. F. Ng, and K. N. Yu. “Photo-degradation of PADC by UV radiation at various wavelengths”. In: *Polymer Degradation and Stability* 91.10 (2006), pp. 2380 –2388. ISSN: 0141-3910. DOI: 10.1016/j.polymdegradstab.2006.03.017. URL: http://www.sciencedirect.com/science/article/pii/S0141391006000991.

[Val20] P. Puyuelo Valdesaldes. “Laser-driven ion acceleration with high-density gas-jet targets and application to elemental analysis”. Theses. Université de Bordeaux; Institut national de la recherche scientifique (Québec, province), Oct. 2020. URL: https://tel.archives-ouvertes.fr/tel-03053720.

[Vol+19] L. Volpe et al. “Generation of high energy laser-driven electron and proton sources with the 200 TW system VEGA 2 at the Centro de Laseres Pulsados”. In: *High Power Laser Sci. Eng.* 7 (2019), e25. DOI: 10.1017/hpl.2019.10.

[Wag+15] F. Wagner et al. “Simultaneous observation of angularly separated laser-driven proton beams accelerated via two different mechanisms”. In: *Physics of Plasmas* 22.6 (2015), p. 063110. DOI: 10.1063/1.4922661.

[Wag+16] F. Wagner et al. “Maximum proton energy above 85 MeV from the relativistic interaction of laser pulses with micrometer thick CH2 targets”. In: *Physical Review Letters* 116 (2016), p. 205002.

[WM05] C. G. Wahl and J. G. McLean. “Response of CR-39 to medium energy electron irradiation”. In: *Radiation Measurements* 40.1 (2005), pp. 43 –49. ISSN: 1350-4487. DOI: 10.1016/j.radmeas.2004.12.003. URL: http://www.sciencedirect.com/science/article/pii/S1350448704002598.

[Wan+14] W. W. Wang et al. *Proton radiography of magnetic field produced by ultra-intense laser irradiating capacity-coil target*. 2014. arXiv: 1411.5933.

[Web+17] S. Weber et al. “P3: An installation for high-energy density plasma physics and ultra-high intensity laser–matter interaction at ELI-Beamlines”. In: *Matter and Radiation at Extremes* 2.4 (2017), pp. 149 –176. ISSN: 2468-080X. DOI: 10.1016/j.mre.2017.03.003. URL: http://www.sciencedirect.com/science/article/pii/S2468080X17300171.

[Wei+20] K. Weichman et al. *Generation of focusing ion beams by magnetized electron sheath acceleration*. 2020. arXiv: 2001.06117.

[Wen+18] S. M. Weng et al. “Optimization of hole-boring radiation pressure acceleration of ion beams for fusion ignition”. In: *Matter and Radiation at Extremes* 3.1 (2018), pp. 28–39. DOI: 10.1016/j.mre.2017.09.002. eprint: https://aip.scitation.org/doi/pdf/10.1016/j.mre.2017.09.002. URL: https://aip.scitation.org/doi/abs/10.1016/j.mre.2017.09.002.

[Whi+89] D. .R. White et al. *Tissue Substitutes in Radiation Dosimetry and Measurement*. 44th ed. Journal of the International Commission on Radiation Units and Measurements. ICRU. 1989. DOI: 10.1093/jicru/os23.1.Report44. URL: http://physics.nist.gov/PhysRefData/.

[Wil+02] I. Wilke et al. “Single-Shot Electron-Beam Bunch Length Measurements”. In: *Phys. Rev. Lett.* 88 (12 2002), p. 124801. DOI: 10.1103/PhysRevLett.88.124801. URL: https://link.aps.org/doi/10.1103/PhysRevLett.88.124801.

[Wil+92] S. C. Wilks et al. “Absorption of ultra-intense laser pulses”. In: *Phys. Rev. Lett.* 69 (9 1992), pp. 1383–1386. DOI: 10.1103/PhysRevLett.69.1383. URL: https://link.aps.org/doi/10.1103/PhysRevLett.69.1383.

[Wil+01] S. C. Wilks et al. “Energetic proton generation in ultra-intense laser-solid interactions”. In: *Physics of Plasmas* 8 (2001), p. 542.

[Wil+20] G. J. Williams et al. “Laser intensity scaling of the magnetic field from a laser-driven coil target”. In: *Journal of Applied Physics* 127.8 (2020), p. 083302. DOI: 10.1063/1.5117162.

[WM11] M. Williams and P. Metcalfe. “Radiochromic film dosimetry and its applications in radiotherapy”. In: *AIP Conference Proceedings*. Ed. by AIP. Vol. 1345. 2011, pp. 75–99.

[Wil+06] L. Willingale et al. “Collimated Multi-MeV Ion Beams from High-Intensity Laser Interactions with Underdense Plasma”. In: *Phys. Rev. Lett.* 96 (24 June 2006), p. 245002. DOI: 10.1103/PhysRevLett.96.245002.

[Wil+09] L. Willingale et al. “Characterization of High-Intensity Laser Propagation in the Relativistic Transparent Regime through Measurements of Energetic Proton Beams”. In: *Phys. Rev. Lett.* 102 (12 Mar. 2009), p. 125002. DOI: 10.1103/PhysRevLett.102.125002.

[WT73] N. K. Winsor and D. A. Tidman. “Laser Target Model”. In: *Phys. Rev. Lett.* 31 (17 1973), pp. 1044–1046. DOI: 10.1103/PhysRevLett.31.1044. URL: https://link.aps.org/doi/10.1103/PhysRevLett.31.1044.

[Wor14] A. Worley. *TASTRAK Material Safety Data Sheet MSDS-070314-1 (Revision 12)*. Tech. rep. Napier House Meadow Grove Shirehampton Bristol BS11 9PJ: Track Analysis Systems Ltd, 2014.

[Wur+16] G. A. Wurden et al. “Magneto-Inertial Fusion”. In: *J Fusion Energ* 35 (2016), pp. 69–77. DOI: 10.1007/s10894-015-0038-x.

[YOM92] T. Yamauchi, K. Oda, and H. Miyake. “An evaluation of the radical life-time in CR-39 track detectors outgassed under vacuum”. In: *International Journal of Radiation Applications and Instrumentation. Part D. Nuclear Tracks and Radiation Measurements* 20.4 (1992), pp. 615–617. ISSN: 1359-0189. DOI: 10.1016/1359-0189(92)90015-N. URL: http://www.sciencedirect.com/science/article/pii/135901899290015N.

[YF13] R. Yasuhara and H. Furuse. “Thermally induced depolarization in TGG ceramics”. In: *Opt. Lett.* 38.10 (2013), pp. 1751–1753. DOI: 10.1364/OL.38.001751. URL: http://ol.osa.org/abstract.cfm?URI=ol-38-10-1751.

[Yas+13] R. Yasuhara et al. “Temperature dependence of thermo-optic effects of single-crystal and ceramic TGG”. In: *Opt. Express* 21.25 (2013), pp. 31443–31452. DOI: 10.1364/OE.21.031443. URL: http://www.opticsexpress.org/abstract.cfm?URI=oe-21-25-31443.

[Yin+06] L. Yin et al. “GeV laser ion acceleration from ultrathin targets: The laser break-out afterburner”. In: *Laser and Particle Beams* 24.2 (2006), pp. 291–298. DOI: 10.1017/S0263034606060459.

[Yin+11] L. Yin et al. “Break-out afterburner ion acceleration in the longer laser pulse length regime”. In: *Physics of Plasmas* 18.6 (2011), p. 063103. DOI: 10.1063/1.3596555.

[You58] D. A. Young. “Etching of radiation damage in lithium fluoride”. In: *Nature* 182.4632 (1958), pp. 375—377. ISSN: 0028-0836. DOI: 10.1038/182375a0.

[Yun+14] H. Yun et al. “Size- and Composition-Dependent Radio Frequency Magnetic Permeability of Iron Oxide Nanocrystals”. In: *ACS Nano* 8.12 (2014). PMID: 25390073, pp. 12323–12337. DOI: 10.1021/nn504711g.

[ZS+17] A. Zaras-Szydlowska et al. “Complex interferometry application forspontaneous magnetic field determination in laser-produced plasma”. In: *44th EPS Conference on Plasma Physics*. P5.214. 2017. URL: http://ocs.ciemat.es/EPS2017PAP/pdf/P5.214.pdf.

[Zei+13] K. Zeil et al. “Dose-controlled irradiation of cancer cells with laser-accelerated proton pulses”. In: *Appl. Phys.* B.110 (2013), pp. 437–444. DOI: 10.1007/s00340-012-5275-3.

[Zha+19] Y. Zhang et al. “Energy calibration of a CR-39 nuclear-track detector irradiated by charged particles”. In: *NUCL SCI TECH* 30 (2019), p. 87.

[Zhu+18] B. Zhu et al. “Ultrafast pulsed magnetic fields generated by a femtosecond laser”. In: *Applied Physics Letters* 113.7 (2018), p. 072405. DOI: 10.1063/1.5038047.

[Zie] J. F. Ziegler. *Stopping of Ions in Matter*. URL: http://srim.org/.

[Zie99] J. F. Ziegler. “The Stopping of Energetic Light Ions in Elemental Matter”. In: *Rev. Appl. Phys.* 85 (1999), pp. 1249–1272.

[ZBZ13] J. F. Ziegler, J. P. Biersack, and M. D. Ziegler. *SRIM - The Stopping and Range of Ions in Matter*. Ed. by Ziegler. Morrisville, NC, USA: Lulu Press Co., 2013. ISBN: 0-9654207-1-X.

8 Annex

8.1 Additional Material

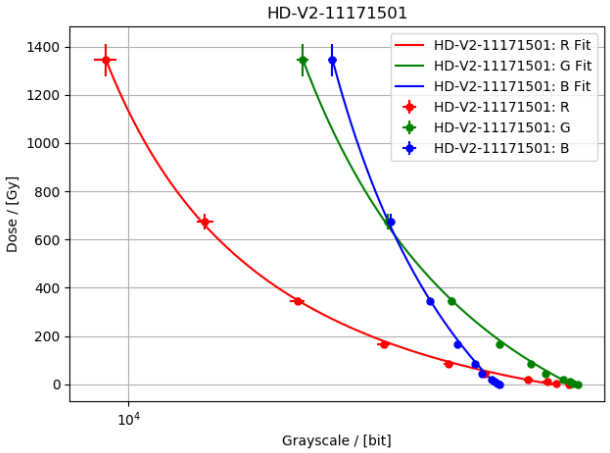

(a) data and fit for all channels

```
HD-V2-11171501 Ch:R
 A = -38360.0 +/- 2690.0
 c = -184.2 +/- 10.5
 g_0 = 43000.0 +/- 2700.0

HD-V2-11171501 Ch:G
 A = -38200.0 +/- 3310.0
 c = -511.7 +/- 29.5
 g_0 = 45910.0 +/- 3350.0

HD-V2-11171501 Ch:B
 A = -25060.0 +/- 2970.0
 c = -870.5 +/- 62.4
 g_0 = 35410.0 +/- 3040.0
```

(b) fit reports for all colour channels

Figure 8.1: Fit of the dose response model proposed by the manufacturer, performed to calibration data for HD-V2 batch number 11171501 for the LIGHT experiment from Paul Neumayer and Abel Blazevic (affiliated to GSI).

	Simulations employing different charge distribution with integral charges of:							
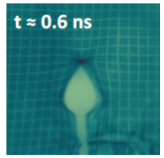  RCF data where B-dot-probe show 129 kA, compared to synthetic RCF with $Q = 0\,\mathrm{nC}$, $I = 21\,\mathrm{kA}$.	−5 nC	−10 nC	−15 nC	−20 nC	−25 nC	−30 nC	−35 nC	−40 nC
Spherical Charge Distribution in the Coil Center	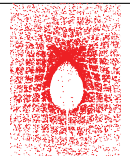 (a) 28 kA	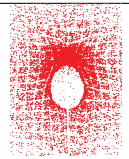 (b) 36 kA	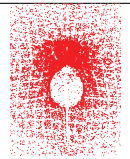 (c) 46 kA	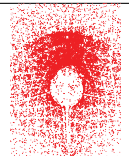 (d) 58 kA	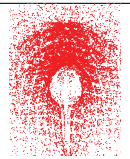 (e) 70 kA	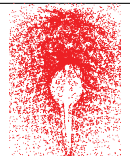 (f) 84 kA	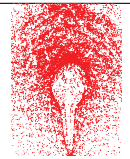 (g) 101 kA	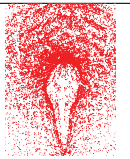 (h) 118 kA
Spherical Charge Distribution between Coil Legs at 250 µm under the coil center	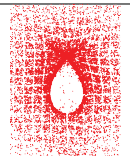 (i) 33 kA	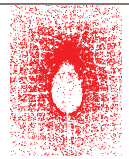 (j) 48 kA	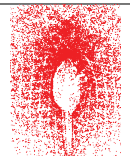 (k) 67 kA	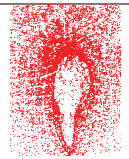 (l) 85 kA	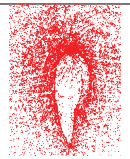 (m) 105 kA	 (n) 130 kA	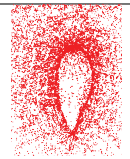 (o) 148 kA	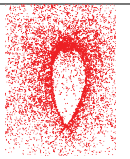 (p) 173 kA
Toroidal Charge Distribution with a main-radius of 275 µm and small-radius of 35 µm oriented in superposition with the coil wire	 (q) 33 kA	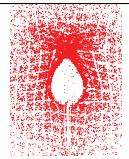 (r) 48 kA	 (s) 67 kA	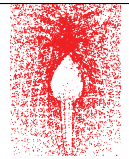 (t) 85 kA	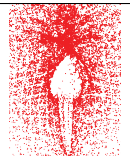 (u) 105 kA	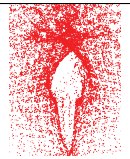 (v) 130 kA	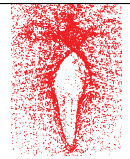 (w) 148 kA	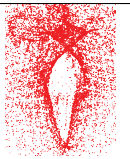 (x) 173 kA

Table 8.1: Screening by different types of charge distributions in the vicinity of the coil. Experimental data (a) of the bulb shaped imprint yields 3.48 mm width at $600 \cdot 10^{-3}$ ns and can be reproduced in synthetic deflectometry simulations (b) with B-field only or (c) – (z) by pairings of various possible charge distributions of integral charge Q and coil current I.

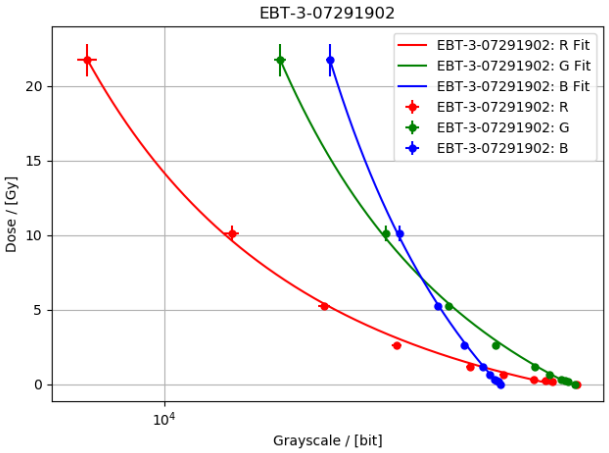

(a) data and fit for all channels

```
EBT-3-07291902 Ch:R
 A = -39620.0 +/- 4490.0
 c = -3.705 +/- 0.327
 g_0 = 41410.0 +/- 4500.0

EBT-3-07291902 Ch:G
 A = -39460.0 +/- 3340.0
 c = -8.138 +/- 0.46
 g_0 = 43980.0 +/- 3380.0

EBT-3-07291902 Ch:B
 A = -27110.0 +/- 1980.0
 c = -15.968 +/- 0.691
 g_0 = 33930.0 +/- 2030.0
```

(b) fit reports for all colour channels

Figure 8.2: Fit of the dose response model proposed by the manufacturer, performed to calibration data for EBT-3 batch number 07291902 for the LIGHT experiment from Paul Neumayer and Abel Blazevic (affiliated to GSI).

RCF			Composition / [atom %]							
Type	d_{RCF} / [µm]	ρ_{RCF} / [g/cm^3]	H	C	O	N	Li	Cl	Na	Others*
HD V2 [Por16b; Sei+15]										
Active	12	1.20	58.4	27.9	11.7	0.1	0.6	0.6	0.5	Al:0.3
Polyester	97	1.35	36.4	45.5	18.2					
MD V2-55 [Kir11; GMI12; Sei+15; Dev+16]										
Polyester	96	1.35	36.4	45.5	18.2					
Active	17.5	1.08	56.8	29.14	7.12	6.94				
Gelatin	0.75	1.30	6.8	50.5	25.5	17.0				
Adhesive	32	1.20	57.1	33.3	9.5					
Polyester	25	1.35	36.4	45.5	18.2					
Adhesive	32	1.20	57.1	33.3	9.5					
Gelatin	0.75	1.30	6.8	50.5	25.5	17.0				
Active	17.5	1.08	56.8	29.14	7.12	6.94				
Polyester	96	1.35	36.4	45.5	18.2					
MD V3 [Lew16; Dev+16]										
Polyester	125	1.35	36.4	45.5	18.2					
Active	10	1.20	58.4	27.9	11.7	0.1	0.6	0.6	0.5	Al:0.3
Polyester	125	1.35	36.4	45.5	18.2					
EBT [Dev+16; Lew10]										
Polyester	97	1.35	36.4	45.5	18.2					
Active	17	1.20	56.89	28.22	5.61	5.68	1.66	1.51		
Surface	6	1.20	53.3	22.5	11.1	12.7	0.2	0.2		
Active	17	1.20	56.89	28.22	5.61	5.68	1.66	1.51		
Polyester	97	1.35	36.4	45.5	18.2					
EBT 2 [Dev+16; Lew10]										
Polyester	50	1.35	36.4	45.5	18.2					
Adhesive	25	1.20	57.1	33.3	9.5					
Active	28 ± 3	1.20	58.33	29.61	10.79	0.06	0.82	0.19	0.11	S:0.03, Br:0.06
Polyester	175	1.35	36.4	45.5	18.2					
EBT 3 [Por16a; Dev+16]										
Polyester	125	1.35	36.4	45.5	18.2					
Active	28	1.20	58.33	29.61	10.79	0.06	0.82	0.19	0.11	S:0.03, Br:0.06
Polyester	125	1.35	36.4	45.5	18.2					
U EBT 3 [Ehr]										
Active	28	1.20	58.33	29.61	10.79	0.06	0.82	0.19	0.11	S:0.03, Br:0.06
Polyester	125	1.35	36.4	45.5	18.2					

Table 8.2: Atomic composition and geometry of GAFCHROMIC RCF films, for older batches or film types see [Das17; Kir11; Lew10; Gca]. Main constituents are H, Carbon, Oxygen, N, Lithium, Chlorine and Sodium. Compositions of layers are good faith estimates not taking into account errors due to moisture during production *etc.*, based on the manufacturer's identification of the constituents, without independent spectroscopic verification. Composition and thickness of individual layers may vary from batch-to-batch. (*) Only Films produced after November 2011 contain traces of Al, common are traces of Bromine and Sulphur.

8.2 SilverFast 8.8 Parameters

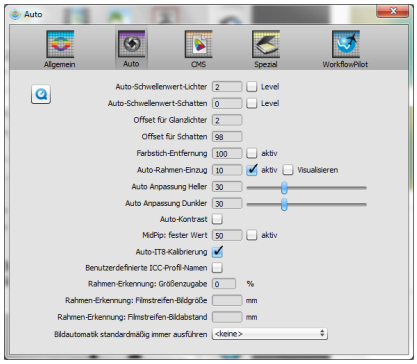

(a) Settings in tab 'Auto'

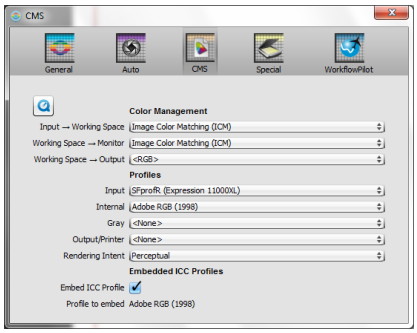

(b) Settings in tab 'CMS'

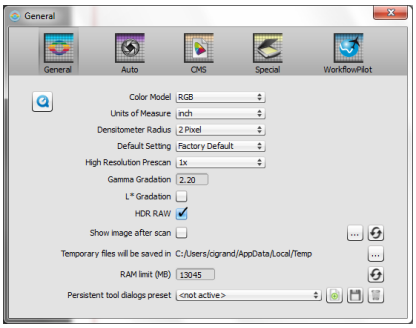

(c) Settings in tab 'General'

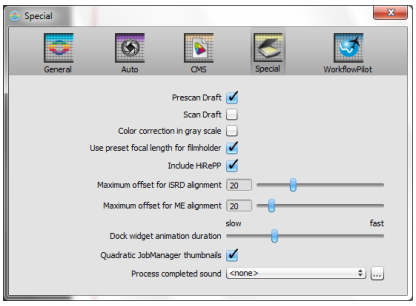

(d) Settings in tab 'Special'

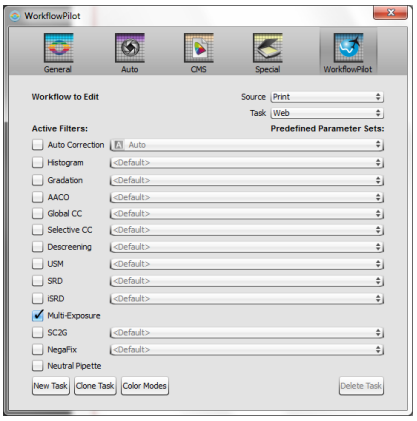

(e) Settings in tab 'WorkflowPilot'

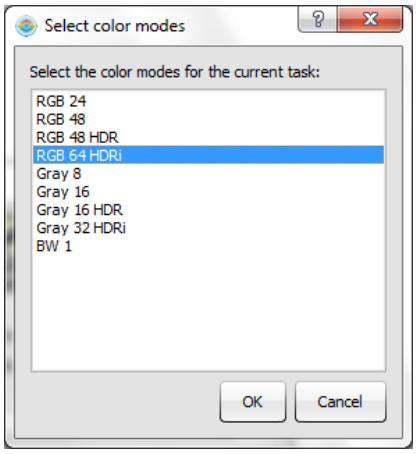

(f) Settings in tab 'SelectColor-Modes'

Figure 8.30: Settings and options for scans in SilverFast 8.8

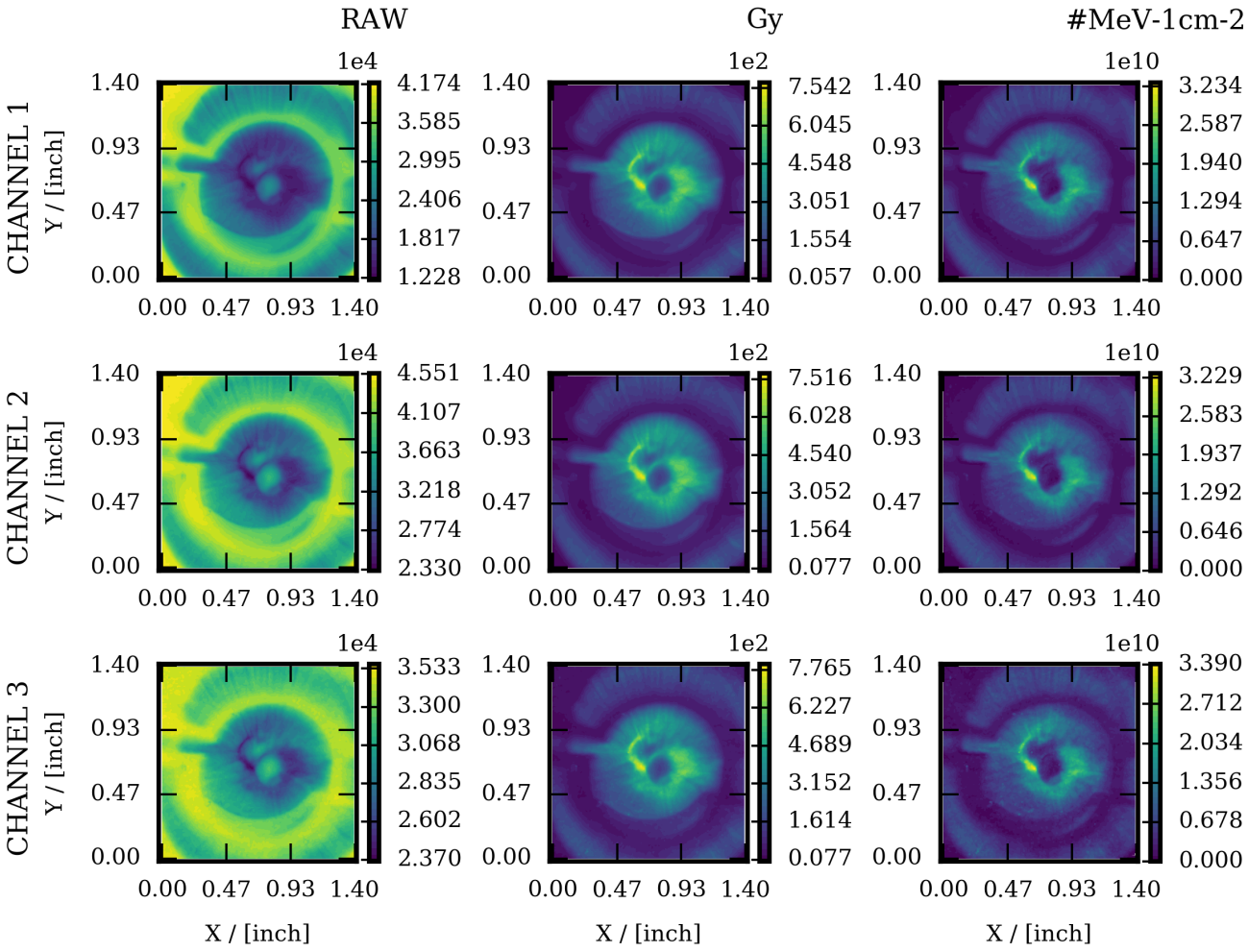

Figure 8.3: RCF layer 1 for $4.1(6)\,\mathrm{MeV}$ protons, from shot #61 with micro-compressor at the LIGHT experiment discussed in section 5.3.2.1. The first column shows the RAW data, the second the dose converted film and the third the pixel-wise deconvolution to proton number density per unit energy of $1\,\mathrm{MeV}$ as calculated with decon_RCF. The rows contain data from red, green and blue colour channel

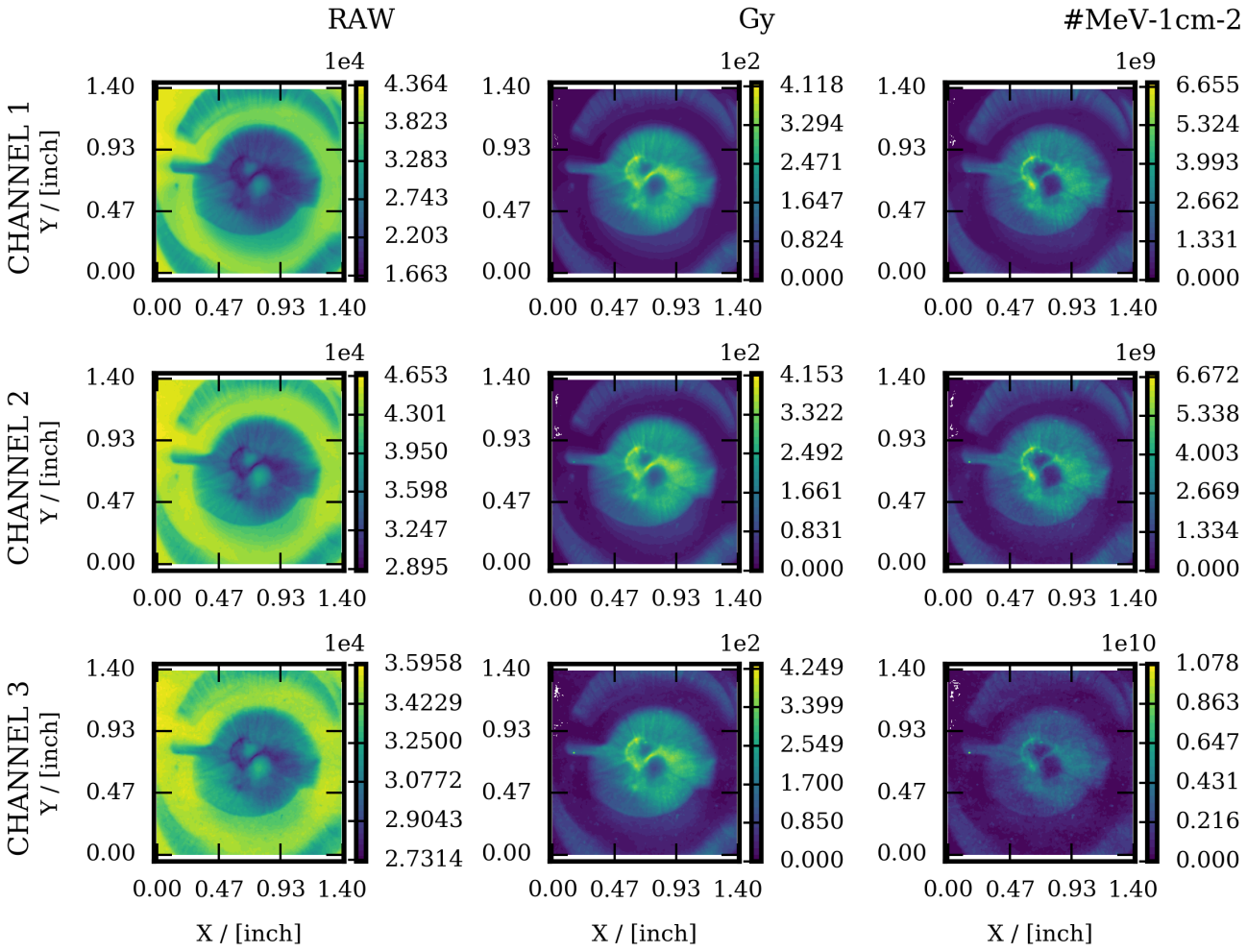

Figure 8.4: RCF layer 2 for $5.4(3)\,\mathrm{MeV}$ protons, from shot #61 with micro-compressor at the LIGHT experiment discussed in section 5.3.2.1. The first column shows the RAW data, the second the dose converted film and the third the pixel-wise deconvolution to proton number density per unit energy of $1\,\mathrm{MeV}$ as calculated with decon_RCF. The rows contain data from red, green and blue colour channel

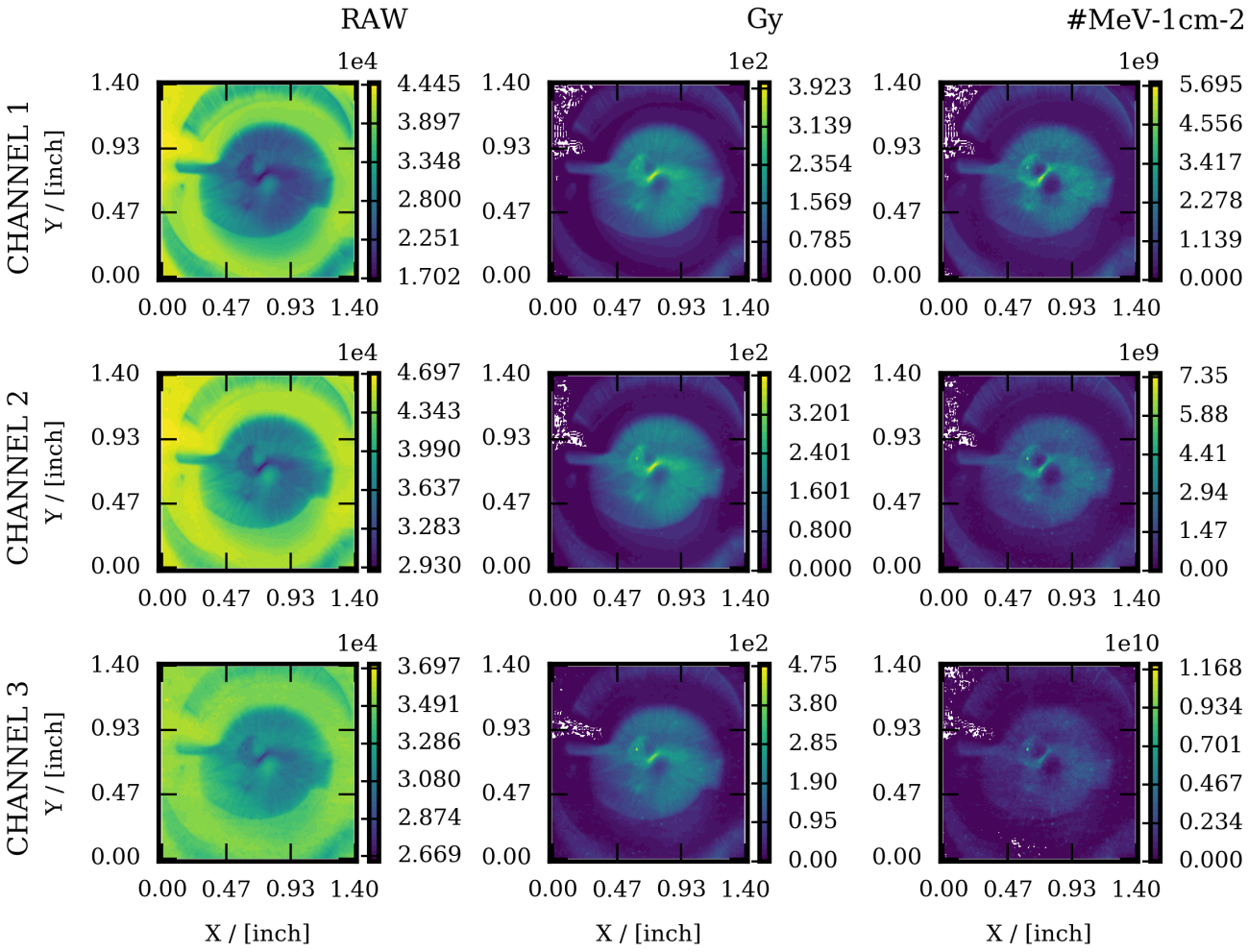

Figure 8.5: RCF layer 3 for $6.5(3)\,\mathrm{MeV}$ protons, from shot #61 with micro-compressor at the LIGHT experiment discussed in section 5.3.2.1. The first column shows the RAW data, the second the dose converted film and the third the pixel-wise deconvolution to proton number density per unit energy of $1\,\mathrm{MeV}$ as calculated with decon_RCF. The rows contain data from red, green and blue colour channel

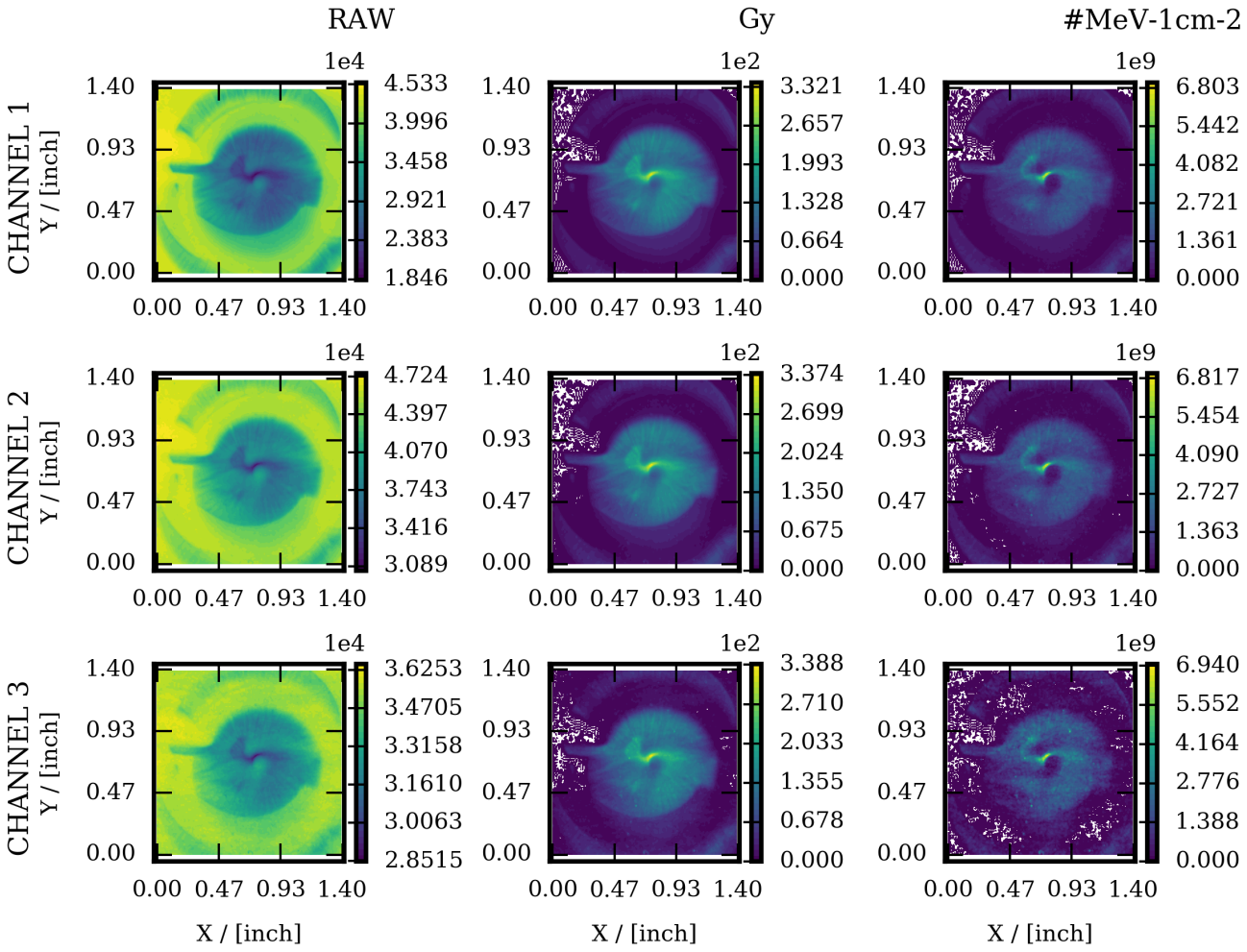

Figure 8.6: RCF layer 4 for $7.3(4)\,\mathrm{MeV}$ protons, from shot #61 with micro-compressor at the LIGHT experiment discussed in section 5.3.2.1. The first column shows the RAW data, the second the dose converted film and the third the pixel-wise deconvolution to proton number density per unit energy of $1\,\mathrm{MeV}$ as calculated with decon_RCF. The rows contain data from red, green and blue colour channel

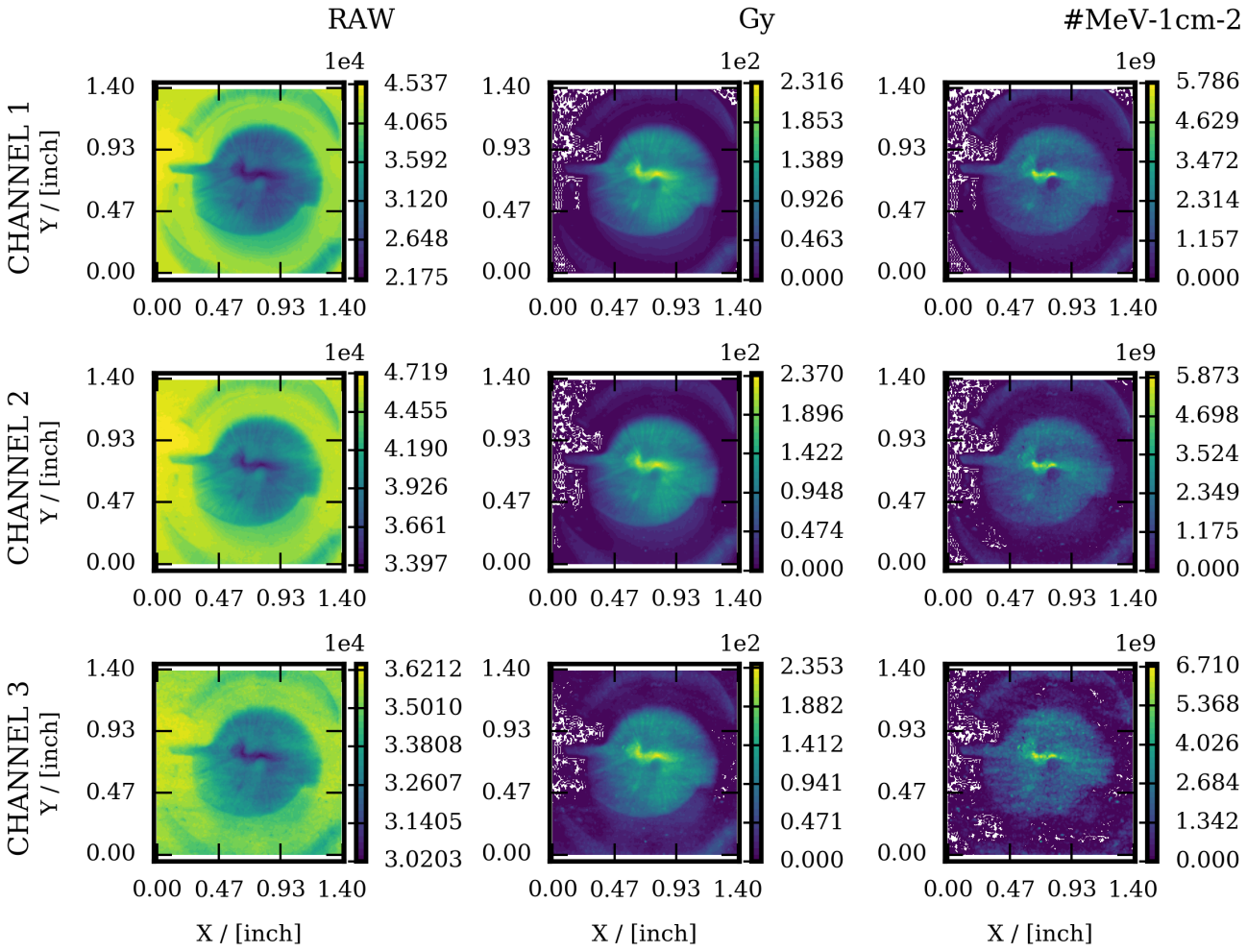

Figure 8.7: RCF layer 5 for $8.1(3)\,\mathrm{MeV}$ protons, from shot #61 with micro-compressor at the LIGHT experiment discussed in section 5.3.2.1. The first column shows the RAW data, the second the dose converted film and the third the pixel-wise deconvolution to proton number density per unit energy of $1\,\mathrm{MeV}$ as calculated with decon_RCF. The rows contain data from red, green and blue colour channel

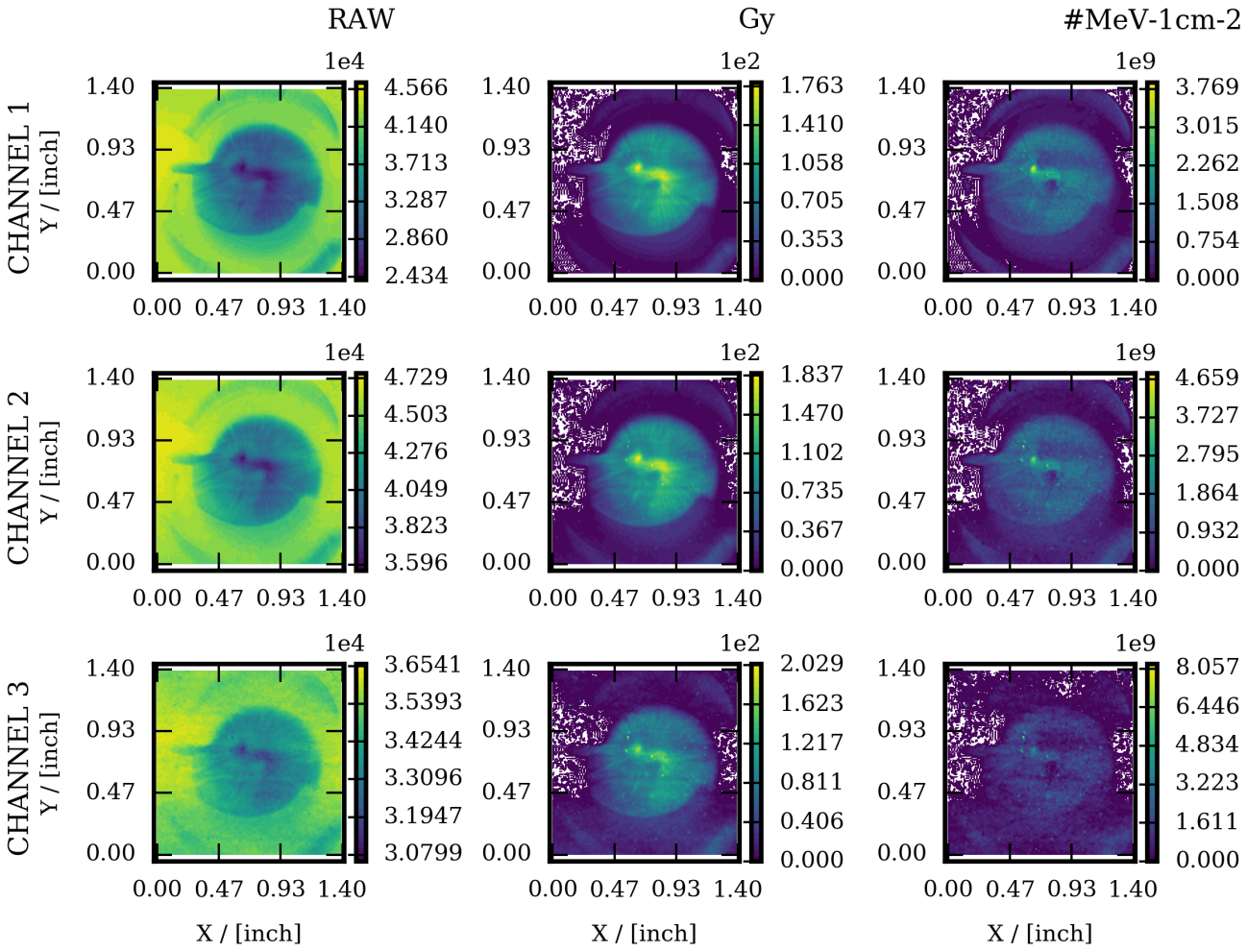

Figure 8.8: RCF layer 6 for $8.9(5)\,\mathrm{MeV}$ protons, from shot #61 with micro-compressor at the LIGHT experiment discussed in section 5.3.2.1. The first column shows the RAW data, the second the dose converted film and the third the pixel-wise deconvolution to proton number density per unit energy of $1\,\mathrm{MeV}$ as calculated with decon_RCF. The rows contain data from red, green and blue colour channel

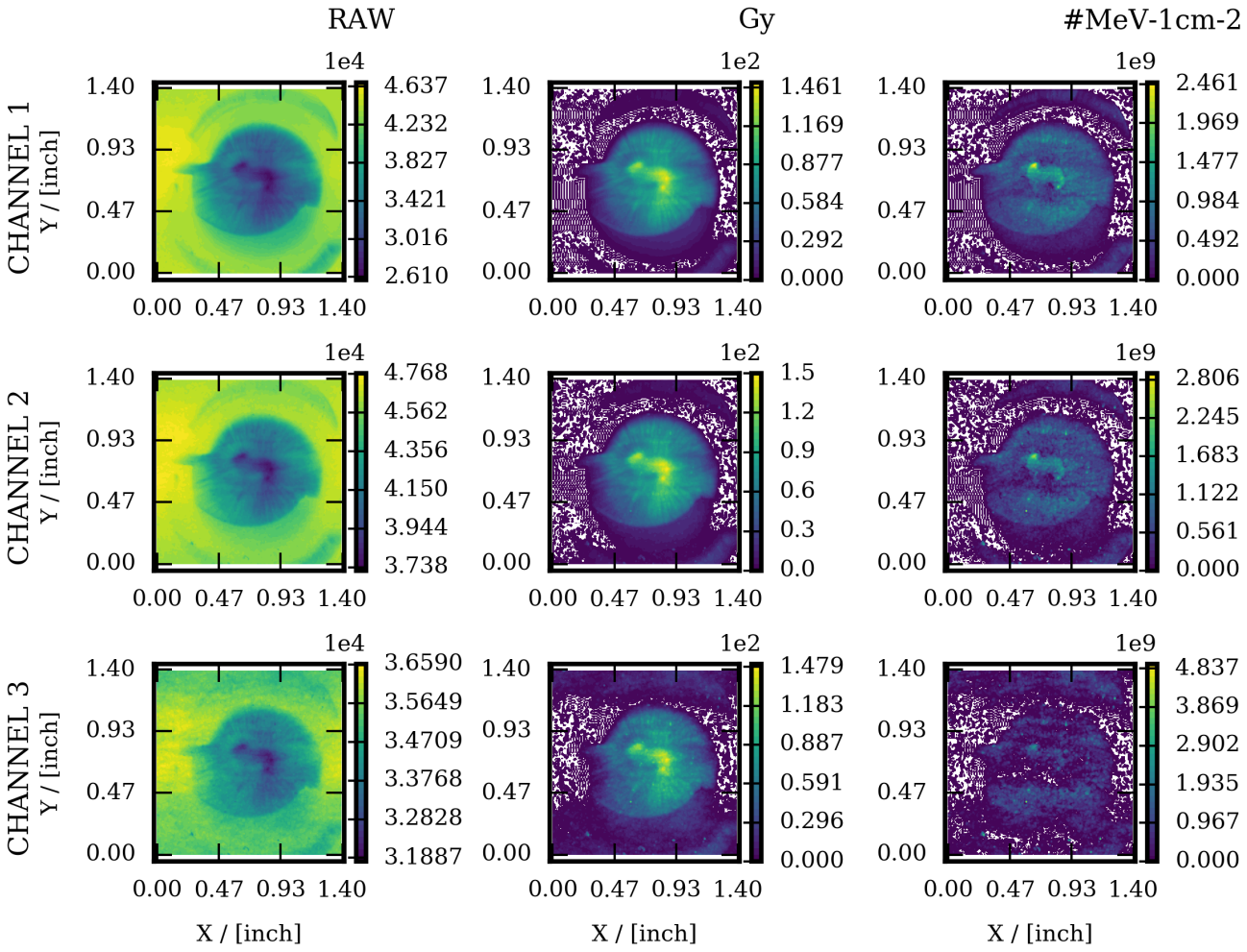

Figure 8.9: RCF layer 7 for $9.5(3)\,\mathrm{MeV}$ protons, from shot #61 with micro-compressor at the LIGHT experiment discussed in section 5.3.2.1. The first column shows the RAW data, the second the dose converted film and the third the pixel-wise deconvolution to proton number density per unit energy of $1\,\mathrm{MeV}$ as calculated with decon_RCF. The rows contain data from red, green and blue colour channel

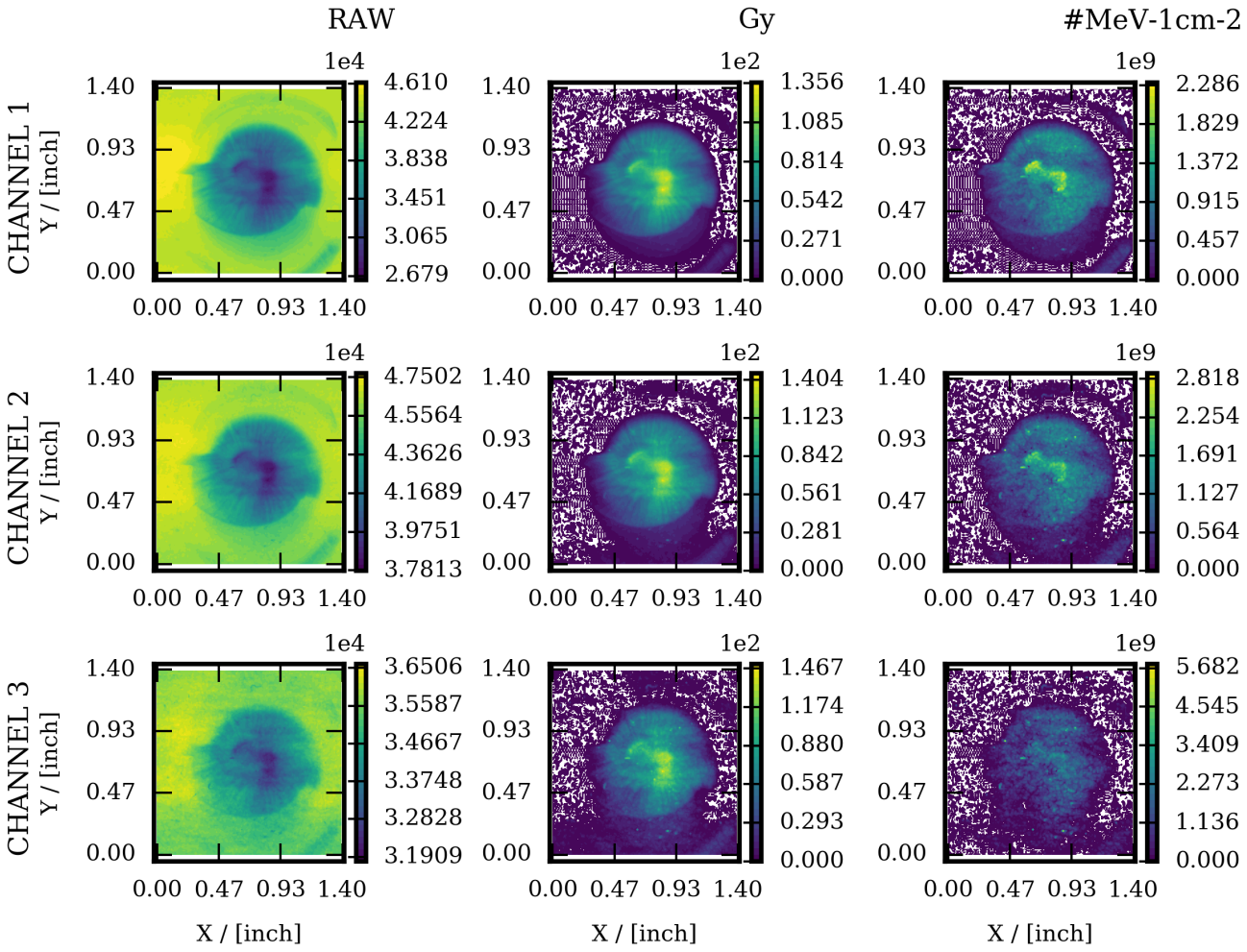

Figure 8.10: RCF layer 8 for $10.2(3)\,\mathrm{MeV}$ protons, from shot #61 with micro-compressor at the LIGHT experiment discussed in section 5.3.2.1. The first column shows the RAW data, the second the dose converted film and the third the pixel-wise deconvolution to proton number density per unit energy of $1\,\mathrm{MeV}$ as calculated with decon_RCF. The rows contain data from red, green and blue colour channel

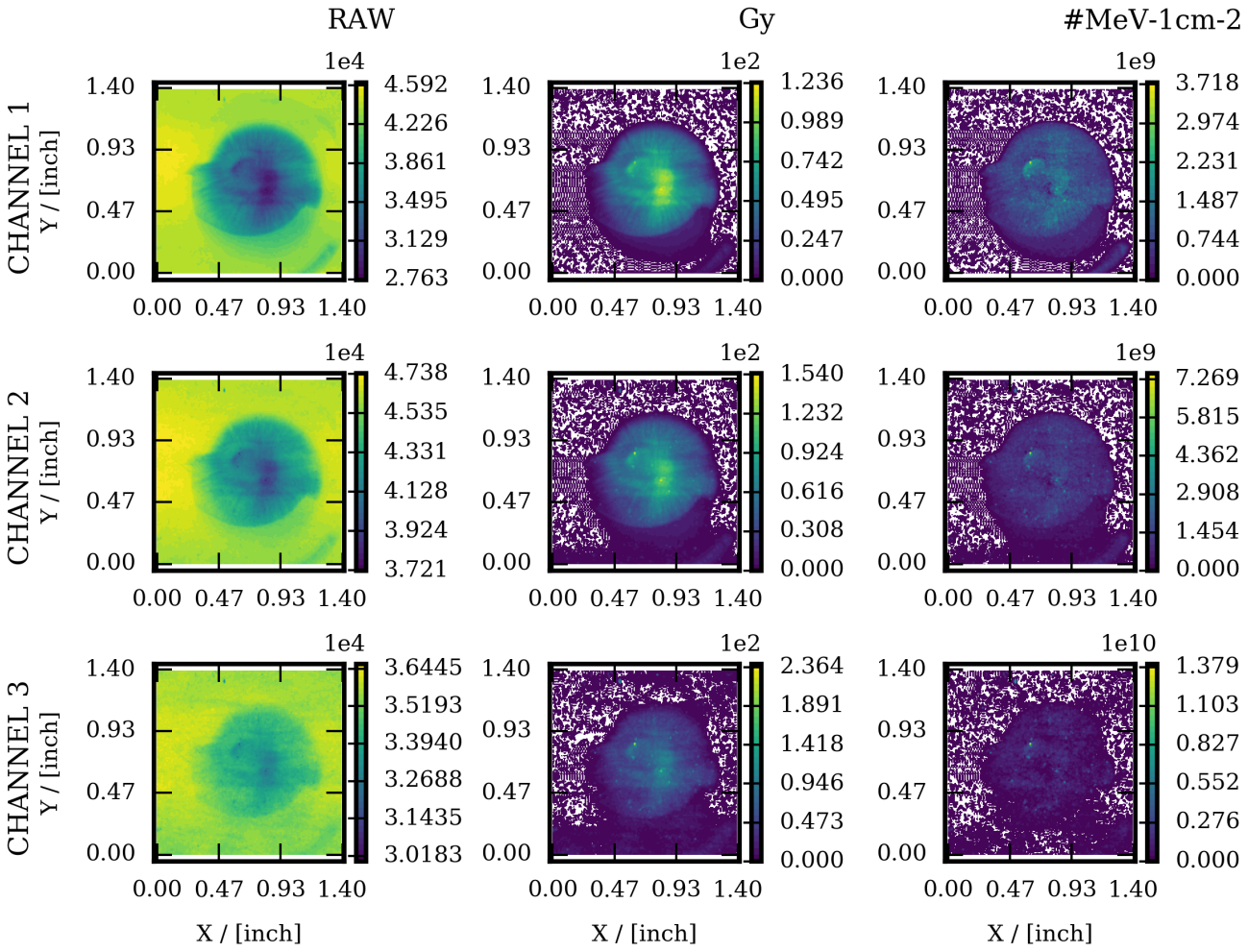

Figure 8.11: RCF layer 9 for $10.8(4)\,\mathrm{MeV}$ protons, from shot #61 with micro-compressor at the LIGHT experiment discussed in section 5.3.2.1. The first column shows the RAW data, the second the dose converted film and the third the pixel-wise deconvolution to proton number density per unit energy of $1\,\mathrm{MeV}$ as calculated with decon_RCF. The rows contain data from red, green and blue colour channel

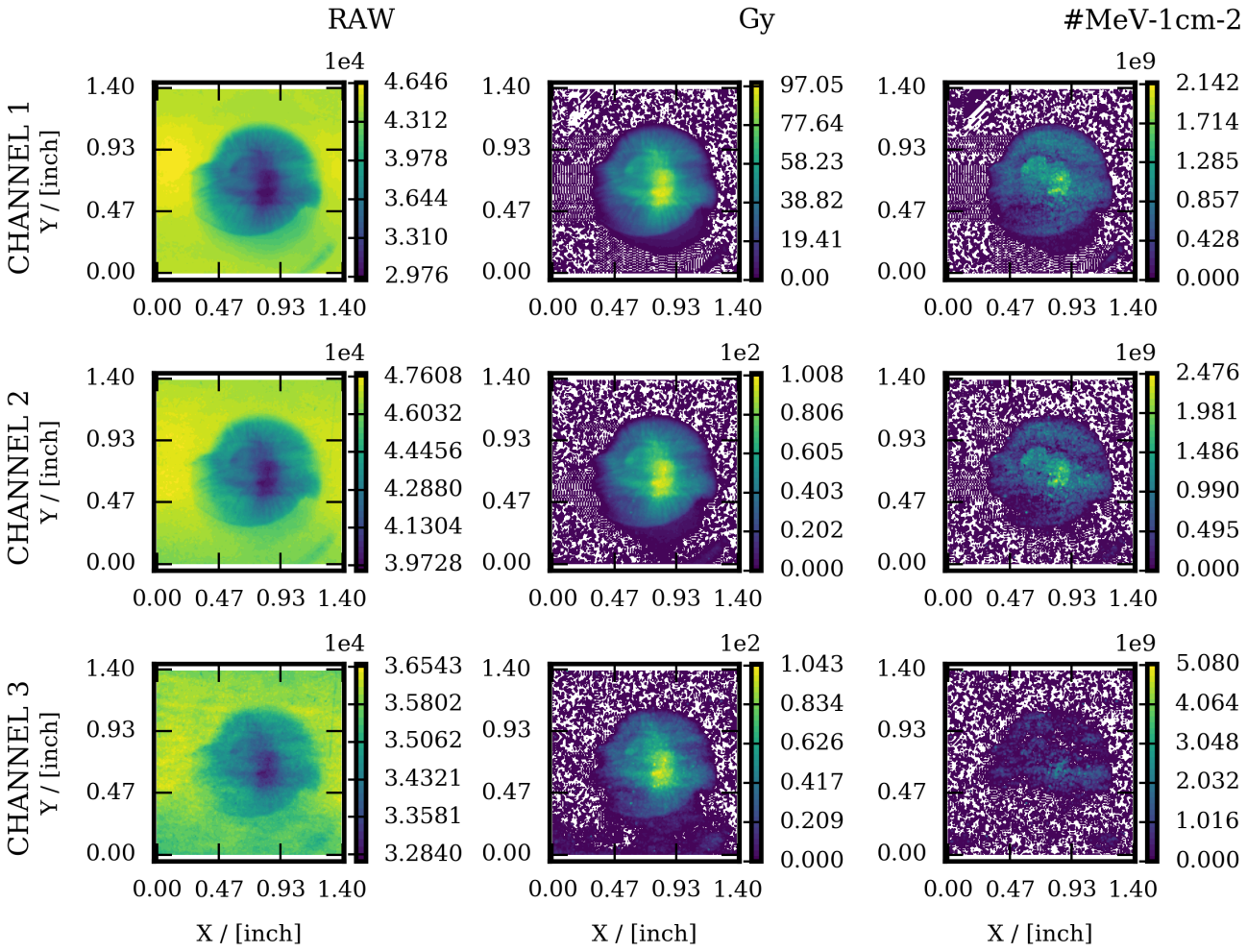

Figure 8.12: RCF layer 10 for $11.3(4)\,\mathrm{MeV}$ protons, from shot #61 with micro-compressor at the LIGHT experiment discussed in section 5.3.2.1. The first column shows the RAW data, the second the dose converted film and the third the pixel-wise deconvolution to proton number density per unit energy of $1\,\mathrm{MeV}$ as calculated with decon_RCF. The rows contain data from red, green and blue colour channel

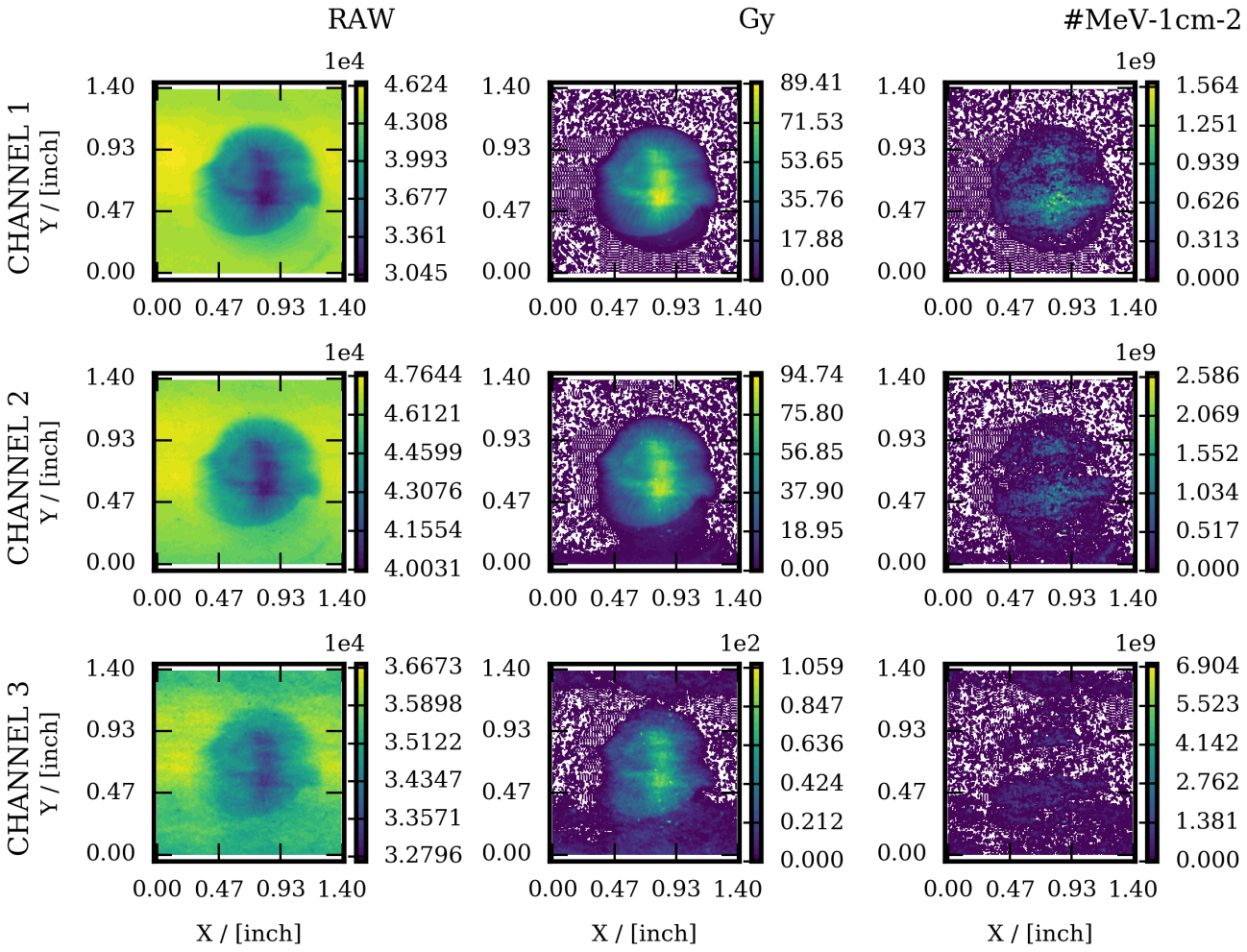

Figure 8.13: RCF layer 11 for $11.9(5)\,\mathrm{MeV}$ protons, from shot #61 with micro-compressor at the LIGHT experiment discussed in section 5.3.2.1. The first column shows the RAW data, the second the dose converted film and the third the pixel-wise deconvolution to proton number density per unit energy of $1\,\mathrm{MeV}$ as calculated with decon_RCF. The rows contain data from red, green and blue colour channel

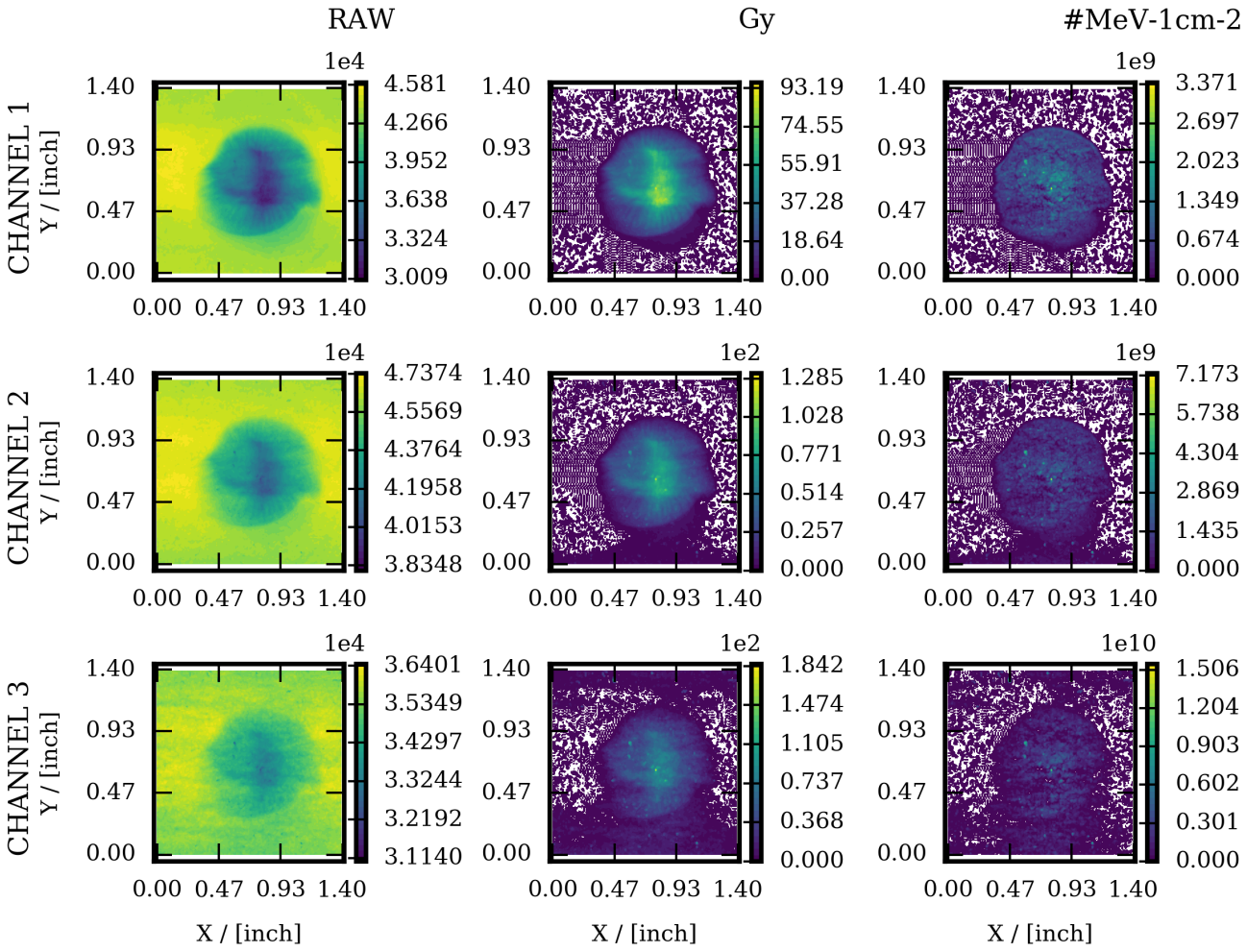

Figure 8.14: RCF layer 12 for $12.5(5)\,\mathrm{MeV}$ protons, from shot #61 with micro-compressor at the LIGHT experiment discussed in section 5.3.2.1. The first column shows the RAW data, the second the dose converted film and the third the pixel-wise deconvolution to proton number density per unit energy of $1\,\mathrm{MeV}$ as calculated with decon_RCF. The rows contain data from red, green and blue colour channel

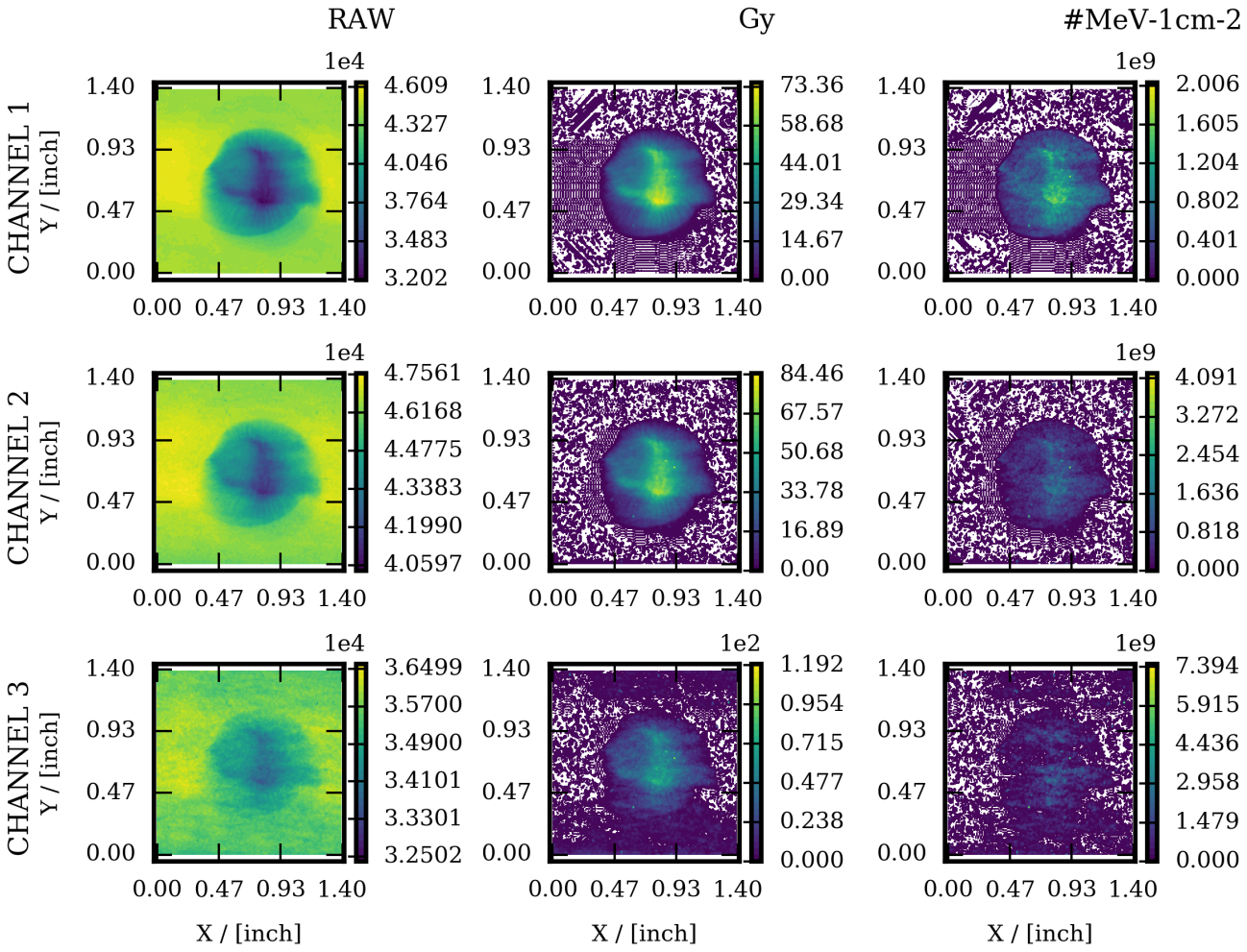

Figure 8.15: RCF layer 13 for $13.0(5)\,\mathrm{MeV}$ protons, from shot #61 with micro-compressor at the LIGHT experiment discussed in section 5.3.2.1. The first column shows the RAW data, the second the dose converted film and the third the pixel-wise deconvolution to proton number density per unit energy of $1\,\mathrm{MeV}$ as calculated with decon_RCF. The rows contain data from red, green and blue colour channel

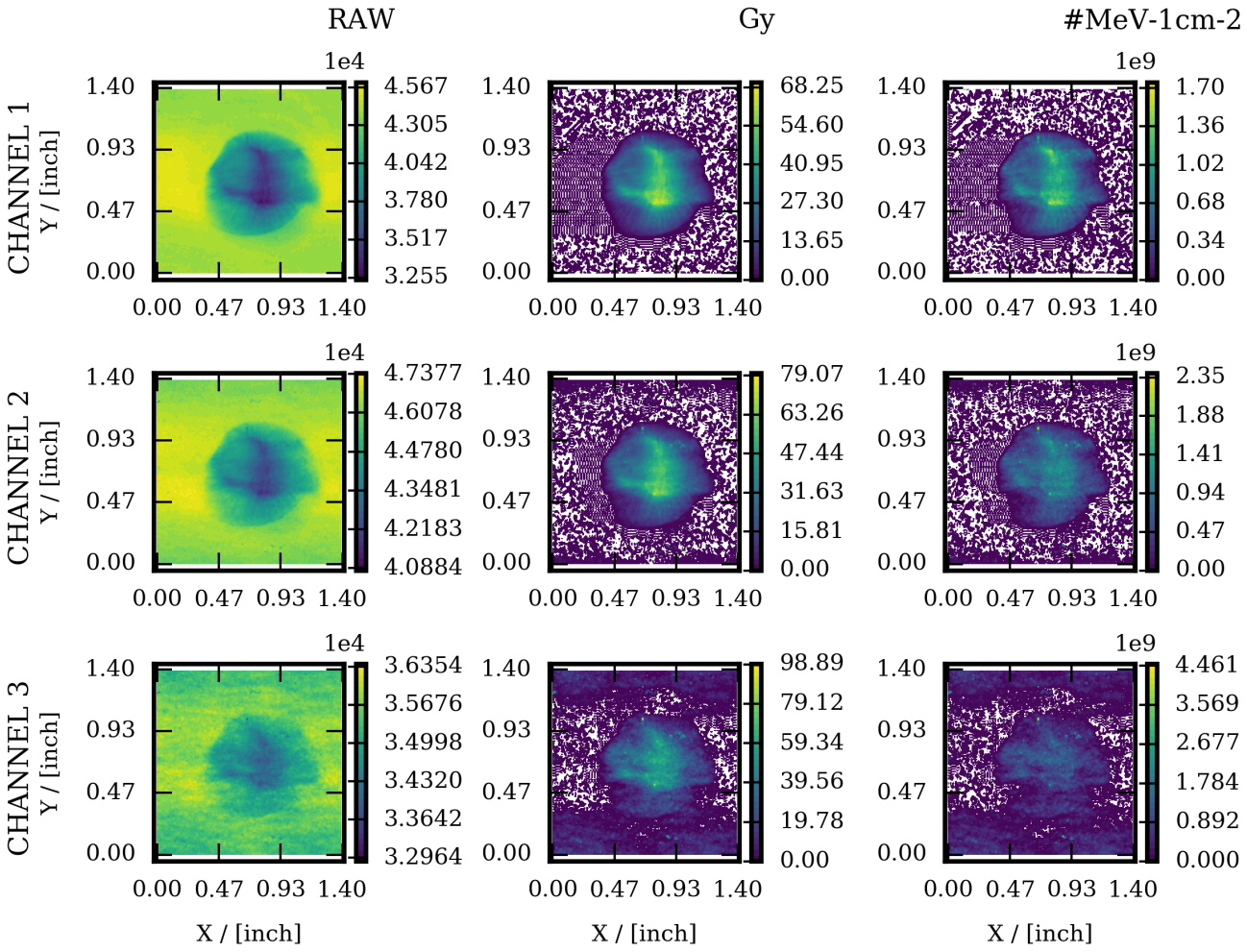

Figure 8.16: RCF layer 14 for $13.5(5)\,\mathrm{MeV}$ protons, from shot #61 with micro-compressor at the LIGHT experiment discussed in section 5.3.2.1. The first column shows the RAW data, the second the dose converted film and the third the pixel-wise deconvolution to proton number density per unit energy of $1\,\mathrm{MeV}$ as calculated with decon_RCF. The rows contain data from red, green and blue colour channel

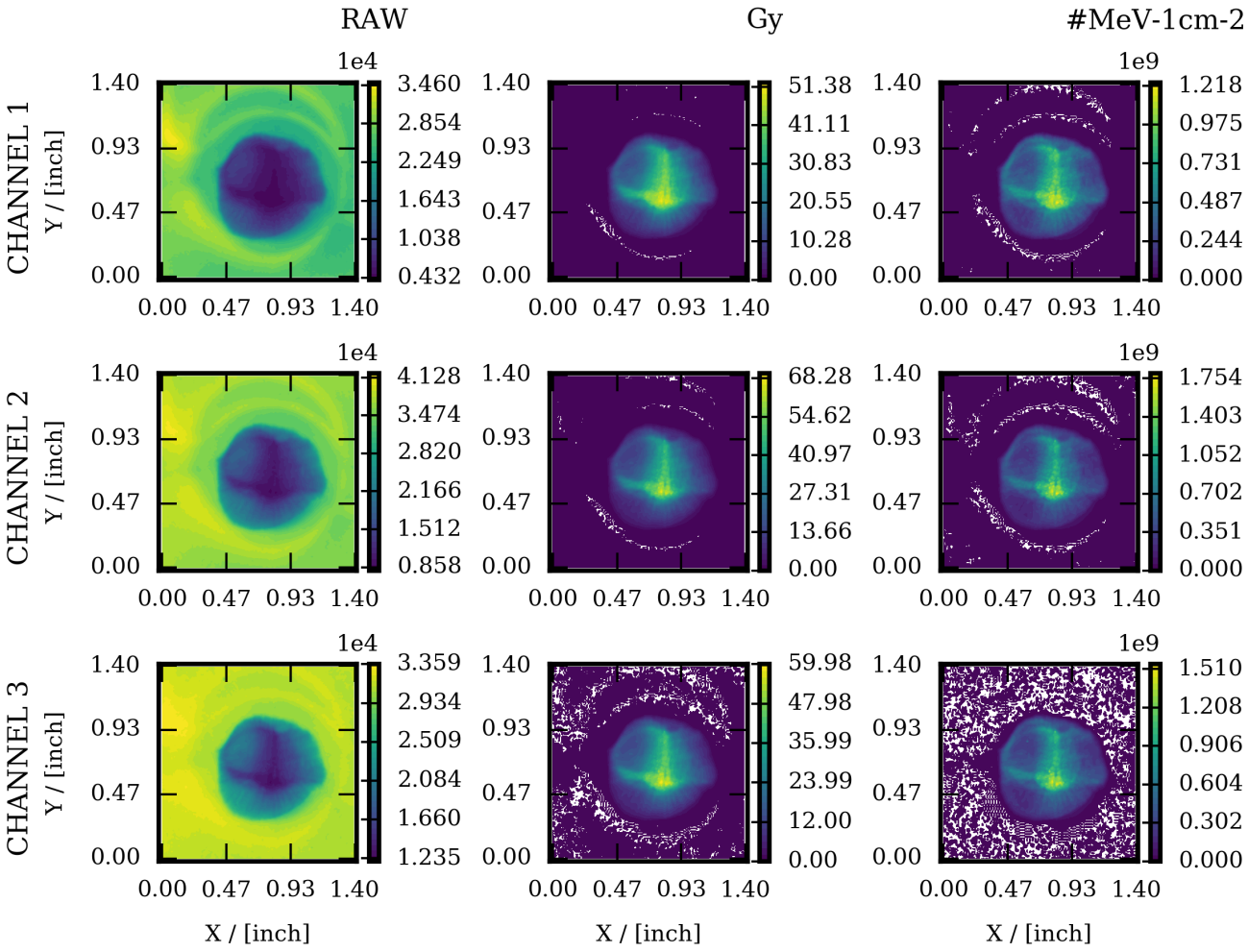

Figure 8.17: RCF layer 15 for $14.6(5)\,\mathrm{MeV}$ protons, from shot #61 with micro-compressor at the LIGHT experiment discussed in section 5.3.2.1. The first column shows the RAW data, the second the dose converted film and the third the pixel-wise deconvolution to proton number density per unit energy of $1\,\mathrm{MeV}$ as calculated with decon_RCF. The rows contain data from red, green and blue colour channel

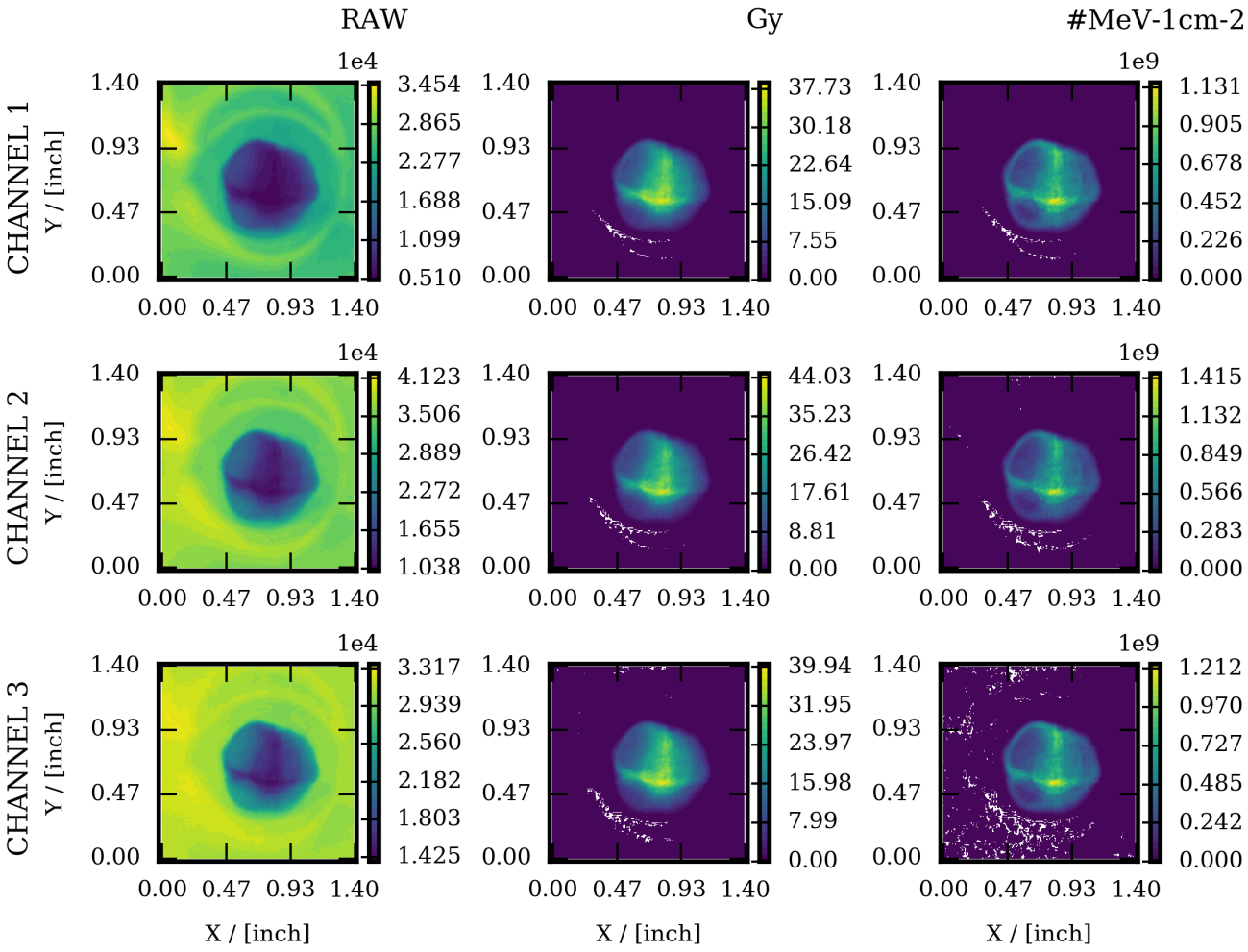

Figure 8.18: RCF layer 16 for $15.8(5)\,\mathrm{MeV}$ protons, from shot #61 with micro-compressor at the LIGHT experiment discussed in section 5.3.2.1. The first column shows the RAW data, the second the dose converted film and the third the pixel-wise deconvolution to proton number density per unit energy of $1\,\mathrm{MeV}$ as calculated with decon_RCF. The rows contain data from red, green and blue colour channel

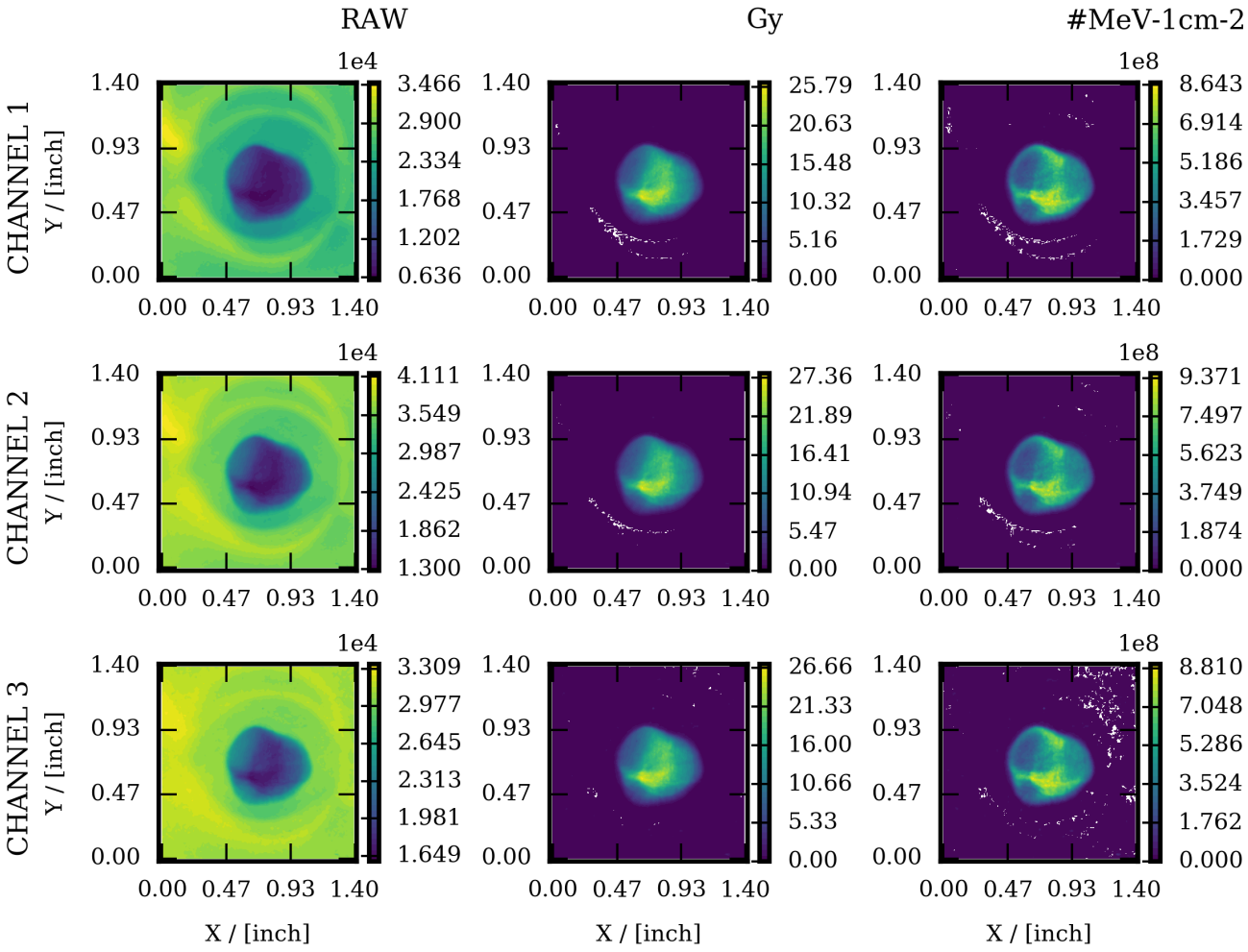

Figure 8.19: RCF layer 17 for $16.9(5)\,\mathrm{MeV}$ protons, from shot #61 with micro-compressor at the LIGHT experiment discussed in section 5.3.2.1. The first column shows the RAW data, the second the dose converted film and the third the pixel-wise deconvolution to proton number density per unit energy of $1\,\mathrm{MeV}$ as calculated with decon_RCF. The rows contain data from red, green and blue colour channel

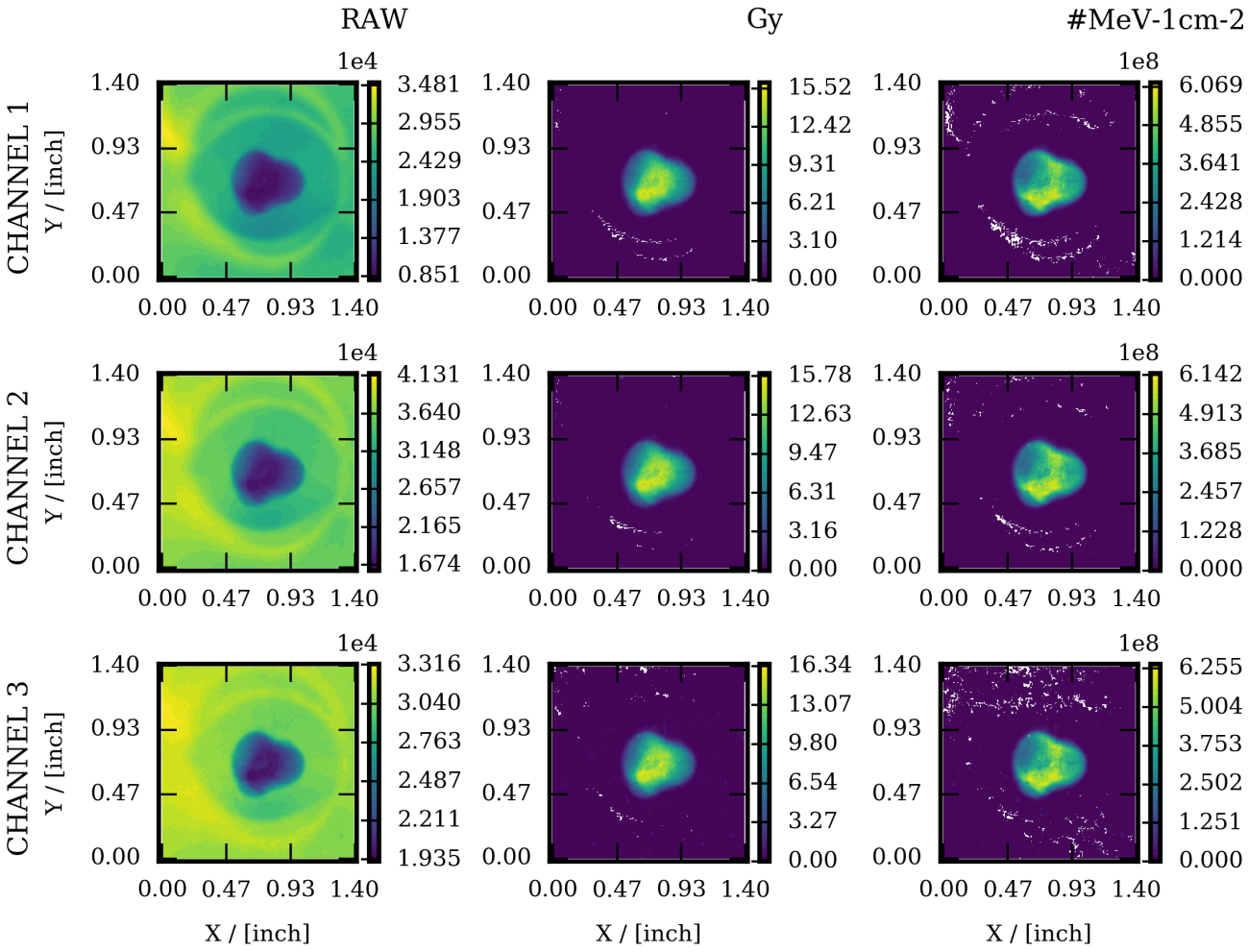

Figure 8.20: RCF layer 18 for $17.9(5)\,\mathrm{MeV}$ protons, from shot #61 with micro-compressor at the LIGHT experiment discussed in section 5.3.2.1. The first column shows the RAW data, the second the dose converted film and the third the pixel-wise deconvolution to proton number density per unit energy of $1\,\mathrm{MeV}$ as calculated with decon_RCF. The rows contain data from red, green and blue colour channel

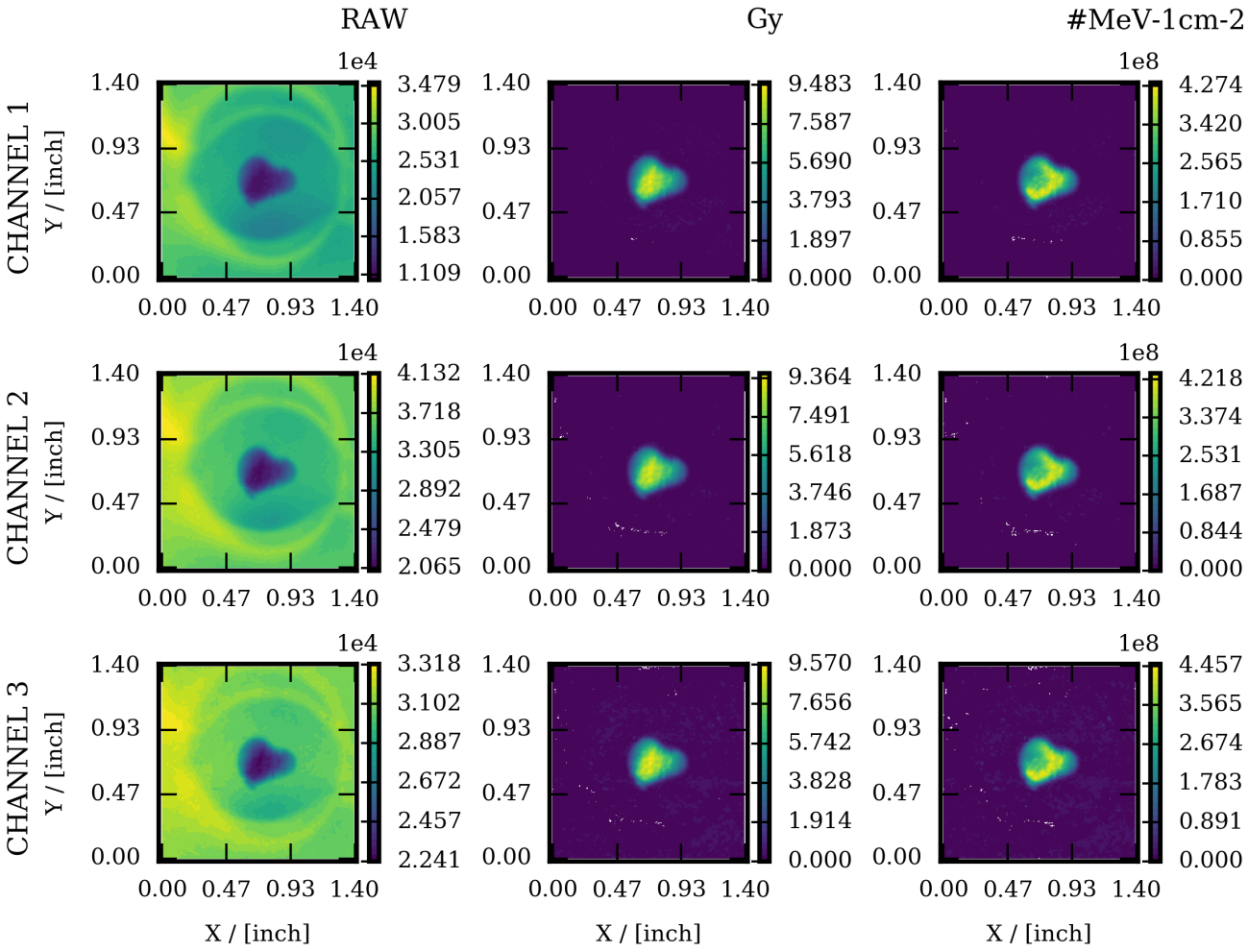

Figure 8.21: RCF layer 19 for $18.9(5)\,\mathrm{MeV}$ protons, from shot #61 with micro-compressor at the LIGHT experiment discussed in section 5.3.2.1. The first column shows the RAW data, the second the dose converted film and the third the pixel-wise deconvolution to proton number density per unit energy of $1\,\mathrm{MeV}$ as calculated with decon_RCF. The rows contain data from red, green and blue colour channel

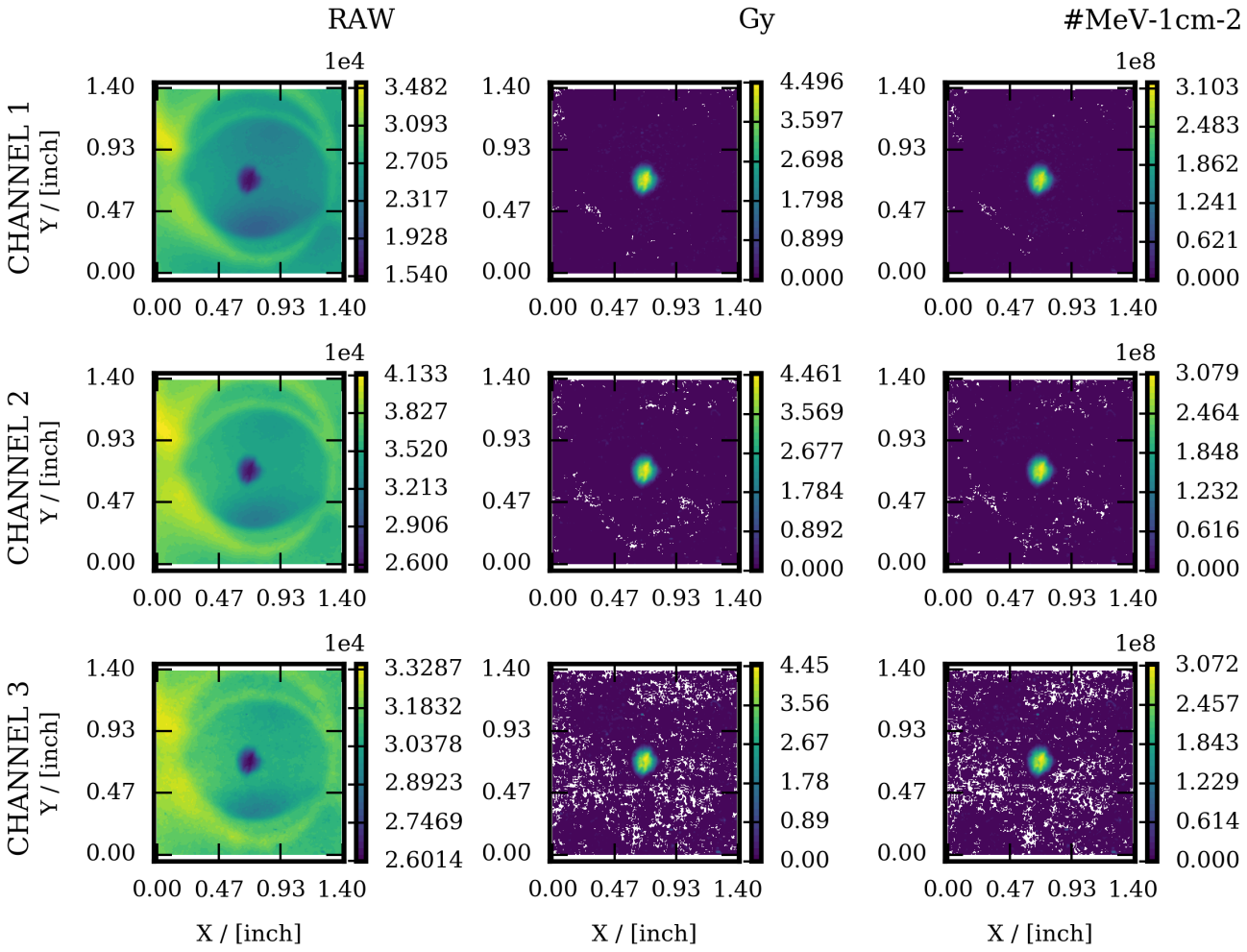

Figure 8.22: RCF layer 20 for $19.8(5)\,\mathrm{MeV}$ protons, from shot #61 with micro-compressor at the LIGHT experiment discussed in section 5.3.2.1. The first column shows the RAW data, the second the dose converted film and the third the pixel-wise deconvolution to proton number density per unit energy of $1\,\mathrm{MeV}$ as calculated with decon_RCF. The rows contain data from red, green and blue colour channel

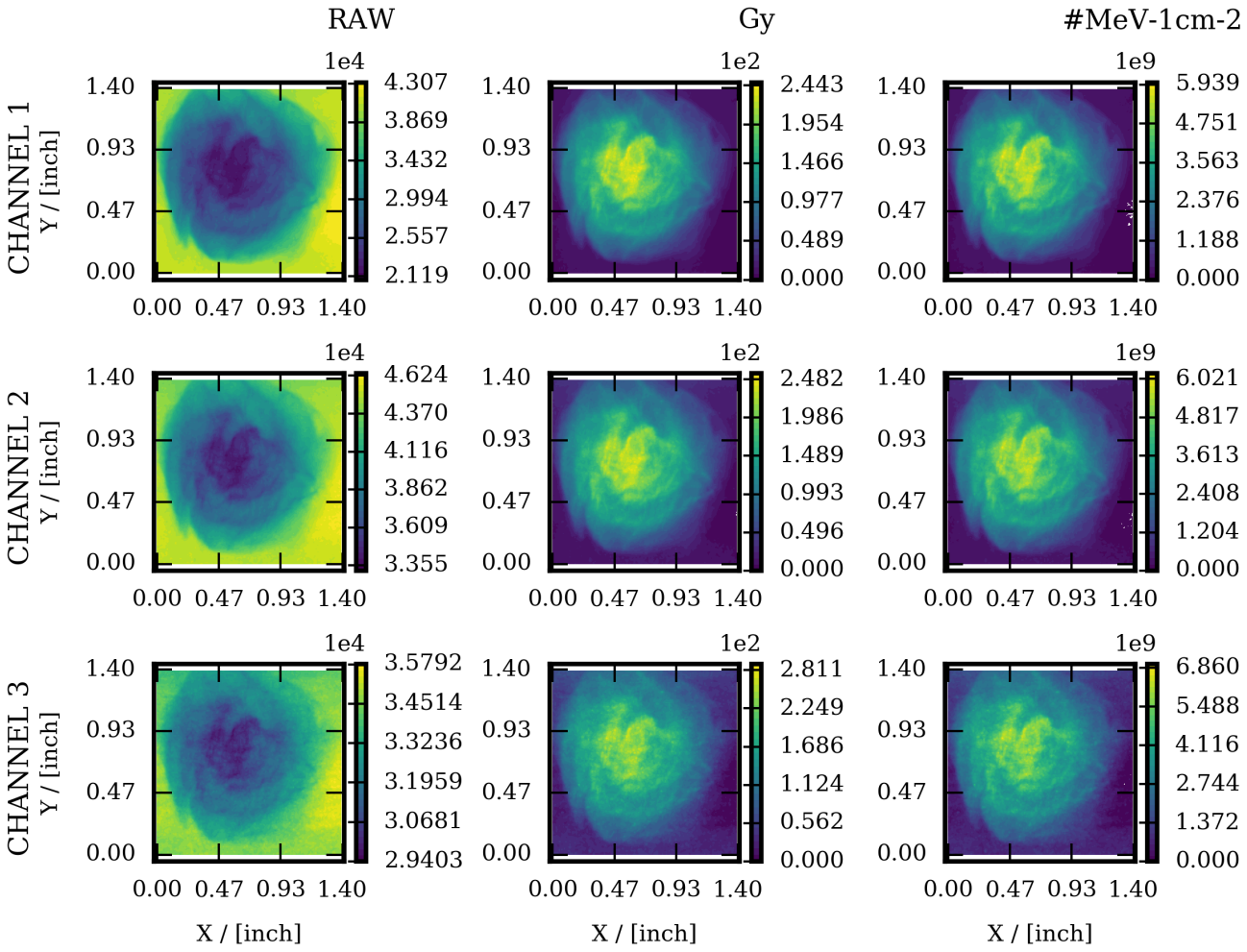

Figure 8.23: RCF layer 1 for $7.7(6)\,\mathrm{MeV}$ protons, from reference shot #01 of the LIGHT experiment discussed in section 5.3.2.1. The first column shows the RAW data, the second the dose converted film and the third the pixel-wise deconvolution to proton number density per unit energy of $1\,\mathrm{MeV}$ as calculated with decon_RCF. The rows contain data from red, green and blue colour channel.

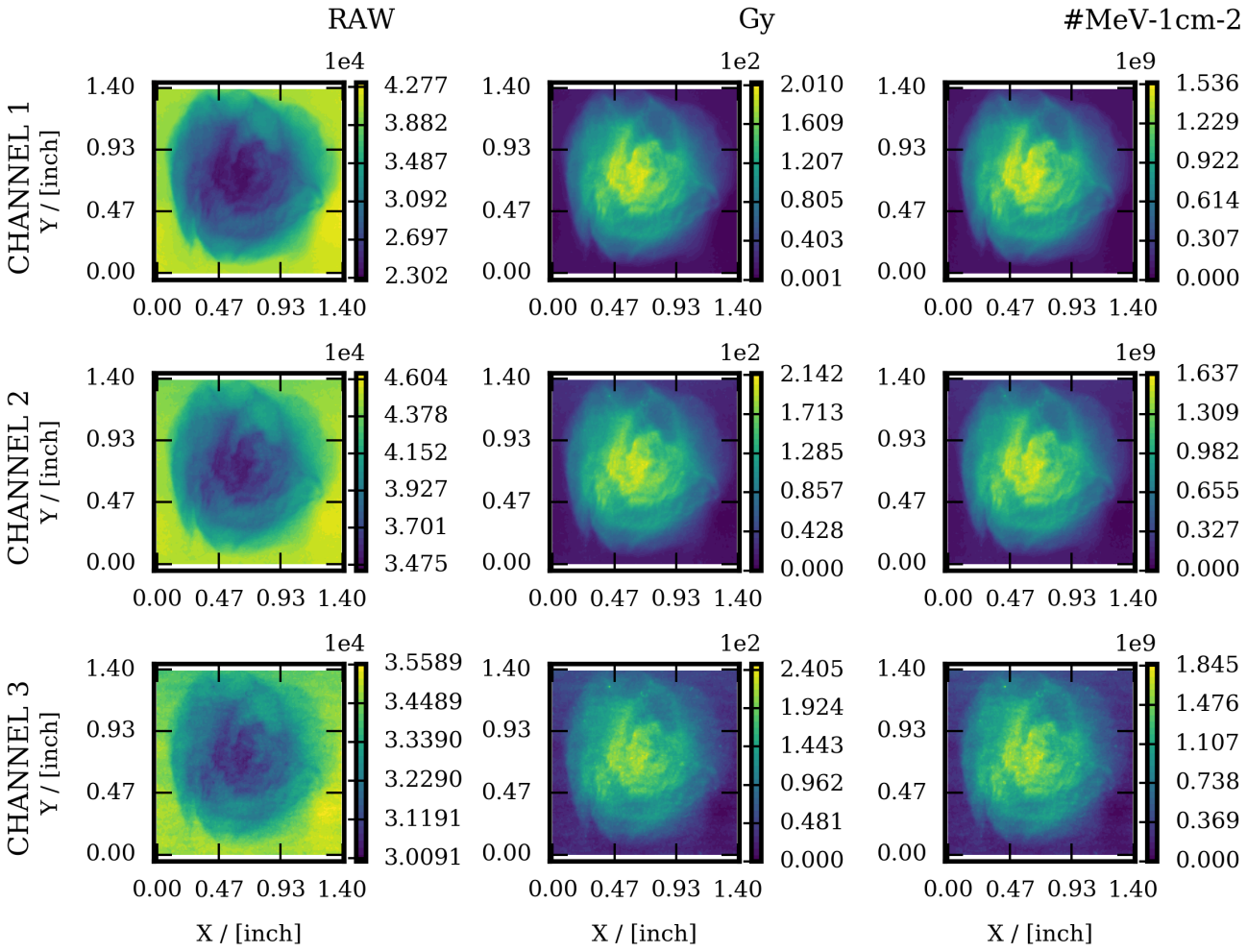

Figure 8.24: RCF layer 2 for $8.5(3)\,\mathrm{MeV}$ protons, from reference shot #01 of the LIGHT experiment discussed in section 5.3.2.1. The first column shows the RAW data, the second the dose converted film and the third the pixel-wise deconvolution to proton number density per unit energy of $1\,\mathrm{MeV}$ as calculated with decon_RCF. The rows contain data from red, green and blue colour channel.

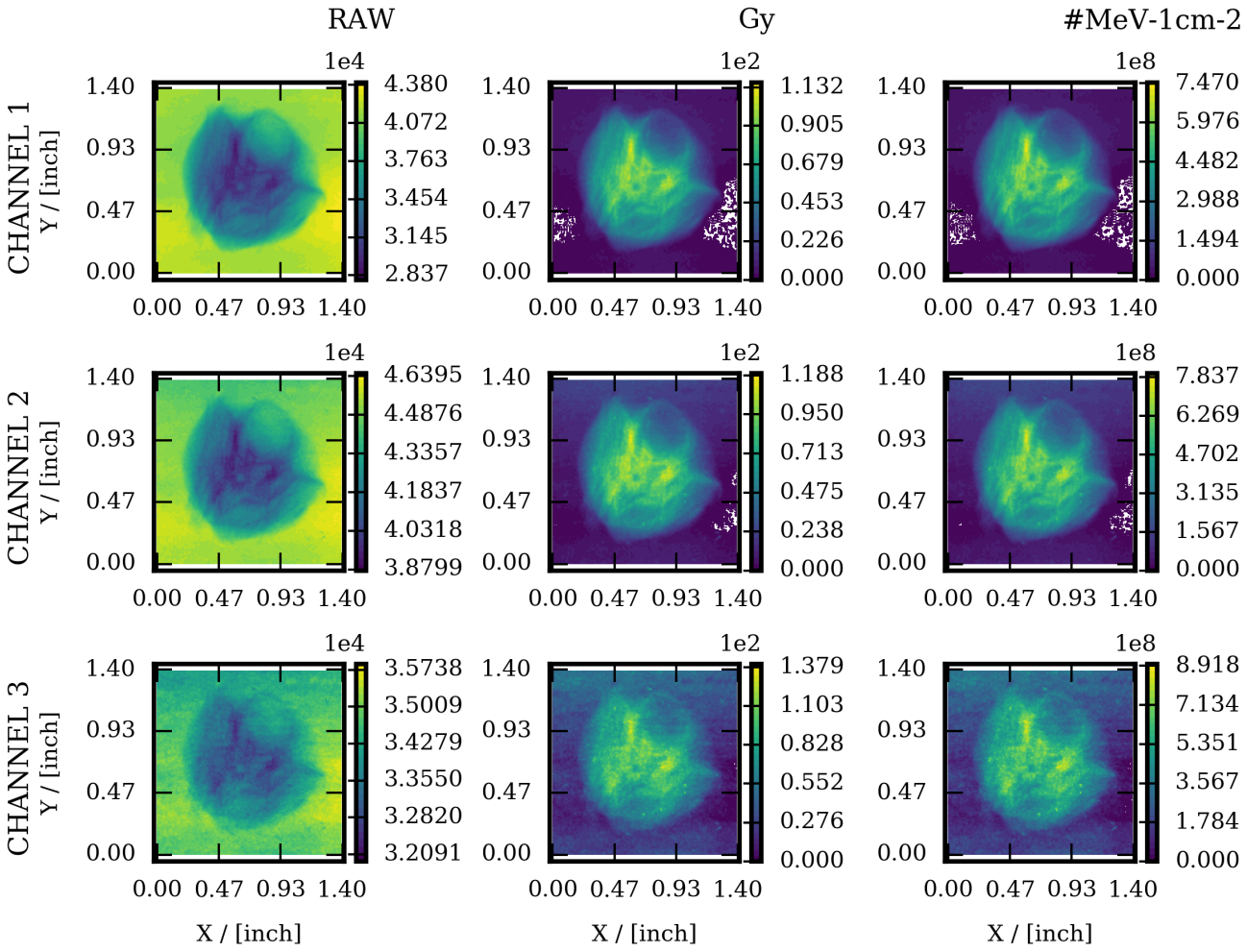

Figure 8.25: RCF layer 3 for $12.6(3)\,\mathrm{MeV}$ protons, from reference shot #01 of the LIGHT experiment discussed in section 5.3.2.1. The first column shows the RAW data, the second the dose converted film and the third the pixel-wise deconvolution to proton number density per unit energy of $1\,\mathrm{MeV}$ as calculated with decon_RCF. The rows contain data from red, green and blue colour channel.

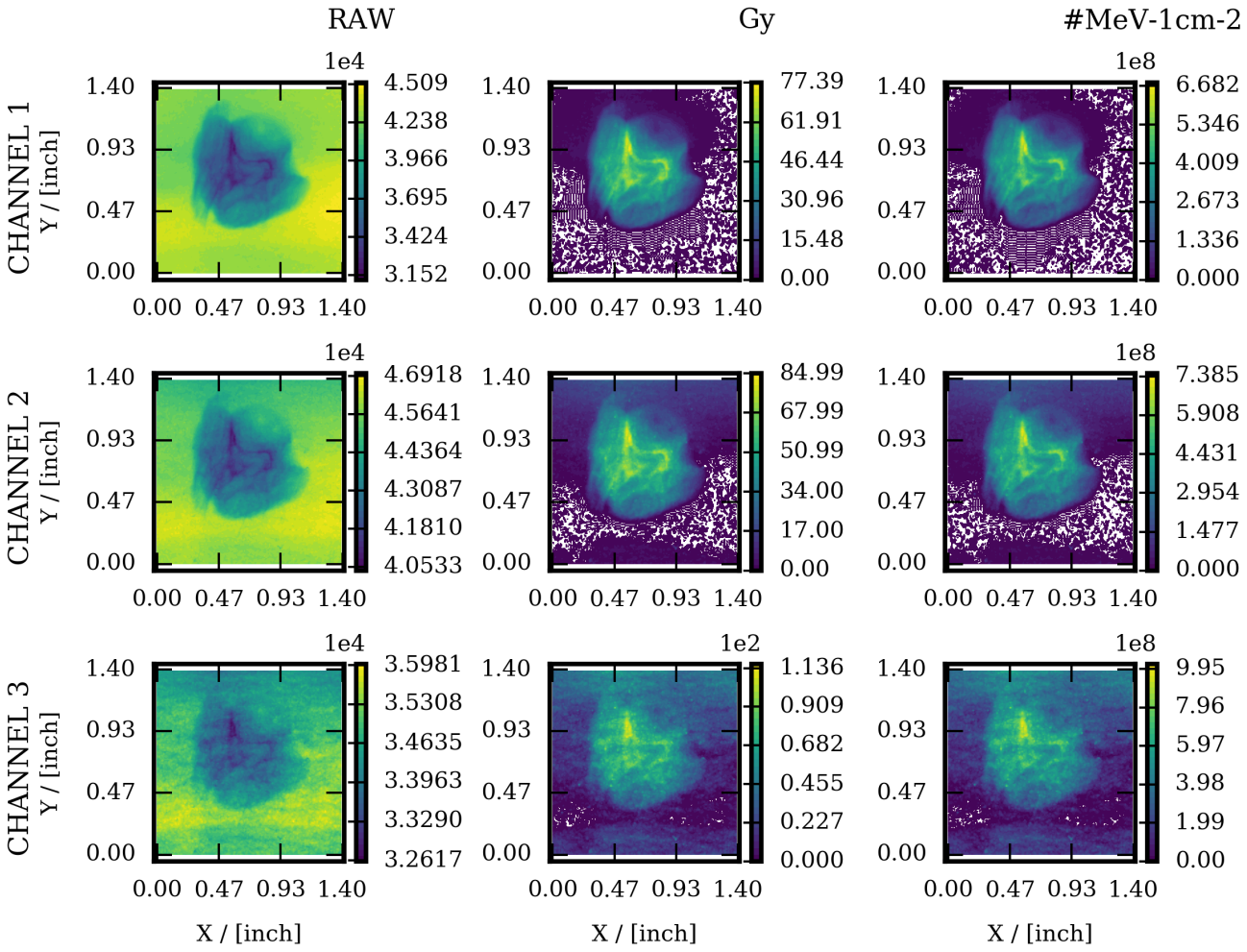

Figure 8.26: RCF layer 4 for $16.1(4)\,\mathrm{MeV}$ protons, from reference shot #01 of the LIGHT experiment discussed in section 5.3.2.1. The first column shows the RAW data, the second the dose converted film and the third the pixel-wise deconvolution to proton number density per unit energy of $1\,\mathrm{MeV}$ as calculated with decon_RCF. The rows contain data from red, green and blue colour channel.

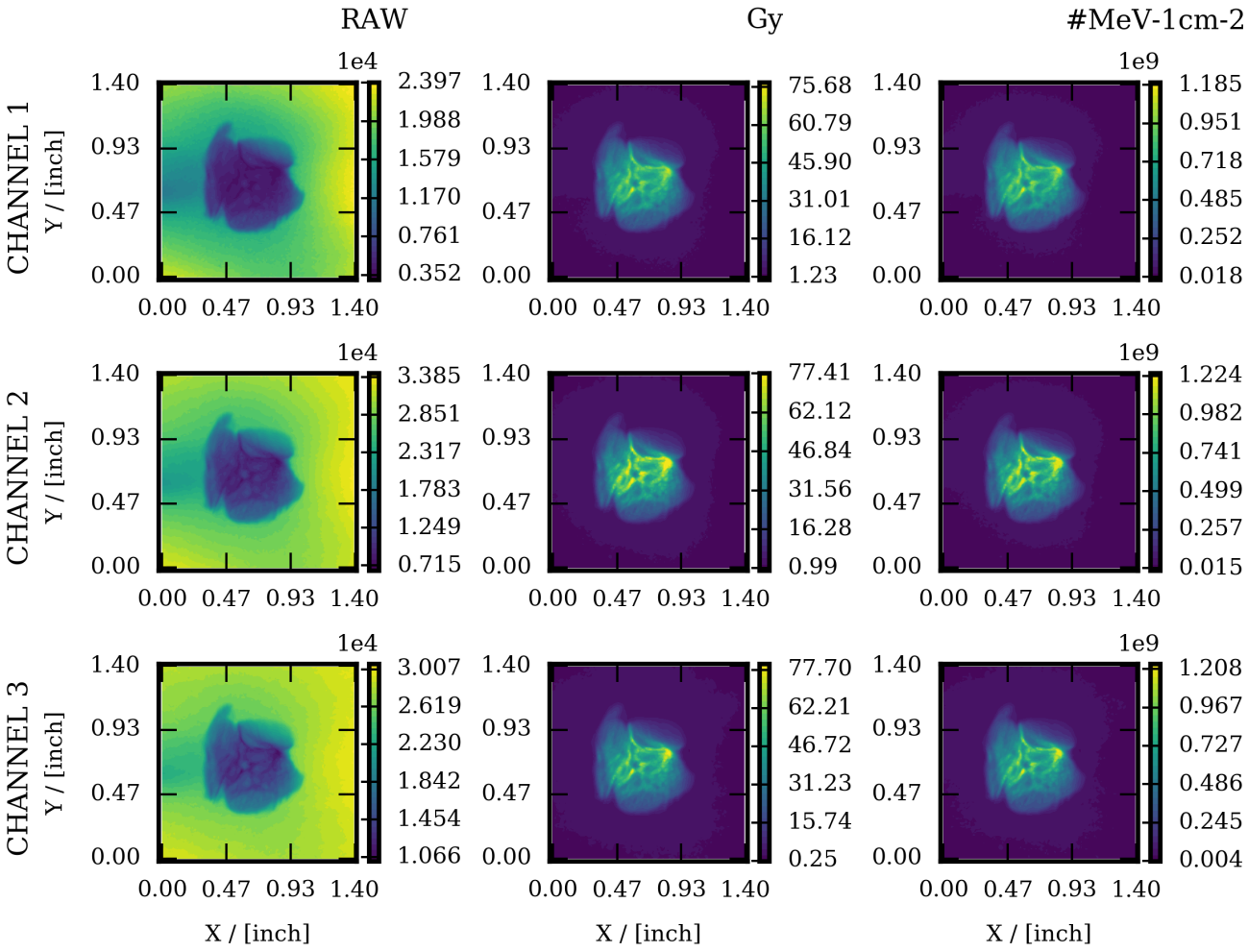

Figure 8.27: RCF layer 5 for $19.3(3)\,\mathrm{MeV}$ protons, from reference shot #01 of the LIGHT experiment discussed in section 5.3.2.1. The first column shows the RAW data, the second the dose converted film and the third the pixel-wise deconvolution to proton number density per unit energy of $1\,\mathrm{MeV}$ as calculated with decon_RCF. The rows contain data from red, green and blue colour channel.

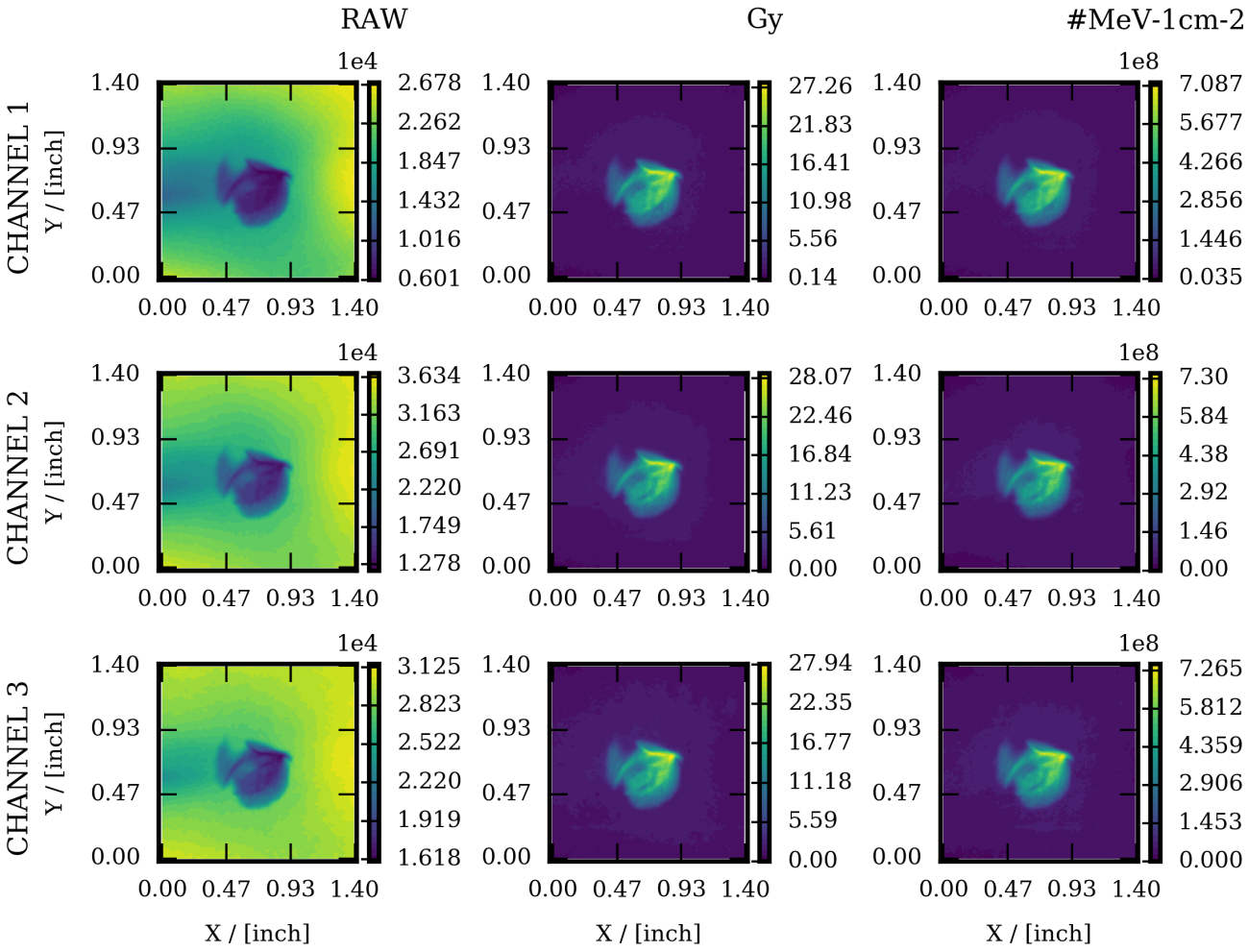

Figure 8.28: RCF layer 6 for $22.6(5)\,\mathrm{MeV}$ protons, from reference shot #01 of the LIGHT experiment discussed in section 5.3.2.1. The first column shows the RAW data, the second the dose converted film and the third the pixel-wise deconvolution to proton number density per unit energy of $1\,\mathrm{MeV}$ as calculated with decon_RCF. The rows contain data from red, green and blue colour channel.

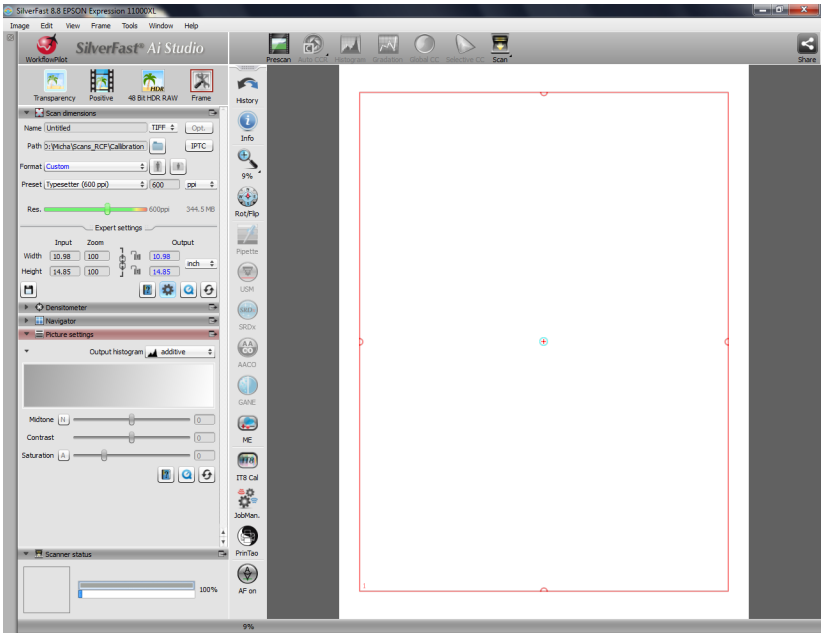

Figure 8.29: Software interface in SilverFast 8.8

Acknowledgements

The thesis project would not have come to live without the ERASMUS Student Grants of the European Union, that allowed me to get to know the host laboratory CELIA.

PAFIN, originally written on the basis of Emmanuel D'Humiéres numerics course during the French national Master Fusion in 2014/15, became a collaborative project with the Insititute for Plasma Physics, University of York. It was only thanks to the many good ideas from Nigel Woolsey, Peter Hill, Philip Bradford and Hal Garland that it was possible to make the code more portable. The rather primitive reprogramming of the original code was improved by Peter's engagement. Phil and Hal have worked on testing routines and ensured that calculations in the scope of their work were correct. It was only because of Nigel's hospitality that the collaboration was a complete success. Many thanks to Emmanuel D'Humiéres and Philipp Korneev, both of which were tireless in supporting me with PIC simulations and many hours of analytical work to pursuit the nature of experimental results.

I would like to thank Ashland to produce and deliver unlaminated EBT-3 radio-chromic films for experimental work done in the course of this thesis project, without their engagement it would not have been possible to visualize the low dose at low particle energies and slim spectral range. Many thanks to Jérome Caron that allowed me to take calibration data for radio-chromic films any time needed. The effort was a major inconvenience with days of waiting for the acquisition of high dose values at the end of the calibration curves – only bearable with a well made pizza. RCF calibration data for scan-to-dose conversion concerning a scanner at LULI was made available by Lorenzo Romagnani, for data scanned at GSI by Paul Neumayer and Pascal Boller. Scanning and conversion of data obtained at CMAM was performed by Marine Huault.

The analysis of CR-39 was only possible due to Fazia Hannachi, Claire Sergeant and Philippe Barberet at CNBG laboratory that were willing to make accessible their equipment without constraints. Furthermore, the technical staff of the UFR de Chimie in building A22, 4th floor proofed that an university environment allows fruitful interdisciplinary exchanges. I thank you for valuable practical help with the etching procedure and help and advice for the use of precision laboratory tools. I was made aware of the usefulness of CR-39 during the very experimental campaign by Marine Huault, who lent us some for building a detector. Thank you very much for the inspiration. PiN ToF detectors used in this work could only be analysed due to calibration data and work done by Valeria Ospina. Detailed microscope pictures of nozzles shown in this work were made available by Carlos Salgado, Jose Luis Henares, Jocelyn Domange and Medhi Tarisien. I navigated through the shallows of Complex Interferometry together with Tadeusz Pisarczyk, Zofia Rusiniak and Tomasz Chodukowski, a team effort which was essential for successful data analysis. Thanks to Michal Krupka for his exhaustive work on electron spectrometers at PALS, essential to measure temperatures used in this work.

Measurements with the LIGHT beamline were only possible working with the LIGHT collaboration, which I like to thank for their unconditional willingness to let me test the micro-cavity during valuable beamtime and for the comparison of a standard focal spot and a focal spot with micro-cavity performed with their standard analysis tools, guaranteeing comparability.

Curriculum Vitae

Personal Data

Name	**Michael Ehret**
Date of birth	**24/09/1990**
Place of birth	**Mannheim**
Citizenship	**deutsch**
Website	**michelmaxx.de**

Education

06/2016 - 07/2021	**Doctoral Fellow**, TU-Darmstadt and Univ. Bordeaux
10/2014 - 03/2016	**M.Sc. Physics**, TU-Darmstadt, Grade 1.77, conducted with CELIA
09/2014 - 08/2015	**M2 Sciences de la Fusion**, Univ. Bordeaux, in the framework of ERASMUS
10/2011 - 11/2014	**B.Sc. Physics**, TU-Darmstadt, Grade 1.9
09/2001 - 06/2010	**Abitur**, Werner Heisenberg Gymnasium Weinheim, Grade 1.2

Experimental Campaigns

Conducted

1. Type: experiment with a high-intensity laser; Title: Ultra-strong magnetic field generation and characterization; facility: TITAN at JUPITER in LLNL, Livermore, USA; role: conceptualization, preparation and implementation of optical diagnostics and charged particle beam deflectometry diagnostics, as well as target manufacturing and alignment; year: 2016; publication: `https://doi.org/10.1038/s41598-019-50401-y`
2. Type: R&D work; Title: Characterization of near critical density targets produced by supersonic shock nozzles; facility: Sourcelab at LOA in Palaiseau, France; role: online implementation of an optical diagnostic, further support to target control and alignment; year: 2017

3. Type: experiment with a high-intensity laser; Title: Ultra-strong magnetic field generation and characterization; facility: TITAN at JUPITER in LLNL, Livermore, USA; role: design and dimensioning of technical aspects of the campaign, further conceptualization, preparation and implementation of optical diagnostics and charged particle beam deflectometry diagnostics, as well as target manufacturing and alignment; year: 2017

4. Type: experiment with a high-intensity laser; Title: Optical generation of quasi-stationary electromagnetic structures in plasma from snail targets; facility: PHELIX in GSI, Wixhausen, Germany; role: conceptualization, preparation, implementation of all diagnostics and beam transport schemes, as well as co-lead of the campaign and target alignment; year: 2017; publication: `https://arxiv.org/pdf/1908.11430`

5. Type: R&D work; Title: Characterization of near critical density targets produced by supersonic shock nozzles; facility: Optical Laboratory at CLPU in Salamanca, Spain; role: online implementation of optical diagnostics for a facility specific target metrology, further target control and alignment; year: 2017

6. Type: experiment with a high-intensity laser; Title: Ion beam acceleration from near-critical density gas jets; facility: VEGA-2 at CLPU, Salamanca, Spain; role: conceptualization, preparation and implementation of all diagnostics, target operation and beam transport schemes, as well as co-lead of the campaign; year: 2018; publication: `https://arxiv.org/pdf/2012.09455`

7. Type: R&D work; Title: Characterization of near critical density targets produced by supersonic shock nozzles; facility: Optical Laboratory at CLPU in Salamanca, Spain; role: online implementation of optical diagnostics for a facility specific target metrology, further target control and alignment; year: 2019

8. Type: experiment with a high-intensity laser; Title: Magnetized TNSA and Zeeman splitting in plasma; facility: pico2000 at LULI in Ecole Polytechnique, Palaiseau, France; role: conceptualization, preparation and implementation of all diagnostics, target designs and beam transport schemes, as well as co-lead of the campaign; year: 2019

9. Type: experiment with a high-intensity laser; Title: Transient self-generated electromagnetic fields for pre-compression at LIGHT; facility: PHELIX at Z6-Z4 in GSI, Wixhausen, Germany; role: set-up and implementation of optical diagnostics and passive particle detectors, as well as target alignment; year: 2020

Participated

1. Type: experiment with a high-intensity laser; Title: Near-bragg-peak stopping power in plasmas; facility: PHELIX/nhelix at Z6 in GSI, Wixhausen, Germany; role: student accompanying the nhelix laser transport and metrology; year: 2014; publication: `https://doi.org/10.1038/ncomms15693`

2. Type: experiment with a high-intensity laser; Title: Relativistic electron beam tailoring in magnetized solid density matter; facility: pico2000 at LULI in Ecole Polytechnique, Palaiseau, France; role: laser driven proton deflectometry for metrology of ultra-strong magnetic fields in a large field of view with single-shot multi-frame acquisition during tens of picoseconds, with picosecond time resolution; year: 2015; publication: `https://doi.org/10.1038/s41467-017-02641-7`

3. Type: experiment with a high-intensity laser; Title: High-intensity laser driven electromagnetic discharge pulse generation and characterization; facility: PHELIX in GSI, Wixhausen, Germany; role: experimental

set-up preparation, as well as target manufacturing and alignment; year: 2016; publication: http://dx.doi.org/10.15120/GR-2017-1

4. Type: experiment with a high-intensity laser; Title: Enhanced relativistic electron beam collimation in self-generated magnetic fields using two consecutive laser pulses; facility: ELFI at LULI in Ecole Polytechnique, Palaiseau, France; role: implementation of set-up and optical diagnostics, operational work during the experiment; year: 2016; publication: https://doi.org/10.1038/s41598-019-50401-y

5. Type: R&D work; Title: Characterization of near critical density targetry produced by supersonic shock nozzles; facility: ECLIPSE-3 at ECLIPSE in CELIA, Talence, France; role: online design and dimensioning of technical aspects of the campaign, further conceptualization, preparation and implementation of optical diagnostics, as well as target control and alignment; year: 2016

6. Type: experiment with a high-intensity laser; Title: Ultra-strong magnetic field generation and characterization; facility: LFEX/Gekko at Osaka University, Osaka, Japan; role: support for online analysis of charged particle beam deflectometry diagnostics; year: 2017

7. Type: R&D work; Title: Ultra-strong magnetic field generation and all-optical characterization; facility: PALS, Praha, CZ; role: targetry; year: 2017

8. Type: experiment with a high-intensity laser; Title: Electron acceleration from near critical density targets produced by supersonic shock nozzles; facility: ECLIPSE-3 at ECLIPSE in CELIA, Talence, France; role: conceptualization, preparation and implementation of optical diagnostics, further support to spectrometric diagnostics, as well as target control and alignment; year: 2017

9. Type: experiment with a high-intensity laser; Title: Laval nozzles for ion acceleration from near-critical density gas jet targets; facility: pico2000 at LULI in Ecole Polytechnique, Palaiseau, France; role: set-up of optical diagnostics, and support of the passive particle detectors; year: 2018; publication: https://doi.org/10.1063/1.5093613

10. Type: experiment with a high-intensity laser; Title: Ultra-strong magnetic field generation and characterization of perturbations; facility: West Target Area at VULCAN in RAL, Didcot, England; role: online design, dimensioning and implementation of optical diagnostics, electromagnetic field probes, and charged particle beam deflectometry diagnostics, as well as laser and target alignment; year: 2018; publication: https://doi.org/10.1017/hpl.2020.9

11. Type: experiment with a high-intensity laser; Title: Ion acceleration from near-critical density gas jet targets using Laval nozzles; facility: pico2000 at LULI in Ecole Polytechnique, Palaiseau, France; role: set-up of optical diagnostics, and support of the passive particle detectors; year: 2018; publication: https://doi.org/10.1063/1.5116337

12. Type: experiment with a high-intensity laser; Title: Ultra-strong magnetic field generation and simultaneous all-optical characterization of induced fields and spontaneous magnetic fields; facility: PALS, Praha, CZ; role: online target manufacturing and alignment; year: 2018; publication: https://iopscience.iop.org/article/10.1088/1748-0221/14/11/C11024

13. Type: experiment with a high-intensity laser; Title: Alternative targets for ultra-strong magnetic field generation and simultaneous all-optical characterization of induced fields and spontaneous magnetic fields (1/2); facility: PALS, Praha, CZ; role: set-up support and target alignment; year: 2019

14. Type: experiment with a high-intensity laser; Title: X-ray phase contrast imaging of a shock wave in magnetized conditions; facility: West Target Area at VULCAN in RAL, Didcot, England; role: online dimensioning and implementation of optical diagnostics and charged particle beam deflectometry diagnostics, as well as target alignment; year: 2019
15. Type: experiment with a high-intensity laser; Title: Alternative targets for ultra-strong magnetic field generation and simultaneous all-optical characterization of induced fields and spontaneous magnetic fields (2/2); facility: PALS, Praha, CZ; role: set-up support and target alignment; year: 2019
16. Type: experiment with a high-intensity laser; Title: Optical generation of quasi-stationary electromagnetic structures in plasma from chiral targets; facility: PHELIX in GSI, Wixhausen, Germany; role: online preparation and implementation of all diagnostics, as well as target alignment; year: 2019

Scientific Contribution

Publications

- M. Ehret *et alia*, News and Reports on HEDgeHOB GSI-2017-2 19, https://indico.gsi.de/event/5681/material/10/1, 2017
- M. Ehret *et alia*, GSI Scientific Report 2016 GSI-2017-1 277, http://dx.doi.org/10.15120/GR-2017-1, 2017
- M. Ehret *et alia*, GSI Scientific Report 2016 GSI-2017-1 278, http://dx.doi.org/10.15120/GR-2017-1, 2017
- A. Morace *et alia*, SPIE Proceedings 10328, Selected Papers from the 31st International Congress on High-Speed Imaging, https://doi.org/10.1117/12.2270530, 2017
- W. Cayzac *et alia*, Nature Communications 8, 15693, https://doi.org/10.1038/ncomms15693, 2017
- J. J. Santos *et alia*, Physics of Plasmas 25, 056705, https://aip.scitation.org/doi/10.1063/1.5018735, 2018
- M. Bailly-Grandvaux *et alia*, Nature Communications 9, 102, https://www.nature.com/articles/s41467-017-02641-7, 2018
- P. Puyuelo-Valdes *et alia*, SPIE Proceedings 11037, Laser Acceleration of Electrons, Protons, and Ions V; 110370B, https://doi.org/10.1117/12.2520799, 2019
- J. Pasley *et alia*, High Power Laser Science and Engineering 7, e23, https://doi.org/10.1017/hpl.2019.7, 2019
- D. Batani *et alia*, Journal of Fusion Energy 38, 299–314, https://doi.org/10.1007/s10894-019-00218-4, 2019
- J. L. Henares *et alia*, Review of Scientific Instruments 90, 063302, https://doi.org/10.1063/1.5093613, 2019
- S. Malko *et alia*, Scientific Reports 9, 14061, https://doi.org/10.1038/s41598-019-50401-y, 2019

- T. Pisarczyk *et alia*, JINST 14 C11024, https://iopscience.iop.org/article/10.1088/1748-0221/14/11/C11024, 2019
- P. Puyuelo-Valdes *et alia*, Physics of Plasmas 26, 123109, https://doi.org/10.1063/1.5116337, 2019
- P. Bradford *et alia*, High Power Laser Science and Engineering, Vol. 8, e11, https://doi.org/10.1017/hpl.2020.9, 2020
- K. F. F. Law *et alia*, Phys. Rev. E 102, 033202, https://link.aps.org/doi/10.1103/PhysRevE.102.033202, 2020
- N. D. Bukharskii *et alia*, J. Phys.: Conf. Ser. 1686 012004, https://doi.org/10.1088/1742-6596/1686/1/012004, 2020
- T. Pisarczyk *et alia*, Plasma Phys. Control. Fusion 62 115020, https://doi.org/10.1088/1361-6587/abb74b, 2020
- Ph. Korneev *et alia*, submitted to MRE, Special Issue on Magnetized Plasmas in HEDP, 2021
- M. Ehret *et alia*, in preparation, https://arxiv.org/pdf/1908.11430, 2021
- M. Ehret *et alia*, in preparation, https://arxiv.org/pdf/2012.09455, 2021
- M. Ehret *et alia*, in preparation, Guided Electromagnetic Discharge Pulses Driven by Short Intense Laser Pulses: Characterisation and Modelling, 2021

Conferences

- Personal presentation of a poster, titled ”TNSA Proton Beam Guidance in Strong LASER Driven Coil Target Fields”, for the 36th International Workshop on High Energy Density Physics with Intense Ion and Laser Beams, 2016
- Personal oral presentation of a status report, titled ”Laser-driven B-field generation platform for LIGHT”, at the Laser Ion Generation, Handling and Transport meeting, aiming at development and operation of a laser-driven charged particle source for standard accelerator beamlines, 2016
- Personal presentation of a poster, titled ”ps and ns Laser Driven Discharges in Coil Targets Probed by Proton-Deflectometry”, for the 2nd European Conference on Plasma Diagnostics
- Personal presentation of a poster, titled ”ps Laser Driven Transient Discharges in Coil Targets with Application to TNSA Beam Micro Lensing”, for the 2nd summer school of the pan-european Extreme Light Infrastructure on high energy density laser-plasma physics, 2017
- Personal oral presentation of a talk in a parallel session, titled ”Transient Electromagnetic Fields for High Energy-Density Beam Tailoring Driven by ps-Laser Pulses”, for the 10th International Conference on Inertial Fusion and Applications, 2017
- Personal practical presentation of experimental physics methodology for intensive training on plasma physics theory and experiments for Erasmus+ PowerLaPs Bordeaux, 2018
- Personal presentation of a poster, titled ”ps Laser Driven Transient Discharges in Coil Targets with Application to TNSA Beam Micro Lensing”, for the 9th laser plasma forum of the French national scientific service, 2018

- Personal presentation of a poster, titled ”Transient Electromagnetic Fields for High Energy-Density Beam Tailoring Driven by ps-Laser Pulses”, for the 45th Conference on Plasma Physics of the European Physical Society, 2018
- Personal oral presentation of a talk in a parallel session, titled ”Picosecond Laser-Driven Transient Electromagnetic Fields for High Energy-Density Beam Tailoring”, for the 18th Advanced Accelerator Concepts Workshop for innovations in the field of charged particle beam acceleration and beam shaping, 2018
- Personal presentation of a poster, titled ”ps-Laser Driven Transient Electromagnetic Fields for High Energy-Density Beam Tailoring”, for the 2nd summer school of the pan-european Extreme Light Infrastructure on high energy density laser-plasma physics, 2018
- Personal oral presentation of a talk in the main session, titled ”Targets for Chromatic Lensing of Laser Accelerated Particle Beams by ps-Laser Driven Electromagnetic Fields”, for the 7th Target Fabrication Workshop, 2018
- Personal oral presentation of a status report, titled ”PETRUX au Centre Lasers Intenses et Applications (UMR 5107)”, at the 1st French national meeting for the project Accélérateurs Plasma PompÉs par Laser, aiming at a collaborative research plan for laser-driven plasma accelerators, 2019
- Personal oral presentation of a talk in the main session, titled ”Picosecond Laser-Driven Transient Electromagnetic Fields for High Energy-Density Beam Tailoring”, for the 3rd European Conference on Plasma Diagnostics, 2019
- Personal oral presentation of a status report, titled ”Near-critical plasmas from supersonic gas jets for enhanced ion acceleration by ultra-intense laser interaction”, at the 1st French national meeting of the ION working group for the project Accélérateurs Plasma PompÉs par Laser, aiming at a collaborative research plan for laser-driven plasma accelerators, 2019
- Personal oral presentation of a talk in a parallel session, titled ”Near-critical plasmas from supersonic gas jets for enhanced ion acceleration by ultra-intense laser interaction”, for the 25th Congrès Général de la Société Française de Physique, 2019
- Personal presentation of a poster, titled ”ps-Laser Driven Transient Electromagnetic Fields for High nergy-Density Beam Tailoring”, for the 25th Congrès Général de la Société Française de Physique, 2019
- Personal oral presentation of a talk in the main session, titled ”Strong Laser-Driven Magnetostatic Fields for Magnetized High Energy-Density Physics”, for the 40th International Workshop on High Energy Density Physics with Intense Ion and Laser Beams, 2020